Transverse Flux Machines For High Torque Applications

Christopher Paul Maddison

A thesis submitted for the degree of
Doctor of Philosophy

Department of Electrical and Electronic Engineering
University of Newcastle upon Tyne
November 1999

To Jo,

My little "*knife du pain*"

Whose support and love

knows no bounds

Abstract

Transverse Flux Machines (TFM) present some interesting problems to the machine designer, electro-magnetically and mechanically. They offer the lure of an extremely high specific output, but only, apparently, at the price of intricate three dimensional flux paths, a complicated construction and a low power factor. The research covered by this thesis was concerned with the study, development and improvement of these machines with a view to reducing the detracting aspects of the marque whilst accentuating its advantages.

Extensive three dimensional finite element analysis into a wide range of TFM topologies, was coupled with practical investigations into three prototype TFMs constructed at Newcastle University. The result of this work was an improved TFM topology with comparatively good power factor, a simple single sided geometry and a very high specific output.

Acknowledgements

First and foremost I should like to thank my supervisors, Barrie Mecrow and Alan Jack. Their enthusiasm, innovation and breadth of knowledge, was both stimulating and inspiring. I would especially like to thank Barrie for his advice and his comments regarding this thesis, particularly with regard to the English what that I did write.

My appreciation to my co-sponsors, Rolls Royce International Research & Development and the Engineering and Physical Sciences Research Council, cannot be over stressed, without their support none of this work would have been carried out.

After the construction of three prototype machines, special thanks must also be heaped upon the department's technical staff, in particular Dave Branch, John Robinson, Jack Noble and Allan Wheatley. Their looks of despair as I described 'our' next excursion into the world of TFM 'bit part' construction, were only surpassed by their howls of derision when confronted by my 'technical drawings'. But without their skill and dedication, my work would have been very much harder.

A begrudging but heartfelt thanks goes to the stalwart members of the UG Lab, Chris F, Christian ('do we get lunch'), Elliott, Hassan, Ken ('Of The Glen'), Matthew and his "Magic Boots", Øystein the Nog, Phil the "Mechanical Marvel", and last but not least, Sarky Simon and his travelling soapbox. Their constructive, destructive, moral and immoral advice, friendship and drinking sprees have been invaluable to my sanity as well as my work.

A thank you also gallops out to the Aged P's for their concern and unwavering belief in my meagre abilities.

Last but definitely not least, I'd like to thank my wife, Jo, for her love, her patience, her smile at the end of a long day and for carting around that little person in her tummy. Oh yes, and for occasionally doing the washing-up.

Table of Contents

List of Symbols

A	Area *or* Magnetic Potential
B_m	Magnet Operating Flux Density
B_g	Airgap Flux Density
B_r	Residual Flux Density
H	Magnetic Field Strength
H_m	Magnet Operating Field Strength
H_c	Magnet Coercive Field Strength
h	2D Unmodelled Magnet Dimension
I	Current
i	Instantaneous Current
K	Fringing Constant
ℓ	Length
ℓ_g	Airgap Length
ℓ_m	Active Magnet Length
ϕ	Flux
ϕ_T	Total Flux
Ψ	Flux Linkage
N	Number of Conductor Turns
R	Resistance
ρ	Resistivity
S	Reluctance
T	Torque
θ	Angular Displacement
μ_m	Magnet Permeability
μ_o	Permeability of Free Space
μ_r	Relative Permeability
μ_{2D}	2D FE Equivalent Magnet Permeability
W	2D Modelled Magnet Dimension
ω_{elec}	Angular Velocity - Electrical
ω_{rot}	Angular Velocity - Mechanical

Chapter 1

Introduction

1.1 The Transverse Flux Machine

The current interest in and development of Transverse Flux Machines (TFM) was instigated by a need to fully utilise the extremely high coercive forces being produced by modern rare earth magnets. The ability to fully exploit these magnetic materials will enable electrical machines to possess levels of torque which easily outstrip those achieved in existing machines of the same size or weight. Magnet utilisation was where the TFM began to excel, due to its inherent ability to maintain a high per pole magnetomotive force (MMF) even at very large pole numbers. This allowed the magnet's useful flux to interact with a much higher level of electrically produced MMF.

The TFM's unique topology lends itself to high-powered direct drive applications such as ship propulsion [26, 28] electric vehicle hub drives [2, 38, 46] and power generation through wind turbines. [44] However, little of the topological characteristics of how and why TFMs work and why one design works so differently to another have been explored. Through investigation into alternative TFM designs and the loss mechanisms inherent in those designs, this project aimed to produce a prototype TFM machine that would outperform all of the existing topologies in categories of torque per unit mass, torque per unit volume and power factor.

There has been some debate as to the validity of the term 'transverse flux' when referring to this type of machine. The phrase was used by Weh in his first paper on the topic in 1986 [42] and he explains the crux of its meaning in a paper published in 1988 [44] in the following way, '. . *the magnetic flux closes itself mainly in a direction transverse to the direction of motion. From this the term "transverse flux" (TF) machine is used.*' When considering this statement it is useful to compare and contrast a TFM's flux to the 'normal' or longitudinal flux that one would find in an induction or synchronous machine. In conventional induction and synchronous machines, the active airgap flux moves orthogonally to the rotor. However, the bulk of

the flux in the stator travels in the same direction as the rotor, longitudinally around the coreback (figure 1.1a) hence the term Longitudinal Flux Machine (LFM). However, in a TFM, (figure 1.1b) the bulk of the flux in the stator travels in a direction orthogonal or transverse to that of the rotor, either radially or axially through the stator cores. There is obviously some circumferential flux related to fringing and leakage flux, but this is small.

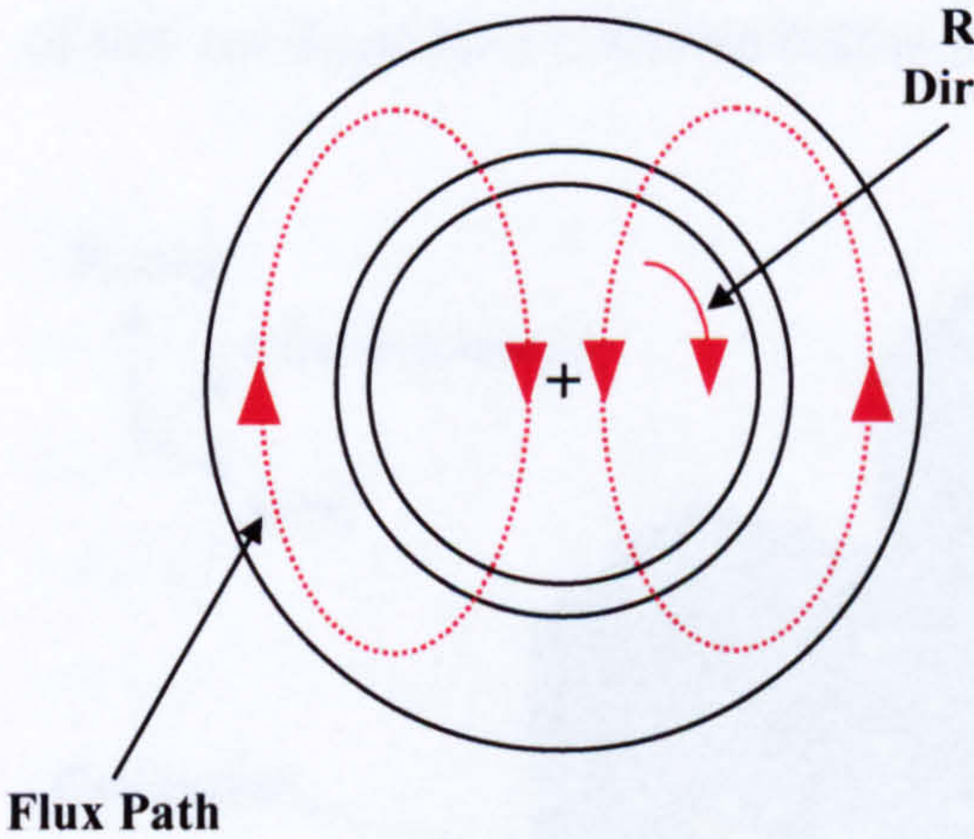

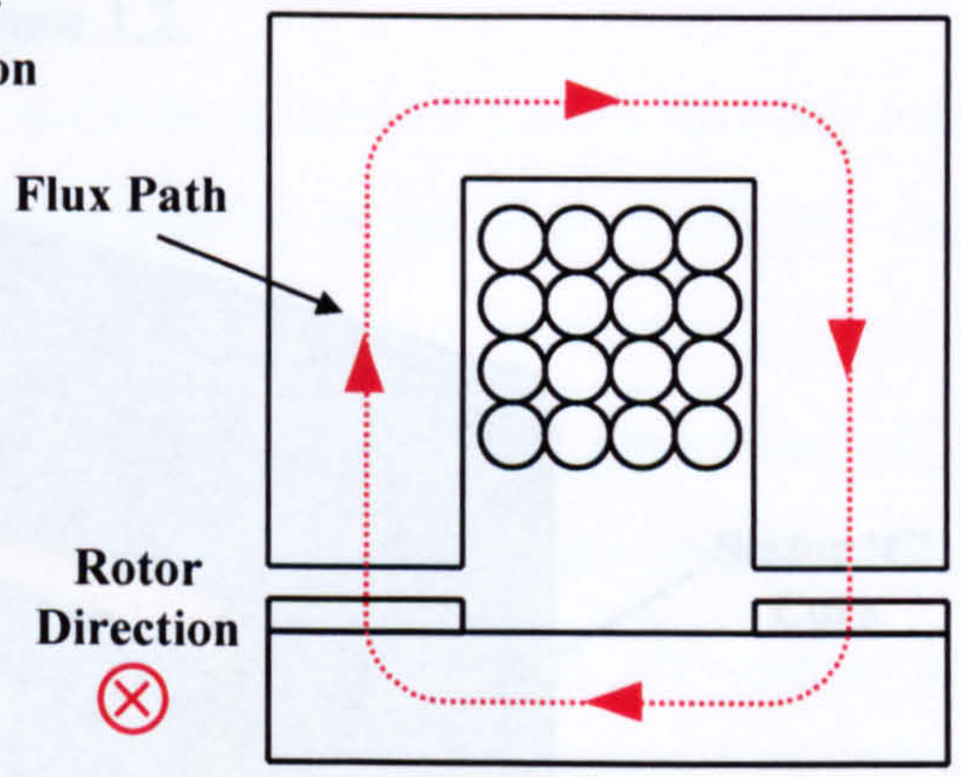

Figure 1.1a. Circumferential / Radial view of a longitudinal flux machine

Figure 1.1b. Axial / Radial view of a transverse flux machine

This explanation of the phrase transverse flux does have its shortcomings, but because of the singular qualities of these machines, a 'family' classification is a necessity. Harris et al [9] have put forward the name Variable Reluctance Permanent Magnet (VRPM) Machine. This does adequately describe the method of torque production in this type of machine, as the permanent magnet rotor is presented with alternate high and low reluctance paths, but this term could also be used to describe other Brushless DC Machines (BDCM) which exhibit stator saliency and as such does not 'button-hole' the genre. However, the term Transverse Flux Machine, despite its inaccuracies, has come into common usage when describing these unique machines and so fulfils that role.

1.2 Basic Principle of Operation

Since their inception in the mid-eighties, numerous variations on the modern Transverse Flux theme have been presented. One of the first configurations presented

by Weh, was a TFM with one active side [45]. This variation is simple enough to allow a ready explanation of the basic principle of operation.

The model consisted of individual 'C' cores of laminated steel positioned around the periphery of the machine. Encompassed within these 'C' cores ran a toroidal winding mounted radially above a rotor. The rotor comprised of two rows of alternately polarised surface mounted permanent magnets. Situated on the rotor below the magnets were a series of laminated steel elements, which channelled the rotor flux axially between these two rows of magnets. A rectilinear representation of one phase of this configuration is shown below in figure 1.2.

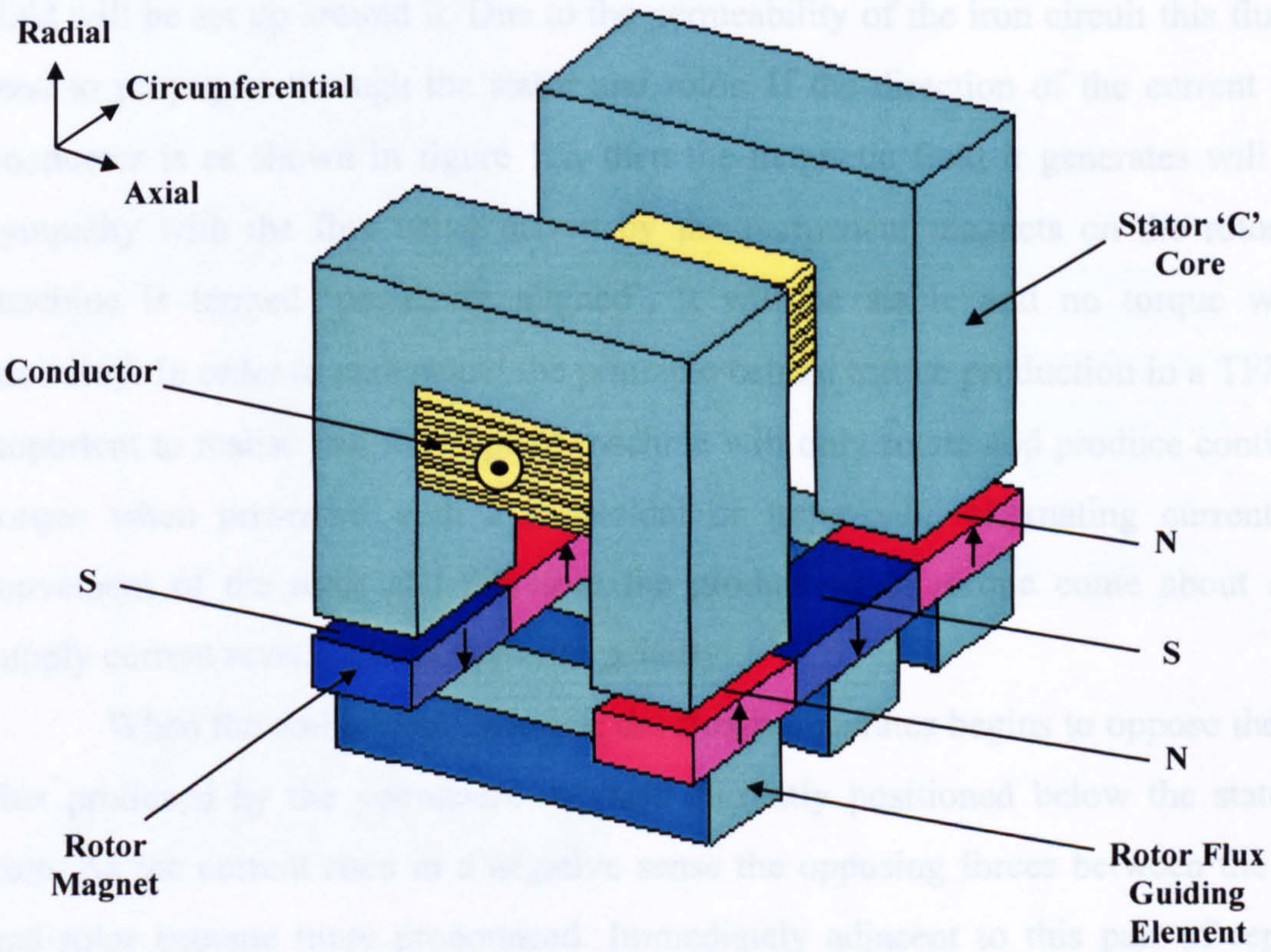

Figure 1.2 Rectilinear model of a single sided TFM

So, simply, how does the TFM work? The easiest way to envisage the principle of operation of this type of machine is to view it in two distinct states. Firstly, in the aligned position in the +ve 'd' axis and then in the –ve 'd' axis aligned position. In order to describe the +ve aligned position it is best to initially imagine an unexcited machine. In figure 1.2, the flux due solely to the magnets will take the following route around the model:

- Radially across the right-hand airgap
- Radially up the right-hand leg of each 'C' core
- Axially across the top of each 'C' core
- Radially down the left-hand leg of each 'C' core
- Across the second airgap into the left-hand magnet
- Axially along the flux guiding element, completing the magnetic circuit in the right-hand magnet

If the conductor is excited, then according to Lenz's Law a rotating magnetic field will be set up around it. Due to the permeability of the iron circuit this flux will tend to propagate through the stator and rotor. If the direction of the current in the conductor is as shown in figure 1.2, then the magnetic field it generates will be in sympathy with the flux being driven by the permanent magnets on the rotor. The machine is termed 'positively aligned', it will be stable and no torque will be produced. In order to understand the principle behind torque production in a TFM it is important to realise that this type of machine will only rotate and produce continuous torque when presented with a sinusoidal or trapezoidal alternating current. The movement of the rotor and therefore the production of torque come about as the supply current reverses to its opposite polarity.

When the coil current reverses, the flux it generates begins to oppose the rotor flux produced by the permanent magnets currently positioned below the stator 'C' core. As the current rises in a negative sense the opposing forces between the stator and rotor become more pronounced. Immediately adjacent to this pair of repelling magnets on the rotor are another pair of magnets polarised to drive flux in the opposite direction through the iron path in the machine, this is now the same direction as the flux produced by the winding. As the rotor is free to move, the opposition to the armature generated flux by the first pair of magnets and the attraction towards the second pair will produce an angular rotation towards the attracting magnets. It should be noted however, that without more than one phase or some form of biasing the direction of rotation will be completely arbitrary. The level of torque produced

depends upon the coercive force of the permanent magnets and the level of electric loading present in the winding as they interact in the airgap.

1.3 The Inductor Alternator

Inductor Alternators [39, 48] were used in the early days of radio telegraphy to generate high frequency carrier waves. One of the first of these, the Alexanderson-Fessenden machine [48] was developed in about 1910. This machine's physical similarity to a Double Sided-Sided TFM (DSTFM) is most apparent when viewed in the axial / radial plane as seen in figure 1.3a.

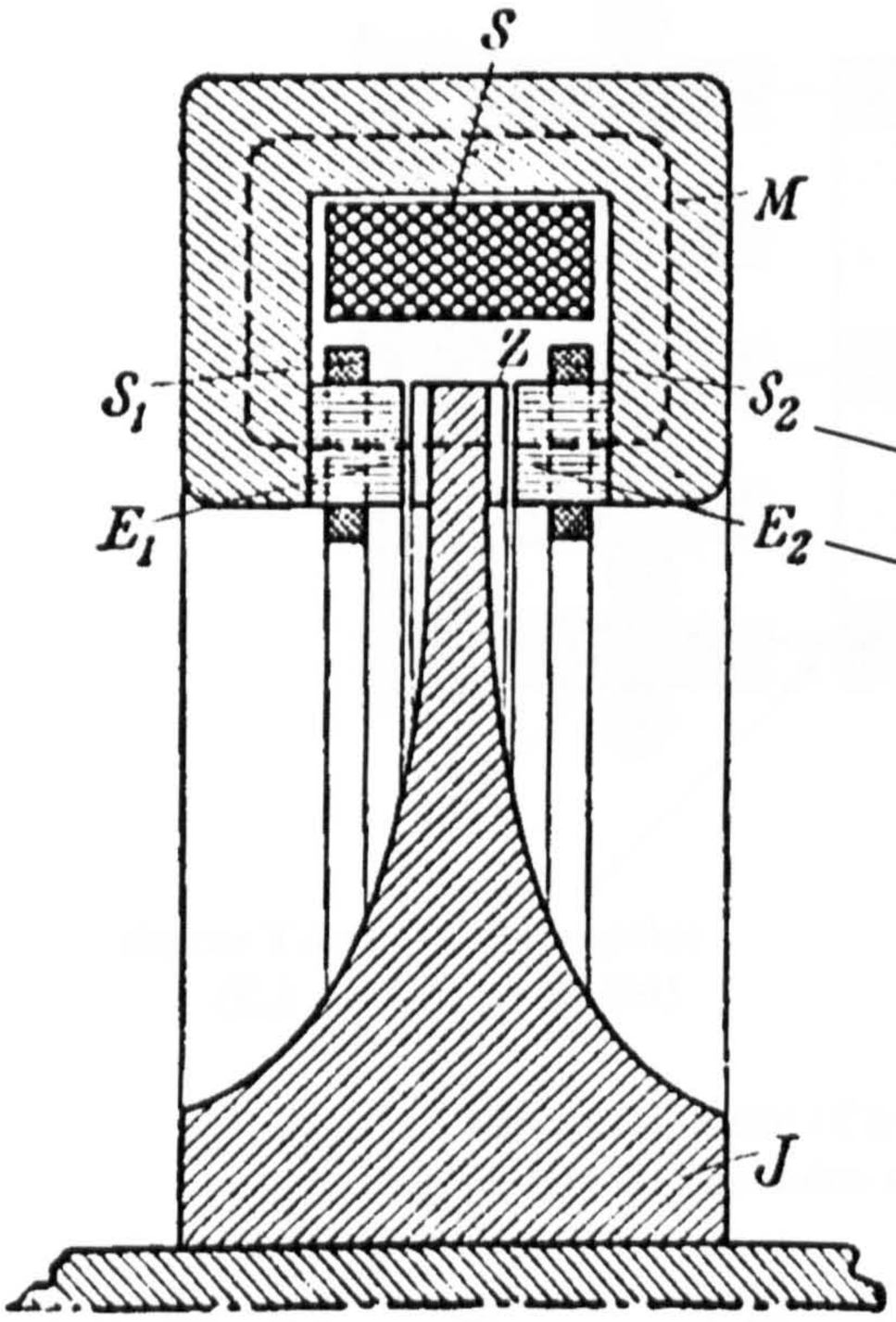

Figure 1.3a Axial / Radial diagram of the Alexanderson-Fessenden machine

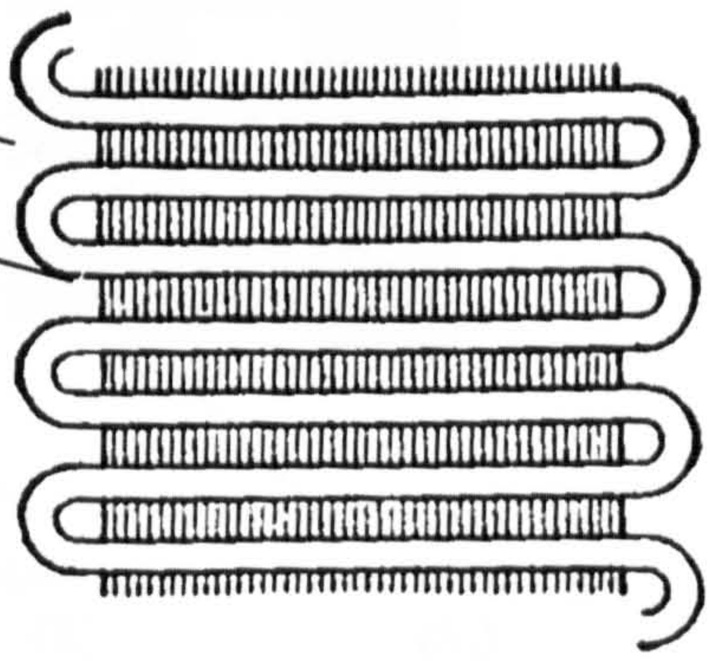

Figure 1.3b Circumferential / Radial diagram of the stator teeth and high frequency winding

(***Figures 1.3a & 1.3b reproduced from reference [48]***)

The Alexanderson-Fessenden machine produced high frequency current in two series connected coils (S_1 and S_2) from a homopolar flux (M) generated from the toroidal DC coil (S). This was achieved by presenting a variable reluctance path to the flux as it passed from the stator teeth (E_1 ,E_2) into the rotor iron (Z) and then back into the stator. The AC winding (S_1 ,S_2) was not a coil as such, but was in effect a single

wire wound 'serpentine-like' through the stator teeth (figure 1.3b). Viewing a set of two consecutive 'U' shaped wires could be regarded as looking at the opposing sides of a coil pair. Current is induced and flows, first in one side and in one direction, then in the other side and the opposite direction. This alternating action occurs as the rotor teeth move past the appropriate stator teeth. Figure 1.4 illustrates the configuration of the rotor and stator teeth. The rotor was designed to be driven at a maximum speed of 20,000rpm, producing an output frequency of between 50 – 100kHz, depending on tooth number and outside diameter.

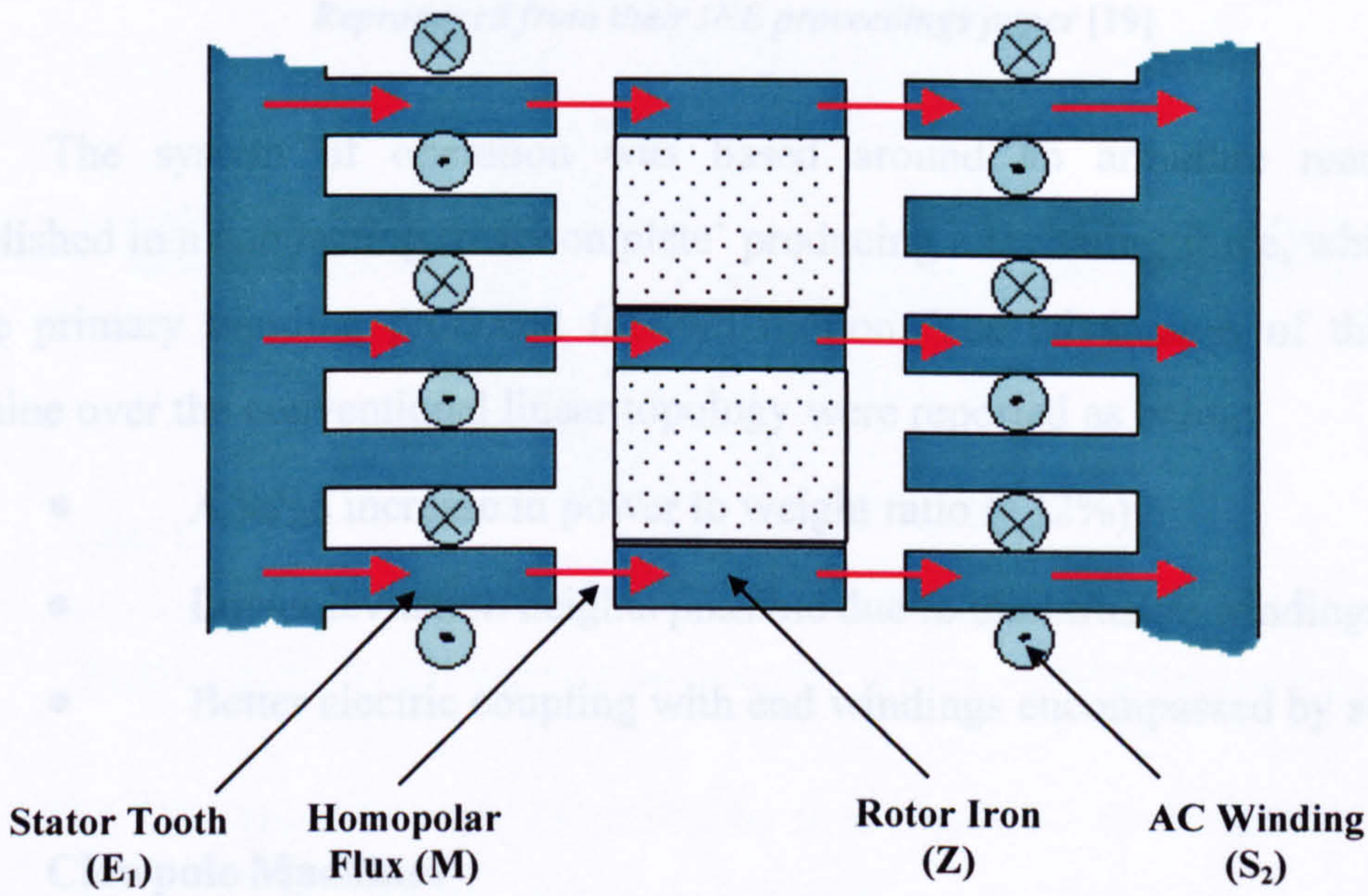

Figure 1.4 Axial / Circumferential schematic of the Alexanderson-Fessenden machine, with annotated flux paths

1.4 The Linear Transverse Flux Machine

In 1971, Laithwaite et al [19] reported on their experimental results into linear induction motors using transverse flux configurations for high speed transportation. Their paper on the topic expounded a number of TFM topologies for this purpose based around laminated 'C' and 'E' core primary circuits. They progressed however, with the 18 pole, single wound, 'E' core prototype machine illustrated in figure 1.5. This was quickly followed by a 72 pole machine of the same overall size, when it was discovered that the first model exhibited higher than expected losses. These were caused by the wide primary teeth enabling large leakage fields to be established in the airgap.

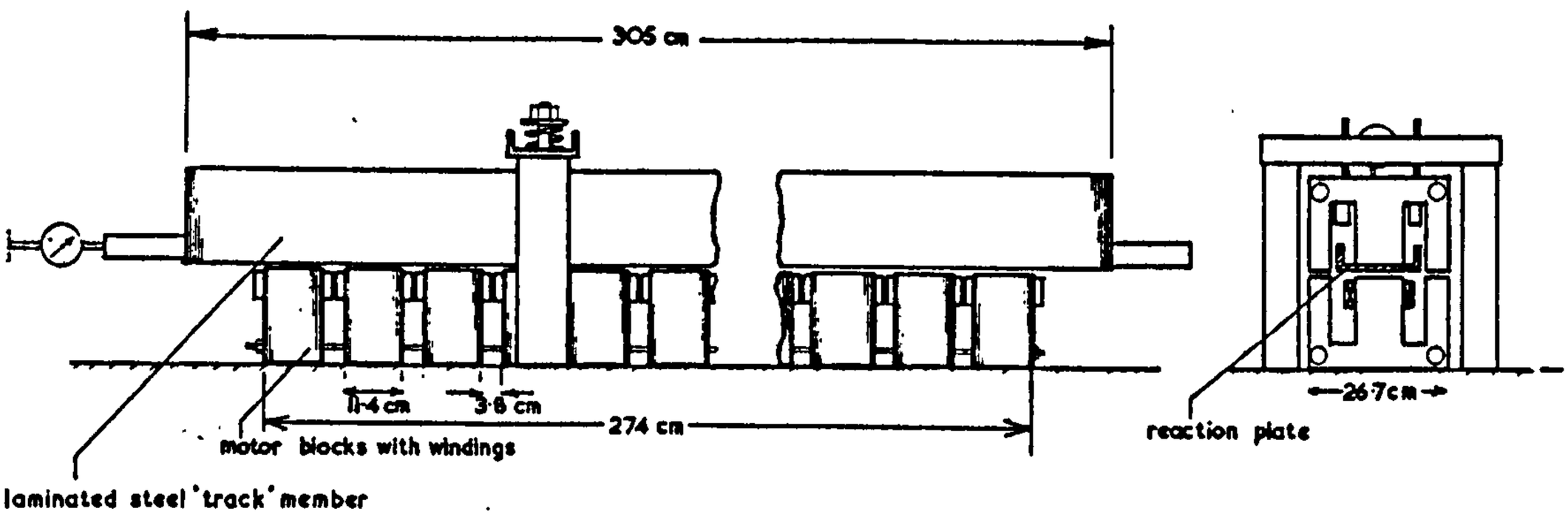

Figure 1.5 Diagram of the experimental linear TFM produced by Laithwaite *et al* in 1971.
***Reproduced from their IEE proceedings paper* [19]**

The system of operation was based around an armature reaction flux established in a conducting 'reaction plate' producing a levitating force, whilst a three phase primary winding produced forward motion. The advantages of this type of machine over the conventional linear topology were reported as being:

- A large increase in power to weight ratio (+32%).
- Lower levitation heights possible due to unobtrusive windings.
- Better electric coupling with end windings encompassed by steel.

1.5 Clawpole Machines

The Clawpole or Lundell Alternator is used to generate electrical power in almost all internal combustion driven vehicles [4]. The stator of a Clawpole Alternator has a standard three phase distributed winding which supplies a three phase bridge rectifier in order to produce a 12V DC automotive supply. However, the method of rotor field flux generation and distribution that is used to excite the three phase winding is where the similarity to the TFM manifests.

The field winding in a Clawpole Alternator is in the form of a circumferentially positioned, toroidal conductor supplied with direct current via a pair of slip-rings. The winding is encapsulated axially and radially by iron, which provides a low reluctance path for the generated magnetic flux. The radial section of rotor iron adjacent to the active airgap and hence closest to the three phase stator does not close on itself but instead forms overlapping "claw" sections. Because of the direct current supplied to the field winding, a homopolar magnetic flux is produced in the iron

circuit. The break in the rotor's magnetic circuit adjacent to the airgap causes alternate North and then South poles to be created on the overlapping "claws" (figure 1.6). As the rotor rotates, flux from the North poles crosses the airgap, passes through the stator, then re-crosses the airgap to complete the magnetic circuit with the South poles. As the rotor rotates, the homopolar flux sweeps circumferentially around the stator inducing a three phase alternating voltage.

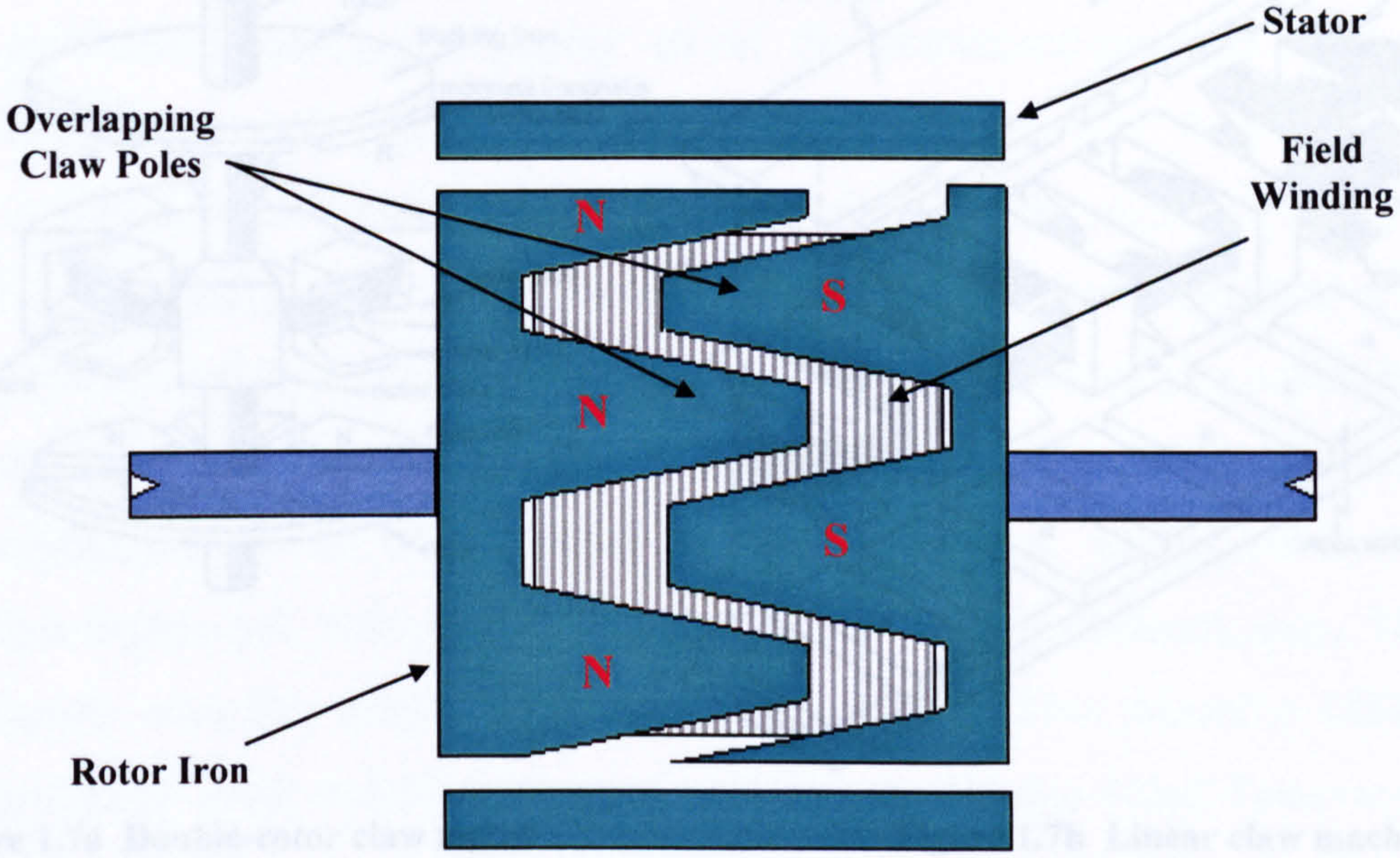

Figure 1.6 Axial / Circumferential schematic of a Clawpole Alternator rotor

The Clawpole Alternator's similarity to a transverse flux machine, is that it can be viewed as an "inside out" TFM. Picture the field winding and associated magnetic circuit of the Clawpole Alternator's rotor inverted so that the winding lies radially outside, instead of inside, the claw teeth. The teeth in turn will now face an active airgap positioned radially towards the central axis of the machine. This configuration would be almost identical to that of a Single-Sided TFM stator. Adding a permanent magnet rotor would complete the transformation.

In the late 1970's this step was taken by McLean et al [21, 22, 23], with the development of a 600W, 1000rpm, permanent magnet, axial field, double sided claw motor. They also reported on a 200Hz, permanent magnet linear motor capable of producing 100N at a velocity of 4m/s (figures 1.7a and 1.7b respectively).

The double-rotor claw motor utilises the principles of transverse flux by guiding the armature produced flux through 'inner' and 'outer' claw members. This sets up successive north and south poles on both of the axial faces of the claw stator.

The alternating supply to the armature winding allows these magnetic stator poles to interact with the two permanent magnet rotors, producing rotational movement and torque.

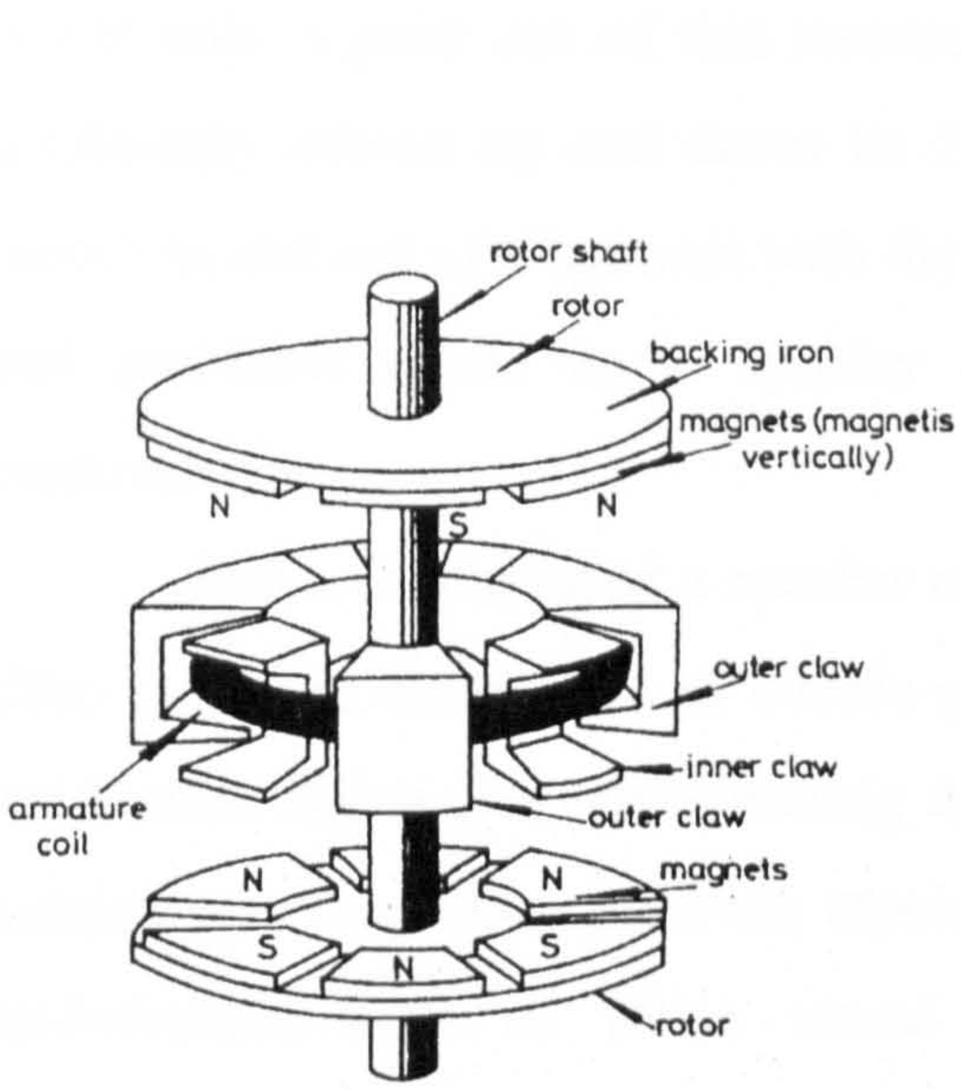

Figure 1.7a Double-rotor claw motor produced by McLean *et al*

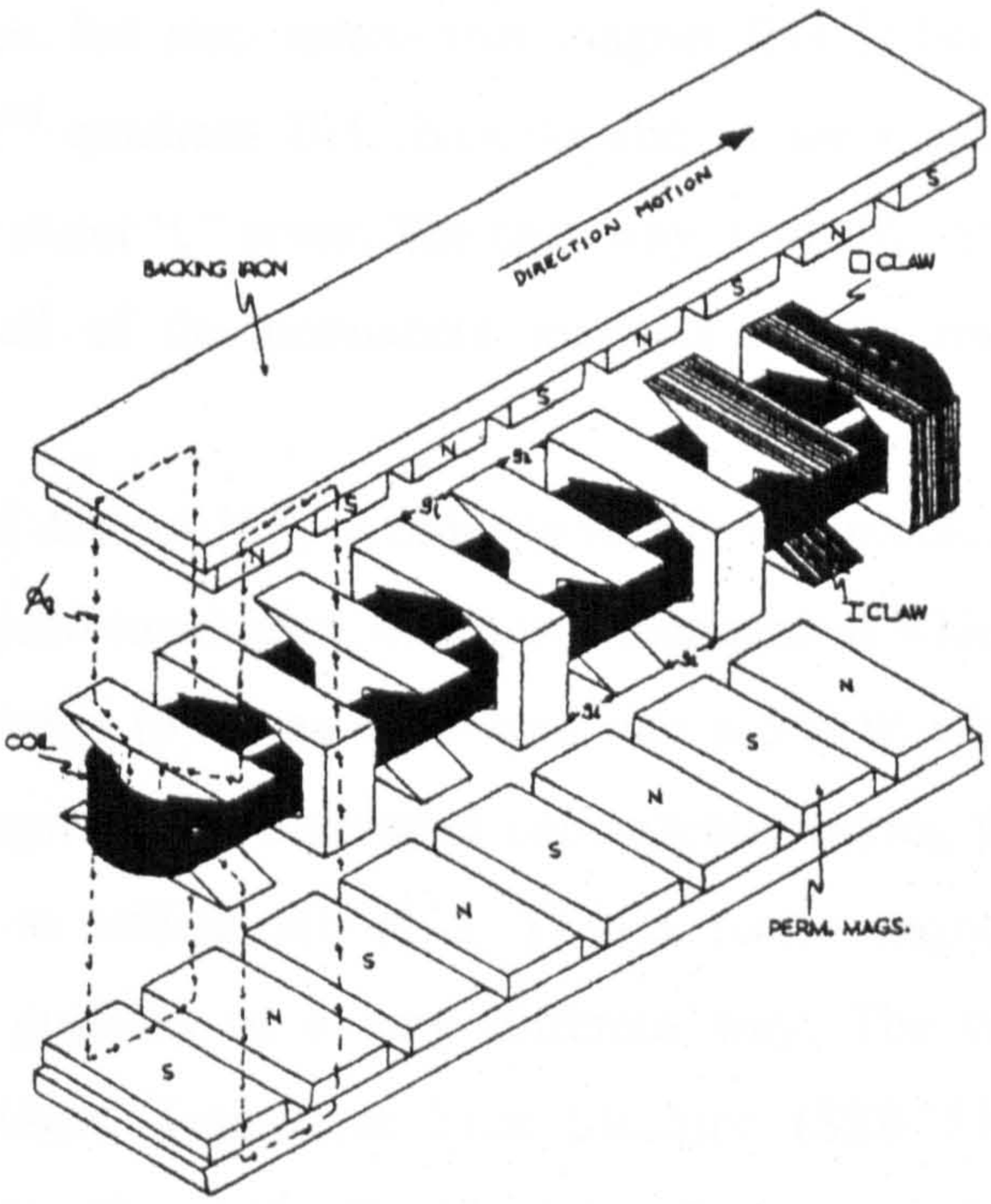

Figure 1.7b Linear claw machine produced by McLean et al

(***Diagrams reproduced from original publications***)

The linear claw motor works on a similar principle, with flux being guided either clockwise or anti-clockwise (see dotted lines in figure 1.8b) around the AC armature winding. This has the effect of producing alternate North and South poles on the stator iron faces, which again interact with two permanent magnet components, this time producing linear, instead of rotational movement. Both of these configurations will self start, but the direction of movement will be arbitrary without some additional input such as a displaced secondary phase or some form of 'pole shading'.

1.6 Recent Developments

The modern TFM topology emerged in the late Eighties in the form of the "TFM with one active side" [45] or Single-Sided Transverse Flux Machine (SSTFM) which was discussed briefly in section 1.2. As with all of the major TFM topologies,

the SSTFM will be discussed in greater depth in Chapter 5. The SSTFM suffered from a limited output due to poor utilisation of its rotor magnets. With reference to figure 1.2, it is apparent that only 50% of the magnet material is in use at any one time. This is not only a poor use of this resource, but also means that magnet flux is being continually driven up and down its 2nd quadrant BH characteristic as the magnet moves in and out of alignment with the stator 'C' cores. The only way to rectify these two problems would be to employ all of the permanent magnets on the rotor continuously.

Weh *et al* produced a number of designs [45] in order to rectify this problem. They consisted in the main of double-sided topologies, the most successful of which, the Double-Sided flux concentrating design [44] was developed into a 5.8kW wind turbine generator. Two alternate topologies were developed concurrently during the mid-nineties, each of which aimed to utilise all of a TFM's rotor magnets simultaneously, yet both tackled the problem in a very different way. The two topologies were the Single-Sided Bridged Transverse Flux Machine (SSBTFM) expounded by Bork and Henneberger [1, 2] and the Double-Sided Transverse Flux Machine (DSTFM) proposed by Mecrow *et al* [25]. The SSBTFM was of the same form as the SSTFM but the redundant magnets were brought into play through the use of axial 'bridges' between the 'C' cores. As with the SSTFM, this topology will be discussed in greater depth in Chapter 5. The DSTFM employed a new Soft Magnetic Composite (SMC) material in its construction, allowing a solid stator coreback and therefore the possibility of higher levels of coreback flux. However, all of the designs suffered to a greater or lesser extent from complex constructional problems.

Additional work has been carried out in this field by a number of institutes and companies. Southampton University have constructed an inverted two phase, 40 pole SSTFM prototype [10] on which they have performed extensive analysis. Rolls Royce, International Research and Development's (IRD) interest has been in the ongoing development of a 20MW TFM for ship propulsion. Their research is based around a 16 phase, 130 pole DSTFM [26]. In Germany, Voith Turbo GmbH have utilised Weh's double-sided design [44] to produce drive motors for electric buses [38].

1.7 What are the Advantages of the TFM?

There are three main advantages associated with TFMs. Firstly, the pole number in a TFM has a fundamental effect on its level of output. Simple analysis predicts that increasing the number of poles in a TFM will give rise to a linearly proportional rise in output torque. This is not true of most other classes of electrical machine, where the output torque is largely independent of pole number. This principle will be discussed in detail in Section 1.8. Secondly, the toroidal nature of the conductor means that the circumferential path it follows around the machine is the shortest and hence most economical route. Therefore copper losses are minimised and the absence of end windings means that the conductor is more efficiently utilised within the machine. Thirdly, high-powered rare earth magnets and the use of flux concentration techniques have given rise to the possibility of very high magnetic loadings in electrical machines. In order to exploit these high flux densities, an equally high level of MMF is required from the armature winding. This requires a larger cross-sectional area (c.s.a) of conductor in order to allow operation at realistic current densities and thereby limit thermal losses. The conductors in LFMs are normally positioned between the stator teeth and so to increase the copper c.s.a would entail enlarging the conductor area either radially or circumferentially. A circumferential increase would reduce stator tooth width and so increase saturation effects, whereas a radial increase would elongate stator tooth length, increasing stator reluctance and overall machine diameter.

Because of the finite amount of space in a machine, there will always be a trade-off in an LFM between the saturation losses caused by insufficient iron in the teeth and the I^2R losses due to a small conductor c.s.a. It can be seen therefore that the LFM will always have to make a compromise between its electric and magnetic loadings in order to attain good levels of efficiency, but at the expense of higher outputs. This is not the case with the TFM.

1.8 Method of Torque Production

The generally accepted method of analysing the force production in an electrical machine is the product of the airgap flux density (B), the electric loading (i) and the length (l) of the conductor carrying the current in the magnetic field. In order

to convert this into a torque, the force must be multiplied by the mean airgap radius (r) and then the result integrated around the machine. Transverse Flux Machines, because of their unique topologies, cannot always be defined using this method of torque analysis. Therefore, in order to evaluate the torque in a TFM a more fundamental formula must be employed. The torque produced in any electrical machine is given by the rate of change of co-energy of its winding with respect to position [5], where:

$$T = i \frac{\partial \Psi}{\partial \theta} \qquad = N i \frac{\partial \phi}{\partial \theta} \qquad \{1.1\}$$

This indicates that the torque produced by a machine is the product of the electric current (i) and the rate of change of flux linkage per phase (Ψ) with respect to the angular displacement (θ) between positions of maximum and minimum flux linkage. In reality this formula is an approximation, as it is only true in a wholly linear model, so throughout this thesis theoretical torque will be evaluated using Ψ-I curves derived from non-linear Finite Element (FE) results. The formula does, however, allow the principle of torque production in TFMs to be evaluated, and shows why such high levels of torque can be attained.

In a standard Longitudinal Flux Machine the winding MMF per pole is reduced as pole number increases. The flux linkage of each turn reduces roughly proportionally to the reduction in change of angular position brought about by the increased pole number (ie. as $\partial\Psi$ reduces, so does $\partial\theta$). The overall effect of this is that torque production is relatively independent of pole number. However, this is not the case when dealing with TFMs and their variants. In a TFM, the flux of each pole links with all of the conductors, so maintaining flux linkage at a maximum. This means that as the pole number increases the flux per pole will reduce. However, despite this reduction in flux per pole, the overall flux linking with the winding remains relatively constant because there are more poles. Thus, as pole number increases and so the change in pole arc diminishes, the overall torque increases proportionally (ie. although $\partial\theta$ reduces, $\partial\Psi$ remains constant). Therefore, for a constant level of electric loading the torque will increase. It may therefore appear that increasing the pole number towards infinity would have a similar effect on the torque. This does not happen, although optimum pole numbers are quite high, because of the physical as well as

electromagnetic limitations placed on the machine, such as tooth width, saturation, and leakage effects.

1.9 The use of Powder Metallurgy

One of the main differences between the work detailed in this thesis and work carried out elsewhere on TFMs is the use of Powder Metallurgy in both the construction and simulation of the machines being analysed. Its use appears to take the form of a double-edged sword, with both substantial advantages and disadvantages. Nevertheless, the three dimensional nature of the flux paths in TFMs made them an obvious test ground for this technology. Because the use of Powder Metallurgy in this work has been vital, an appendix (A) has been included to cover the basic principles of the material's manufacture and characteristics.

1.10 Finite Element Analysis

Non-linear three dimensional finite element (FE) analysis has been used extensively throughout this research. All of the topologies investigated were reproduced as 3D FE rectilinear models. Each model was solved over a wide range of current load steps using non-linear materials in order to ascertain its electromagnetic characteristics. Prospective performance was determined from coreback flux linkage against MMF curves, corresponding to the positive and negative 'd' axis aligned positions in the model. The 3D FE magneto-static package used for all of the simulation work during this research uses the magnetic scalar potential with currents and magnets imposed through the use of an electric vector potential (Appendix D.6).

A further avenue of exploration was the 2D FE simulation of TFMs. With fully three dimensional flux paths, modelling a TFM satisfactorily in two dimensions is difficult. It is common place in electrical machines such as Switched Reluctance Motors or Induction Machines, to use 2D FE analysis. This is because the main flux paths in these machines are two dimensional. However, they also possess 3D flux paths, generally associated with leakage fields and end effects. In order to evaluate these unmodelled fluxes, empirical knowledge is employed in conjunction with 2D analysis. As part of this thesis, a study was carried out to discover how accurately a TFM supporting fully three dimensional flux can be modelled in two dimensions.

1.11 Aims of the Thesis

The overwhelming drive behind this thesis was to understand the characteristics of a Transverse Flux Machine, its shortcomings and potential and use that knowledge to design and build a TFM with the ability to outperform all existing TFM topologies.

To fulfil this task a large amount of detailed analysis was carried out on each major TFM topology: the Single-Sided TFM, the Single-Sided Bridged TFM, the Claw Pole TFM and the Double-Sided TFM. The analysis involved both two dimensional and three dimensional finite element studies of the topologies and extensive optimisation of flux paths in each model. Some of the areas covered by the investigation were the effect of:

- Pole number
- Circumferential tooth overlap of rotor magnets
- Circumferential tooth width
- Axial tooth overlap
- Radial rotor magnet depth
- Stator coreback thickness
- Airgap length

This analysis was achieved by creating 3D FE models of each topology and each variation on that topology. Each model was then subjected to a suitably wide electric loading (MMF) range in order to determine its performance characteristics. The flux paths and loss mechanism in each of the models were then studied in detail. This enabled conclusions to be drawn as to why one particular topology exhibited better or worse characteristics than another, be it more mean torque, lower armature reaction or higher saturation effects.

To ensure that valid and fair comparisons could be made between each type of machine, every topology investigated was evaluated on a par with its fellows and each model was optimised within the given parameters of the study. From this work, an optimised high performance TFM topology was produced.

1.12 Prototype Machines

In order to validate the extensive 3D FE analysis that was carried out, three prototype machines have been built. These were respectively:

1. Double Sided TFM (DSTFM)
2. Claw Pole TFM (CPTFM)
3. Claw Pole Hybrid TFM (CPHTFM)

Both the DSTFM [25] and CPHTFM [20] are non-rotating 100 pole, single phase machines. The CPTFM [17], is a 24 pole, single phase, rotating machine. Analysis of these machines took the form of static torque tests and heat runs. The results of these practical investigations allowed comparisons to be made between actual and theoretical results, enabling the validation of both 2D and 3D FE analysis. The close correlation between practical and theoretical work meant that further FE investigations into this class of machine could be carried out with confidence.

1.13 Contributions of this Work

This three-year study of the Transverse Flux Machine has enabled a detailed picture to be drawn of how this family of machines operate.

- How they produce such high specific outputs
- Which aspects of machine topology affect the level of output
- Which aspects of machine topology affect Power Factor
- Why one topology outperforms another

The ability to answer these questions has enabled a totally original Transverse Flux Machine, that displays an extremely high specific output to be designed and built.

Chapter 2

TFM Two Dimensional Finite Element Analysis

2.1 Introduction

One of the most accurate methods of modelling electromagnetic fields is with three-dimensional Finite Element Analysis (FEA). However, constructing 3D models and producing 3D FEA solutions can be very expensive in terms of both man-hours and computer run-time. Because of these constraints, many problems are analysed and solved using two dimensional software and any three dimensional electromagnetic effects evaluated using empirical data. The empirical knowledge used is generally based on many years of research into a particular machine topology. For most electrical machines the bulk of the magnetic field flows in a single plane. If the correct plane of reference is selected then a full electromagnetic analysis can be carried out. As previously stated, the flux paths in a Transverse Flux Machine (TFM) are fully three-dimensional, so there is no two dimensional plane that will wholly model the active flux paths in the machine. As well as this, if a two dimensional plane were used, there is not yet the depth of research that allows *a priori* assumptions to be made regarding the effects of unmodelled leakage flux.

If a methodology could be formulated to allow accurate two dimensional analysis of TFMs the initial design procedure could be substantially improved, with non-viable topologies being "weeded out" and promising designs progressing forward for more stringent three dimensional analysis. The 2D design methodology presented in this chapter used empirical and mathematical procedures to achieve a close approximation to a 3D result, without the labour intensive and time consuming need to construct a 3D model. It must be stated however that the evaluation of three-dimensional finite element problems using two dimensions will always lead to some form of compromise.

The 2D methodology considered one pole pitch of the machine, encompassing the stator, rotor and conductor area. The finalised 2D model was evaluated by impressing an MMF onto the conductor in the model, equal to the actual MMF experienced by the machine. The average magnetic vector potential of the model was

ascertained at a series of current increments, enabling a picture of flux linkage against current to be produced over the entire operating range of the machine. Analysis of flux densities and saturation effects in the machine could also be carried out at any of the predetermined load steps.

2.2 Establishing the Two Dimensional Model

The first problem encountered when attempting to produce a two dimensional model of a TFM, was to decide in which plane of the proposed three dimensional machine to create the FEA model. Figures 2.1a and 2.1b represent two planes in a simple SSTFM. Taken individually, each of the planes omits essential electromagnetic characteristics when describing the action of the complete topology. When viewed in the axial/radial plane (figure 2.1a) the circumferential slotting of the teeth is unmodelled. In the circumferential/radial plane (figure 2.1b) the stator MMF cannot be imposed on the conductor, in addition to an incomplete main flux path.

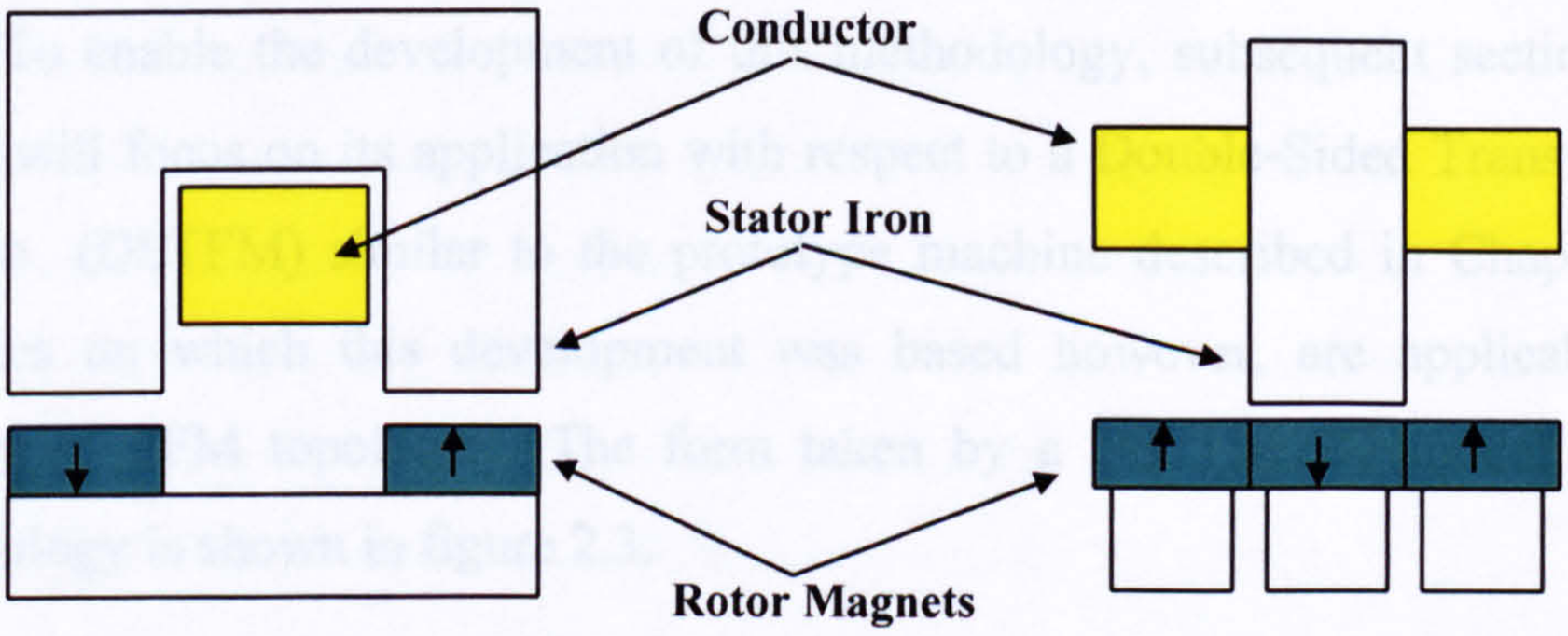

Figure 2.1a Axial/radial view of a simple SSTFM

Figure 2.1b Circumferential/radial view of a simple SSTFM

With a small amount of lateral thinking, the problem was circumnavigated by creating a 2D model that incorporates elements of all three dimensions. This was achieved by viewing the rotor and the stator in two separate orthogonal planes, the axial/radial and the axial/circumferential, and then combining these two planes in one model (figure 2.2). The conductor area was modelled in the axial/radial plane, which in a TFM is normal to the direction of current flow around the machine, whilst the magnets and stator teeth were modelled in the axial/circumferential plane. Unfortunately, both planes may also support magnetic fluxes that are not normally adjacent to one another and so could give rise to unrealistic flux paths being

established. Non-magnetic barrier regions were therefore required to prevent the passage of magnetic flux between these areas. These barrier regions, which possess very low permeability in order to inhibit the passage of magnetic flux, must be positioned at the planar interface.

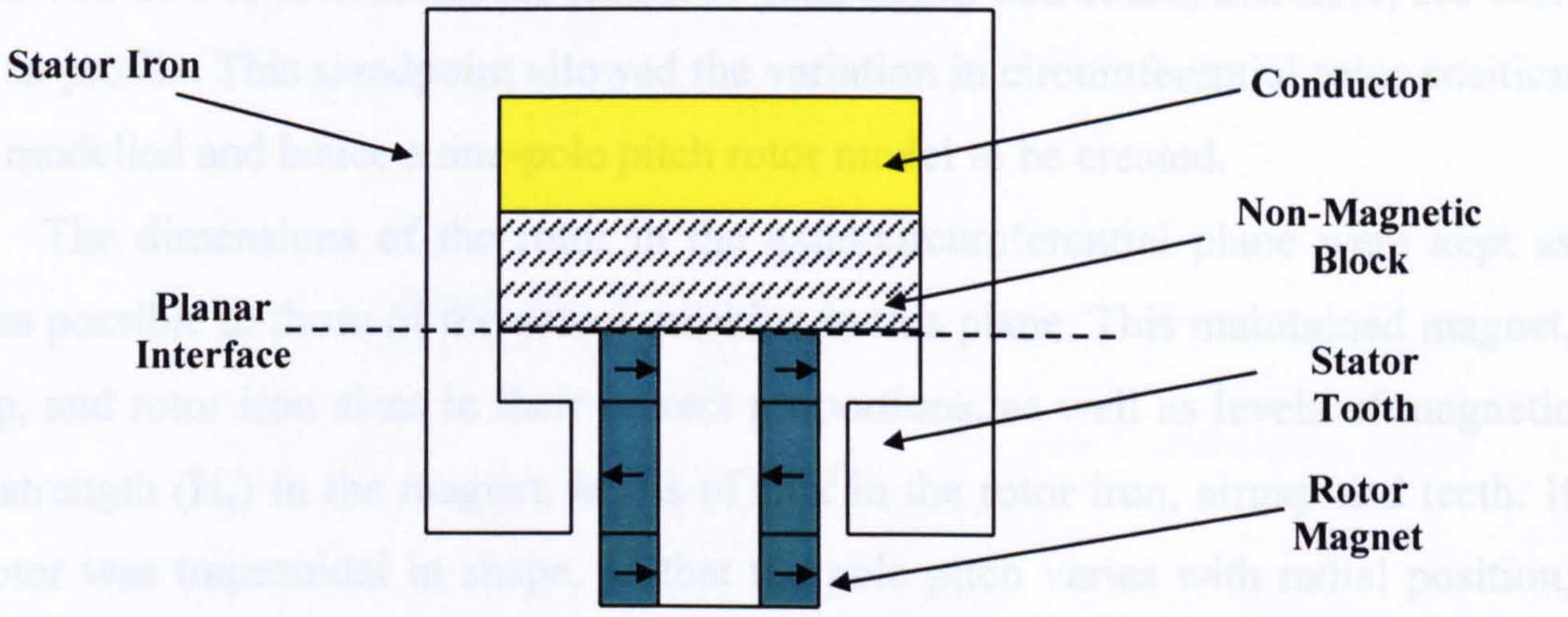

Figure 2.2 A single pole of a simple SSTFM, incorporating two orthogonal planes, viewed as a 2D model

To enable the development of this methodology, subsequent sections of this chapter will focus on its application with respect to a Double-Sided Transverse Flux Machine (DSTFM) similar to the prototype machine described in Chapter 3. The principles on which this development was based however, are applicable to the majority of TFM topologies. The form taken by a DSTFM 2D model using this methodology is shown in figure 2.3.

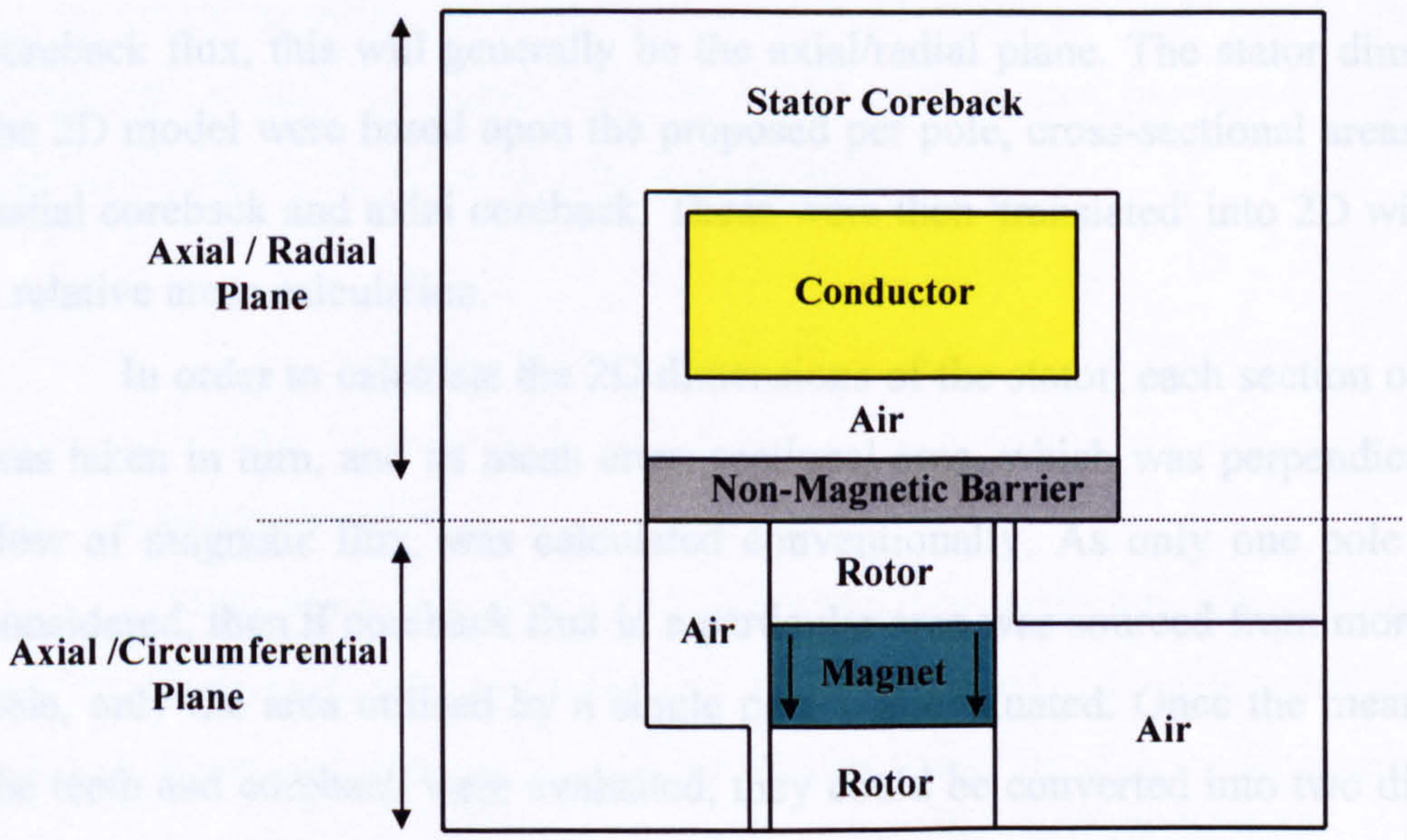

Figure 2.3 Typical single pole layout for the 2D model of a DSTFM

2.3 Rotor Orientation

The orientation of the rotor in the 2D model was dependent upon the orientation of the teeth and airgaps in the machine. The two dimensional view of the rotor was such that both active airgaps could be seen. From this perspective the viewer was able to look along the length of each airgap and could, therefore, see each tooth in profile. This standpoint allowed the variation in circumferential rotor position to be modelled and hence a one-pole pitch rotor model to be created.

The dimensions of the rotor in the axial/circumferential plane were kept as near as possible to those of the actual machine in this plane. This maintained magnet, airgap, and rotor iron sizes in their correct proportions, as well as levels of magnetic field strength (H_c) in the magnet, levels of flux in the rotor iron, airgap and teeth. If the rotor was trapezoidal in shape, so that the pole pitch varies with radial position, then mean rotor dimensions were be used for modelling.

2.4 Stator Orientation and Sizing

A fundamental consideration in determining the dimensions of the 2D model was that the two orthogonal planes invariably had different depths. This meant that relevant areas in the 2D model had to be suitably scaled in order to reflect these differences and so more accurately emulate the three-dimensional problem. The following sections of this chapter, which describe the model's construction, cover the incorporation of these dimensional differences into the 2D model.

The 2D stator should be viewed in a plane that runs parallel to the main coreback flux, this will generally be the axial/radial plane. The stator dimensions in the 2D model were based upon the proposed per pole, cross-sectional areas for teeth, radial coreback and axial coreback. These were then 'translated' into 2D widths using a relative areas calculation.

In order to calculate the 2D dimensions of the stator, each section of the TFM was taken in turn, and its mean cross sectional area, which was perpendicular to the flow of magnetic flux, was calculated conventionally. As only one pole pitch was considered, then if coreback flux in a particular area was sourced from more than one pole, only the area utilised by a single pole was evaluated. Once the mean areas for the teeth and coreback were evaluated, they could be converted into two dimensional widths for the 2D model.

Rather than using arbitrary widths, stator dimensions were derived from the cross sectional area at the airgap interface of the rotor and the stator. Two variables were required to calculate the 2D stator dimensions (figure 2.4).

1. The unmodelled radial dimension of the rotor (h)
2. The modelled dimension used in the rotor section of the 2D model (W)

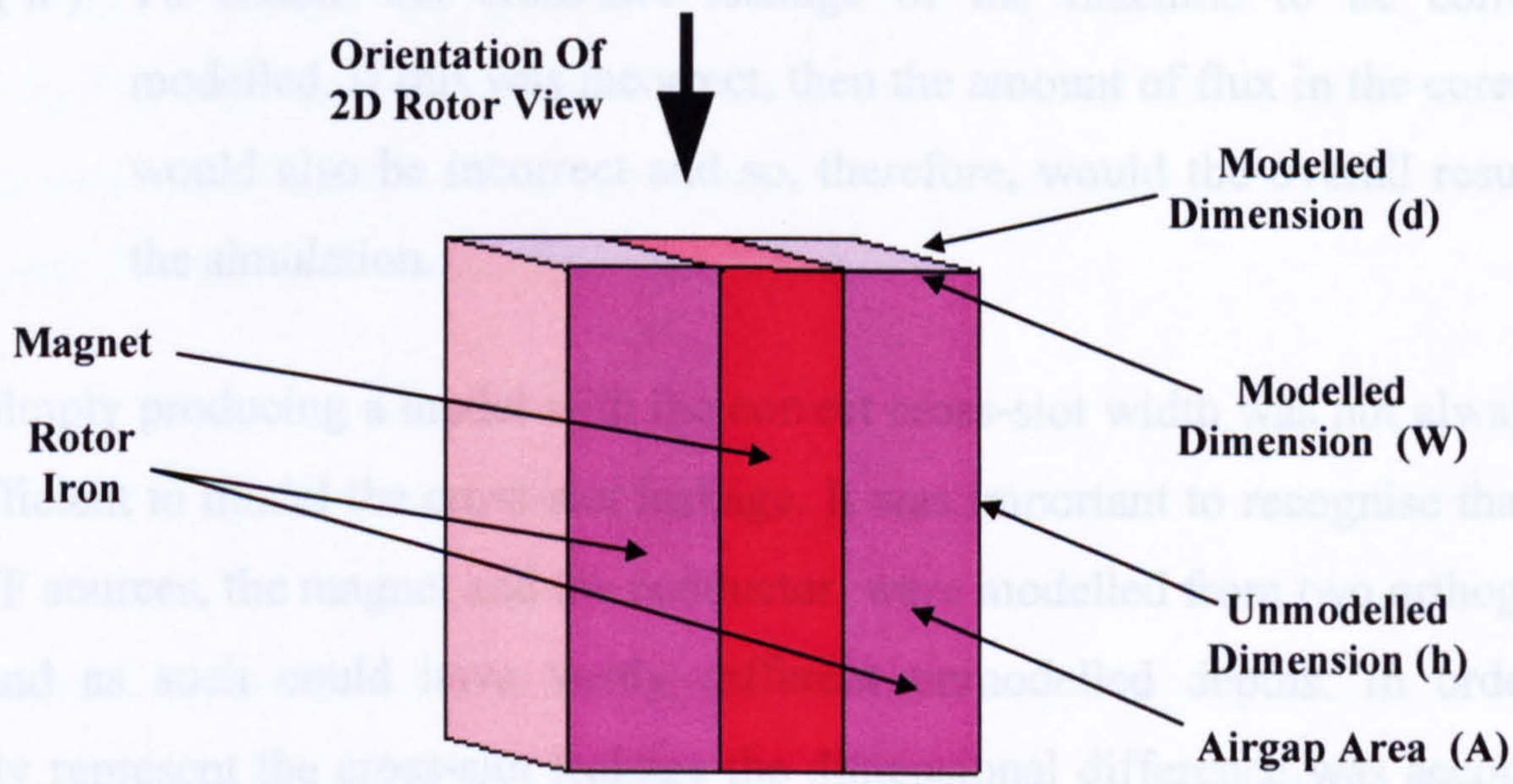

Figure 2.4 Segment of rotor iron and magnet demonstrating the position of the airgap area datum

The airgap area (A) and modelled dimension (W) were used as a datum in order to calculate the widths of the 2D stator. The individual calculations were based upon each of the mean cross-sectional areas in the proposed machine. If the 2D width is termed 'x' and the mean cross sectional area of that particular section of the machine is 'A_x' then 'x' is calculated as follows:

$$x = W \times \frac{A_x}{A} \qquad \{2.1\}$$

2.5 Electric Loading

Correct simulation of the conductor area was important when producing FEA models of electromagnetic circuits, so the dimensions of this area should be kept accurate; these included not only the conductor itself, but also the air space around it.

There were two reasons for accurately reproducing the actual conductor area in the FEA model:

(i) To enable the correct level of current density to be impressed upon the conductor, without the need to scale the value, or take account of its altered dimensions when evaluating the effect of the electric field on the magnetic circuit.

(ii) To enable the cross-slot leakage of the machine to be correctly modelled. If this was incorrect, then the amount of flux in the coreback would also be incorrect and so, therefore, would the overall result of the simulation.

Simply producing a model with the correct cross-slot width was not always in itself sufficient to model the cross-slot leakage. It was important to recognise that the two MMF sources, the magnet and the conductor, were modelled from two orthogonal planes and as such could have vastly different unmodelled depths. In order to accurately represent the cross-slot leakage the dimensional difference was accounted for by scaling the relative permeability of the conductor area, by the ratio of unmodelled conductor length (generally equivalent to the pole pitch), to the unmodelled magnet length (h – see figure 2.4). For example, if one pole pitch =10mm, and 'h' = 20mm, then this gave a scaled value for the relative permeability in the conductor area of 0.5 instead of the relative permeability of free space figure of 1.0. So, altering the relative permeability in the conductor area from unity to this new scaled value should produce a more accurate value of cross-slot leakage and hence coreback flux.

It should be noted that for low values of MMF (≤10,000Ampereturns) it was not necessary to scale the relative permeability of the conductor area as the effect of cross-slot leakage was not significant.

2.6 Magnetic Loading

One of the major causes of analytical inaccuracy encountered when performing 2D analysis of 3D problems comes from leakage and fringing flux that propagates in the unmodelled third dimension of the 2D model. The most prominent

of these third dimensional leakage paths was found in the vicinity of the source magnet. The unmodelled leakage flux was equivalent to a flux path in parallel with the magnet and these parallel reluctance paths combined to produce an overall lower magnet reluctance.

In order to model this leakage and operate the magnetic circuit at a more realistic level, the magnet's characteristics were altered to reduce the level of flux in the machine. This was achieved by increasing the relative permeability (μ_r) of the magnet, which increased the gradient of the second quadrant B-H characteristic (figure 2.5), thus reducing the value of H_c for a given residual flux density (B_r). This procedure could also be viewed as a reduction of the magnet's reluctance value by changing the denominator of the reluctance equation:

$$S = \frac{\ell}{\mu_o \mu_r A} \qquad \{2.2\}$$

The next problem considered is by how much the value of μ_r should be altered.

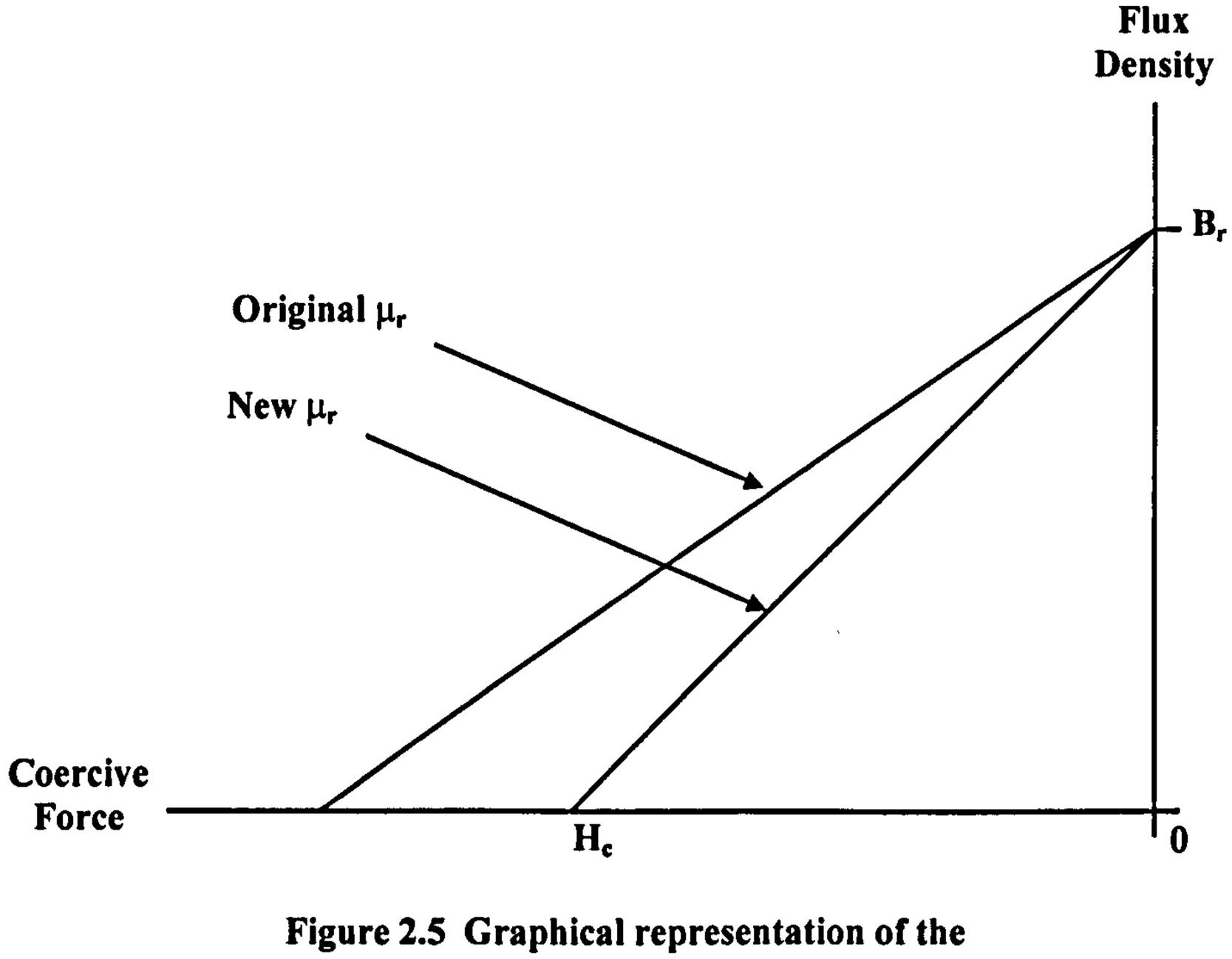

Figure 2.5 Graphical representation of the effect of altering a magnet's relative permeability

The unmodelled leakage paths could be viewed as parallel reluctance paths, which combined to reduce the overall reluctance of the magnet. The leakage paths were shown to increase the effective height of the magnet (h) by a distance K at each

end (figure 2.6). This concept can be further explained in terms of the magnet source equivalent circuit (figure 2.7).

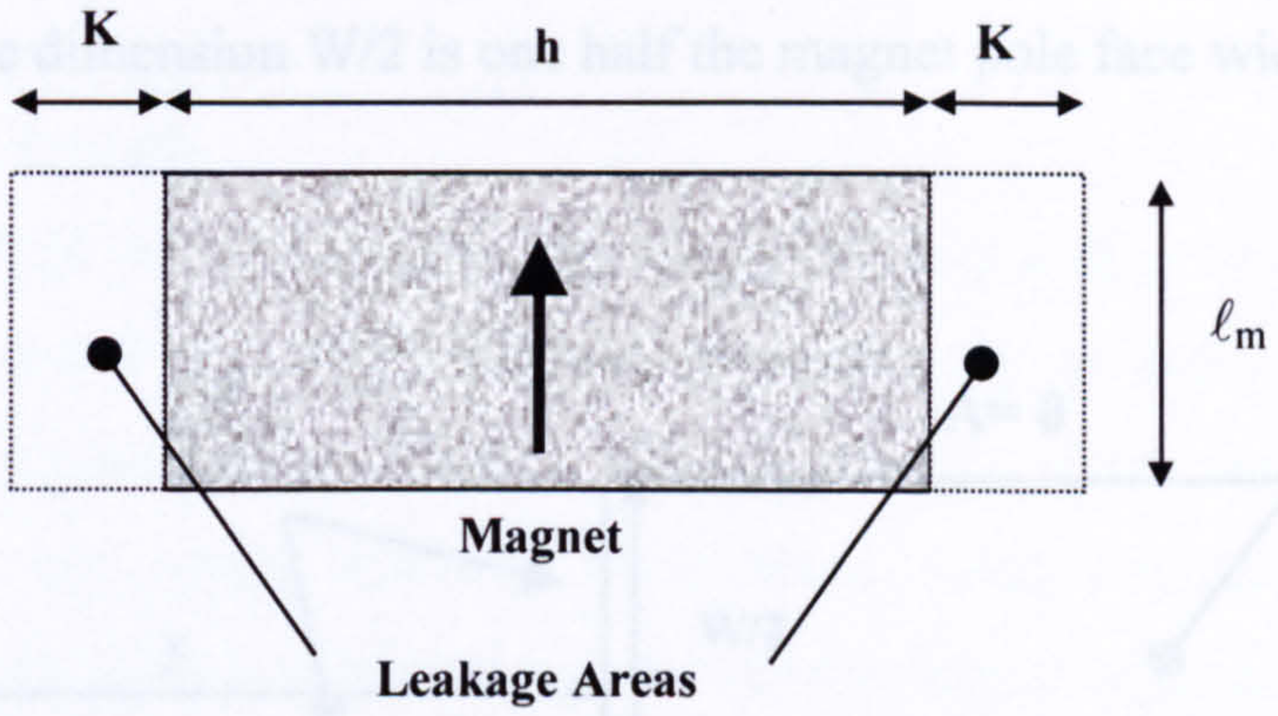

Figure 2.6 Diagram showing the parallel leakage areas on either side of the source magnet

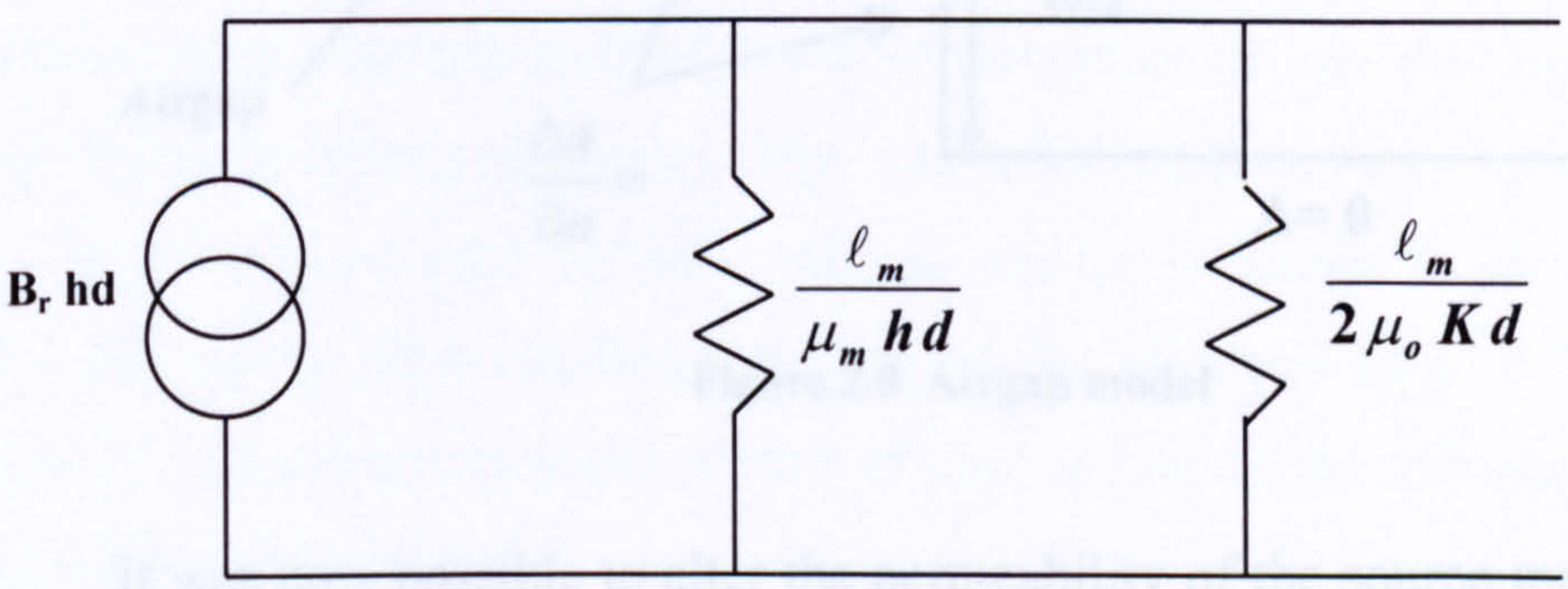

Figure 2.7 Source magnet's equivalent circuit showing the magnet's reluctance and the parallel leakage path reluctance

The value of K was derived using a simple 'Airgap Model' (figure 2.8), constructed and analysed using FEA. Boundary conditions were applied to force a net flux across the gap. With reference to figure 2.8, the procedure for obtaining this value was as follows:

(i) Using FEA measure the MMF drop (MMF_{meas}) across the airgap (ℓ_m)

(ii) Assume ϕ = 1Wb per metre and so to ascertain the value of y+K, transpose the equation:

$$MMF_{meas} = \phi S \qquad \{2.3\}$$

(iii) The arbitrary length, y, needs to be at least three times the length of the gap (ℓ_m) in order to allow the MMF drop across the airgap to stabilise.

(iv) The dimension W/2 is one half the magnet pole face width.

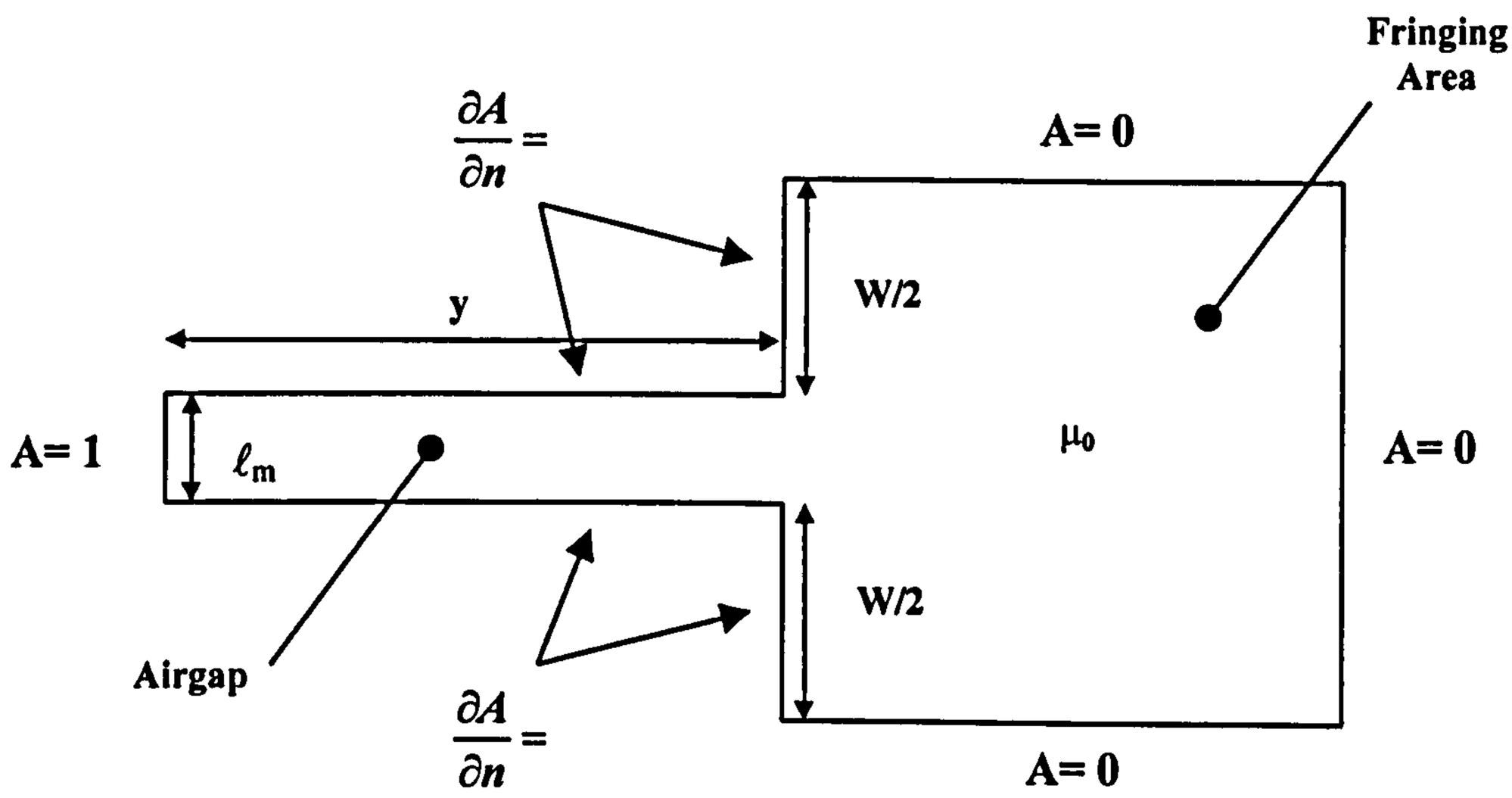

Figure 2.8 Airgap model

It was now possible to alter the permeability of the source magnet based upon the variables K, h and ℓ_m.

ie. $$\mu_{2D} = \mu_r \times \frac{h + 2K}{h} \qquad \{2.4\}$$

This new value, μ_{2D}, was used to redefine the magnet's characteristics.

2.7 Non-Magnetic Barriers

In this form of composite two dimensional model there was a strong possibility that unrealistic flux paths could be established at the interface of the two orthogonal planes. For example, in an actual TFM, the flux paths are such that there is no substantial radial path between the top of the rotor and the bottom of the conductor, however in the 2D model, the end-effect rotor flux was oriented towards the conductor, and so had to be blocked. In FEA, creating non-magnetic barriers may be achieved using an area with a very low relative permeability of, for example, 0.01.

This barrier area would be placed between the conductor area and rotor, preventing unrealistic flux paths being established.

2.8 Flux Path Length

The length of the coreback in the 2D model was a direct translation of the mean path length the flux took through the three dimensional machine. This meant that the level of reluctance and hence flux in the 2D stator iron was a better representation of the actual machine when these mean lengths were used in conjunction with the widths calculated by the "relative areas" approach expounded in Section 2.4.

The stator was discreetised into linear sections, then the path lengths of these sections were summed to give the total stator path length in the 2D model. Calculating the mean path took into account areas of redundant or low flux usage iron such as those found at radial extremities. This was achieved by measuring only straight line flux paths through each section, with no curves or bends in the path. A typical representation of the mean flux path through the 3D stator of a DSTFM is shown in figure 2.9. This diagram shows a view of the machine in the axial/radial plane, which is parallel to the flux path.

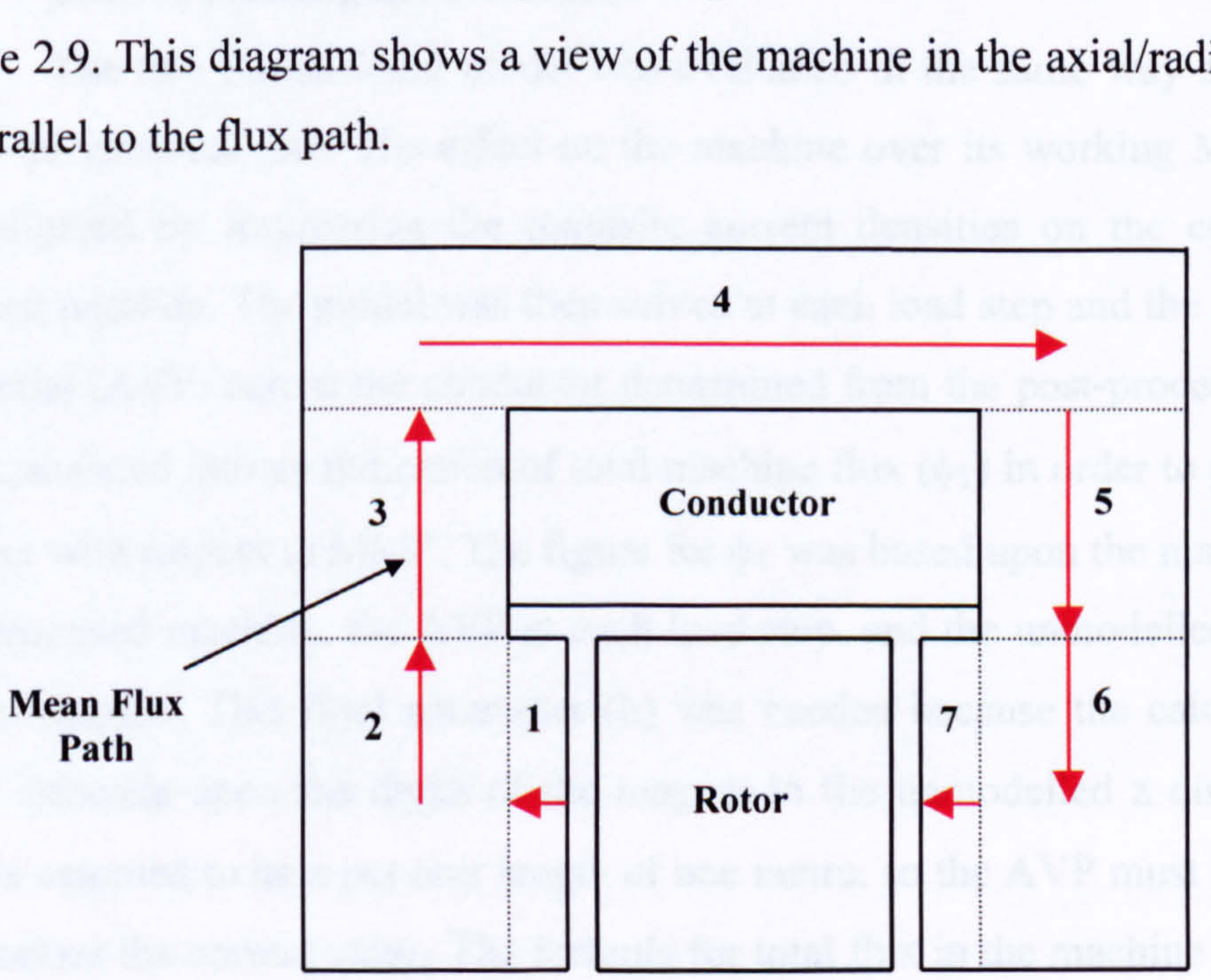

Figure 2.9 Mean flux paths around the 3D stator viewed in the axial/radial plane

The mean flux path length in the 2D model was equivalent to the summation of lengths 1 to 7 in the 3D geometry. When applied to the 2D model, this length was equivalent to the distance around the internal periphery of the model; that is, around

the conductor area and the inner boundaries of the teeth. The 2D model was constructed using the following data:

- As the model represents one pole of the machine and assuming that there is no mutual flux linking with any adjacent poles, the boundary conditions on the external periphery of the model should be given a magnetic potential (A) of zero.
- Rotor and Airgap dimensions from the proposed 3D model.
- Conductor Area dimensions from the proposed 3D model.
- Conductor Area relative permeability value.
- Magnet characteristics based upon its scaled relative permeability.
- Non-magnetic barriers to prevent unrealistic flux paths being established.
- 2D widths derived from the relative areas method.
- Mean Flux Path Length from the proposed 3D model.

2.9 Post-Processing the 2D Model

The two dimensional model was evaluated in the same way as an equivalent three-dimensional one. The effect on the machine over its working MMF range was investigated by impressing the requisite current densities on the conductor in the aligned position. The model was then solved at each load step and the Average Vector Potential (AVP) across the conductor determined from the post-processor. This value was translated into an indication of total machine flux (ϕ_T) in order to produce a graph of flux with respect to MMF. The figure for ϕ_T was based upon the number of poles in the proposed machine, the AVP at each load step, and the unmodelled dimension (h) of the magnet. This final parameter (h) was needed because the calculated value of AVP depends upon the depth of the magnet in the unmodelled z direction. Initially this is assumed to be a per unit length of one metre, so the AVP must be scaled by 'h' to produce the correct value. The formula for total flux in the machine is therefore:

$$\phi_T = \text{N}^{\text{o}}\text{. of Poles} \times \text{AVP} \times \text{h} \qquad \{2.5\}$$

The value of flux linkage at each load step was determined from the product of total machine flux and number of conductor turns. It is a feature of the TFM that the

levels of flux in the coreback for the positive and negative aligned positions are mirror images of one another and therefore the model needed only to be solved for one position to give a complete Ψ- I envelope.

As well as Ψ- I data, MMF drops and levels of flux density could also be determined from the 2D model, in the same way that they could be in a 3D FEA model, with a reasonable degree of accuracy. This means that the 2D version may be used to fully examine the potential of any TFM topology under investigation.

2.10 Results

This methodology was used with some success to evaluate a number of TFM configurations. Figures 2.10 and 2.11, compare 2D and 3D Flux-MMF curves for two separate TFM topologies. In figure 2.10, three sets of curves are shown, two 2D and one 3D. These represent three separate analyses of the same double-sided topology.

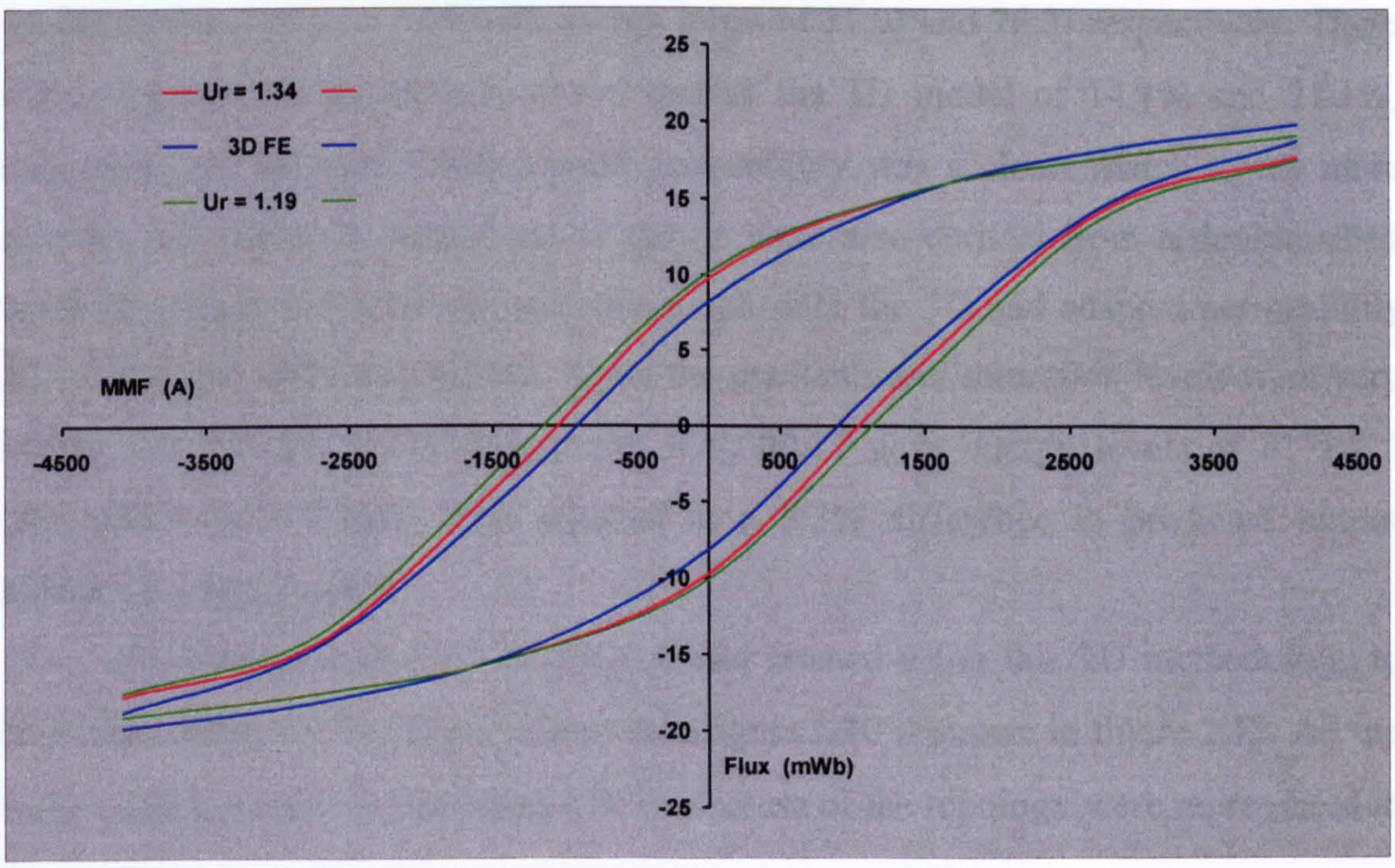

Figure 2.10 Flux-MMF curves from the 3D FEA and 2D FEA of a single topology. There are two sets of 2D curves, one with $\mu_r = 1.19$ and one with $\mu_r = 1.34$

The reason that there are two 2D curves is to demonstrate the effect of altering the relative permeability of the magnet. The original value of magnet relative permeability was 1.19, but after adjustment using the "leakage factor," K, it was altered to 1.34. It should be noted that the magnet in the 3D model also had a relative permeability of 1.19. From examination of the graph, it may be observed that the

three sets of curves have very similar gradient and saturation characteristics, which would indicate that they also have similar electromagnetic characteristics. Another indication of their similarity is the area enclosed by each pair of curves. This area indicates the mean output of the modelled machine, based on the following two equations:

$$\textit{Area of Loop} = \textit{VoltSeconds} \times \textit{Amperes} = \textit{Energy in Joules} \qquad \{2.6\}$$

$$\textit{Mean Torque} = \frac{\textit{Energy}}{\Delta\theta} \qquad \{2.7\}$$

(where $\Delta\theta$ = Angle between an aligned position ($+_{ve}$ 'd' axis) and the next aligned position)

The narrowest envelope was derived from the 3D FEA model and has an area equivalent to 63.0 Joules. This was followed by the 2D model with $\mu_r = 1.34$ and then the 2D model with $\mu_r = 1.19$ with energy loops of 71.9J and 76.3J respectively. These values represented an increase above that of the 3D model of 14.1% and 21.1%, indicating that the model with altered permeability was a closer match to the more accurate 3D model. A second set of curves were also derived from a double-sided topology (figure 2.11). However in this graph only the 3D and adapted permeability 2D FEA model were represented. Again the gradients and saturation levels were very similar and the area enclosed between ±15,000AT gave energy levels of 8171.1 J (3D) and 8441.4 J (2D). This equated to a 3.3% difference in predicted output between the two models.

An annotated no-load 2D FEA model created using this 2D methodology to determine the $\mu_r = 1.34$ 2D curve shown in figure 2.10 is shown in figure 2.12. All the main requirements for electromagnetic evaluation of the topology were represented in this model:

- Airgap flux density
- Rotor, Tooth and Magnet Leakage fluxes
- Cross Slot Leakage
- Saturation areas
- Coreback flux density

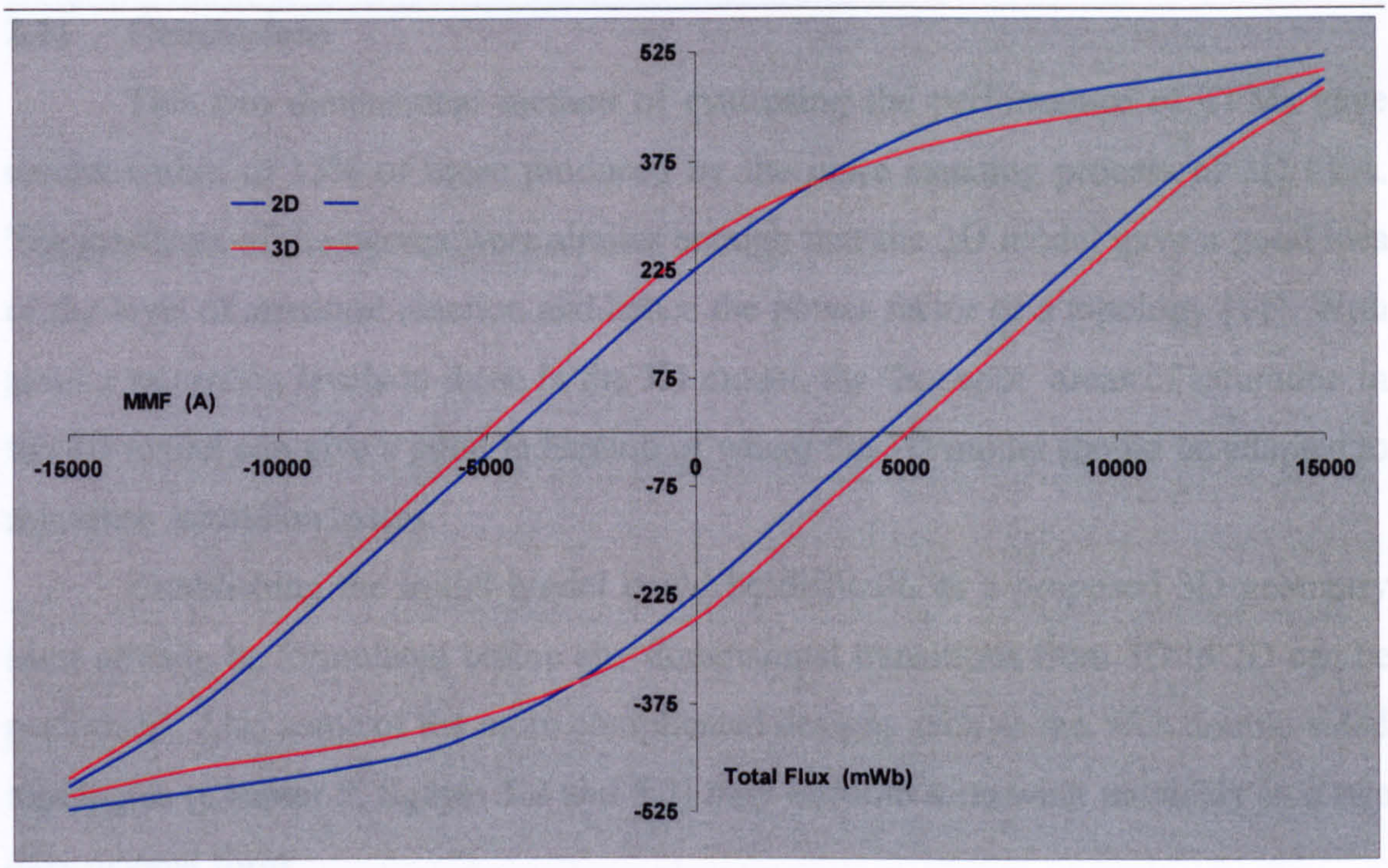

Figure 2.11 Flux-MMF curves from the 3D FEA and 2D FEA of an alternate DSTFM topology

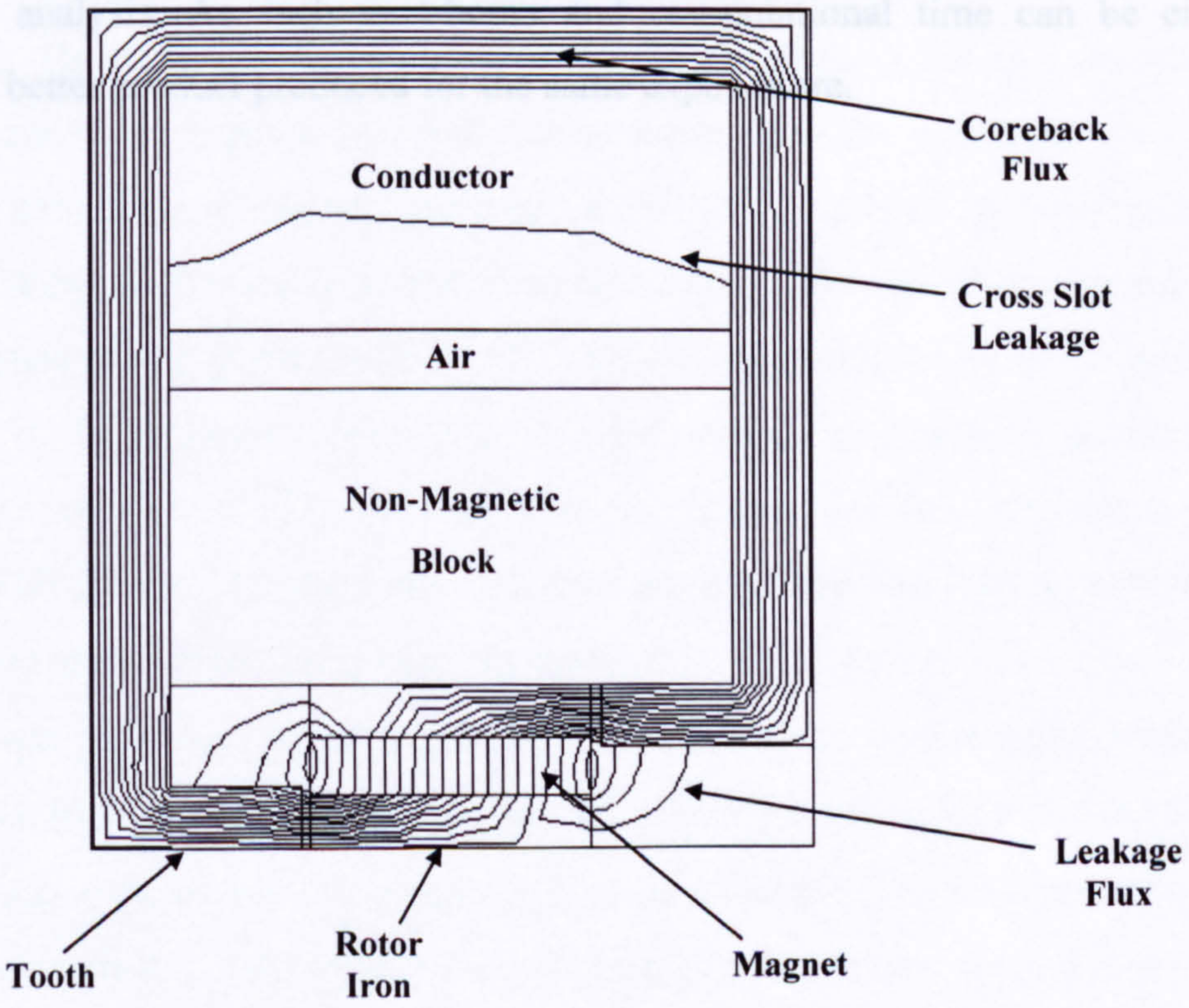

Figure 2.12 A non-excited 2D FEA flux contour plot of a DSTFM

2.11 Conclusions

This two dimensional method of evaluating the performance of TFMs gave results within of 15% of those produced by the more exacting process of 3D FEA. The gradients of the curves were similar enough that the 2D model gave a good idea of the level of armature reaction and hence the power factor of a topology [11]. With similar saturation levels to those in the 3D model, the 'hot-spot' areas of saturation in the 2D model can give a good indication of where the 3D model should be adapted to minimise saturation losses.

Establishing the initial model could be difficult, as a proposed 3D geometry must already be formulated before any dimensional transitions from 3D to 2D can be performed. Also some of the more complicated designs such as the Weh double-sided topologies (Chapter 5, figures 5.2 and 5.3) may become somewhat unwieldy in a two dimensional form.

However, use of this methodology in the initial design analysis of new TFM topologies could be a worthwhile exercise. It allows the time set aside for the evaluation of a new topology to be used for additional optimisation of the original 'rough' designs before the most promising model is subjected to a more rigorous three dimensional analysis. As such man-hours and computational time can be either reduced or a better product produced for the same expenditure.

Chapter 3

The Double Sided Transverse Flux Machine

3.1 Introduction

In 1986, Weh and May [42] first raised the principle of the Double-Sided Transverse Flux Machine (DSTFM). They referred to the configuration as a "double face version," which incorporated alternate 'U' cores and bridging pieces on either side of a rotor that was comprised of two sets of surface mounted magnets. Two years later they had adapted the design, by using two sets of flux concentrating magnets on the rotor and thereby allowing the removal of the design's bridging pieces [45]. This new configuration was the basis for a 5.8kW prototype wind turbine generator [44]. This two-phase machine consisted of a cylindrical rotor with four sets of stator cores positioned radially above and below the rotor's outer and inner surfaces respectively. The machine consisted of 144 poles per phase and produced a rated torque of 284Nm at 195rpm, with an active mass of 27.2kg, giving a torque per unit mass of 10.44Nm/kg. The design was, however, relatively complicated but this complexity appeared a small price to pay for the high output achieved by the prototype.

Full utilisation of magnet material in the DSTFM built at Braunschweig University, indicated that using a rotor with two active sides would greatly enhance the performance of any given topology of TFM, although complexity was a problem that needed to be addressed. With this in mind, design studies were initiated at Newcastle University [6, 24, 37] in order to further examine transverse flux principles, with the view to producing a simpler machine that had least an equivalent level of output to that of the Braunschweig machine.

A major difference between previous TFM's and the double-sided prototype built at Newcastle University, was the use of a Soft Magnetic Composite (SMC) material for all of the active iron components of the machine. The main advantage of SMC over laminations, is its ability to support the TFM's inherent three dimensional flux paths. Also SMC allows the use of a solid coreback, thereby introducing more

iron into the flux paths, which helps to reduce coreback saturation. The properties associated with SMC materials are presented in Appendix A.

3.2 Initial Design Parameters

Analysis of the previous research carried out at Newcastle suggested the following design configuration. A flux concentrating rotor positioned axially between two sets of staggered stator teeth, displaced from their circumferentially adjacent teeth by two pole pitches, and by one pole pitch from the tooth axially opposite. The conductor was then positioned radially above the rotor and was in turn fully encompassed by the stator coreback. A rectilinear diagram of this basic configuration is shown in figure 3.1. The merits of this topology over the Braunschweig double-sided TFM include:

- One magnet per pole, instead of two, leading to half the number of active airgaps.
- A single flux concentrating rotor, as opposed to two mechanically linked flux concentrating rotors.
- A solid coreback, instead of isolated 'C' cores, by virtue of the SMC material used.

This facilitated higher coreback flux density levels and so greater flux linkage in the machine. However, shortcomings envisaged for the design centred around the electromagnetic and mechanical properties of the new SMC material, whose use was fundamental to this topology.

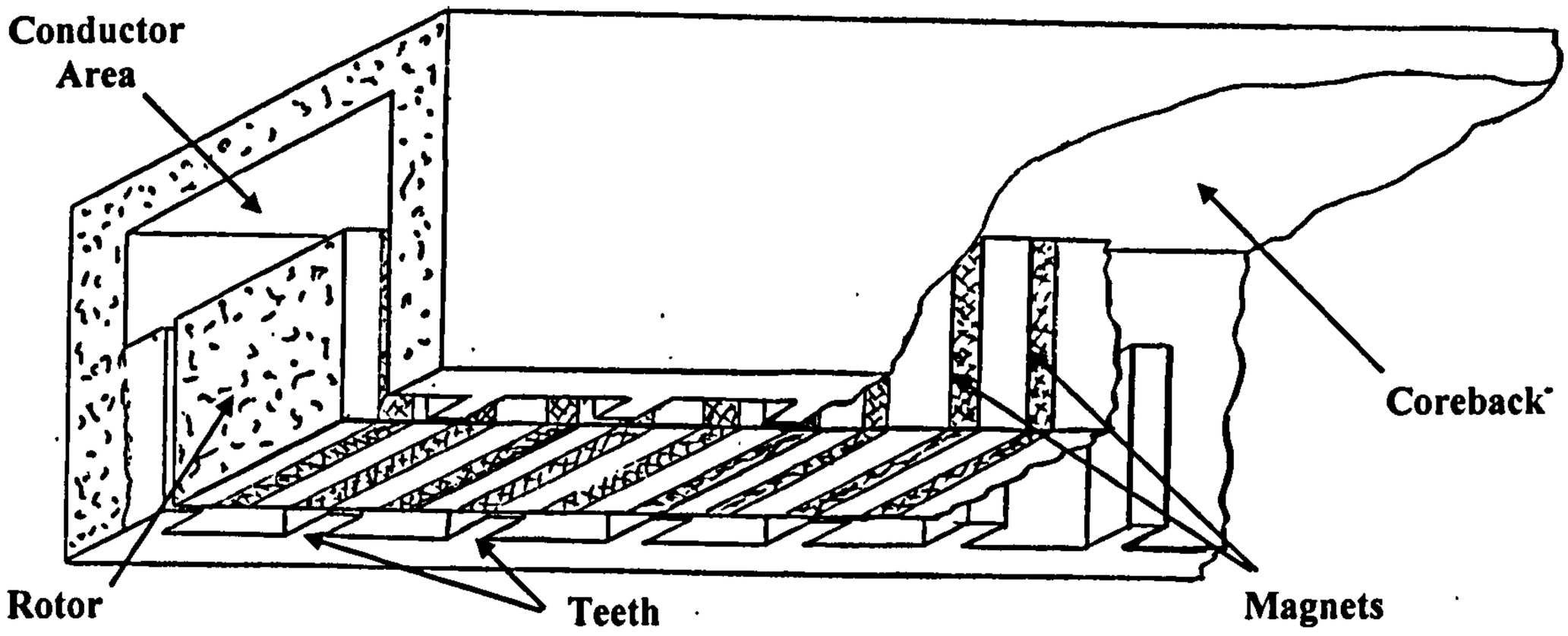

Figure 3.1 Rectilinear schematic of the proposed DSTFM topology

Initially, a number of decisions needed to be made with regard to the overall machine design. From these fundamental requirements the design for the complete machine was derived. The three main design parameters were:

a) Pole number
b) Rotor outside diameter
c) Magnet and Airgap length

3.2.1 Pole Number Constraints

How does the pole number affect the design? The specification for the prototype demanded a high output machine suitable for a direct drive application. With reference to equation 1.1, a high torque output in a TFM necessitates a high pole number in order to maximise the rate of change of flux linkage with respect to position. However, there is a limit imposed on the electrical frequency that the machine can operate at because of the drive's power electronics and iron loss. Therefore, because of these limitations, a high pole number would necessitate a low rotational velocity, characteristic of a direct drive machine.

Although it was agreed that the pole number should be high, the choice of pole number was firmly linked to the overall dimensions of the finished machine. The constraints imposed by laboratory testing facilities, covering both physical size as well as torque handling capabilities, limited the prototype machine to a stator outside diameter in the region of 0.4m (rotor OD $\approx$ 0.3m) and an output of approximately 500Nm. Therefore, pole number was based on these values and per pole dimensions governing:

- Ratio of magnet/airgap length
- Minimum airgap length
- Ratio of magnet/pole width

3.2.2 Ratio of Magnet/Airgap Length

The active length of the magnets and the airgap length in a machine design are closely linked, and the relative values of the two are largely dependent on the coercive force of the magnet being used. The choice of rare earth magnet for this machine was

narrowed down to Samarium Cobalt (SmCo) or Neodymium Iron Boron (NdFeB). Neodymium Iron Boron magnets have a much lower Curie temperature than SmCo magnets and start to partially demagnetise at approximately 100°C. However, NdFeB is less than half the cost of SmCo. This is a considerable saving in capital outlay in a large permanent magnet machine. If close attention was paid to the thermal design of the machine, then the NdFeB magnets could be used without penalty, but with a considerable saving in cost.

After selecting NdFeB as the magnet material, the active length of magnet (ℓ_m) needed to be chosen, and this dimension would have a direct bearing upon the airgap length (ℓ_g) required for a specific airgap flux density (B_g). A large value for ℓ_m would have allowed a proportionally larger airgap length, making mechanical construction less exacting. As the magnets were to be an integral part of a toroidal rotor, increasing their length increased the rotor circumference. With a fixed rotor diameter, this would have reduced the number of poles, longer magnets would also have given a higher magnet volume and hence increased cost.

In order to employ the magnet efficiently, its assumed operating point was considered to be half that of its residual flux density (B_r), so that, $H_m = -\frac{1}{2}H_c$. A further assumption was to allow all of this MMF to be dropped across the two airgaps. Using these two approximations enabled the length of each airgap to be determined, based on the following relationships:

$$\frac{\textbf{Magnet Coercive Force } (mmf_m)}{2} \approx \textbf{2} \times \textbf{Airgap MMF } (mmf_g) \qquad \{3.1\}$$

$$mmf_m = H_C \times \ell_m = \frac{B_r\ \ell_m}{\mu_o\ \mu_m} \qquad \{3.2\}$$

$$mmf_g = \frac{B_g\ \ell_g}{\mu_o} \qquad \{3.3\}$$

From {3.1} . . . . $$\frac{B_r\ \ell_m}{2\ \mu_o\ \mu_m} \approx \frac{2\ B_g\ \ell_g}{\mu_o} \qquad \{3.4\}$$

$$\therefore \quad \ell_g \approx \frac{B_r\ \ell_m}{4\ B_g\ \mu_m} \qquad \{3.5\}$$

In order to select a suitable value for ℓ_m, equation 3.5 was evaluated using a predetermined airgap length. As a high airgap flux density (≈1.5T) was desirable a small airgap length was required. The minimum value deemed mechanically acceptable was 0.5mm per airgap. Taking the magnet characteristics for NdFeB from Appendix B.1 (B_r = 1.2 T and μ_r = 1.19) equation 3.6 gave a magnet active length of 2.98mm (≈3mm).

$$\ell_m \approx \frac{4 B_g \mu_m \ell_g}{B_r} \qquad \{3.6\}$$

3.2.3 Ratio of Magnet/Pole Width

With a fixed circumferential magnet length (3mm), the per pole length of the rotor iron could be determined. Inefficient utilisation of the iron could have occurred if there was too much rotor iron in the machine, which would have also reduced the magnitude of flux concentration. If there had been insufficient rotor iron, there would have been additional problems resulting from leakage flux fields and saturation. Previous work carried out on permanent magnet machines at Newcastle University, [24] suggested that a rotor iron width of at least twice the magnet length would give optimal performance; this indicated a pole pitch of 9mm.

The predetermined rotor outside diameter of 300mm, equated to an outer circumference of 942mm, which implied a pole number of 104 based upon a 9mm pole pitch. Reducing this number to 100 increased the pole pitch to 9.42mm, increasing the rotor iron width by 7% per pole.

3.2.4 Rotor Iron Dimensions

The active portion of the rotor may be considered a hoop or toroid, and as such has an inner and outer diameter. The rotor outside diameter (OD) was set at 300mm, with an OD pole pitch of 9.42mm, which enabled the other active dimensions, radial height (RH) and axial width (AW) to be established. The length of RH was limited by the rotor iron width narrowing at its inner radius. Restricting the ratio of rotor outer/inner radius iron width to 70% gave a rotor inner radius width of 4.5mm, equating to an RH figure of 30mm.

3.2.5 Flux Concentration

In figure 3.2, a segment of toroidal rotor is shown. It can be seen from this diagram that increasing either RH or AW would increase the surface area of the magnet. The level of flux concentration presented to the airgap depended upon the mean rotor width (RW) and the value of AW, whereas the predominant effect of RH was seen in the stator iron depth.

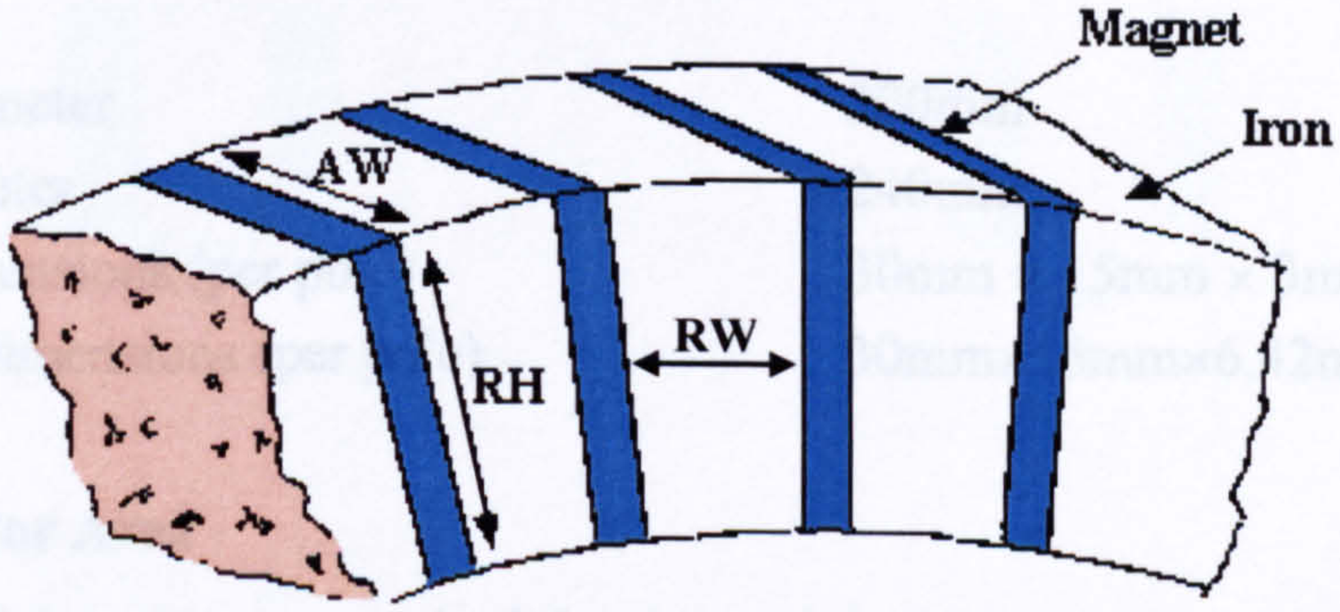

Figure 3.2 Annotated rotor section of the DSTFM

The level of flux concentration depended upon a number of factors; the saturation level in the rotor iron, the operating point of the magnet, the physical dimensions of the rotor and the magnitude of the rotor leakage fields. The large magnet peripheral length indicated a high degree of rotor leakage, which meant a low level of airgap flux and hence stator tooth flux. Therefore, flux concentration had to be high in order to compensate for these leakage fields, but not so high that the magnet was pushed too far down its second quadrant BH characteristic, risking some permanent demagnetisation. Selecting a minimum magnet operating point (B_m) of 0.3T, 25% of the residual value, gave the NdFeB magnet a coercive force of 200kA/m (see Appendix B.1). Coupling that value of B_m with an airgap flux density (B_g) of 1.5T (equation 3.7) indicated a value of flux concentration in the region of five was appropriate.

$$\textit{Flux Concentration} = \frac{B_g}{B_m} \qquad \{3.7\}$$

$$\textit{Flux Concentration} \approx \frac{2\ AW}{RW} \qquad \{3.8\}$$

The affect of this level of flux concentration on the rotor parameters (figure 3.2) was determined from equation 3.8. A mean rotor width of 5.5mm, based upon outer and inner iron widths of 6.42mm and 4.5mm respectively, together with a flux concentration of five required an axial width (AW) of approximately 15mm.

Bringing together the parameters determined throughout section 3.2 gave the following overall dimensions for a 100 pole DSTFM rotor:

- Outside Diameter 300mm
- Inside Diameter 240mm
- Magnet Dimensions (per pole) 30mm × 15mm × 3mm
- Rotor Iron Dimensions (per pole) 30mm×15mm×6.42mm×4.54mm

3.2.6 Conductor Area

The initial parameter required for determining the stator's dimensions is the conductor area, as a TFM stator is formed around this area. Preliminary calculations derived from the magnet data (Appendix B.1) suggested that with an active length of 3mm, the operating MMF of the magnet would be around 2000Ampereturns. To prevent demagnetisation of the magnet the conductor MMF was also restricted to this value. Assuming a fill factor of 0.5 and a current density of $10A/mm^2$, this pointed to a conductor area of $400mm^2$.

3.2.7 Stator Coreback Dimensions

A major consideration in determining the stator coreback thickness was the low physical strength of the SMC material in shear or tensile load situations (Appendix B.1). The high torque expected from the prototype machine, meant that preliminary mechanical calculations were made, which suggested a coreback thickness of 15mm would be sufficient to ensure mechanical integrity. This was a larger value than the electromagnetic requirements of the machine would have warranted, which meant that coreback flux density would be low.

3.2.8 Stator Tooth Dimensions

Stator teeth have two parameters; width and length. Tooth width is a compromise between the effect of leakage flux if the tooth is too wide (figure 3.3a)

and saturation if the tooth is too narrow (figure 3.3b). The tooth length is also a compromise, between leakage flux if the tooth is too short (figure 3.3c) and reluctance if the tooth is too long (figure 3.3d).

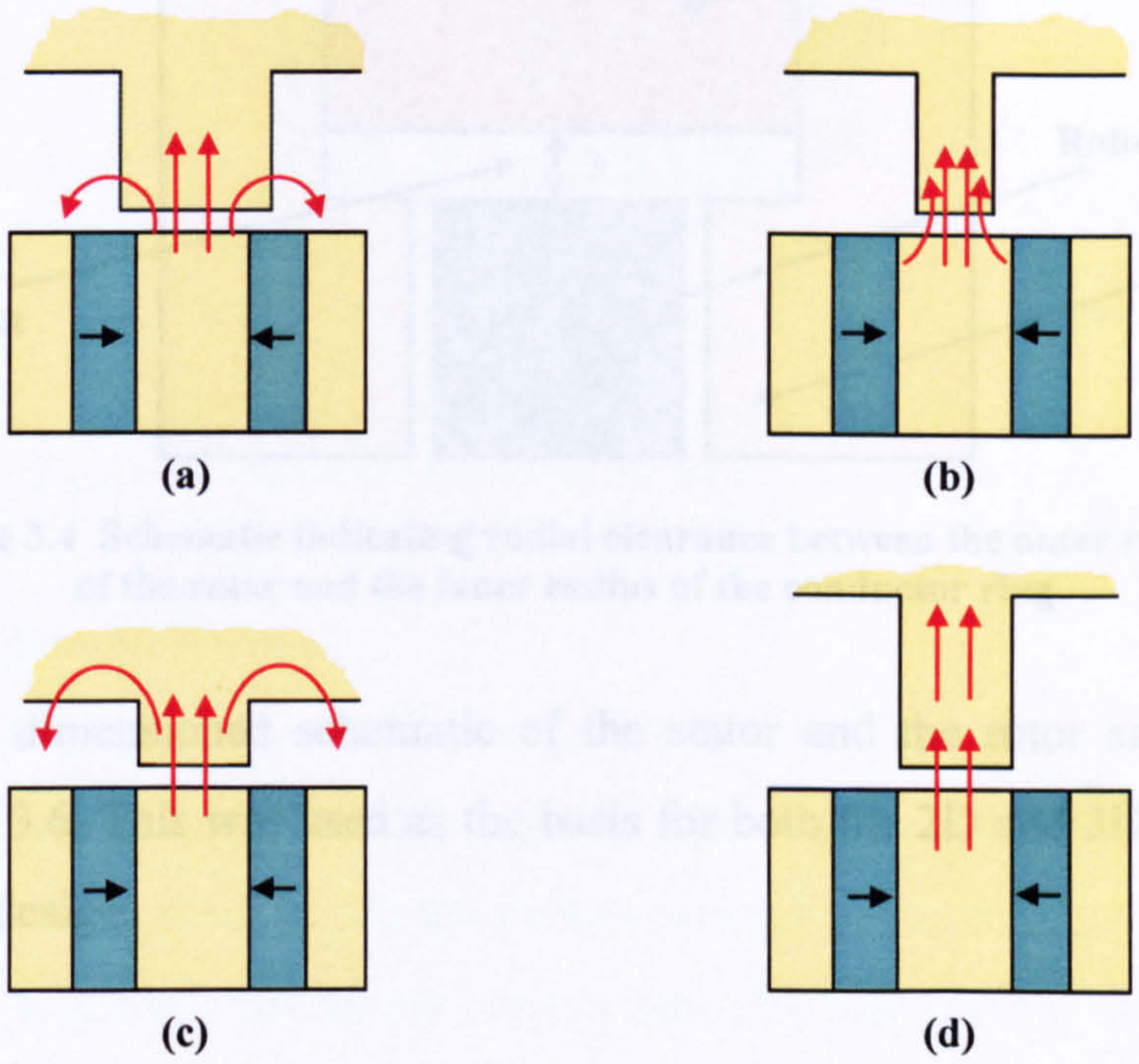

Figure 3.3 The effect of tooth shape on the passage of flux in a TFM

Choosing the tooth length was based upon the criteria above and their affect on the overall dimensions of the machine. The teeth were dimensioned to match the width of the rotor iron at the outside diameter, namely 6.5mm. The tooth width for this particular machine design was to be kept uniform rather than tapering radially in sympathy with the rotor iron segments. This reduced demands on physical machining as well as producing a slight overlap on the magnets on the inner radius, which should theoretically reduce the level of cogging torque experienced in the prototype. As a starting point, teeth were designed to be as deep as they were wide [8]. With a rotor iron width of 6.42mm already proposed, a tooth 7mm long seemed appropriate.

3.3 Overall Dimensions

The clearance required between the conductor and the top of the rotor (figure 3.4) had to be large enough to allow for possible 'banding' of the outer circumference of the rotor, and to allow actual clearance between the stationary conductor and the spinning rotor. An 'airgap' of 3mm was considered adequate clearance. Linking this

clearance value with the stator iron thickness of 15mm allowed the proposed geometry to be fully defined.

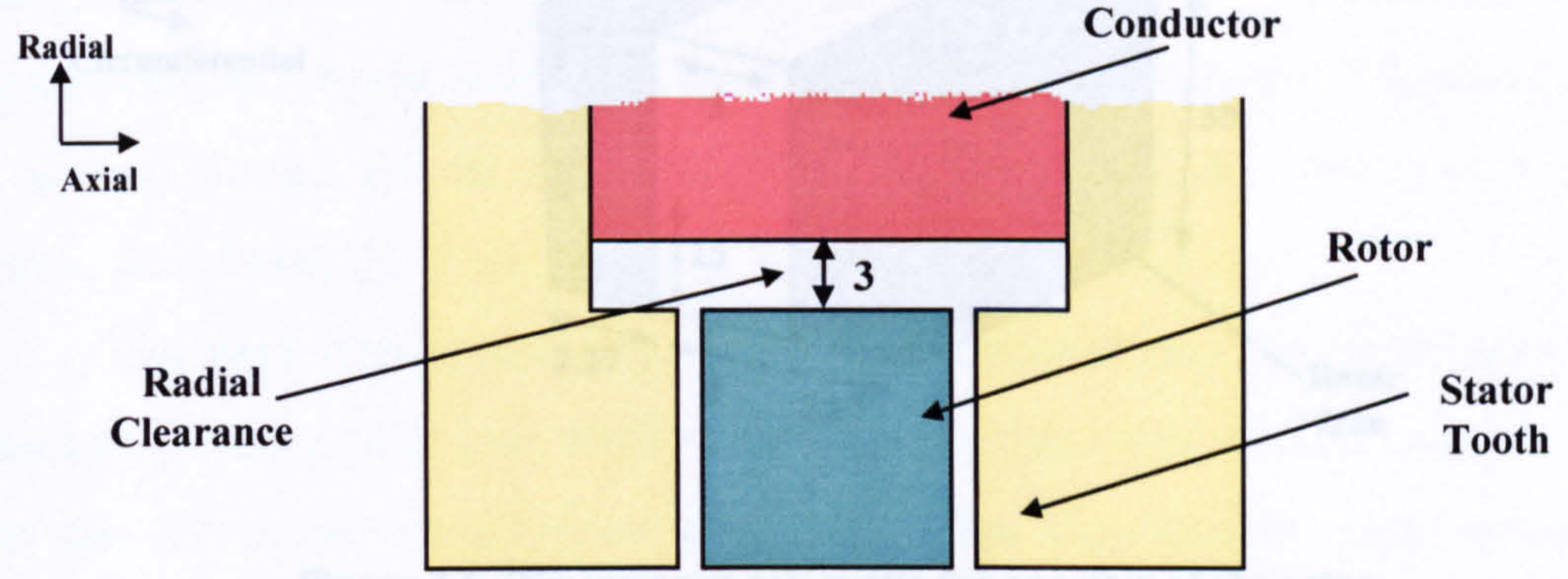

Figure 3.4 Schematic indicating radial clearance between the outer radius of the rotor and the inner radius of the conductor ring

A fully dimensioned schematic of the stator and the rotor are presented in figures 3.5 and 3.6. This was used as the basis for both the 2D and 3D finite element analysis of the design.

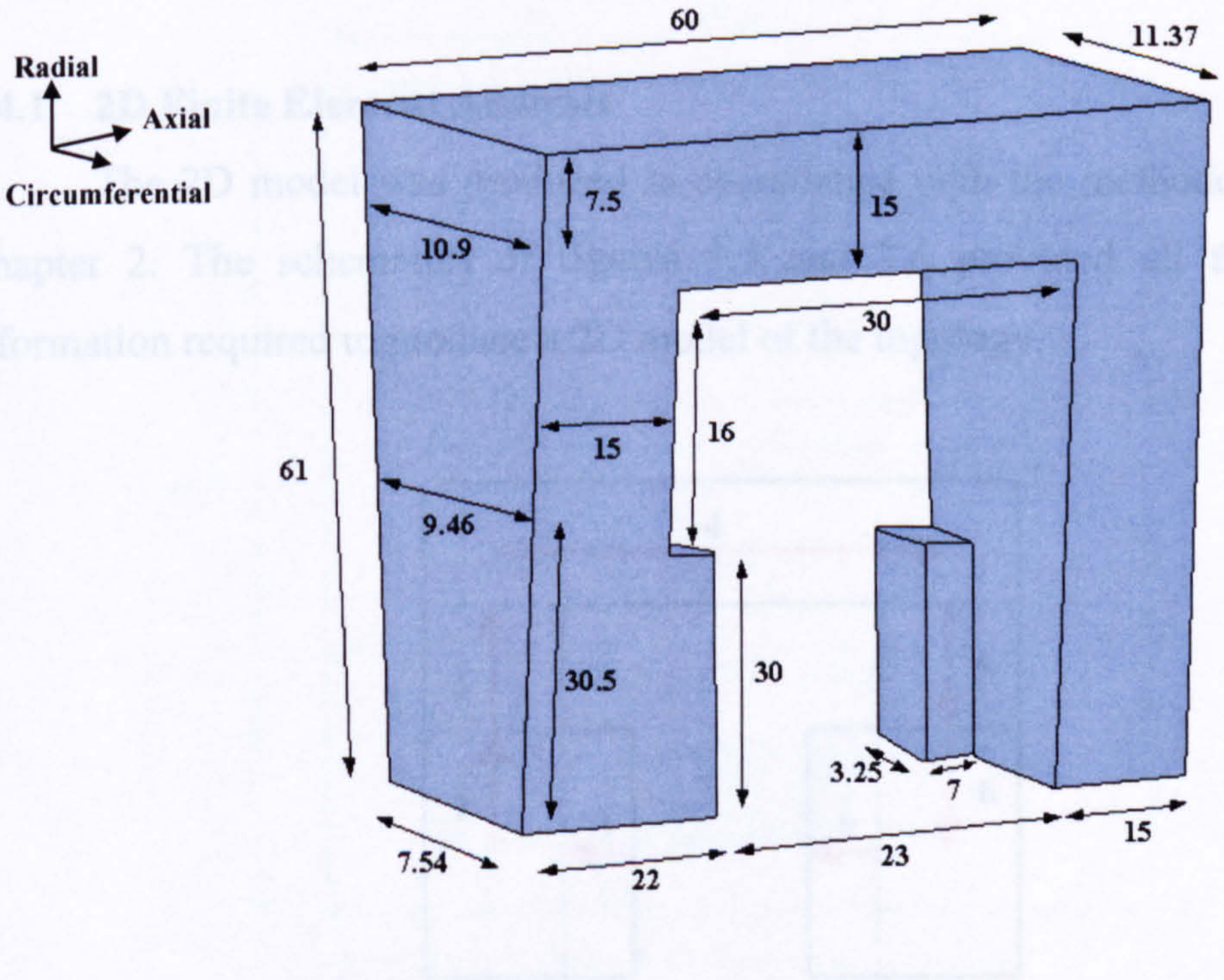

Figure 3.5 Dimensioned schematic for one pole of the stator

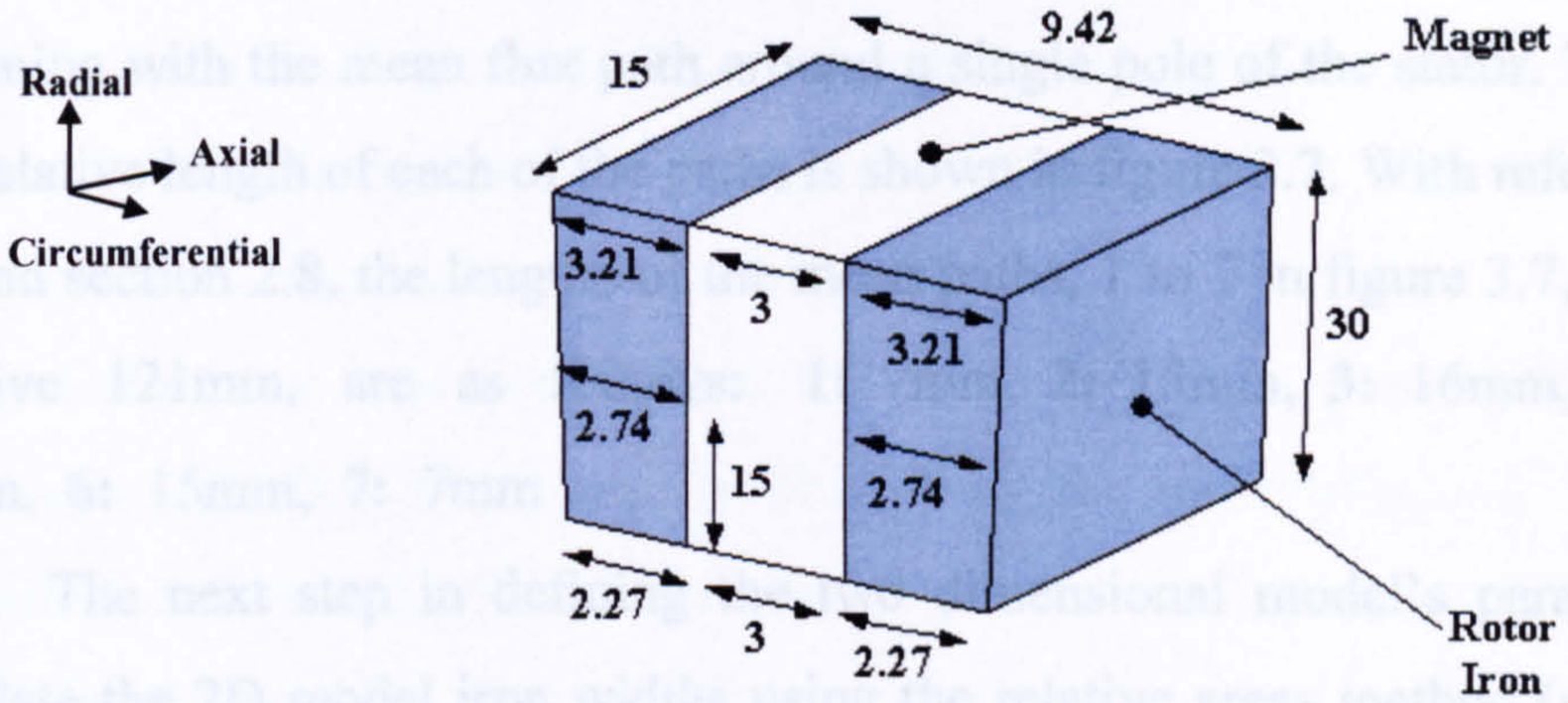

Figure 3.6 Dimensioned schematic for one pole of the rotor

3.4 Finite Element Analysis

With the dimensions for the proposed DSTFM established, finite element models were developed for analysis. Initially, this was in 2D, then in 3D for final verification before construction on the prototype began. The main aim of the 2D FE simulation was to gather data on the performance characteristics of the machine and the flux densities experienced by different sections of the model.

3.4.1 2D Finite Element Analysis

The 2D model was produced in accordance with the methodology set out in Chapter 2. The schematics of figures 3.5 and 3.6 provided all the dimensional information required to produce a 2D model of the topology.

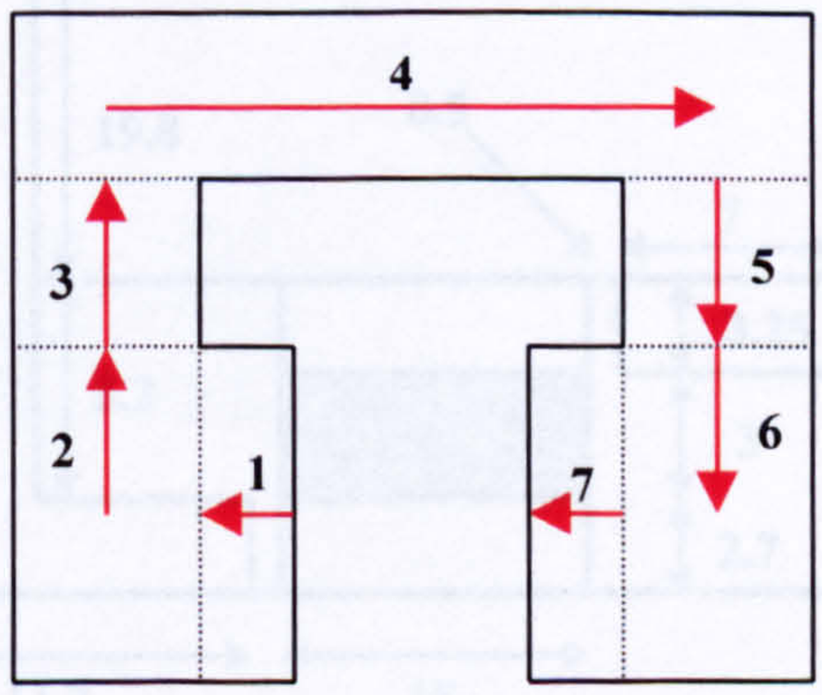

Figure 3.7 Stator mean flux paths

The methodology proceeded with the derivation of the 2D model dimensions, beginning with the mean flux path around a single pole of the stator. The orientation and relative length of each of the paths is shown in figure 3.7. With reference to figure 3.5 and section 2.8, the lengths of the mean paths, 1 to 7 in figure 3.7, which sum up to give 121mm, are as follows: **1:** 7mm, **2:** 15mm, **3:** 16mm, **4:** 45mm, **5:** 16mm, **6:** 15mm, **7:** 7mm

The next step in defining the two dimensional model's parameters was to calculate the 2D model iron widths using the relative areas method (section 2.4), so that the 2D model would have appropriate flux densities in each section. The calculations to derive these widths are presented in Appendix D.8.1. These dimensions were incorporated into the 2D model, along with the mean flux path lengths which defined the path length around the internal periphery of the stator iron. The 2D FE model, illustrated in figure 3.8, was produced from these dimensions. It should be noted that the model had an envelope of air around the teeth, magnet, and rotor iron to allow the passage of leakage and fringing fluxes.

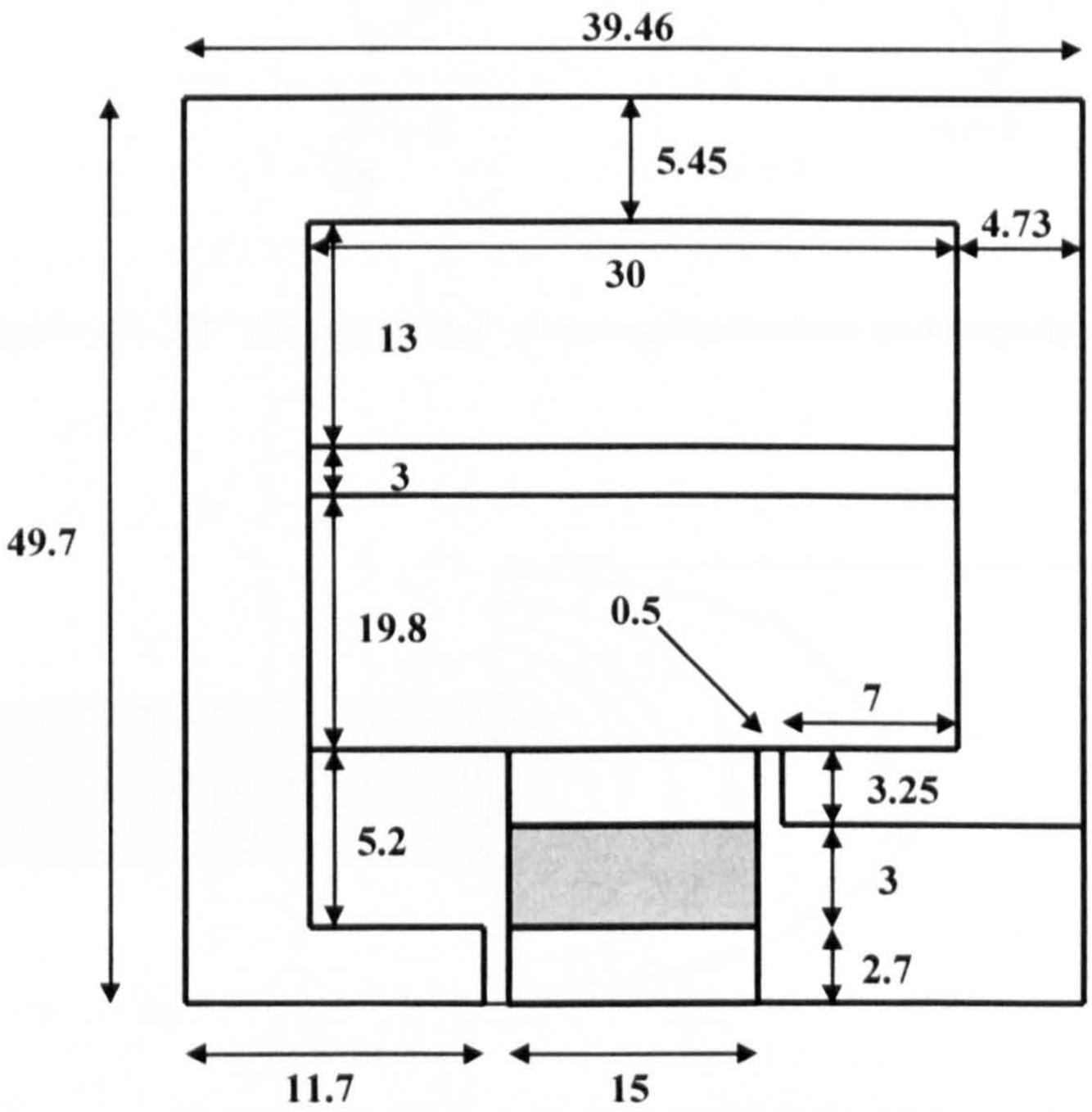

Figure 3.8 Fully dimensioned 2D FE model of the DSTFM

As stated in section 3.2.6, the rated MMF in the prototype would be 2000Ampereturns. Simple calculations (Appendix D.8.2) predicted that the cross slot leakage fields contributed to less than 5% of the machine flux at rated load and therefore did not need to be accurately modelled.

There was, however, a need to scale the magnet permeability in order to incorporate the effect of the leakage flux along the unmodelled sides of the magnet (Chapter 2, section 2.6). Therefore, a two dimensional 'airgap model' (figure 3.9) was created for this purpose.

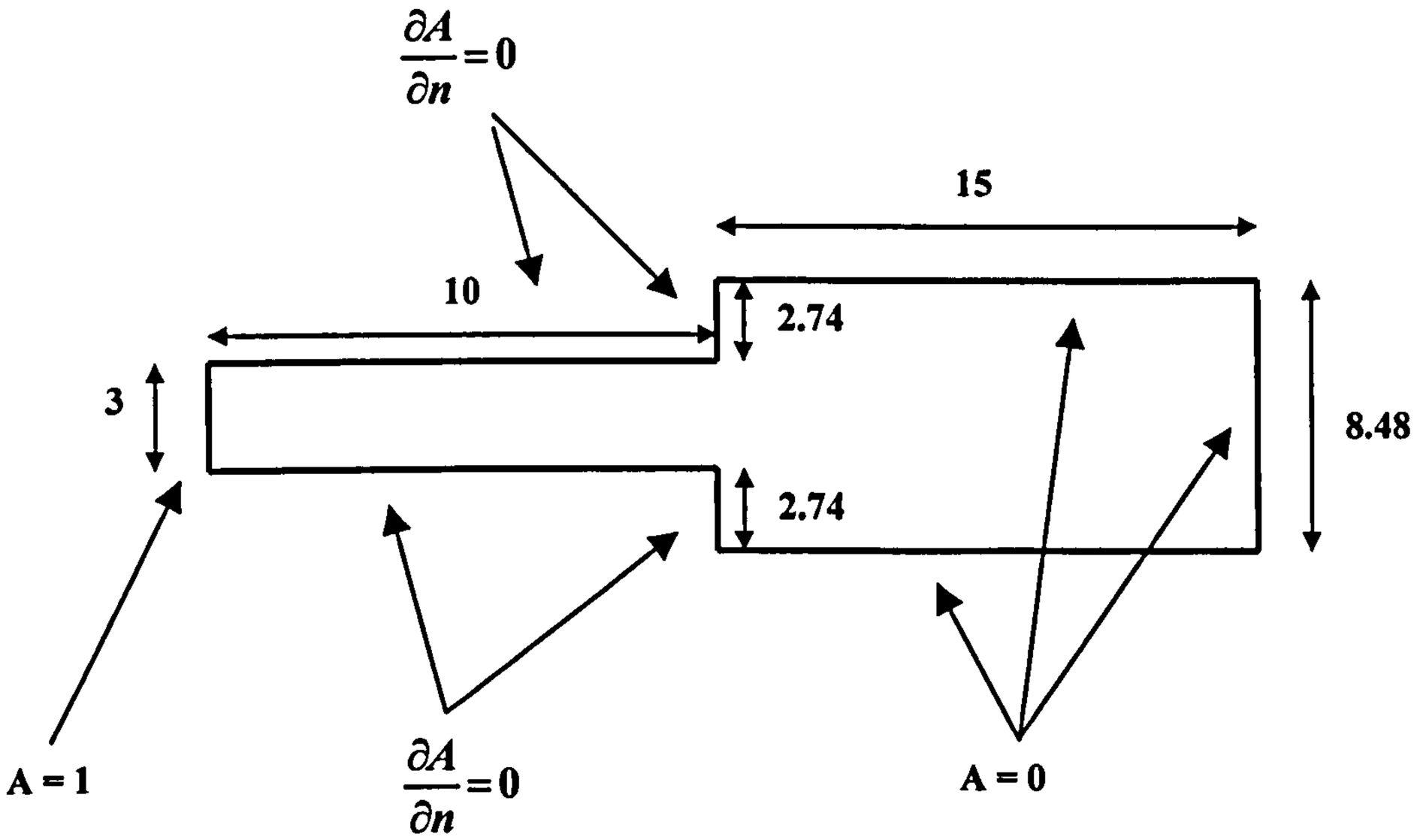

Figure 3.9 2D "Airgap Model" showing dimensions and boundary conditions

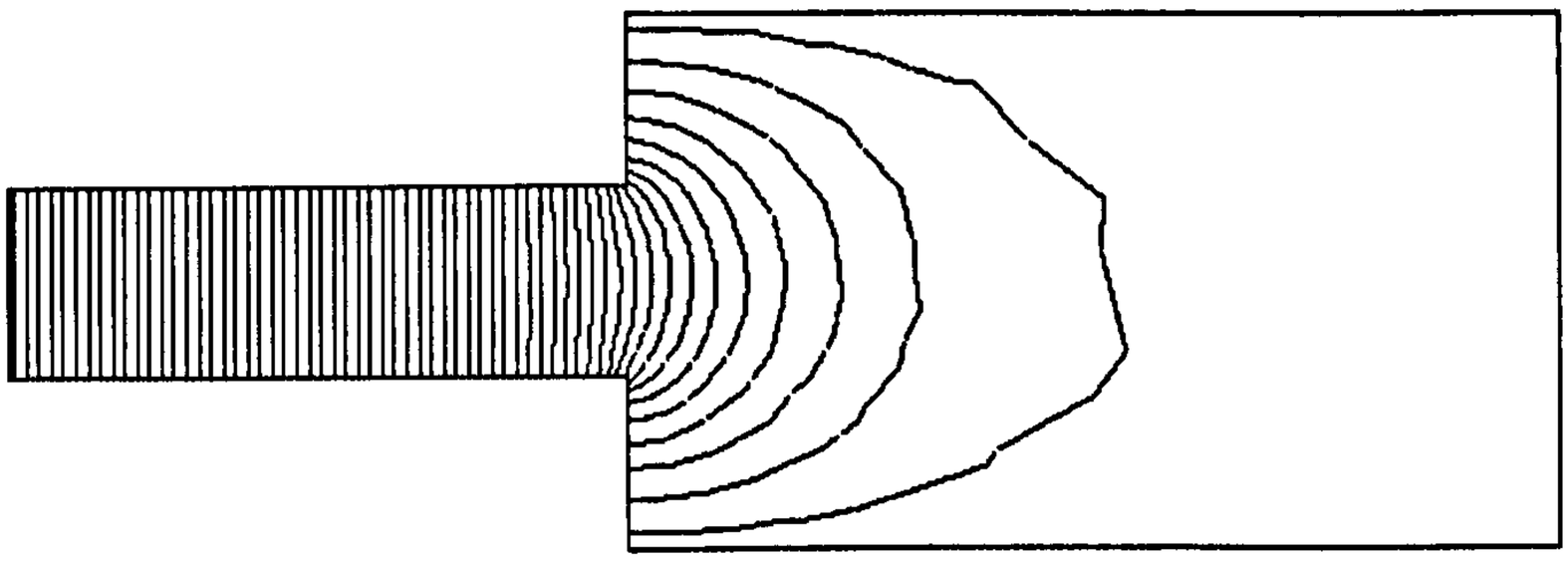

Figure 3.10 FE flux contour plot for the airgap model

The flux contour plot produced from the FE model is shown in figure 3.10 for a fixed total flux of 1.0 Wb/m flowing through the model. Using the same procedures presented in section 2.6, this model gave the following data:

Measured MMF 0.201×10^6 Ampereturns

Effective Length $\dfrac{3 \times 10^{-3}}{4\pi \times 10^{-7} \times 0.201 \times 10^6} = 11.877 \times 10^{-3}\, m$

Actual Length $= 10 \times 10^{-3}\, m^2$

The difference between the actual length and effective length was 1.877mm. This effect occurred at both the inner and outer radii of the magnets, making their effective length 33.8 mm. Using this value the modified magnet permeability, μ_{2D}, was calculated using equation 2.4.

$$\mu_{2D} = 1.19 \times \frac{33.8 \times 10^{-3}}{30 \times 10^{-3}} = 1.34$$

All the information required to build a 2D model of the DSTFM had now been gathered. The boundary conditions and materials data for the model were as follows:

- The model was shown in the fully aligned position.
- The entire periphery of the model was fixed at zero magnetic potential (A = 0) in order to channel the flux along the paths it would naturally follow in the real stator iron.
- The data used for the materials in this finite element simulation were as follows:

Magnet Data:	Flux Density	1.2T (in 'y' axis)
	Relative Permeability	1.34 (originally 1.19)
Iron Data:	Relative Permeability	Non-linear ABM100.32 data (see Appendix B.1)
Non-Magnetic Barrier:	Relative Permeability	0.01
Conductor / Air:	Relative Permeability	1

Using this information a 2D model was constructed and analysed over an MMF range of ±4000 AT, which was double the mean stator MMF and chosen because it took the coreback iron into saturation. This allowed the characteristics of the model to be fully explored. The results from the 2D FE simulation are presented in Appendix E.1.1.

Figure 3.11a shows the no-load flux contour plot for the model. Examining the flux paths in the model revealed the leakage and fringing fields around the magnet and airgap areas. Figure 3.11b is a plot of the 2D FE mesh, which contained 1292 nodes and 2479 elements, used to determine the prototype's electromagnetic characteristics. Detail of the mesh around the rotor/airgap/tooth area is shown in figure 3.11c.

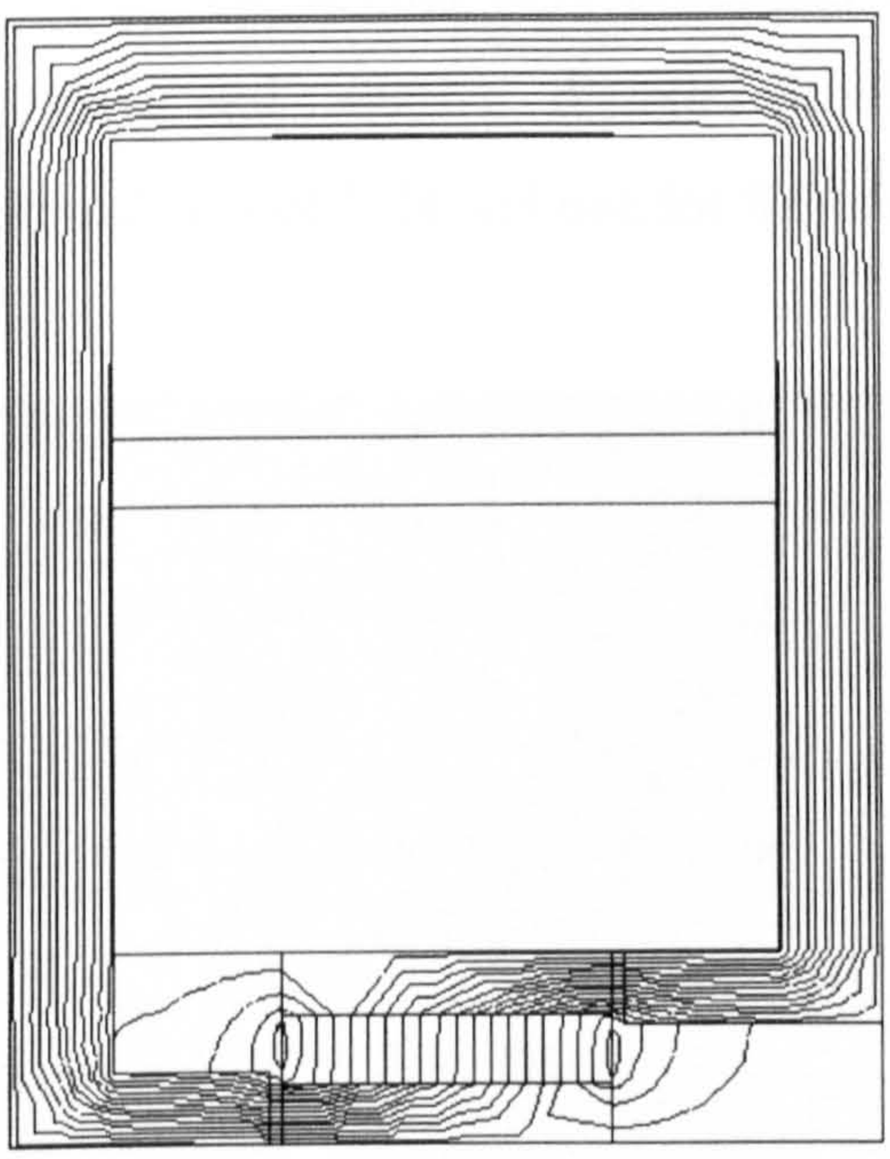

Figure 3.11a No-load flux contour plot of the 2D DSTFM finite element model

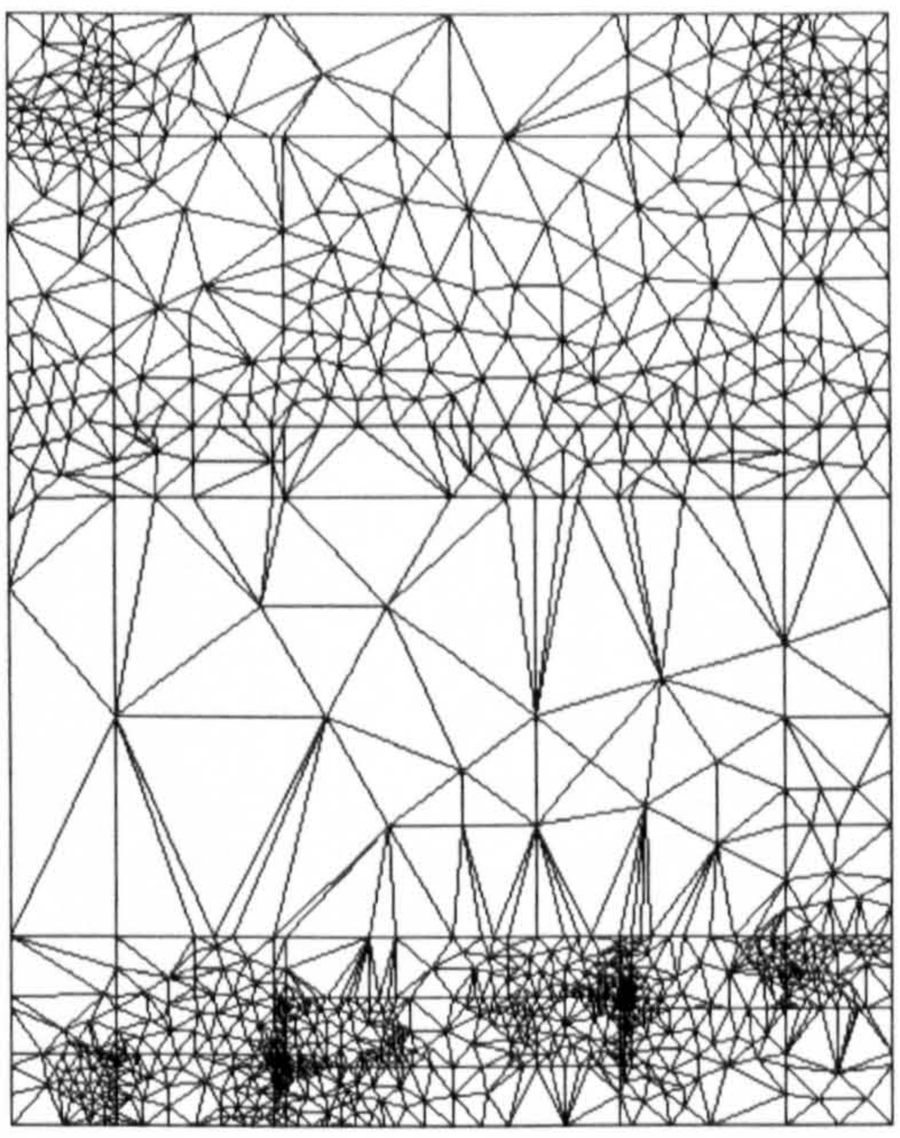

Figure 3.11b Finite element mesh for the 2D model

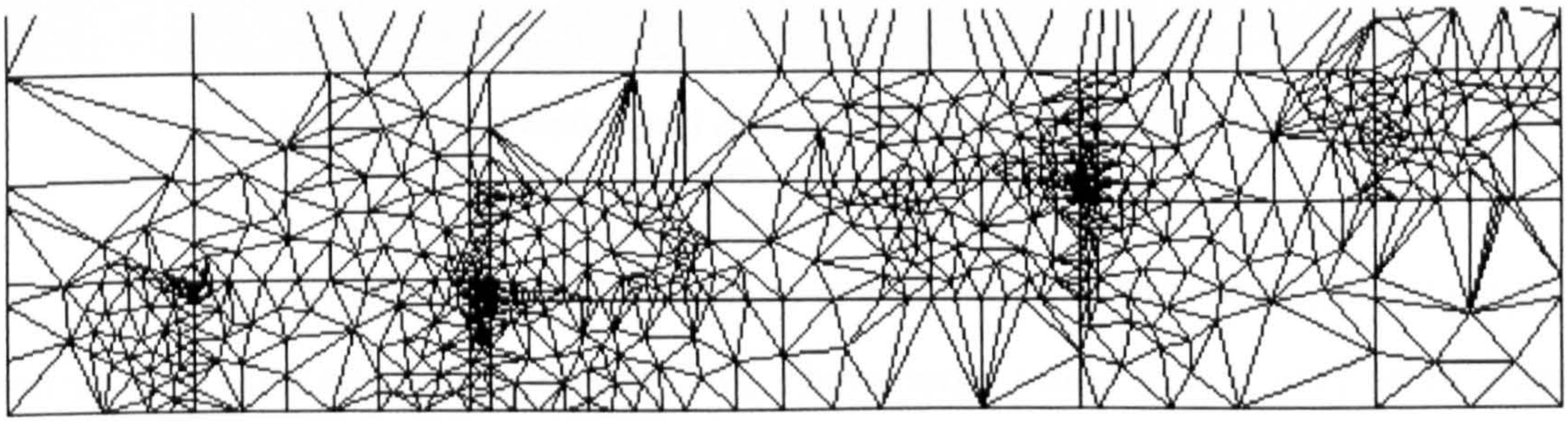

Figure 3.11c Detail of the 2D FE mesh around the rotor

3.4.2 2D Finite Element Results

Gathering data on the performance characteristics of the machine to enable reasonable evaluation of the topology's capabilities, was the main task of the 2D analysis. Examination of the no load flux, produced the following modulus levels of flux density in the 2D model:

Magnet	-	0.56T
Airgap	-	1.47T
Teeth	-	1.5T
Coreback	-	0.43T
Rotor Iron	-	1.51T

These results were processed to produce two sets of aligned and unaligned (positive and negative 'd' axis) flux/MMF curves (figure 3.12), one for a magnet permeability of 1.34 and one for the unaltered model with magnet μ_r of 1.19.

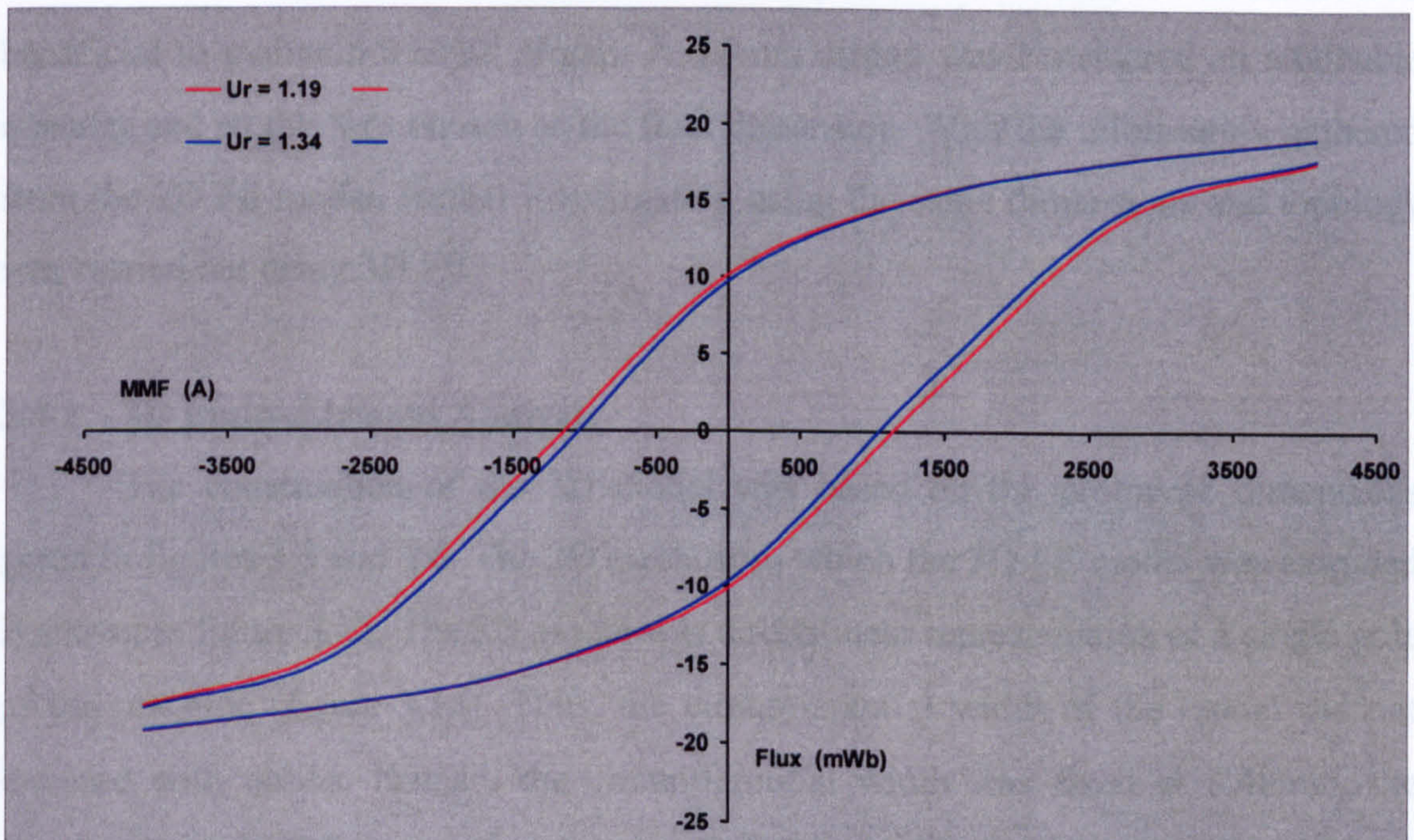

Figure 3.12 Positive and negative 'd' axis Flux-MMF curves for 2D models with μ_r = 1.19 and μ_r = 1.34

The area enclosed by the two curves is equivalent to the mean energy output of the machine (section 2.10, equation 2.6). This energy value was converted into mean torque using equation 2.7. Two output values were calculated, one for the entire area

enclosed by the flux/MMF curves and a second for the area bounded by the positive and negative "working MMF" limit of the prototype (±2000AT). Both the energy envelope results and equivalent mean torque value, based upon a value for $\Delta\theta$ of $(2\pi)/50$, are given in table 3.1.

Table 3.1 2D model Ψ-I energy and torque results

	Energy (Joules)	Mean Torque (Nm)
Flux/MMF Limit	70.71	562.7
Working Limit	43.08	342.9

The 2D results confirmed that a double-sided TFM of this geometry would produce very high levels of output. With such high forces, a larger airgap would be easier to maintain than a small one. Therefore, an additional investigation was carried out into the effect of increasing the airgap length from 0.5mm to 1mm. The results of this simulation showed a reduction in overall output of 29%. Thus, it was considered beneficial to maintain a small airgap. A 0.5mm airgap was considered an attainable quantity and so this was chosen as the final dimension. With the information gathered from the 2D FE model, further investigation using the same dimensions and topology was carried out using 3D FE.

3.4.3 3D Finite Element Analysis

The construction of the 3D model was based on the prototype dimensions given in figures 3.5 and 3.6. The 2D mesh from which the 3D FE model was extruded is shown in figure 3.13. The 3D model was a rectilinear representation of a single pole of the machine (figure 3.14). Thus, the circumferential width of the model did not increase with radius. Instead, the circumferential width was fixed at 8.48mm, the mean pole pitch of the rotor. For reasons of clarity, the 3D model is shown without its radial and axial envelope of air.

Once more, the MMF in the model was varied to determine the winding flux linkage in the aligned position. Flux against MMF data was used to determine the magnitude and characteristics of the model's output. Leakage mechanisms were also examined in order to gauge their effect on the machine's overall performance. As this

was a three-dimensional model, surrounded radially and axially by a 10mm envelope of air, there should be no unmodelled flux leakage paths. Consequently, none of the material data from the original specification needed to be scaled or adapted in any way. The 3D materials data for this model is presented in table 3.2.

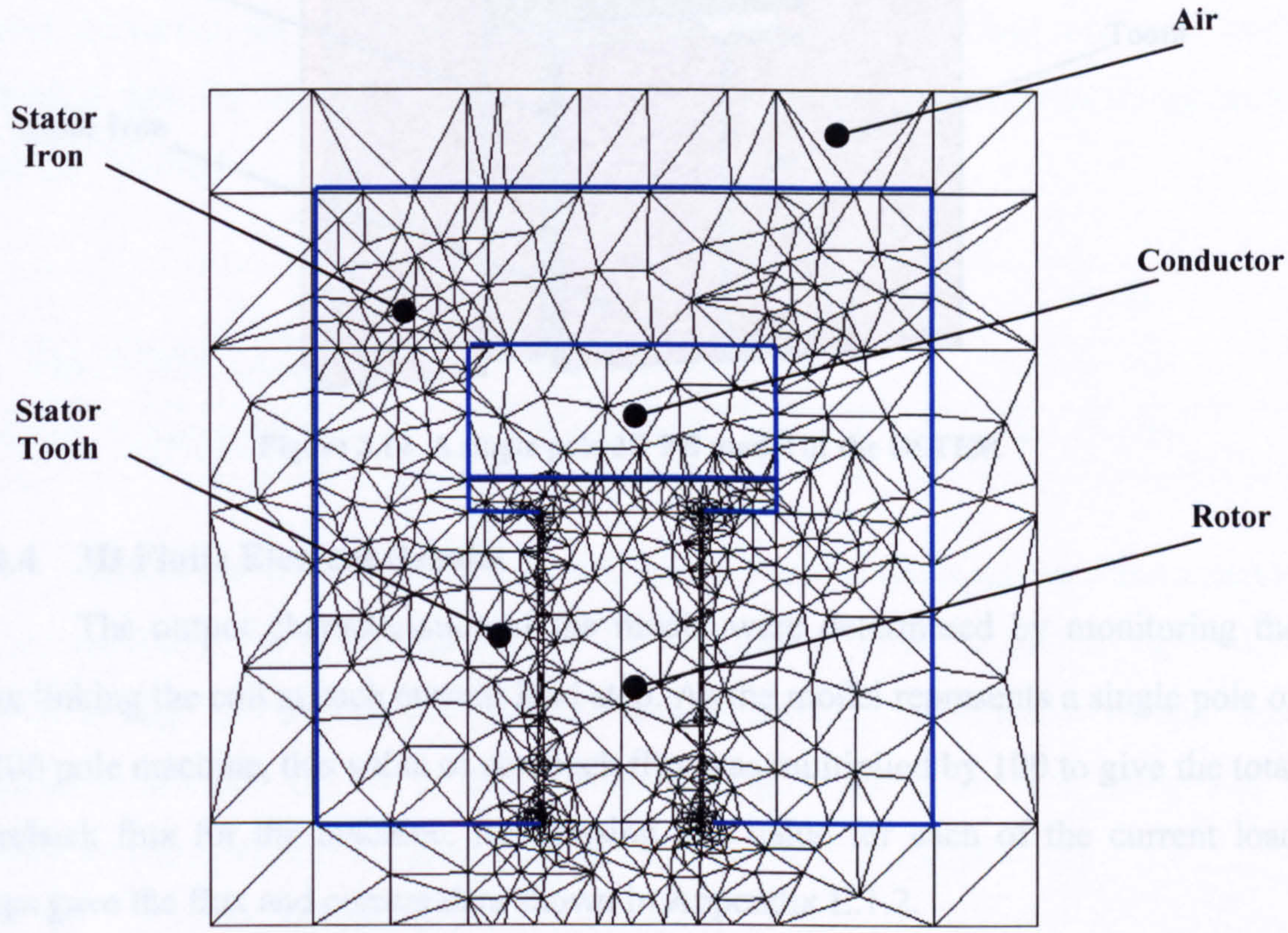

Figure 3.13 DSTFM 2D mesh before extrusion into 3D

Table 3.2 Materials data for the DSTFM 3D FE model

Material	Relative Permeability	Additional Information
Air	1	none
Stator Iron	Non-Linear ABM100.32	see Appendix B.1
Rotor Iron	Non-Linear ABM100.32	see Appendix B.1
Magnet	1.19	B_r = 1.2 Tesla
Conductor	1	copper

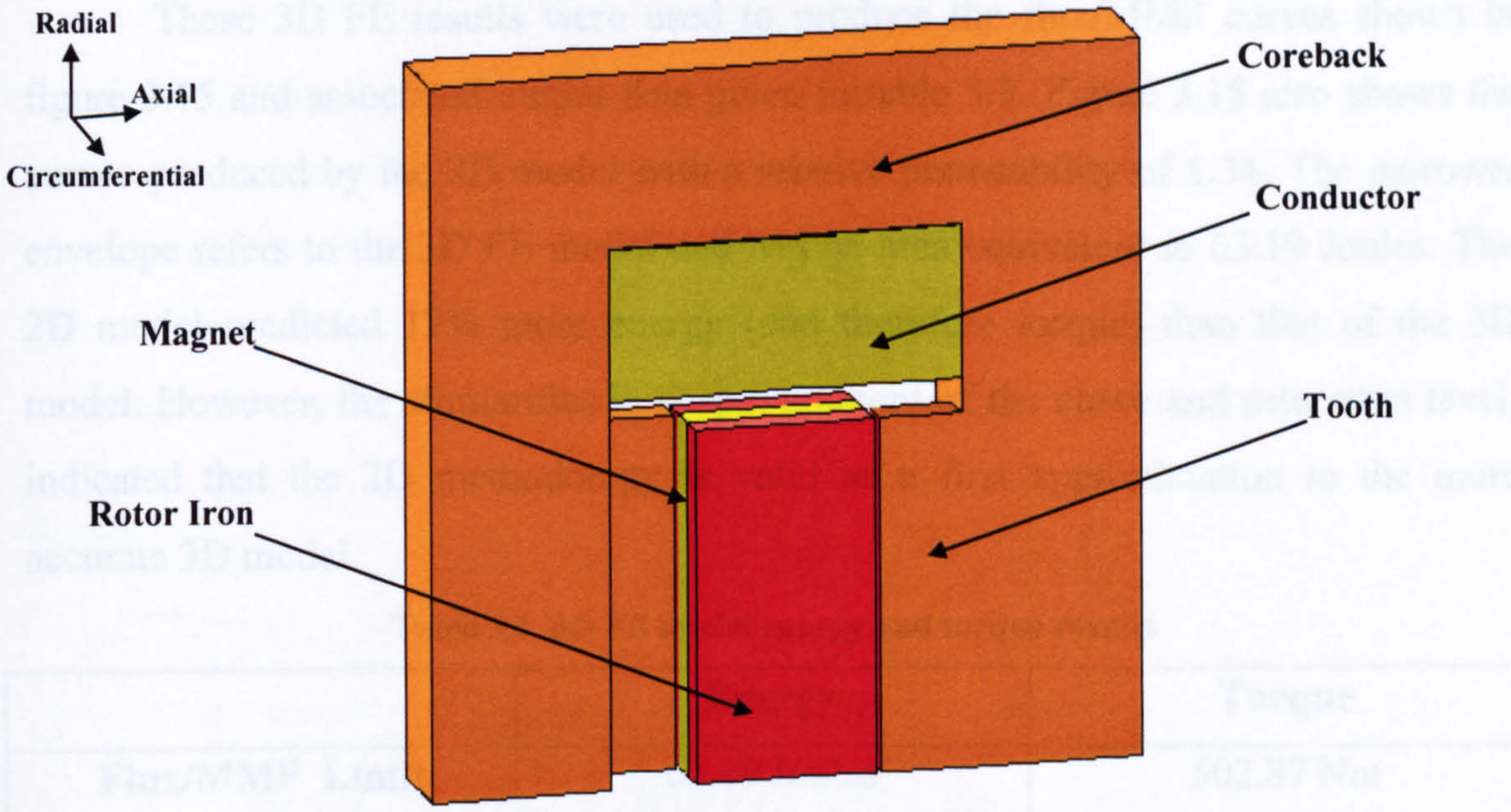

Figure 3.14 A single pole 3D FE model of the DSTFM

3.4.4 3D Finite Element Results

The output characteristics of the model were determined by monitoring the flux linking the coil at each current load step. As the model represents a single pole of a 100 pole machine, this value of coreback flux was multiplied by 100 to give the total coreback flux for the machine. Reassessing this value for each of the current load steps gave the flux and current data shown in Appendix E.1.2.

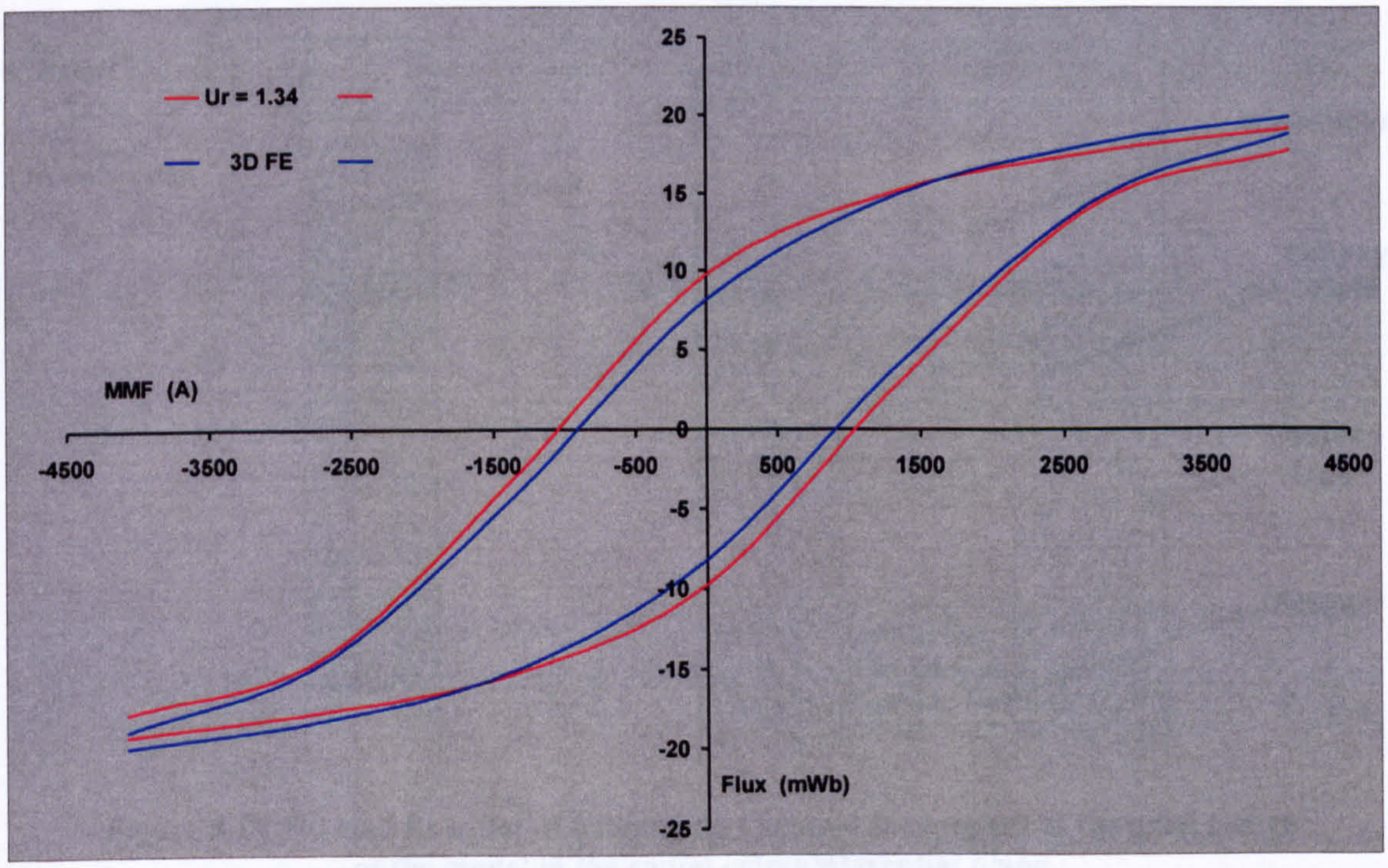

Figure 3.15 2D and 3D FE positive and negative 'd' axis Flux-MMF curves for the DSTFM

These 3D FE results were used to produce the flux/MMF curves shown in figure 3.15 and associated output data given in table 3.3. Figure 3.15 also shows the curves produced by the 2D model with a relative permeability of 1.34. The narrower envelope refers to the 3D FE model and had an area equivalent to 63.19 Joules. The 2D model predicted 12% more energy (and therefore torque) than that of the 3D model. However, the similarities in shape, gradient of the curve and saturation level, indicated that the 2D methodology is valid as a first approximation to the more accurate 3D model.

Table 3.3 3D FE model energy and torque results

	Energy	Torque
Flux/MMF Limit	63.19 Joules	502.87 Nm
Design Limit (±2000AT)	50.42 Joules	401.25 Nm

Analysis of the flux paths in the 3D model enabled the magnitude and location of the leakage paths in the topology to be determined. The flux plot in figure 3.16 shows a large circumferential leakage field around the outer radius of the rotor magnet, equivalent to 19% of the no-load coreback flux (81.6μWb). There was a similar level of leakage flux around the inner radius of rotor magnet.

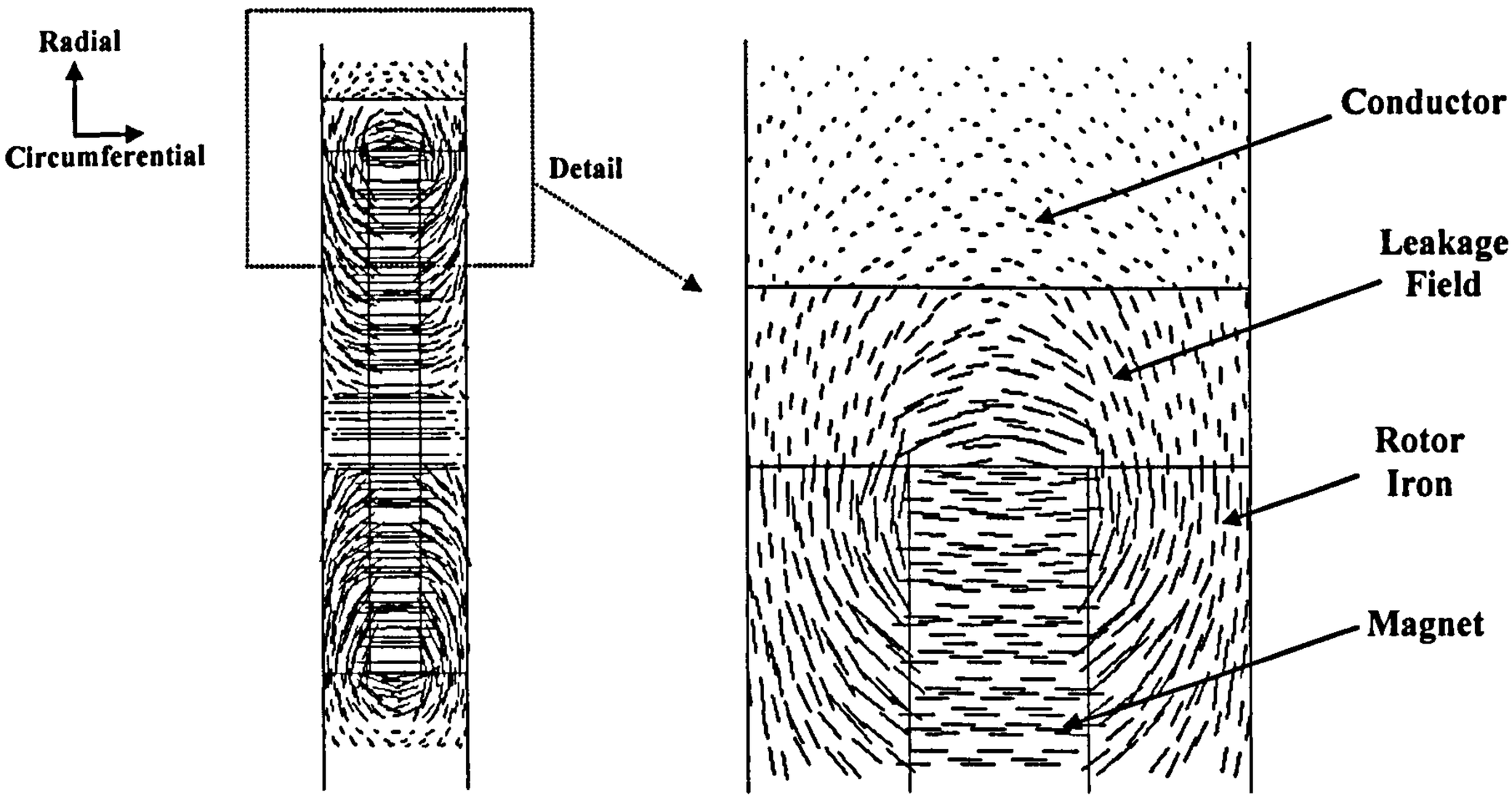

Figure 3.16 No load flux plot of fringing flux around the magnet at the axial centre of the model in the radial / circumferential plane

Viewing the model in the axial/circumferential plane (figure 3.17) allowed the flux leaking along both the radial sides of the magnet to be monitored. These leakage paths, although similar to the radial ones, had a lower reluctance due to the inclusion of stator teeth in their paths. Examining the detailed flux plot of figure 3.18 indicated that the first 20% of the magnet merely sourced the circumferential leakage path, creating a circulating leakage flux around the axial faces of the magnet.

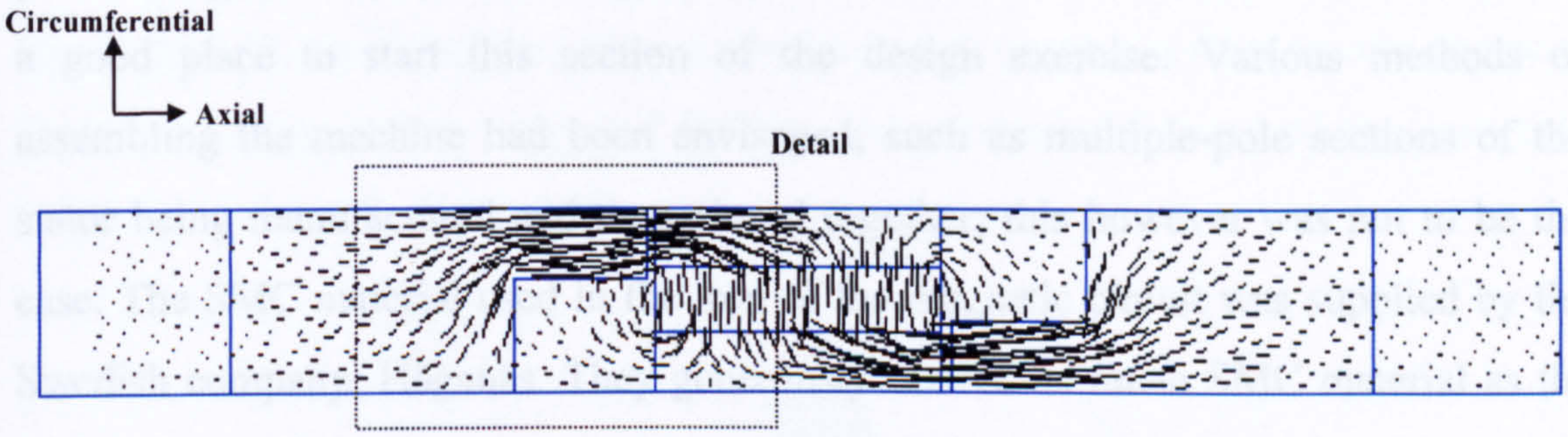

Figure 3.17 No load flux plot of leakage around the magnet in the axial / circumferential plane

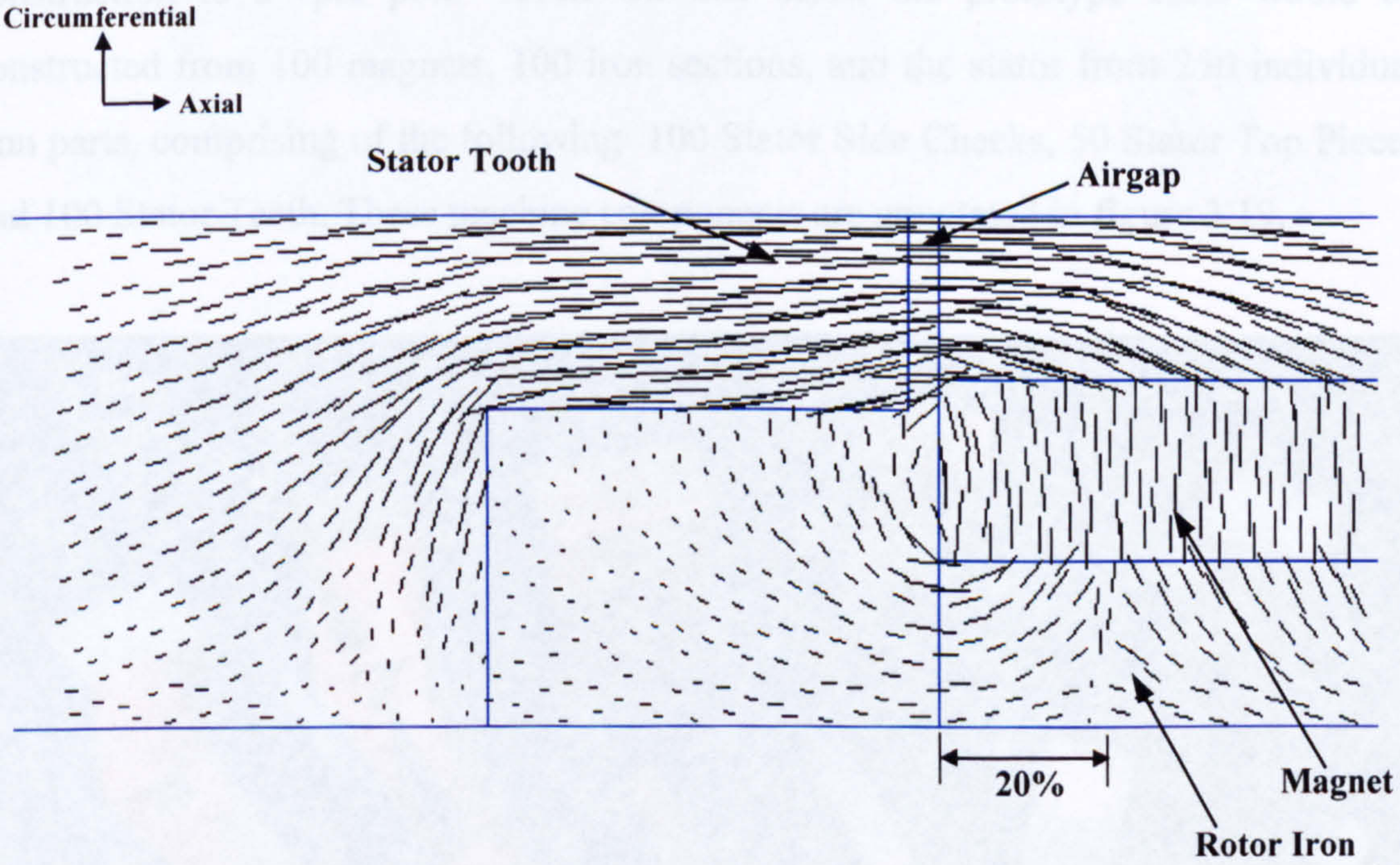

Figure 3.18 Detail of no load flux plot showing leakage around the magnet in the axial / circumferential plane

The 3D FE analysis of the proposed DSTFM showed promising results. Saturation flux densities were only evident at higher MMFs and then limited to the stator teeth and rotor iron. The no load flux leakage fields around the rotor accounted

for 38% of the magnet flux, but despite the magnitude of these rotor leakage fields the model predicted a substantial mean torque output. Therefore, design work on a prototype machine was commenced.

3.5 Constructional Design

With all the theoretical dimensions of the machine finalised, it was time to produce a practical physical design. Determination of the method of construction was a good place to start this section of the design exercise. Various methods of assembling the machine had been envisaged, such as multiple-pole sections of the stator being manufactured and then pieced together; this however was not to be the case. The SMC material used in the iron of the magnetic circuit was supplied by the Swedish company, Höganäs. They generously offered as much SMC material as the project required *free-gratis*, however, they could only supply SMC in 120mm×30mm×2→40mm billets. This effectively restricted the method of construction to a "per pole" level. On this basis, the prototype rotor would be constructed from 100 magnets, 100 iron sections, and the stator from 250 individual iron parts, comprising of the following: 100 Stator Side Cheeks, 50 Stator Top Pieces and 100 Stator Teeth. These machine components are annotated in figure 3.19.

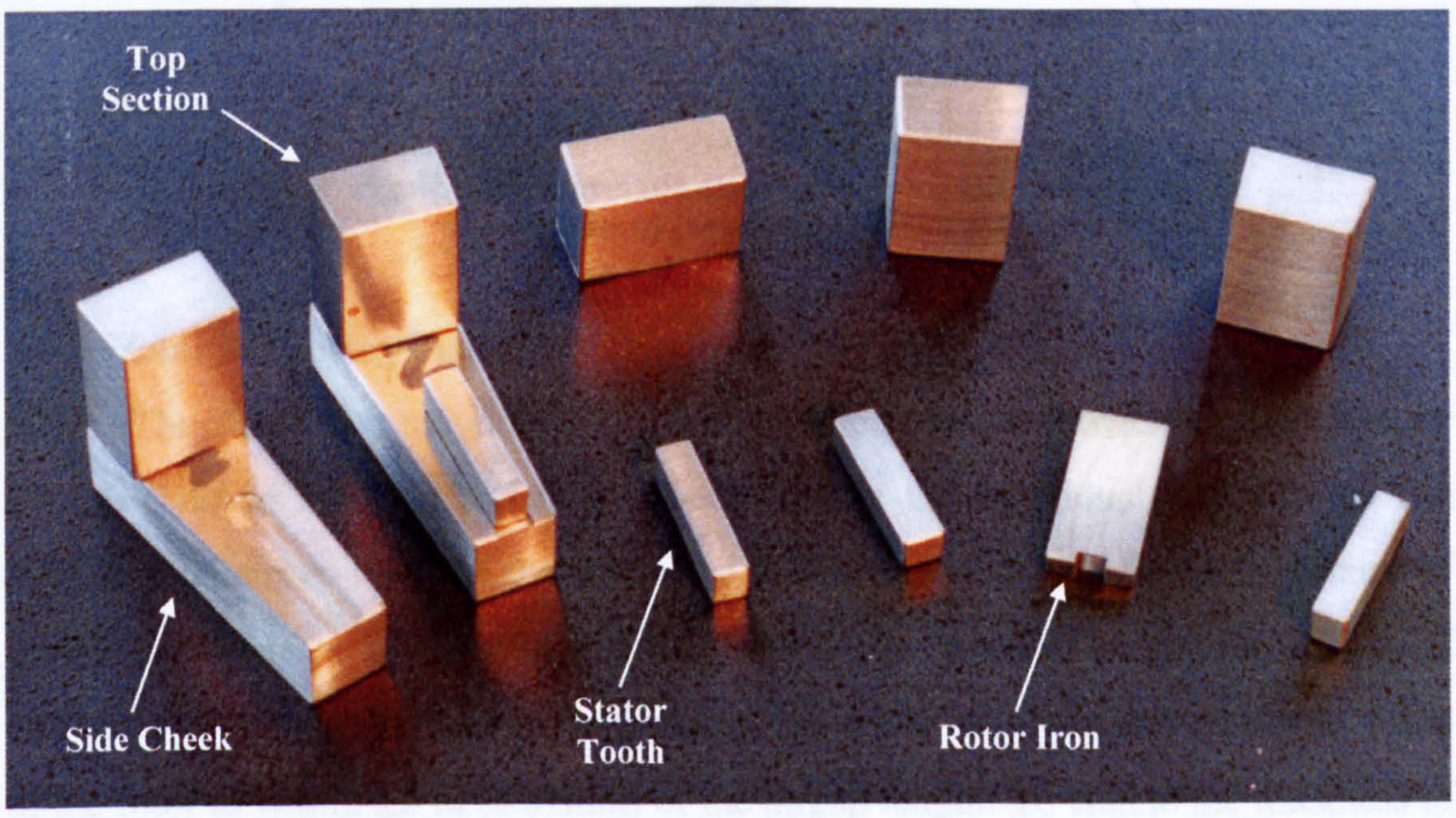

Figure 3.19 Component SMC pieces of the DSTFM

The construction of the new DSTFM was not a simple task for a number of reasons. Both the stator and the rotor were comprised of a large number of component pieces that needed to be positioned relative to one another with a high degree of accuracy. The forces inherent in the prototype were high and the physical framework around the electromagnetically active parts of the machine had to be sufficient to contain these forces. A further problem was the ability to ensure the integrity of the airgap over repeated assembly and disassembly operations. Finally, a test bed was required which could measure angular displacements down to a fraction of a degree at levels of torque in the region of 500Nm. A schematic diagram of the complete assembly is shown in figure 3.20.

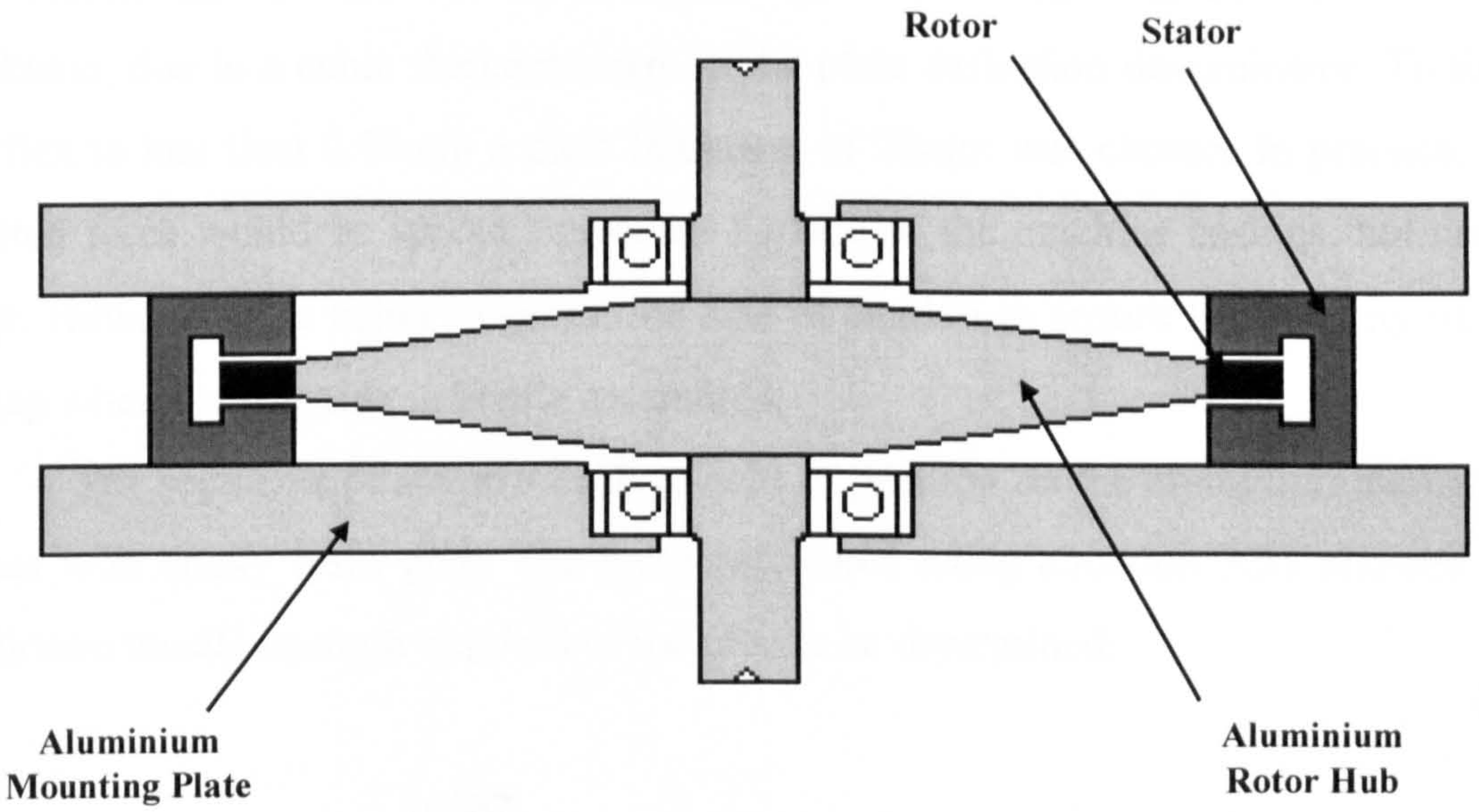

Figure 3.20 Schematic diagram showing the major components of the assembled DSTFM

3.5.1 Stator Mounting Plates

The aluminium mounting plates had two purposes, to provide physical rigidity for the finished machine and to accurately secure the individual pole pieces. The 0.5mm axial airgap between the stator and rotor determined the flexing tolerance of the mounting plates. Erring on the side of caution, the plates were produced to be of sufficient strength to limit any axial bending due to the attractive and repulsive forces of the rotor to within ±2 % (0.01mm) of the airgap length. To enable the thickness of the plates to be calculated, the force that was exerted upon them by the rotor magnets was determined using Maxwell's Stress Tensor {3.9}. Assuming a flux density of

1.5T in the airgap and a total airgap tooth area of 16.4×10^{-3} m^2, the force exerted by the rotor magnets on the stator using equation 3.21, was 14.682kN.

Maxwell's Stress Tensor: $$\textbf{Force} = \frac{B_g^2 A}{2 \mu_o} \quad \{3.9\}$$

Where: B_g = Airgap flux density
A = Total tooth area in the airgap

In order to determine the minimum thickness of aluminium casing required to limit axial flex to an acceptable level, mechanical stress and strain formulae were utilised (Appendix D.2). Results presented in table D.2.1, were calculated using a worst case scenario, ie. with all the axial force applied at the lower edge of the stator. The results showed that the reduction in flex did not fall linearly with material thickness, due to a cubic thickness term in the plate deflection denominator. To limit the flex to less than 0.01mm a plate thickness of 20mm was chosen. In practice, the exerted force would be spread across the surface of the machine casings, not on an edge. However, it is better to err on the side of caution to ensure the integrity of the airgap when the machine is finally assembled.

The segments of stator iron were held in position on the aluminium mounting plates with epoxy resin glue. The force calculated using equation 3.21 allowed the minimum tensile strength required of the glue to be determined:

$$\frac{14682}{16.4\times10^{-3}} = 895 kN/m^2 = 0.9 N/mm^2$$

This figure was well within the tolerances of most epoxy resin adhesives. For example, 'Ciba Polymers' indicated values of tensile strength [3] for their Araldite 2011 epoxy adhesive in the range of 5 to 10N/mm^2.

In order to clamp the stator halves together when the prototype was assembled, the aluminium side casings were of a larger diameter than the active stator. This enabled ten 12mm securing bolts to be positioned around the periphery of the machine. A casing overlap of 40mm provided sufficient space around the outside of the stator to position these clamping bolts. With an active outside diameter of 362mm, the 40mm overlap increased the overall machine diameter to 442mm. Placing the

securing bolts in the centre of this overlap region gave a 'rigid' outside diameter of 402mm.

3.5.2 Stator Assembly

Each pole of the stator comprised a tooth and a trapezoidal side cheek, both machined from SMC material. Fifty poles were positioned onto each mounting plate, forming a ring of iron segments. On to one of these rings, fifty top pieces were positioned on the side cheeks. The photograph in figure 3.21 shows a section of the component pieces arranged on one of the aluminium mounting plates prior to adhesive application. To ensure correct radial positioning of the side cheeks, a 61mm wide, 0.5mm deep circular channel with an internal radius 120mm was machined into each of the mounting plates. Each set of side cheeks were positioned, glued and clamped into the channel. This procedure was repeated for the stator teeth on each assembly and then for the top pieces on one of the assemblies. Once all of the components had been successfully attached to the aluminium casings, the stator was ready for assembly around the rotor.

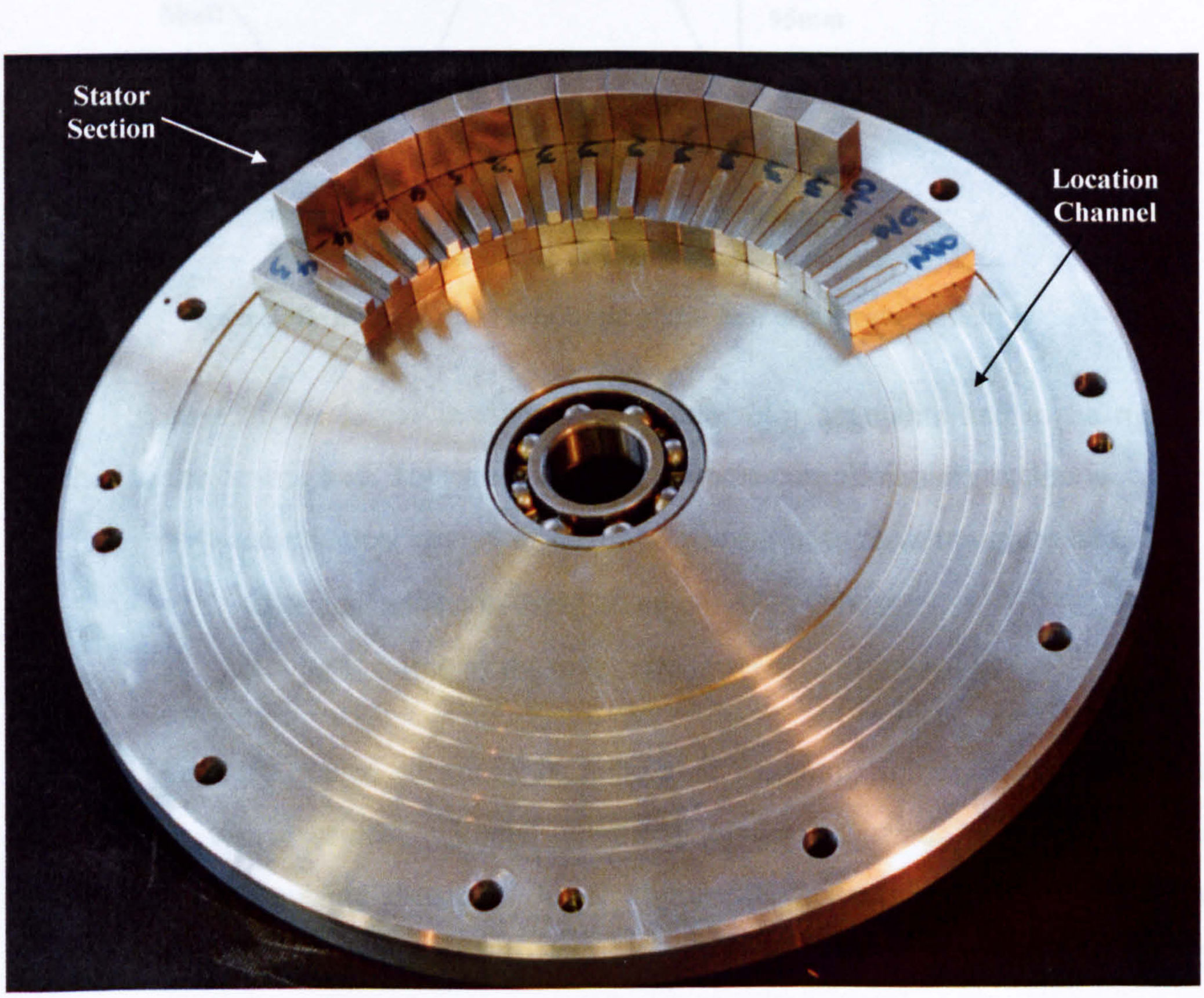

Figure 3.21 Component SMC pieces arranged on one of the aluminium mounting plates

3.5.3 Rotor and Shaft Assembly

The active part of the rotor was mounted on a single aluminium disc centred on a 50mm diameter steel drive shaft. To minimise both mass and axial bending moments, the rotor iron and magnet segments were mounted on a tapered aluminium hub (figure 3.22). The hub's dimensions were governed by the axial width of the stator and the rotor. The axial width of the hub at its outer diameter was 15mm to match that of the active rotor. The hub widened at its inner diameter to a dimension close to the 60mm stator width. With a drive shaft radius of 25mm, these values gave an inherently stiff, short trapezoidal shaped aluminium hub with a radial length of 95mm.

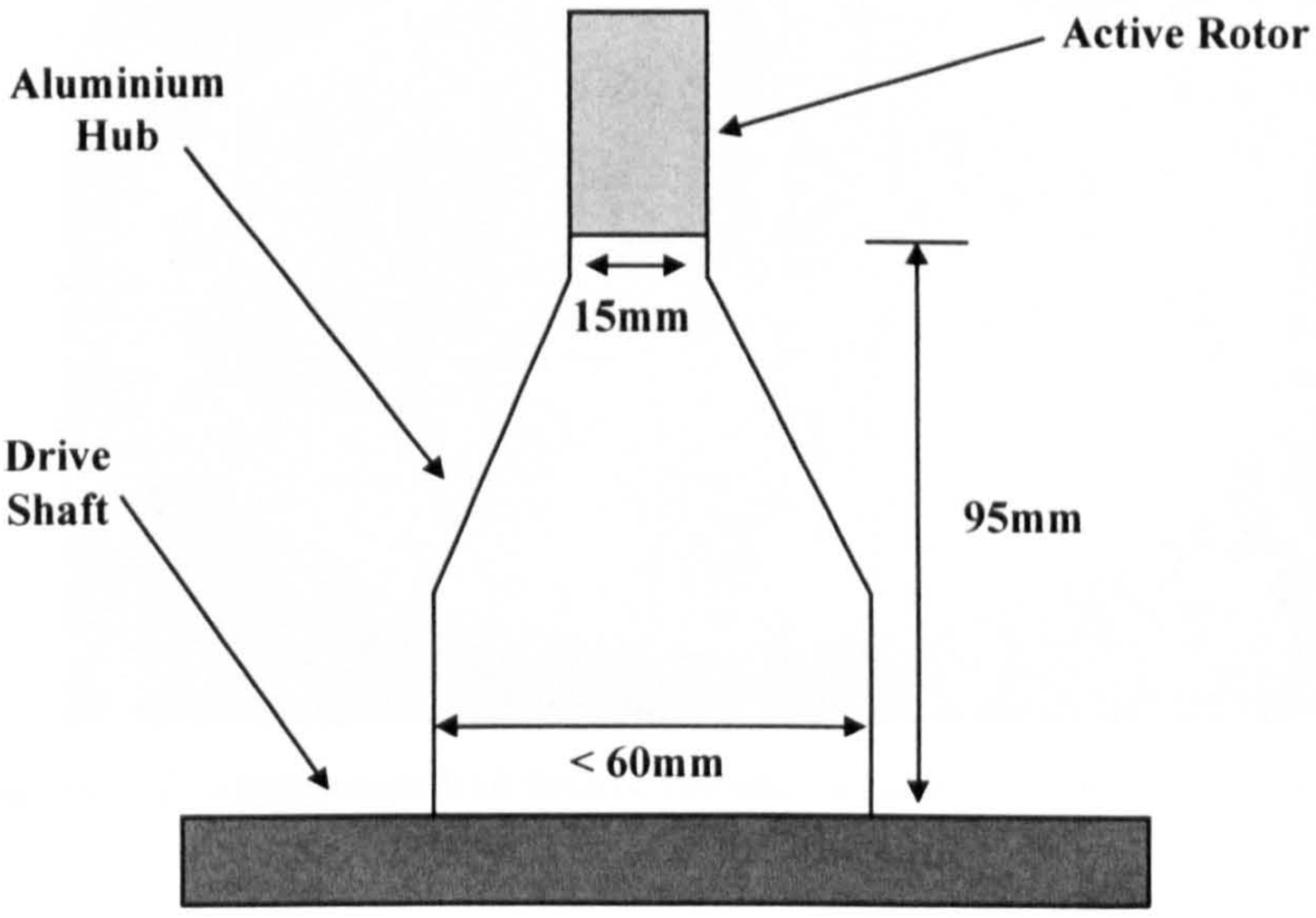

Figure 3.22 Radial / Axial schematic of one half of the rotor assembly

Because of the forces involved, the active rotor segments had to be rigidly attached to the central hub. This was achieved by three complimentary methods.

- Mechanical keying of the SMC rotor iron to the aluminium hub.
- Chemical adhesion using an epoxy resin adhesive.
- Kevlar banding of the outer circumference of the rotor.

As with the stator, accurate positioning of the rotor iron and magnets in all three planes was essential. Radial positioning was achieved by virtue of the aluminium hub's outside diameter. Axial alignment was ensured by machining a datum on each side of the hub to be used in conjunction with two machined clamping rings. In the circumferential plane, positioning was achieved by milling one hundred

axially orientated slots in the outer rim of the aluminium hub. These slots were then used to key the rotor iron segments into their correct circumferential position. This method of positioning also increased the mechanical strength of the aluminium/SMC epoxy adhesive bond. Figure 3.23 shows the rotor hub on its drive shaft. Indicated in the picture are the axial datum surfaces and the milled slots around the rotor's circumference. The completed rotor is shown in figure 3.24. To enable a better view of the individual rotor and magnet segments, the circumferential Aramid Kevlar band is omitted in this photograph.

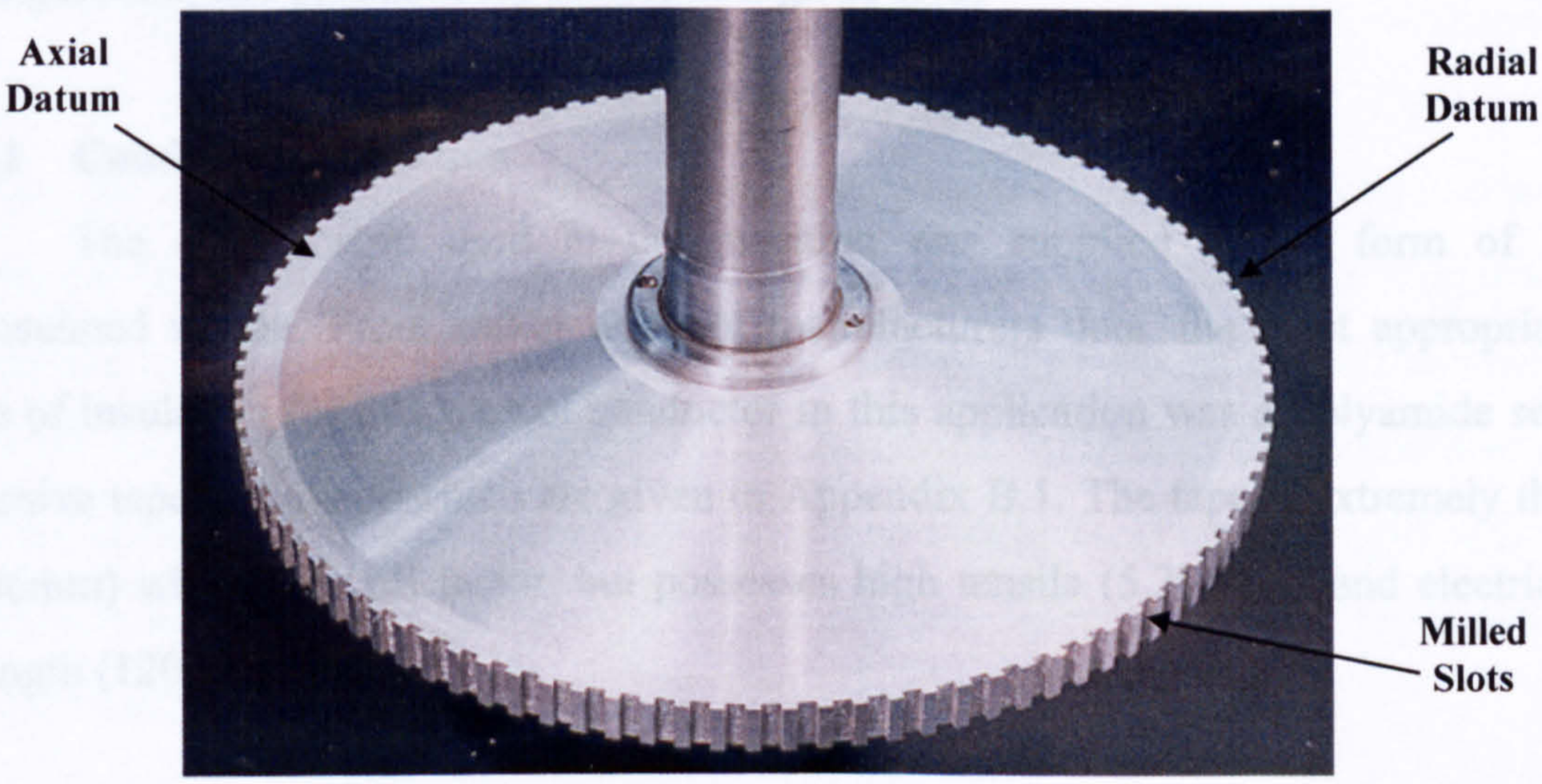

Figure 3.23 Aluminium hub before the active rotor components are attached

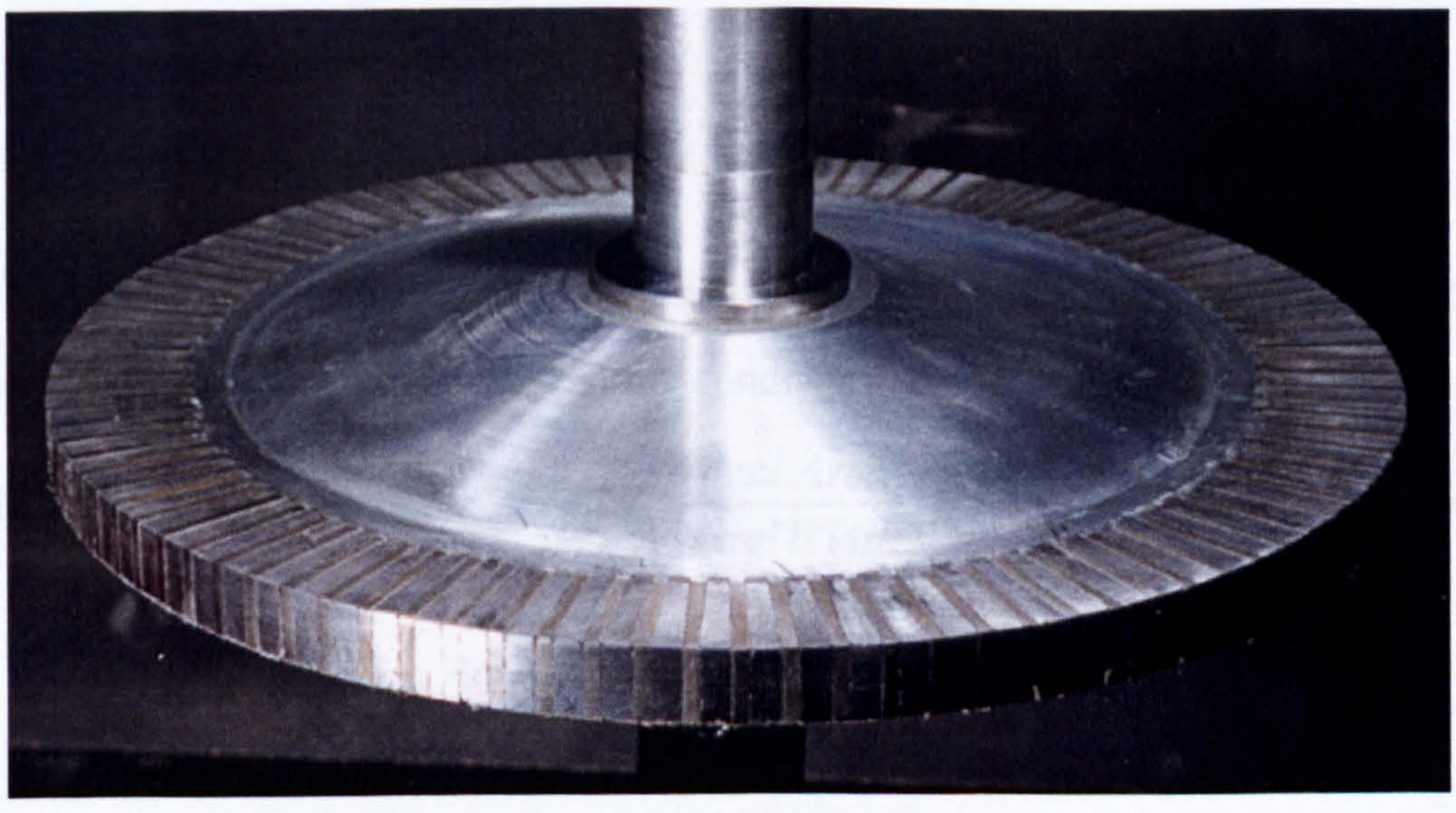

Figure 3.24 Assembled rotor prior to Kevlar banding

3.6 Conductor Sizing

The main limitation on conductor sizing is the working current. This was pre-set, based on the capabilities of the test equipment available, at a maximum value of 30A rms. The conductor parameters were defined on the basis of this current level and the area available for the winding in the prototype. The rectangular cross-sectional winding area (see figure 3.1) meant that the finished conductor toroid would be a rectangular-section hoop. Therefore, this shape was wound using insulated flat copper strip, previous experience using strip copper conductors with this winding configuration, had produced fill factors as high as 0.75.

3.6.1 Conductor Insulation

The copper strip used in the machine was supplied in the form of an uninsulated ribbon. From examination of manufacturers data, the most appropriate type of insulation for this type of conductor in this application was a Polyamide self-adhesive tape, details of which are given in Appendix B.1. The tape is extremely thin (0.06mm) which aids fill factor, but possesses high tensile (5.3kg/cm) and electrical strength (120kV/mm).

3.6.2 Conductor Sizing, and Current Level

The number of turns required to give an MMF of 2000AT at an rms current of 30A is:

$$\textit{No.Of Turns} = \frac{2000}{30} = 66.67 \approx 67\textit{Turns}$$

The area allowed for the conductor was $400mm^2$, with an axial width of 30mm. Therefore the radial height of the conductor area was:

$$\textit{Radial Height Of Conductor Area} = \frac{\textit{Ideal Area}}{\textit{Axial Width}} = \frac{400mm^2}{30mm} = 13.33 \approx 13mm$$

$$\therefore \quad \textit{Actual Area} = 30 \times 13 = 390mm^2$$

Instead of a single conductor winding, two series linked, axially adjacent, windings were used, each of 14mm width. This allowed 2mm axial clearance for any excess insulation in this plane. Two 34 turn series connected windings were

employed, which increased the number of turns to 68, this had the advantage of slightly reducing the current density required to attain the specified level of MMF. These parameters led to the following sizes:

$$\textit{Overall Insulation Thickness}, \quad 0.06 \times 35 = 2.1mm$$

$$\textit{Individual Conductor Thickness}, \quad \frac{(13 \times 0.75) - 2.1}{34} = 0.225mm$$

$$\textit{Individual Conductor c.s.a.} \quad 0.225 \times 14 = 3.15mm^2$$

A cross-sectional area of $3.15mm^2$ enabled the current density to be reduced, whilst still maintaining the specified rms current of 30A, which would improve the copper loss in the machine. The conductor toroid was produced by winding two rows of the flat insulated copper strip around a wooden former. The OD of this former was machined to enable the internal and external diameters of the stator and conductor respectively, to form an interference fit. A tight radial interface was required to aid thermal conduction from the conductor into the coreback. To produce a rigid coil, the conductor toroid was sealed using a non-conducting adhesive shellac resin, which served to stiffen and further insulate the sixty-eight turn winding.

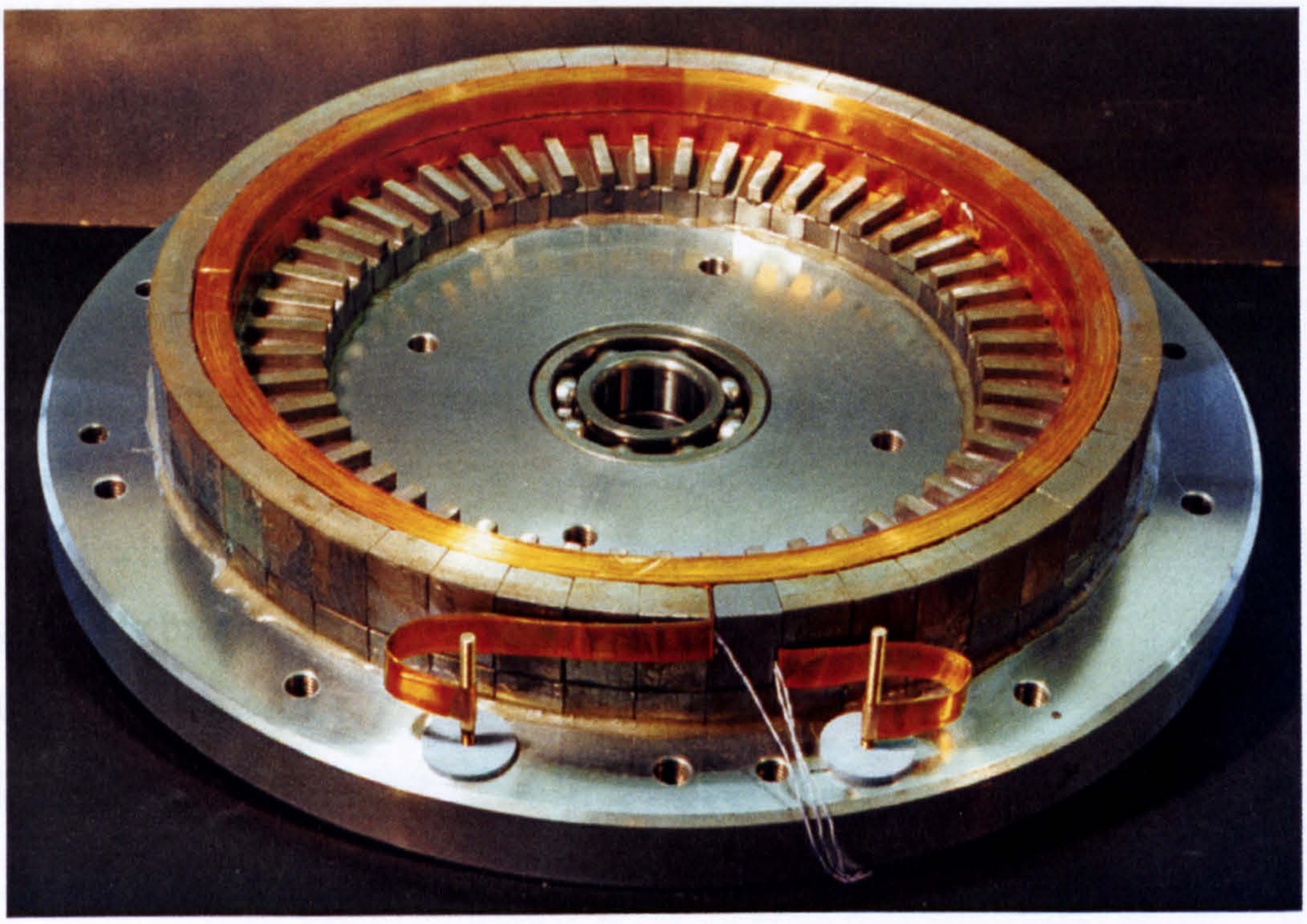

Figure 3.25 Stator half complete with terminated toroidal conductor

3.7 Assembling the Machine

In order to complete the machine, the component pieces of the machine had to be brought together. This involved pressing the pre-formed conductor into the 'L' shaped stator half and electrically terminating its ends, then inserting the rotor within the two stator halves. Figure 3.25 shows the assembled 'L' shaped stator half and terminated conductor ring.

High axial forces were produced by the rotor magnets as they closed on the iron circuits of the two stator halves. Therefore, a great deal of care and precision was required bringing the stators together around the rotor. To achieve this, two purpose built mechanical pullers and an aligning tool were designed and built.

With reference to figure 3.26, the method of assembly was as follows:

- The aligning tool was substituted for the rotor.
- The two stator halves were bolted together allowing the aligning tool to protrude through the bearings.
- Each puller was lubricated and then slid onto the exposed 'bearing surface' of the tool on its respective side of the stator.
- With the pullers aligned and concentric to the stator, they were bolted to the aluminium backing plates.
- The stator was split, the aligning tool removed and each of the puller's 'jacking bolts' was wound in fully.
- Orientating the machine so that the axial plane was vertical, the rotor shaft was lowered through the stator bearing and into the 'bottom' puller.
- The second stator half was then lowered onto the exposed upper shaft of the rotor.
- The 'jacking bolts' in the two pullers were then sequentially unwound which gradually brought the two stator halves together.
- Once this procedure had been completed, the two stator halves were bolted together to complete the whole assembly.

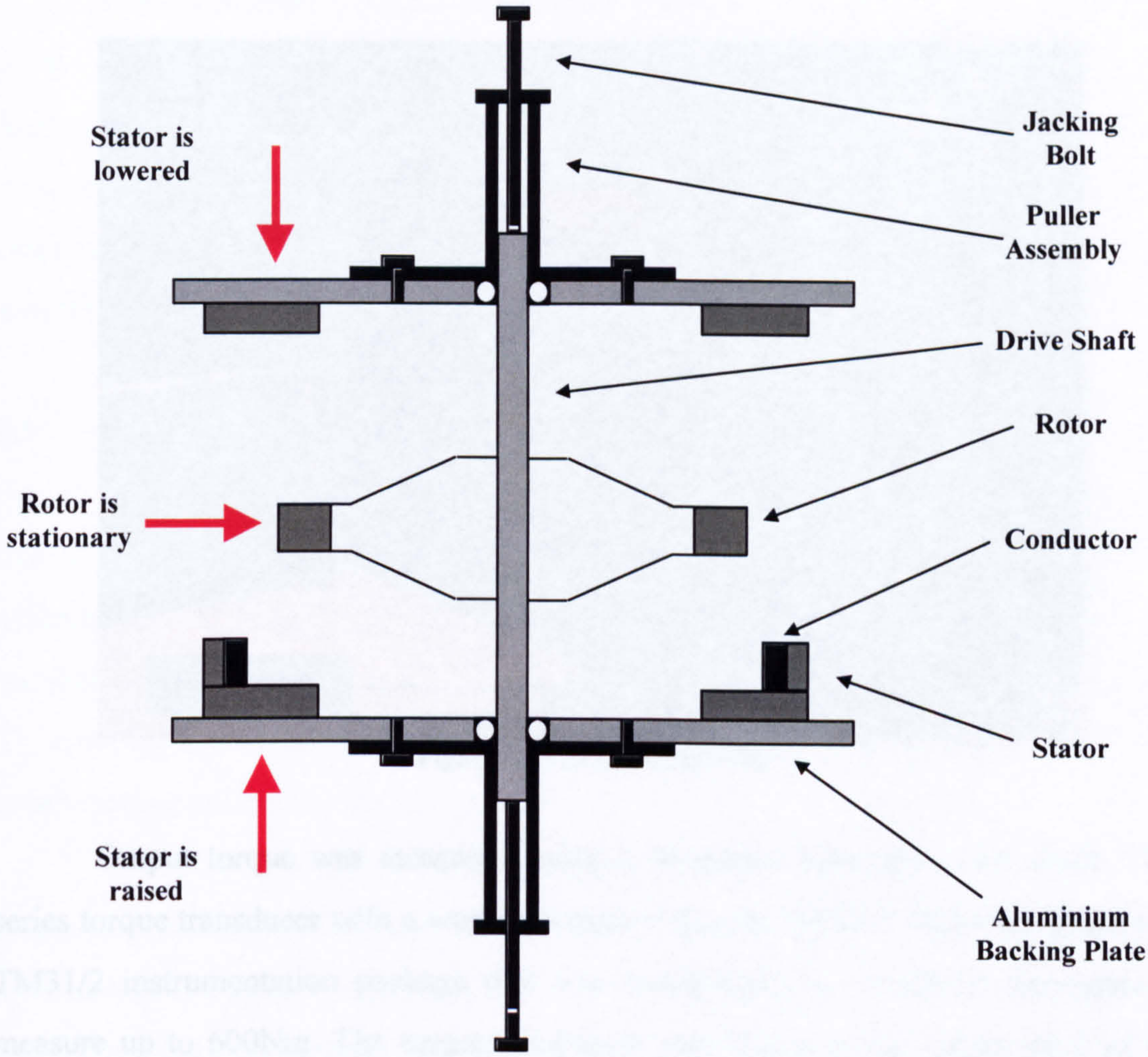

Figure 3.26 Schematic illustrating the DSTFM assembly procedure

3.8 Test Bed Design and Construction

The rig had to be physically strong and rigid in order to cope with the expected levels of output torque from the prototype machine. There was also a requirement for the rotor to be turned through fractions of a degree so that incremental values of output torque could be measured.

The bed plate was a simple construction incorporating two parallel U section beams (6mm×150mm×1830mm), with four cross beams (6mm×100mm×480mm) welded between them to form the basic bed plate. Milled slots were machined into the uppermost section of the parallel U beams and four 6mm thick box-section cross beams with matching orthogonal slots on their lower faces were bolted onto the bed. The prototype machine and torque transducer were attached to the two pairs of cross beams.

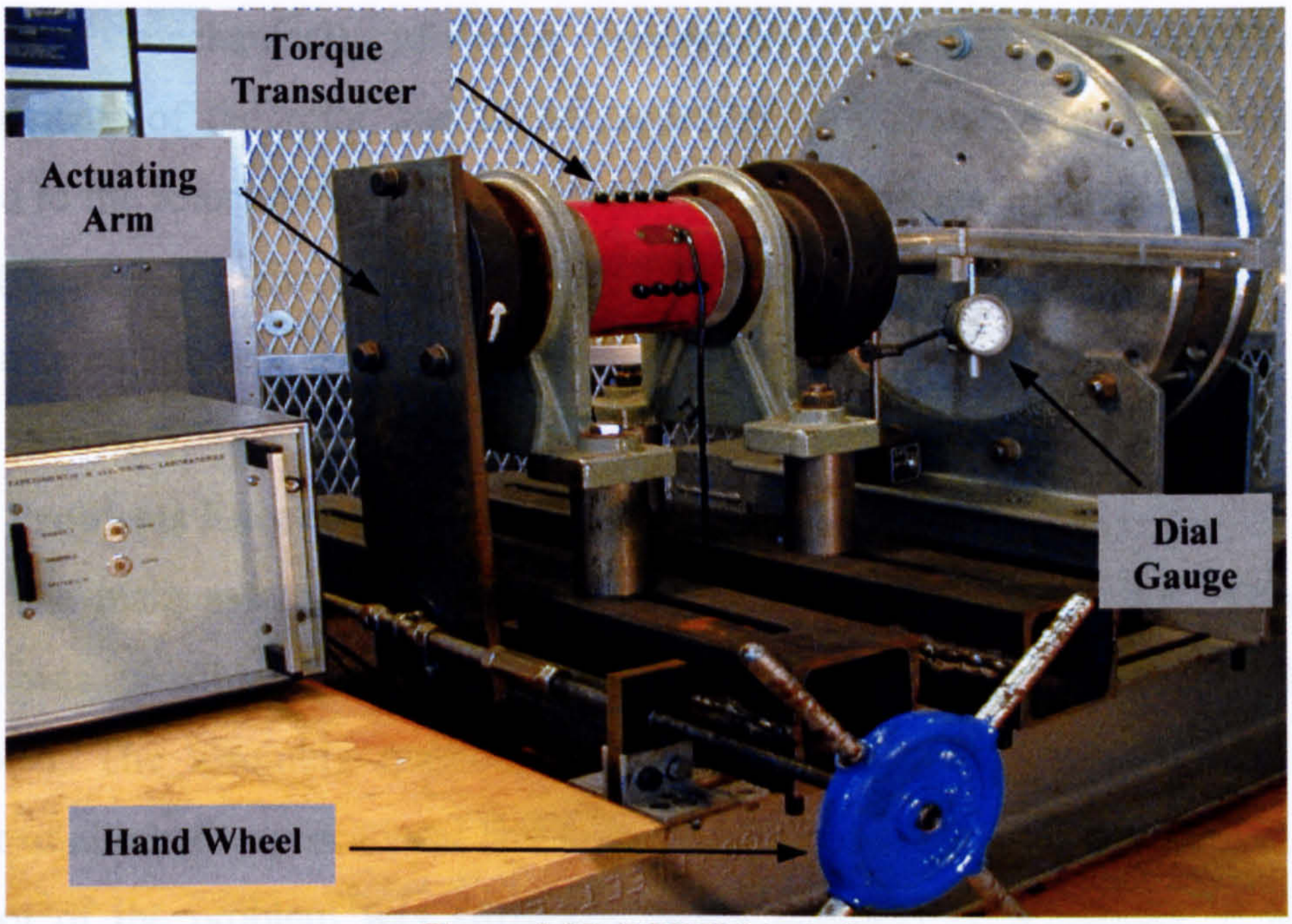

Figure 3.27 DSTFM test rig

Output torque was measured using a Westland Aerospace EEL 2400 / DB series torque transducer with a working range of zero to 800Nm. This was linked to a TM31/2 instrumentation package that was recalibrated by Westland Aerospace to measure up to 600Nm. The torque transducer was linked to the output shaft of the machine via a 180mm diameter coupling, attached with taper-lock bushes. The output shaft of the torque transducer was connected to an actuating arm (9mm×150mm×410mm). A pivot and slot at the opposite end to the coupling, was linked through a length of ½" UNF studding to a hand-wheel. Rotating this hand-wheel slowly rotated the torque transducer shaft and so the input shaft of the DSTFM. One complete turn of the hand-wheel moved the rotor through 0.26° (mechanical).

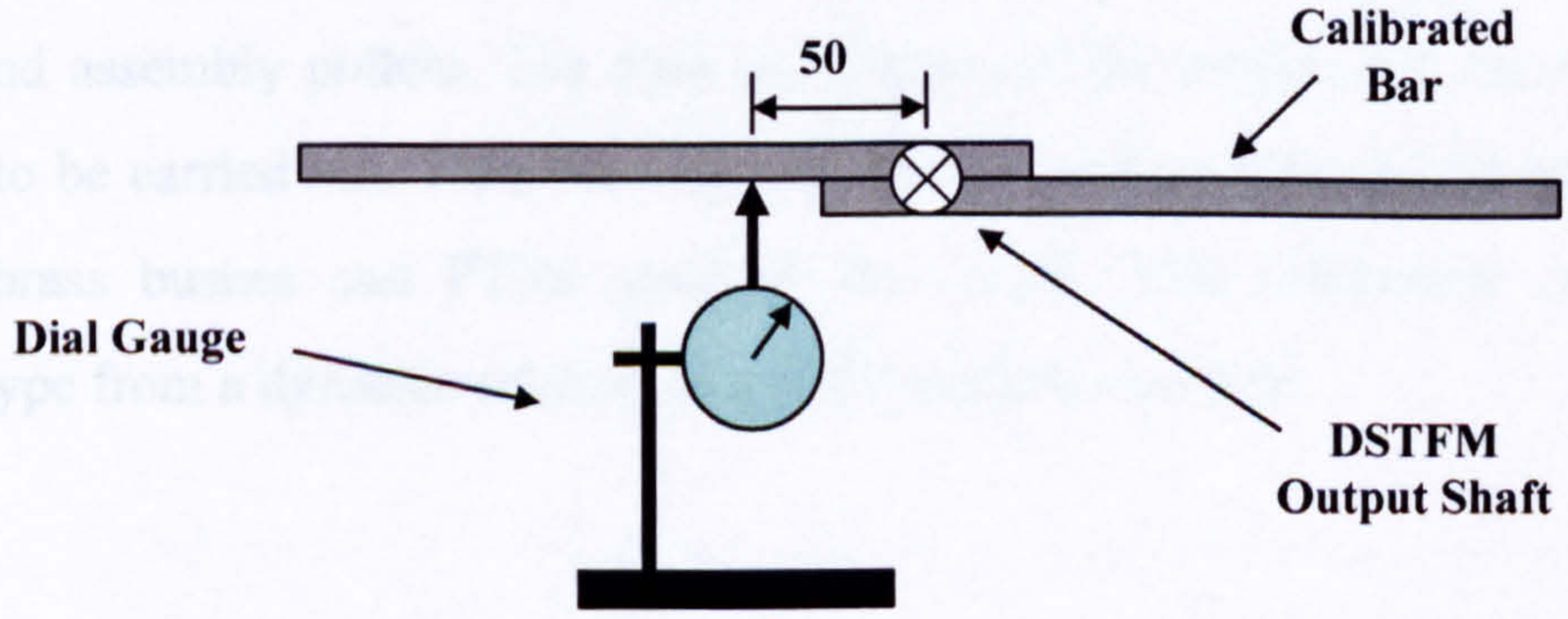

Figure 3.28 Schematic diagram of angular displacement measurement set-up

A high number of input and output readings were taken over a single pole pitch (3.6° mechanical) of rotor movement. Therefore, fractional angular displacements of the rotor had to be measured. A calibrated aluminium bar was clamped to the rotor shaft and a dial gauge positioned below it, 50mm from its radial centre (figure 3.28). Using trigonometry, the vertical movement of the calibrated bar was translated into angular displacements of the rotor.

3.9 Problems Encountered During Assembly

The main assembly difficulty experienced was rotor alignment. This meant that it was possible to compromise the active airgap when the machine was assembled. The assembly method described in section 3.7 was finalised after a number of alternative procedures had failed to produce consistently repeatable results. The root of the problem was attributed to the mechanical advantage of the rotor magnets over the radial tolerance of the thrust bearings on the output shaft.

The original assembly procedure assumed that as the stators came together, the magnetic force exerted by each side of the rotor balanced and so the bending moment applied on the bearings was negligible; this was not the case. If the rotor approached the stator at any angle other than parallel then the unbalanced forces pulled the rotor over to one side, taking up all radial play in the bearings. The bending moment and radial force experienced by the thrust bearings was calculated to be 1098Nm and 13.23kN respectively (Appendix D.3). The only realistic method of reducing this radial force would be to increase the axial separation of the bearings. Doubling the distance between the bearings from 83mm to 166mm would half the radial force to 6.615kN. To carry out this modification would involve fabricating a new rotor output shaft and two completely new bearing housings, as well as re-machining the aligning tool and assembly pullers. The time constraints on the project did not allow for this work to be carried out. Therefore, the decision to replace the original thrust bearings with brass bushes and PTFE washers was made. This effectively converted the prototype from a dynamic rotating to a static rotating machine.

3.10 Testing the Prototype

Two sets of physical tests were planned for the DSTFM prototype. Initially the thermal capabilities of the machine were evaluated, followed by measurements of torque against angular position. These enabled the dynamic characteristics of the machine to be predicted.

3.10.1 Thermal Time Constants

There are two thermal time constants associated with the DSTFM, one derived from the winding and one from the casing. To determine these two values involved impressing a fixed DC current onto the single phase winding and monitoring the temperature rise from ambient to a steady-state level. Three 'T' type thermocouples with a working range of -200°C to +400°C and an accuracy of ±1°C were used to monitor the temperature in different parts of the machine. The three positions chosen were:

(i) Outer radius of the conductor coil.

(ii) Inner radius of the conductor coil.

(iii) Centre of the conductor coil.

Two 'heat runs' were performed on the naturally ventilated machine, one at 15A and then another at 20A. From ambient, the temperature of each thermocouple was recorded every minute due to the initially steep temperature gradient. Readings were then taken every five minutes and then later, every fifteen minutes. This continued until a steady state was reached. The data gathered from the 15A and 20A tests is presented in Appendix E.1.3 and E.1.4 respectively. The thermal time constants derived from this data were calculated using the following equations:

$$T_{rise} = T_{steady\ -state} \times \left(1 - e^{\frac{-t}{\tau}}\right) \qquad \{3.10\}$$

Therefore at $t = 0$

$$\tau = \frac{T_{steady\ -state}}{d\,T_{rise}/d\,t} \qquad \{3.11\}$$

Where $\frac{d\,T_{rise}}{d\,t}$ = Maximum gradient of the temperature rise

From the data in Appendix E.1.3 and E.1.4 the time constants derived for the winding and casing from the 15A and 20A tests respectively are:

15A **τ for winding** = 2.83 minutes

τ for casing = 102.5 minutes

20A **τ for winding** = 3.37 minutes

τ for casing = 90 minutes

These four values were then used to calculate curves, which could be compared to the two thermal test curves produced from measurements. Figures 3.29 and 3.30 show the graphs of these comparisons. The thermal time constants associated with the prototype's winding are represented in figure 3.29. This shows that the time constants calculated from the two 'heat runs' compare favourably with the actual winding temperature dissipation. There is good correlation over the initial ten minute period and the final period from 100 to 450 minutes where temperature dissipation remained a constant 32 °C. It should be noted that for reasons of clarity, the x axis of the graph was truncated at '120 minutes', also that the two calculated time constants were so close that one is positioned on top of the other. The second graph (figure 3.30) shows the measured and calculated thermal time constants associated with the casing temperature. It indicates that neither of the calculated time constants matched the measured curve exactly and so the actual time constant must lie between the two values. Experimenting with the value for the casing time constant produced a 'best fit' figure of 95 minutes. This curve is shown in figure 3.31.

Realistically, the winding should be limited to a 100°C temperature rise. On the basis that $t_{rise} \propto i^2$, the results from the thermal analysis (Appendix E.1.3 and E.1.4) were extrapolated to produce a °C/Amp calculation. Therefore, from the 20A current data:

$$dt_{rise} = 92 - 19 = 73^{\circ}C$$

And so;

$$\frac{i^2}{20^2} = \frac{100^{\circ}C}{73^{\circ}C} \quad \therefore \quad i = \sqrt{\left(\frac{100}{73}\right)} \times 20 = 23.4A$$

So the rms current associated with a 100°C temperature rise is 23.4A (33.1A peak, assuming a sinusoidal current).

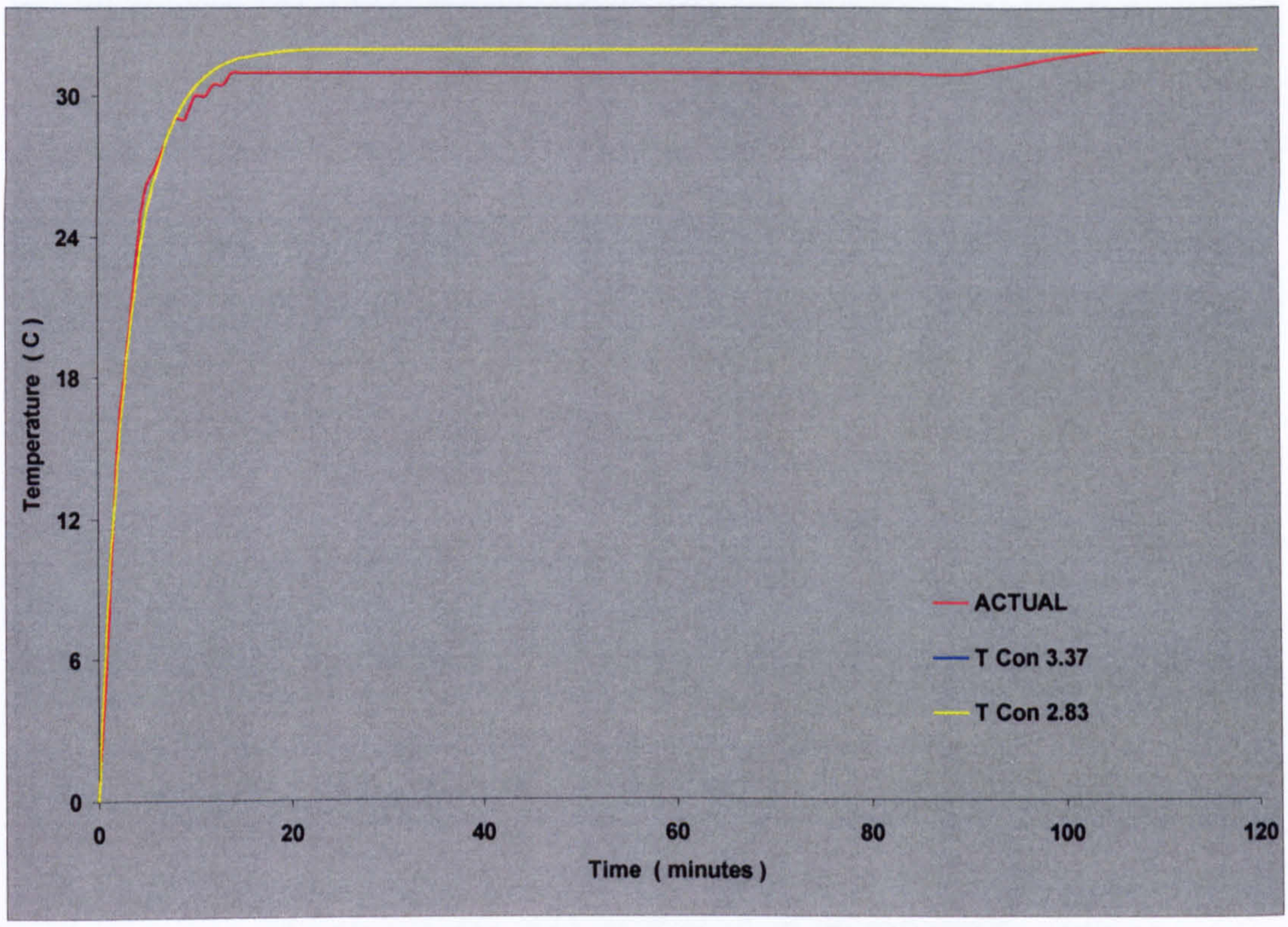

Figure 3.29 Comparison of theoretical and actual DSTFM winding time constants

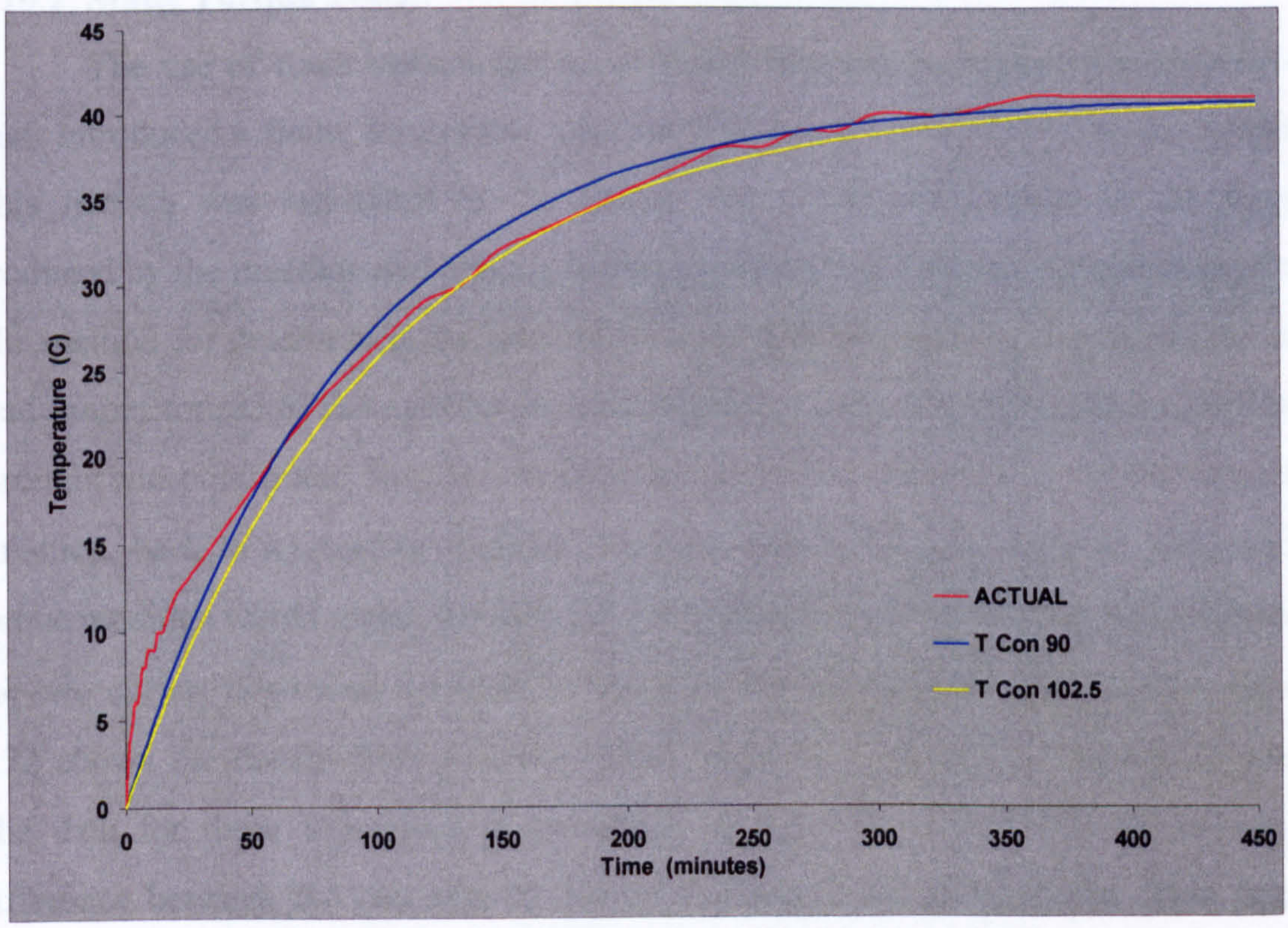

Figure 3.30 Comparison of theoretical and actual DSTFM casing time constants

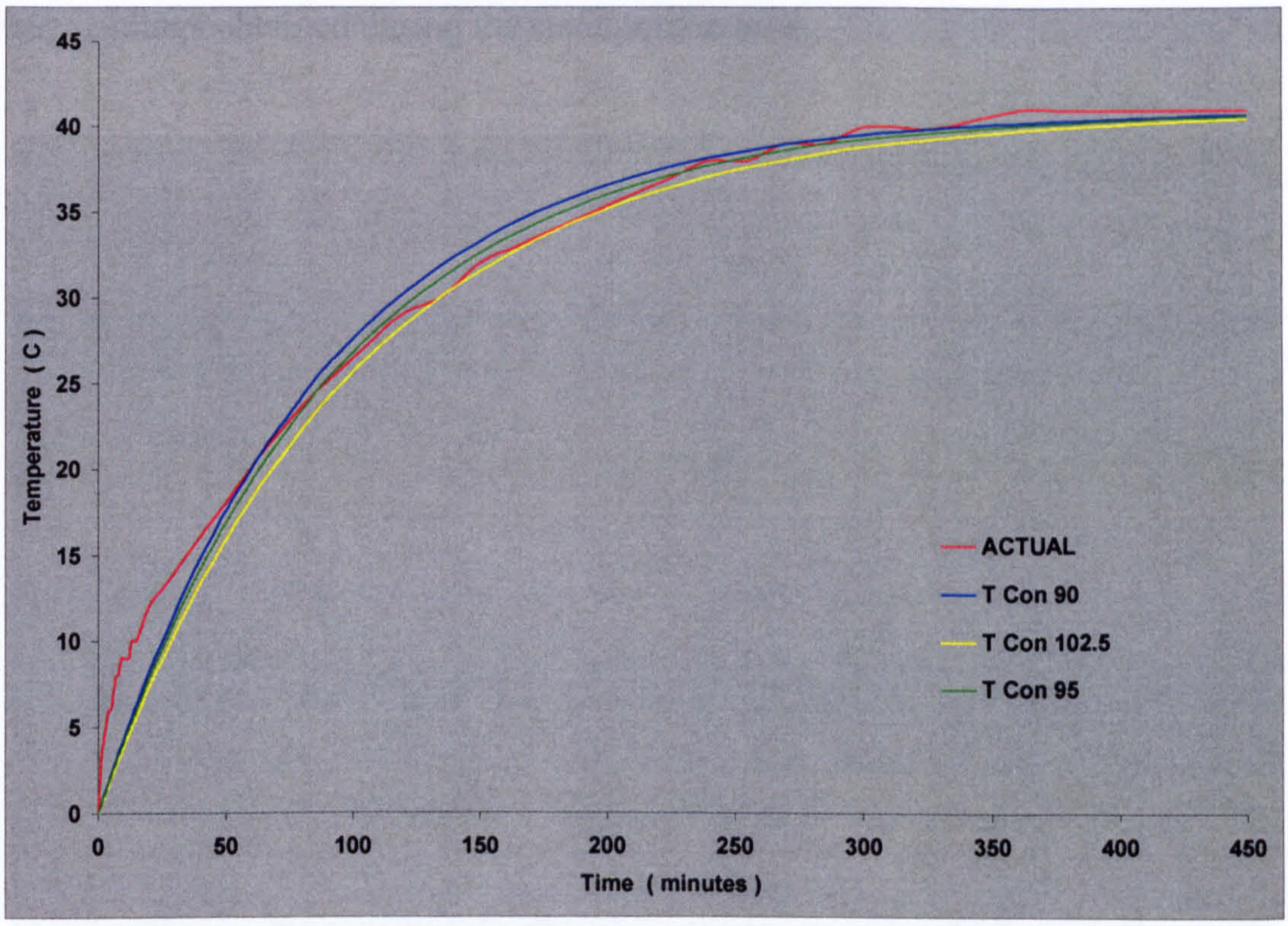

Figure 3.31 Comparison of theoretical and actual DSTFM casing time constants showing the '95 minute best fit'

3.10.2 Static Torque Tests

The use of brass bushes instead of thrust bearings to support the rotor drive shaft introduced a finite, measurable amount of friction (or 'stiction') into the system. This friction was registered by the torque transducer in addition to the torque produced by the machine and as such had to be subtracted from the measured reading. The method for determining the level of this 'stiction' torque was to measure the no-load output torque of the machine in both directions, whilst rotating the output shaft through one pole pitch, first in one direction and then immediately in the opposite direction, back to its starting position. With no 'stiction' in the machine, the reverse torque readings would match the forward readings exactly. Any discrepancies between the two curves illustrated the level of constant friction present. The graph in figure 3.32 shows the results from four-and-a-half transitions through a single pole pitch. The data for these transitions is presented in Appendix E.1.5. The mean torque difference between the two sets of curves was calculated to be 85Nm. This figure represents the 'stiction' in both directions, so half this value (42.5Nm) was due to the

inherent friction in one direction. This value was subtracted from all subsequent torque readings obtained during the static torque tests.

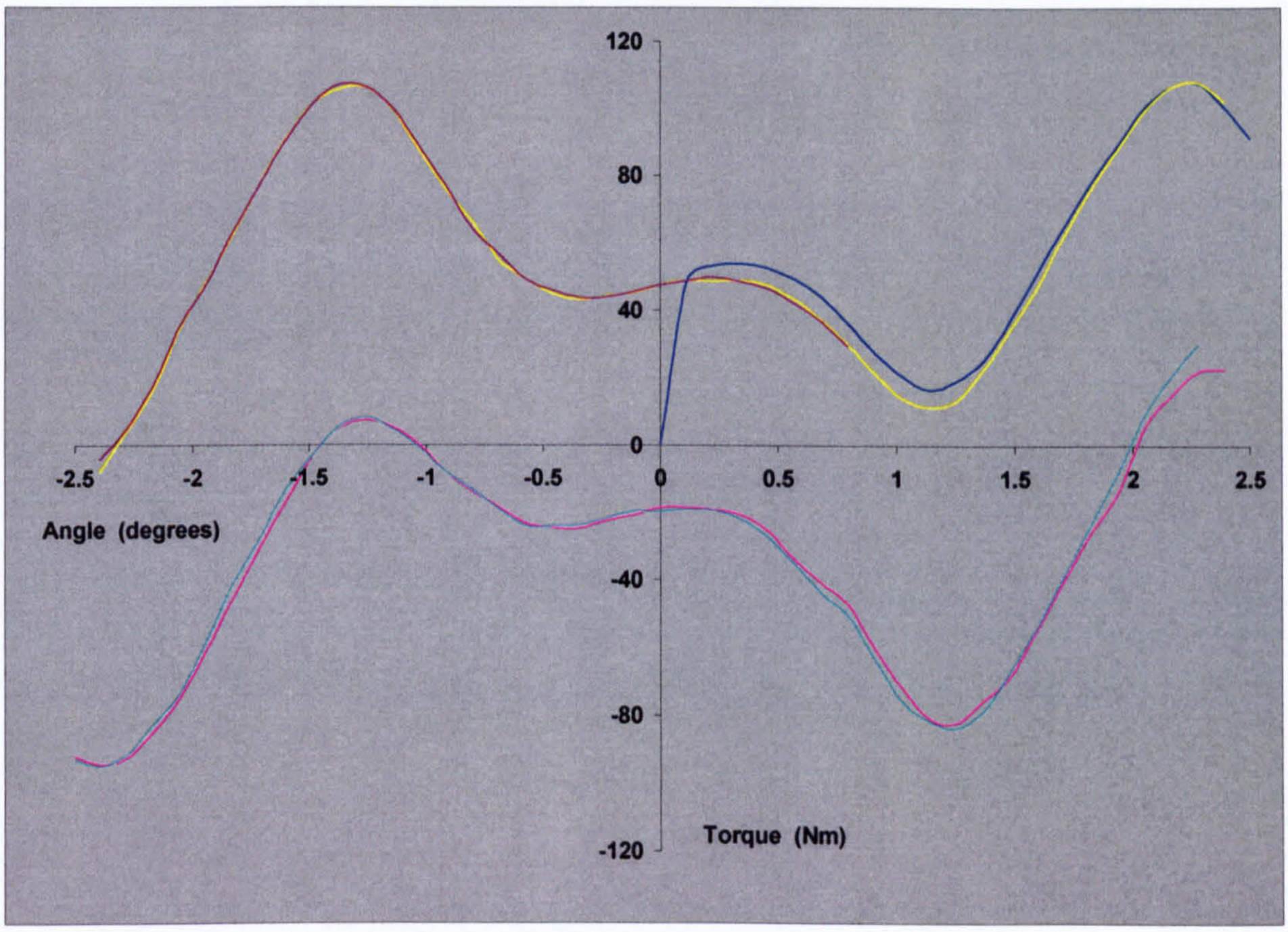

Figure 3.32 Graph highlighting the level of 'stiction' in the DSTFM

The procedure followed for each of the static torque tests was identical:

(i) Disengage the actuating arm from the drive shaft so that the machine was free to rotate.

(ii) Impress the winding with a current equivalent to one third the rated value (≈10A). This caused the rotor to move to a position of alignment.

(iii) Reconnect the actuating arm to the drive shaft, ensuring that any inherent backlash in the drive chain couplings was taken up in the direction of shaft rotation.

(iv) Set the supply resistors for the required test current.

(v) Confirm datum readings on the dial gauge, ammeter and torque transducer instrumentation.

(vi) The drive shaft was slowly rotated via the actuating arm, and readings were taken from all instruments at each increment of angular position.

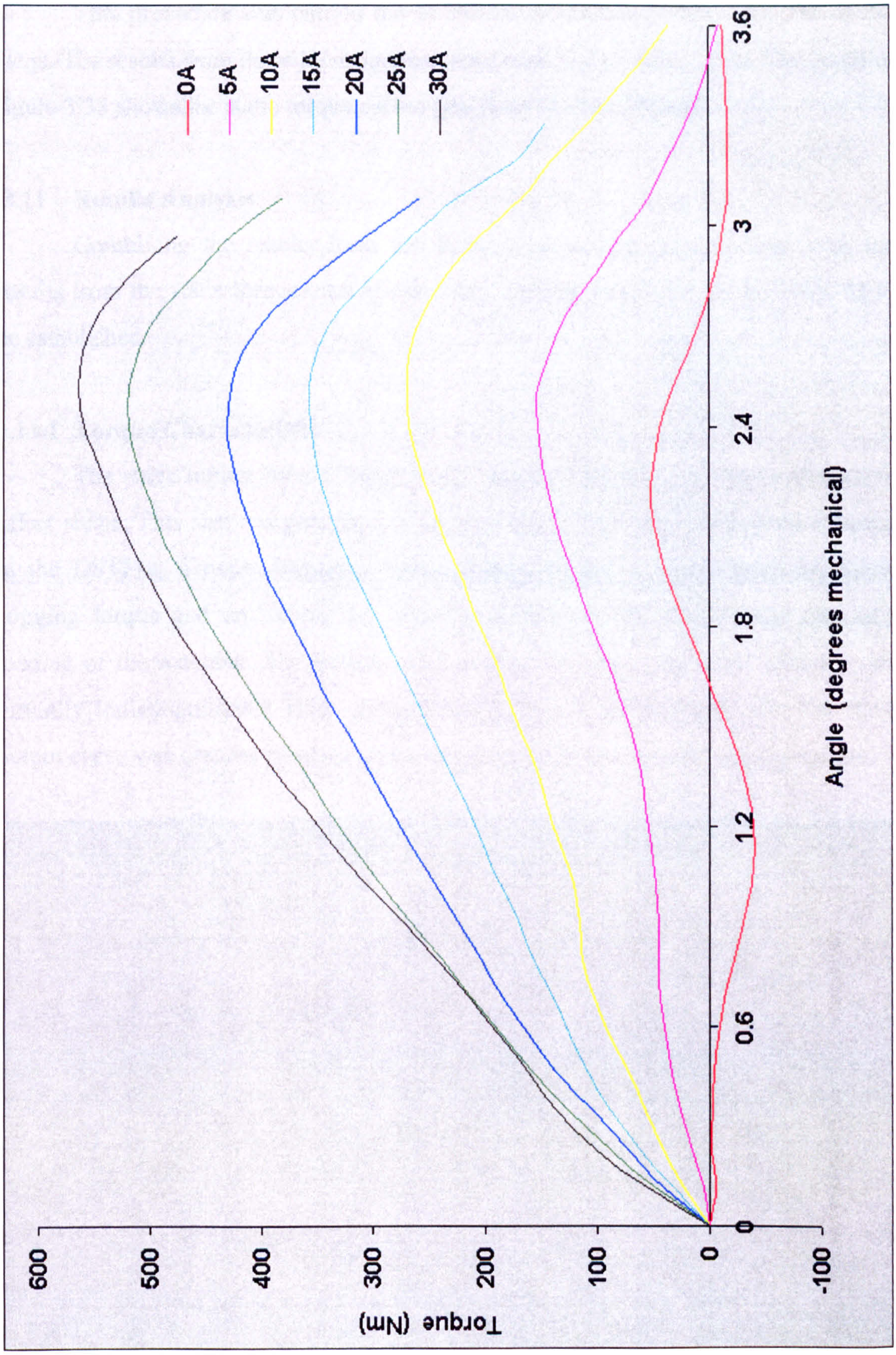

Figure 3.33 Static torque curves for the DSTFM (42.5Nm 'stiction' offset removed)

This procedure was carried out at current levels from 0A to 30A DC in 5A steps. The results from these investigations are given in Appendix E.1.6. The graph in figure 3.33 shows the static torque curves generated by these results.

3.11 Results Analysis

Combining the results from the thermal analysis of the machine with the results from the static torque tests enabled the working parameters of the DSTFM to be established.

3.11.1 Torque Characteristic

The static torque curves shown in the graph of figure 3.33 have a distinctive offset shape. This shape is generated by three torque producing mechanisms inherent in the DSTFM, a twice frequency rotor saliency torque, a twice frequency stator cogging torque and an interaction torque produced by the electric and magnetic loading of the machine. The torques produced by the rotor and stator saliency, are virtually indistinguishable from one another. Figure 3.34 illustrates how the static output curve was derived from the interaction torque and the double saliency torque.

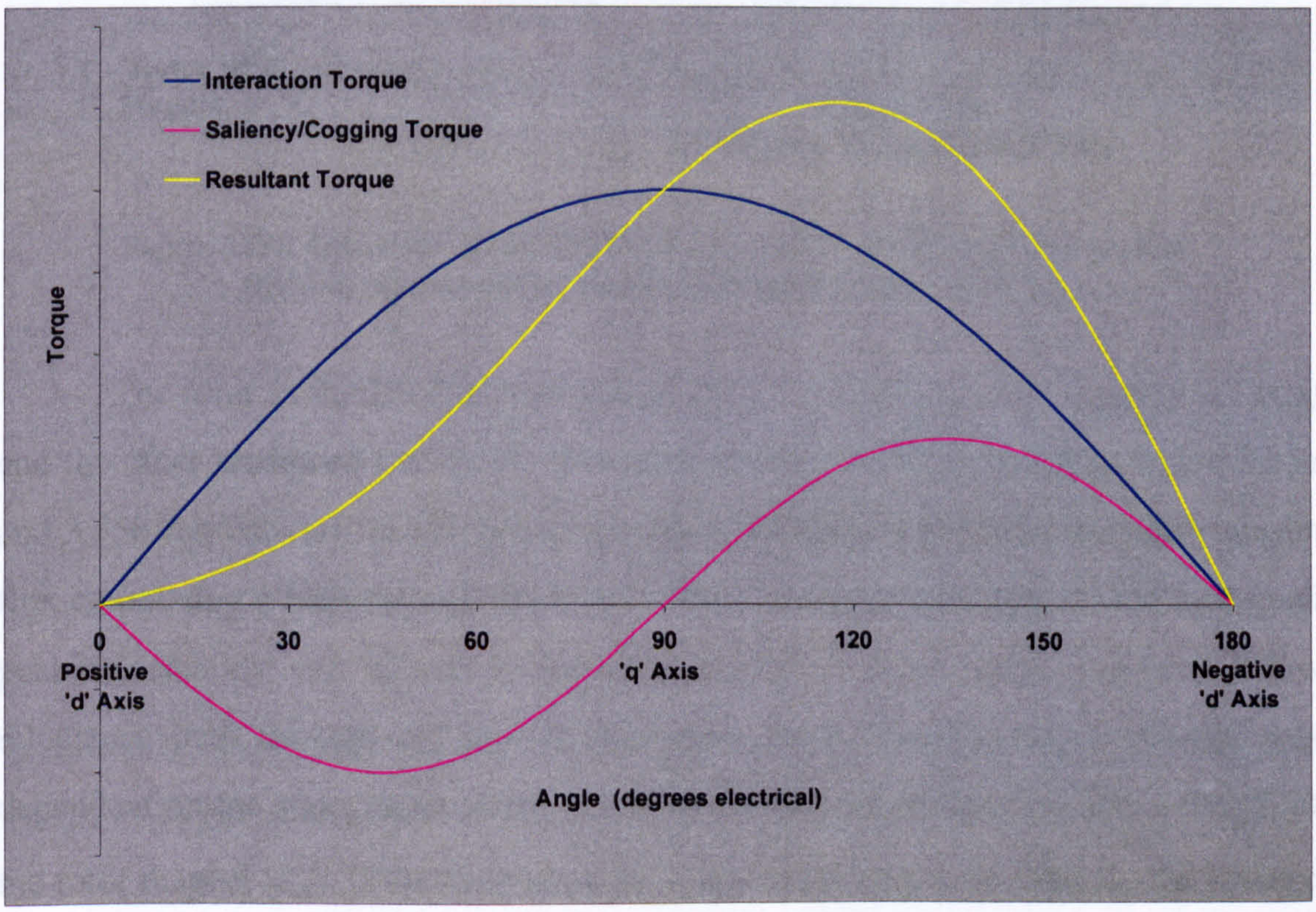

Figure 3.34 Schematic graph demonstrating the composition of a DSTFM torque curve

Adding the twice frequency saliency/cogging torques to the interaction torque produces a resultant torque curve with an offset peak. With reference to figure 3.33, the effect of the saliency/cogging torque became less pronounced as the interaction torque rose, although the offset peak was still in evidence. However, what caused the rotor saliency and the stator cogging torque to operate at twice frequency?

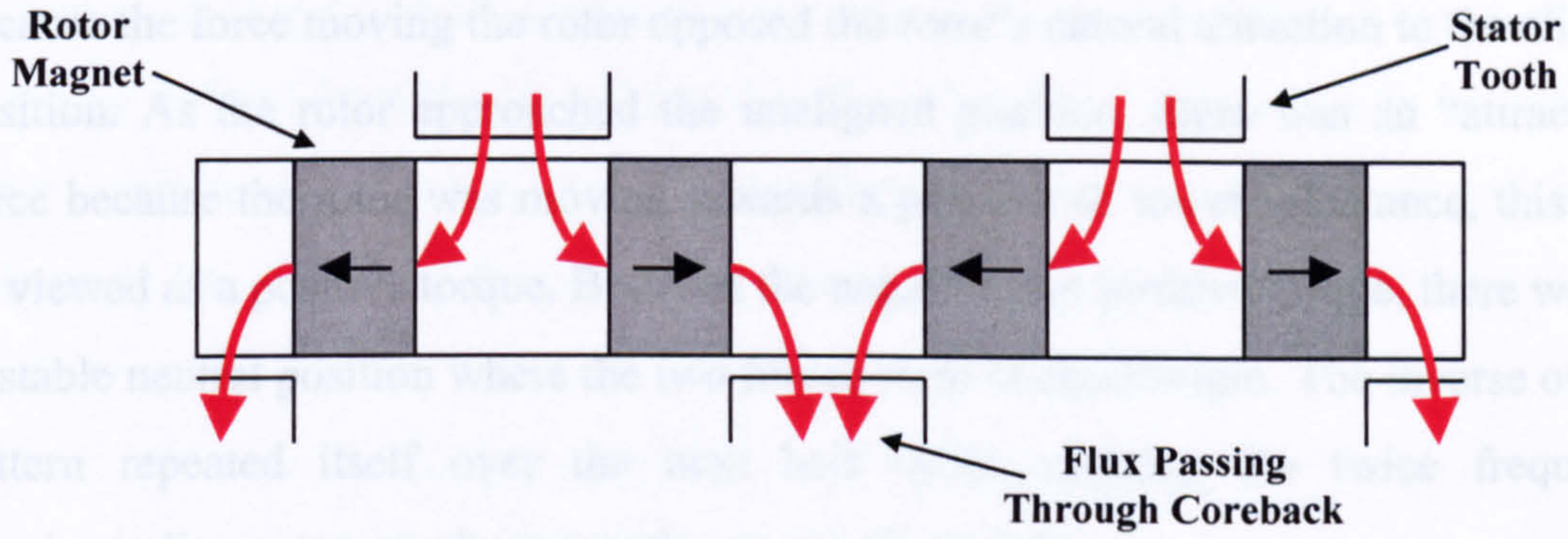

Figure 3.35a Schematic of the DSTFM rotor in an aligned ('d' axis) position showing the magnet flux passing through the stator teeth

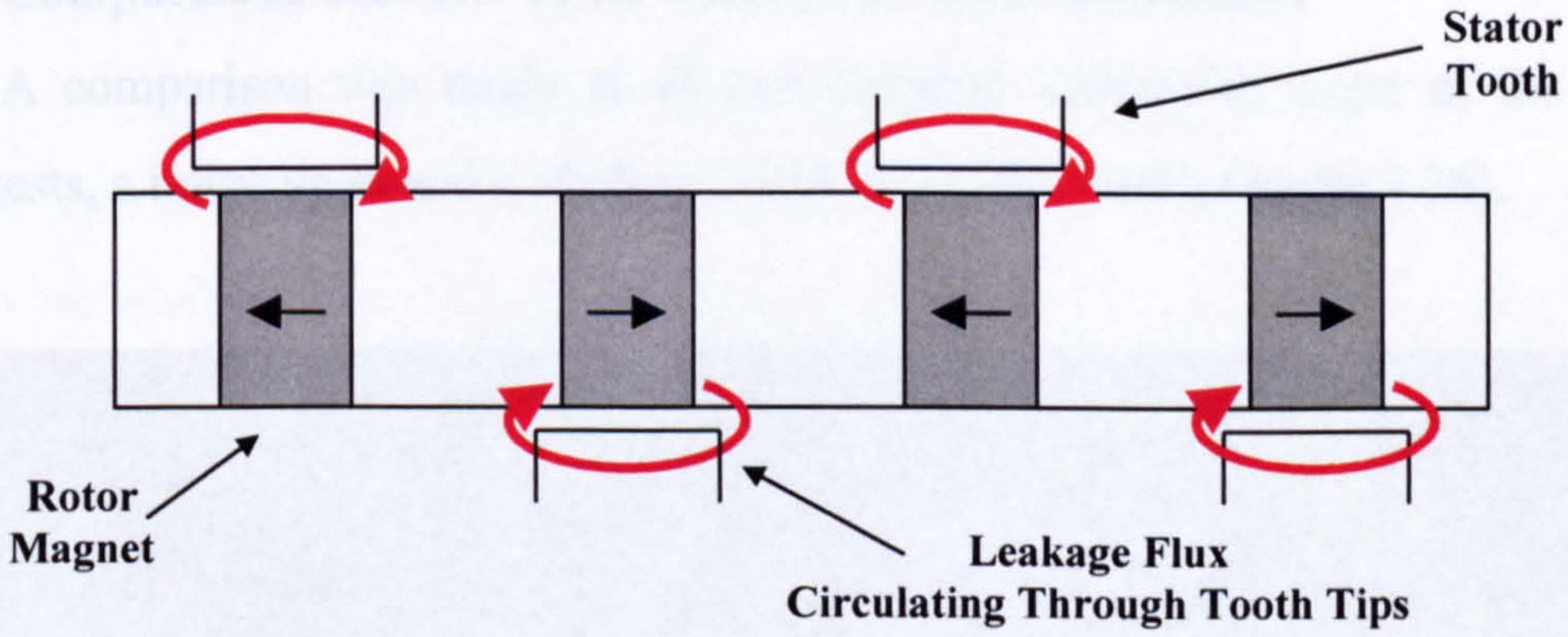

Figure 3.35b Schematic of the DSTFM rotor in an unaligned ('q' axis) position showing the magnet flux passing through the stator tooth tips

The rotor in the DSTFM had two positions of stability, one aligned ('d' axis) and the other unaligned ('q' axis). These two positions are illustrated in figure 3.35a and 3.35b respectively. In the aligned position, stability was due to the rotor magnet flux completing a path through the stator's teeth and coreback iron. In the unaligned position, stability was caused by the rotor magnet leakage fields following a low reluctance path through the base of the stator teeth. The degree of stability was dependent on the stator tooth width in relation to the circumferential active length of the rotor magnet (ℓ_m). If the teeth were the same width or greater than ℓ_m, the leakage path reluctance was lower than the surrounding air and so a position of stability was

reached. However, if the teeth were narrower than ℓ_m, then the position became less stable as the path reluctance was higher.

The twice frequency curve could be described in terms of relative rotor movement. If the rotor were viewed moving away from an aligned position towards an unaligned position, this would initially give rise to a negative torque. This was because the force moving the rotor opposed the rotor's natural attraction to the aligned position. As the rotor approached the unaligned position, there was an "attractive" force because the rotor was moving towards a position of lower reluctance, this may be viewed as a positive torque. Between the negative and positive torque, there was an unstable neutral position where the two forces were in equilibrium. The inverse of this pattern repeated itself over the next half cycle, creating the twice frequency cogging/saliency torque characteristic seen in figure 3.33.

3.11.2 Comparisons between Theoretical and Measured Results

A comparison was made at all rms currents within the scope of the static torque tests, a range up to and including 21.2A rms (30A peak), (figure 3.36).

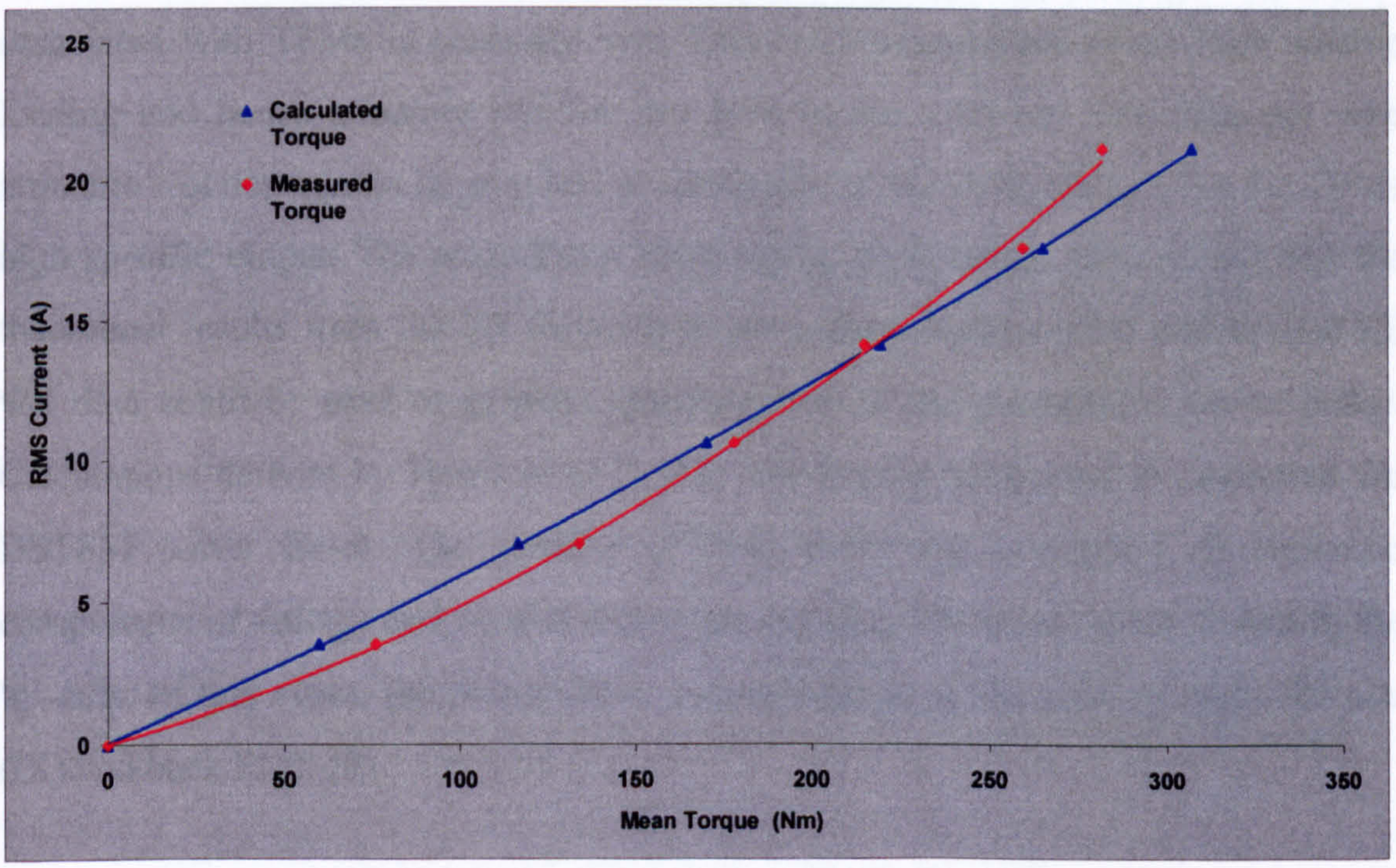

Figure 3.36 Comparison between measured mean torque and 3D FE calculated mean torque

Comparing the calculated and measured mean torque curves in figure 3.36 indicates that the measured curve had a larger unsaturated torque at low levels of

excitation than the calculated curve. This was curtailed at higher MMFs where there was evidence of increased saturation in the measured results. These differences may be attributed to the rectilinear nature of the 3D FE model, increasing the stator reluctance in the first case and imperfect interfacing of the prototype's iron parts in the second. However, a general comparison of the two sets of data showed an average percentage difference of 6% over the entire current range. The thermally limited value of torque derived from the 3D FE analysis (327.2Nm) could therefore be quoted with some confidence. Coupling this value with the active mass (22.7kg) and active volume ($6.18\times10^{-3}m^3$) of the prototype allowed the specific output of the machine to be determined.

- Torque/unit mass = 14.41Nm/kg
- Torque/unit volume = $52.9kNm/m^3$

3.11.3 Power Factor

Power factor has a marked effect on the power handling capacity of a machine drive. A poor power factor will require power electronic devices to be overrated in order to compensate for the increased reactive power in the system. The power factor associated with TFMs is generally low. This is a consequence of the high electric loading and hence armature reaction per pole in the machine. The high per pole armature reaction cannot be avoided, as this is one of the main reasons for the TFMs high specific output. The comparison between the static torque tests results and the theoretical results from the 3D FE analysis were close enough (6%) that the 3D FE Ψ-I data could be used to give an approximation of the prototype's power factor. Calculations derived by Harris *et al* [9, 11] had already been used to determine the DSTFM power factor. The premise of their work was to neglect all harmonic components of voltage and current and to assume that the current is impressed in the 'q' axis. In this event, the power factor is proportional to the ratio of reactive volts (IX) and back EMF (E).

$$\text{Power factor} = \cos\phi \quad \text{and:} \qquad \phi = \arctan\frac{IX}{E} \qquad \{3.12\}$$

This equation (3.12) could be interpreted for use with the 3D FE Ψ-I results in the following way. Neglecting saturation, the ratio of IX/E is equivalent to the ratio of peak stator flux linkage solely due to the armature current and the stator peak flux linkage solely due to magnet flux [29]. In the Ψ-I curve context, the first of these two values is the flux magnitude in the 'q' axis at the value of thermally limited peak current. The second value is represented by the magnitude of flux between the same two positions at no-load. Interpolation of the 3D FE Ψ-I data (Appendix E.1.2) for a peak armature current of 33.1A (23.4A rms) shows these two values to be 981.7mWb (IX) and 554.9mWb (E).

$$\phi = \arctan \frac{981.7\times10^{-3}}{554.9\times10^{-3}} = 60.52^{\circ}$$

$\therefore$ Power Factor (using the assumptions of Harris) $= \cos\phi = 0.49$

The figure quoted by Harris for the DSTFM was 0.55 at a thermally limited current of 21.2A rms, which equates to a power factor of 0.51 using the 3D FE Ψ-I data gathered for this thesis. The slight discrepancy between the two figures could be attributed to differences in the FE models/packages or to the different methods of determining IX and E. The values of back EMF (E) were derived in the same way, from the magnitude of coreback flux, due solely to the magnet in the aligned 'd' axis position. However, the value of IX was a different matter. The method used by Harris involved the creation of a separate 3D FE model in which the magnet was replaced by air and the rotor was placed in the position of maximum torque, the unaligned position. This reduced the saturation effects present in the Ψ-I curves and so increased the value of IX, thereby lowering the model's power factor. Because saturation effects are reduced by this method of power factor derivation, it results in a degree of approximation. If it were possible to determine power factor from the saturated Ψ-I data then a more accurate measure of its value could be established. Therefore, an alternative approach was undertaken.

One method of power factor analysis, utilising the saturated Ψ-I data, was to assume a sinusoidal current variation with position and then impose a locus of that current onto the Ψ-I curves. This current locus was then used to interpolate the flux waveform, which was then differentiated to produce a voltage waveform. From this,

the power factor was easily determined. The above condition corresponds to a drive operating at low speed under current control. An alternative would have been to impose a sinusoidal voltage corresponding to voltage control. This methodology was validated by a simple example using parallel positive and negative 'd' axis curves (Appendix D.4).

3.11.4 DSTFM Power Factor

The interpolated curves for the DSTFM were produced at a thermally limited peak current value of 33.1A (≡ 23.4A rms) and an assumed rotational velocity of 10.47rads/s (100rpm). The values of mean power, rms voltage and rms current derived from these curves were used to calculate a power factor of 0.37.

- DSTFM Mean Power = 5.964kW
- DSTFM rms Voltage = 680.76V
- DSTFM rms Current = 23.4A

$$\text{Therefore Power Factor} = \frac{\textbf{mean Power}}{(\textbf{Vrms} \times \textbf{Irms})} = \frac{\textbf{5964}}{(\textbf{680.76} \times \textbf{23.4})} = \textbf{0.37}$$

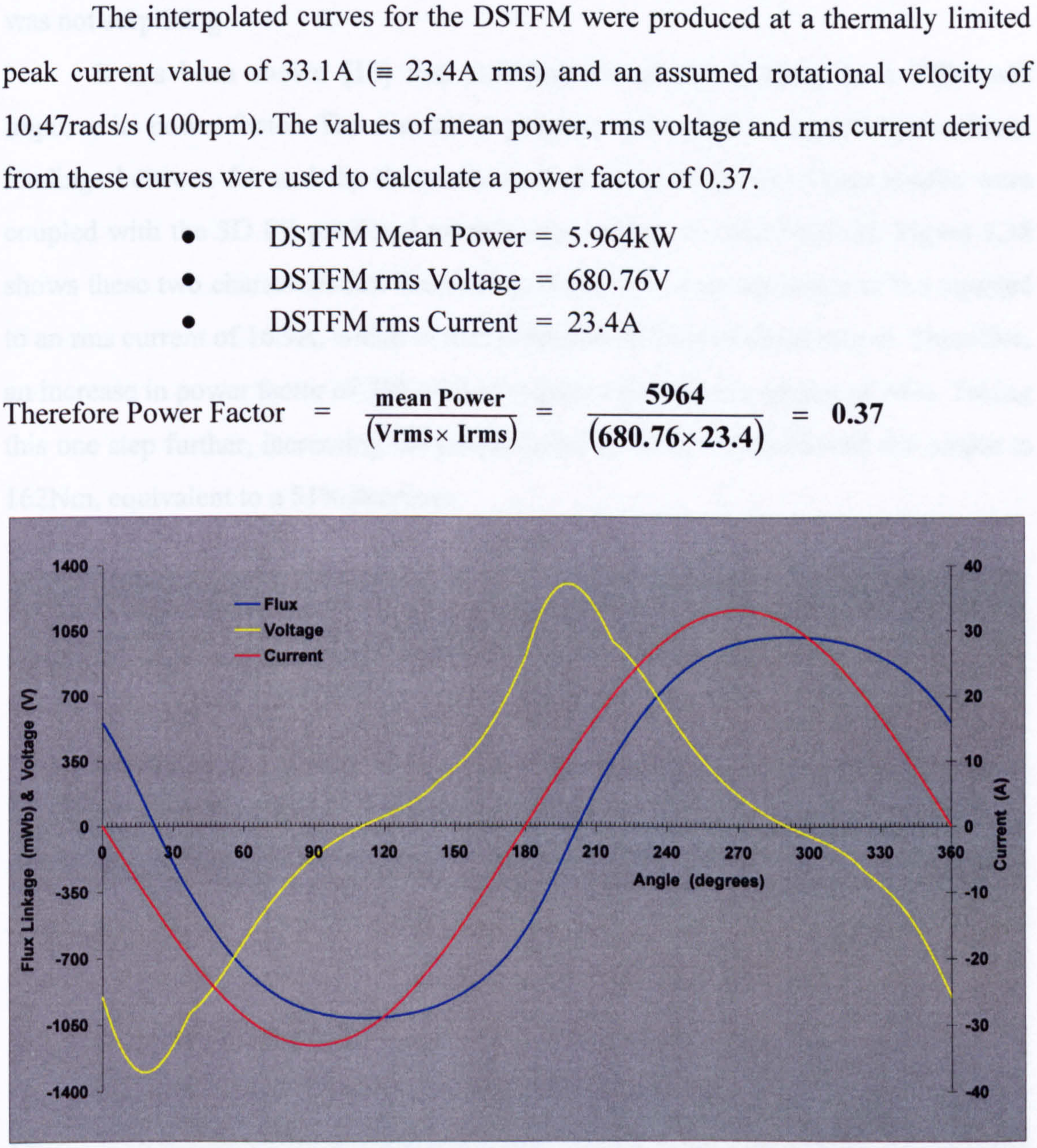

Figure 3.37 Flux and voltage curves generated for the DSTFM

The power factor interpolated from the voltage and current waveforms presented in figure 3.37 confirmed this figure. The distortion evident in the voltage

waveform was caused by the saturation of the 3D FE model at high MMFs. Coupled with a low power factor, this distortion would have a significant effect on the rating of any power electronic drive components used with this machine.

The power factor obtained for the DSTFM by Harris *et al* was derived at a slightly lower value of electric loading of 21.2A. Processing this value through the interpolation system generated a lagging power factor of 0.44. This was still some way below 0.55 (20%) but given the fundamental differences in approach to the problem it was not surprising.

It has been shown [13] that reducing the electric loading in a TFM will improve its power factor. The simulation program was run for a range of rms current loadings between 5A and the thermally limited value of 23.4A. These results were coupled with the 3D FE predicted mean torque outputs for the DSTFM. Figure 3.38 shows these two characteristics. Examining the curves, a power factor of 0.5 equated to an rms current of 16.9A, which in turn produced 250Nm of mean torque. Therefore, an increase in power factor of 35% would require a decrease in output of 24%. Taking this one step further, increasing the power factor to 0.7 (+89%) reduced the output to 162Nm, equivalent to a 51% decrease.

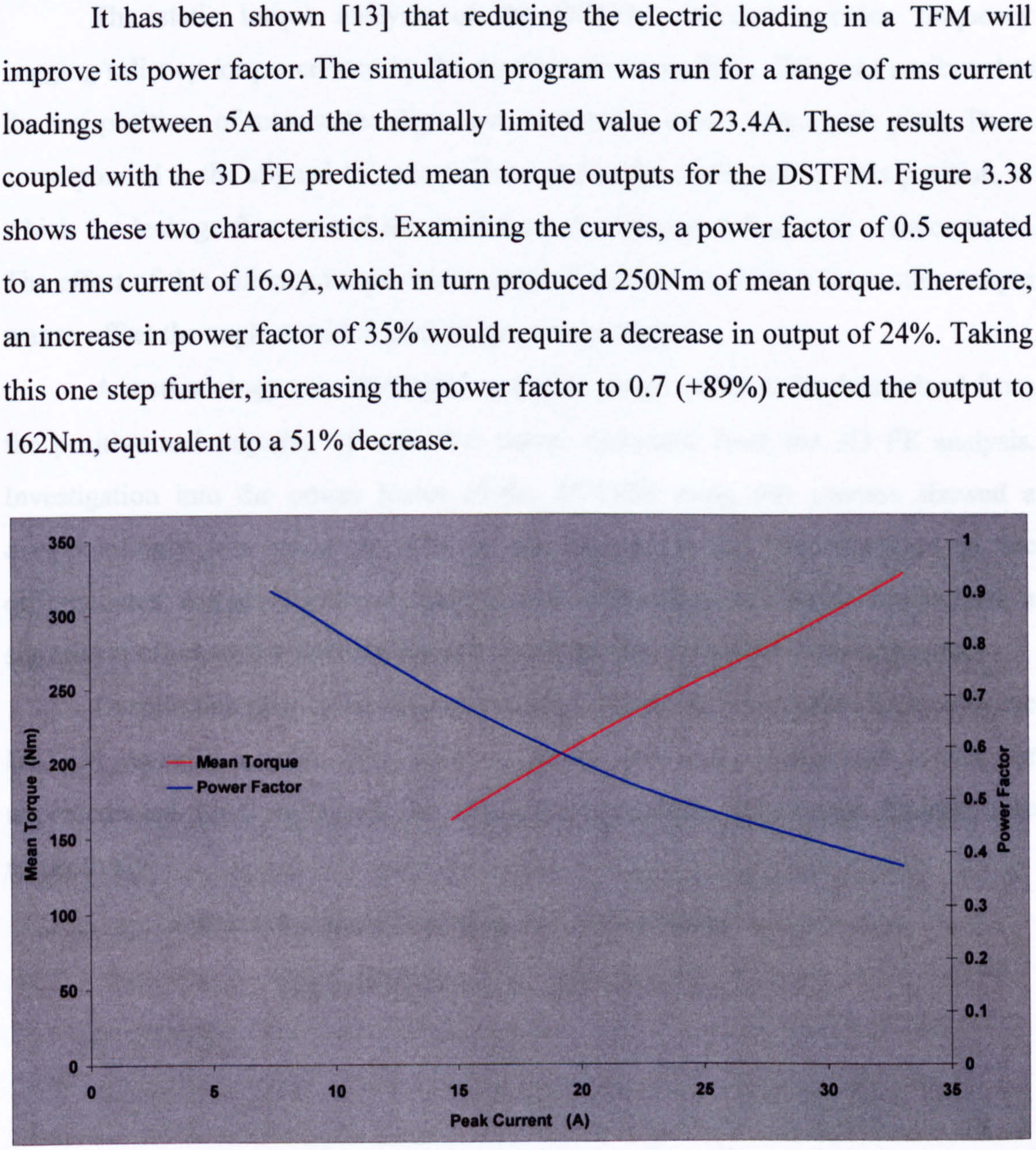

Figure 3.38 Comparison of DSTFM power factor and output energy at different current loadings

3.12 Conclusions

A double-sided Transverse flux machine has been designed and a non-rotating prototype constructed with active iron parts of the machine fabricated from the SMC material ABM100.32. Thermal and static torque testing of the prototype as well as extensive 3D FE analysis, has shown that for a thermally limited 100°C rise the machine will produce a mean torque in the region of 327Nm. There was good correlation between the theoretical and practical analysis of the prototype, with an error of only 6% between the two sets of data in the region of the thermal limit.

The static torque analysis of the DSTFM revealed a twice frequency cogging/saliency torque created by the doubly salient machine. This was attributed to the two positions of rotor/stator alignment, or stability, over a single pole pitch. These corresponded to the aligned 'd' axis position and to the unaligned 'q' axis position, at which the leakage flux around the axial face of a magnet linked with a stator tooth. The effect of this saliency torque when coupled with the machine's interaction torque was to offset the angle at which peak torque was produced.

A methodology was developed to enable power factor to be determined from the positive and negative 'd' axis Ψ-I curves generated from the 3D FE analysis. Investigation into the power factor of the DSTFM using this process showed a disappointingly low value of 0.37 at the thermal limit. The distortion in the differentiated voltage waveform and the low value of power factor would have a significant effect on the rating requirements of any drive coupled to this machine.

Despite this poor value of power factor, calculation of specific outputs for the DSTFM revealed a very high value of torque per unit volume and a thus far unprecedented level of torque per unit of active mass. These two figures were respectively:

- Torque/unit volume = 52.9kNm/m^3
- Torque/unit mass = 14.41Nm/kg

Chapter 4

The Claw Pole Transverse Flux Machine

4. 1 Introduction

There are close topological links between the Transverse Flux Machine (TFM) and electrical machines employing claw pole armatures. The relationship is close enough to regard a TFM as an alternative geometry for a Claw Pole Machine (CPM) or vice versa. Each type of machine incorporates a toroidally wound coil producing an axial and radial flux which is spatially varied in the airgap by an arrangement of flux guiding teeth. Torque production in both machines can be evaluated in a similar fashion (see Section 1.5). This means that, as with the TFM, a CPM's output will rise proportionally with its pole number [21]. The basis for this investigation into claw pole topologies for TFMs was driven by these similarities.

The main application of the CPM is in the Claw Pole Field Car Alternator found in the majority of automobiles produced over the last thirty years. An explanation of its operation can be found in Section 1.5 (pp. 8–9). The Car Alternator employs a simple solid steel claw pole rotor. The rotor is unlaminated because the field winding carries DC current and so produces a homopolar flux. There is a fluctuation of flux in the claw teeth themselves due to airgap reluctance variations but the effect of these on the machine's performance is considered minimal. However, if claw pole tooth structures were to be used on the AC side of the machine they would have significant drawbacks. The armatures of claw pole machines have high frequency alternating flux fields due to their high pole number. This means that the iron losses in a solid tooth would be prohibitive. The orientation of the stator flux fields makes lamination of the teeth and coreback difficult. Consequently, the claw tooth arrangement in machine armatures to date has been limited to small stepping motors and very low speed applications [22]. The use of powder metallurgy and Soft Magnetic Composite (SMC) materials (Appendix A) has removed this restriction.

Claw pole armature machines offer the promise of high specific torque output using a simple and yet mechanically strong arrangement of soft magnetic armature components. The major drawbacks of the CPM are the same as those generally

associated with the TFM, namely high operating frequency losses, high per unit reactance, hence low power factor [21] and high leakage flux. The high frequency losses will be partly offset by the good high frequency performance of powder iron composites, but high per unit reactance and high leakage are inherent problems of this type of topology. A reduction in the severity of these problems would be advantageous and the most logical way to determine their cause is through the detailed 3D FE analysis of the Claw Pole Transverse Flux Machine's (CPTFM) capabilities and operating parameters. Therefore, this chapter deals with the 3D FE analysis of the CPTFM and the testing of the completed prototype machine.

4. 2 The Claw Pole Machine Prototype

The design and construction of a single phase, 24 pole Claw Pole Transverse Flux Machine (CPTFM) was carried out by Professor A.G. Jack, Professor B.C. Mecrow and Mr Norhasbi Abdul Wahab. The Author's involvement began part way through the testing of the newly completed prototype machine.

The machine was comprised of a 40 turn toroidal winding enclosed by a stator made from the SMC material ABM100.32 produced by the Swedish company Höganäs. The stator has 24 fully overlapping claw teeth, each with a mean circumferential width equivalent to 120° electrical. These teeth are positioned radially above 24 alternately polarised surface mounted Samarium Cobalt permanent magnets, which are in turn attached to a solid steel rotor. Full specifications and engineering drawings for the machine can be found in Appendix C.2. Annotated photographs of the completed prototype are presented in figures 4.1 and 4.2.

4. 3 Testing the Prototype Machine

Three forms of practical analysis were carried out on the CPTFM: a no load test to determine the back EMF of the machine, followed by a heat run in order to evaluate its thermal characteristics and finally static torque tests to ascertain the prototype's output capabilities.

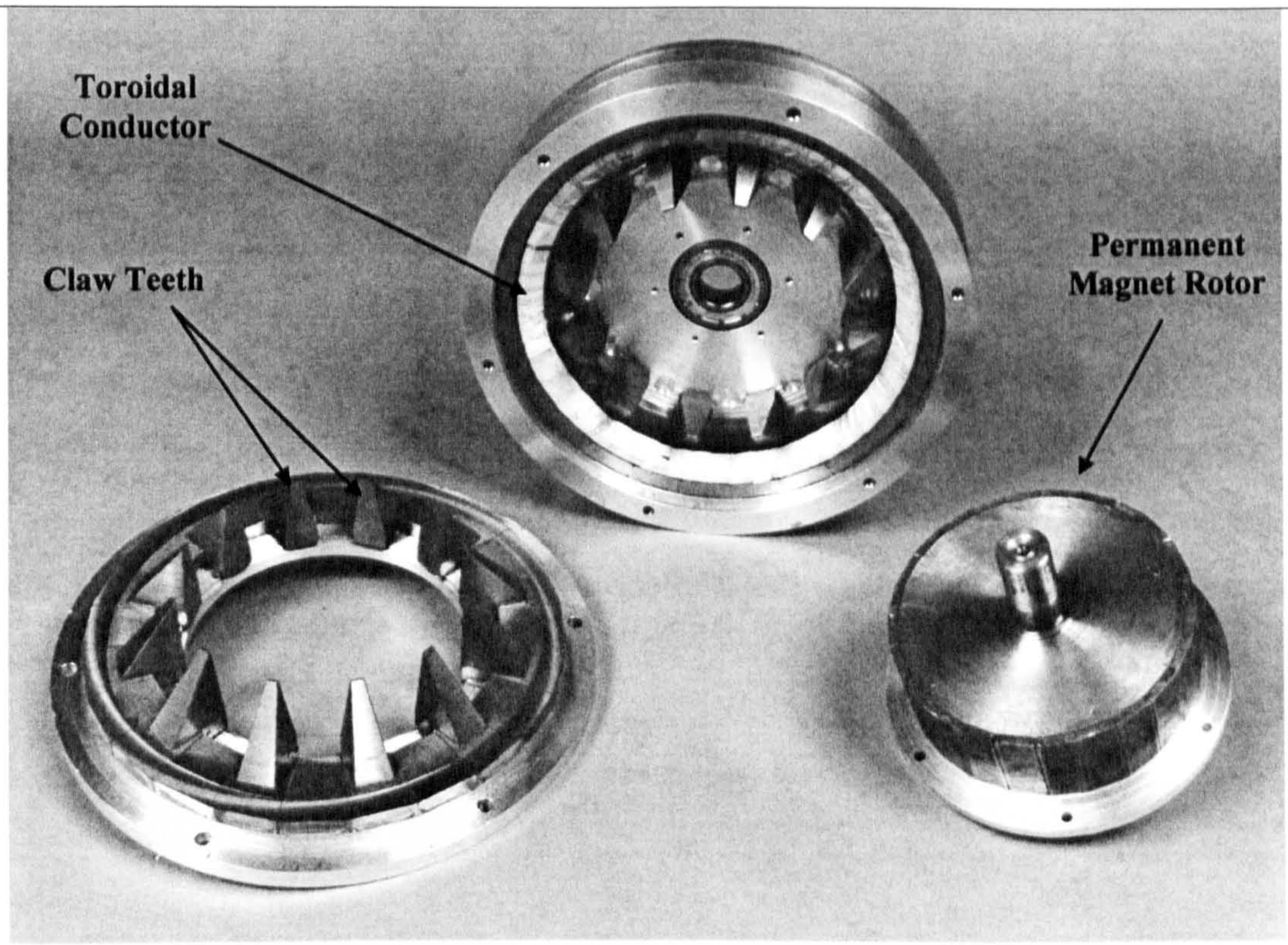

Figure 4.1 Two stator halves and the rotor of the CPTFM

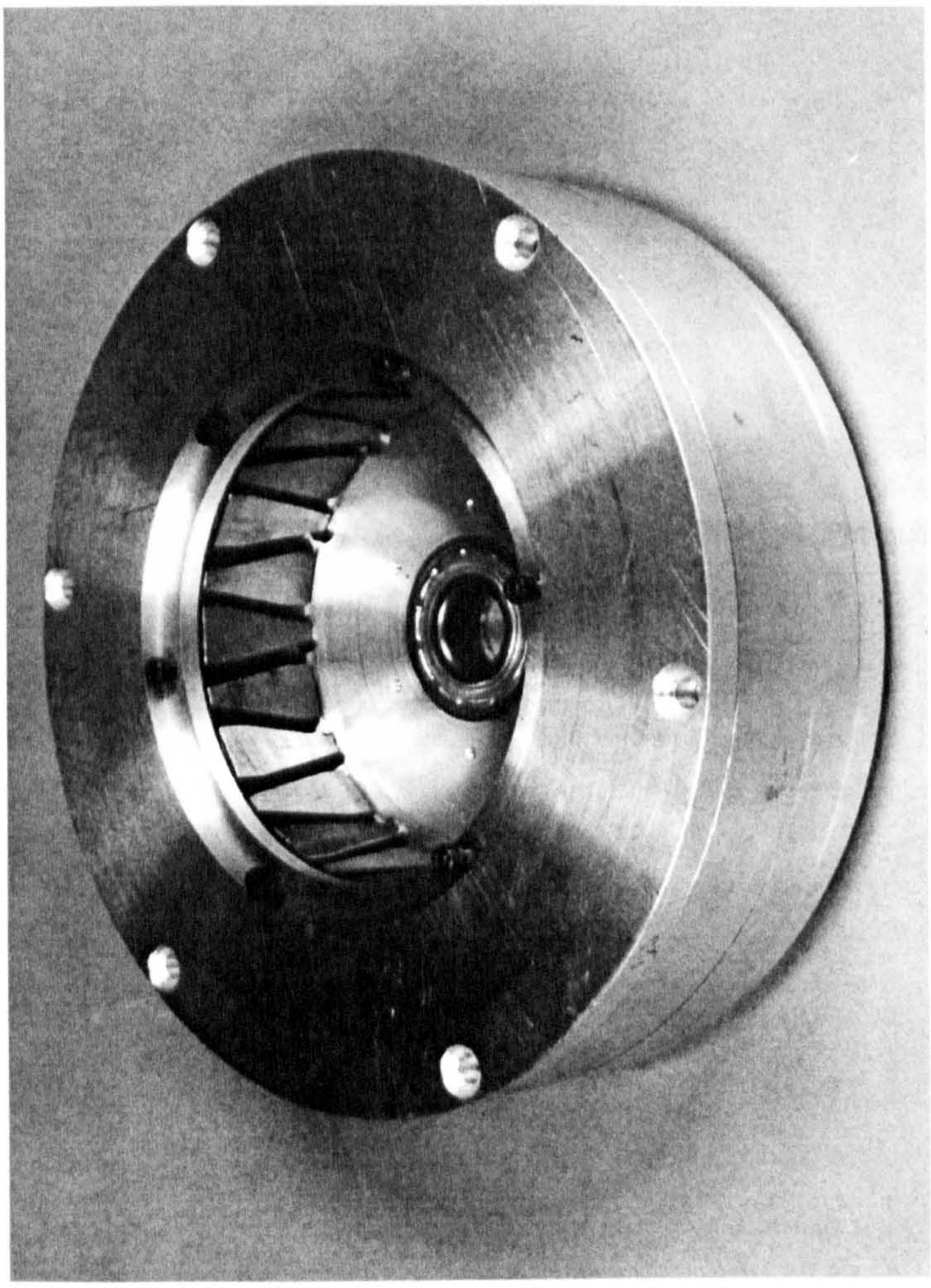

Figure 4.2 Assembled stator illustrating the interleaved claw teeth

4.3.1 Back EMF

Despite the trapezoidal nature of the flux produced by the permanent magnet rotor, the back EMF waveform produced by the prototype was a very close approximation to a sinusoid. This was because of the circumferentially sloped nature of the stator teeth and a high degree of pole to pole leakage (discussed in Section 4.5.3) creating a gradual flux transition between adjacent poles. In order to determine the form of the back EMF waveform, the prototype was mechanically coupled to a DC machine and driven with no load at approximately 800rpm. The output of the prototype was connected to an oscilloscope and the waveform produced is shown in figure 4.3.

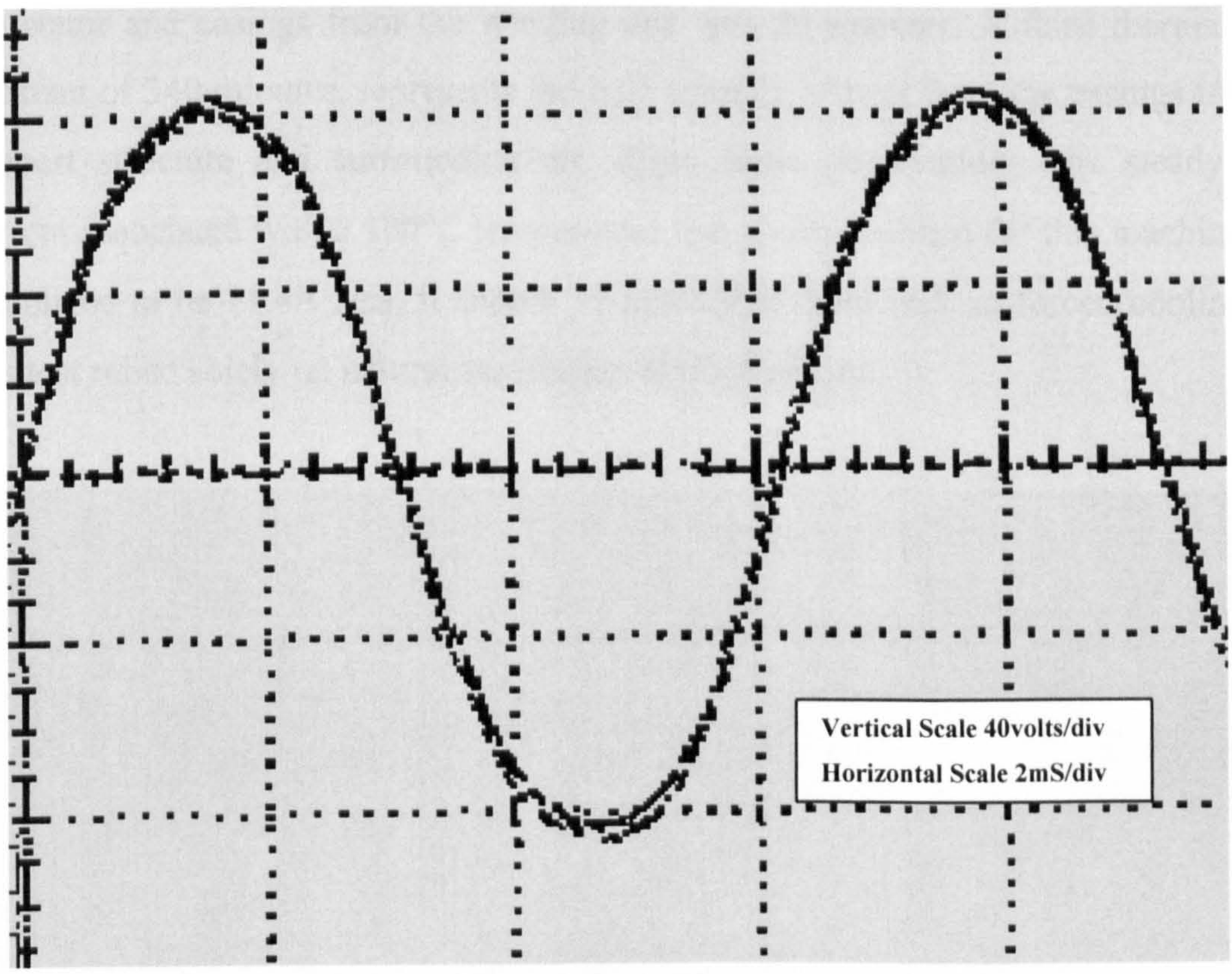

Figure 4.3 Back EMF waveform from CPTFM (56.5V_{rms} at 833rpm)

4.3.2 Thermal Characteristics

The thermal characteristics of the CPTFM were determined by performing a heat run on the machine. The prototype was subjected to a constant 7A (dc) current over a period of 7 hours. At regular intervals throughout the test period the values of voltage and current supplied to the single phase winding were recorded. Using the

thermal co-efficient of resistance for copper ($0.00392°C^{-1}$) and by transposing equation 4.1 the temperature rise of the winding above ambient could be determined.

$$R = R_o\ (1 + 0.00392 \times \text{Temp Rise}) \qquad \{4.1\}$$

where: R = instantaneous winding resistance
R_o = initial winding resistance

The results from this test are presented in appendix E.2.2 and in the graph of figure 4.4. Analysis of the characteristic revealed that there were three thermal time constants associated with the machine. The first, 5.5 minutes, related to the initial temperature rise in the winding. The second was governed by the transfer of heat into the stator and casings from the winding and was 80 minutes. A third thermal time constant of 340 minutes, represents the bulk transfer of heat from the casings into the support structure and surrounding air. From these observations, the steady state current associated with a 100°C temperature rise above ambient for this machine was calculated to be 11.4A rms. It should be noted that there was no forced cooling and this test relied solely on natural ventilation of the machine.

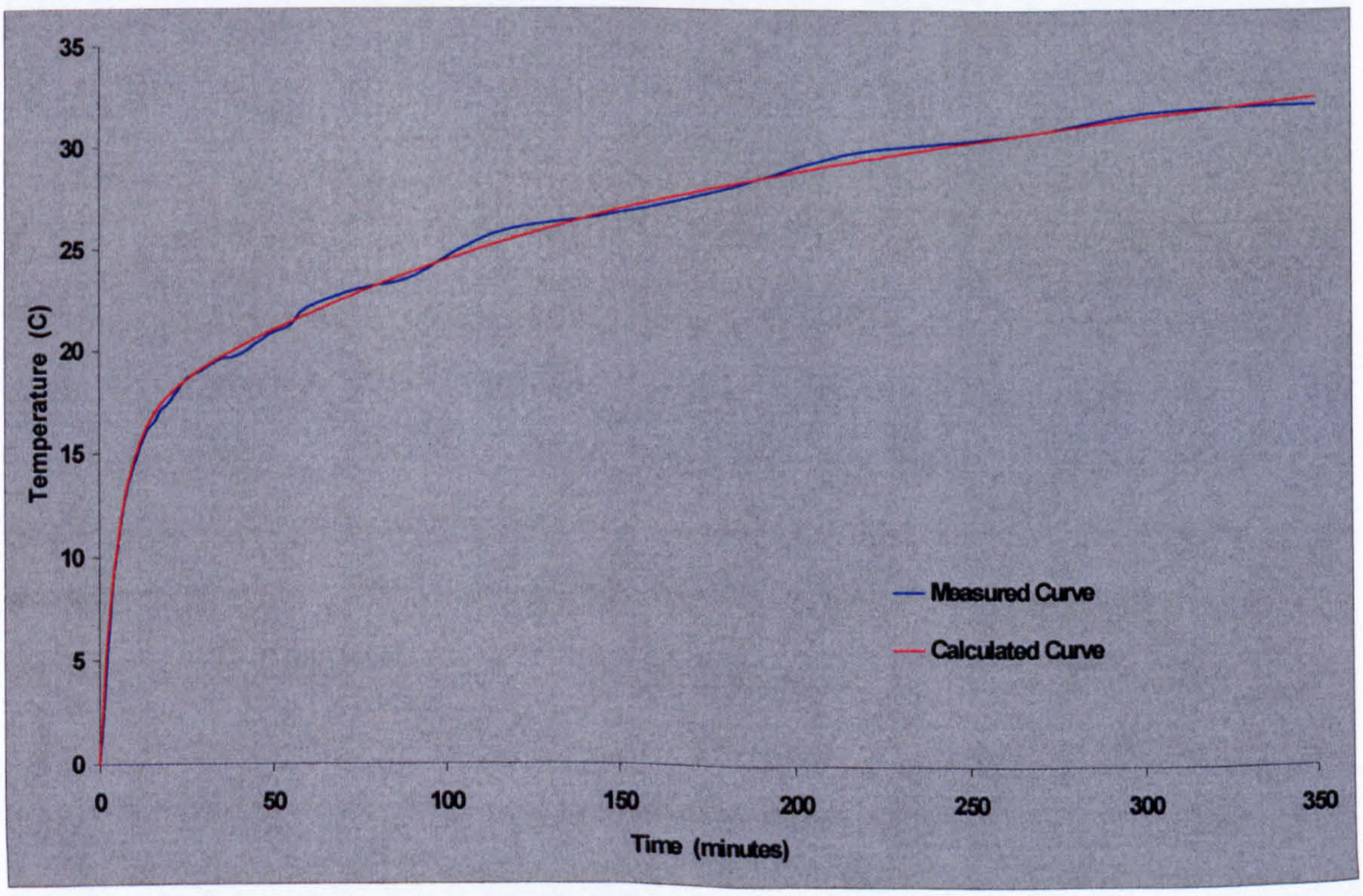

Figure 4.4 The CPTFM thermal characteristic for a DC current of 7A

4.3.3 Static Torque Test

This test was carried out by exciting the machine's winding with increasing levels of DC current. At each current step the rotor of the prototype was incrementally turned through one pole arc. A spring balance indicated the force being exerted on a torque arm by the machine at each angular step. This reading was then converted to a value of torque. The graphical results of torque against angular position are reproduced in figure 4.5. Examining the shape of these curves showed a close resemblance to the static torque curves produced by the DSTFM (figure 3.33). Again there was a twice frequency cogging torque which was most easily discernible in the no-load curve. The reasons for this distinctive characteristic were again attributable to two positions of "stability" one in the aligned position and one in the unaligned as described in section 3.11.1. Because of the constraints of the testing apparatus available, it was not possible to obtain torque readings above an angle of 120° (electrical). However, there was sufficient graphical information in figure 4.5 to show the no-load curve passing through two zero transitions, one at 0° (aligned) and one at 90° (unaligned) and the effect of this second transition on the other torque curves. The data gathered from the physical analysis of the CPTFM is presented in table 4.1.

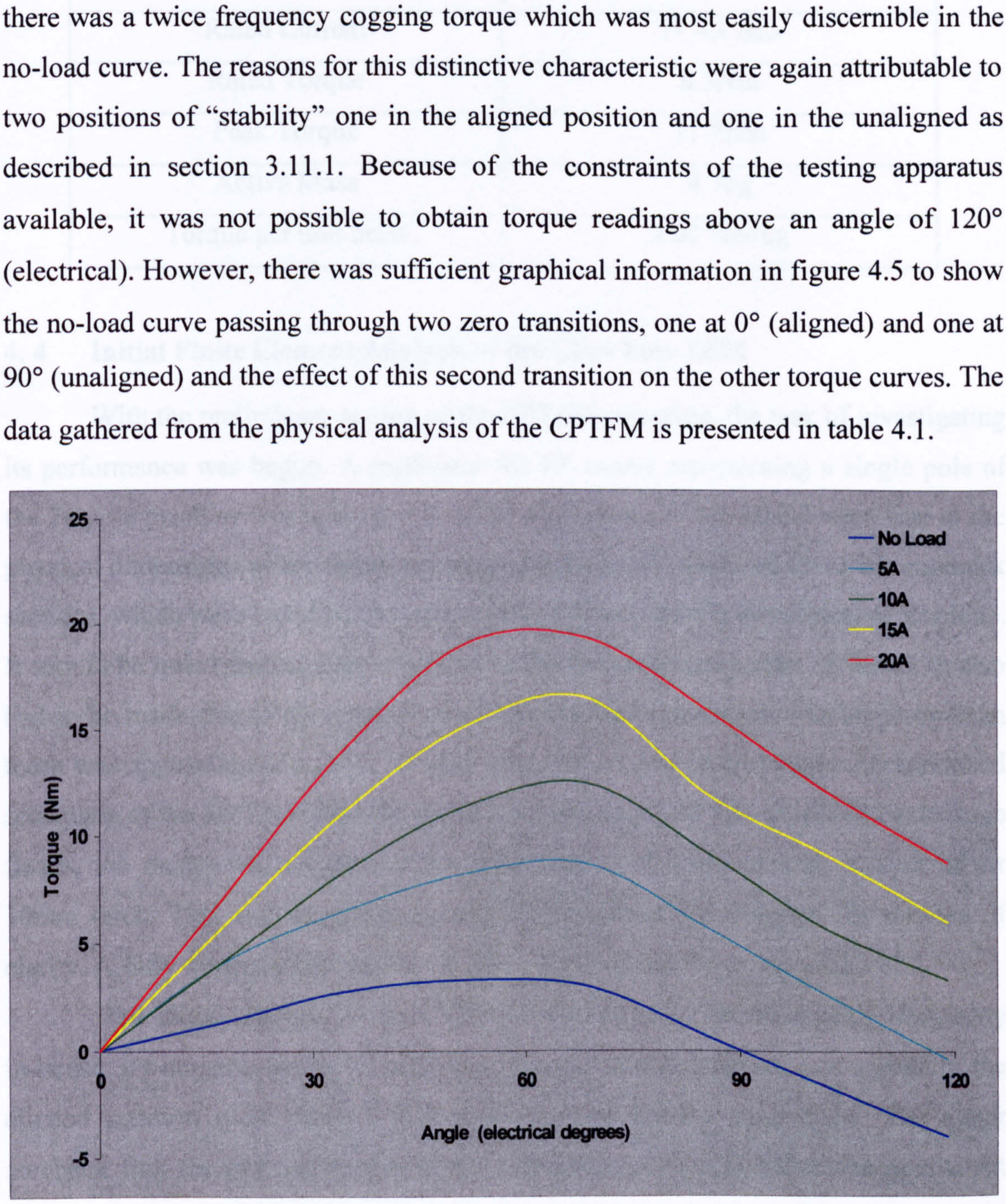

Figure 4.5 Static torque curves for the CPTFM

Table 4.1 CPTFM Parameters

Number of Poles	24
Outside Diameter	200mm
Bore	117mm
Air gap Length	0.5mm
Axial Length	37.5mm
Magnets	Neodymium Iron Boron (see Appendix B.2)
Open circuit Volts @ 800rpm	56.6 V
Rated Current	11.4A rms
Rated Torque	8.3Nm
Peak Torque	11.7Nm
Active Mass	4.1kg
Torque per unit mass	2.02 Nm/kg

4. 4 Initial Finite Element Analysis of the Claw Pole TFM

With the preliminary testing of the CPTFM complete, the task of investigating its performance was begun. A rectilinear 3D FE model representing a single pole of the 24-pole machine was created. All of the dimensions in the model were true to the physical dimensions of the machine, except the circumferential width of the coreback sections, which were based on the mean cross-sectional area in the prototype machine. It should be noted that an approximation to the circumferential rake of the tooth also had to be made due to the constraints of the 3D mesh generator. The slope on each tooth was approximated to five 1.25mm steps of varying axial length. An annotated schematic of the 3D FE rectilinear model is shown in figure 4.6. To allow for leakage fluxes, the model was encased on its radial and axial surfaces with a layer of air 10mm thick. This and the conductor are omitted from the diagram for reasons of clarity. A fully dimensioned version of figure 4.6 is presented in Appendix C.2.

The initial analysis of the CPTFM involved using the Newcastle University in-house 3D magneto-static FE package. The non-linear problem was solved in the aligned position over nineteen individual current density load steps. The stator coreback flux for each of these models was noted and converted to the equivalent value of flux linkage in order to produce a graph of flux linkage (Ψ) against current

(I), (figure 4.7). The flux data gathered from the nineteen load steps is presented in Appendix E, table E.3.1.

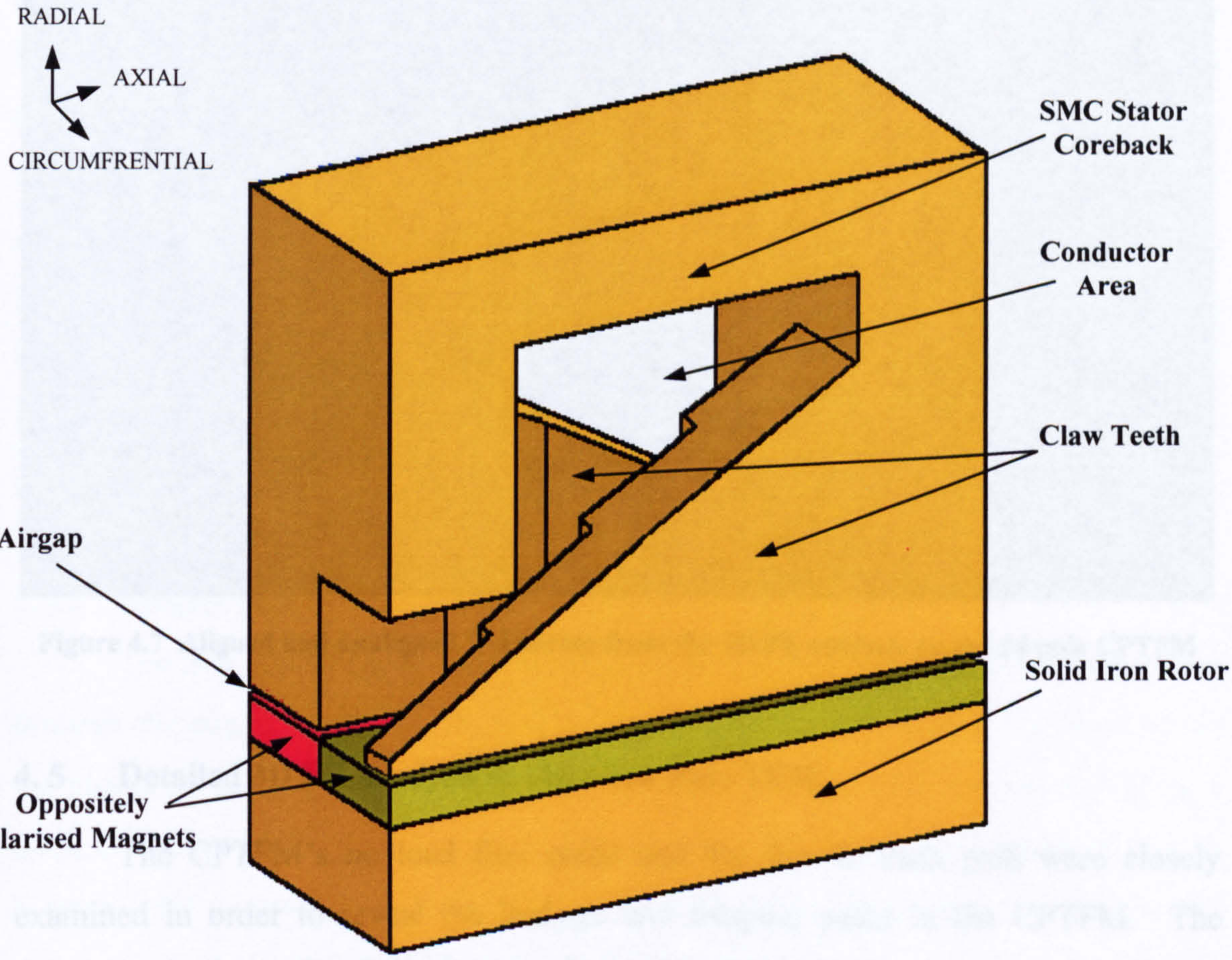

Figure 4.6 Annotated rectilinear diagram of the 3D FE model

The rated current of the CPTFM is 11.4A. The area enclosed by transposing this value as a positive and negative limit (±11.4A) on the Ψ-I curves (as indicated by the dotted lines in figure 4.7) enabled the theoretical mean energy per cycle and hence torque of the CPTFM to be determined, assuming square wave excitation.

- Mean Energy = **4.52 Joules**
- Mean Torque = **8.64 Nm**

Comparing this value with the rated torque of 8.3Nm derived from the static torque test showed good correlation between the two values; the Ψ-I derived torque was 4.1% higher than the measured value.

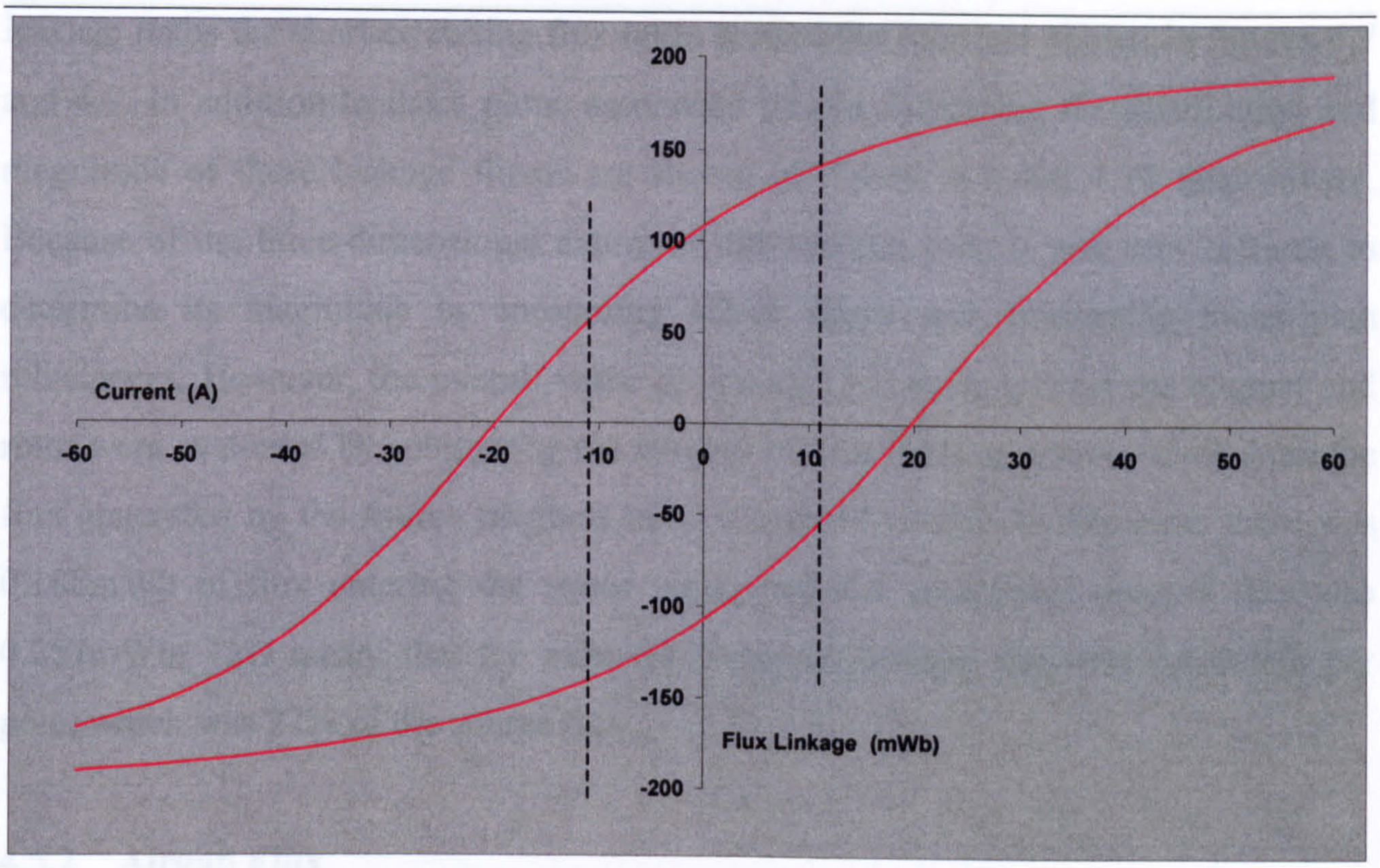

Figure 4.7 Aligned and unaligned Ψ-I curves from the 3D FE analysis on the 24 pole CPTFM

4. 5 Detailed 3D FE Analysis of the Claw Pole TFM

The CPTFM's no load flux paths and the flux in each path were closely examined in order to reveal the leakage and fringing paths in the CPTFM. The following sections of model were be individually investigated.

- Rotor Iron
- Magnet
- Airgap
- Tooth
- Stator Flanking Iron
- Stator Coreback

4.5.1 Rotor and Magnet Flux

The radial and axial extremities of the surface mounted permanent magnet rotor were prime areas for magnet leakage flux to circulate. This was especially true when the stator was formed from an SMC material such as ABM100.32 with an unsaturated permeability of around 300, which is much less than that of high grade magnetic steels. Rotor flux plots from an unexcited 3D FE model illustrating the

leakage paths the short-circuiting flux takes around the rotor are shown in figures 4.7 and 4.9. In addition to these plots, associated graphs indicating the distribution and magnitude of these leakage fluxes are shown in figures 4.8 and 4.10 respectively. Because of the three-dimensional nature of this leakage flux, it was very difficult to determine its magnitude by measuring MMF drops and calculating mean path reluctances. However, the overall value of leakage, per pole, around the magnet and rotor were evaluated by subtracting the amount of flux entering a stator tooth from the flux generated by the source magnets in an unexcited model. In this case, there was 0.188mWb of flux entering the stator tooth, and the permanent magnet flux was 0.257mWb. This meant that the total rotor/magnet leakage flux was 0.69mWb per pole, which was 27% of the source flux.

4.5.2 Airgap Flux

The flux plot of figure 4.11, shows the flux passing from the rotor to the stator through the airgap in the 3D FE model of the CPTFM. The plane-slice, from which the plot is taken, is at the circumferential centre of the tooth and magnet and gives a good indication of the peak airgap flux values. The plot shows the passage of flux as it turns from circumferential to radial in the rotor, radially through the magnet and airgap, then as it spreads radially and axially through a tooth towards the coreback. There is some indication of axial leakage flux at either end of the airgap and the effect of this can be more readily seen in the levels of flux density shown in the graph of figure 4.12. The graph of flux density (B) against distance shows the level of B along a line drawn from the extreme left-hand side of the model in figure 4.11 to its extreme right-hand side, passing through the radial centre of the airgap. The length and position of the airgap is denoted by dotted lines on the graph. The levels of B_{mod} shown outside these dotted lines are indicative of the leakage flux present. It should be noted that there was a higher leakage flux density on the right-hand side of the model than on the left. This was due to the tapered end of the tooth presenting a higher stator reluctance path than the non-tapered side of the tooth. The peak value of B_{mod} shown on the graph is 0.964T and the average airgap flux density is 0.93T.

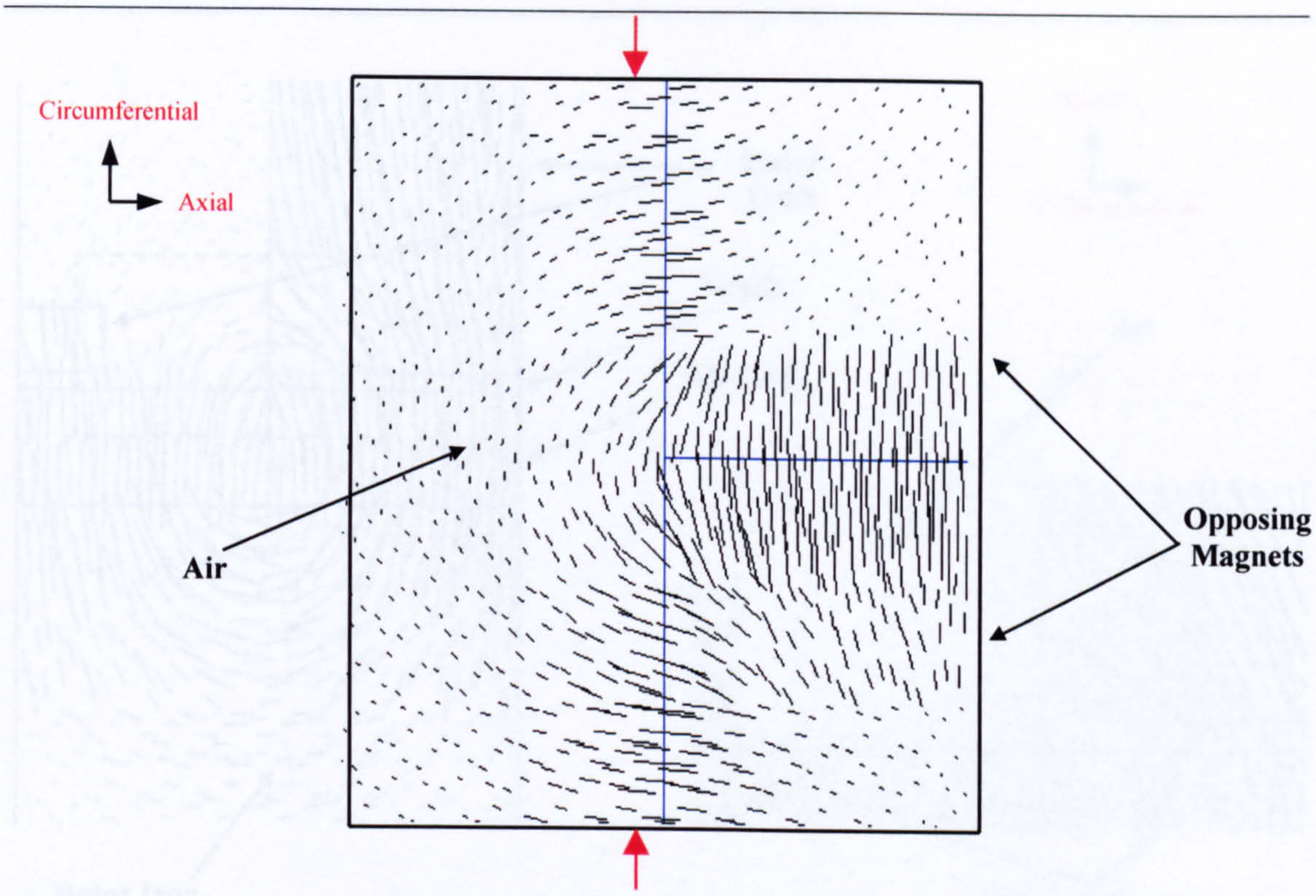

Figure 4.7 A view looking radially down on the two magnets, 0.5mm below the active airgap shows circumferential and beginnings of radial leakage.

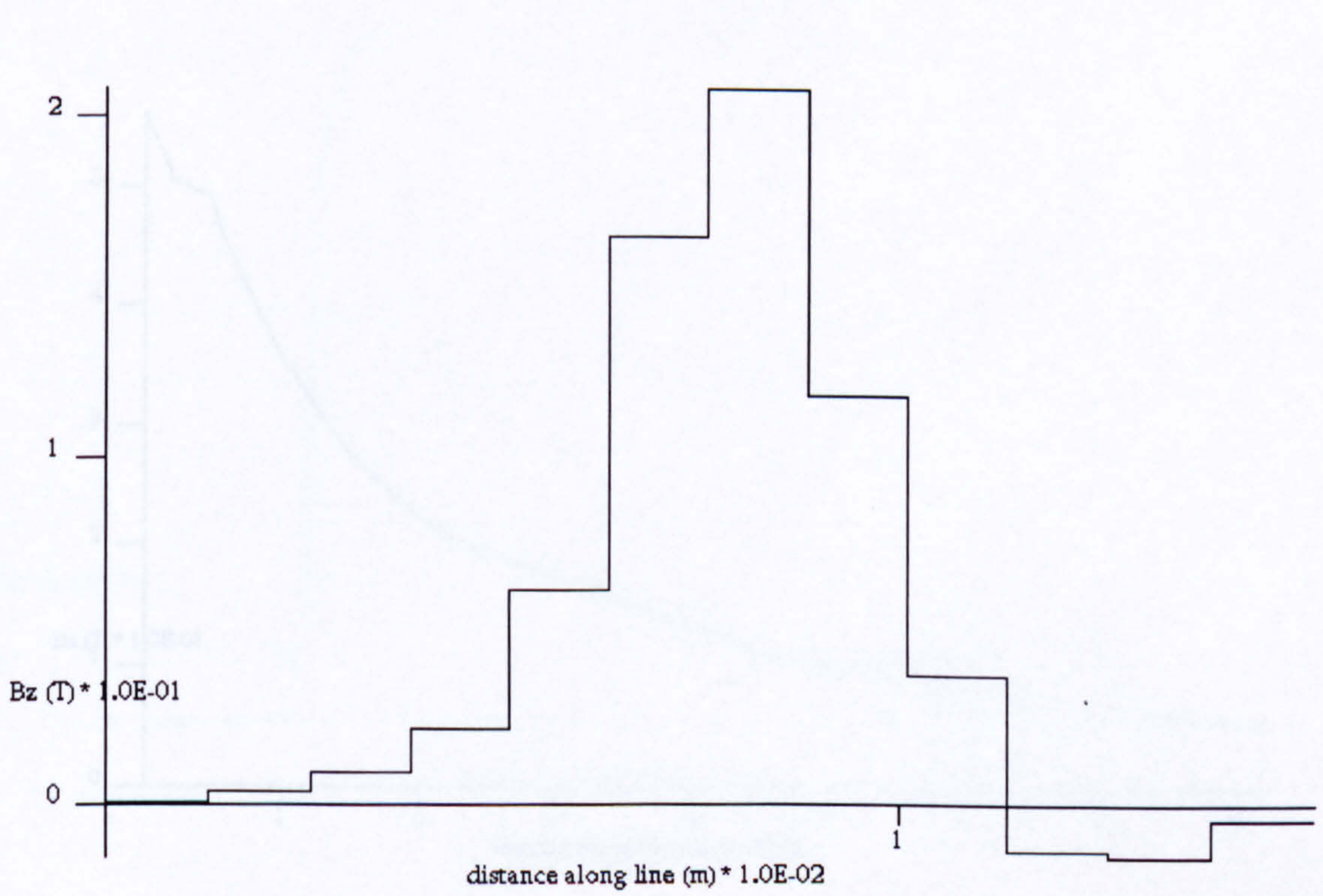

Figure 4.8 Plot of the circumferential variation of flux density between the arrows indicated, 0.5mm to the left of the two magnets in figure 4.7. The peak value shown is 0.209T:

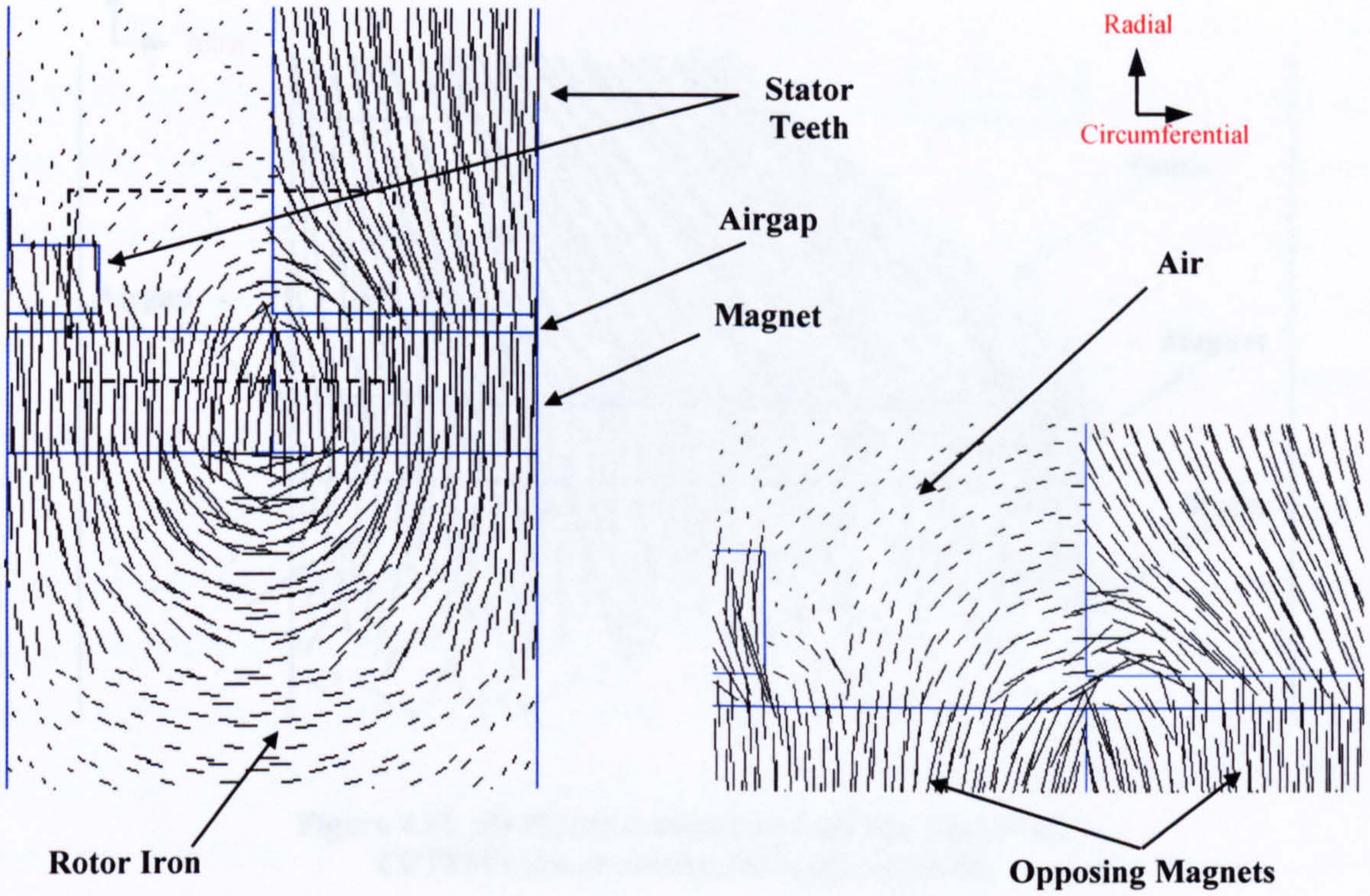

Figure 4.9 A view looking axially and detail view of the rotor and stator 0.5mm into the axial surface. The flux plot shows circumferential / radial leakage flux

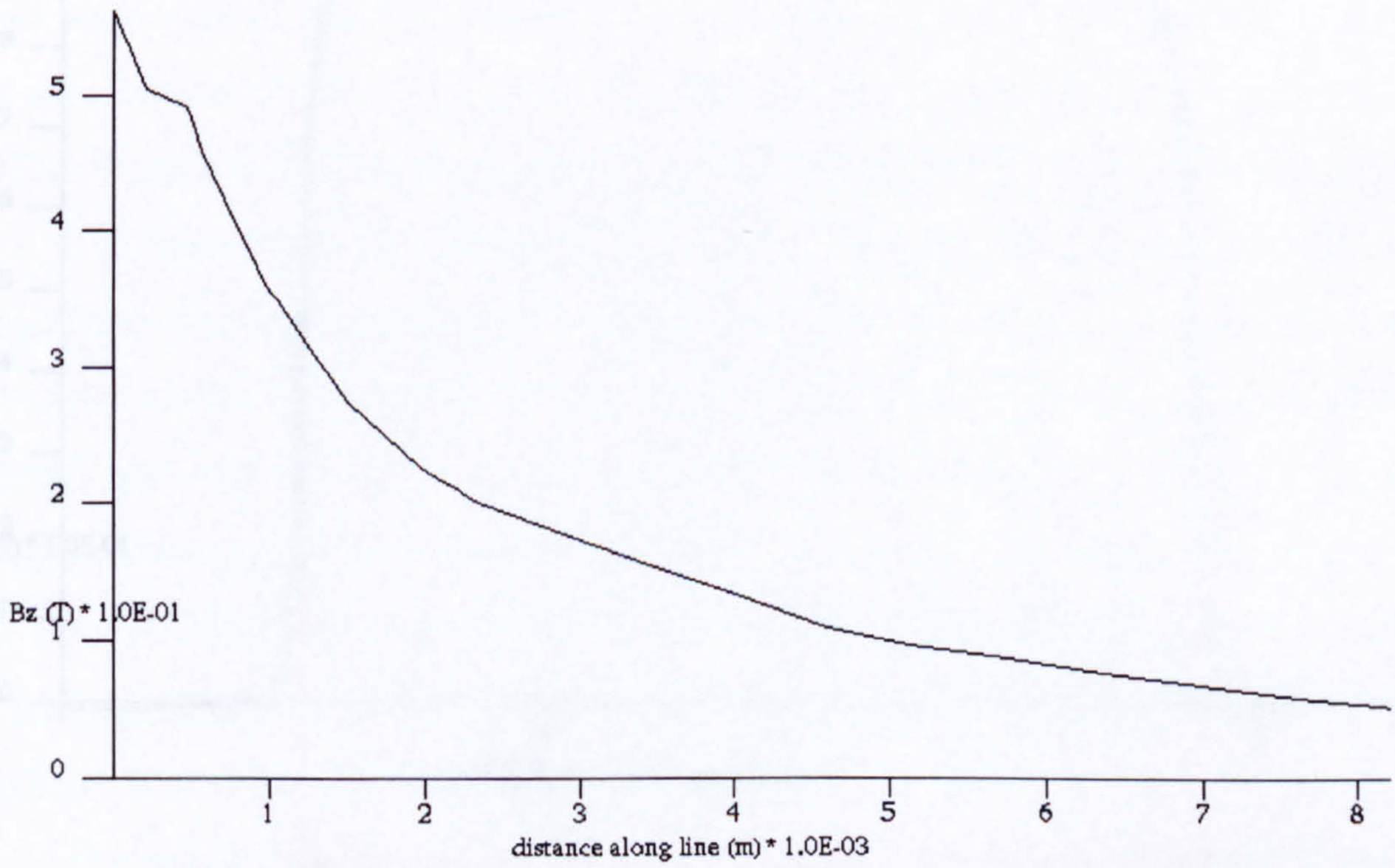

Figure 4.10 Plot of the radial variation of flux density in the air, 0.5mm to the left of the larger tooth in figure 4.9. The peak value shown is 0.56T and the minimum value is 0.05T

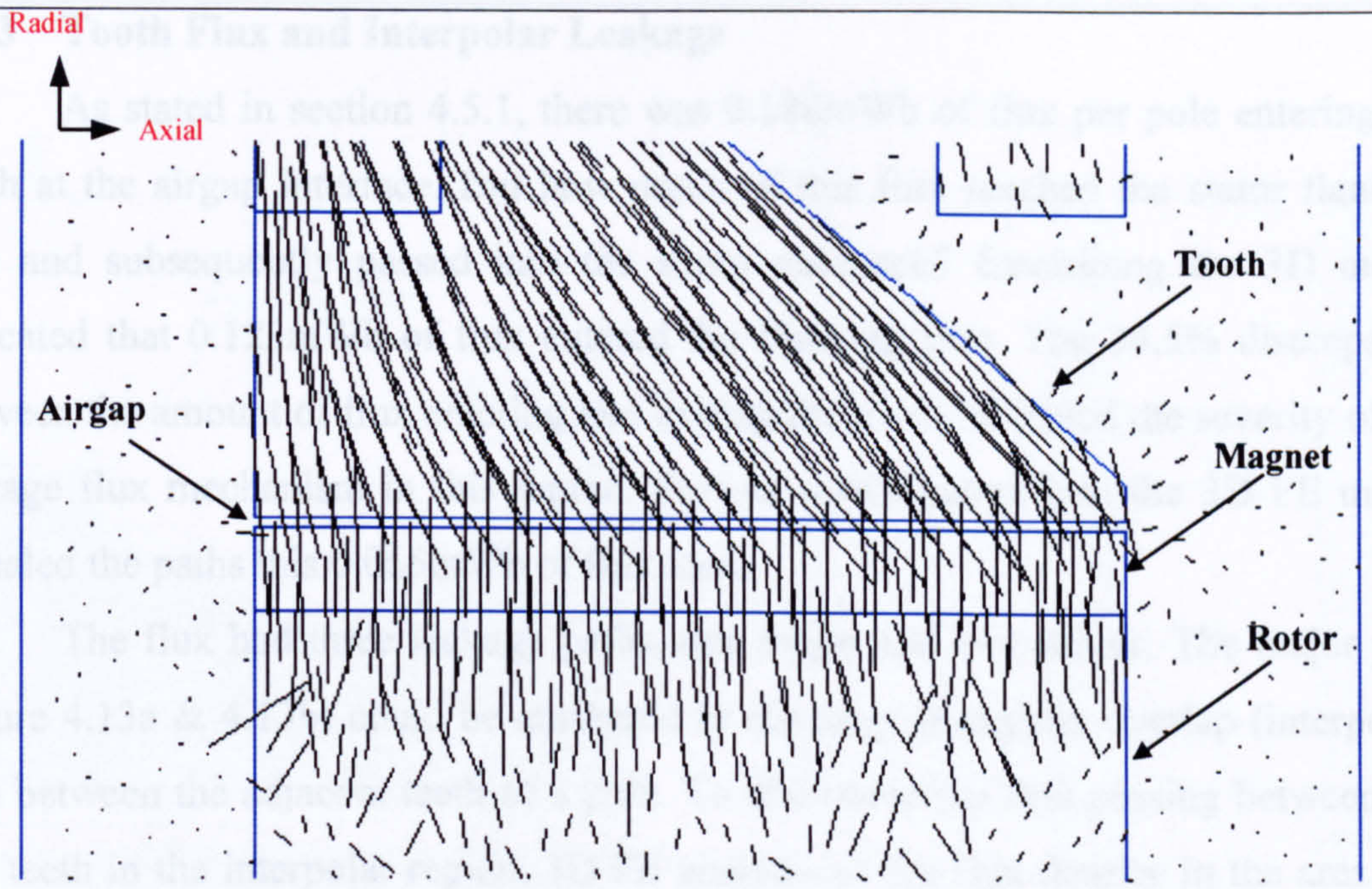

Figure 4.11 3D FE axial /radial no load flux plot of the CPTFM centred around the airgap (d-axis)

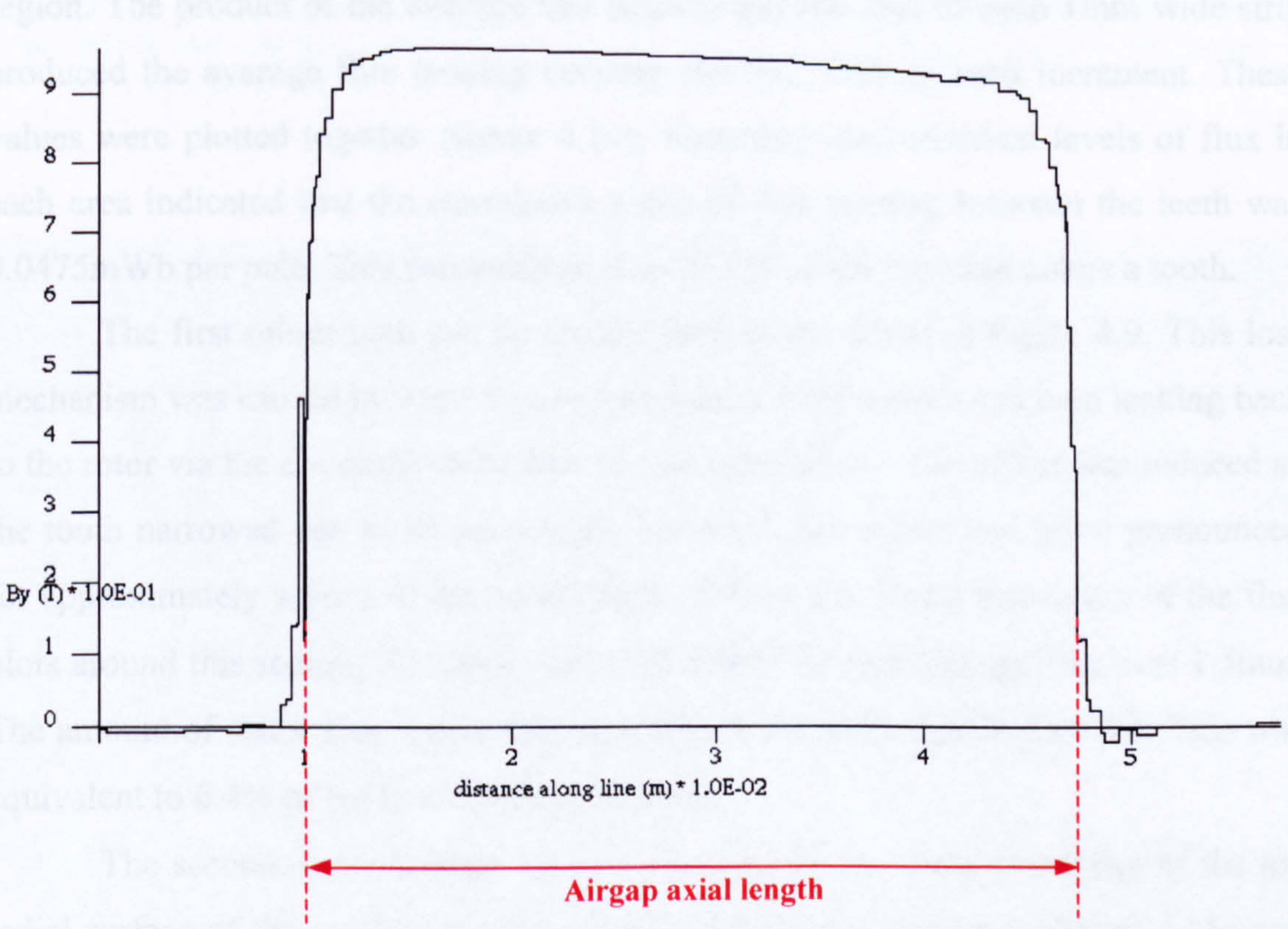

Figure 4.12 Radial flux density along the centre of the airgap and extending axially into the surrounding air (peak B = 0.964T)

4.5.3 Tooth Flux and Interpolar Leakage

As stated in section 4.5.1, there was 0.188mWb of flux per pole entering the tooth at the airgap interface. But how much of this flux reached the stator flanking iron and subsequently passed into the stator coreback? Examining the 3D model indicated that 0.123mWb of flux entered the flanking iron. The 34.5% discrepancy between the amount of flux entering and exiting the tooth indicated the severity of the leakage flux mechanism in this region. Further investigation into the 3D FE model revealed the paths this 0.065mWb of flux took.

The flux had three leakage paths, one major and two minor. The major path (figure 4.13a & 4.13b) could be attributed to the large triangular overlap (interpolar) area between the adjacent teeth of a pole. To determine the flux passing between the two teeth in the interpolar region, 3D FE analysis of the flux density in the area was carried out. The method of analysis was to determine the average flux density axially between the teeth at 1mm radial intervals. The measurements commenced 1.5mm radially above the sole of the tooth, in order to discount the effect of leakage flux (discussed in the next paragraph) and finished at the radial apex of the interpolar region. The product of the average flux density and the area of each 1mm wide strip produced the average flux passing between the two teeth at each increment. These values were plotted together (figure 4.14). Summing the individual levels of flux in each area indicated that the cumulative value of flux passing between the teeth was 0.0475mWb per pole. This was equivalent to 25.3% of the flux that enters a tooth.

The first minor path can be readily seen in the detail of figure 4.9. This loss mechanism was caused by rotor flux entering the sole of a tooth and then leaking back to the rotor via the circumferential face of that same tooth. The effect was reduced as the tooth narrowed due to its axial taper. However, the effect was quite pronounced for approximately a third of the axial length of the tooth. From inspection of the flux plots around this region, the radial "cut-off" height for this leakage flux was 1.5mm. The amount of stator flux lost in this region for both teeth was 0.012mWb. This was equivalent to 6.4% of the flux entering the tooth.

The second minor leakage path was caused by the close proximity of the top radial surface of the tooth to the lower edge of the stator coreback (figure 4.15a and 4.15b). The remaining 2.8% of missing flanking iron flux was attributable to this minor leakage path. The calculated value of this flux over this section was 0.0078mWb, equivalent to 4.1% of the flux entering the stator tooth.

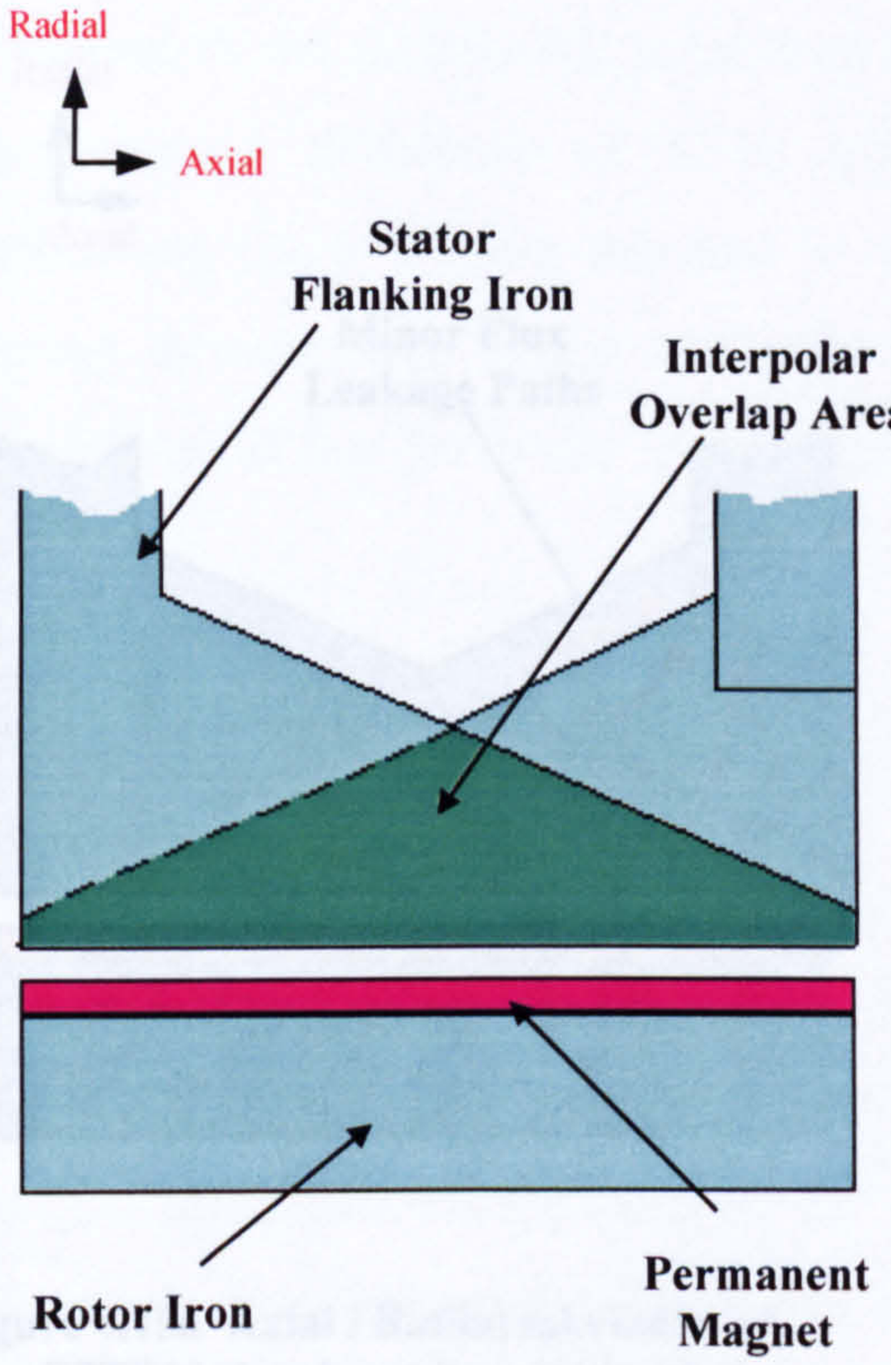

Figure 4.13a Axial / Radial schematic of the CPTFM showing the tooth overlap or interpolar region

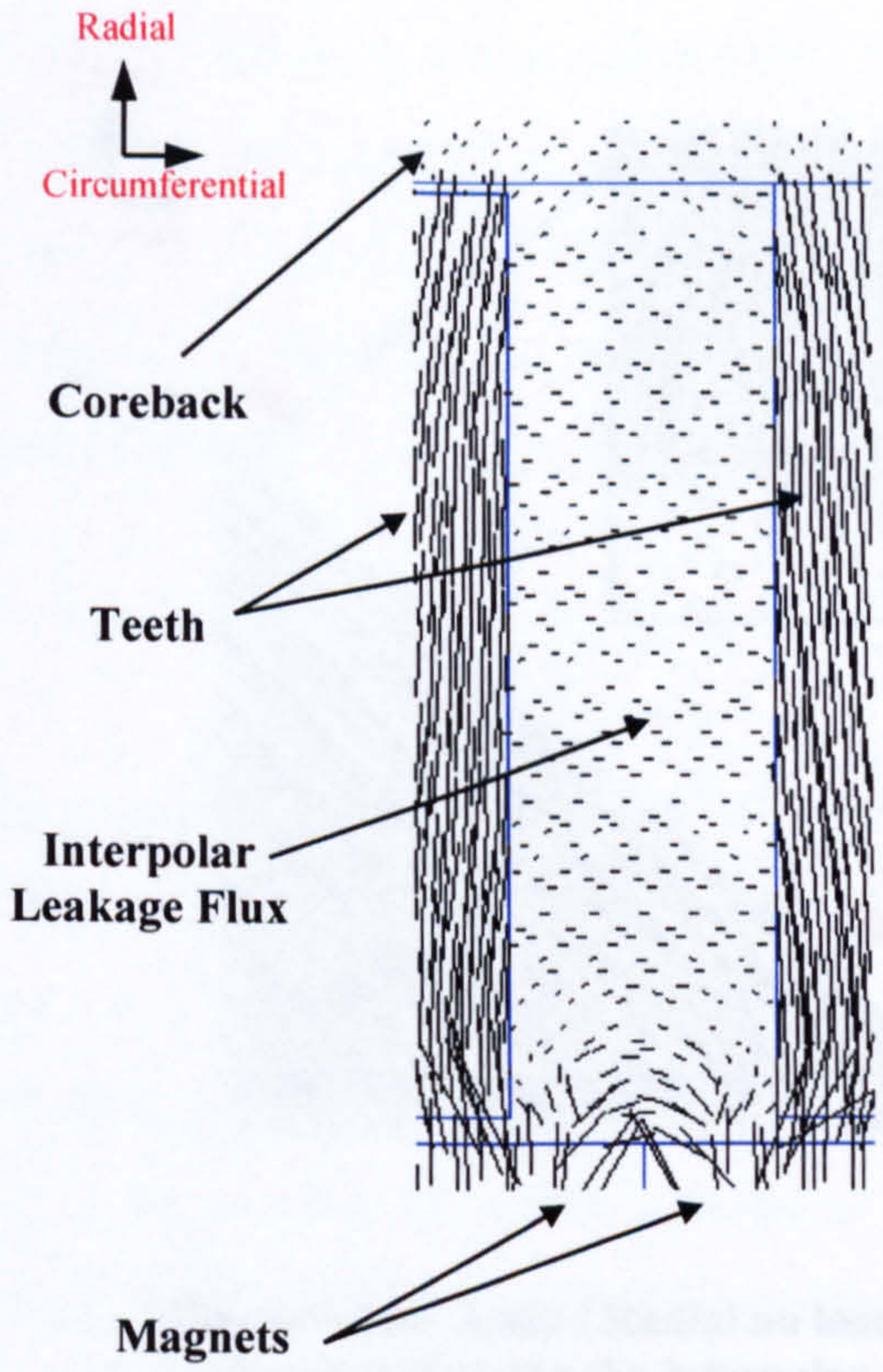

Figure 4.13b Circumferential / Radial no load flux plot showing the interpolar leakage flux

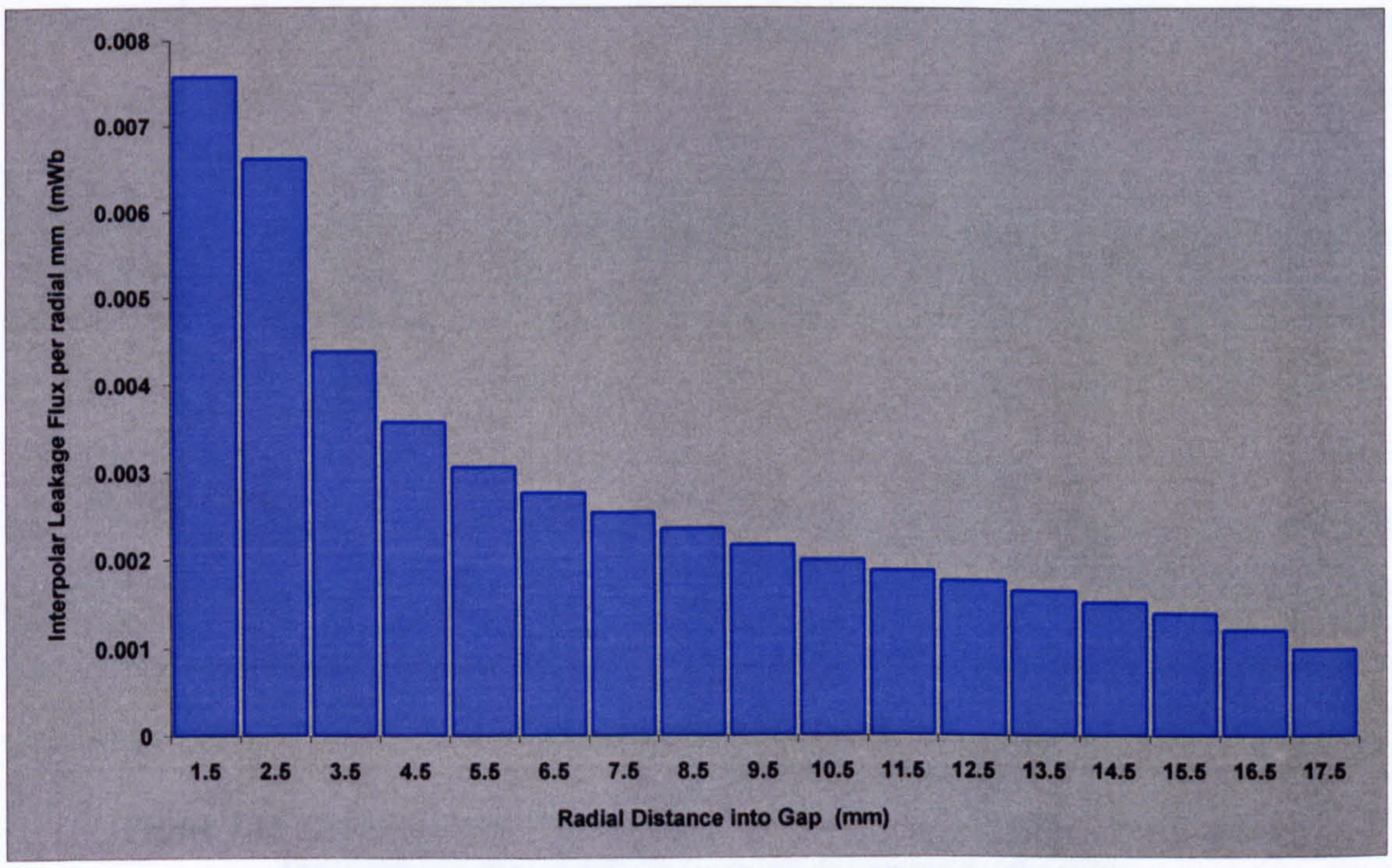

Figure 4.14 Radial variation of leakage flux in the interpolar region

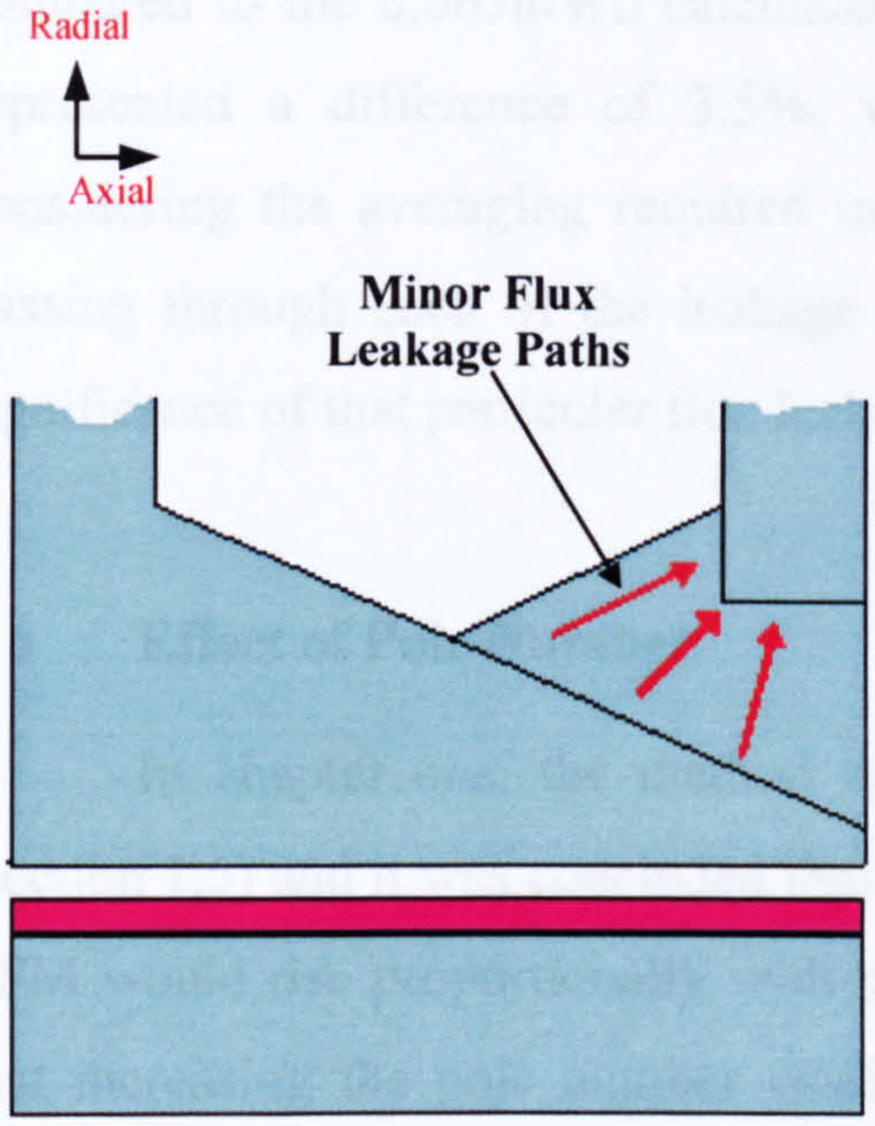

Figure 4.15a Axial / Radial schematic of the CPTFM showing minor interpolar leakage paths

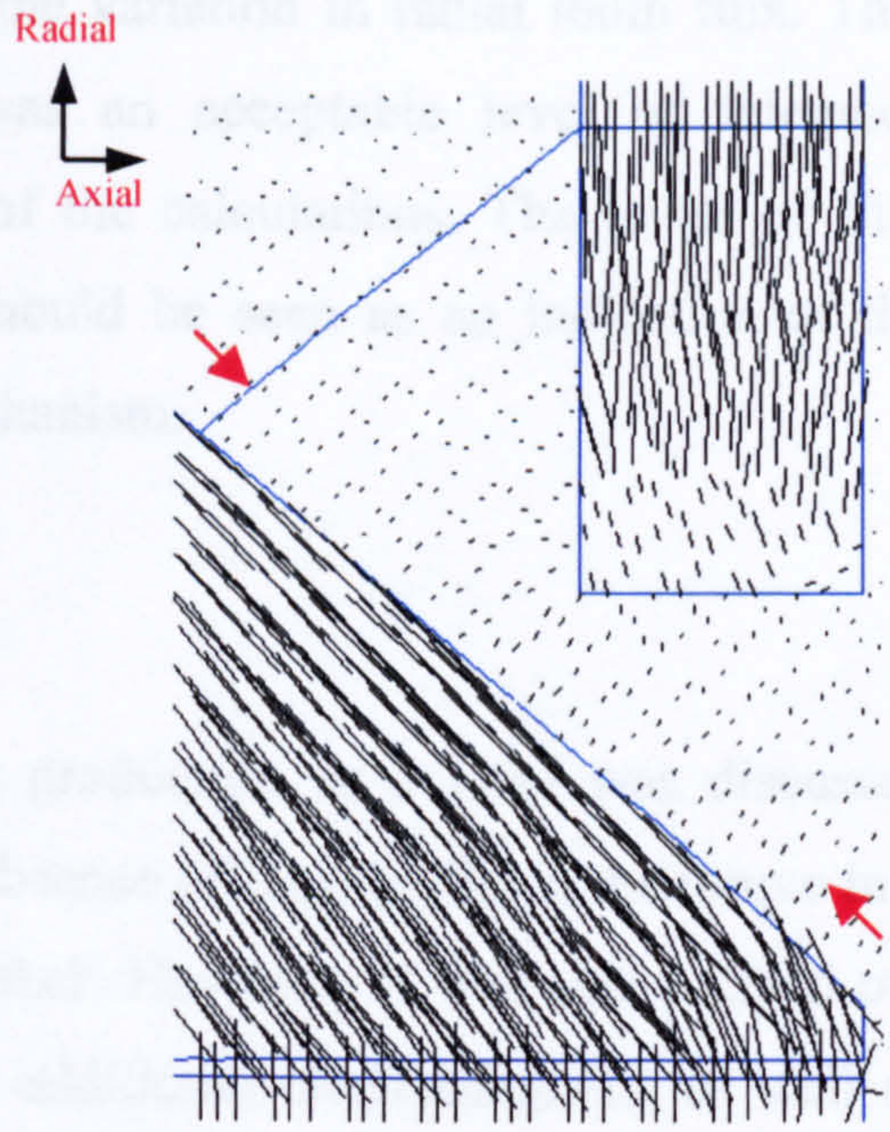

Figure 4.15b Axial / Radial no load flux plot showing the interpolar leakage flux

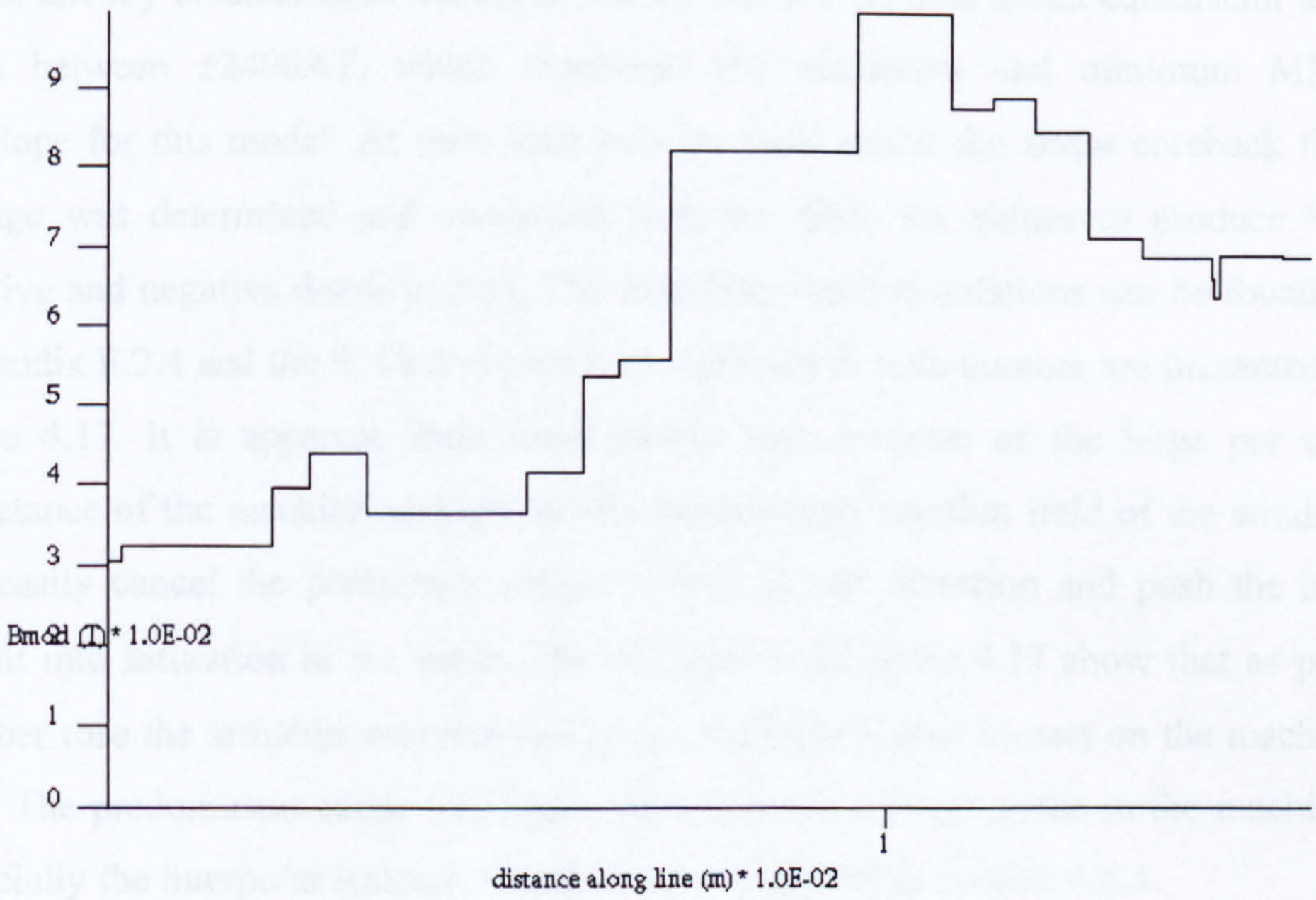

Figure 4.16 Graphical plot of the flux density along a line parallel to the slope of the tooth in figure 4.15b between the two arrows indicated (peak value is 0.1T, average is 0.06T)

Summing the flux in the three leakage paths gave a total flux of 0.0673mWb compared to the 0.065mWb calculated from the variation in radial tooth flux. This represented a difference of 3.5%, which was an acceptable level of tolerance considering the averaging required in some of the calculations. The levels of flux passing through each of the leakage paths should be seen as an indication of the significance of that particular flux leakage mechanism.

4.6 Effect of Pole Number

In chapter one, the method of torque production in a TFM was discussed (section 1.5) and it was concluded that in the absence of leakage fields the torque in a TFM would rise proportionally with pole number. However, it was also pointed out that increasing the pole number would place additional electromagnetic as well as physical constraints on the machine. In order to validate this statement a series of 3D FE models were created. The models were based upon the 24 pole CPTFM geometry (Section 4.2). Each model encompassed one pole pitch of the topology and was scaled to represent differing pole numbers for a fixed stator outside diameter (OD). Four different pole numbers were investigated, 12, 18, 30 and 36, in addition to the 24 pole model already created. Each additional model was solved over seven equidistant load steps between ±2400AT, which represents the maximum and minimum MMF envelope for this model. At each load step for each model the stator coreback flux linkage was determined and correlated with the other six values to produce Ψ-I positive and negative d-axis curves. The data from these simulations can be found in Appendix E.2.4 and the Ψ-I curves for each variation in pole number are presented in figure 4.17. It is apparent from these curves that, because of the large per unit inductance of the machine, at high MMFs the armature reaction field of the winding can easily cancel the permanent magnet's field in one direction and push the iron circuit into saturation in the other. The Ψ-I curves of figure 4.17 show that as pole number rose the armature reaction had an increasingly higher impact on the machine flux. The predominant cause was again, the increased leakage paths in the machine, especially the interpolar leakage, which will be discussed in Section 4.6.1.

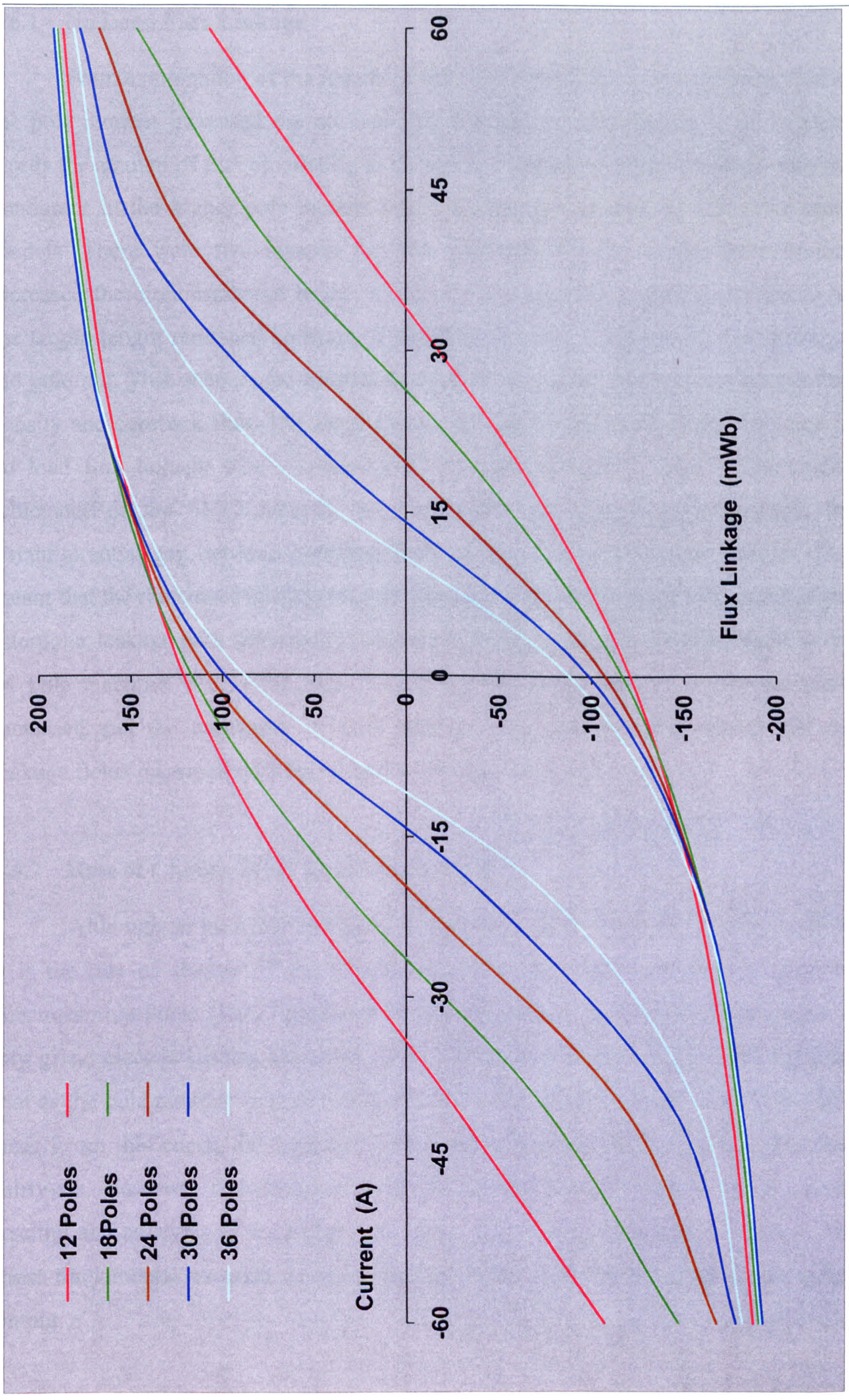

Figure 4.17 Effect of Pole Number on the aligned and unaligned Ψ-I curves of the CPTFM

4.6.1 No Load Flux Linkage

From examination of the results of the 3D FE analysis, it was apparent that as the pole number increased the no load flux linkage reduced (figure 4.18). In other words the amount of flux circulating in the stator coreback and hence linking with the conductor in the higher pole models was consistently less than in the lower order models. There were two reasons for this reduction. Firstly, as the pole number increased the circumferential length of the surface mounted magnets decreased. As the airgap length remained constant, it started to become a substantial proportion of the pole arc. This encouraged magnet leakage fields and so reduced the airgap flux density and coreback flux. The second and most significant cause of the reduction in no load flux linkage with increased pole number was closely tied to the higher reluctance of the SMC material. In the models with higher pole numbers, the circumferential gap between opposing teeth of the same pole became smaller. This meant that the reluctance of that particular leakage path was reduced. The effect of the interpolar leakage path discussed in section 4.5.3 was shown to be significant in the 24 pole machine. So, as the pole number increased the number of leakage paths increased and the reluctance of each leakage path reduced. This means that the leakage fields increased with the square of the pole number.

4.6.2 Rate of Change of No Load Flux Linkage

Although no load flux linkage is an indication of the capabilities of a machine, it is the rate of change of that flux linkage ($d\Psi$) that fundamentally governs the Electromotive Force (EMF) produced in the machine and hence its overall output at any given electric loading (equation 1.1). The curve shown in figure 4.19 indicates that as the pole number increased, the rate of change of no load flux linkage actually rose. From this curve, the optimum pole number appeared to be much higher than thirty-six. However, this machine could not operate without some form of electric loading and as levels of excitation rose, other parameters moderated this effect. The most fundamental measure of pole number impact was its effect on mean torque output.

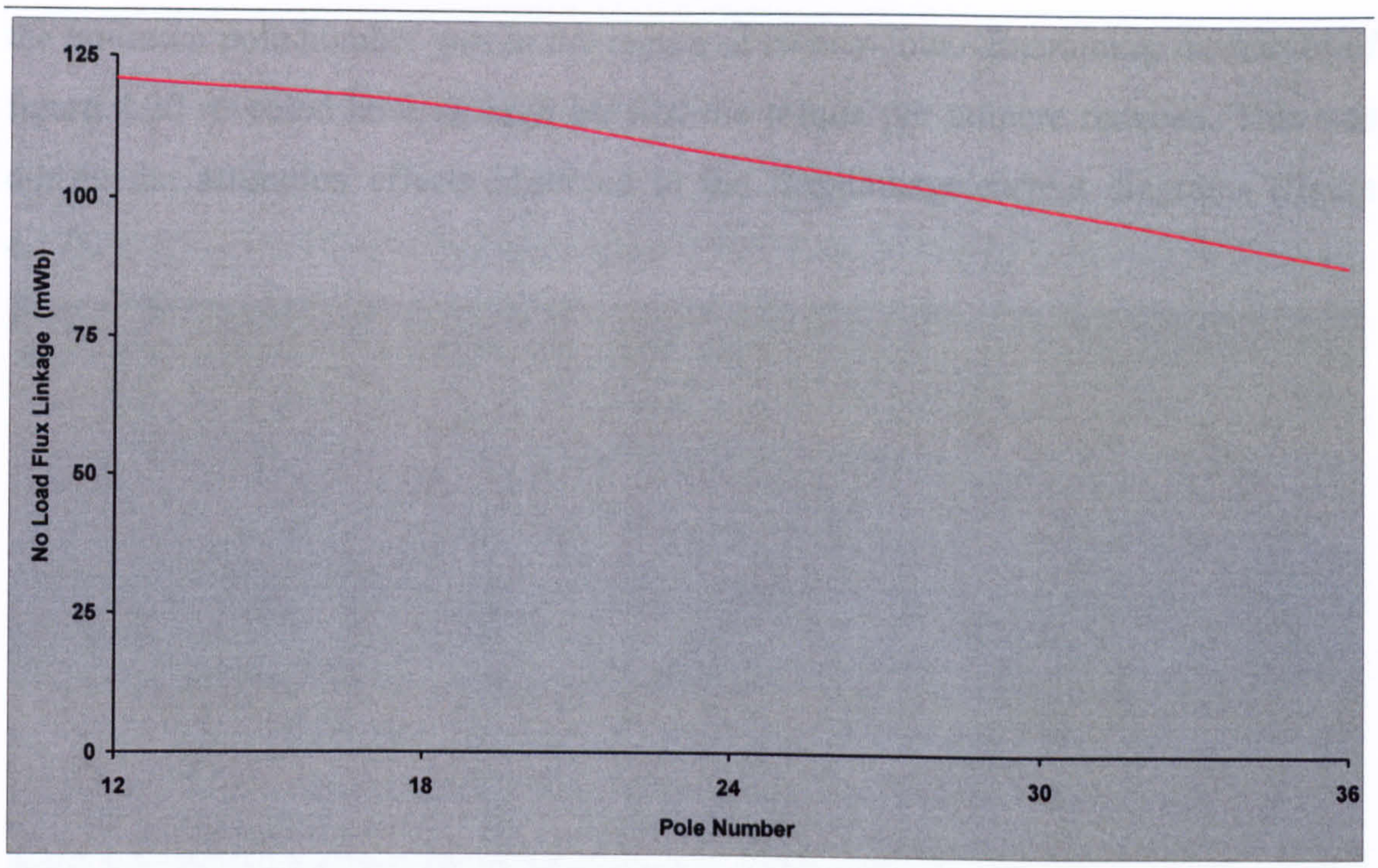

Figure 4.18 Reduction in no load flux linkage with increased pole number in the CPTFM

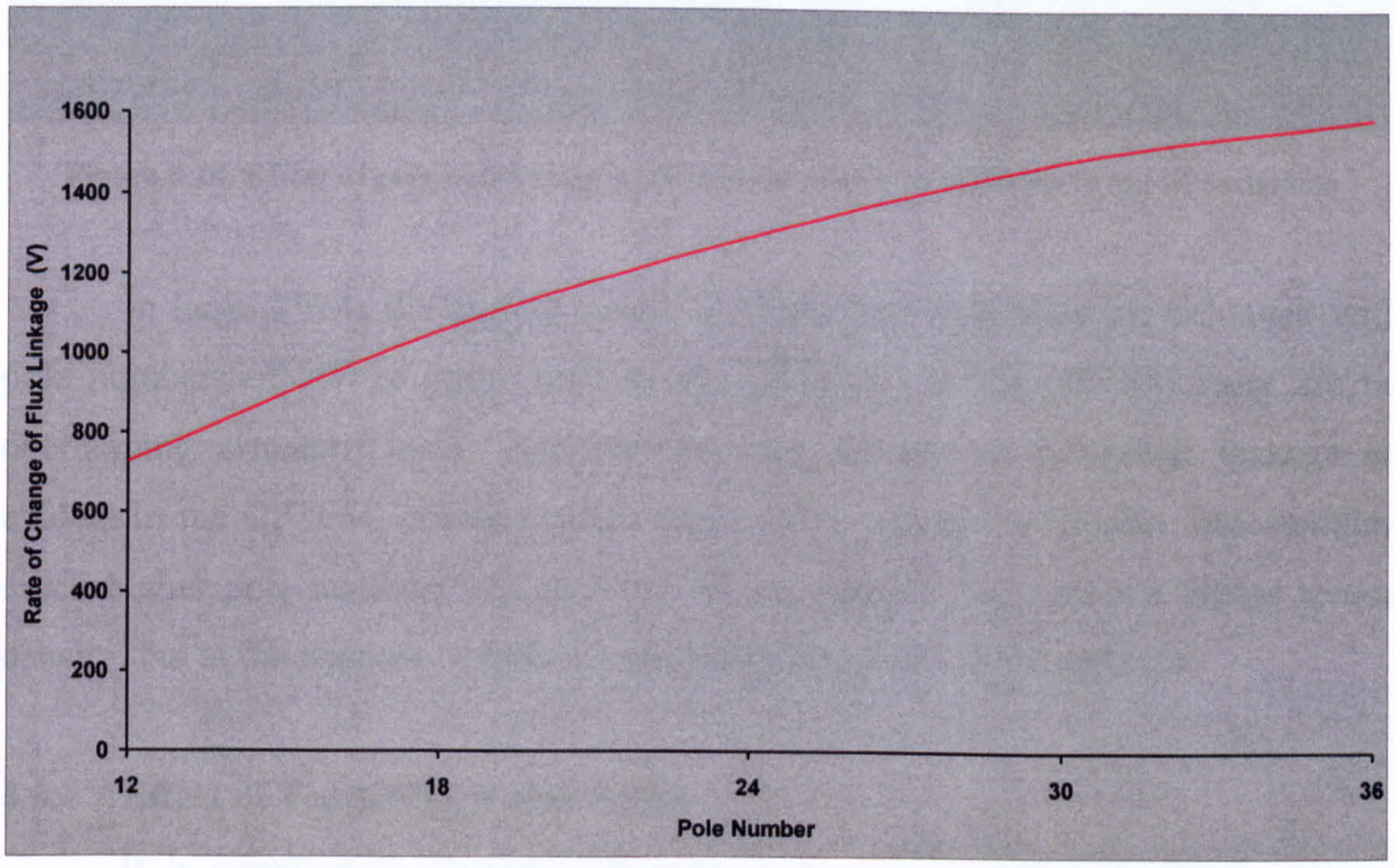

Figure 4.19 Effect of pole number on the rate of change of no load flux linkage in the CPTFM

4.6.3 Torque Production

Evaluating the area encompassed by each of the Ψ-I envelopes of figure 4.17, enabled the mean torque variation with pole number to be determined. The graph of figure 4.20 shows how the maximum value of torque occurred at progressively lower pole numbers as the level of winding excitation increased. At high excitation levels

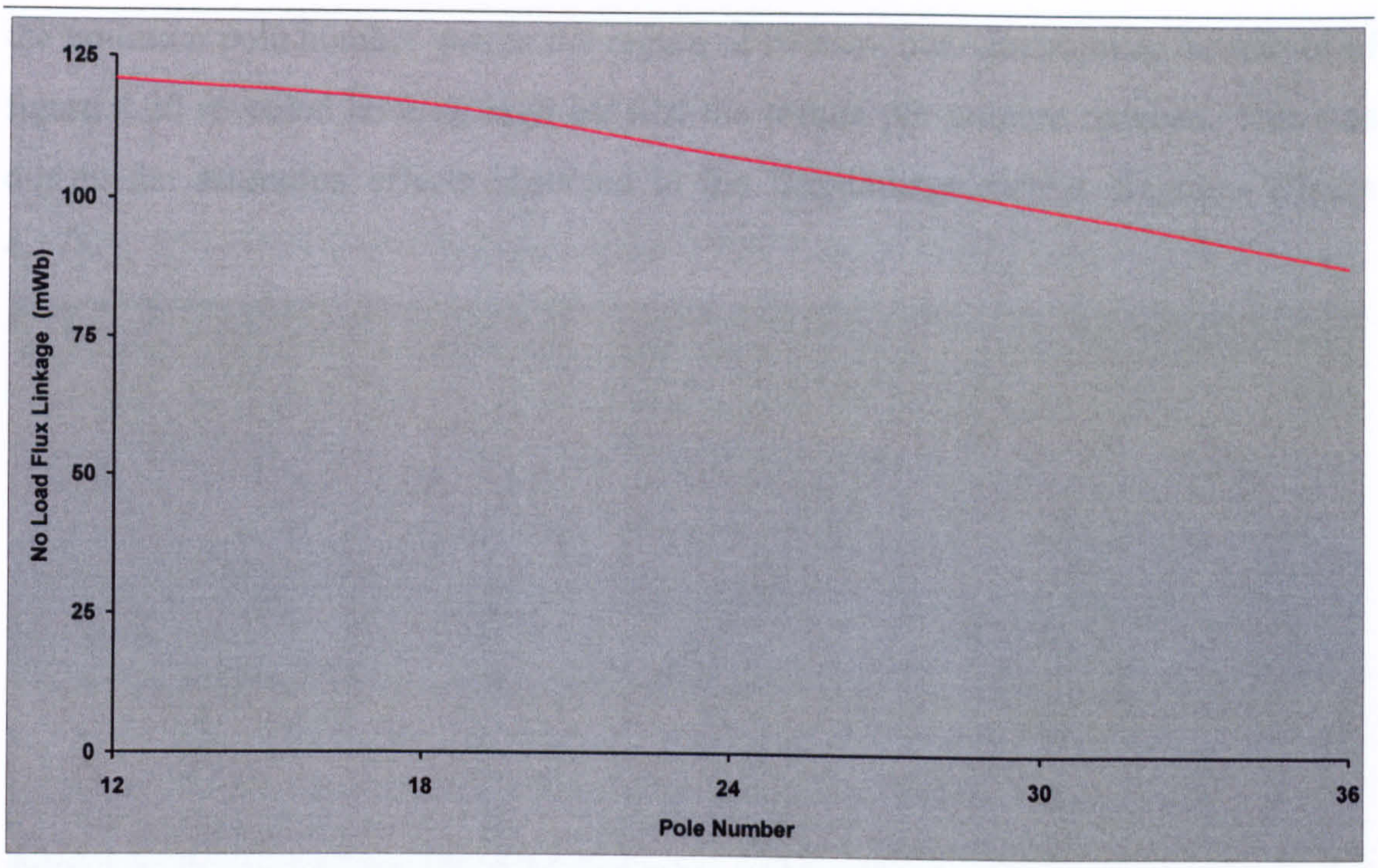

Figure 4.18 Reduction in no load flux linkage with increased pole number in the CPTFM

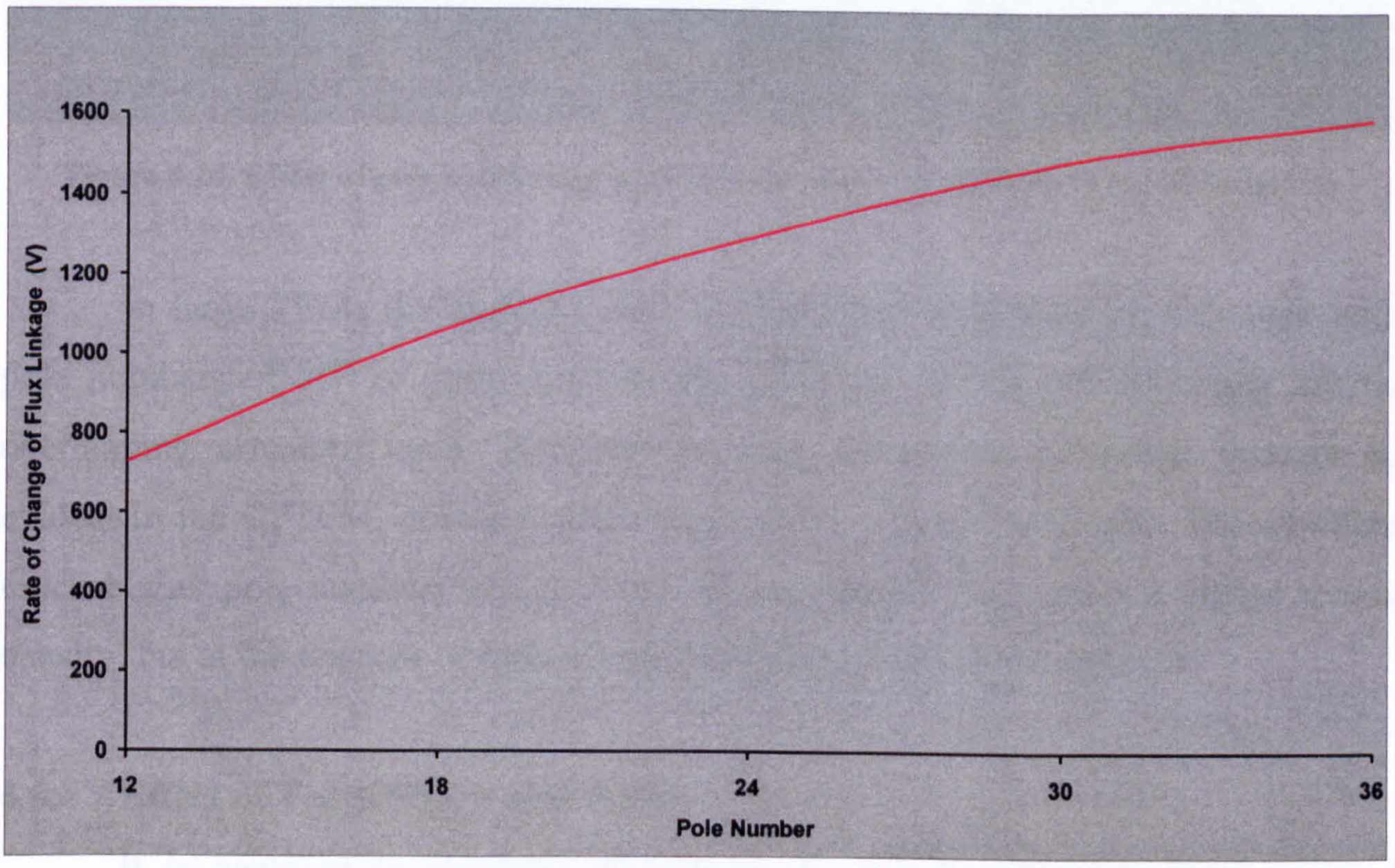

Figure 4.19 Effect of pole number on the rate of change of no load flux linkage in the CPTFM

4.6.3 Torque Production

Evaluating the area encompassed by each of the Ψ-I envelopes of figure 4.17, enabled the mean torque variation with pole number to be determined. The graph of figure 4.20 shows how the maximum value of torque occurred at progressively lower pole numbers as the level of winding excitation increased. At high excitation levels

the optimum pole number was in the region of twenty-four. Examining the curves of figure 4.20 revealed how, at high MMFs, the torque per ampere reduced. This was due to the saturation effects observed in the flux-linkage/current diagrams (figure 4.17).

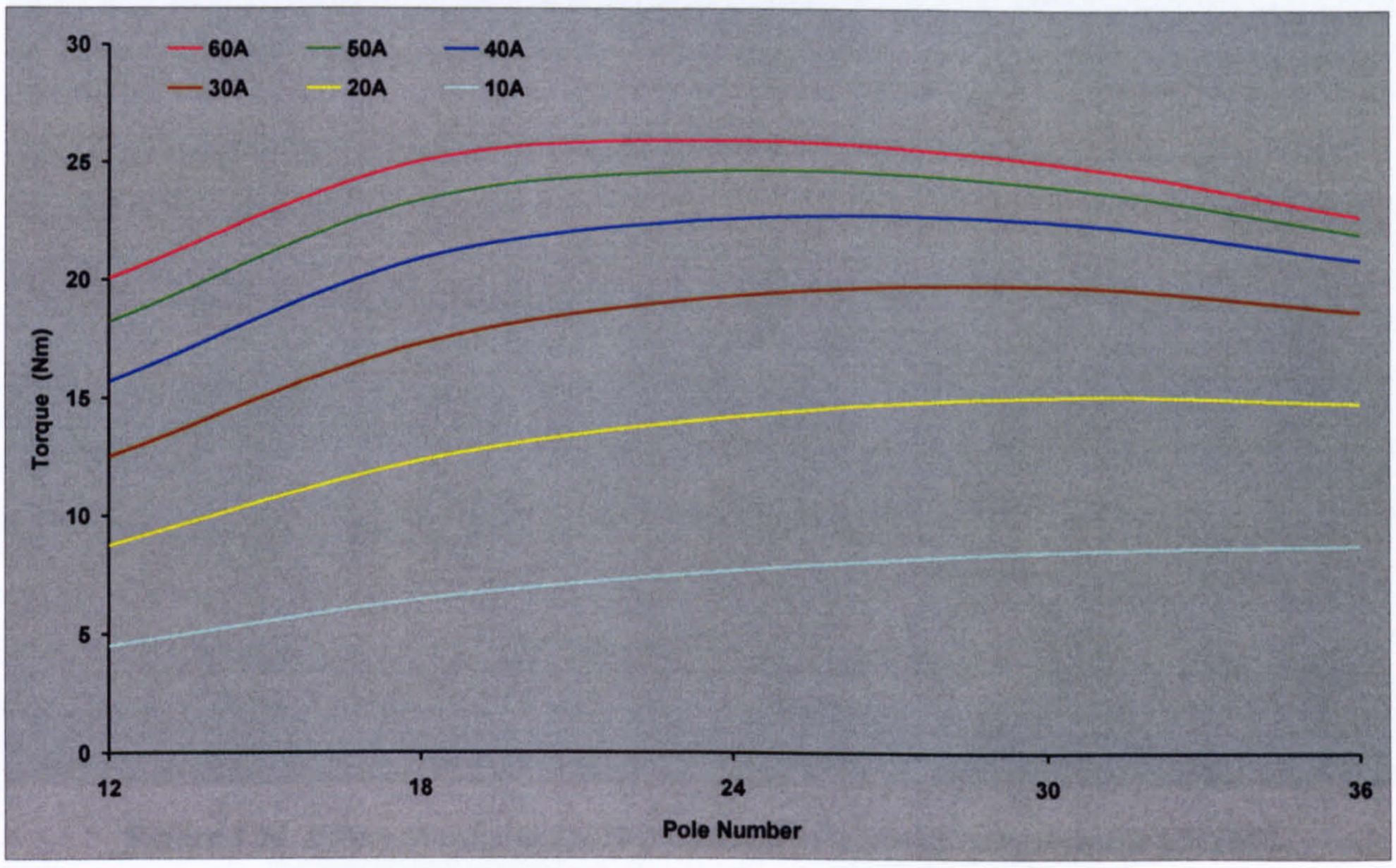

Figure 4.20 Effect of pole number on mean torque output at different levels of excitation

In large TFMs the highest levels of torque per unit mass are achieved with pole numbers of 100 or more, such as the DSTFM. In the DSTFM there are no overlapping armature teeth. This removes the debilitating interpolar leakage so evident in the CPTFM, giving a much lower stator leakage reactance, thus enabling much higher pole numbers and so much higher torques. This gives a higher torque density, but at the expense of reduced mechanical strength in the machine.

4.6.4 Effect of Tooth Shape and Width

It is common in clawpole alternators to employ circumferentially tapered teeth. For the same reasons as slot skewing, [33, 36] this helps to reduce cogging torque in the machine and may also reduce harmonic voltages induced in the armature by providing a more gradual commutation of the air gap flux. Does it provide any other advantages, particularly in relation to the level of flux linkage in the machine and hence overall output? Each individual tooth in the CPTFM covered 120 electrical degrees of a pole. What was the effect of increasing or decreasing this coverage? An

investigation into the effect of tooth shape and pole arc coverage was carried out using a series of 3D FE models, the results of which are presented in figure 4.21 and Appendix E.2.5.

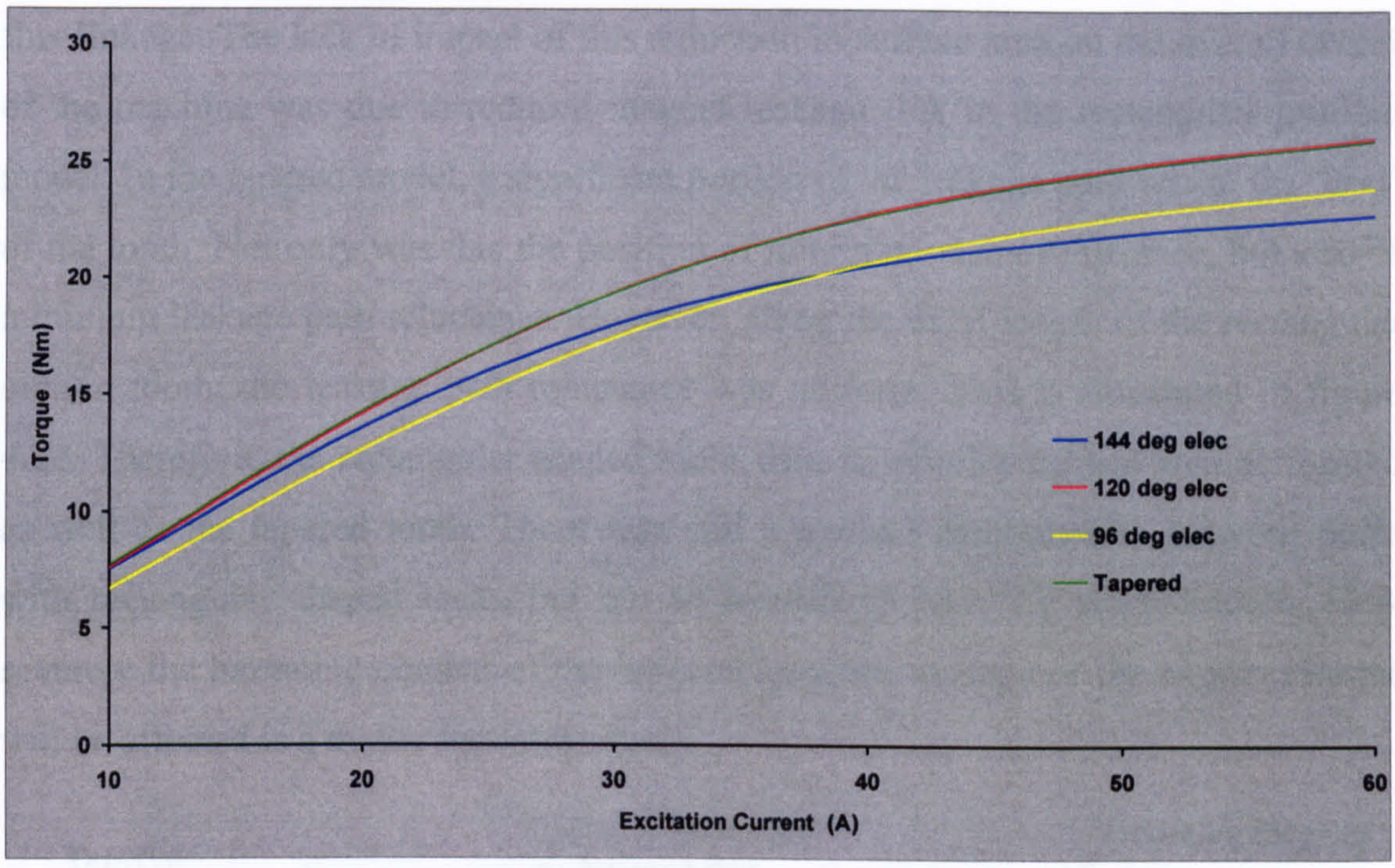

Figure 4.21 Effect of varying tooth parameters on output torque in the CPTFM

Table 4.2 Variation of tooth shape and pole arc coverage

Tooth Shape	Tapered	Rectangular	Rectangular	Rectangular
Pole Arc Coverage (°elec)	120	96	120	144
Tooth Area (mm^2)	420.5	298.4	373	447.6
Interpolar Distance (mm)	5	7.2	5	3.2
No Load Flux Linkage (mWb)	107.6	92.4	105.6	108

A 3D FE model was created which allowed the shape of the tooth in the circumferential / axial plane, to be altered from the tapered profile of the prototype machine to that of a rectangle. The radial / axial slope of the tooth as it rises towards the coreback was maintained. Examining two of the output curves in figure 4.21 ('Tapered' and '120 deg elec') showed that there was a negligible difference in output

over the entire excitation range. Although this was true, table 4.2 reveals some counteracting effects at work. The table shows that the 120° rectangular tooth had 11% less surface area in the airgap than the 120° tapered tooth yet only had 2% less flux linkage. The lack of impact of this reduction in surface area on the overall output of the machine was due to reduced magnet leakage flux in the rectangular profiled model. In the tapered model, a significant portion of the leakage path was at the 'heel' of the tooth. Not only was this the position of minimum stator reluctance, but also of minimum leakage path reluctance. However, along the axial length of the rectangular section tooth, the leakage path reluctance was uniform. This is illustrated in figure 4.22. Therefore, the rectangular shaped tooth with its smaller surface area performed as well as the tapered tooth. There was still a gradual commutation between poles with rectangular shaped teeth, but not as smooth as with the tapered tooth. How severely the harmonic content of the induced armature voltage or the cogging torque will be affected is a matter for future study.

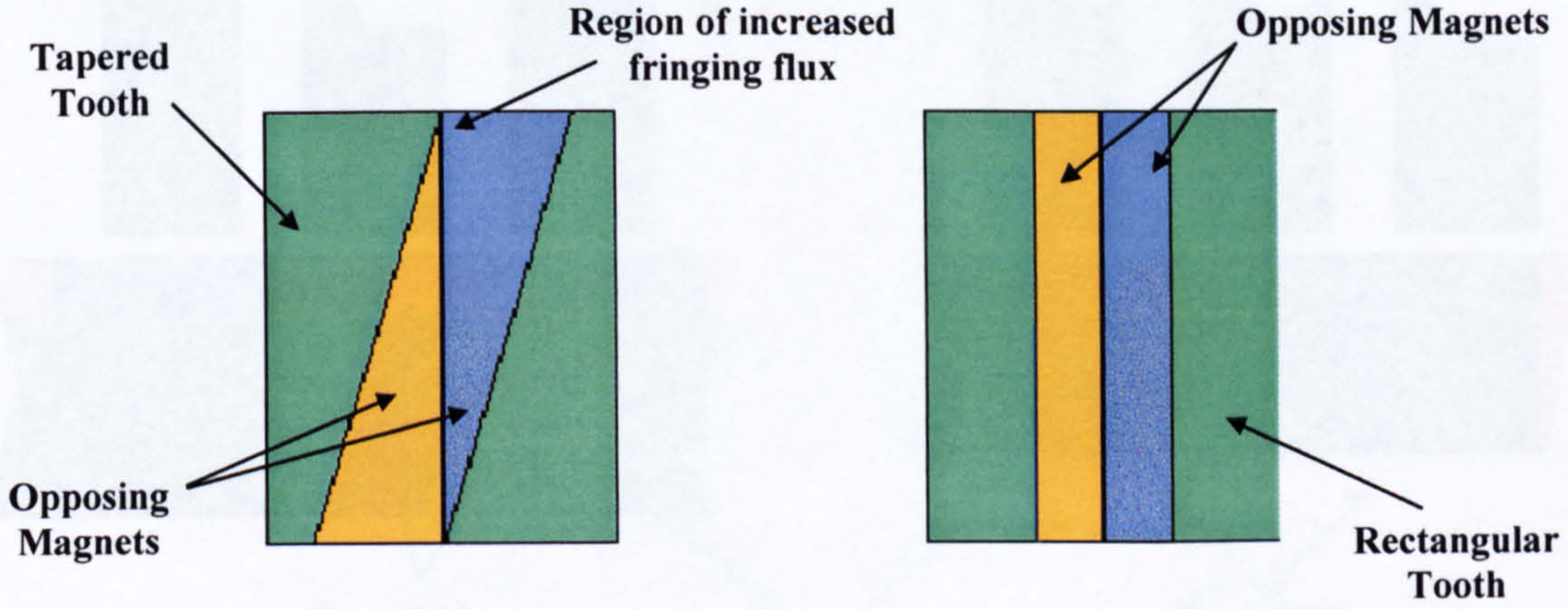

Figure 4.22 Two single pole pitch schematics viewed in the circumferential / axial plane indicating the areas of increased magnet fringing flux via tooth iron

Further analysis of the data gathered in table 4.2 showed that decreasing the pole arc to 96° reduced the no load flux linkage by 14%. This was due to the increased reluctance and reduced flux gathering capabilities of a tooth with 29% less airgap surface area. This was despite a 31% increase in the length and hence reluctance of the interpolar leakage path. The curve for this tooth coverage shows how these parameters limit the output potential of the model throughout the excitation range (figure 4.21). Increasing the degree of pole arc coverage to 144° provided a 6% increase in tooth 'sole' area with which to gather flux, but afforded only a 0.4%

increase in no load flux linkage. This tooth enlargement reduced the interpolar path length by 36% allowing a greater degree of stator flux to follow this short circuit path. The 144° curve of figure 4.21 illustrates how this lower reluctance path had a more pronounced effect on the output of the model at higher excitation levels.

4.7 Effect of Flux Concentration in the CPTFM

The existing prototype machine had twenty-four surface mounted permanent magnets. Could improvements in performance be achieved by reconfiguring the rotor magnets in a flux concentrating arrangement? To maintain a valid datum from which the comparison could be based, the same number of magnets with the same dimensions and properties were used in the 3D FE flux concentrating model.

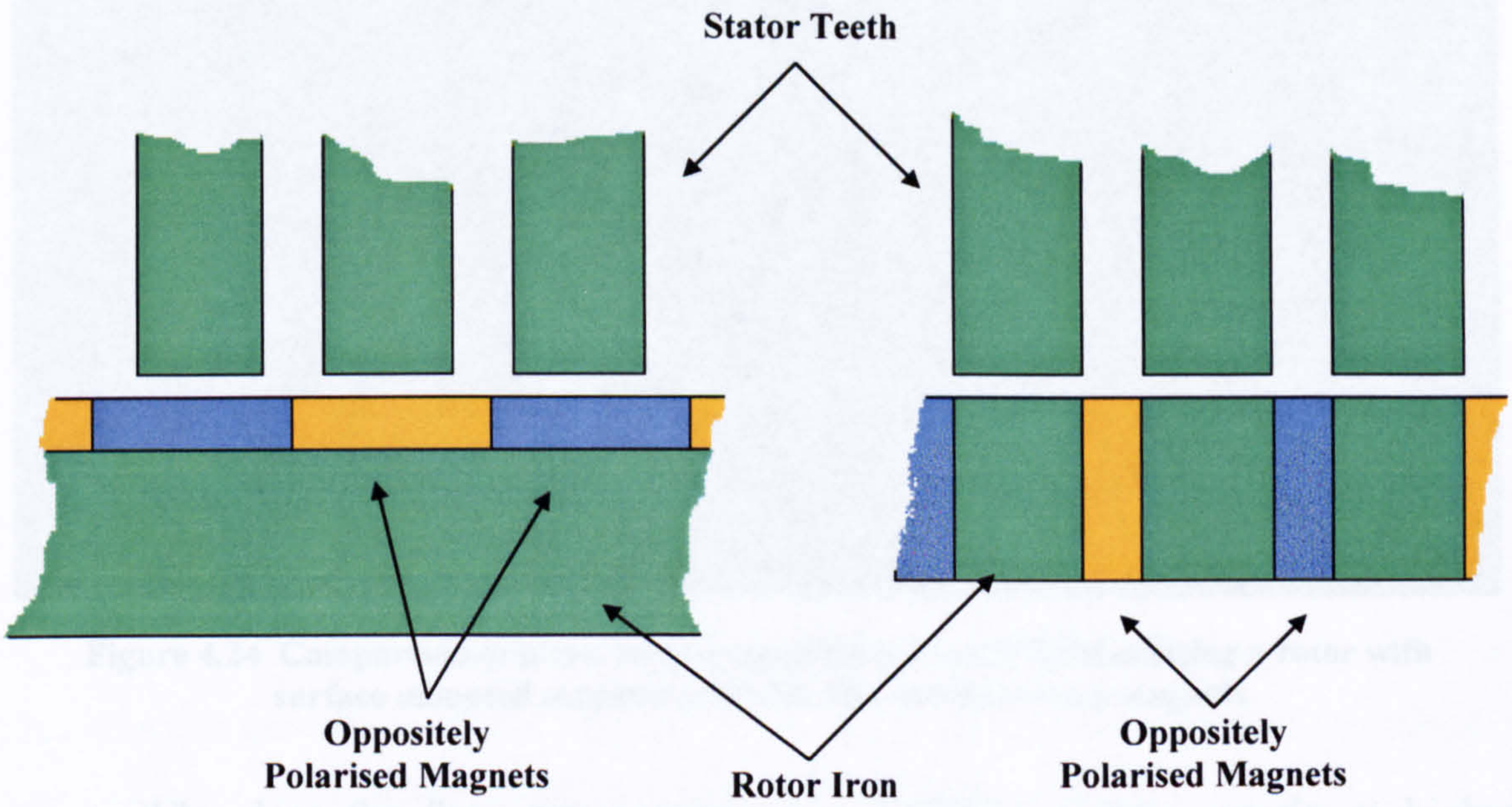

Figure 4.23 Schematic of surface mounted and flux concentrating rotor magnet configurations in the radial / circumferential plane

The flux concentrating arrangement can be seen in comparison with the surface mounted configuration in figure 4.23. Using this formation gave a flux concentration factor of 2.6. The same rotor configuration was used in the DSTFM (section 3.2). Three-dimensional finite element analysis was utilised over a suitably wide range of MMFs in order to determine the characteristics of this topology; the results of this Ψ-I study are presented in appendix E.2.6.

Direct comparisons were made between this model and the model representing the original prototype. Comparing the Ψ-I derived mean output of the two machines,

showed that the flux concentrating model had an initial increase in mean output over the original surface mounted model of 5% at 10A, (400Ampereturns) but this improvement decayed to 1% at 30A. Above this excitation level, the surface mounted model outperformed the flux concentrating model, culminating in a 9% higher value at 60A. Figure 4.24 illustrates this data. However, as previously stated, the thermal excitation limit for this CPTFM is 11.4A, a value equivalent to a higher output in the flux concentrating model.

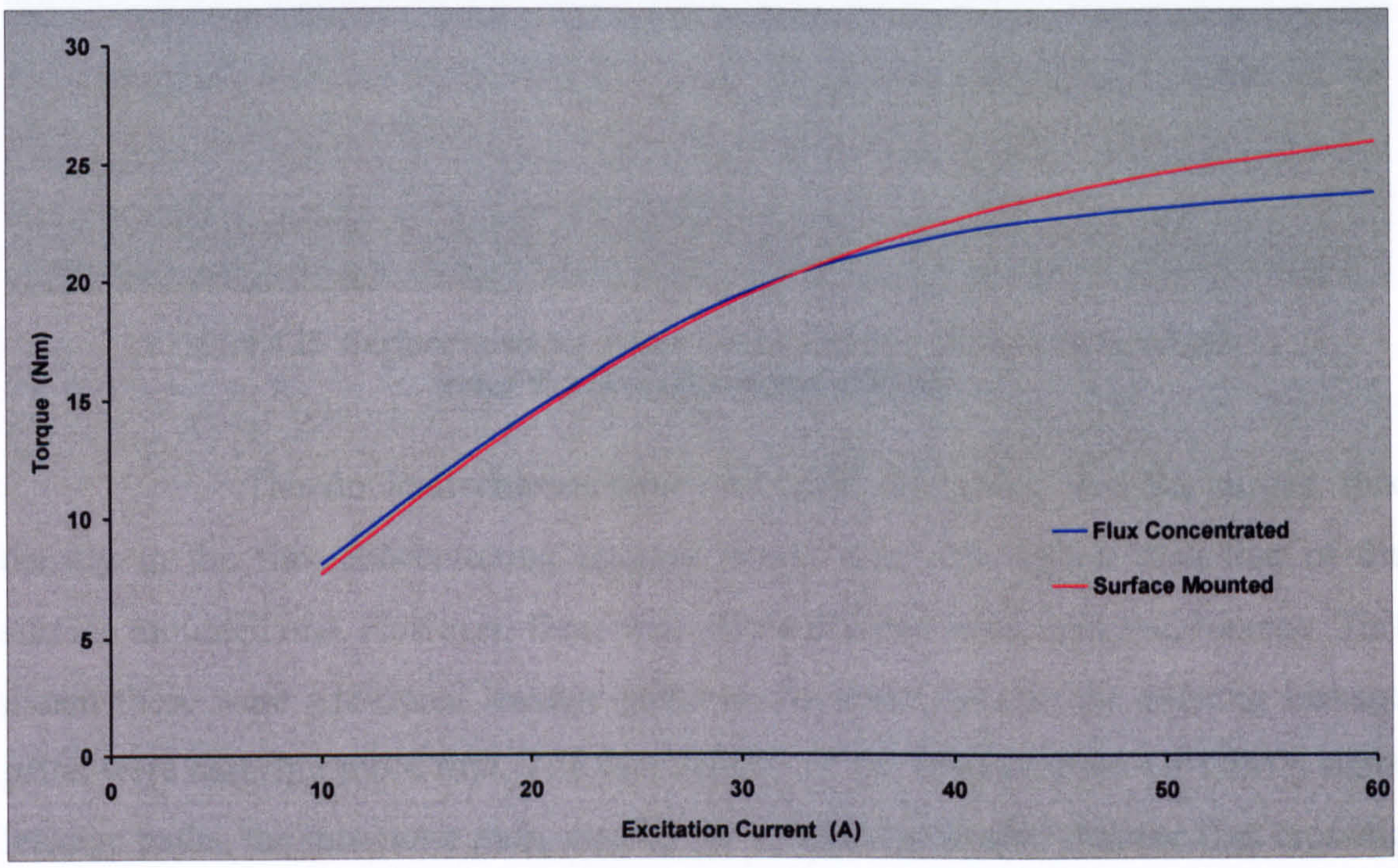

Figure 4.24 Comparison of mean torque capabilities of a CPTFM utilising a rotor with surface mounted magnets and with flux concentrating magnets

Why does the flux concentrating rotor CPTFM perform poorly at higher excitation levels? Looking at the aligned (±d axis) Ψ-I curves for the two models (figure 4.25) revealed that when the magnet and winding induced fluxes were additive to one another (ie. +ve MMF) the flux concentrating model saturated magnetically much sooner than the surface mounted model due to saturation in the rotor pole pieces. For the same reason, the negative portion of the same curve shows that the onset of coreback saturation was delayed but had a more pronounced effect. However, between approximately ±19A there was a noticeable enlargement of the Ψ-I envelope. As the naturally ventilated thermal limitations on the CPTFM were in the region between ±11.4A, this increase in output was produced with no additional electrical or magnetic costs.

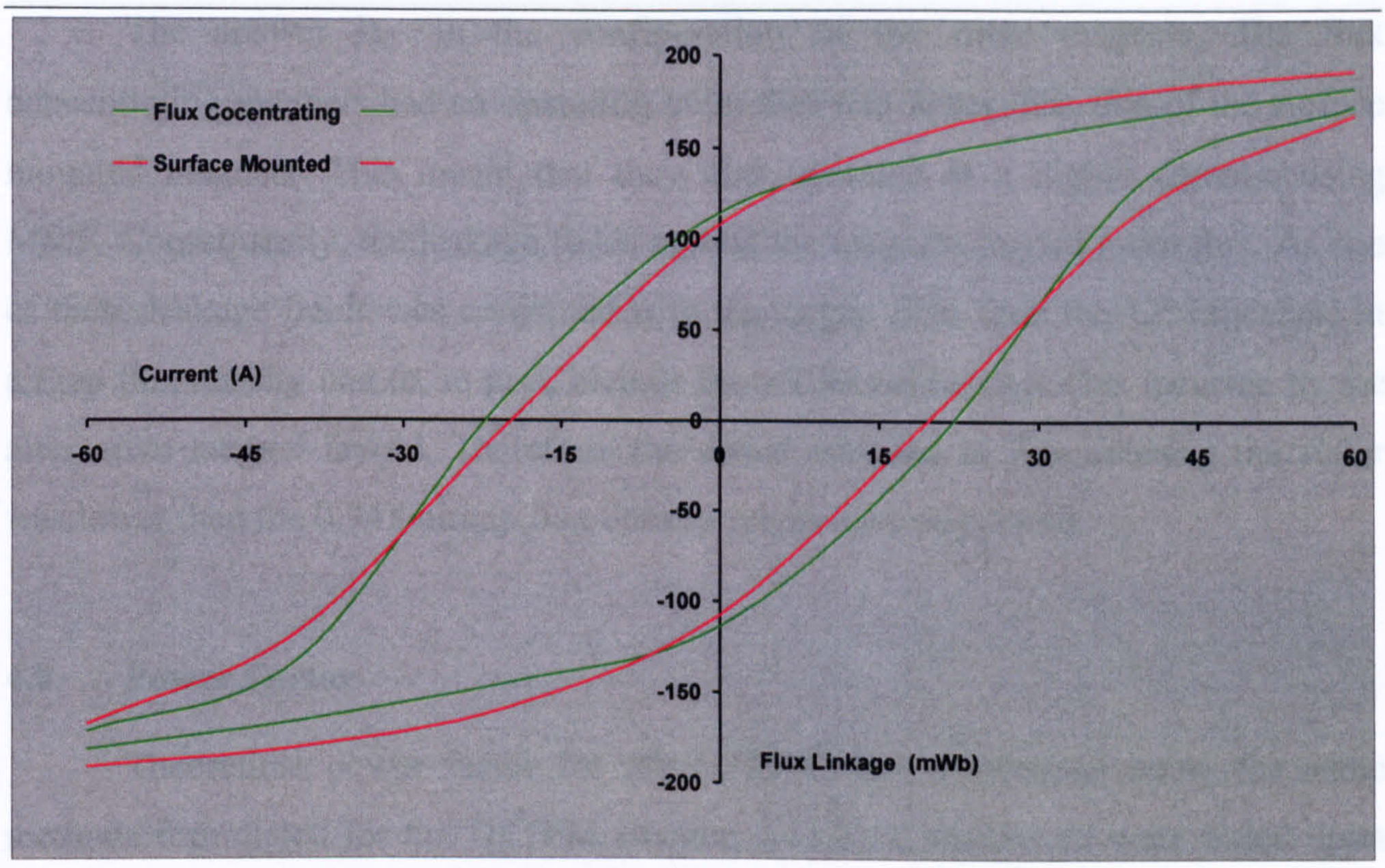

Figure 4.25 Surface mounted magnet rotor and flux concentrating magnet rotor Ψ-I envelopes for the CPTFM

The no load characteristics of table 4.3, show that the airgap flux density in the flux concentrating magnet model was 12% higher than that of the surface mounted one. However, there was only a 6% rise in no load flux linkage. This meant there were additional leakage paths in the stator, or that the existing leakage paths were carrying more flux. The flux density of the largest of the CPTFM's stator leakage paths, the interpolar path, rose by 38%, which indicated that the flux crossing between the teeth had increased by a similar amount. If the percentage rise in airgap flux density and coreback flux linkage were taken into account, then the interpolar leakage should have risen from its original value of 0.065mWb (see section 4.5.3) to a new value of 0.0802mWb. In fact the 38% increase in interpolar flux density put this value at 0.0897mWb, 12% higher, so why was there a discrepancy?

Table 4.3 3D FE no load operating comparison for the CPTFM with a surface mounted magnet rotor and with a flux concentrating magnet rotor

	Surface Mounted Magnet Rotor	Flux Concentrating Magnet Rotor
No Load Flux Linkage	107.6mWb	114.0mWb
Interpolar Leakage Flux Density	0.086T	0.119T
Air Gap Flux Density	0.84T	0.94T

The answer lay in the configuration of the rotor magnets. The flux concentrating magnets had an operating point that was lower than that of the surface mounted magnets. This meant that they also operated at a higher demagnetising MMF. Consequently, the leakage fields around the magnets carried more flux. As one of these leakage fields was conjoined with the airgap flux, then the 12% increase in airgap flux density had to, in part, include the additional leakage flux incurred by the alternative magnet layout. Therefore, the actual increase in flux entering the stator was lower than the 0.94T airgap flux density might have suggested.

4.8 Power Factor

Theoretical power factor for the CPTFM was determined using the same methods formulated for the DSTFM (section 3.11.3). Calculations were based upon the thermally limited current of 11.4A at 800rpm. The Ψ-I derived analysis produced the flux, voltage and current curves shown in figure 4.26. The calculated values of rms voltage, rms current and mean power were:

- RMS Voltage 574V
- RMS Current 11.4A
- Mean Power 5.518kW

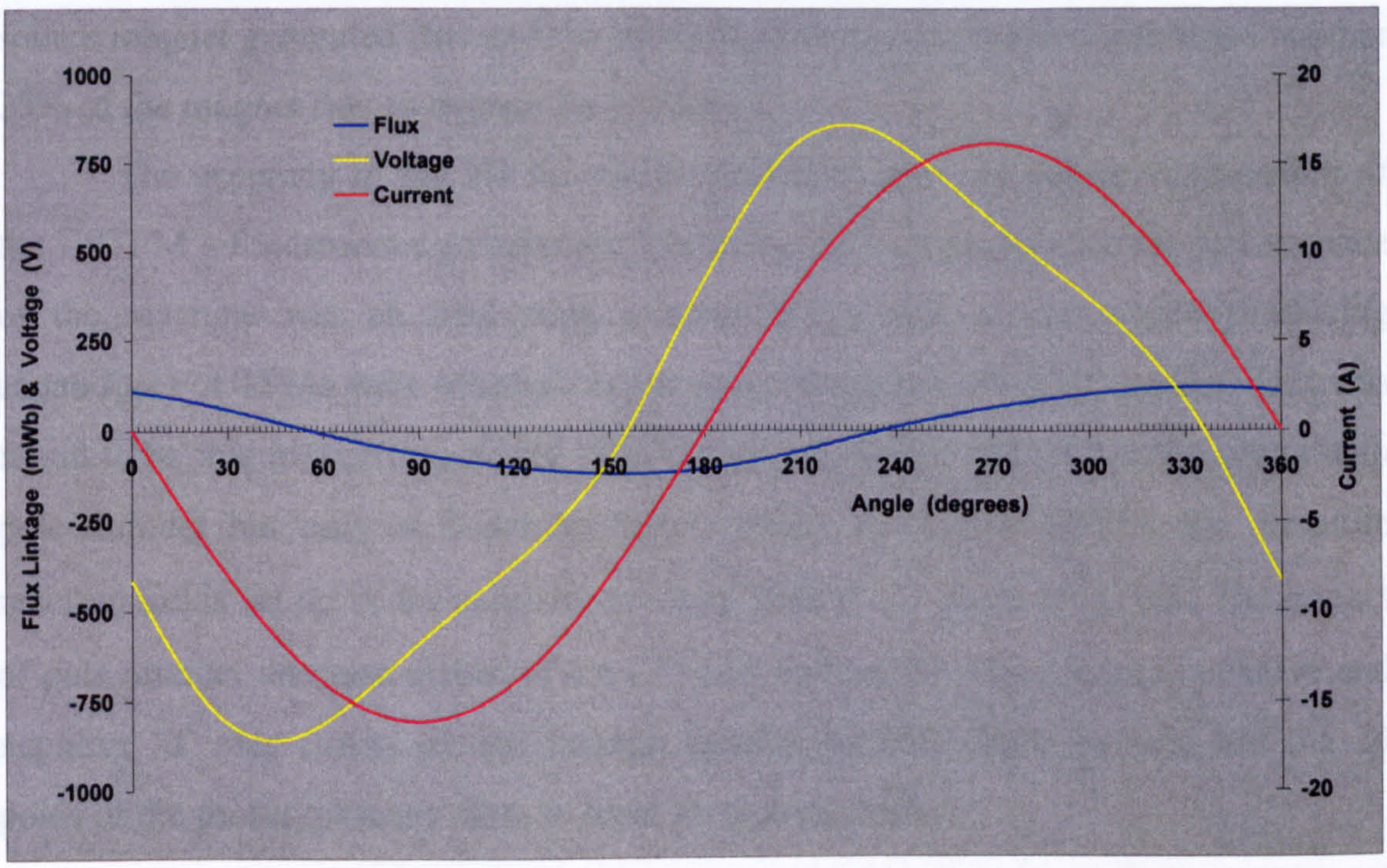

Figure 4.26 Derived curves showing the theoretical voltage/current phase angle

These values combined to give a power factor of 0.843. Comparing values with the DSTFM (0.37) showed a vast differential. Theoretically, the high interpolar leakage inherent in the CPTFM, should have produced a lower power factor than the DSTFM. The reason behind this discrepancy lay in the level of electric loading experienced in the model. With reference to figure 4.7, the thermally limited operating range imposed on the Ψ-I curves was very narrow and in an area of low saturation. Because of this, the positive and negative 'd' axis curves in that region were almost parallel to one another, which led to a higher power factor.

4.9 Conclusions

A prototype Claw Pole Transverse Flux Machine exhibiting a torque per unit of active mass of 2.02Nm/kg has been built and tested. In order to explore the parameters of the machine a large number of 3D finite element models have been produced and evaluated. A close correlation was found between the mean torque calculated from the original CPTFM 3D FE model and the results of the static torque tests on the prototype machine. This provided some measure of confidence in the validity of the FE model. Consequently, the model was employed to analyse the overall flux distribution in the CPTFM. This investigation revealed a number of distinct leakage paths that were being utilised by the rotor and stator fluxes. The most substantial of these were the magnet leakage fields which accounted for 27% of the source magnet generated flux and the interpolar leakage path which permitted another 25% of the magnet flux to bypass the coreback.

The accuracy of the 3D FE model enabled a more extensive examination of the CPTFM's fundamental parameters. The effect of pole number on the performance of the machine was an interesting avenue of research as the torque producing capabilities of TFMs were assumed to rise proportionally with pole number. This was found to be true to a certain extent, with the rate of change of flux linkage rising with pole number but only at lower excitation levels. At higher MMFs, the armature reaction fields set up in the machine severely limited the value of $d\Psi/d\theta$. The impact of pole number on mean output of the CPTFM was derived from aligned positive and negative 'd' axis curves of flux linkage against current. These showed that the 24 poles of the prototype were close to ideal for this machine.

A number of 3D FE models were constructed in order to investigate the significance of tooth shape and width in the CPTFM. The circumferentially tapered teeth in the prototype machine covered 120 electrical degrees. This type of tooth was directly compared to a rectangular profile tooth which also had 120° pole arc coverage. There was no discernible difference in output from the two models, despite the fact that the rectangular profiled tooth had an 11% smaller airgap surface area. The tapered tooth would be expected to have a higher output as a result of increased surface area, but this was lost due to increased airgap leakage flux. Although not proven in the text, there is a school of thought which suggests that a tapered tooth may reduce the harmonic content of the induced back EMF in the stator. The effect of varying pole arc coverage showed little increase in net output, as increased airgap surface area was generally offset by increased interpolar leakage.

An investigation was also carried out into the consequences of converting the existing, surface mounted permanent magnet rotor, into a flux concentrating permanent magnet rotor. The study showed that at light load, an improvement of *circa* 5% in output could be made from using the flux concentrating configuration.

Power factor calculations for the 3D FE model revealed a value of 0.843. This high figure was attributed to the low armature current rating. As the level of electric loading was determined from thermal tests carried out on the prototype machine, this pointed to a poor utilisation of the thermal conduction paths in the machine. As the winding was produced as a pre-formed toroid, the most likely area for this failure was the conductor/coreback interface. Disassembling the prototype, showed that the coil was indeed a loose fit in the stator and hence had poor thermal conduction paths. This meant that the electric loading of the machine could realistically be pushed up if the conduction paths were improved.

Chapter 5

Topology Evaluation and Comparison

5. 1 Introduction

Since 1986 a number of distinct Transverse Flux topologies have been proposed. Some have been merely postulated as designs, whilst some have been developed and taken forward to be constructed as fully operational machines for commercial applications. Four of the main centres for TFM design are Braunschweig University, Aachen University, Southampton University and Newcastle University. A prolific source of TFM designs originates from Professor Weh and his colleagues at Braunschweig University. They formulated a great deal of the early work in this field, producing a number of unique topologies. The design team at Aachen under Professor Henneberger have produced and developed a variation of one of the Braunschweig models, which has proven popular with some commercial organisations [38]. Southampton University have also produced a prototype based on a Braunschweig topology, but their main interest has been in the analytical evaluation of different models particularly with regard to power factor. Newcastle University has taken a slightly different approach to the underlying design rationale of TFMs by employing Soft Magnetic Composite (SMC) materials (see Appendix A). These materials have opened the possibilities of utilising three dimensional flux paths within the rotor and stator iron. Without the two dimensional constraints of laminations, this means the machine designer can be given, within reason, carte blanche with respect to new three dimensional designs. Newcastle have taken advantage of this freedom to explore a number of novel TFM designs, including the Double-Sided Transverse Flux Machine (DSTFM) and the Claw Pole Transverse Flux Machine (CPTFM) presented in chapters three and four respectively.

This chapter contrasts and compares the four most fundamental topologies. This was be achieved by redesigning each TFM variant to the same specific set of parameters and then producing and analysing a set of 3D Finite Element (FE) models for each design.

The four models to be analysed are:

- Single-Sided TFM (SSTFM)
- Single-Sided with Bridges TFM (SSBTFM)
- Claw Pole TFM (CPTFM)
- Double-Sided TFM (DSTFM)

5.2 The Designs of Braunschweig University

Professor Weh and his associates at Braunschweig produced an array of TFM designs. Each design incorporated discrete stator 'C' cores fashioned from laminated steel. In three of the cases, laminated steel 'I' pieces, either on the stator or rotor, served to complete the magnetic flux path around the ever present circumferential conductor. The most basic and well known of the designs produced at Braunschweig was the Single-Sided TFM (SSTFM). There is an explanation of its method of operation in Section 1.2 of Chapter One. However, in order to aid comparison with the subsequent models under scrutiny in this chapter, radial/axial and radial/circumferential schematics of the topology are presented in figure 5.1a and 5.1b respectively. A single-sided prototype was also produced at Southampton University [10]. The two phase, 40 pole, machine comprised of a liquid cooled stator positioned within an outer rotor. The machine required 160 rotor magnets, these were mounted on the inner circumference of the rotor drum. Test results showed a rated torque of 70Nm at 10A rms, which equated to a torque per unit active mass of 7.14Nm/kg.

A major point to note concerning the SSTFM topology is that only 50% of the magnet material was used at any one time. This was not only a poor use of resources, but caused the permanent magnets to oscillate between their aligned flux density and their unaligned operating point. This oscillation induced voltages and hence eddy currents in the magnets, causing I^2R associated heating. This could be a particular problem in some rare earth magnets, due to their low Curie temperatures. At best, there could be a loss of performance and at worst, complete demagnetisation of the permanent magnet.

The first alternative to the SSTFM (figures 5.2a and 5.2b) attempted to rectify this problem by using both sides of the rotor. For clarity, figures 5.2a and 5.2b are arranged in the same planes of references as those of figures 5.1a and 5.1b. This

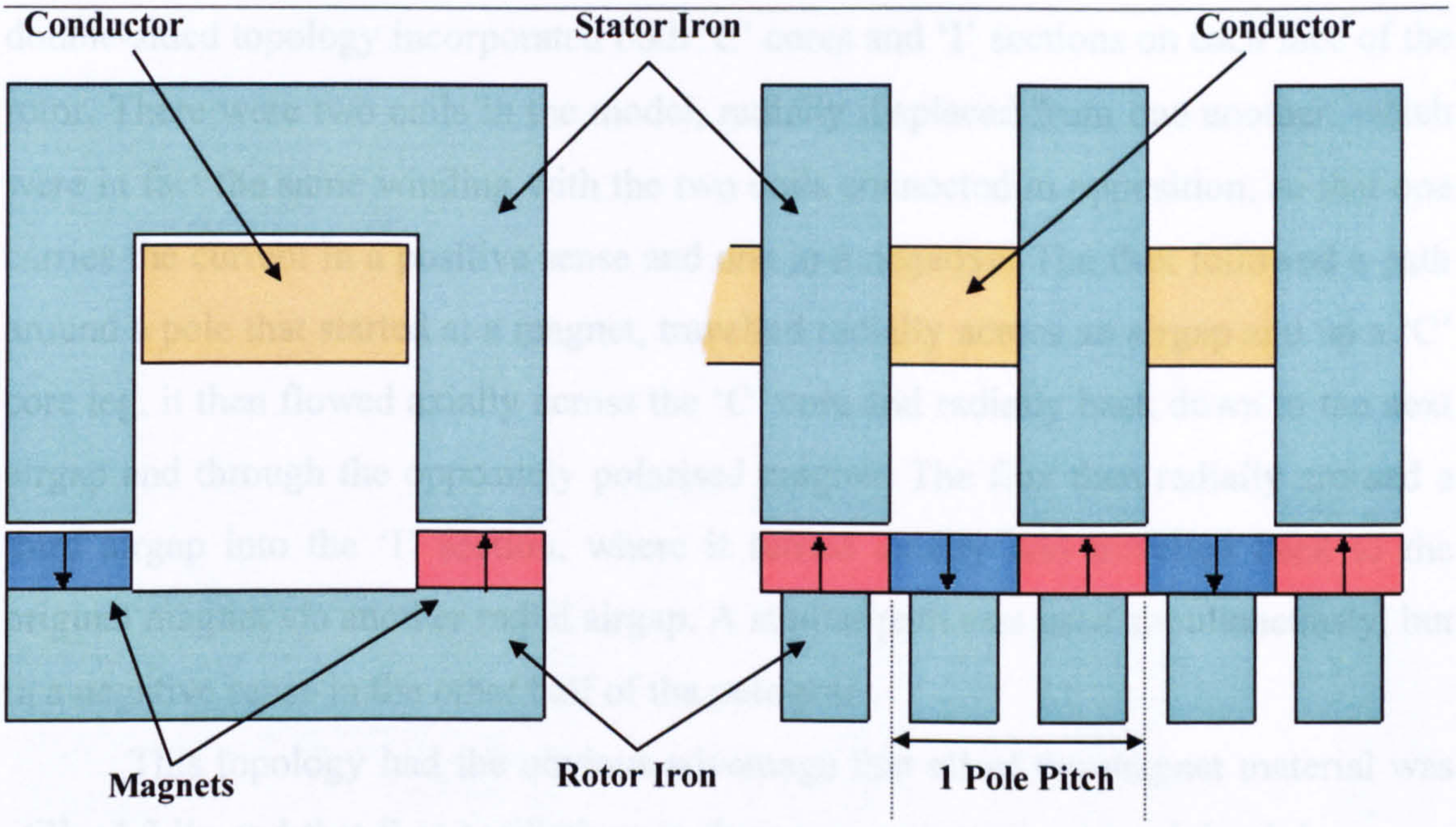

Figure 5.1a Radial/Axial view of the SSTFM

Figure 5.1b Radial/Circumferential view of the SSTFM

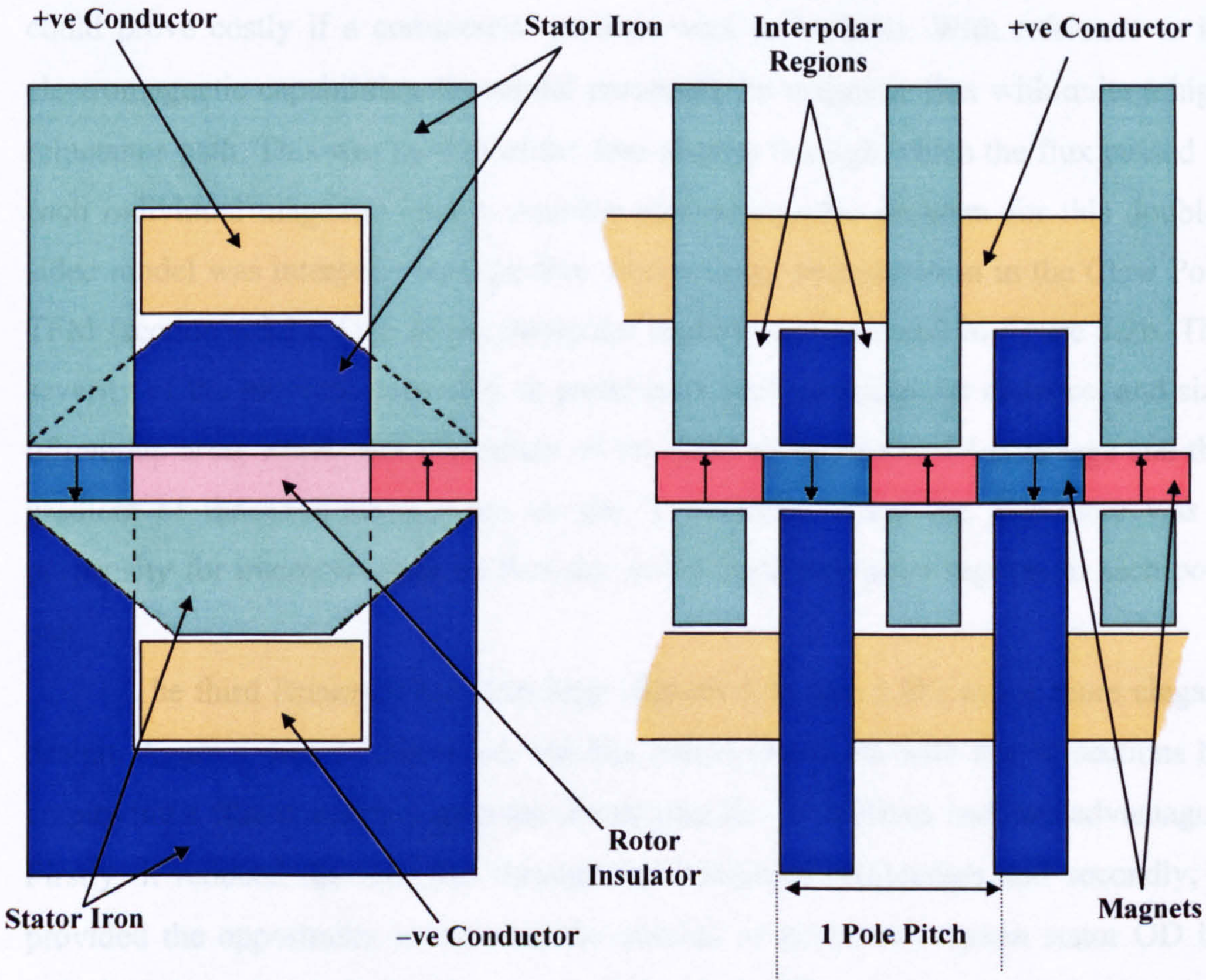

Figure 5.2a Radial/Axial view of a double-sided TFM

Figure 5.2b Radial/Circumferential view of a double-sided TFM

double-sided topology incorporated both 'C' cores and 'I' sections on each face of the rotor. There were two coils in the model, radially displaced from one another, which were in fact the same winding with the two coils connected in opposition, so that one carries the current in a positive sense and one in a negative. The flux followed a path around a pole that started at a magnet, travelled radially across an airgap and up a 'C' core leg, it then flowed axially across the 'C' core and radially back down to the next airgap and through the oppositely polarised magnet. The flux then radially crossed a third airgap into the 'I' section, where it turned axially and travelled back to the original magnet via another radial airgap. A similar path was used simultaneously, but in a negative sense in the other half of the pole pair.

This topology had the obvious advantage that all of the magnet material was utilised fully and that flux oscillations in the source magnets were minimal, however, it did have some shortcomings. It was a complex design, comprising of four distinct stator iron sections and four rotor magnets per pole pair. It also incorporated two conductor windings. For a high pole number TFM, this number of component parts could prove costly if a commercial product were to be built. With reference to its electromagnetic capabilities, the model presented the magnetic flux with quite a high reluctance path. This was by dint of the four airgaps through which the flux passed in each individual magnetic circuit. Another electromagnetic problem for this double-sided model was interpolar leakage flux, also a major consideration in the Claw Pole TFM (section 4.5.3). Two of the interpolar regions are indicated in figure 5.2b. The severity of the problem depended on parameters such as interpolar distance, and size of overlap area; which was dependant on the axial width of the 'C' core legs and the gradient of the axial/radial slope on the 'I' sections. None the less there was a propensity for interpolar leakage flux due to the eight interpolar regions in each pole pair.

The third Braunschweig topology (figures 5.3a and 5.3b) was a more elegant design. Again it was double-sided, but this model dispensed with the 'I' sections by employing a flux concentrating rotor. Removing the 'I' sections had two advantages. Firstly, it reduced the flux lost through the interpolar mechanism and secondly, it provided the opportunity to increase the number of poles for a given stator OD by reducing the pole pitch. If this was carried out sensibly then these two advantages were not necessarily mutually exclusive and the pole number could increase without the interpolar path compromising the stator flux. The advantages of this topology over

the two previous models would be a higher airgap flux density, hence flux linkage, for the same volume of magnet material, a relatively low interpolar leakage flux and a lower level of complexity. In relation to the DSTFM built at Newcastle University, its double rotor and 'stand alone' 'C' cores not only reduced its mechanical strength but, along with the double conductor winding, made it more complicated to build.

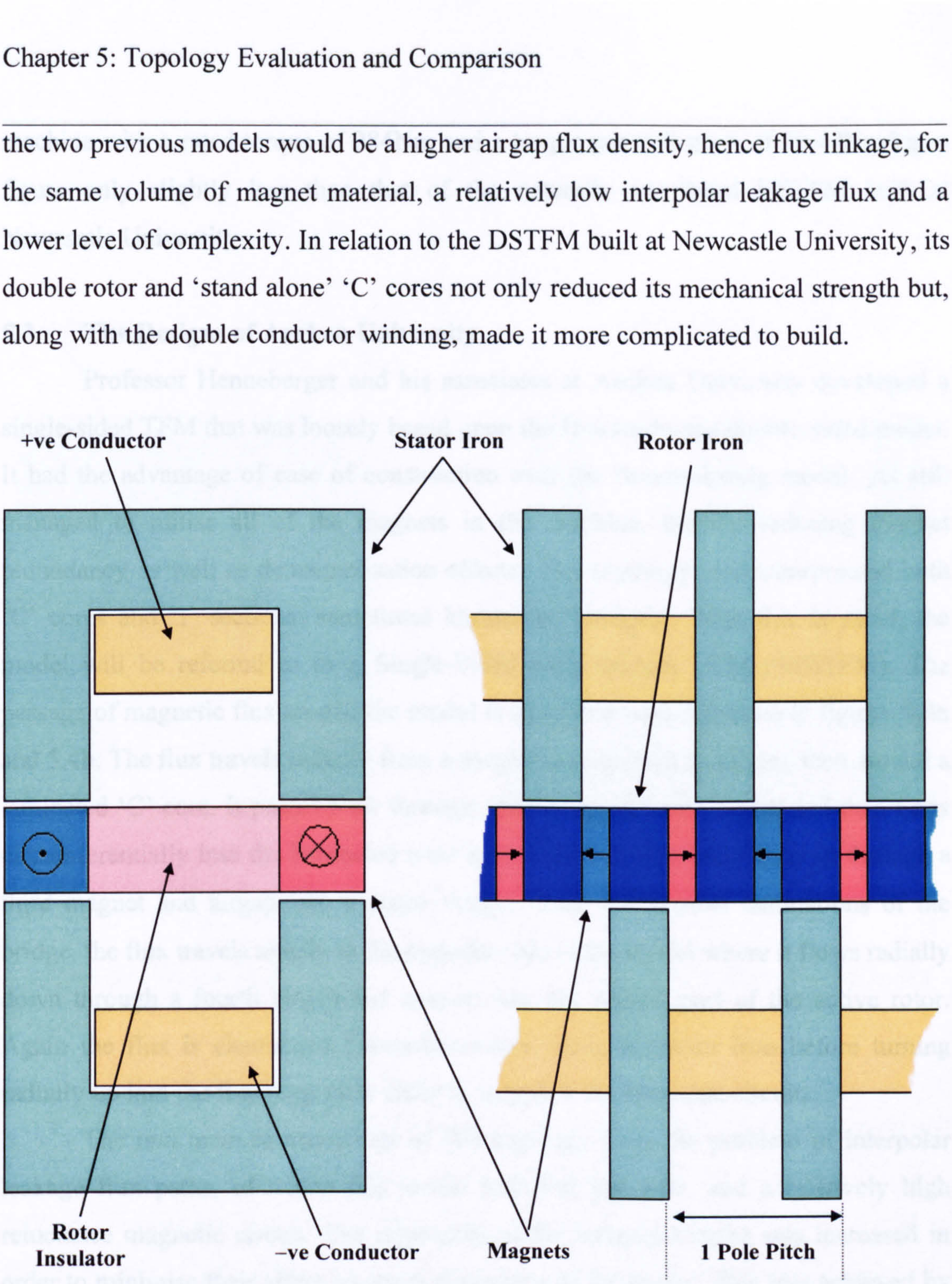

Figure 5.3a Radial/Axial view of a flux concentrating double-sided TFM

Figure 5.3b Radial/Circumferential view of a flux concentrating double-sided TFM

The double-sided TFM was the most promising of the Braunschweig designs and was developed into a 5.8kW wind turbine generator [44]. The prototype was a two phase 144 pole machine, with the stators axially displaced from one another. The two flux concentrating rotor sections were mounted on the opposing axial faces of a radial rotor disc which passed between the two stators and was connected at the axis of the machine to the drive shaft. The rated speed of the prototype was 195rpm, which coupled with the rated output of 5.8kW and an active mass of 27.2kg equated to a

machine with a rated torque of 284Nm and a torque per unit mass of 10.44Nm/kg; a figure only slightly less than that of the naturally ventilated DSTFM built at Newcastle University.

5.3 The Designs of Aachen University

Professor Henneberger and his associates at Aachen University developed a single-sided TFM that was loosely based upon the Braunschweig double-sided model. It had the advantage of ease of construction over the Braunschweig model, yet still managed to utilise all of the magnets in the machine, thereby reducing magnet redundancy as well as demagnetisation effects. This topology also incorporated both 'C' cores and 'I' sections, sometimes known as 'Bridges'. With this in mind, the model will be referred to as a Single-Sided with Bridges TFM (SSBTFM). The passage of magnetic flux around the model is described with reference to figures 5.4a and 5.4b. The flux travels radially from a magnet and through an airgap, then around a laminated 'C' core. It passes back through another airgap and magnet and then turns circumferentially into the laminated rotor iron, followed by a radial turn up through a third magnet and airgap into a stator bridge. Once in the steel laminations of the bridge, the flux travels axially to the opposite side of the model where it flows radially down through a fourth airgap and magnet into the second part of the active rotor. Again the flux is channelled circumferentially along the rotor iron before turning radially up into the first magnet in order to complete the magnetic circuit.

The two main shortcomings of this topology were the problem of interpolar leakage flux paths, of which this model had four per pole, and a relatively high reluctance magnetic circuit. The reluctance of the interpolar paths was increased in order to minimise their affect on the performance of the model. This was achieved by chamfering the axial ends of the bridges, effectively halving the interpolar area. The high reluctance of the magnetic circuit was the result of having four magnets and so four airgaps per pole, positioned in series around the circuit.

A good deal of investigative optimisation was carried out by the Aachen team, resulting in a finalised design for a prototype machine. The prototype was a three-phase outer rotor machine with a rotating outer casing supporting 120 magnets, 40 pole per phase. The 'C' cores were mounted on an internal stator, presenting three channels into which the three separate phases were wound. The stator was completed by the addition of the bridge sections. The hollow centre of the stator enabled cooling

water to be pumped through the machine to aid its thermal properties. Unfortunately, published results of the prototype's performance were unavailable, so no direct comparisons can be made with any of the other topologies.

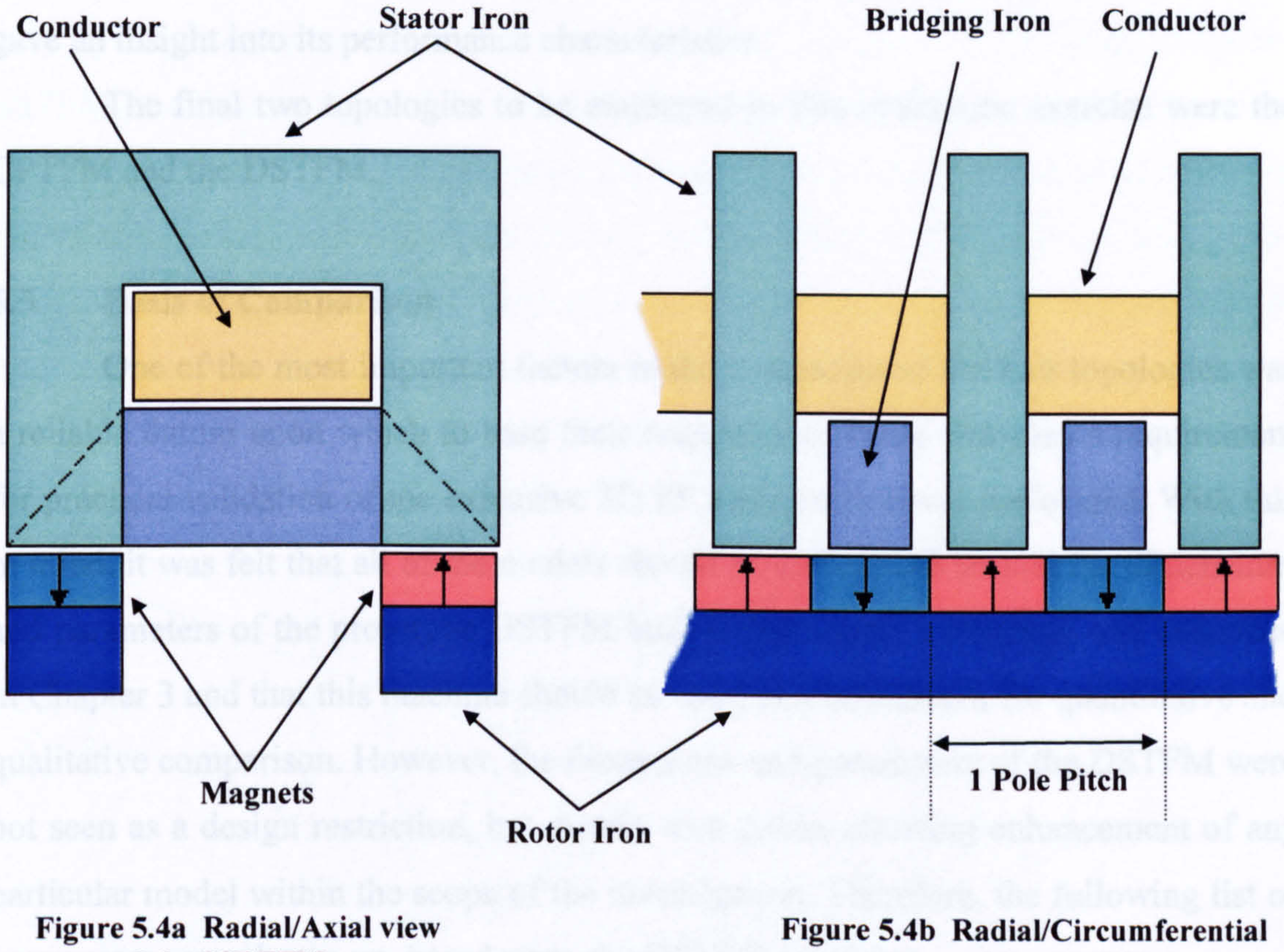

Figure 5.4a Radial/Axial view of the SSBTFM

Figure 5.4b Radial/Circumferential view of the SSBTFM

5.4 Choice of Designs for Comparison

As stated in section 5.1, four designs were selected for in depth evaluation and comparison. The choice was based upon obtaining as wide a database of TFM topological characteristics as possible. The first model selected was the SSTFM of Braunschweig University. The simplicity of its single-sided design and the opportunity to gauge the effect on output of only using the magnets for 180° of the electrical cycle made this model an interesting prospect for study. A further reason for choosing this topology was that it was the formulating topology of the past decade's studies into TFMs.

The second selection for this design study was the SSBTFM produced at Aachen University. The reason for this choice of topology over the double-sided and flux concentrating models produced at Braunschweig, was based upon simplicity of design and duplication of data. Essentially, the SSBTFM is a simpler version of the double-sided design and possesses half the number of stator 'C' cores for a given

circumferential dimension. However, its similarity enabled the general topology of the two machines to be explored. The double-sided flux concentrating model was neglected due to of its generic similarity to the DSTFM built at Newcastle and because the data produced from the prototype machine built at Braunschweig already gave an insight into its performance characteristics.

The final two topologies to be employed in this evaluation exercise were the CPTFM and the DSTFM.

5.5 Basis of Comparison

One of the most important factors in the evaluation of the four topologies was a reliable datum upon which to base their comparison. There was also a requirement for practical validation of the extensive 3D FE analysis that was performed. With this in mind, it was felt that all of the models should be formulated around the dimensions and parameters of the prototype DSTFM built at Newcastle University and described in Chapter 3 and that this machine should be used as a benchmark for quantitative and qualitative comparison. However, the dimensions and parameters of the DSTFM were not seen as a design restriction, but merely as a guide, allowing enhancement of any particular model within the scope of the investigation. Therefore, the following list of parameters were drawn up, based upon the DSTFM topology.

- Model to represent one pole of a 100 pole machine
- Model's active axial width = 60mm
- Model's active radial height = 61mm
- Active airgap at a radius of 135mm (equivalent to the mean radius of DSTFM airgap)
- Airgap length of 0.5mm
- Magnet active length of 3mm
- Per pole magnet volume of $1.35\times10^{-6}m^3$
- Magnet properties: $B_r = 1.2T$ $\mu_r = 1.19$
- B-H iron data to be derived from the SMC material, ABM100.32
- All models to maintain identical electric loading

5.6 The Single-Sided TFM

The original form of the SSTFM was easily recognisable with its discrete 'C' cores and surface mounted magnets. Employing powder metallurgy transformed this machine, giving it a continuous SMC coreback encasing the conductor, interrupted only by the indexed stator teeth above the rotor. A schematic sketch of the proposed SSTFM is shown in figure 5.5. The DSTFM incorporated a flux concentrating rotor, however, it would not be possible to do the same with this topology. A solid rotor was out of the question because of the short-circuiting effect on the magnets, and a twin rotor configuration could not support a continuous flux path without the use of bridging sections. The topology was therefore tied to surface mounted magnets.

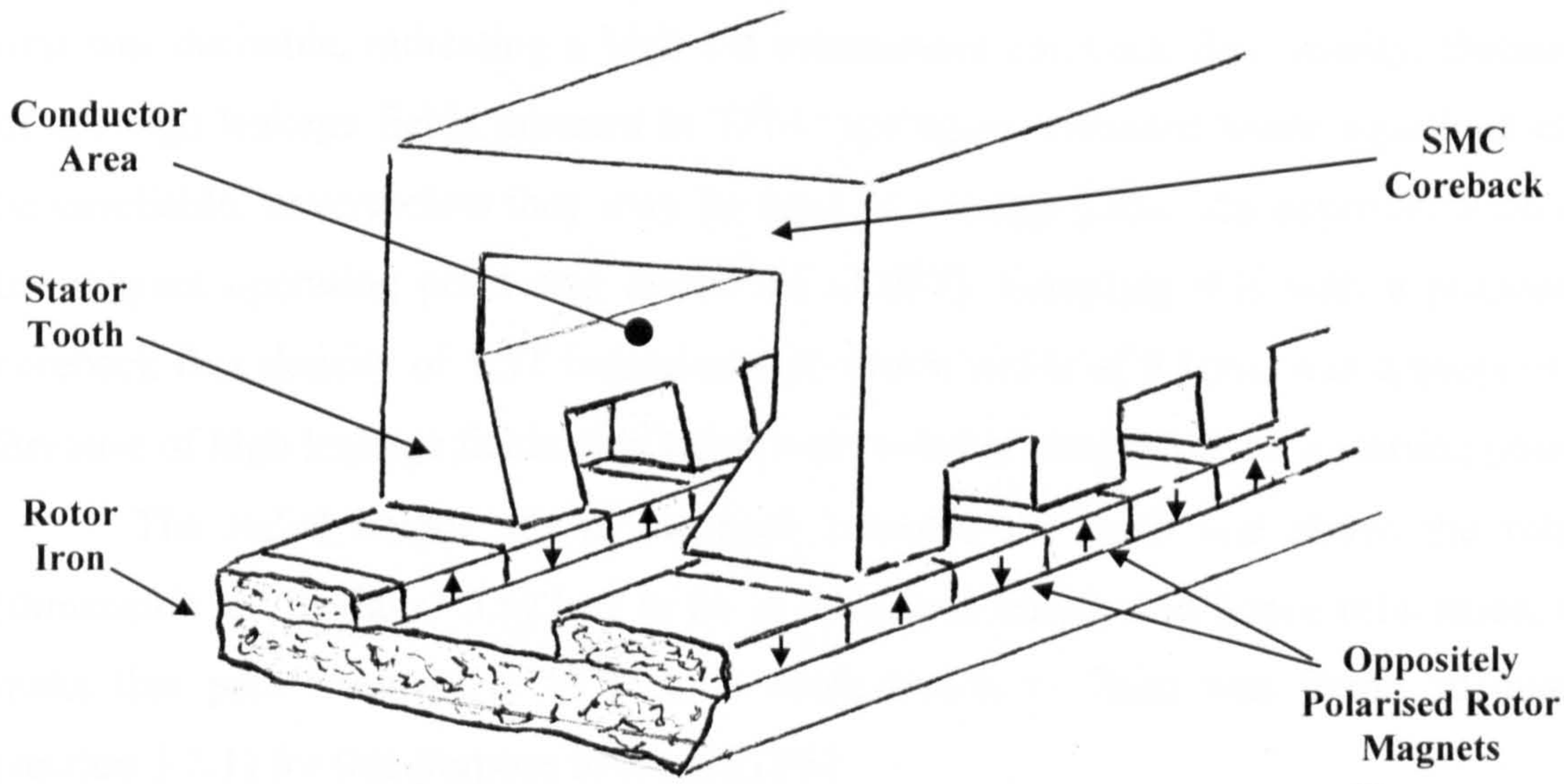

Figure 5.5 Rectilinear sketch of the proposed SSTFM

5.6.1 Initial Sizing of the SSTFM

The prime consideration of any design is the per unit cost of the material. In this context, it means obtaining the highest coreback flux linkage possible in the machine, with the most economical use of material. Some simple calculations can provide a useful guide to the minimum coreback thickness required for maximum output. Before these calculations were carried out, the dimensions of the magnets had to be decided upon. In the SSTFM there were four magnets per 'C' core, whereas in the DSTFM there was only one. Therefore, in order to compare like for like the volume of magnet material had to remain constant. The DSTFM magnet had an active length of 3mm and a volume of 1350mm^3. If the active length of each surface

mounted magnet was also set at 3mm in the SSTFM, then the combined surface area of the four magnets should be as close to 450mm^2 as possible. As the airgap radius was set at 135mm, the pole pitch was 8.48mm. Dividing this equally between two circumferential magnets gave 4.24mm per magnet. To produce an overall surface area of 450mm^2, the axial dimension for each magnet was 26.5mm (≡ 449.5mm^2). As the model had an axial width of 60mm, this left a generous 7mm spacing between the opposing teeth and magnets.

5.6.2 Coreback Sizing of the SSTFM

To estimate the coreback size, a prediction of the coreback flux density (B_{cb}) and the magnet operating point (B_m) was made. A high flux linkage with minimum iron was desirable, indicating a high but unsaturated coreback flux density. Because of the high leakage fields inherent in TFM topologies, standard linear equations can be unreliable, nevertheless they may be used as a rough guide. An approximation of the magnet operating point was calculated (1.03T). Coupling this with a proposed coreback flux density of 1.5T indicated a coreback width of 9.1mm was appropriate. Because of high leakage fields, this value was probably excessive, but a starting point.

The radial height of the coreback between the teeth and above the rotor (dimension 'z' in figure 5.6) had to be of sufficient length and hence reluctance, to make that path unattractive to flux. A tooth length of 7mm was found adequate (section 3.3.1) for this purpose in the DSTFM.

The conductor area (390mm^2) was the final dimensional component. Maintaining the same axial/radial envelope of the DSTFM (60mm × 61mm) produced a very large conductor area. It seemed prudent therefore to reduce the radial height of the model making the conductor area an exact fit within the stator.

5.6.3 Tooth / Coreback Interface

As the flux traversed between a stator tooth and the radial coreback iron, it was important to ensure that the cross-sectional area of the crossover interface was as close as possible to that of the tooth's sole. This was accomplished by embedding both radial and axial surfaces of the teeth into the core sides, as shown in figure 5.6, and extruding area 'A' along the axial faces of all the teeth in direction 'x'.

With these requirements taken into consideration, the axial/radial 2D template of figure 5.7 and the circumferential/radial 2D template of figure 5.8 were produced. The effect of increasing the coreback in the 'x' direction enlarged the interface area from 102mm^2 (55% smaller than the tooth sole area) to 144mm^2 (35% smaller). Although there was still some discrepancy in area, saturation was not severe. Increasing the radial length of the teeth by 35%, from 7mm to 9.5mm, raised the tooth reluctance but lowered the rotor to coreback leakage path reluctance by a similar amount. These dimensions were then adapted and extruded to form the 3D finite element model shown in figure 5.9.

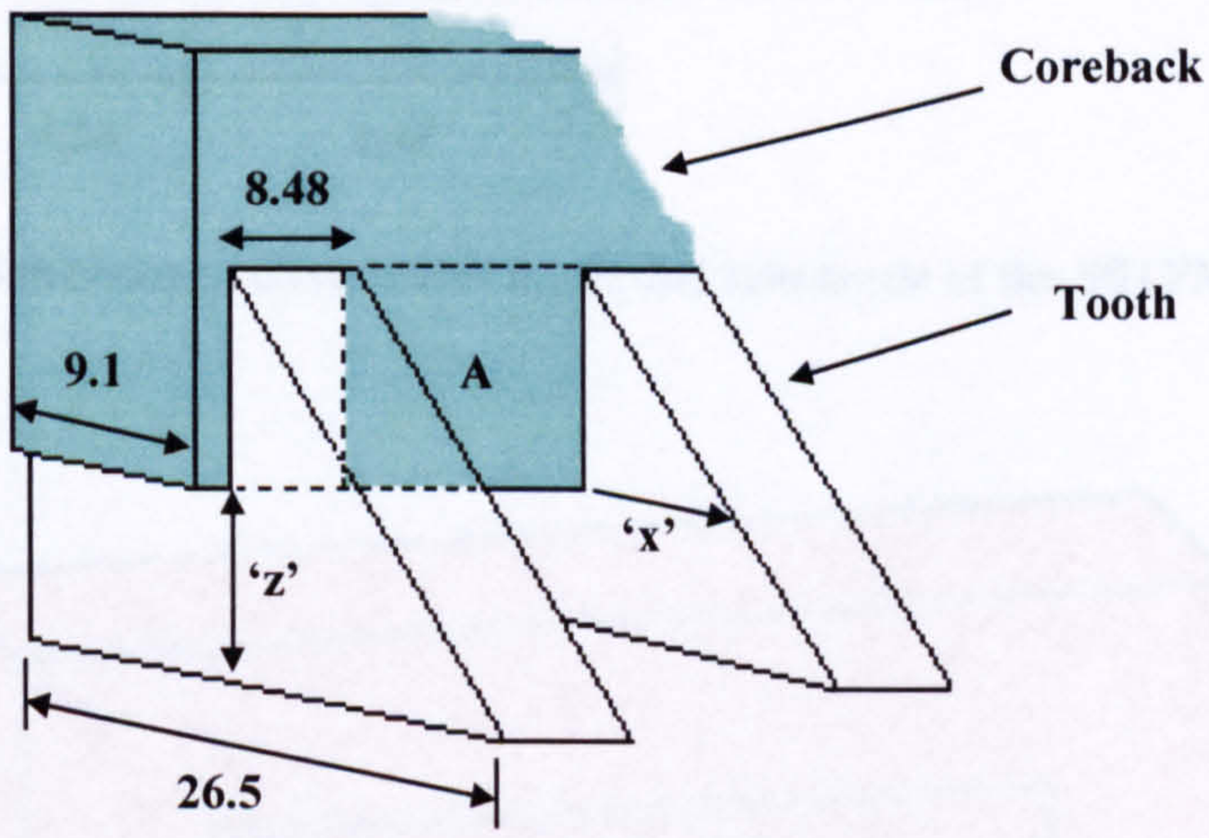

Figure 5.6 Schematic of tooth and coreback interface region

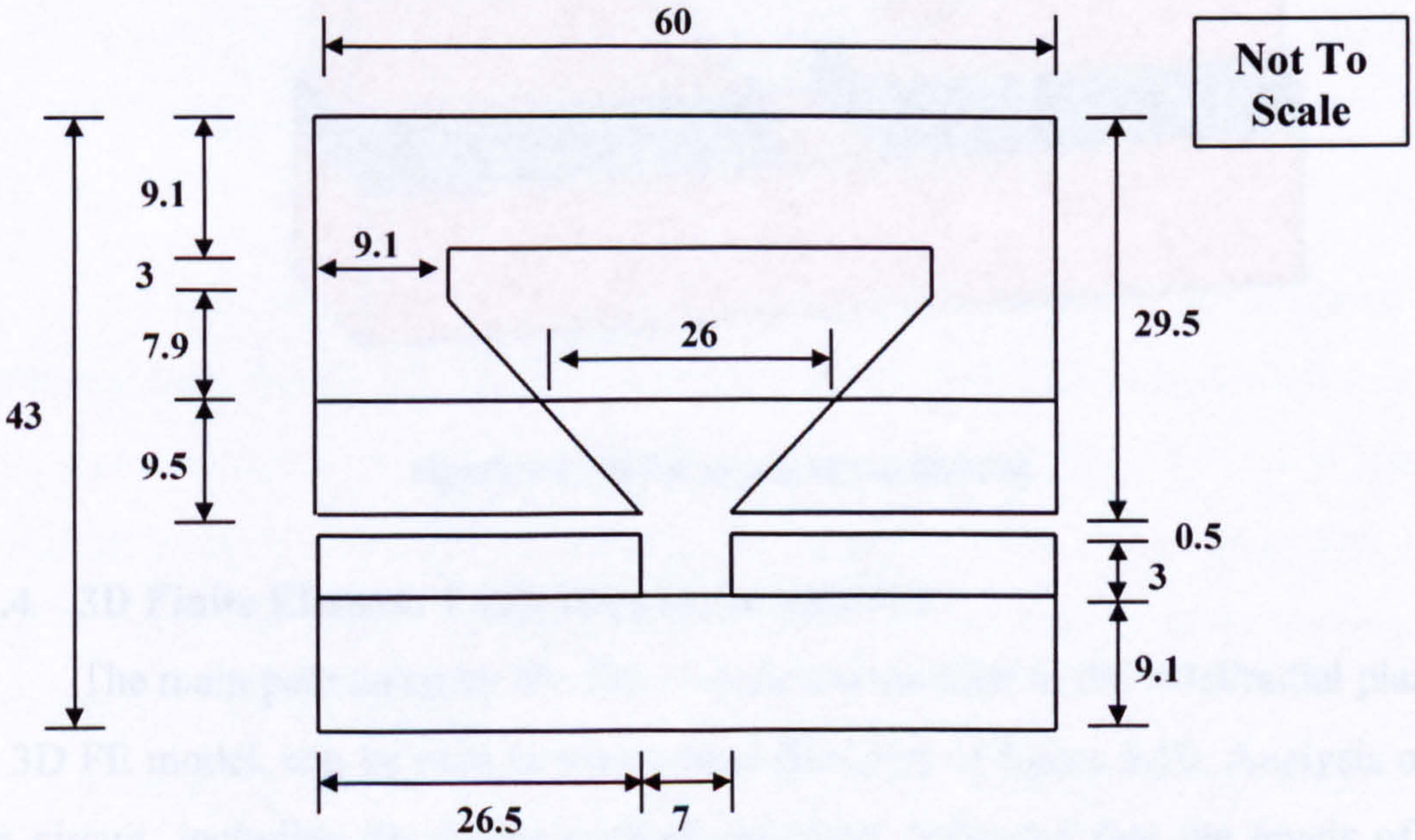

Figure 5.7 Dimensioned axial/radial schematic of the SSTFM

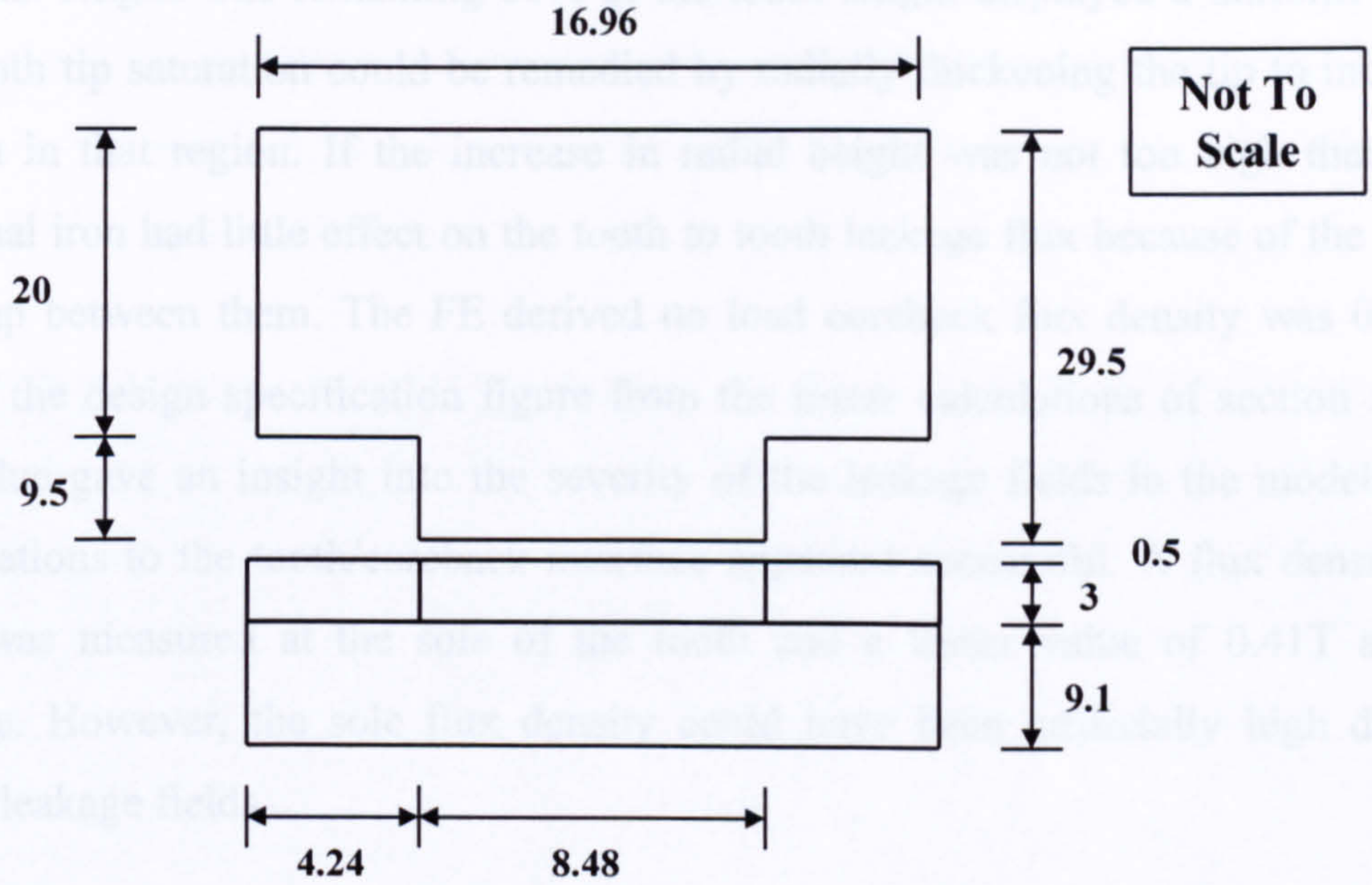

Figure 5.8 Dimensioned circumferential/radial schematic of the SSTFM

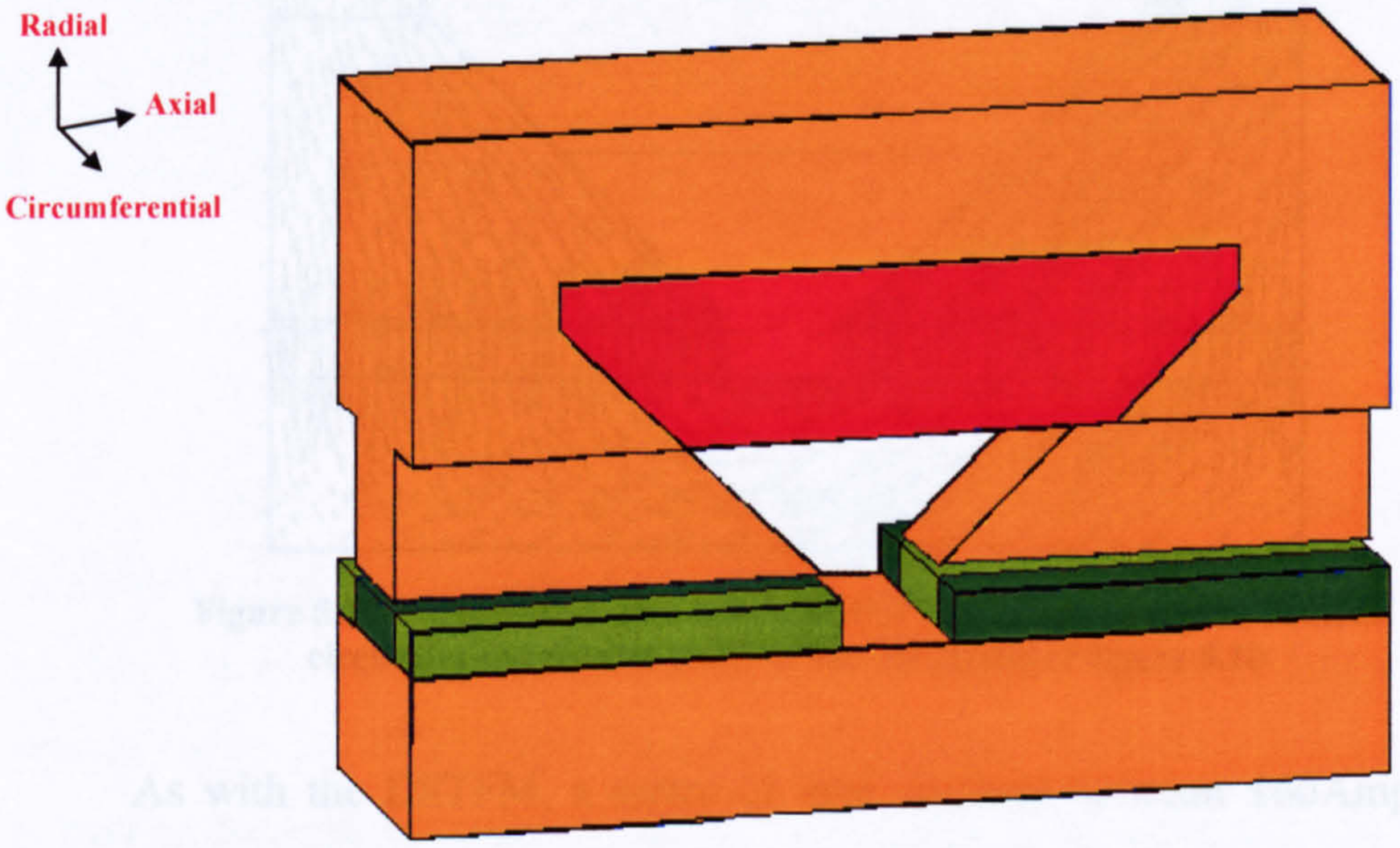

Figure 5.9 3D FE model of the SSTFM

5.6.4 3D Finite Element Evaluation of the SSTFM

The main path taken by the flux, which was parallel to the axial/radial plane of the 3D FE model, can be seen in the no load flux plot of figure 5.10. Analysis of the iron circuit, including the tooth/coreback interface, indicated that the levels of flux were well within its capabilities. The only exceptions were the tooth tips. For a radial depth of 1mm from the airgap, they exhibited flux densities up to 1.2T for 20% of

their axial length. The remaining 80% of the tooth length displayed a uniform 0.8T. This tooth tip saturation could be remedied by radially thickening the tip to increase the iron in that region. If the increase in radial height was not too high then this additional iron had little effect on the tooth to tooth leakage flux because of the large axial gap between them. The FE derived no load coreback flux density was 0.39T, 25% of the design specification figure from the linear calculations of section 5.6.2. This value gave an insight into the severity of the leakage fields in the model. The modifications to the tooth/coreback interface appeared successful. A flux density of 0.54T was measured at the sole of the tooth and a lesser value of 0.41T at the interface. However, the sole flux density could have been artificially high due to magnet leakage fields.

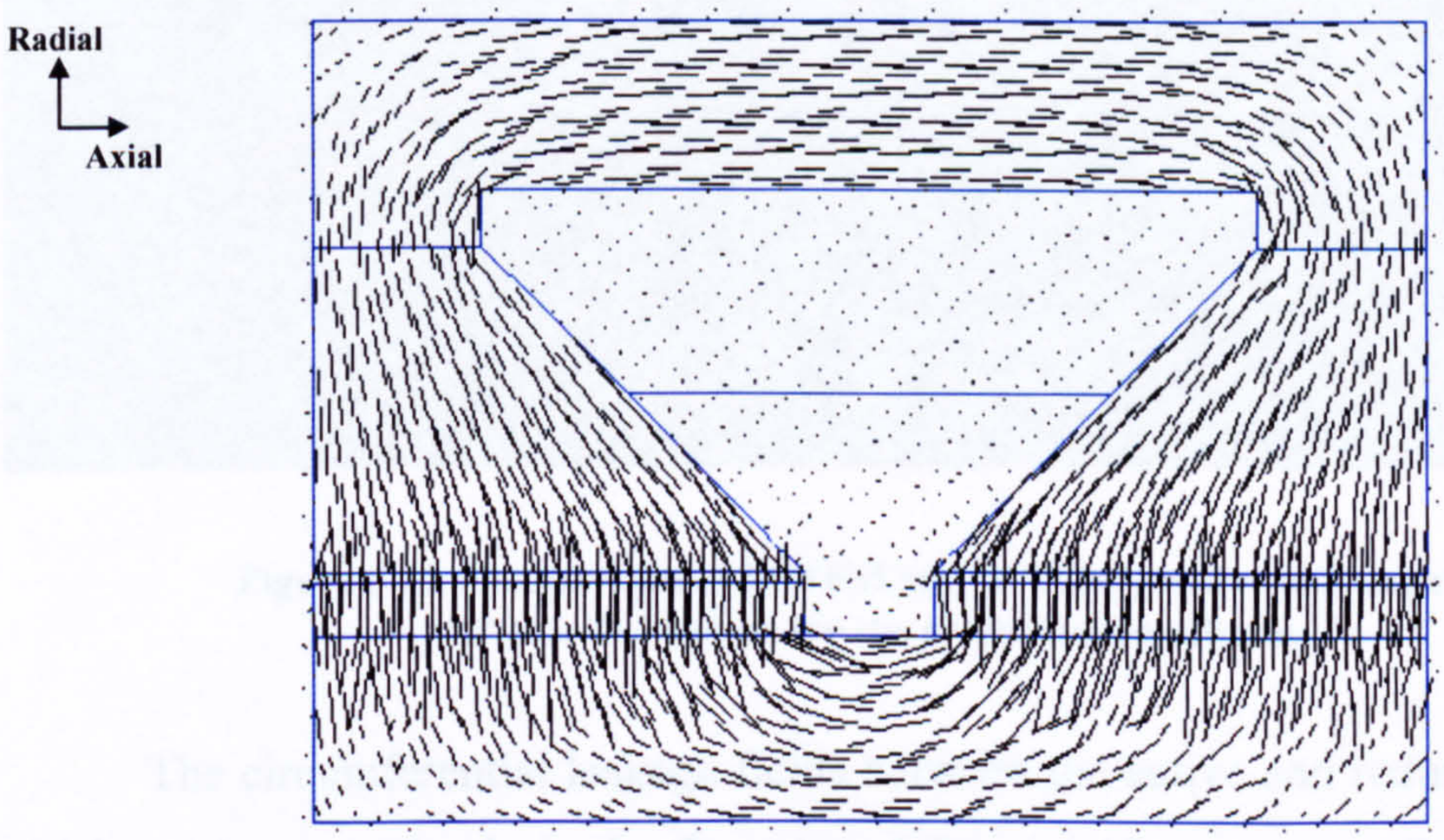

Figure 5.10 No load flux plot from the SSTFM, taken along the central circumferential/axial plane of the 3D model of figure 5.10

As with the DSTFM, a series of load currents between ±60Amperes were impressed upon the 3D FE model, enabling its electromagnetic characteristics as well as its mean output to be determined. The positive and negative 'd' axis Ψ-I curves derived from these load steps are shown in comparison to the curves generated by the DSTFM under the same load conditions(figure 5.11). The data from the investigation is presented in appendix E.4.1.

Examining the two sets of curves in figure 5.11 revealed a marked difference between the two topologies. The area enclosed by the SSTFM curves equated to 30.76 Joules whereas the DSTFM area, as stated in section 3.8.4, was 62.95 Joules. Virtually all of this 51% deficit could be attributed to the 50% reduction in magnet

utilisation. However, the no load flux linkage (Ψ) of the two topologies examined indicated that the SSTFM had 64% less flux linkage than the DSTFM (199mWb as opposed to 555mWb). This was the result of three separate factors, only one of which was the 50% magnet utilisation.

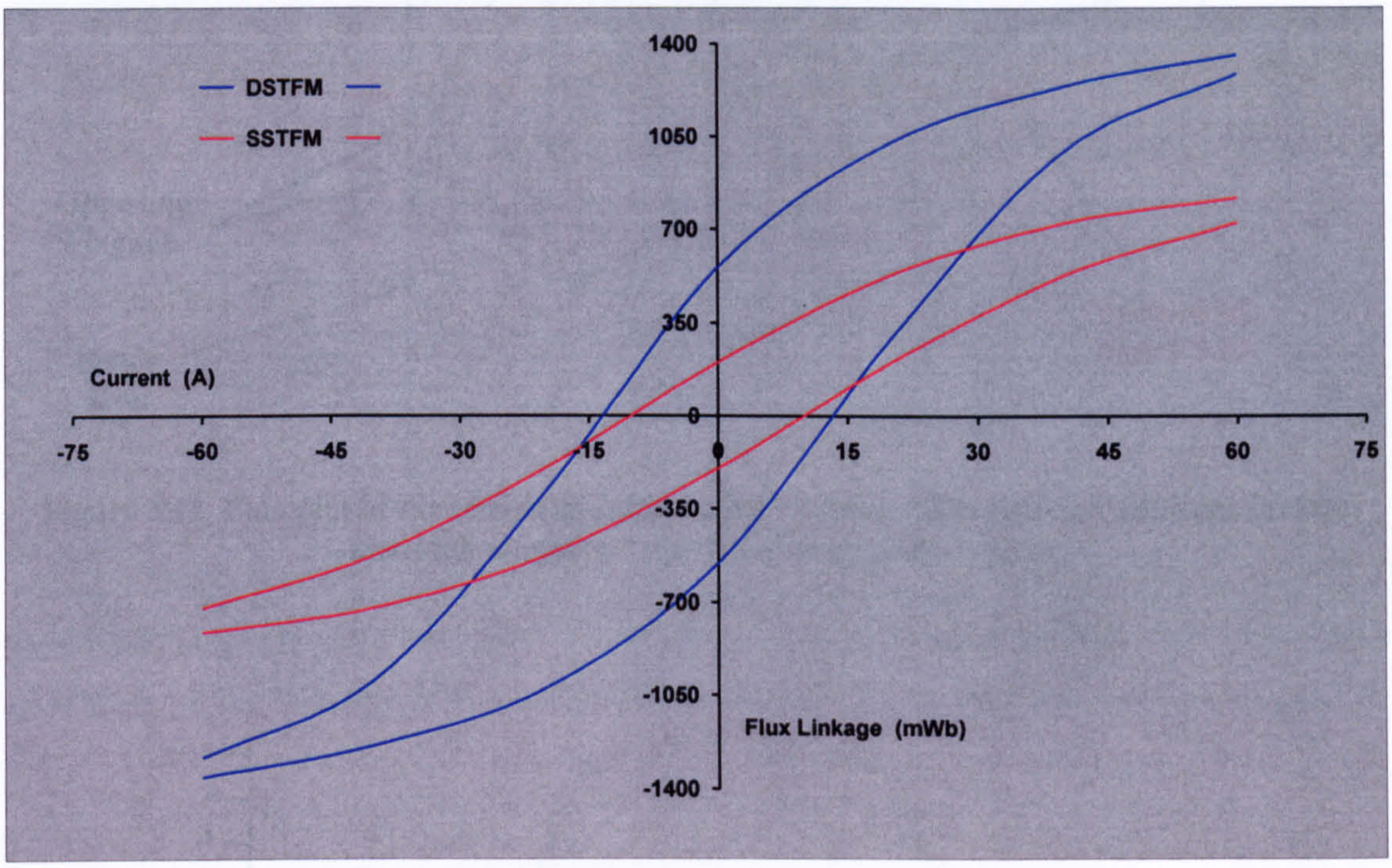

Figure 5.11 Comparison of DSTFM and SSTFM positive and negative 'd' axis Ψ-I curves for the same load conditions

The circumferential leakage fields between the active and redundant magnets, which can be seen clearly in the flux plot of figure 5.12, were one other source of no load flux linkage shortfall. A graph indicating the level of these fringing fields is shown in figure 5.13. The graph shows the variation in flux density along a horizontal line passing through the centre of the airgap from the left-hand side to the right-hand side of the plot of figure 5.12.

In order to determine the severity of these leakage fields, the magnitude of per pole flux travelling radially up a tooth at 1mm intervals was ascertained from the 3D FE model. This data was converted to the graphical form shown in figure 5.14. The analysis showed that there was 0.117mWb of flux entering the tooth at the airgap, but only 0.061mWb leaving the tooth for the coreback. This means that 48% of the flux was lost in leakage fields. An additional reason for the low value of no load flux linkage was the lower airgap flux density (0.93T average) due to the use of

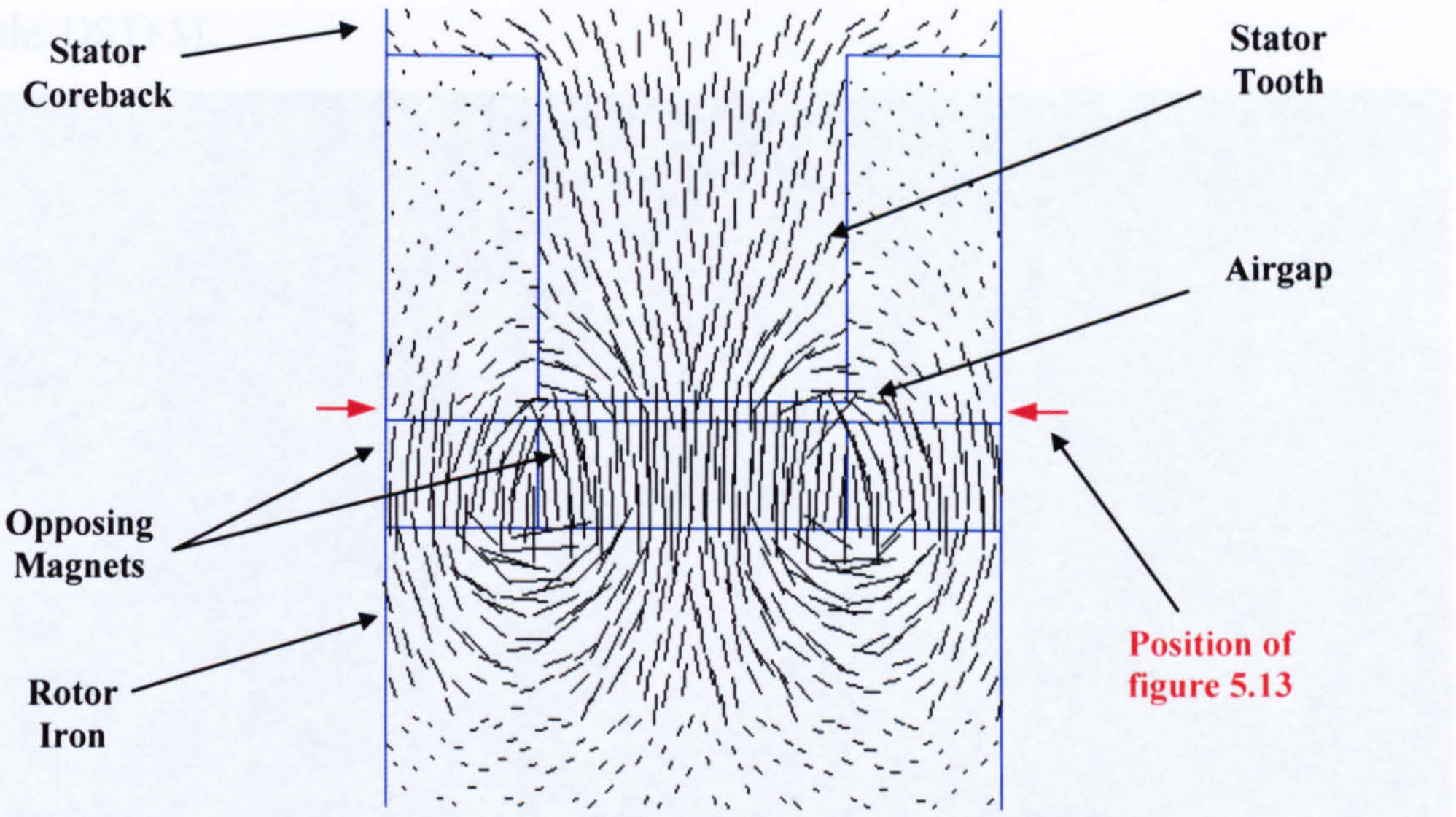

Figure 5.12 Flux plot of the circumferential/radial fringing fields between adjacent surface mounted magnets, 1mm from an axial extremity

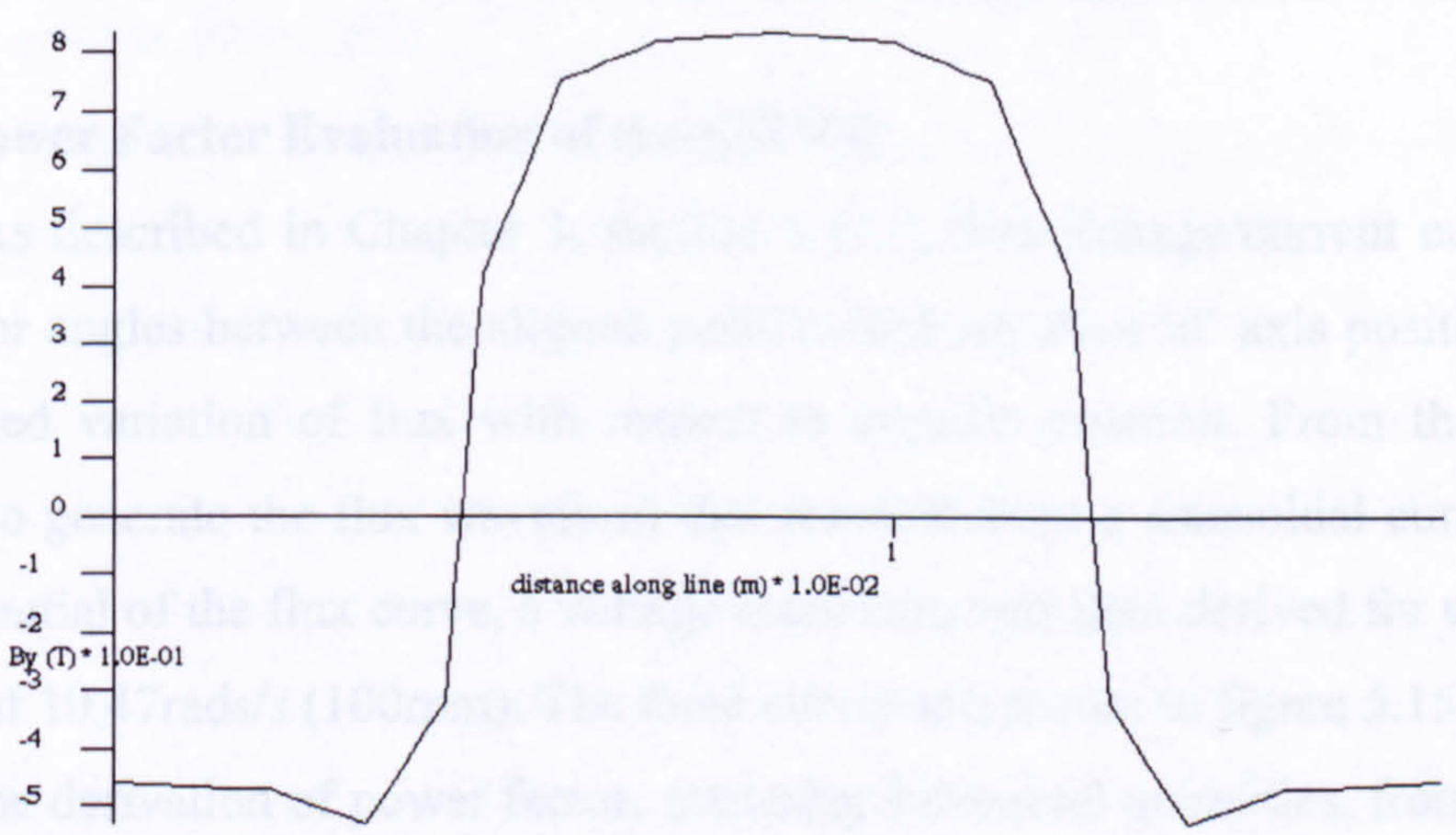

Figure 5.13 Variation of radial flux density in the plot of figure 5.12 between the indicated circumferential extremities and through the airgap. (B_{max} = 0.83T B_{min} = -0.53T)

surface mounted magnets over a flux concentrating configuration. In comparison, at 1.33T, the DSTFM had a 30% higher average airgap flux density (Chapter 3,section 3.8.4). However, using surface mounted magnets did have some advantages. With surface mounted magnets, all airgap fields generated by the armature had to cross the full depth of the magnet, reducing the armature reaction field, compared to a flux concentration configuration. This is evident in the comparative gradients of the Ψ-I

curves in figure 5.11, with the SSTFM exhibiting a much shallower gradient than that of the DSTFM.

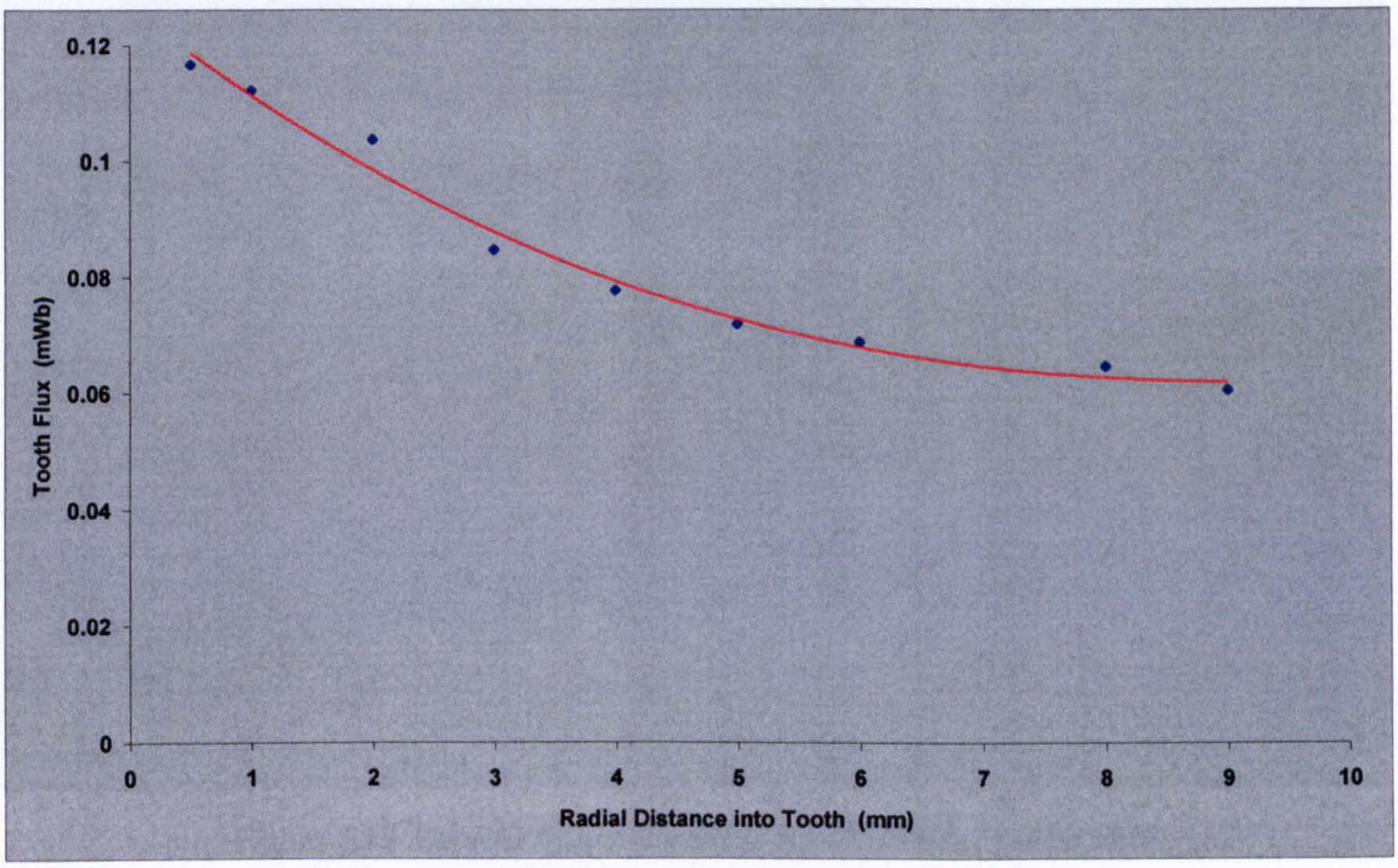

Figure 5.14 Variation of no load tooth flux with radial distance from the active airgap

5.6.5 Power Factor Evaluation of the SSTFM

As described in Chapter 3, section 3.11.3, flux linkage/current curves were derived for angles between the aligned positive and negative 'd' axis positions, using an assumed variation of flux with respect to angular position. From these it was possible to generate the flux waveform that resulted from a sinusoidal current. From the differential of the flux curve, a voltage waveform was then derived for a rotational velocity of 10.47rads/s (100rpm). The three curves are shown in figure 5.15.

The derivation of power factor, assuming sinusoidal quantities, from the mean power and rms quantities of voltage and current, produced a value of 0.29, this value was confirmed by the 73° phase angle between the voltage and current.

$$pf = \frac{mean\ Power}{(rms\ Voltage \times rms\ Current)} = \frac{2425.9}{(353 \times 23.4)} = 0.294$$

The SSTFM power factor was 22% less than that of the DSTFM. This may be attributed to the large magnet leakage fields, which substantially reduced the no load flux linkage of the model.

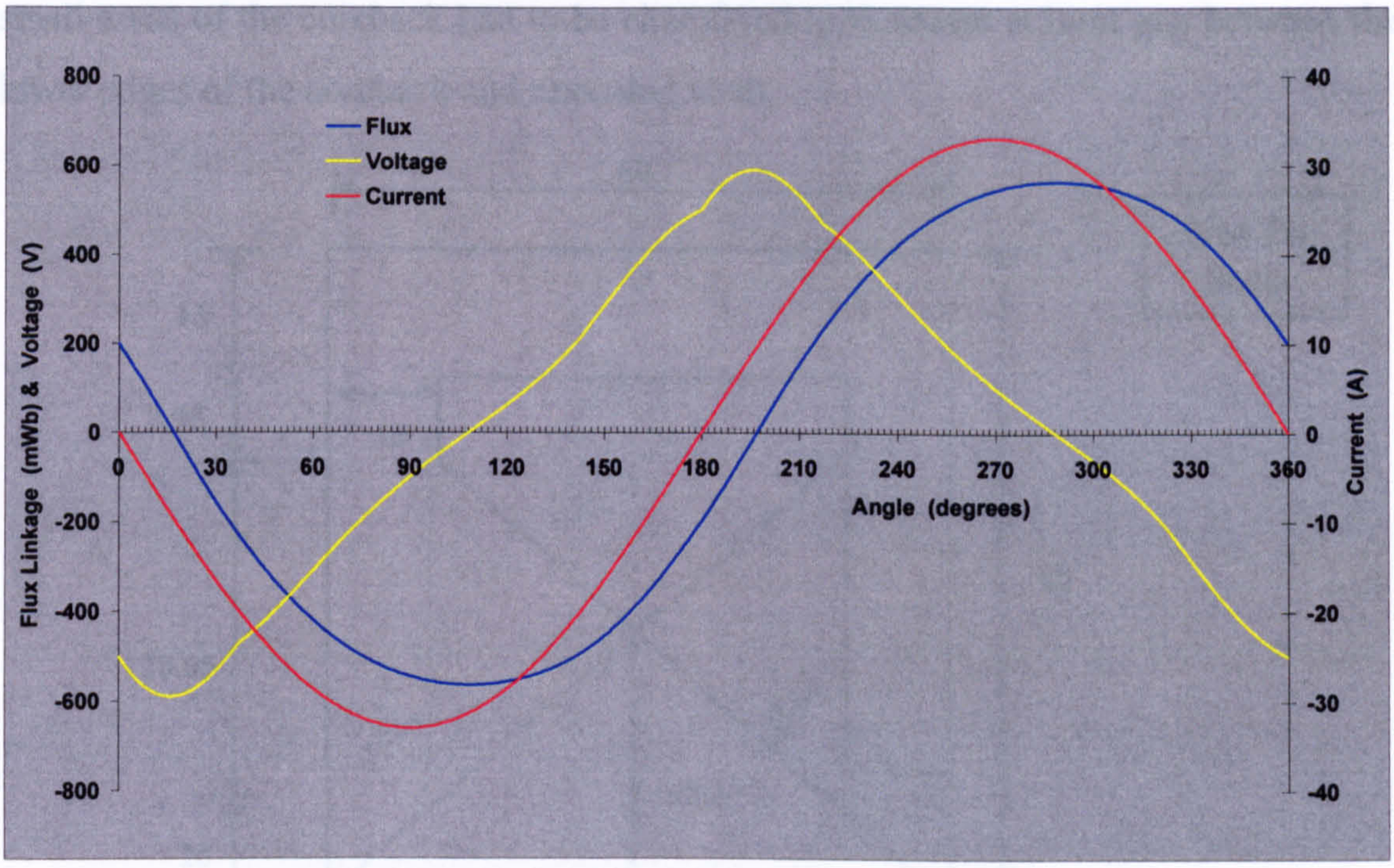

Figure 5.15 Derived flux and voltage waveforms for the SSTFM

5.7 The Claw Pole TFM

Although Chapter 4 has been devoted to the claw pole topology already, this particular evaluation was useful for a number of reasons. Firstly, it allowed the CPTFM to be 'benchmarked' along with the other topologies under investigation in this chapter, due to the similarity in specifications imposed upon them. Secondly, there was the ability to adapt the geometry and dimensions of the model to their best advantage. However, the main difference between this model and the claw pole model of Chapter 4, apart from resizing to match the DSTFM specifications, was the use of a flux concentrating rotor. A direct comparison with a surface mounted magnet configuration was also made.

5.7.1 Initial Sizing of the CPTFM

In order to give as close a comparison as possible, the coreback axial and radial widths were identical to those of the DSTFM. The axial length of the model was maintained at 60mm and the radial height at 61mm. With the same airgap radius and pole number, the pole pitch was 8.48mm. As in the SSTFM, it was important to ensure that the tooth/coreback interface area was comparable in size to that of the tooth/airgap interface. The dimensions used for the CPTFM model are shown in

figures 5.16 and 5.17. The 3D model is shown in figure 5.18. It should be noted that small areas of the coreback had to be chamfered to maintain a 5mm gap between the lower edges of the coreback and opposing teeth.

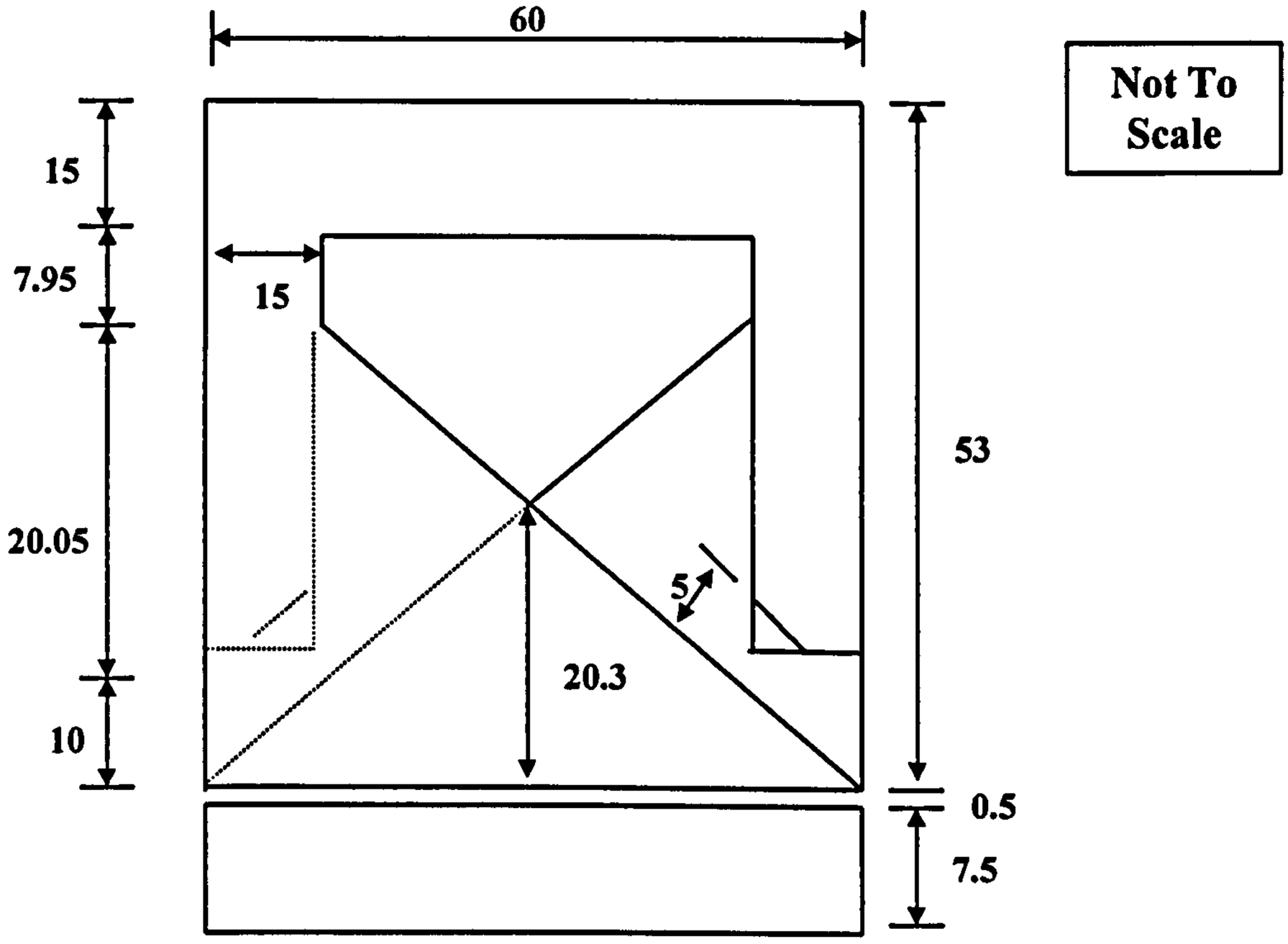

Figure 5.16 Dimensioned axial/radial schematic of the CPTFM

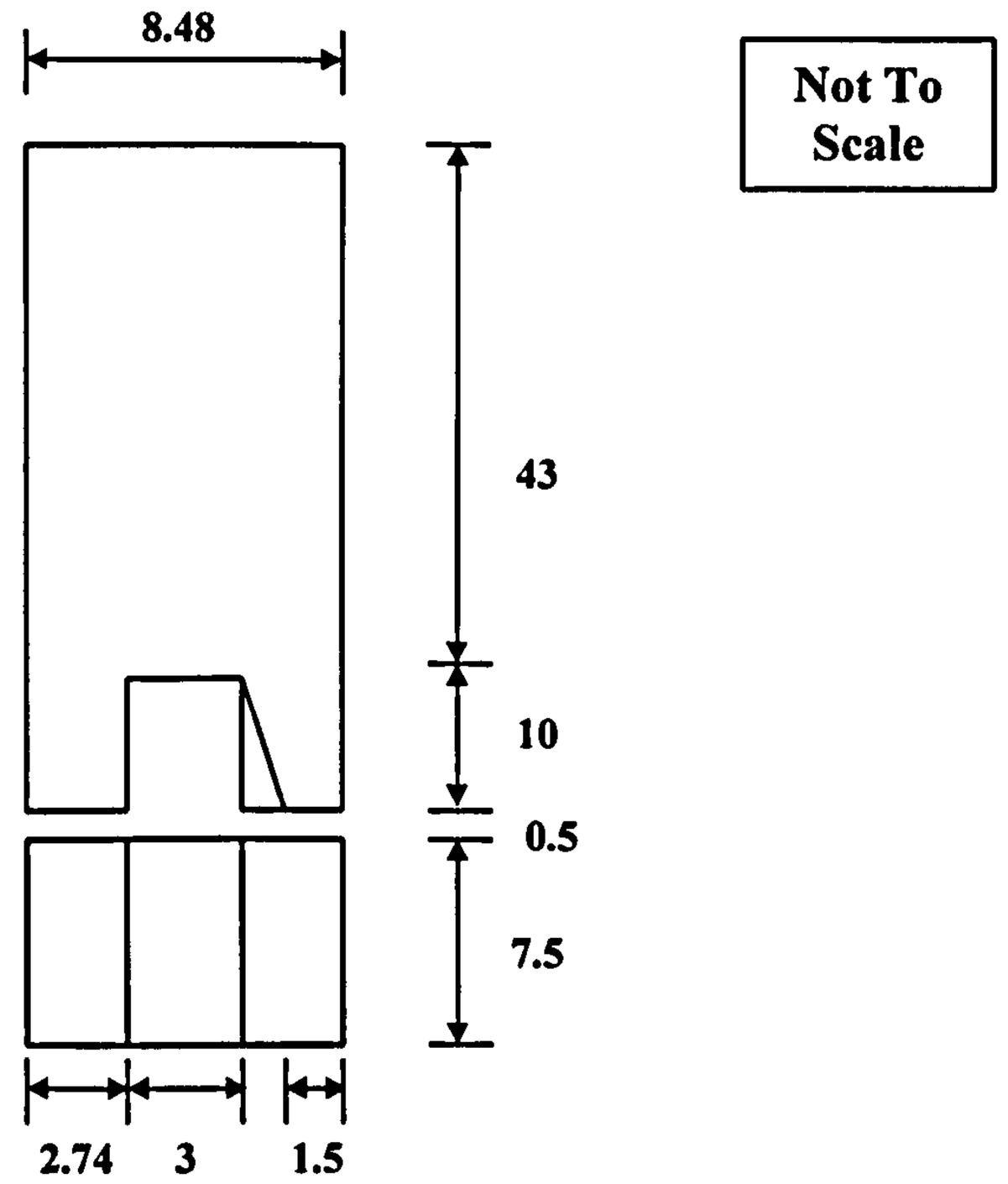

Figure 5.17 Dimensioned circumferential/radial schematic of the CPTFM

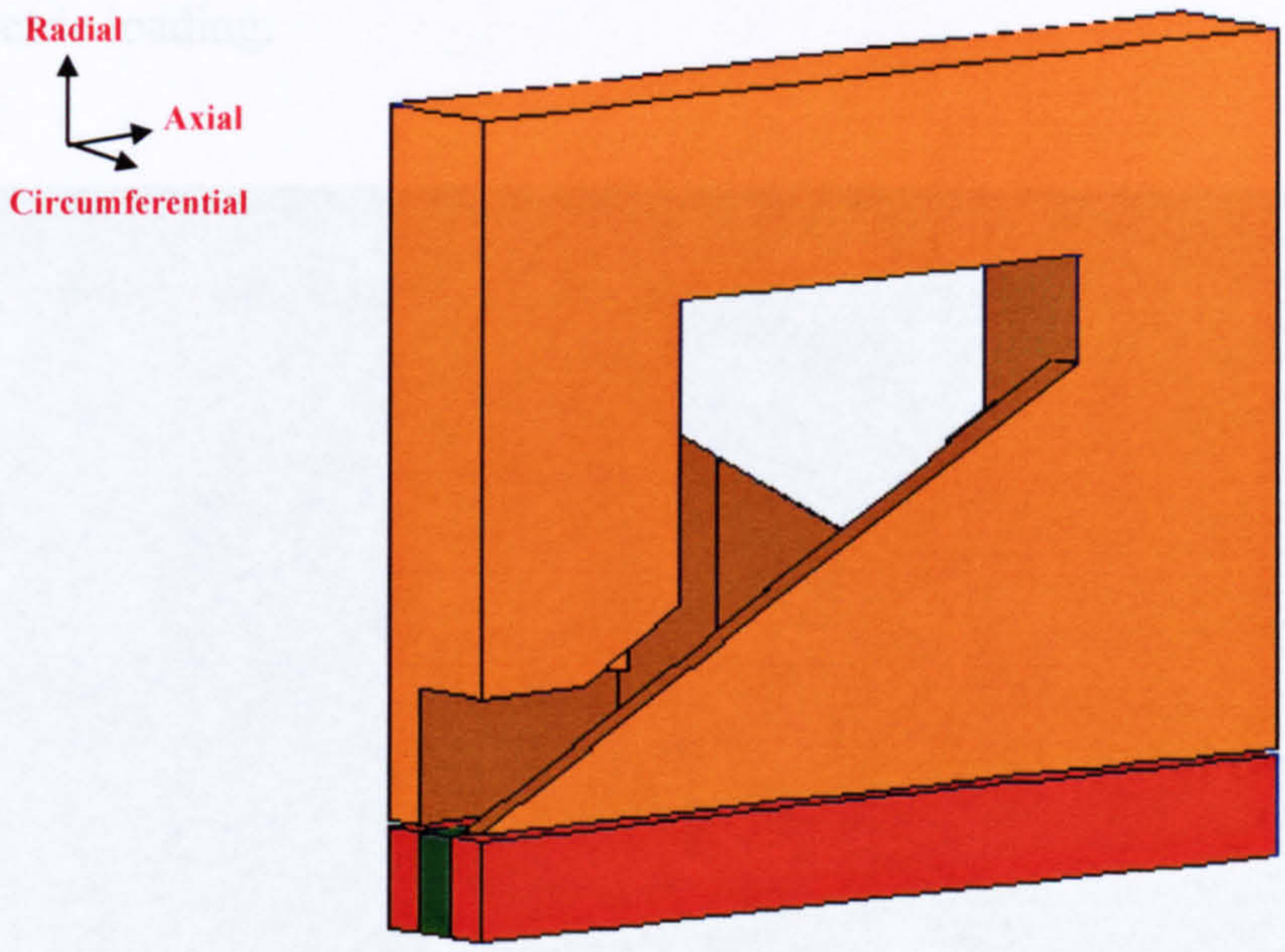

Figure 5.18 3D FE model of the CPTFM

5.7.2 Comparing the Flux Concentrating Magnet CPTFM and Surface Mounted Magnet CPTFM

To remain consistent with past models, the completed 3D FE model of figure 5.20 was exposed to a series of currents between ±60A. The results from these current loadings are presented in Appendix E.4.2. As mentioned at the beginning of this section, an additional 3D FE model of a CPTFM with surface mounted magnets was also constructed. The stators of the two models were identical. The rotors differed only in configuration and radial depth. In the surface mounted configuration, there was no restriction to the rotor iron radial depth and consequentially it was made 15mm deep radially to ensure that saturation would not occur. The Ψ-I data for the surface mounted magnet CPTFM is given in appendix E.4.3. Figure 5.19 compares the Ψ-I aligned positive and negative d-axis curves for these two CPTFM configurations.

The equivalent energy encompassed by the two Ψ-I loops was very similar 28.38 Joules (surface mounted) and 28.40 Joules (flux concentrating). However, at low MMFs the flux concentrating configuration performance was better than that of the surface mounted magnet configuration. At 30A the flux concentrating topology encompassed 7.2% more energy (26.84 Joules) and at 20A there was 9.8% more energy (23.53 Joules). The general shape of the curves and the saturation levels were almost identical but, as shown in section 4.7, the flux concentrating configuration

outperformed the surface mounted configuration at all but the highest levels of electric loading.

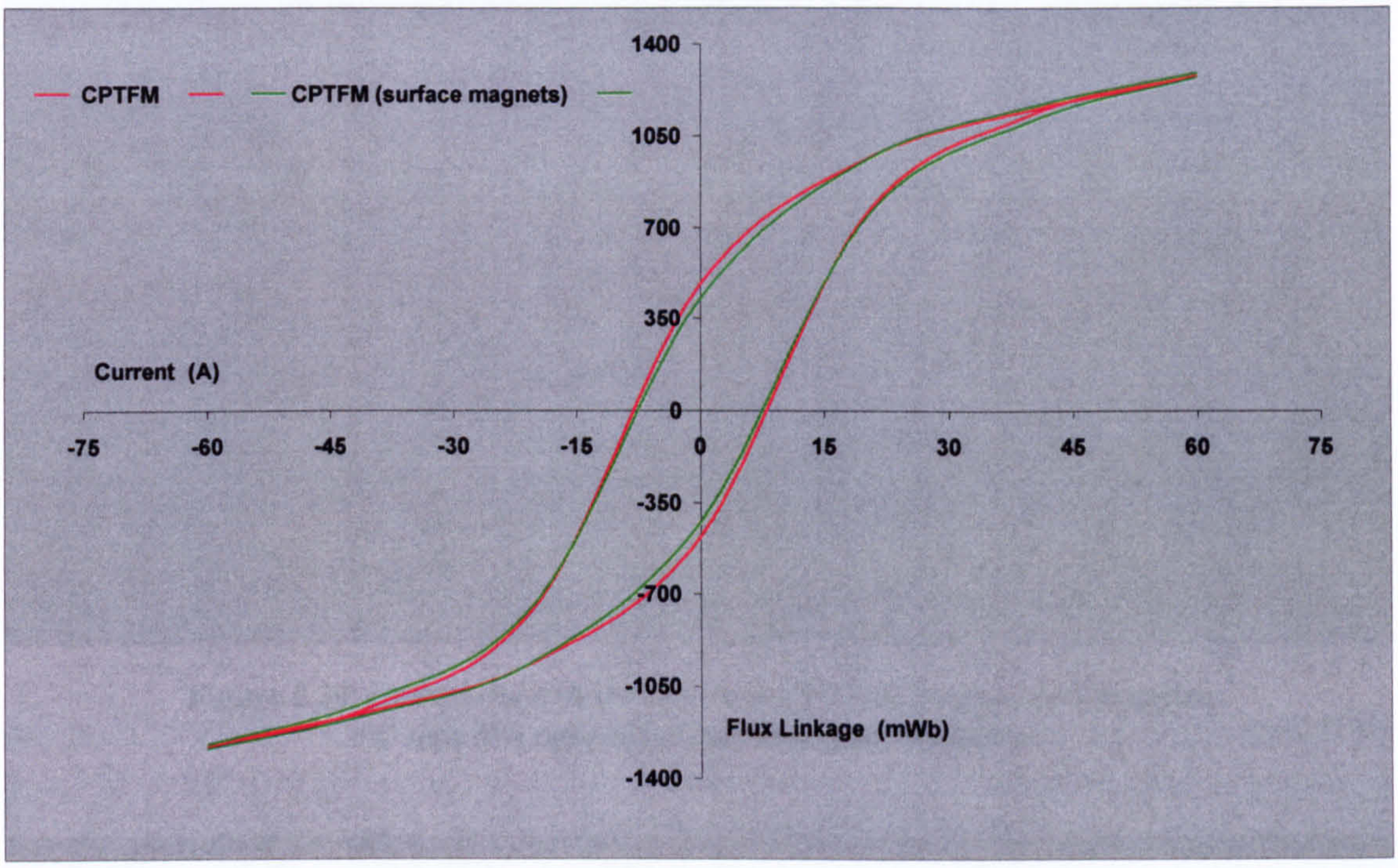

Figure 5.19 Comparison of the surface mounted and flux concentrating magnet configurations of the CPTFM, positive and negative 'd' axis Ψ-I curves for the same load conditions

5.7.3 Comparison between the DSTFM and CPTFM

Comparing the CPTFM and DSTFM topologies, (figure 5.20) revealed a similarity in form between the first quadrant, positive 'd' axis, curves and also a comparable value of no load flux linkage between the two models (13% less in the CPTFM). However, the significant interpolar leakage inherent in this topology (see Chapter 4, section 4.5.3) produced a much higher level of armature reaction and hence a steeper curve gradient and narrower energy envelope than that of the DSTFM. The CPTFM saturated with 6% less flux, and a negative 'd' axis 'knee' at a current of 21.3A as opposed to 39A (ie. 45% lower). Thus, the CPTFM energy envelope was 55% smaller than that of the 62.95 Joules of the DSTFM. A large proportion of this reduction was attributed to the interpolar leakage path in the model. Figure 5.21 illustrates the magnitude of flux passing radially up a tooth in this model, from the sole of the tooth to a position level with the top of the conductor area there was a steady decline in tooth flux as it rose through the interpolar overlap region and leaked across the connecting airgap. The end of the overlap region (at a radial height of 20mm) was clearly defined by the stabilisation of the flux level. However, the flux

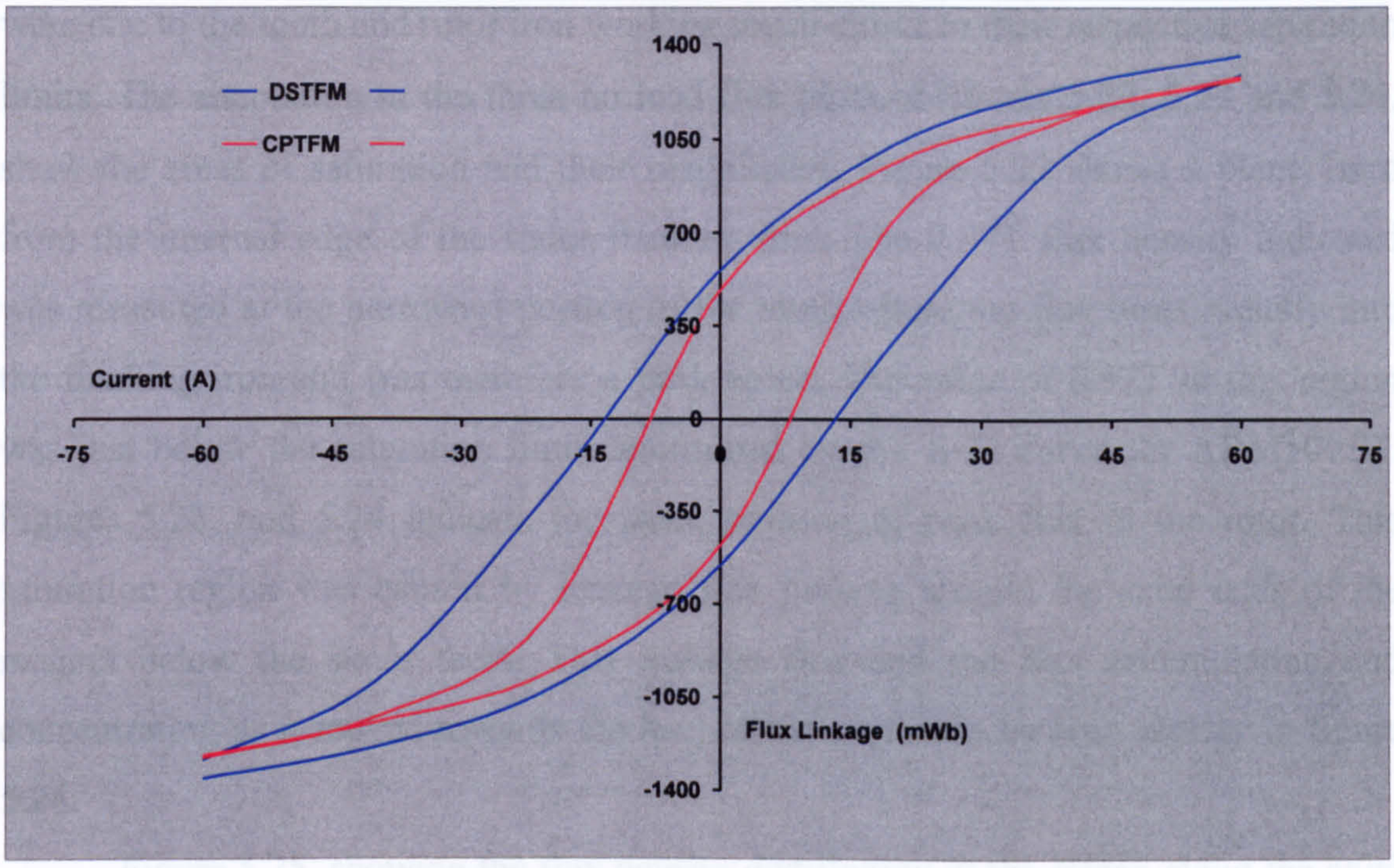

Figure 5.20 Comparison of DSTFM and CPTFM positive and negative 'd' axis Ψ-I curves for the same load conditions

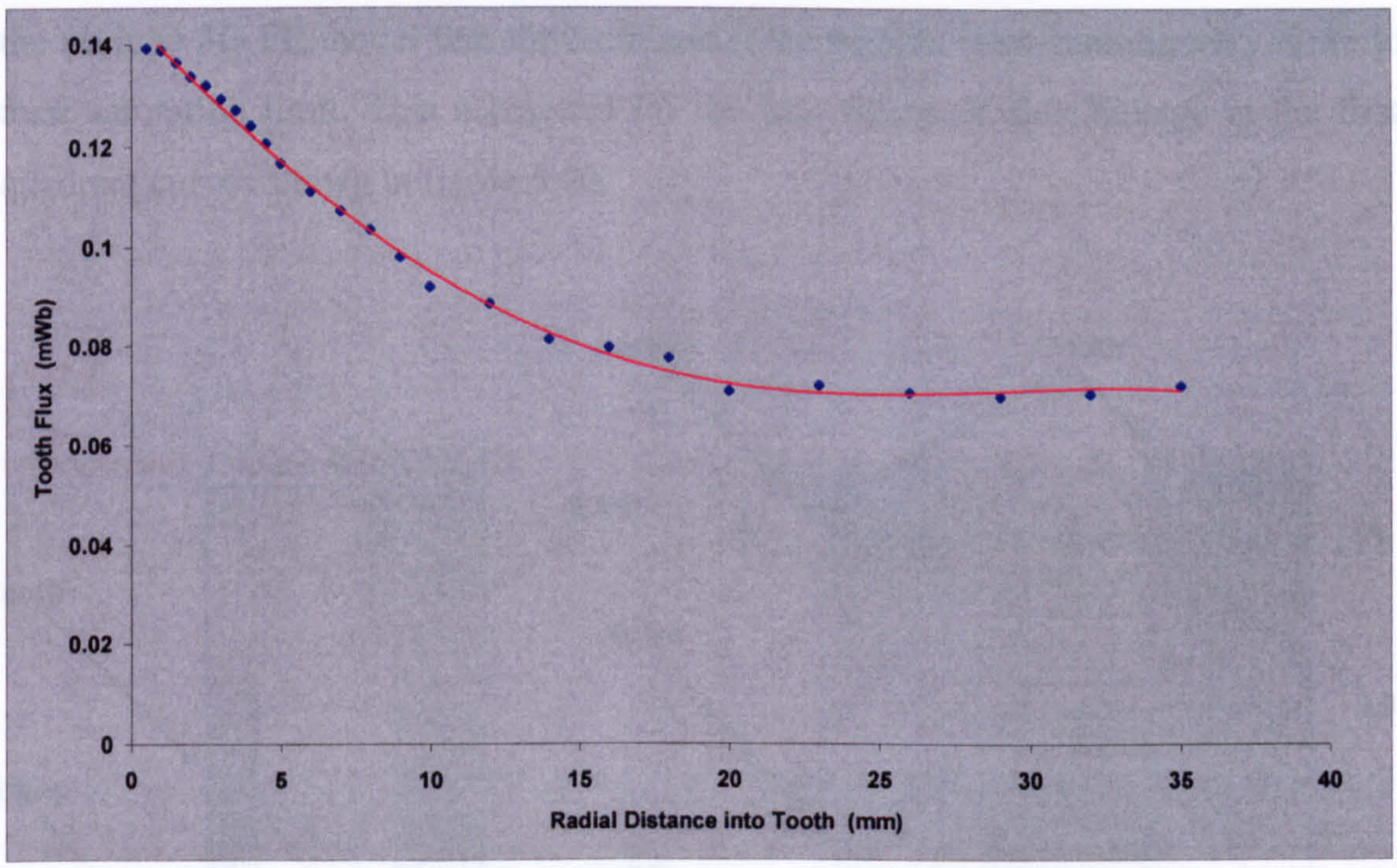

Figure 5.21 Variation of CPTFM no load tooth flux with radial height, graph shows measured points and best fit curve

reduction from 0.139mWb at the sole of the tooth to 0.0708mWb at 20mm, equated to a decrease of 49.2%.

Another contributing factor to the CPTFM's reduced output was related to the utilisation of tooth and rotor iron. The low Ψ-I curve saturation levels in the CPTFM

were due to the tooth and rotor iron working much closer to their respective saturation limits. The annotation in the three no load flux plots of figures 5.22, 5.23 and 5.24, show the areas of saturation and their magnitudes. Figure 5.22 shows a plane 1mm from the internal edge of the stator flanking iron. The 0.97T flux density indicated was measured at the narrowest portion of the tooth where the flux turns radially into the flanking iron and was therefore a peak value. The value of 0.97T in this region was just below the saturation limit determined by the B–H curve for ABM100.32. Figures 5.23, and 5.24 indicate the same position of peak flux in the rotor. This saturation region was caused by leakage flux passing around the axial ends of the magnet below the stator teeth. This leakage flux and the flux accumulating and concentrating as it moved towards the heel of the tooth can be seen clearly in figure 5.24.

Figure 5.25, showing the flux density distribution in the airgap along the axial centre of a tooth, reinforced the idea of an axial build up of flux moving towards the ends of the rotor, before turning radially up the tooth. It was clear from the analysis of the no load 3D FE model that the teeth and rotor regions were running very close to their saturation limit. This accounted for the low values of flux linkage in the first quadrant curves shown in figure 5.20.

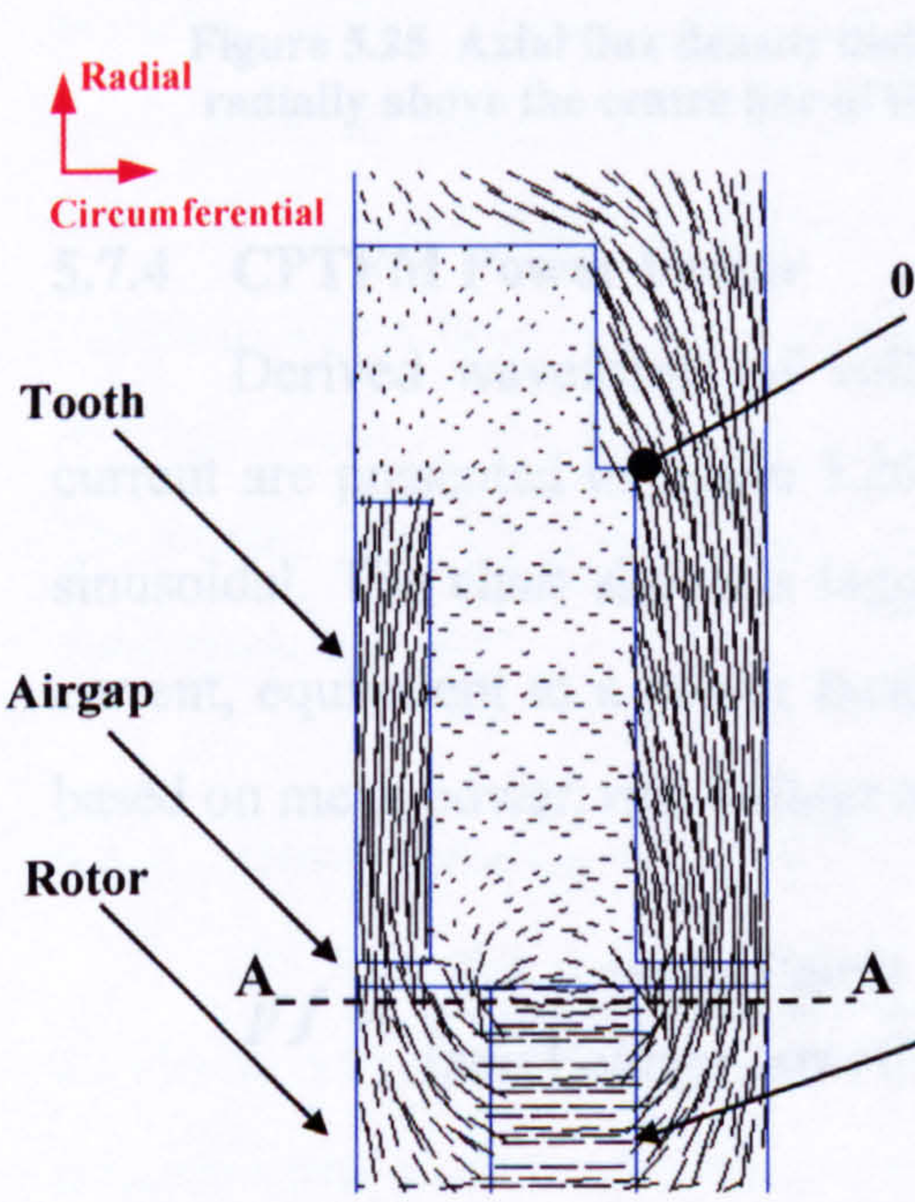

Figure 5.22 Radial/circumferential no load flux plot of the teeth and rotor region 14mm from an axial extremity

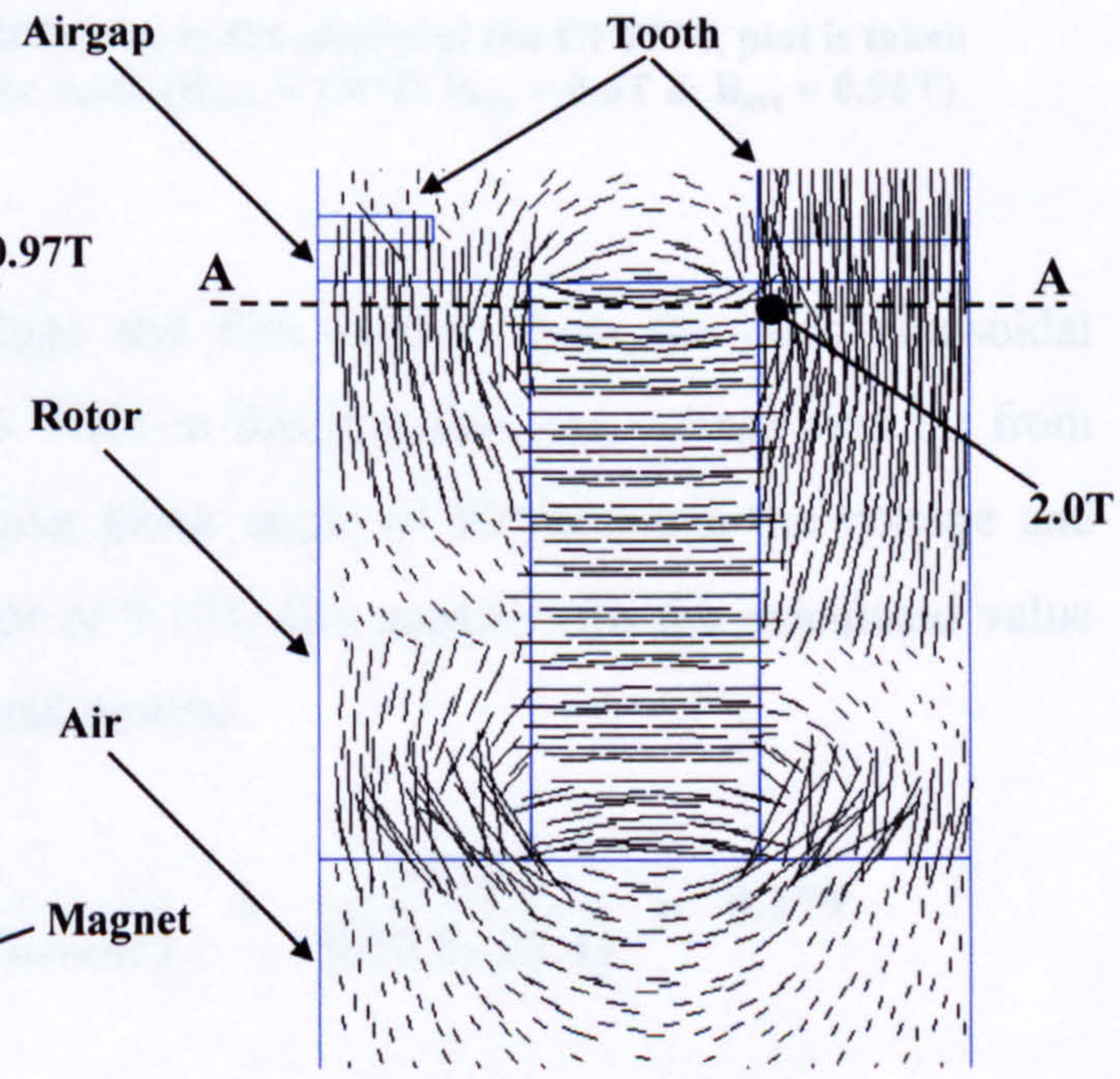

Figure 5.23 Radial/circumferential no load flux plot of the rotor and airgap region, 0.5mm from an axial extremity

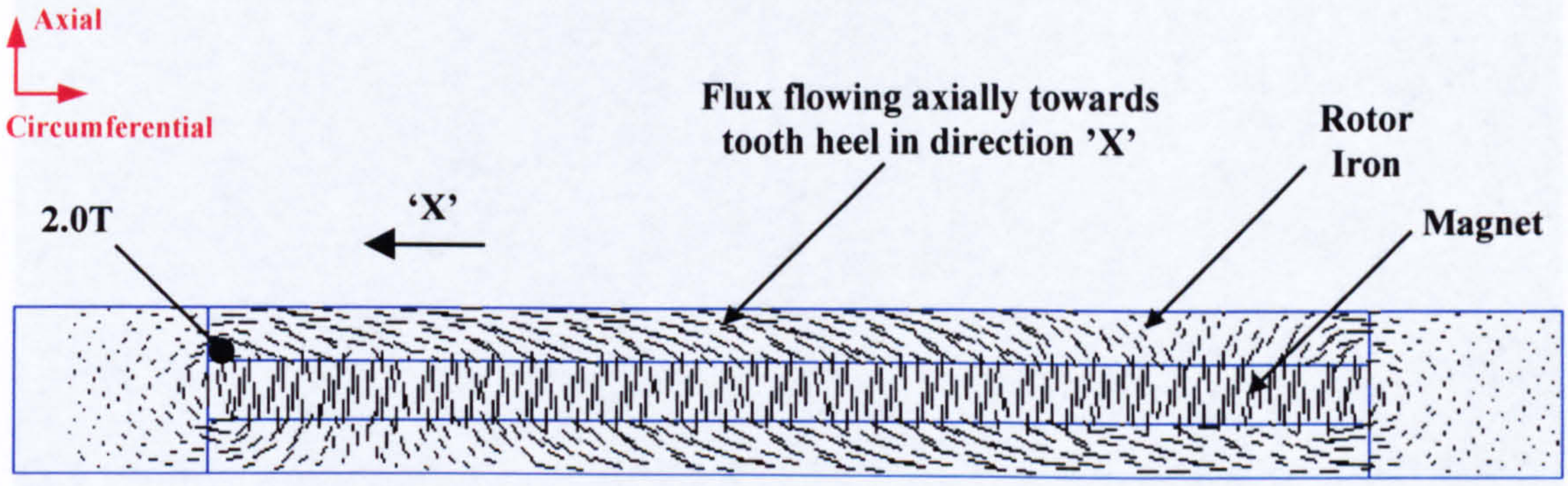

Figure 5.24 Axial/circumferential no load flux plot within the rotor of the CPTFM. The slice is taken along the A–A plane of figures 5.22 & 5.23

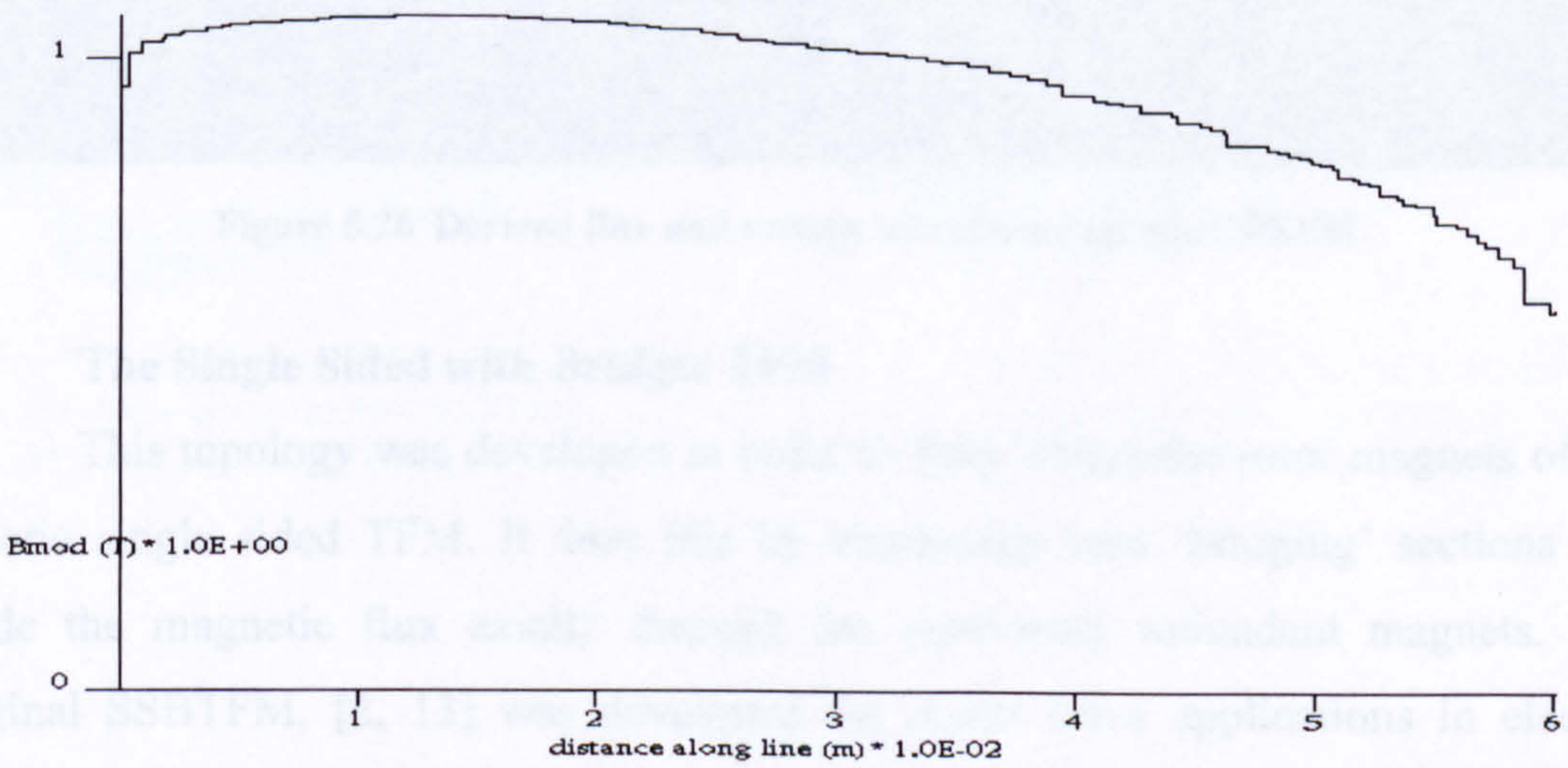

Figure 5.25 Axial flux density distribution in the airgap of the CPTFM, plot is taken radially above the centre line of the tooth (B_{max} = 1.07T, B_{min} = 0.6T & B_{ave} = 0.96T)

5.7.4 CPTFM Power Factor

Derived waveforms of voltage and flux linkage from the rated sinusoidal current are presented in figure 5.26. Note in this machine, the voltage was far from sinusoidal. The chart shows a lagging phase angle of 80° between the voltage and current, equivalent to a power factor of 0.174, this agreed with the calculated value based on mean power, rms voltage and current.

$$pf = \frac{mean\ Power}{(rms\ Voltage \times rms\ Current)} = \frac{3435.3}{(820.8 \times 23.4)} = 0.179$$

The CPTFM power factor was 53% less than that of the DSTFM. This was a result of the high armature reaction fields inherent in the model, due to the large interpolar leakage fields.

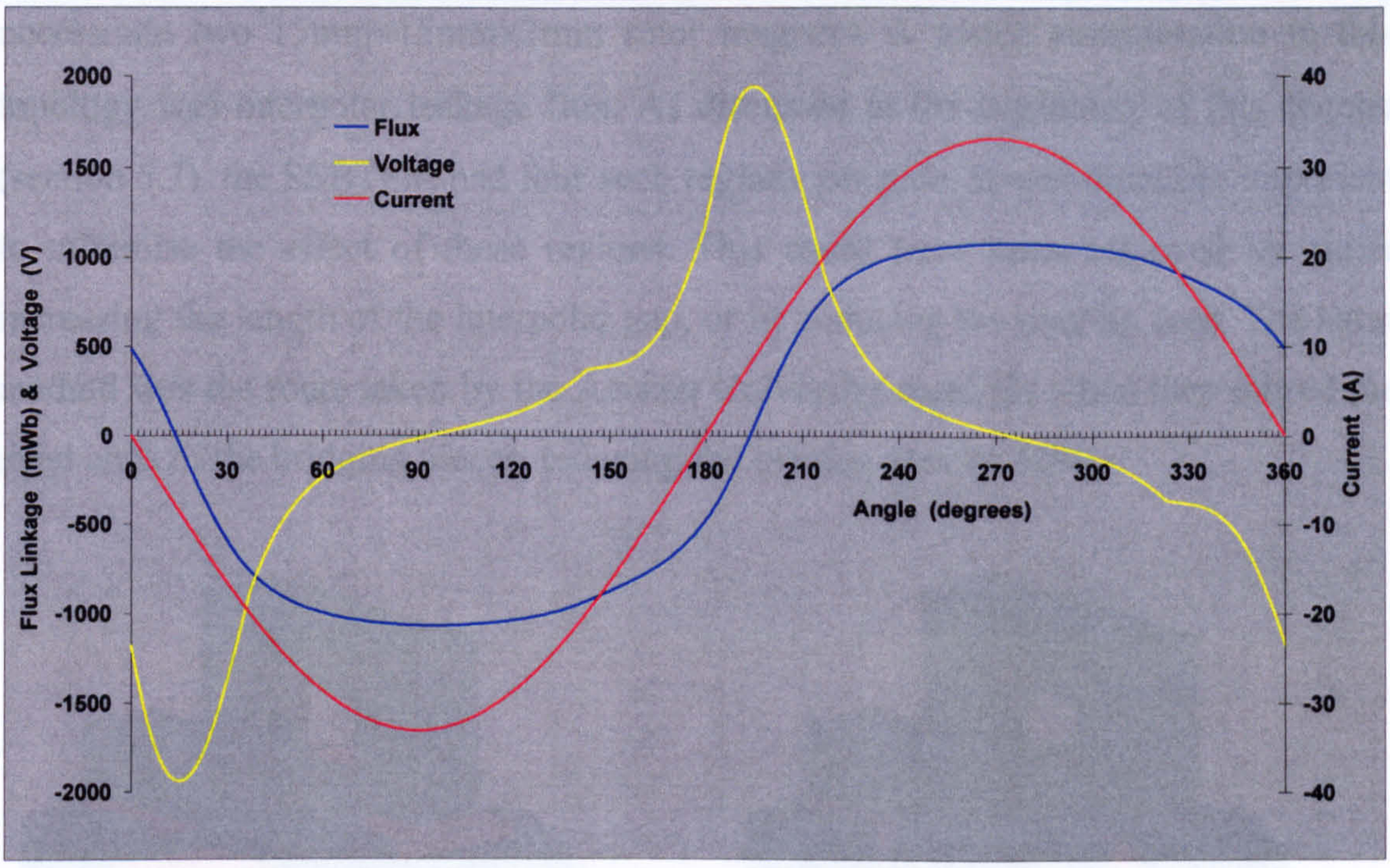

Figure 5.26 Derived flux and voltage waveforms for the CPTFM

5.8 The Single Sided with Bridges TFM

This topology was developed in order to fully utilise the rotor magnets of the generic single sided TFM. It does this by employing iron 'bridging' sections that guide the magnetic flux axially through the previously redundant magnets. The original SSBTFM, [2, 13] was developed for direct drive applications in electric vehicles and a considerable amount of optimisation was carried out with this application in mind. The original 80 pole machine was magnetically driven by two rows of surface mounted magnets. The information gathered so far in this thesis points to a flux concentrating configuration producing a higher output in the working thermal range of the machine (Chapter 4 section 4.7 and Chapter 5 section 5.7.2). Therefore, the 3D FE model produced for this evaluation incorporated a flux concentrating rotor.

5.8.1 Dimensioning the SSBTFM

As with the previous topology under scrutiny, this model comprised a solid coreback and the same upper stator dimensions as the DSTFM. Using a flux concentrating rotor halved the number of magnets required per pole. This is illustrated by the two representations of a basic SSBTFM configuration in figures 5.27 and 5.28. Maintaining an equal magnet volume with the previous models would therefore

necessitate two 15mm×15mm×3mm rotor magnets. A major consideration in this topology was interpolar leakage flux. As discussed at the beginning of this chapter (section 5.3), the SSBTFM had four such regions per pole. It was therefore important to minimise the effect of these regions. This could have been achieved by either increasing the length of the interpolar gap, or by reducing the overlap area. The latter method was the route taken by the Aachen University team [2] when they mitred the axial ends of the bridging pieces, reducing the overlap area by 50%.

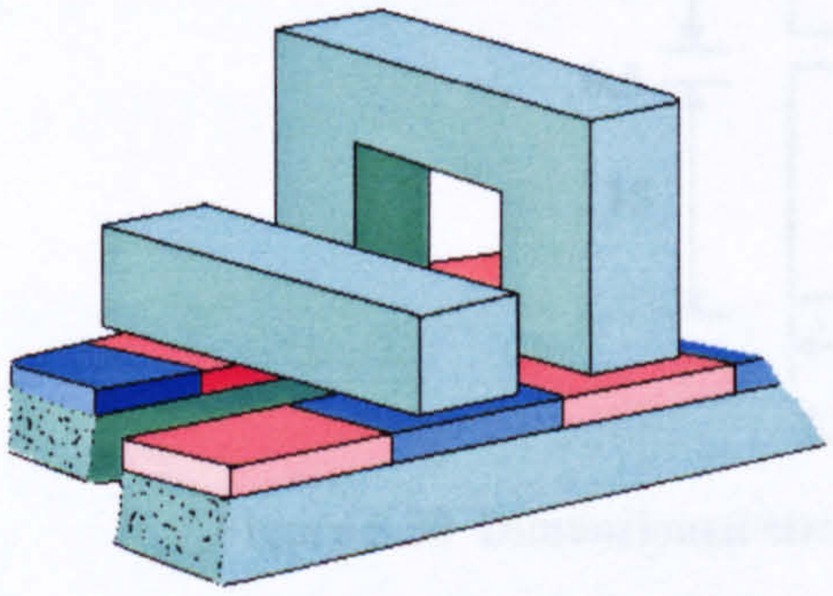

Figure 5.27 Rectilinear schematic of a basic single pole, surface mounted magnet SSBTFM topology

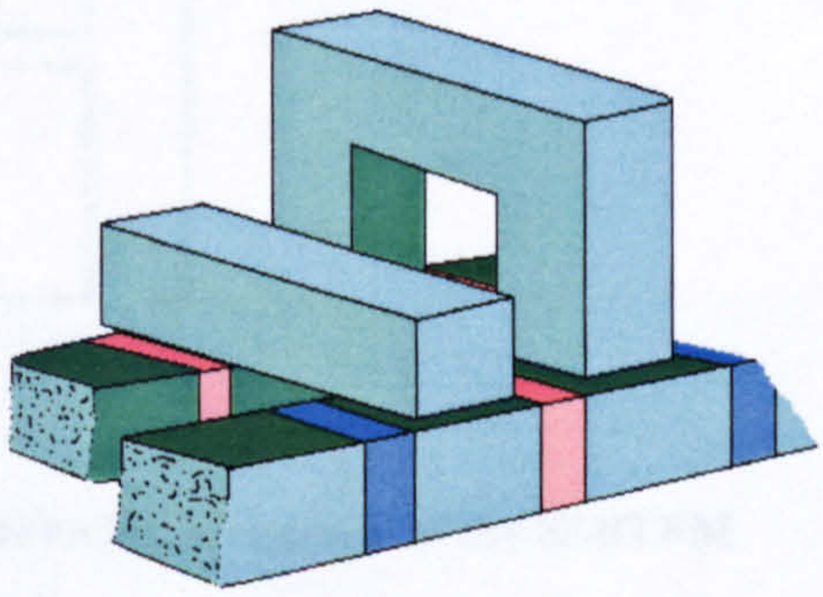

Figure 5.28 Rectilinear schematic of a basic single pole, flux concentrating magnet SSBTFM topology

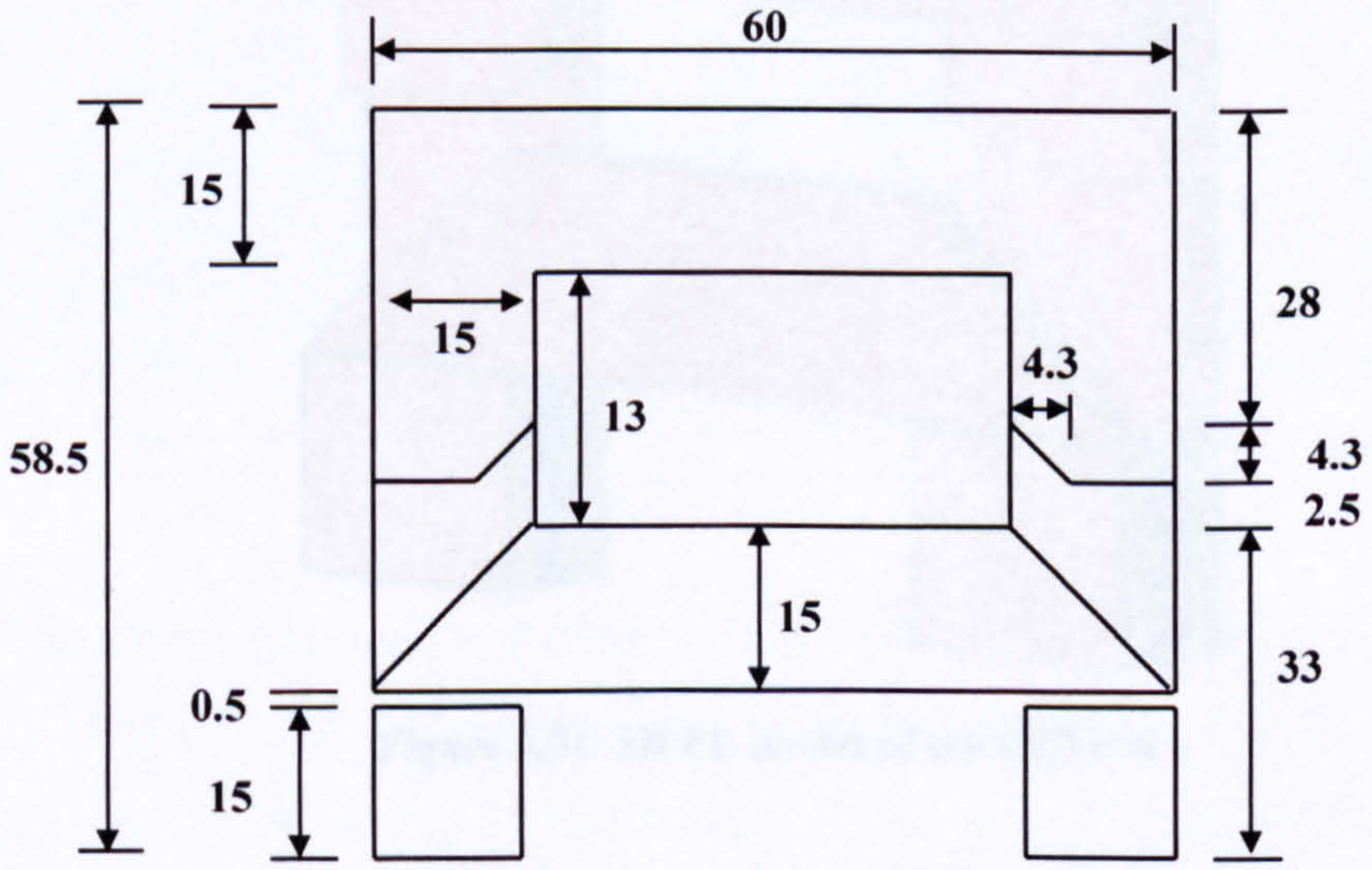

Figure 5.29 Dimensioned axial/radial schematic of the SSBTFM

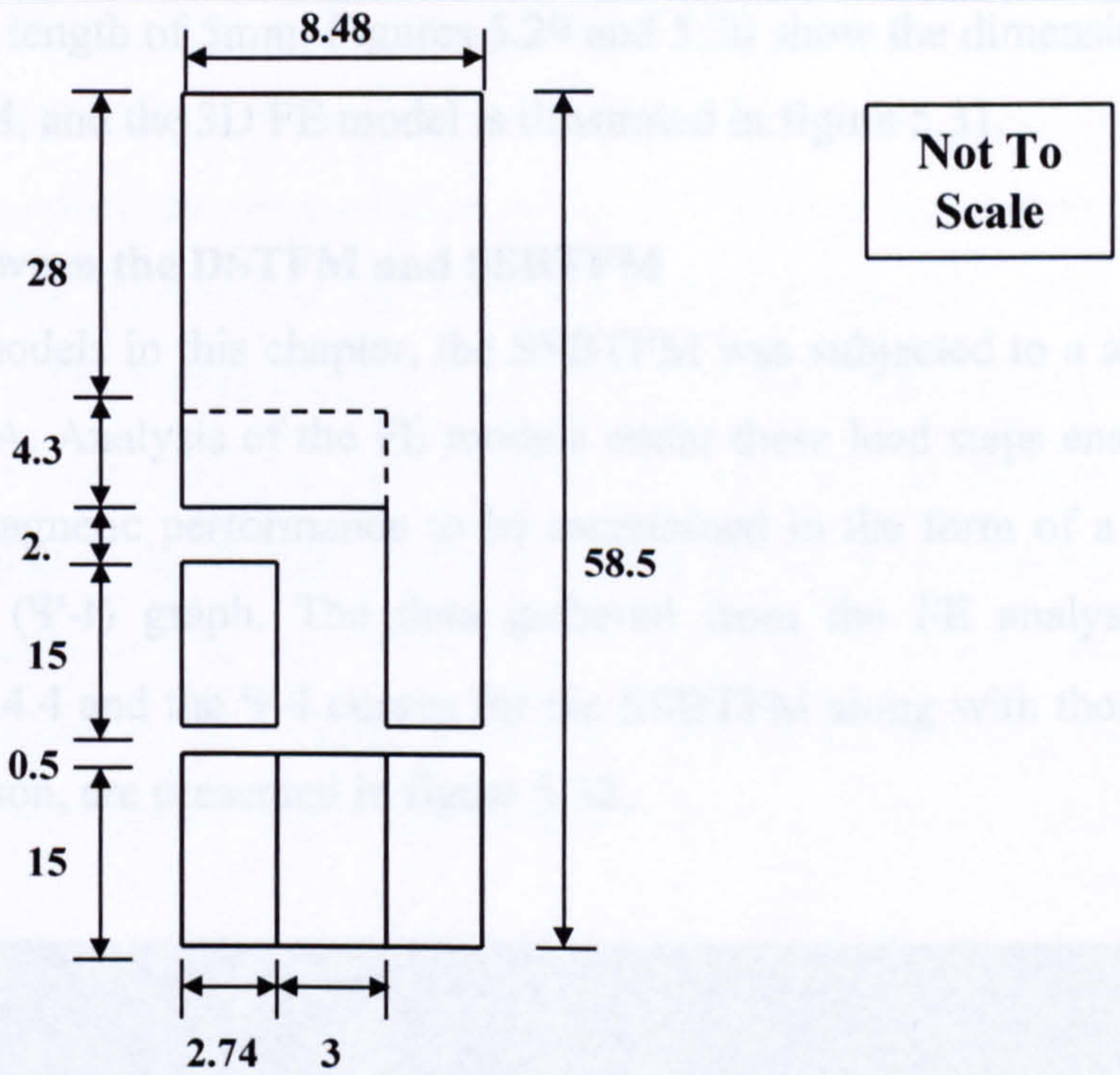

Figure 5.30 Dimensioned circumferential/radial schematic of the SSBTFM

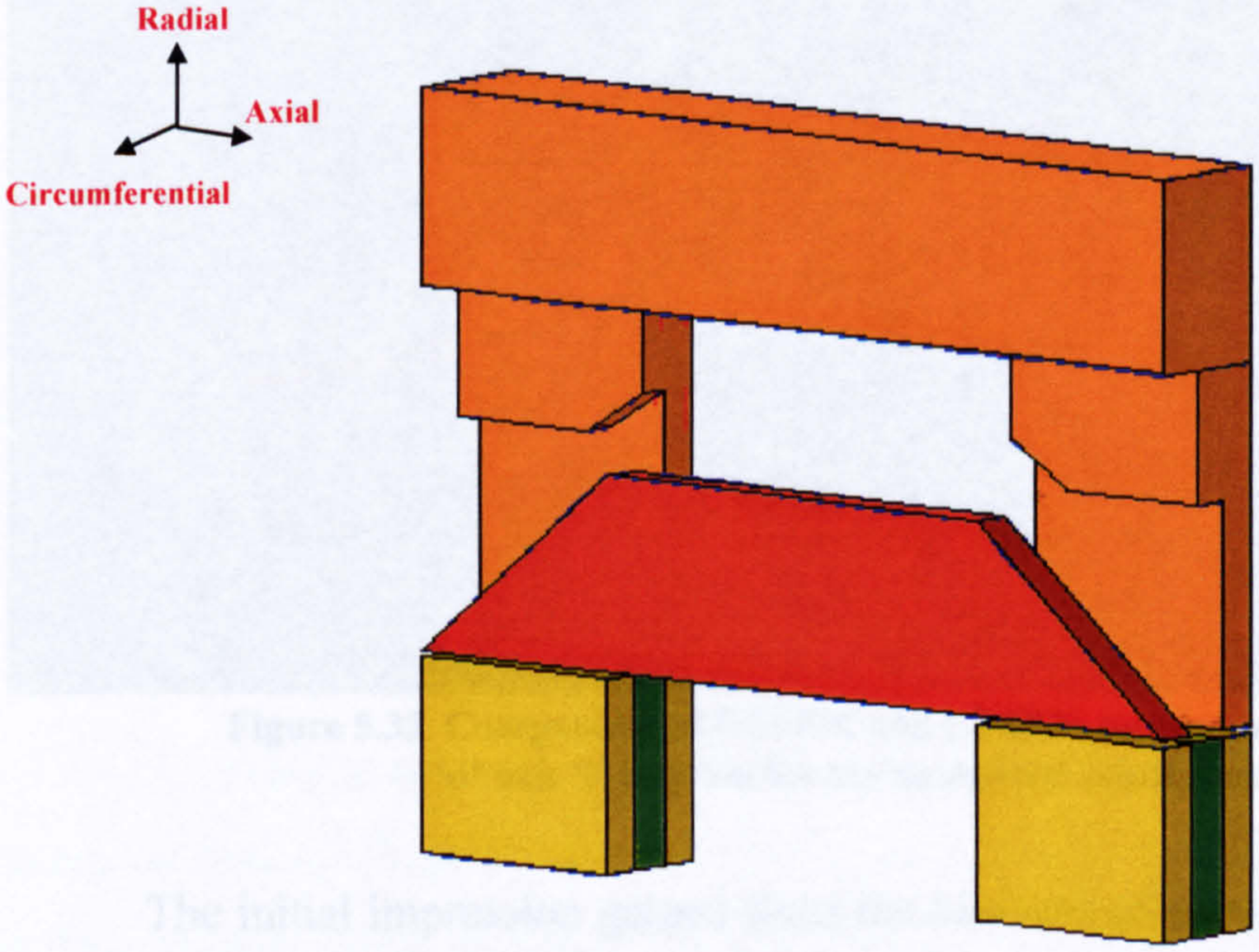

Figure 5.31 3D FE model of the CPTFM

The pole pitch and axial dimensions used were the same as those of the CPTFM and DSTFM. However, to reduce the 'C' core tooth reluctance, the radial height of the model was lowered by 2.5mm. This brought the solid 'body' of the 'C' core closer to the bridging iron. To minimise radial interpolar leakage paths between these two stator sections, the vertical section of the 'C' core was chamfered to ensure

a minimum leakage path length of 5mm. Figures 5.29 and 5.30 show the dimensioned diagrams of the SSBTFM, and the 3D FE model is illustrated in figure 5.31.

5.8.2 Comparison between the DSTFM and SSBTFM

As with all the models in this chapter, the SSBTFM was subjected to a series of currents between ±60A. Analysis of the FE models under these load steps enabled the SSBTFM's electromagnetic performance to be ascertained in the form of a flux linkage against current (Ψ-I) graph. The data gathered from the FE analysis is presented in appendix E.4.4 and the Ψ-I curves for the SSBTFM along with those of the DSTFM for comparison, are presented in figure 5.32.

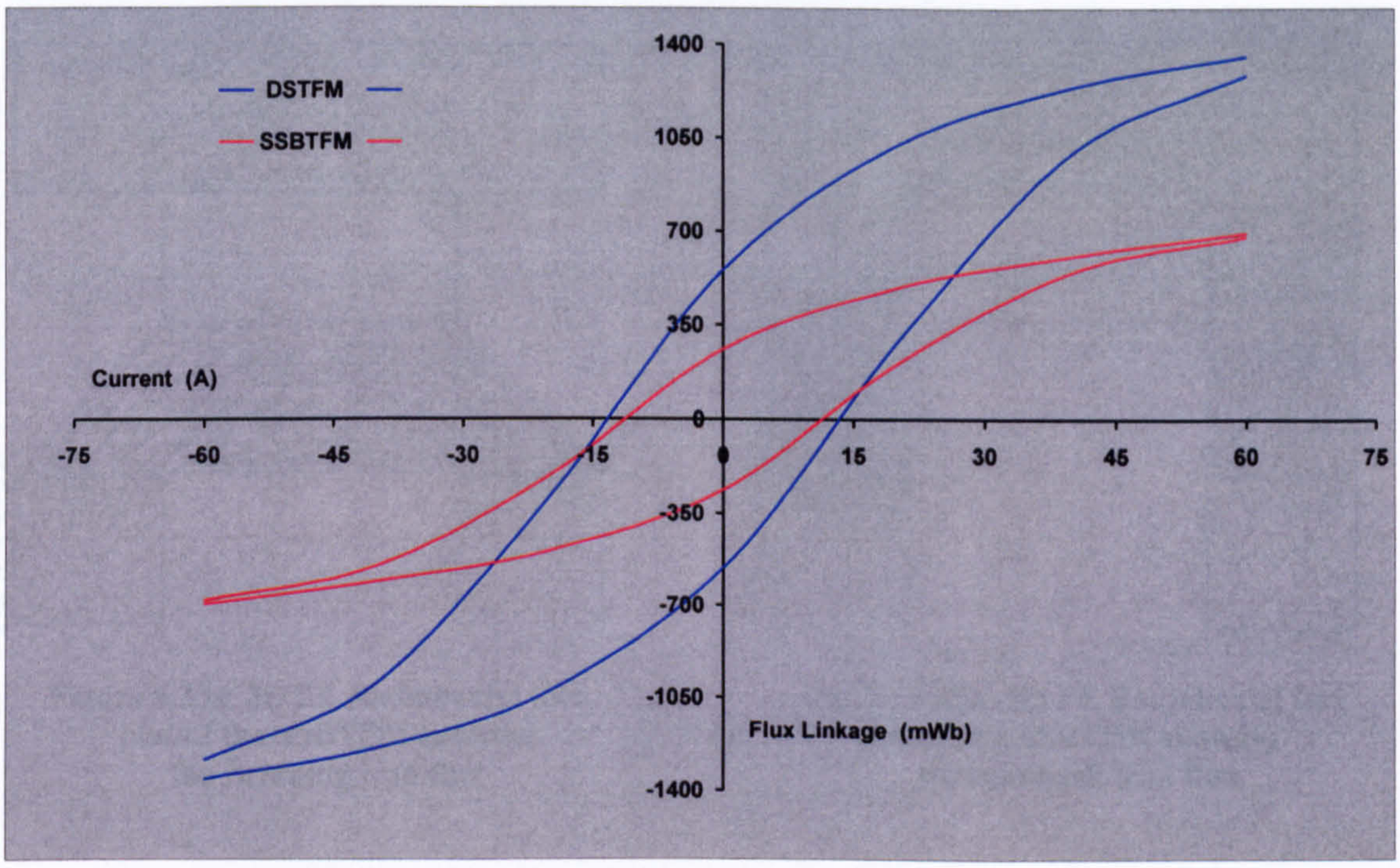

Figure 5.32 Comparison of DSTFM and CPTFM positive and negative 'd' axis Ψ-I curves for the same load conditions

The initial impression gained from the two sets of curves was the larger area of the DSTFM envelope. The overall area encompassed by the SSBTFM curves was equivalent to 24.38 Joules, 61% smaller than that of the DSTFM. As stated previously, the working thermally limited current for the DSTFM was 23.4A. Using this value to determine the working range of the SSBTFM gave a value of 17.6 Joules as opposed to 41.12 Joules for the DSTFM, a reduction of 57%. What caused this marked difference in output considering the similarity in magnetic and electrical parameters?

Firstly, there were four airgaps per pole instead of two, increasing the overall airgap reluctance by a factor of eight. However, the main reduction was caused by this configuration having only half the magnet area per pole. Another loss of flux was associated with the leakage flux around the flux concentrating magnets. With two 15mm × 15mm magnets the area available for fringing flux to travel through was 25% larger than in the single 15mm × 30mm DSTFM magnet. This reduced the operating point of the magnets, making the leakage paths more attractive. Figures 5.33a and 5.33b illustrate the flux paths around the rotor at each extreme of a pole pitch and the flow of flux through each side of the model. In figure 5.33b, it is interesting to note the reduction in flux density as the stator leg widens half way (17.5mm) along its length.

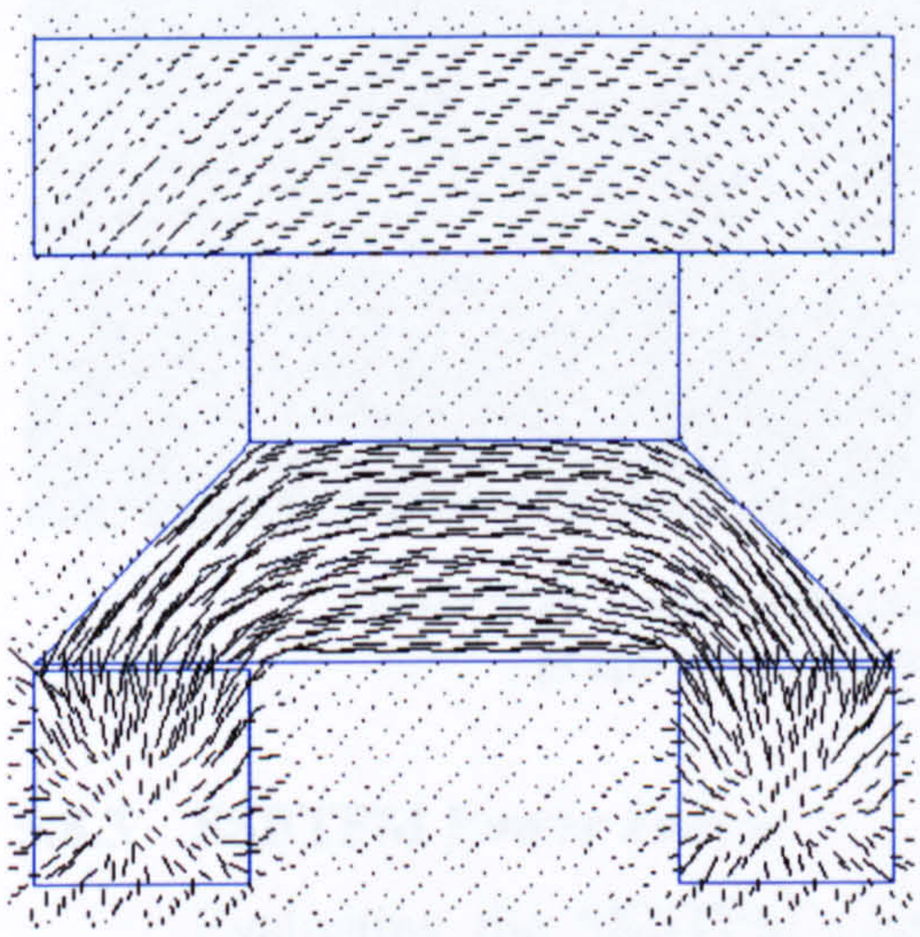

Figure 5.33a 3D FE Radial/axial flux plot of the SSBTFM showing the Bridging iron flux

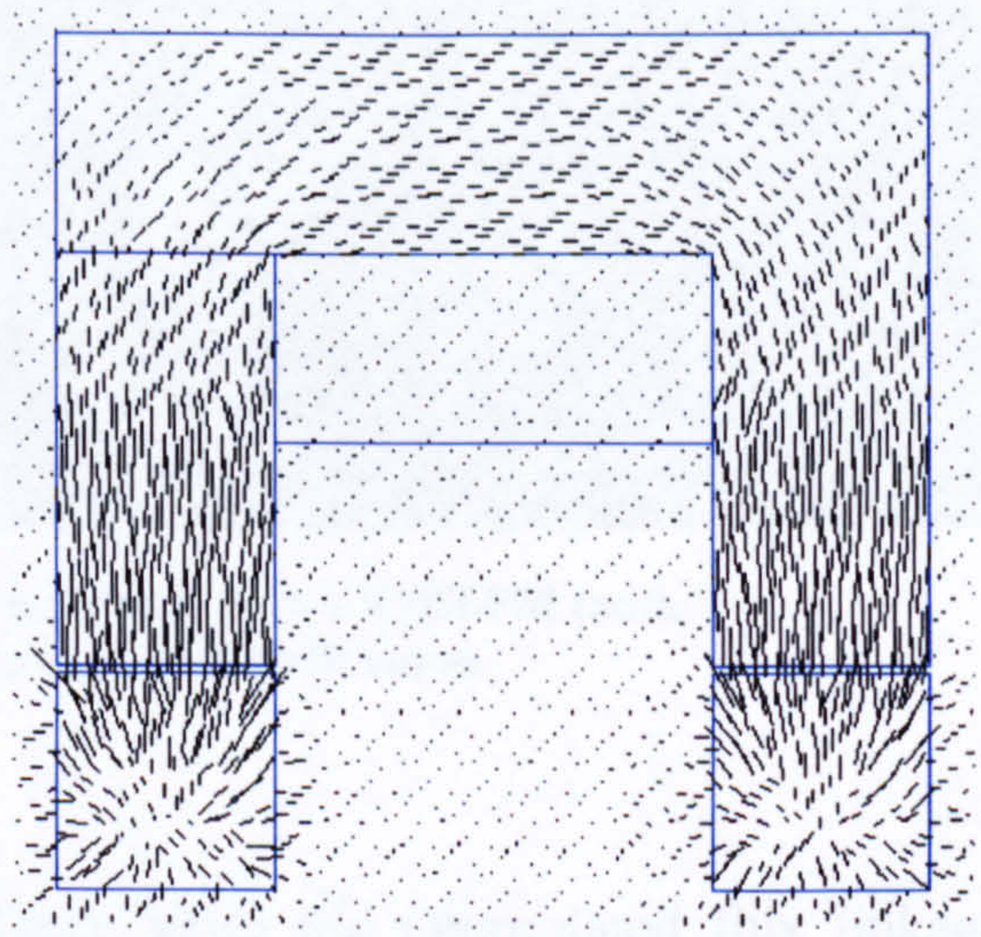

Figure 5.33b 3D FE Radial/axial flux plot of the SSBTFM showing the coreback iron flux

As stated at the beginning of section 5.8.1, the SSBTFM had a propensity for interpolar leakage. Figure 5.34 plots the variation of flux in one stator 'C' core leg as it rises radially from the airgap to the coreback. As expected there was an initial reduction (12%) in flux due to the rotor magnet fringing fields, which were active up to a radial height of approximately 3.5mm. This was followed by a steady decline as flux was passed circumferentially into the adjacent bridging iron. The overlap area was terminated at a distance of 15mm, which is apparent from the graph as the curve levels out. The overall percentage reduction in flux from the airgap to the end of the interpolar region was 28.7%. The CPTFM interpolar leakage accounted for 49.2% (section 5.7.3) of the flux entering a tooth, so this was a marked improvement on that

value (42% less), considering the difference in interpolar areas was only 26%. This apparent reduction in the effect of the flux loss mechanism could be attributed to the flux reduction in the two iron sections and hence the magnetic potential between them.

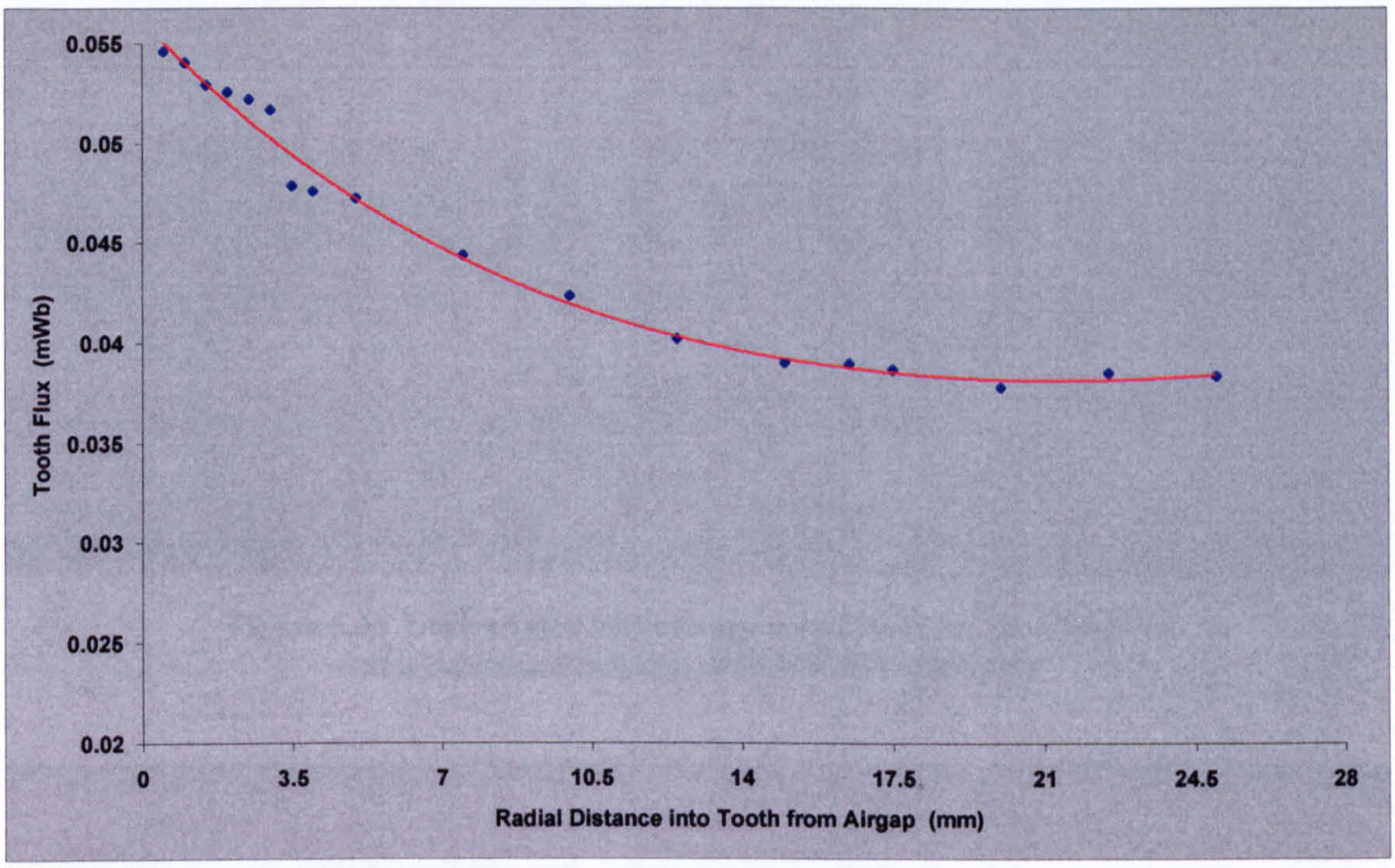

Figure 5.34 Radial distribution of no load flux in a SSBTFM tooth graph shows measured points and best fit curve

5.8.3 SSBTFM Power Factor

Evaluating the SSBTFM's power factor from the interpolated flux linkage waveform, (figure 5.35) revealed a lagging power factor of 0.309, determined from a phase angle of 72°. This agreed with the calculated figure:

$$pf = \frac{mean\ Power}{(rms\ Voltage \times rms\ Current)} = \frac{3606}{(7.42 \times 1591)} = 0.305$$

5.9 Comparisons and Conclusions

The four topologies evaluated in this chapter exhibited very different characteristics with regard to their output, illustrated in figures 5.36 and 5.37. Figure 5.36 indicates the levels of thermally limited mean torque for each of the models. The DSTFM developed 40 to 60 percent more torque than the alternative topologies. However, this cannot be taken at face value and must be put in some common context.

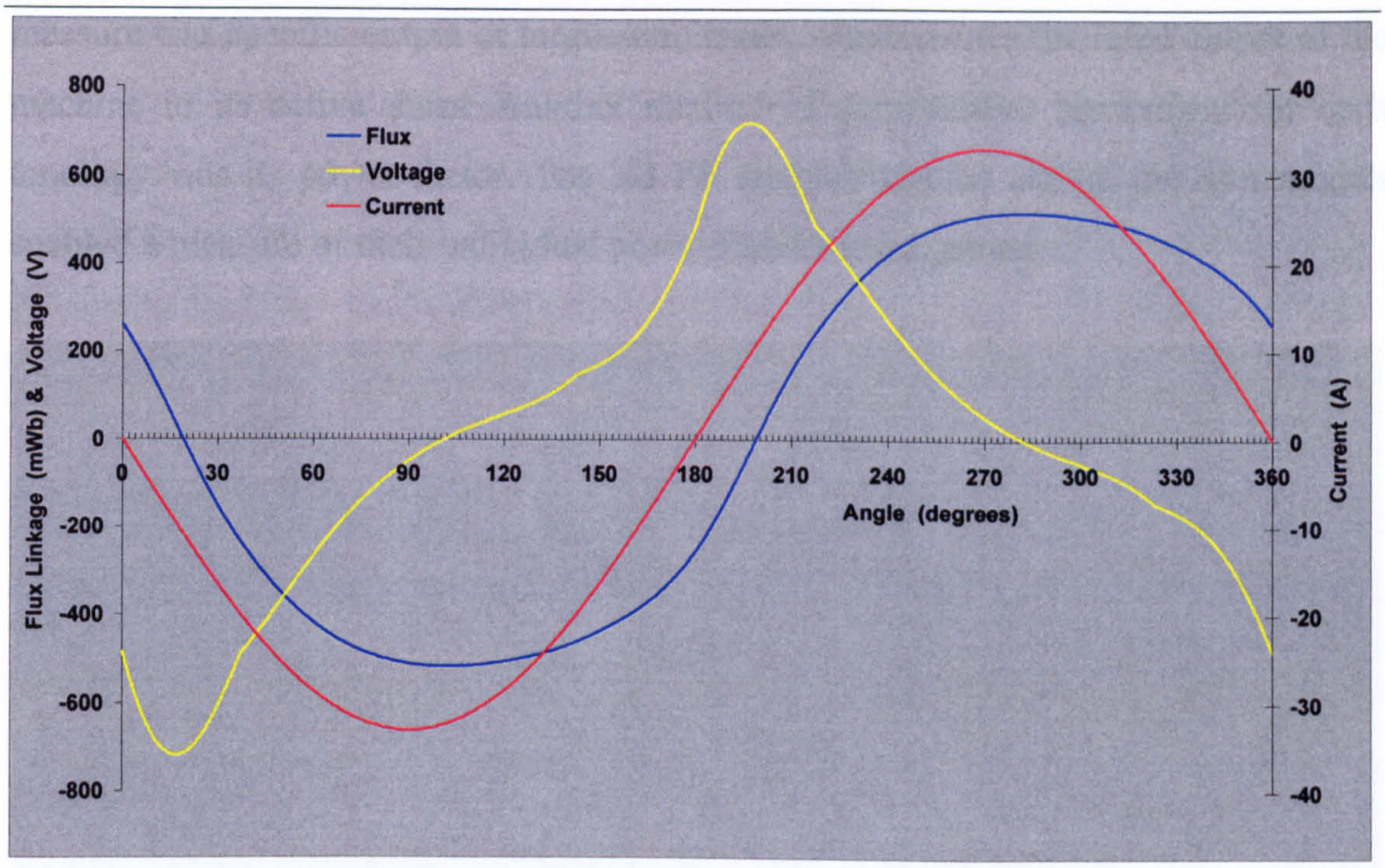

Figure 5.35 Derived flux and voltage waveforms for the SSBTFM at a rotational velocity of 10.47rads/s (100rpm)

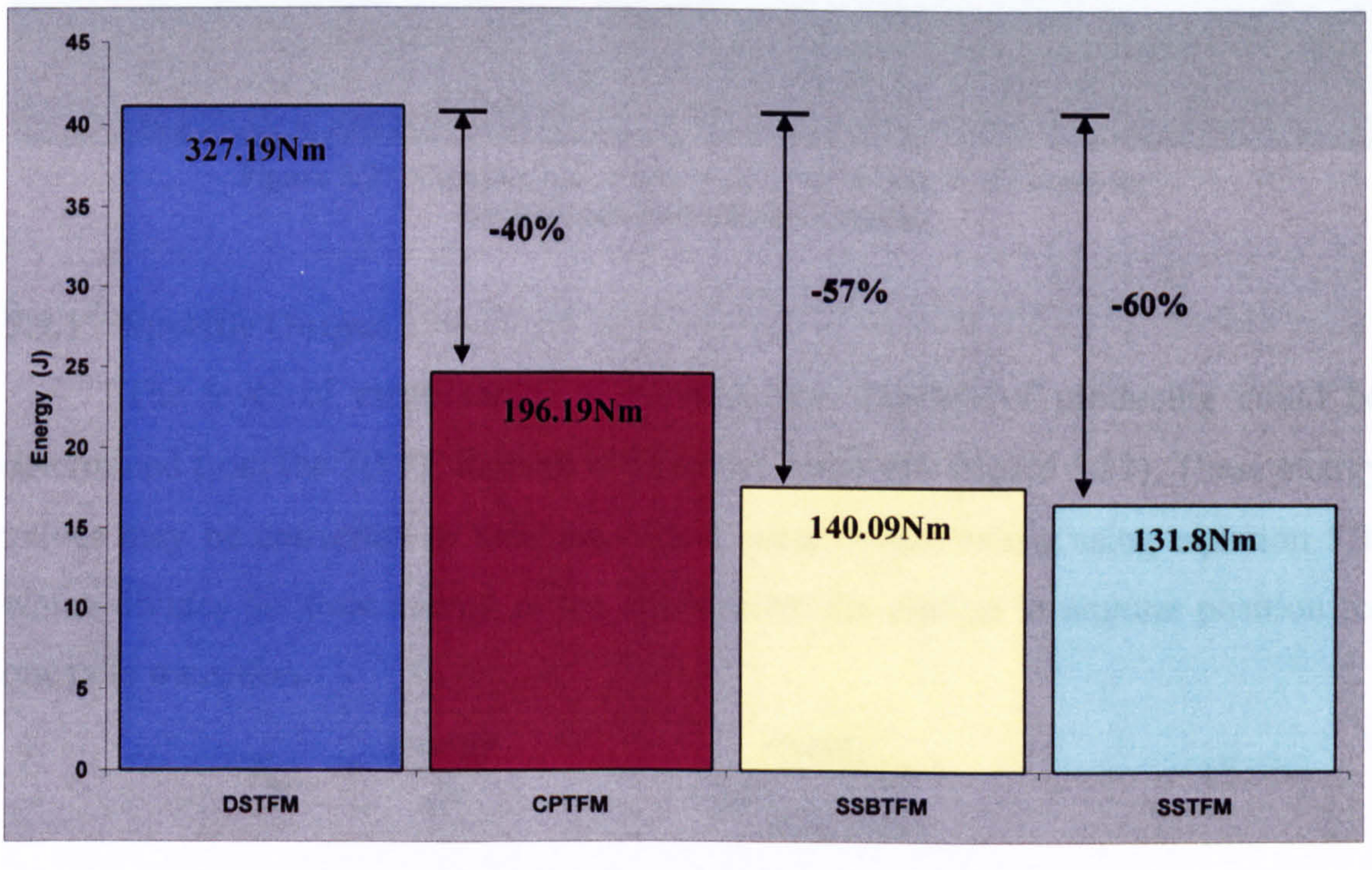

Figure 5.36 Comparison of the thermally limited Ψ-I mean torque for the four 100 pole topologies

The results already had points of reference such as, electric and magnetic loading, pole pitch, airgap length and maximum active envelope size. These benchmarks do allow some degree of qualitative and quantitative assessment, however a more fundamental measure of 'goodness' would be valuable. One such

measure was specific output or torque/unit mass, which relates the rated output of the machine to its active mass. Another method of comparative assessment for each topology was its power factor. The 3D FE analysis carried out on the four models enabled a measure of their individual power factors to be gained.

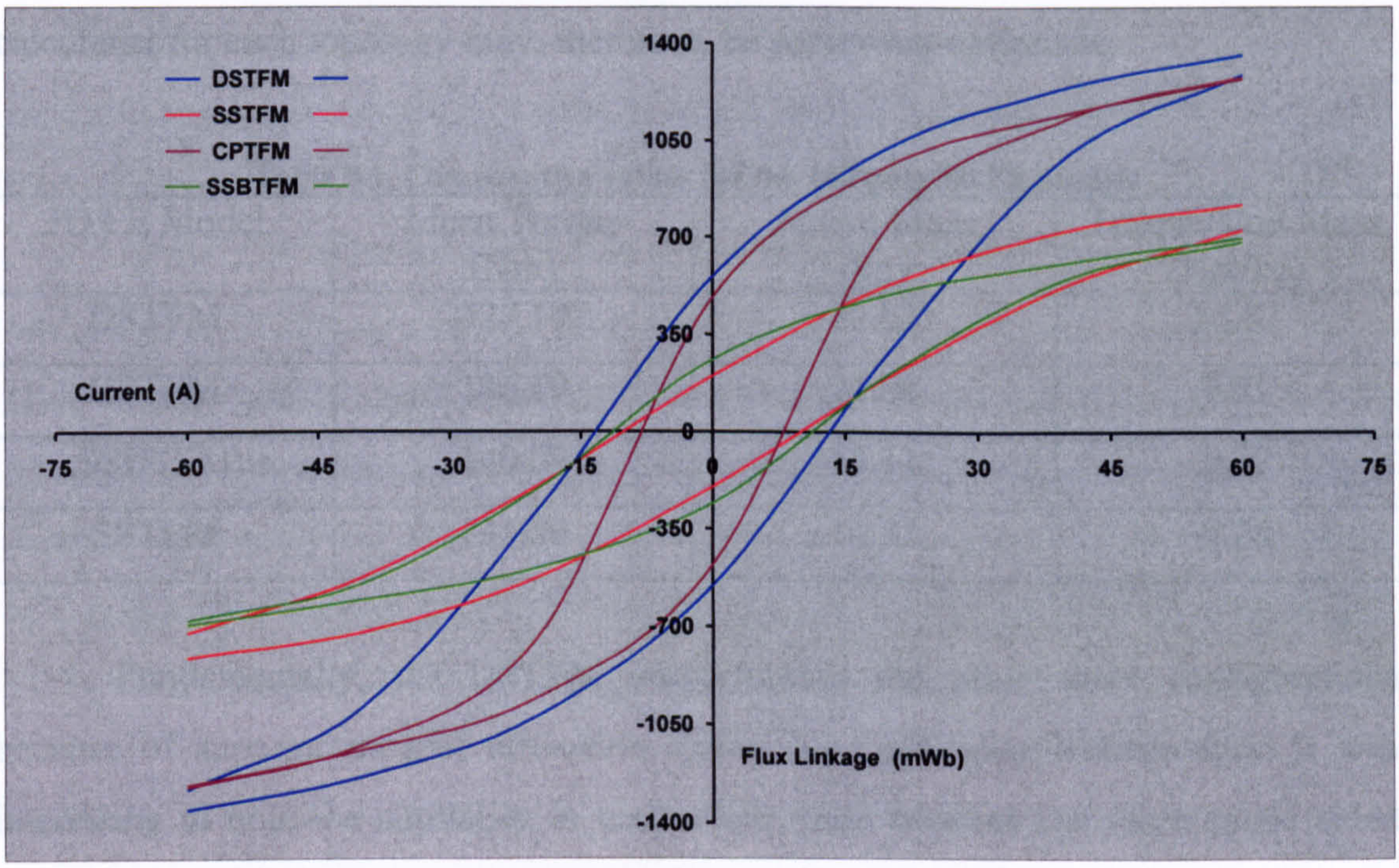

Figure 5.37 Comparison of the +ve & –ve 'd' axis Ψ-I curves for the four 100 pole TFM topologies

5.9.1 Specific Output

The level of mean torque a machine was capable of producing could be determined from the 3D FE derived Ψ-I energy envelopes (figure 5.37). These energy values may be converted to their equivalent mean torque rating using equation 5.3, which divides the total energy in the machine by the change in angular position for one pole transition.

$$T_{mean} = \frac{energy}{d\theta} = \frac{energy}{2\pi / Pole\ Pairs} \qquad \{5.3\}$$

Calculating the active mass of a particular model was slightly more time consuming. To ensure a 'level playing field,' the value of torque/unit mass determined for the DSTFM (14.41Nm/kg) in Chapter 3 was not used. Instead, the active mass for each of the models was calculated from their individual, single pole, rectilinear 3D FE model. These calculations are presented in Appendix D.7. The calculated values of mean torque, active mass and torque/unit mass are given in table 5.1. The calculated

mean torque value of the DSTFM had already been compared favourably with its measured value (Chapter 3, Section 3.10.2). However, the active mass of the DSTFM was actually 2kg greater than the value quoted in table 5.1. This was not of undue concern as the figures presented were for relative comparison and were not intended as absolute values. It should be pointed out however, that the torque/unit mass calculated for each topology may, therefore, be somewhat optimistic.

Table 5.1 Comparative values for the 100 pole 3D FE models

3D FE Model	Mean Torque (Nm)	Active Mass (kg)	Torque/Unit Mass (Nm/kg)
DSTFM	327.19	20.62	15.87
CPTFM	196.19	21.08	9.31
SSBTFM	140.09	15.11	9.27
SSTFM	131.80	14.21	9.28

Fundamentally, the DSTFM outperformed the other three configurations because of superior magnet utilisation and/or low interpolar leakage flux. It was interesting to note the similarity in torque/unit mass between the three single sided TFM topologies. This was despite a mean output range differing by 33%. The fact that the torque/unit mass values were of the same order points to the similarities of the four machines as well as their differences.

5.9.2 Power Factor

All four machines exhibit poor power factor at the thermally rated current loading, as follows:

- CPTFM = 0.179
- SSTFM = 0.294
- SSBTFM = 0.305
- DSTFM = 0.374

The CPTFM had the poorest power factor due to a high armature reaction field, perpetuated by large interpolar leakage paths within the model. The SSTFM and SSBTFM had similar values, but for different reasons. In the case of the SSTFM, surface mounted magnets, with no flux concentration and large leakage fields, led to a low magnet produced field flux. However, the armature produced field remained

large, giving a low power factor. The interpolar regions in the SSBTFM model provided an easy short-circuit path for the armature flux allowing it to bypass the rotor and its magnets, leading to a high armature reaction and poor power factor. The DSTFM had a 22.5% higher power factor than its closest competitor, due to non-existent interpolar paths and relatively good magnet utilisation, yet at 0.374 the power factor was still low.

5.9.3 Claw Pole TFM Conclusions

The CPTFM produced the highest output of the three single-sided models, but was hampered by a large active mass. Realistically, the mass of this model could be reduced by 2kg if the overall radial height of the teeth were reduced by 10mm (with alterations to associated components). This should improve specific output without affecting output unduly. The problem of interpolar leakage flux was harder to rectify, as it was a fundamental aspect of this topology. The only method of stemming its effect would be to increase the reluctance of the leakage path. The two routes to achieving this goal were either to decrease the overlap area or to increase the path length. Reducing the overlap area would generally involve reducing the size of the stator teeth. This could have two detrimental outcomes. Firstly, a reduction in the volume of iron could cause increased saturation effects. Secondly, a reduction in the surface area of the teeth in the airgap could limit the amount of flux entering the teeth and eventually link with the conductors in the stator. In order to increase the leakage path length, one of two eventualities needed to occur. The pole pitch of the machine had to be increased by either reducing the number of poles whilst maintaining the machine's outside diameter, or by maintaining the number of poles and increasing the outside diameter. Whichever route was taken the fundamental parameters of the machine would be compromised in order to increase output.

5.9.4 Single-Sided with Bridges TFM Conclusions

This topology was developed as an improvement on the SSTFM: it succeeded in some aspects but not in others. Utilisation of the magnet, which was left redundant in the original single-sided TFM, should have theoretically doubled the SSBTFM's output; instead, there was only a 6% improvement. However, because the magnets had a similar magnetic circuit reluctance at all rotor positions, there was less likelihood of magnet heating due to induction effects within the magnet material. The

introduction of interpolar regions into the model undoubtedly reduced the machine's output. However, the mechanism with the most substantial impact was the high reluctance of the magnetic circuit compared to the other topologies. There are twice as many airgaps for the flux to flow across and far greater leakage paths, all reducing the performance of the machine.

5.9.5 Single-Sided TFM Conclusions

The simplicity of design in this model and its axially displaced teeth provided a robust machine with a low value of interpolar leakage and armature reaction. One effect of reduced armature reaction was an improvement in the harmonic complexity of the voltage waveform (figure 5.15) compared to the other three topologies. Its main shortcomings were in poor magnet utilisation and the thermal consequences of induced currents as the magnet cycled between its remanent and operating point. A large percentage of the flux produced by the magnet was 'spent' in the leakage fields around its periphery. This was particularly prevalent along the circumferential interface between adjacent magnets. Whilst this flux leakage effect may go someway to reducing the difference between the remanent and operating point, so reducing the risk of inductive losses, it also severely limited the level of flux passing around the stator and linking with the conductor. One method of rectifying this problem could be to reduce the pole arc of the magnets [8]. The resultant airgap would have little effect on the reluctance of the active flux path because of the almost unity value of the magnet permeability. However, it would increase the relative 'appeal' of the stator path as opposed to the leakage path.

5.9.6 General Conclusions

Analysis of the four topologies revealed three major design requirements for an improved TFM geometry.

- Low armature leakage fields
- Low rotor pole to pole leakage
- Single radial airgap

Armature leakage fields tend to propagate most readily through interpolar leakage paths Reducing the effect of these paths should reduce the armature leakage

and so improve both power factor and specific output. High magnet pole to pole leakage fields were particularly prevalent in the SSTFM. Utilising all of the magnets simultaneously and, in the case of surface mounted configurations, reducing the pole arc of each magnet, would limit this flux loss mechanism. A reduction in the viability of rotor pole to pole leakage paths would increase the flux travelling through the coreback and so increase specific output. In addition, a single-sided machine with one radially active airgap would be much easier to assemble than a machine with one or more axially active airgaps.

How else could specific output be improved? An interesting point to note was that the SSTFM only employed half of its magnets. However, if the SSTFM topology could use all of its magnet material simultaneously its theoretical output would double. This would increase its thermally limited mean torque from 131.8Nm (figure 5.36) to 263.6Nm; 19.5% lower than the DSTFM, but 25.6% higher than the CPTFM and 46.9% higher than the SSBTFM. If the same active mass of the original SSTFM were assumed, then the torque/unit mass of this theoretical model would also double to 18.5Nm/kg, a figure 15% greater than that of the DSTFM. Therefore, it would theoretically be possible for a single-sided TFM topology to produce a higher specific output than a double-sided one if certain design criteria could be met.

Chapter 6

The Claw Pole Hybrid Transverse Flux Machine

6.1 Introduction

Analysis outlined in Chapter 5 indicates a number of design characteristics for a successful TFM topology. There are three fundamental requirements.

- Low armature leakage fields
- Single radial airgap
- Low rotor pole to pole leakage

If these requirements could be met in a single TFM design, then that geometry would benefit from improved power factor, a relatively simple mechanical arrangement and a high specific output.

The preliminary designs for the Claw Pole Hybrid Transverse Flux Machine (CPHTFM) were formulated whilst the work presented in Chapter 5 was being carried out. The fundamental premise involved fusing a Single-Sided TFM (SSTFM) with a Claw Pole TFM (CPTFM). It was envisioned that the resultant 'hybrid' would be a flux concentrating machine, which utilised all available magnet material simultaneously without incorporating large interpolar leakage paths. This would provide a relatively 'good' power factor at rated levels of MMF, whilst producing a high specific output. Figure 6.1 shows the basic CPHTFM concept in the form of a rectilinear sketch. It comprises a flux concentrating rotor with circumferentially magnetised magnets and a radial airgap. Indexed claw stator teeth are positioned above the active airgap so that they are above alternately polarised rotor pole pieces. Teeth of the same pole are displaced from one another axially as well as circumferentially. The axial separation is designed to limit leakage flux travelling circumferentially between teeth of the same pole (interpolar leakage flux). The teeth are attached to a circumferentially continuous SMC (Soft Magnetic Composite) coreback, which in turn encompasses the toroidal conductor. The active flux, sourced

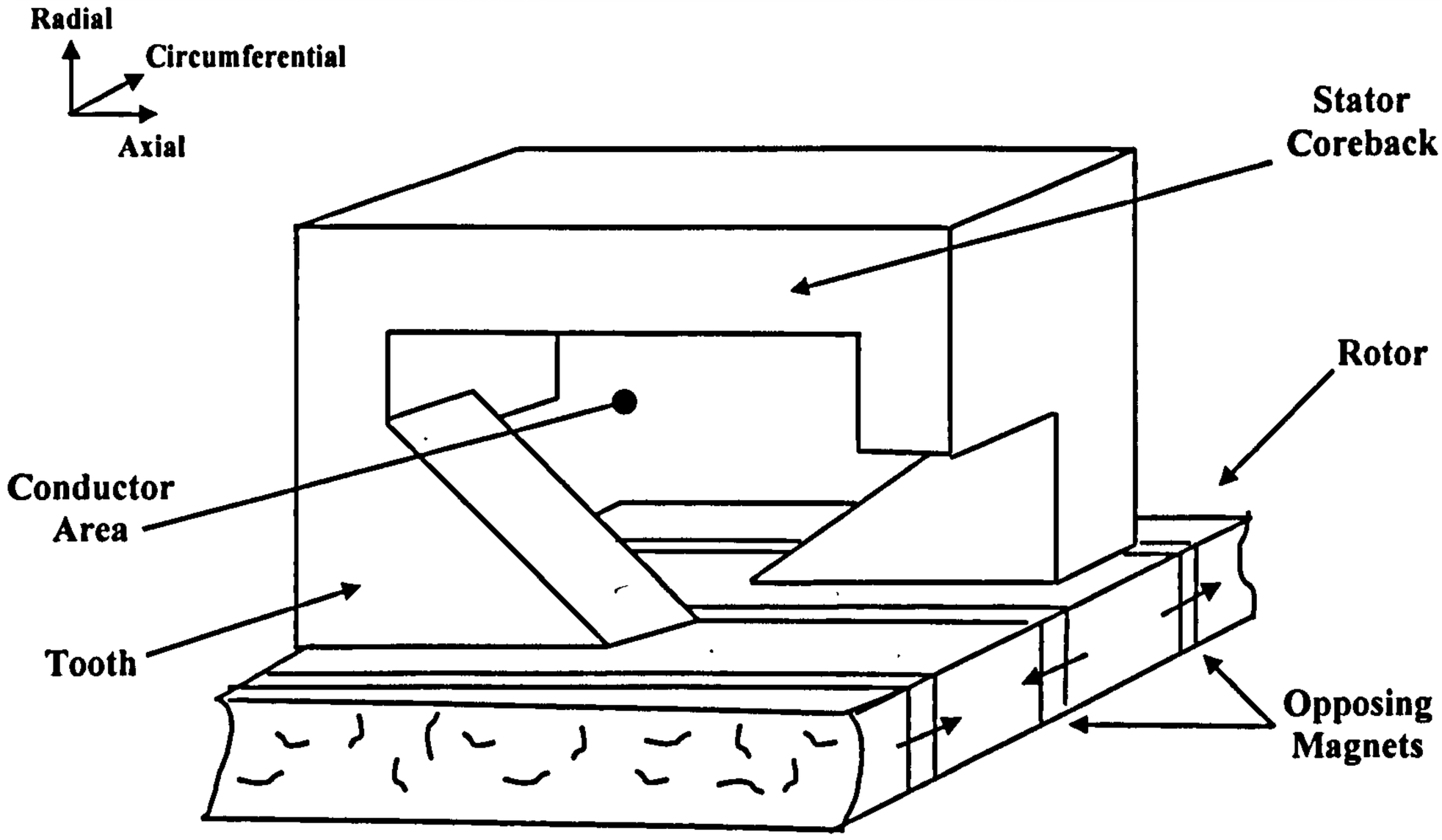

Figure 6.1 Rectilinear sketch of the proposed CPHTFM configuration

from the magnet, travels first circumferentially and then radially through the rotor iron, before radially crossing the airgap and entering a stator tooth; the flux flows radially up the tooth, turning to cross the coreback axially, then radially again down the opposing stator tooth, across the airgap and back into the rotor iron, and finally completing its path at the source magnet.

In this study 3D FE analysis was carried out exploring the new topology in order to produce a finalised prototype design. This design was then taken and constructed as a static, 100 pole machine. Thermal and static testing of the new machine enabled confirmation of the theoretical results as well as proving the validity of the initial design criteria.

6.2 Initial Development

An initial CPHTFM model was produced to explore the potential of the new topology. Basing the new machine's design parameters upon those of the original DSTFM produced at Newcastle University (Chapter 3), enabled a practical comparison between the two configurations. This led to the following design specification:

- 100 Poles
- Airgap length of 0.5mm
- Active magnet length of 3mm

- Magnet volume per pole of 1350mm^2
- $B_r = 1.2T$, $\mu_r = 1.19$
- Conductor area of 390 mm^2
- Stator tooth, 7mm (radial) 6.5mm (circumferential)
- Coreback width 15mm (radial/axial plane)
- Axial length of 60mm
- Rotor outside diameter of 270mm (≡ pole pitch = 8.48mm)
- Stator outside diameter of 362mm

With a design based upon the topology shown in figure 6.1, these parameters enabled the dimensions for the initial 3D FE model to be determined. Schematic diagrams of the model, along with exact dimensions, are reproduced in Appendix C.3.1. The results from this 'first draft' model are shown in figure 6.2 and Appendix E.3.1.

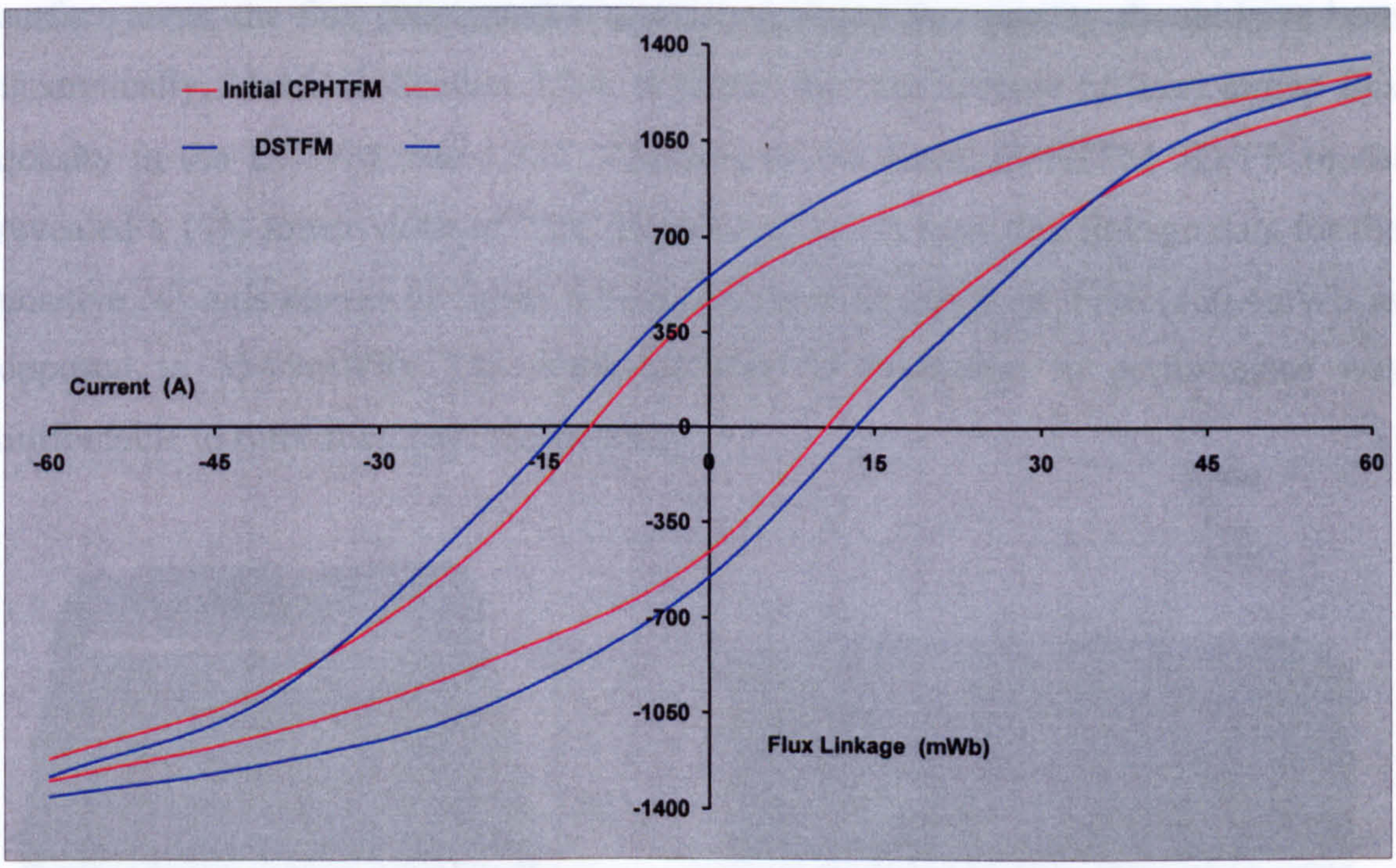

Figure 6.2 Positive and negative 'd' axis Ψ-I curves for the initial 15mm coreback CPHTFM, (based solely upon the DSTFM dimensions) compared with the DSTFM curves

The Ψ-I area bounded by the positive and negative 'd' axis curves for the new topology produced the equivalent of 239.1Nm of mean torque at the predetermined DSTFM thermal limit of 1591Ampereturns, (see Chapter 3, section 3.10). Although this figure was 27% lower than that of the DSTFM, (327.2Nm) it was a considerable

improvement on the three alternate topologies analysed in Chapter 5 (see section 5.9). This new hybrid model exhibited 22% more thermally limited output than the CPTFM, 70% more than the SSBTFM and 81% more than the SSTFM. With such promising results from this initial analysis, it was felt that further investigation was warranted.

6.3 Limiting Factors of the Initial Geometry

Before an improved CPHTFM model could be produced, the shortcomings as well as the benefits of this introductory topology had to be assessed. Examining the comparative curves of figure 6.2, revealed that the CPHTFM had a consistently lower value of flux linkage throughout the current range. Two possible causes for this were a fundamentally lower no load airgap flux density, and/or additional leakage fields inherent in the model.

As the DSTFM and the CPHTFM had identical magnet and stator tooth surface areas, the flux concentration and hence airgap flux density should have been theoretically, identical. Section 3.8.4, indicates that the average no load airgap flux density in the DSTFM was 1.33T. Analysis of the initial CPHTFM 3D FE model revealed a 17% lower value of 1.1T. Evaluating the no load flux linkage data for the positive 'd' axis curves of figure 6.2, also showed a deficit of 17% (460.4mWb as opposed to 554.9mWb). This indicated that the reduction in performance was attributable to rotor flux loss mechanisms.

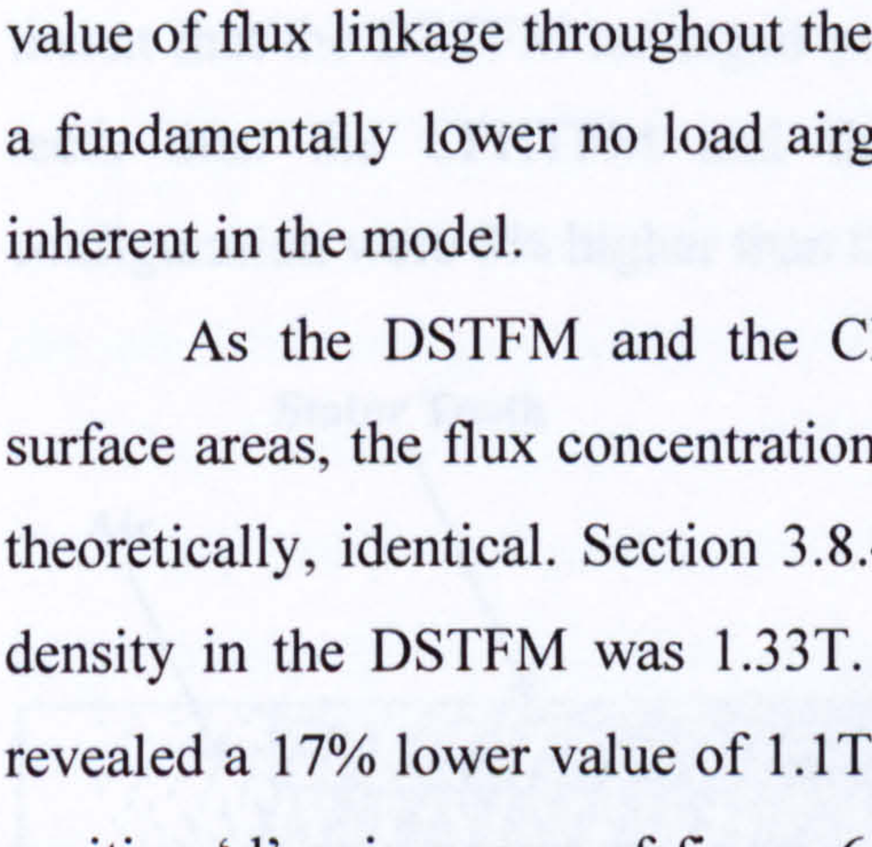

Figure 6.3a Axial/radial schematic of the DSTFM showing rotor dimensions

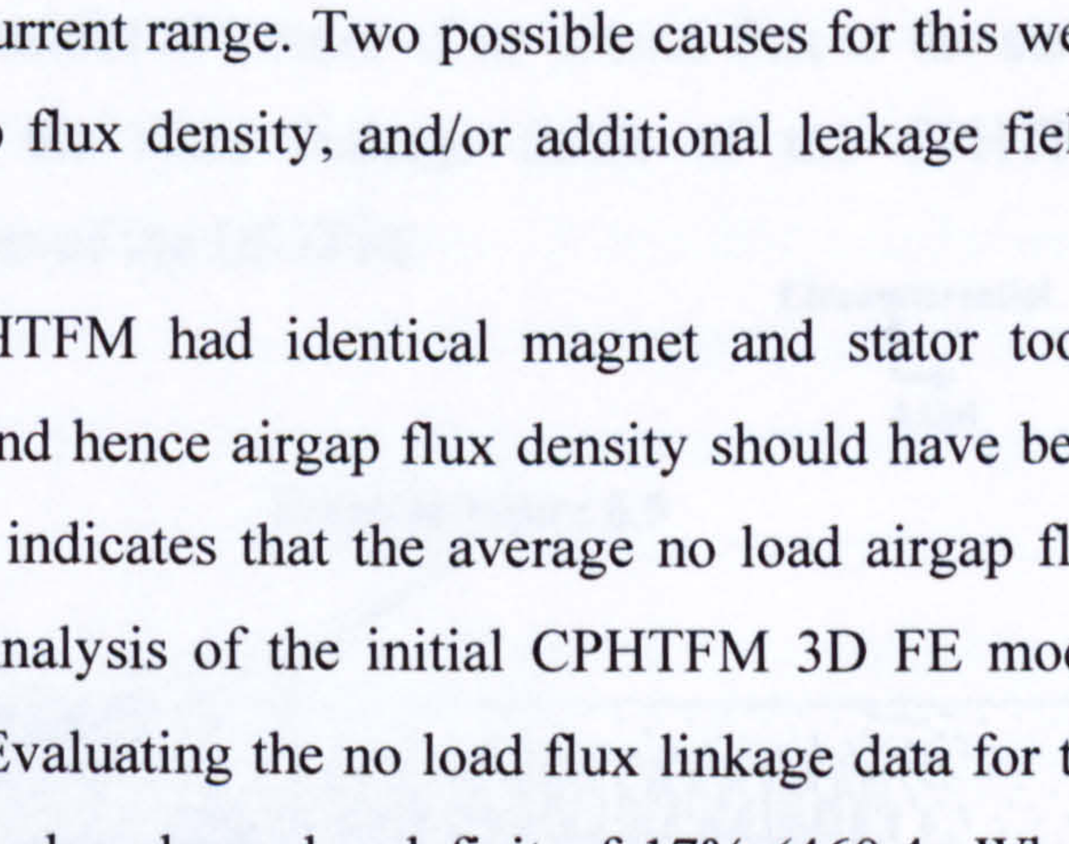

Figure 6.3b Axial/radial schematic of the CPHTFM showing rotor dimensions

The most likely cause of this discrepancy was the 33% increase in the peripheral length of the rotor (figures 6.3a and 6.3b) and the additional magnet

leakage fields that would have ensued. The rotor leakage paths with the lowest reluctance were those that travelled via the stator teeth, as both rotors had the same tooth coverage (60mm), the additional leakage paths in the CPHTFM must have propagated through higher reluctance air paths. Therefore, the effective increase in this leakage flux was not proportional to the overall increase in peripheral rotor length. Analysis of the single pole 3D FE model indicated that 0.29mWb of flux was produced by the source magnet. Further analysis showed that the average flux passing radially along each tooth was 0.095mWb, thus 67% of the magnet flux was not linking with the stator winding. The same analysis on the DSTFM revealed a source flux of 0.32mWb and an individual tooth flux of 0.12mWb (a reduction of 62%). This meant that the DSTFM managed to transfer 8% more of its source flux to the stator teeth than the CPHTFM and that the rotor leakage fields of the CPHTFM configuration were 8% higher than those of the DSTFM.

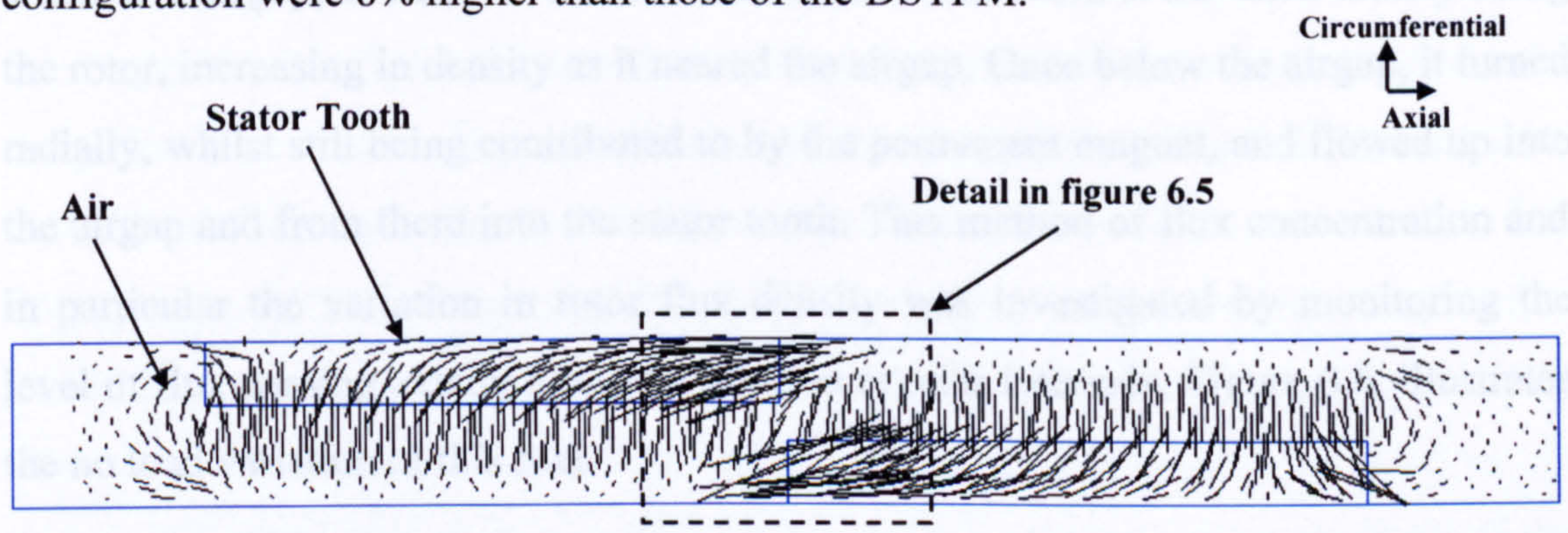

Figure 6.4 Axial/circumferential plot indicating interpolar and rotor leakage flux paths 0.5mm radially above the active airgap

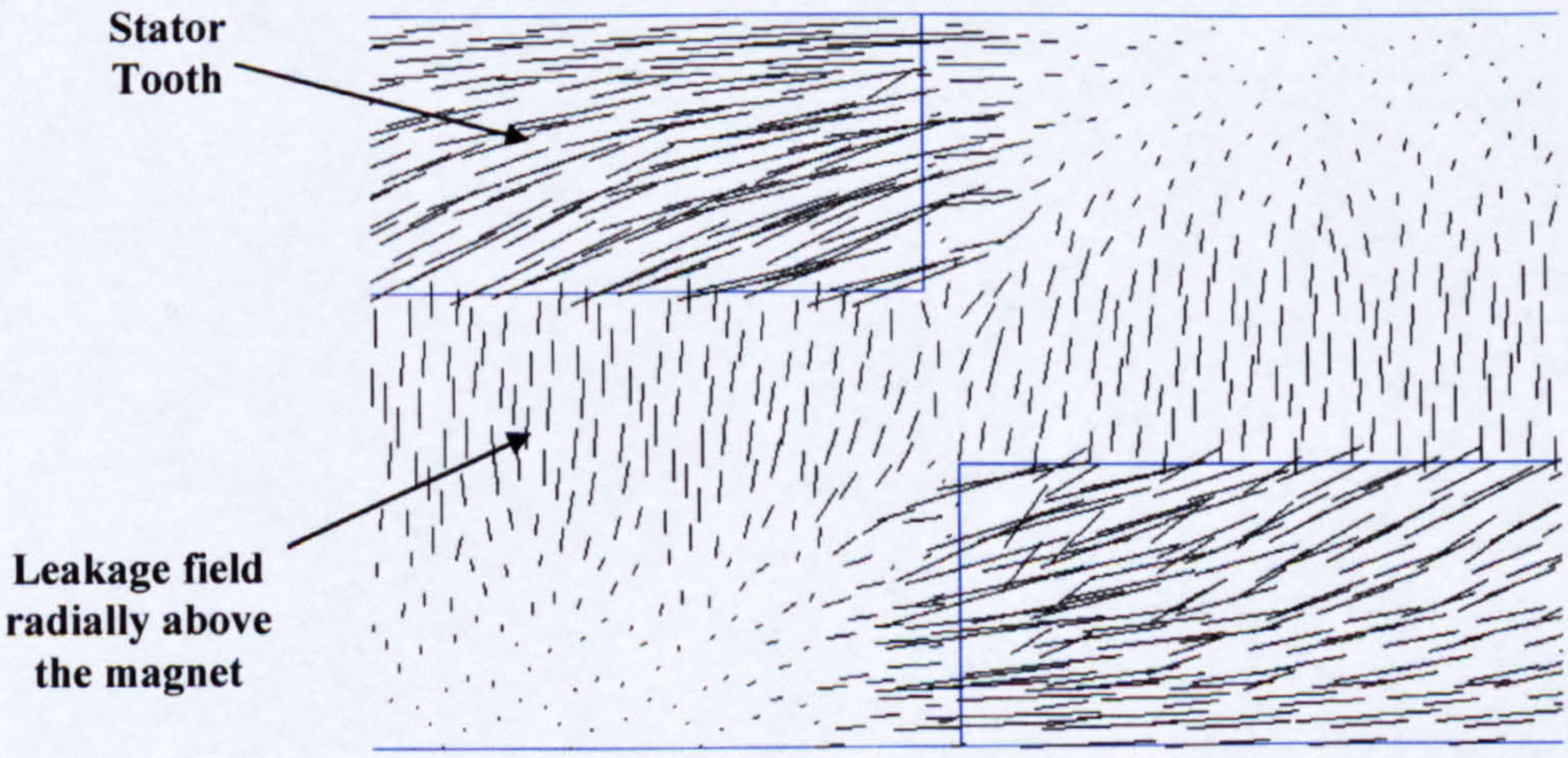

Figure 6.5 Detail of figure 6.4, showing the magnet leakage fields, both stator teeth and the flux passing between them

The CPHTFM tooth layout precluded virtually all interpolar flux leakage paths. Figures 6.4 and 6.5 are flux plots in the axial/circumferential plane, 0.5mm radially above the airgap in the stator teeth. Evident in both of these figures are the circumferential leakage fields which pass through the air radially above the magnet and the axial fringing flux as it enters the two stator teeth. Examining the interpolar region showed that the flux passing between the adjacent teeth was negligible.

6.4 Flux Concentrating Rotor

The mechanism of flux concentration in the CPHTFM was different to that of the DSTFM. In the DSTFM, apart from initial circumferential flux as it left or entered the magnet, the direction of flux movement was predominantly axial. This was not the case in the CPHTFM. The rotor flux started at a point farthest from the stator tooth and active airgap, at either of the two axial ends of the rotor. It travelled axially along the rotor, increasing in density as it neared the airgap. Once below the airgap, it turned radially, whilst still being contributed to by the permanent magnet, and flowed up into the airgap and from there into the stator tooth. This method of flux concentration and in particular the variation in rotor flux density was investigated by monitoring the level of flux passing axially along the rotor at regular intervals. Figure 6.6, illustrates the no load variation of this flux.

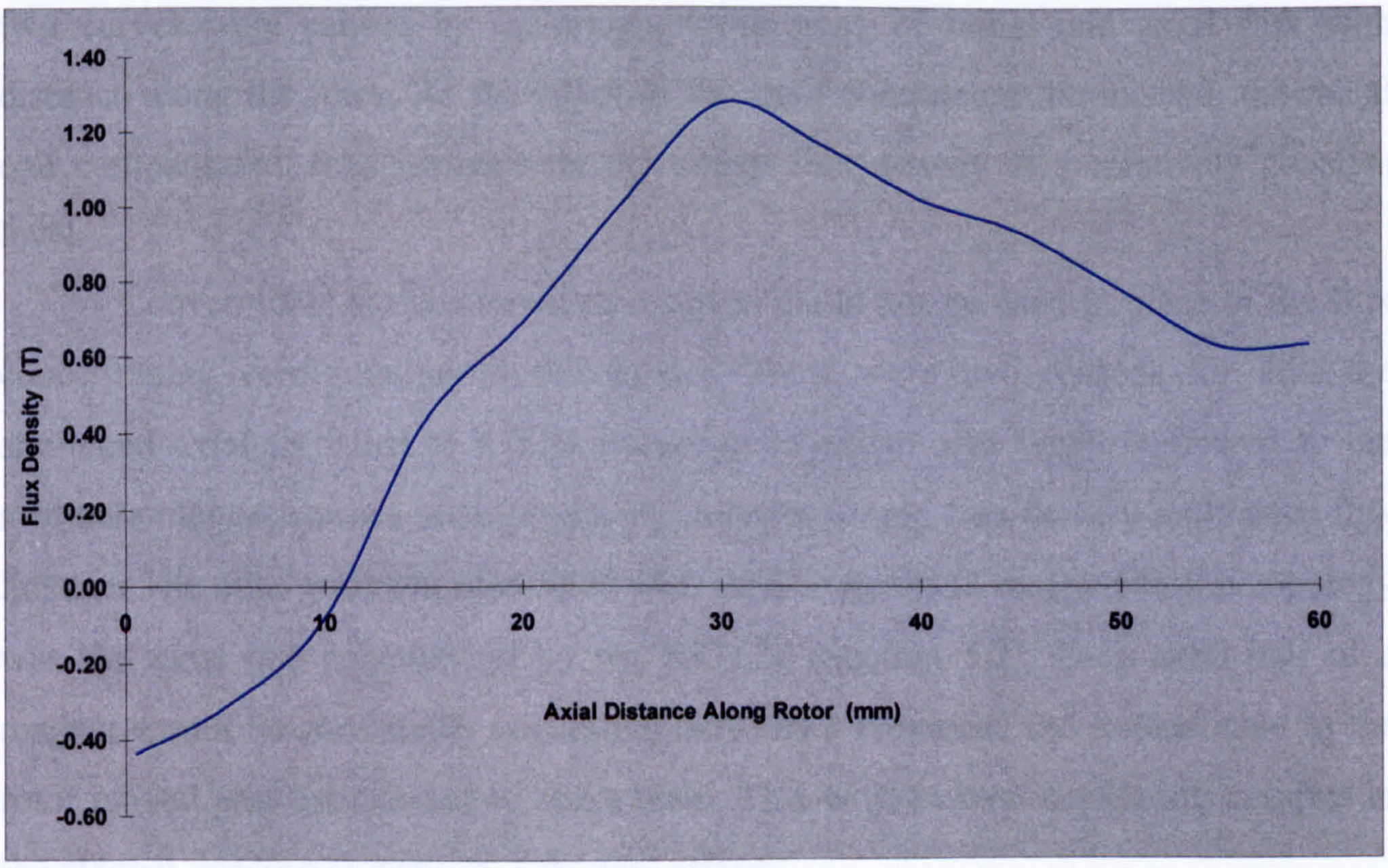

Figure 6.6 Axial variation of no load rotor axial flux density in the CPHTFM

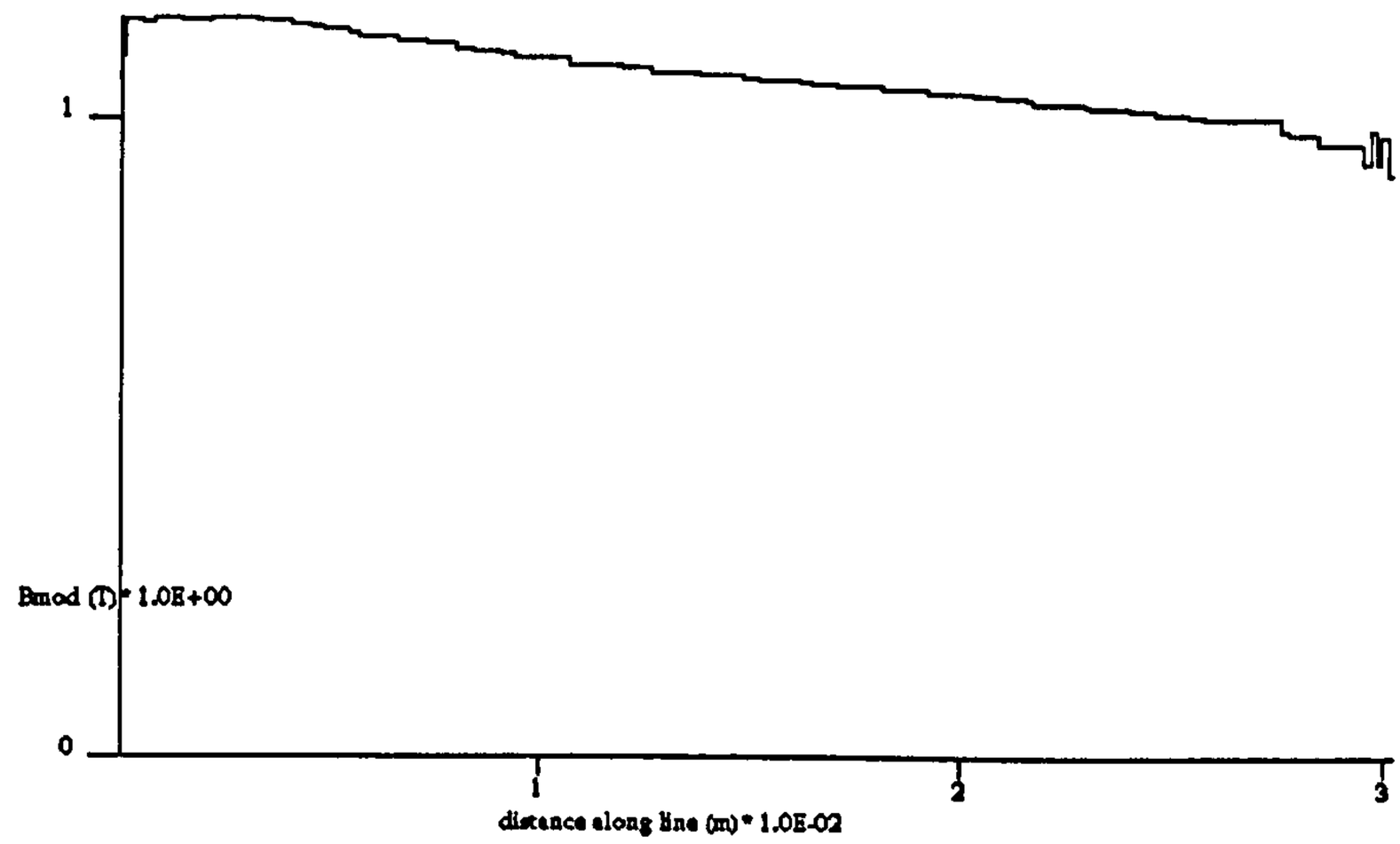

Figure 6.7 Axial variation of no load radial airgap flux density in the CPHTFM (The 0m and 0.03m positions are equivalent to 30mm and 60mm respectively in figure 6.5)

Examining figure 6.6 showed that flux in the first 11mm of rotor iron flowed away from the rotor mid-point (30mm) at the start of the airgap. This 'negative' movement of flux was the source for rotor leakage flux. From 11mm onward, flux density increased to a peak value of 1.3T. This was followed by a steady decay as flux passed from the rotor iron into the airgap. Figure 6.7 shows the effect of this form of flux concentration on the airgap flux density. Maximum and minimum plotted values were 1.16T and 0.94T, with an average value of 1.1T. The dissimilar gradients of the two curves were caused by differing contributions of radial and axial flux with distance along the rotor. As the effect of the axial component diminished, the radial one compensated, thus maintaining the airgap flux density at a relatively constant level.

Conventional surface mounted magnets could not be used in place of the flux concentrating configuration in this model. There were two reasons for this; the shortened axial teeth led to a 50% reduction in airgap area when compared to the available magnet surface area, producing a lower airgap flux density and hence flux linkage. The other problem associated with surface mounted magnets in this topology was the same one encountered by the SSTFM (Section 5.2). Each axial half of a magnet would be continually oscillating between a remanent and loaded state as the rotor moved past the alternating stator teeth. This would cause circulating currents in the magnet, leading to unwanted thermal effects.

6.5 Improving the CPHTFM

Increasing the level of airgap flux density by lowering rotor leakage flux was the first objective for the follow-up CPHTFM design. As with the DSTFM, there was a 0.25mm circumferential magnet overlap on both sides of a stator tooth. Removing this overlap would increase the reluctance of the flux leakage paths around the rotor and improve the airgap flux density. Reducing the width of the teeth would be a counter productive solution. Therefore, the pole pitch was increased, allowing rotor iron width to match that of the stator teeth. This was achieved by enlarging the rotor diameter from 270mm to 304mm, whilst shortening the radial height of the stator to maintain the outside diameter of the machine at the DSTFM dimension of 362mm, this increased the pole pitch from 8.48mm to 9.5mm. The physical constraints of reducing the stator height meant that there was a reduction in coreback width to 10mm. An annotated schematic of this new model is illustrated in Appendix C.3.2 and the positive 'd' axis results from the 3D FE Ψ-I analysis are presented in Appendix E.3.2. The resultant Ψ-I curves for this model are shown in figure 6.8, along with those of the initial 8.48mm pole pitch CPHTFM and the DSTFM.

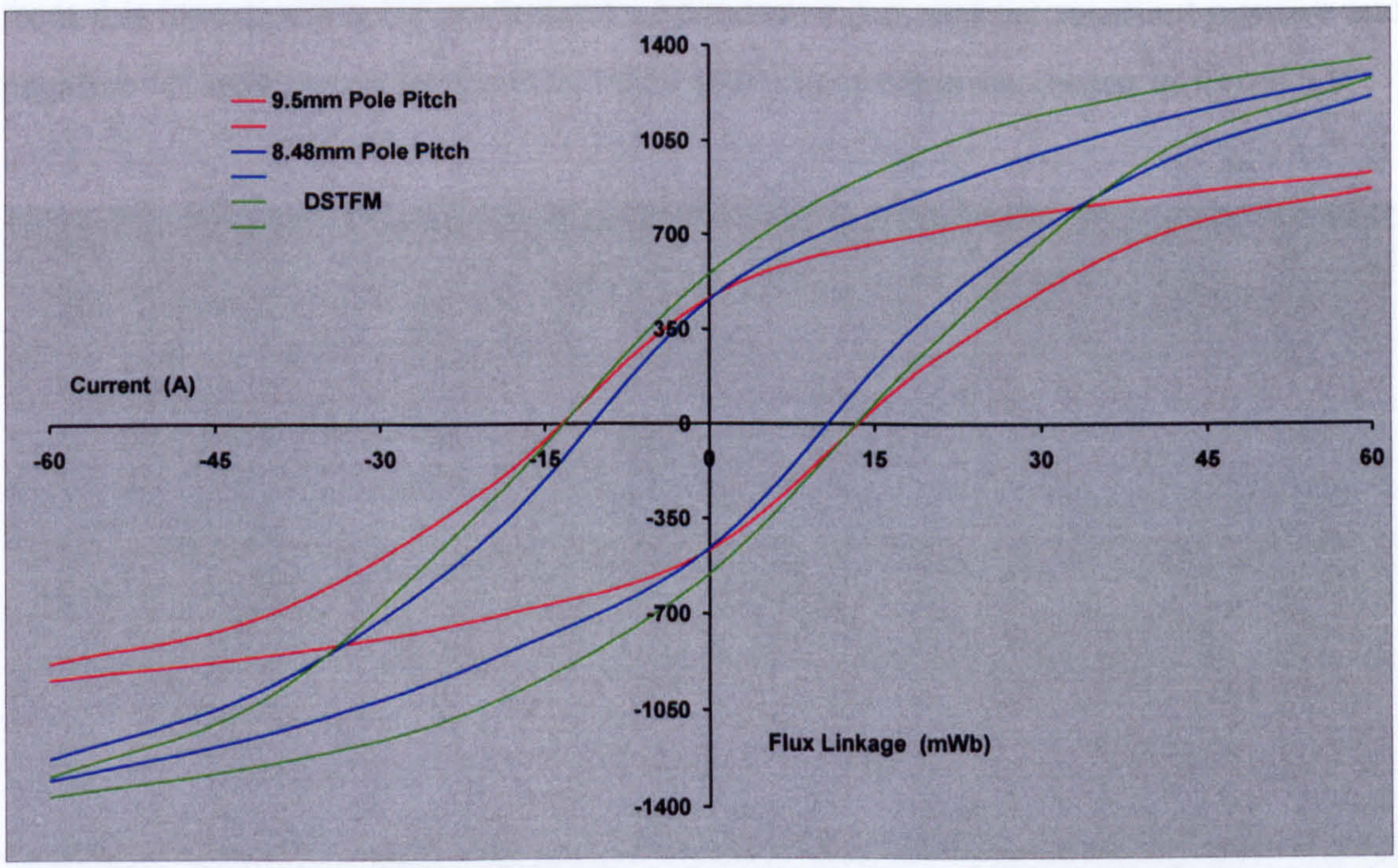

Figure 6.8 Comparison of positive and negative 'd' axis Ψ-I curves between the two CPHTFM designs and the DSTFM

Despite the early onset of saturation in the 9.5mm pole pitch model due to the 10mm coreback, this new configuration exhibited a 3% higher mean torque value

(247.3Nm) at the thermal limit of 23.4A than the 8.48mm pole pitch model. Whilst analysis of the no load 3D FE model showed that the no load flux linkage had increased by only 1.6%. Thus, these design modifications, although producing positive results, had a negligible effect on performance.

6.5.1 Pole Pitch Variation

Increasing the rotor iron volume and removing the circumferential stator tooth/magnet overlap in the 9.5mm pole pitch model produced a slight increase in thermally limited output. If the pole pitch and hence tooth widths were further increased would this generate a worthwhile improvement in output?

Two additional 3D FE models were developed to examine the effect of circumferential tooth width and in a limited way, pole number. The two models, based upon overall dimensions of the 9.5mm pole pitch design, were scaled to represent 80 pole and 90 pole machines, giving pole pitches of 11.9mm and 10.6mm respectively. Stator tooth and rotor iron width were increased, whilst the magnet retained its original dimensions with no stator tooth/magnet overlap. The per pole Ψ-I results from this investigation are presented in Appendix E.3.3, and the resultant positive and negative 'd' axis curves for the 100, 90 and 80 pole models are shown in figure 6.9.

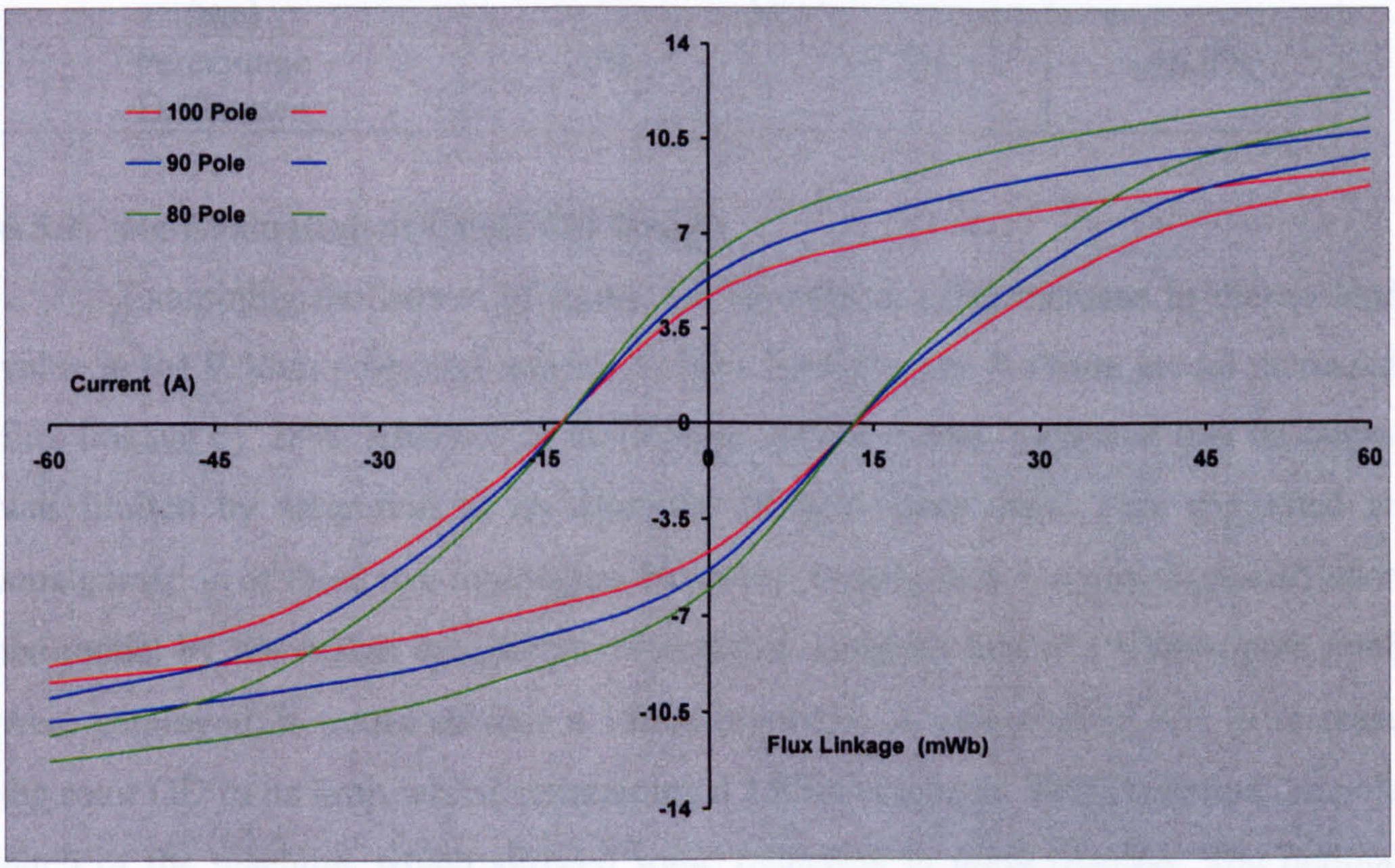

Figure 6.9 Comparison of positive and negative 'd' axis, per pole, Ψ-I curves for the 100, 90 and 80 pole variations of the CPHTFM

Comparative evaluation of the three sets of data showed that the per pole flux linkage increased with pole number due to lower reluctance iron paths (table 6.1). However, the overall output was reduced considerably precisely because of the lower pole number. Increasing pole pitch showed an improvement in output was possible, although only at the expense of enlarging the stator OD in order to maintain pole number.

Table 6.1 Evaluation of 100, 90 and 80 pole CPHTFM models

Pole Number	100	90	80
Per pole No Load Flux Linkage (mWb)	4.67	5.32	6.04
Percentage Difference	0%	13.9%	29.3%
Total No Load Flux Linkage (mWb)	467.16	478.72	482.8
Percentage Difference	0%	2.5%	3.3%
Thermally Limited Output (Joules)	31.07	31.86	32.31
Percentage Difference	0%	2.5%	4%
Thermally Limited Mean Output (Nm)	247.27	228.20	205.66
Percentage Difference	0%	-7.7%	-16.8%

6.5.2 Re-Evaluation of CPHTFM Design

Examining the curves of figure 6.8 revealed a 1.6% increase in the no load value in the 9.5mm pole pitch model. At 60A however, the 8.48mm model increased flux linkage by 28%. Analysis of the 9.5mm 3D FE model, indicated that its output was limited by saturation of its narrower (10mm) stator iron. This suggested an amalgamation of these two topologies. However, the physical constraints placed upon the model by the design specification (section 6.2) meant that if a 9.5mm pole pitch were employed, it would exclude a 15mm coreback. A compromise was to increase the rotor OD to its limit whilst maintaining a 15mm coreback. This increased the pole pitch of the machine, which allowed some reduction in tooth overlap. The optimal rotor radius for this new model was found to be 145mm. This enabled the retention of

the 15mm coreback and a 390mm^2 conductor area, whilst increasing the pole pitch from 8.48mm to 9.1mm. An annotated schematic of the design is presented in Appendix C.3.3 and the positive 'd' axis Ψ-I results in Appendix E.3.4. The three geometric variations examined so far, are illustrated in figure 6.11. The comparative effect on their Ψ-I curves (figure 6.10) are tabulated in table 6.2.

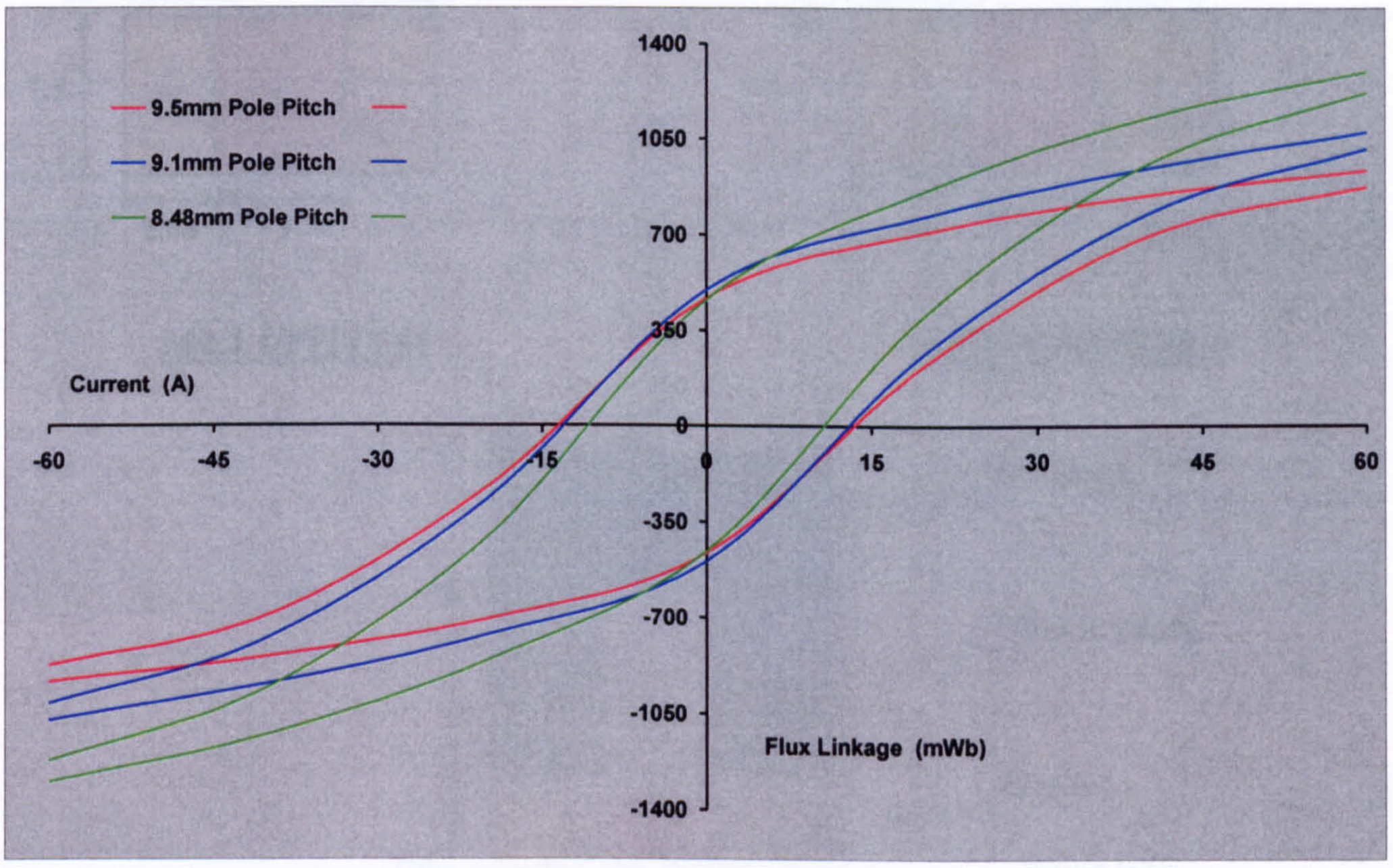

Figure 6.10 Comparison of positive and negative 'd' axis Ψ-I curves between the 8.48mm pole pitch, 15mm coreback, the 9.1mm pole pitch, 15mm coreback and the 9.5 mm pole pitch, 10mm coreback CPHTFMs

Table 6.2 Comparative evaluation of the three initial CPHTFM models

Model	MKI	MKII	MKIII
Pole Pitch (mm)	8.48	9.5	9.1
Coreback Width (mm)	15	10	15
No Load Flux Linkage (mWb)	460.36	467.16	497.76
Thermally limited Torque (Nm)	239.1	247.3	260.5

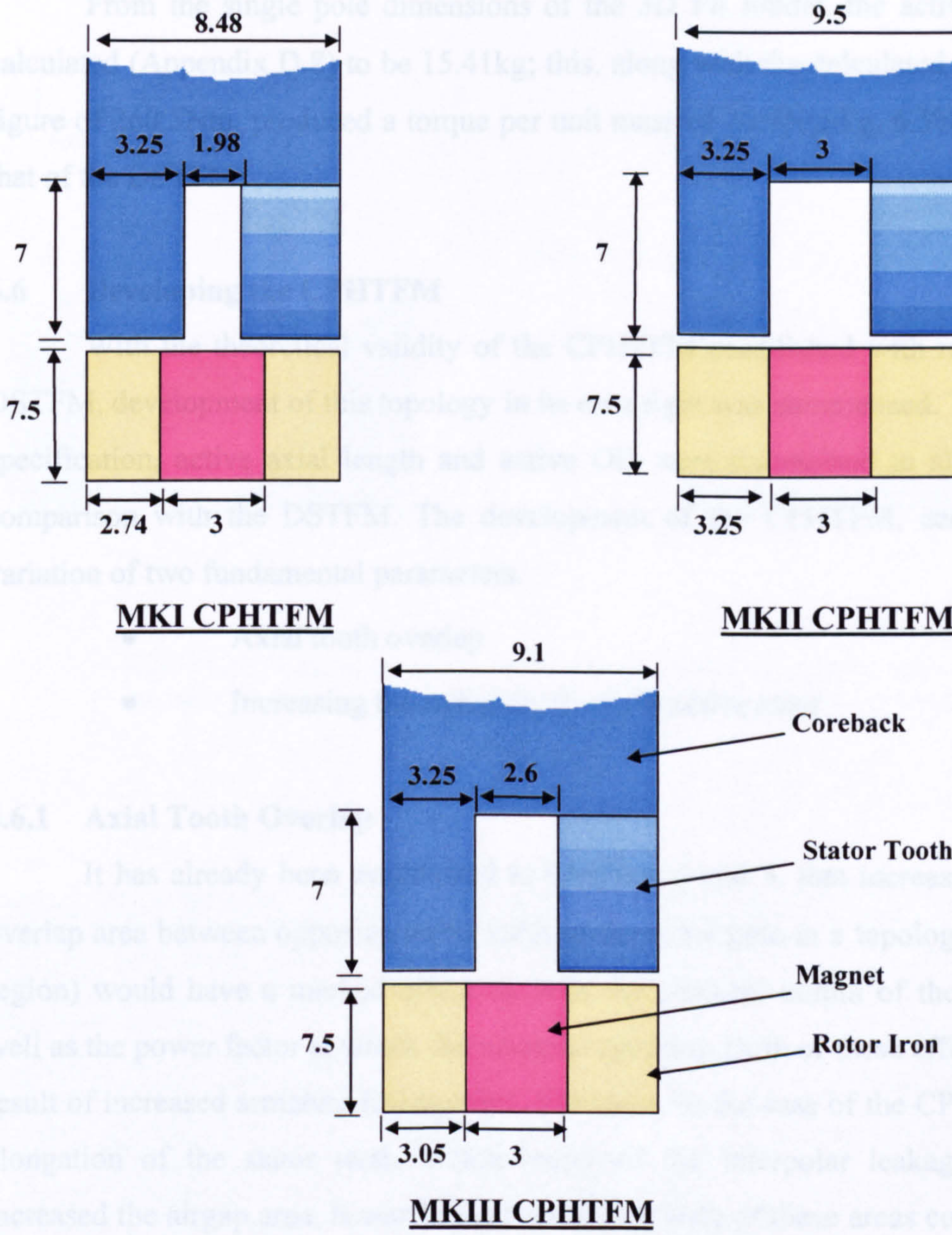

Figure 6.11 Comparative schematics of the three initial CPHTFM topologies. Each diagram is a view in the axial direction, showing the rotor iron and magnet, and the opposing stator teeth

6.5.3 Specific Output Comparison

The 'MKIII' variation of the CPHTFM produced 8.2% more mean torque at the thermal limit than the 8.48mm pole pitch model and 5.1% more than the 9.5mm version. However, this value was still 20% lower than that of the DSTFM.

Referring back to Section 5.9.1, a measure of worth for an electrical machine is the level of rated torque it produces compared to its active mass. Section 5.9.1 indicated that the DSTFM had a specific output of 15.87Nm/kg based upon its thermally limited current. How well did the MKIII CPHTFM compare to this value?

From the single pole dimensions of the 3D FE model, the active mass was calculated (Appendix D.8) to be 15.41kg; this, along with the calculated mean torque figure of 260.5Nm, produced a torque per unit mass of 16.9Nm/kg, 6.5% higher than that of the DSTFM.

6.6 Developing the CPHTFM

With the theoretical validity of the CPHTFM established with respect to the DSTFM, development of this topology in its own right was commenced. The 100 pole specification, active axial length and active OD were maintained to allow a direct comparison with the DSTFM. The development of the CPHTFM, centred on the variation of two fundamental parameters.

- Axial tooth overlap
- Increasing the radial depth of the active rotor

6.6.1 Axial Tooth Overlap

It has already been established in Chapters 4 and 5, that increasing the axial overlap area between opposing stator teeth of the same pole in a topology (interpolar region) would have a marked effect on both the physical output of the machine as well as the power factor at which the machine operates. Both of these effects were the result of increased armature leakage flux. However, in the case of the CPHTFM axial elongation of the stator teeth, which increased the interpolar leakage area, also increased the airgap area. It was felt that enlarging both of these areas could lead to a compromise position that afforded a higher mean output for a small loss in effective power factor.

A series of seven 3D FE models were produced covering axial overlaps from 2.5mm to complete tooth overlap (60mm). Flux linkage data for these models is presented in Appendix E.3.5. As the degree of overlap increased, the geometry of the model changed. This affected ancillary flux paths in the model, in particular axial flux leakage between a tooth and the opposite side of the stator coreback (figure 6.12). To limit this effect, the solid coreback was chamfered in this region to maintain an average axial gap over the seven models of 8.6mm (minimum of 6mm in the 15mm overlap model). Results of power factor and thermally limited output for these models are reproduced in figure 6.13 and table 6.3.

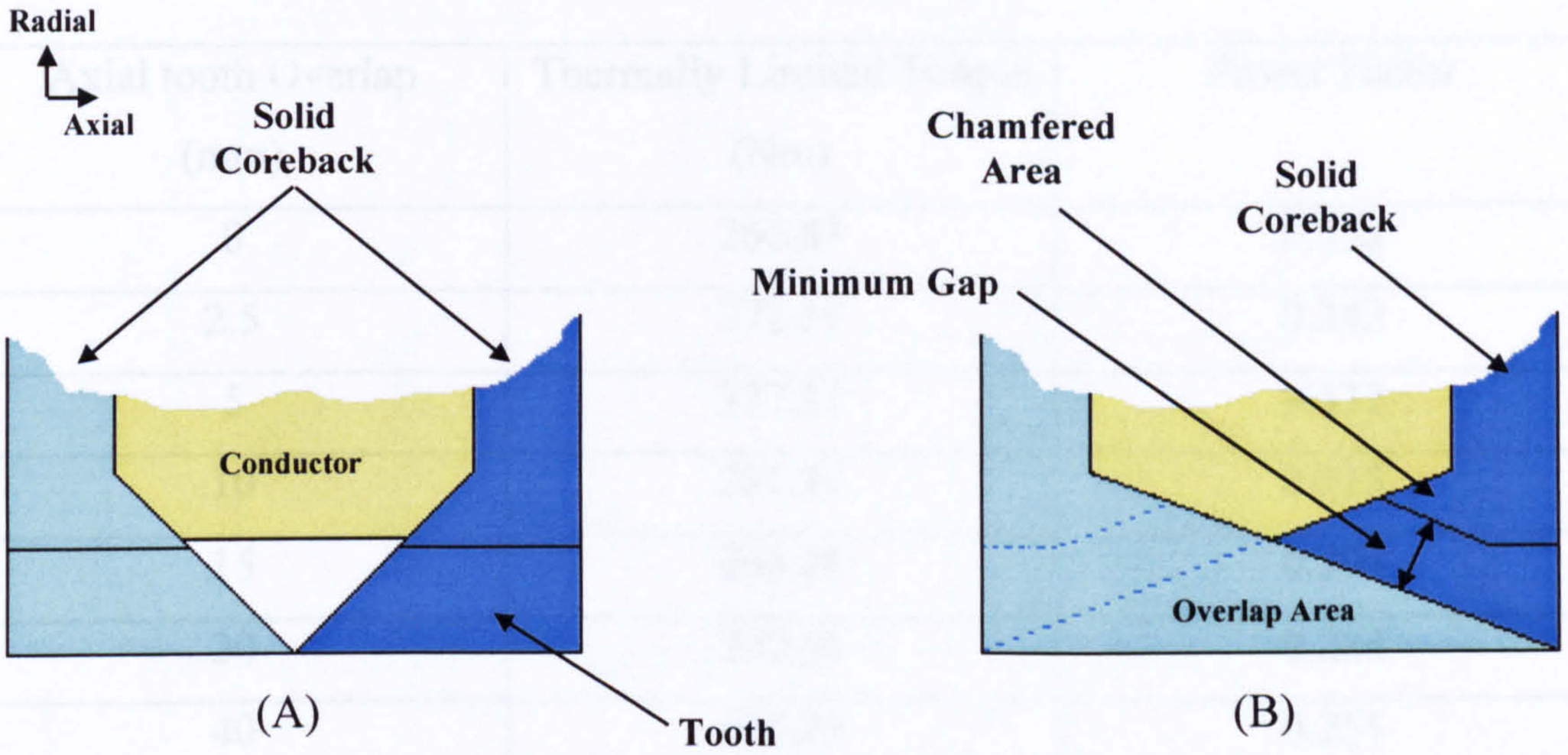

Figure 6.12 Diagrammatic comparison of two CPHTFM stators, one with no axial tooth overlap (A) and one with teeth fully overlapped axially (B)

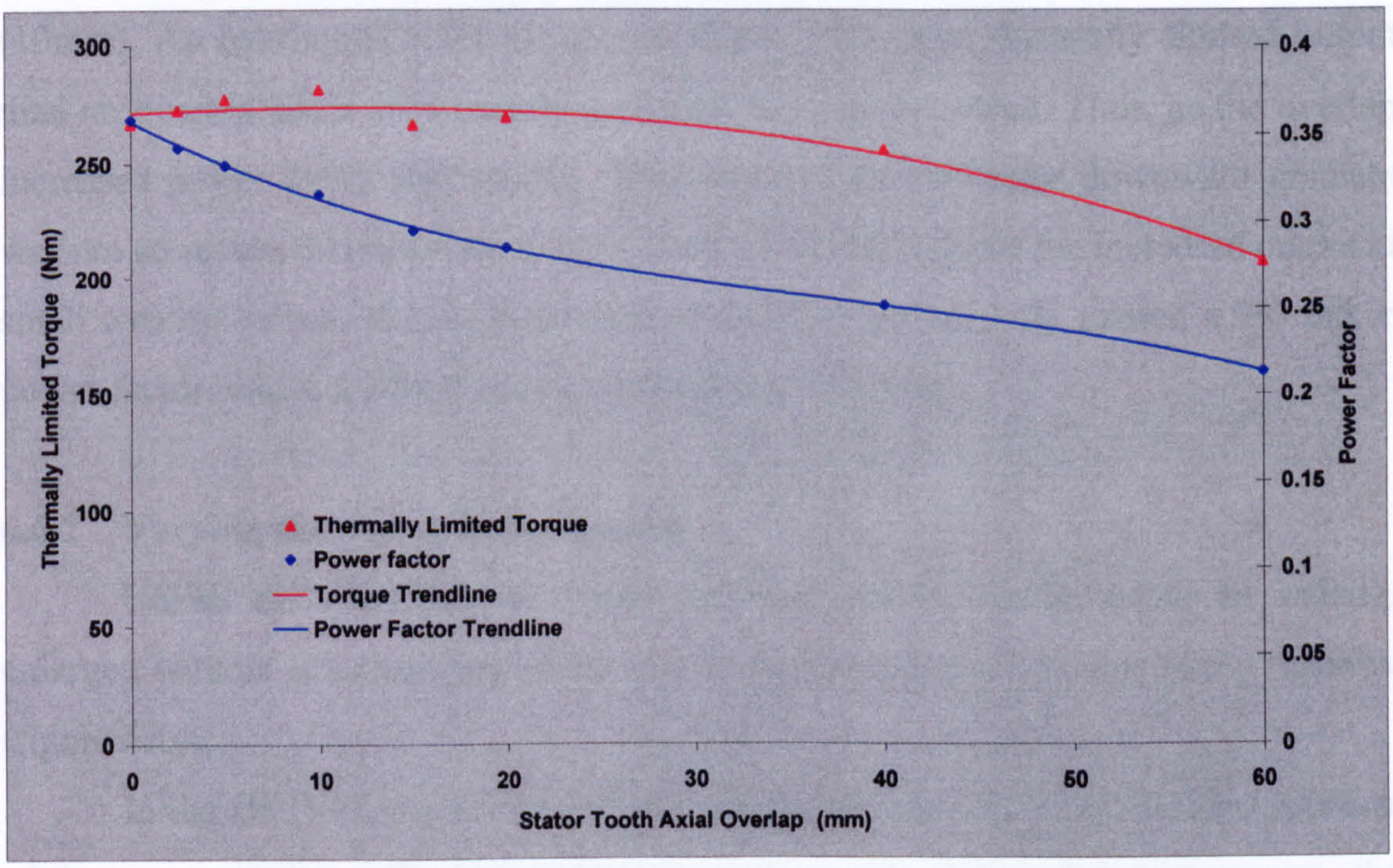

Figure 6.13 Variation of thermally limited output and power factor with axial tooth overlap

Table 6.3 Effect on output and power factor of varying the axial overlap of the stator teeth in the CPHTFM

Axial tooth Overlap (mm)	Thermally Limited Torque (Nm)	Power Factor
0	266.83	0.358
2.5	272.59	0.342
5	277.31	0.332
10	281.37	0.315
15	266.26	0.294
20	269.46	0.284
40	255.83	0.251
60	207.44	0.213

Analysis of the data from these models showed that a small axial overlap produced a rise in output as the airgap area increased. However, the effects of lost flux through interpolar mechanisms became apparent as the overlap rose above 17% (10mm). An overlap of 8.5% (5mm) provided 3.9% more thermally limited output than no overlap and a 17% overlap provided 5.5% more output. Thus, as the overlap increased power factor fell steadily. However, the power factor downward gradient was not so severe that some advantage could not be taken from the increased output at small overlap values. If a 5mm overlap was employed this only caused a 7% fall in power factor, whilst a 10mm overlap produced a 12% drop.

6.6.2 Varying the Active Rotor Depth

Unlike the DSTFM, the active rotor of the CPHTFM could be radially enlarged without affecting any of the physical parameters of the rest of the machine (figure 6.14).

In the DSTFM, the rotor is axially narrow and radially long. A radial increase of the rotor would amplify the axial force acting at its outer radius and increase the shear forces at the support hub interface. On the positive side, unmatched rotor iron and stator tooth lengths could serve to amplify the flux concentration into the stator teeth. Realistically however, a longer rotor necessitates a similar stator tooth radial

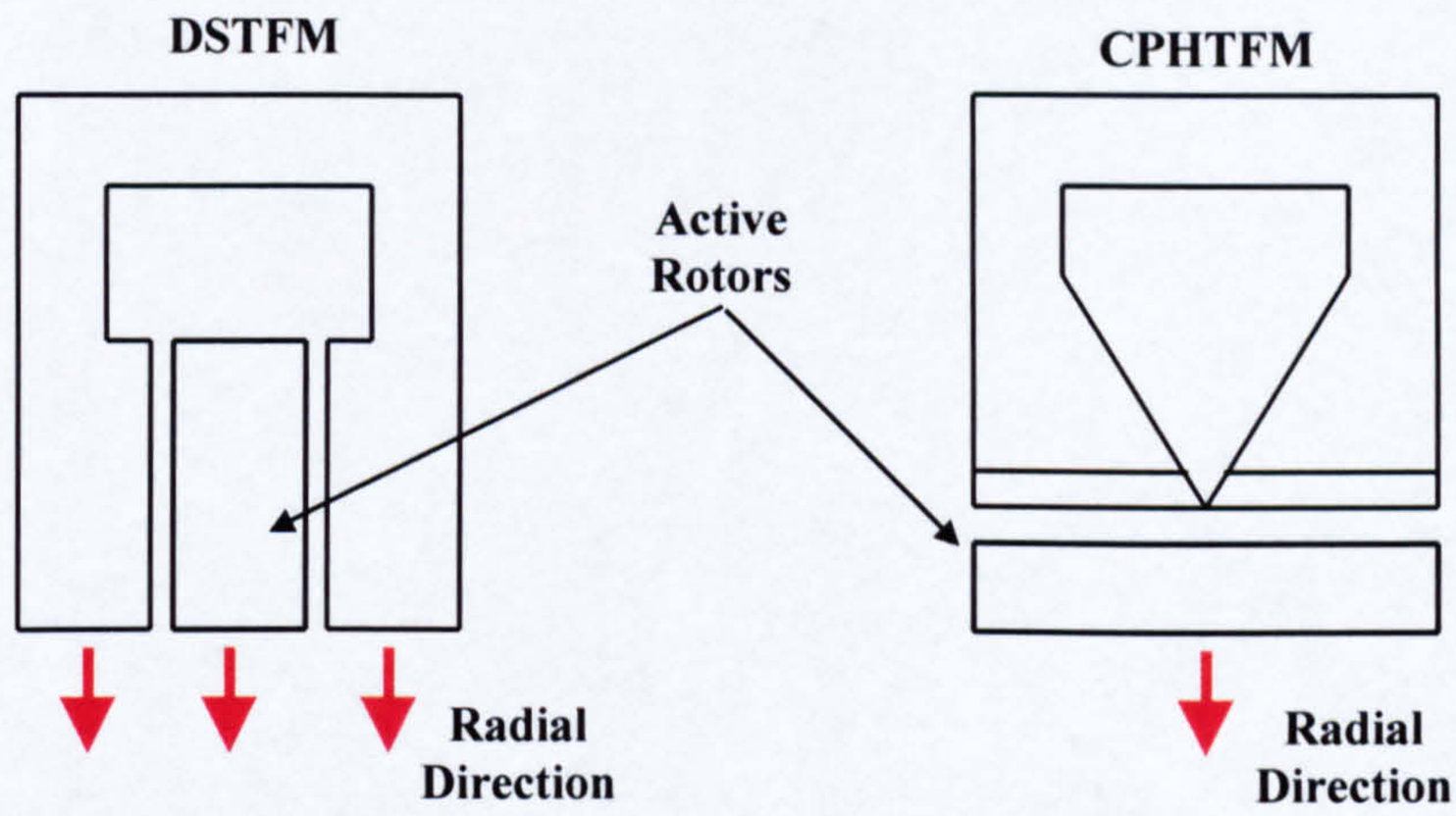

Figure 6.14 Radially elongating the active rotor of a DSTFM and a CPHTFM

increase to prevent saturation at the tooth's inner radius. The aspect ratio of the CPHTFM rotor and the radial direction of the applied force in the airgap, overcomes the mechanical difficulties experienced by the DSTFM. A radial rotor increase in the CPHTFM will produce a higher airgap flux density by virtue of the increased magnet volume and flux concentration. There is a limit to the viable radial depth of the active section because as the rotor approaches the rotor axis the iron becomes circumferentially narrower. Four alternative radial depths were investigated; 10mm, 12.5mm, 15mm and 30mm, in addition to the original 7.5mm rotor model. The Ψ-I results from these analyses are presented in Appendix E.3.6. The analysis of these curves is given in figure 6.15 and table 6.4.

Table 6.4 Effect on output and power factor of varying the active rotor's radial depth in the CPHTFM

Radial Rotor Depth (mm)	Thermally Limited Torque (Nm)	Power Factor
7.5	266.83	0.358
10	308.14	0.391
12.5	340.33	0.416
15	358.57	0.431
30	393.17	0.476

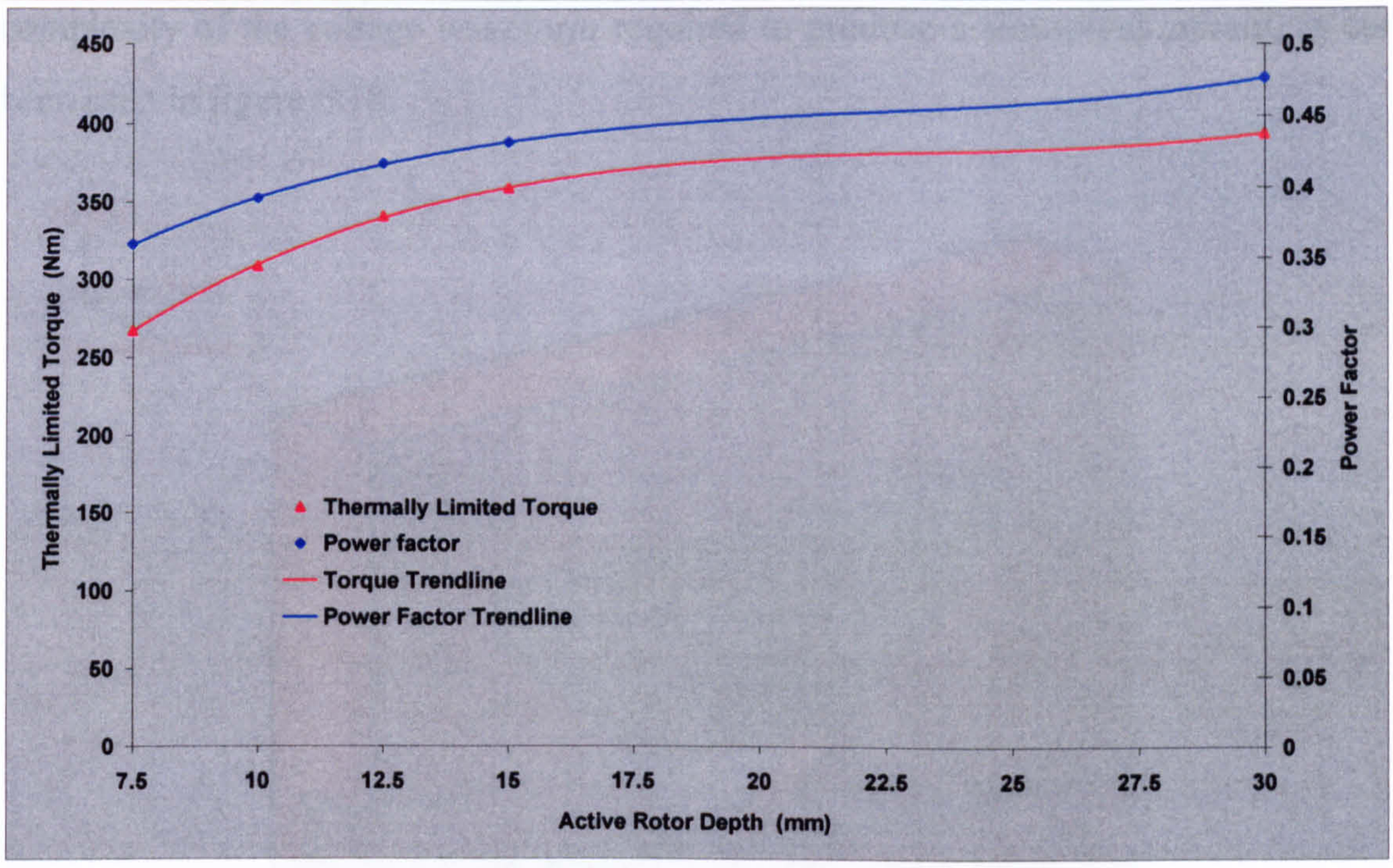

Figure 6.15 Effect on output and power factor of radial elongation of the active rotor in a CPHTFM

The thermally limited output and power factor were seen to rise with rotor depth (figure 6.15). At a rotor depth of up to 15mm, which was equivalent to doubling the rotor depth, there was a substantial increase in both values. The output rose by 34% and the power factor increased by 20%. A further doubling of the rotor depth to 30mm, only provided an extra 9.5% improvement in output and 10% in power factor, but with a further twofold increase in magnet volume and hence cost.

These two investigations pointed to a revised CPHTFM model which should exhibit a higher output and an improved power factor. Therefore, another 3D FE model (figure 6.16) was produced with a 5mm axial overlap and an active rotor depth of 15mm. The Ψ-I data for the model is presented in Appendix E.3.7 and the positive and negative 'd' axis curves, along with those of the DSTFM for comparison, are shown in figure 6.17.

The new CPHTFM configuration demonstrated a 13% higher thermally limited mean output than the DSTFM (369.9Nm and 327.2Nm respectively) and a 39% increase over the original CPHTFM. Average airgap flux density rose from 1.1T in the original CPHTFM to 1.28T in this new model, an increase of 16%. Power factor was improved by 18% (0.441), over the DSTFM (0.374) and 23% over the original CPHTFM (0.358). However there was little improvement in the harmonic

complexity of the voltage waveform required to produce a sinusoidal current, as can been seen in figure 6.18.

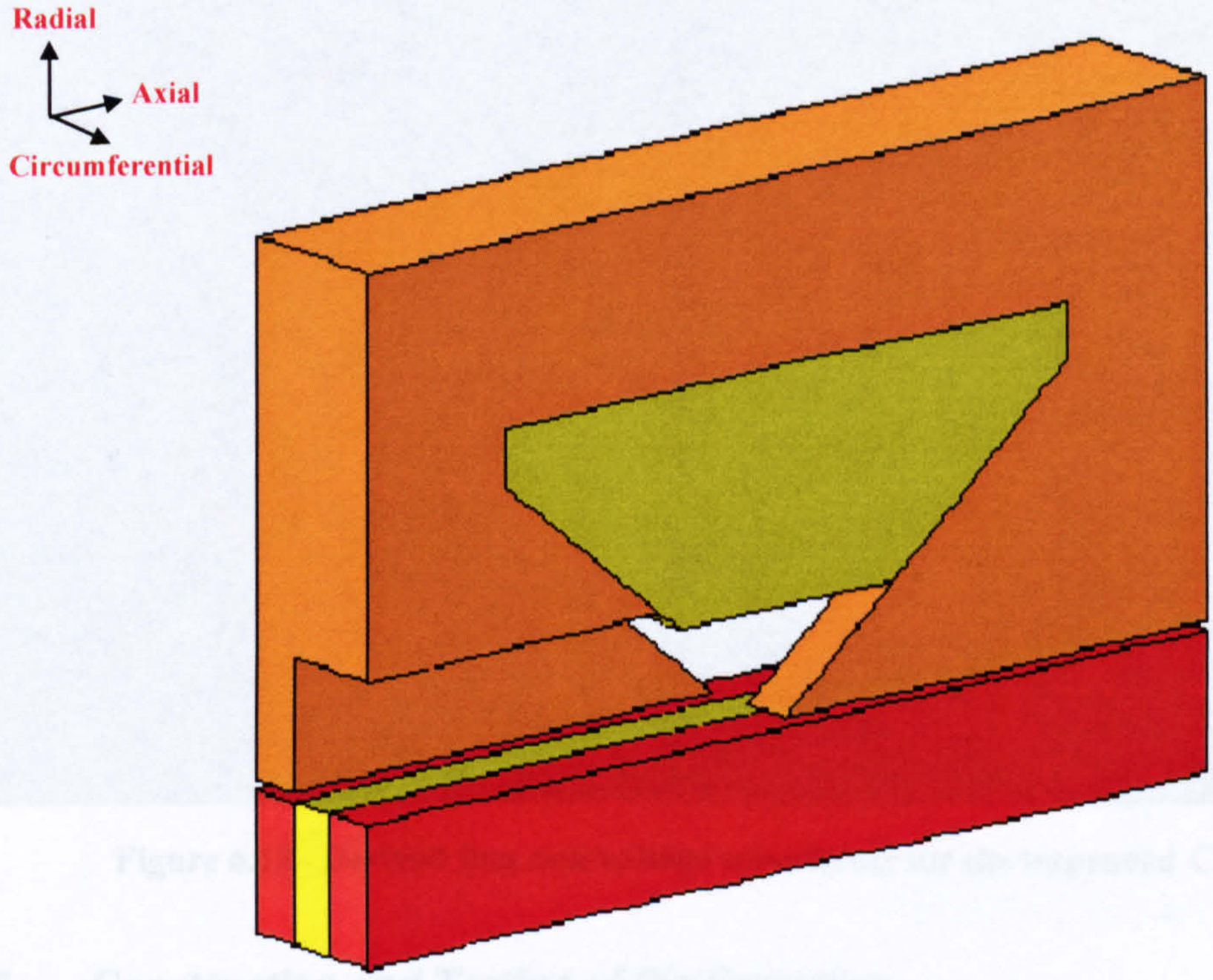

Figure 6.16 3D FE model of the improved CPHTFM topology

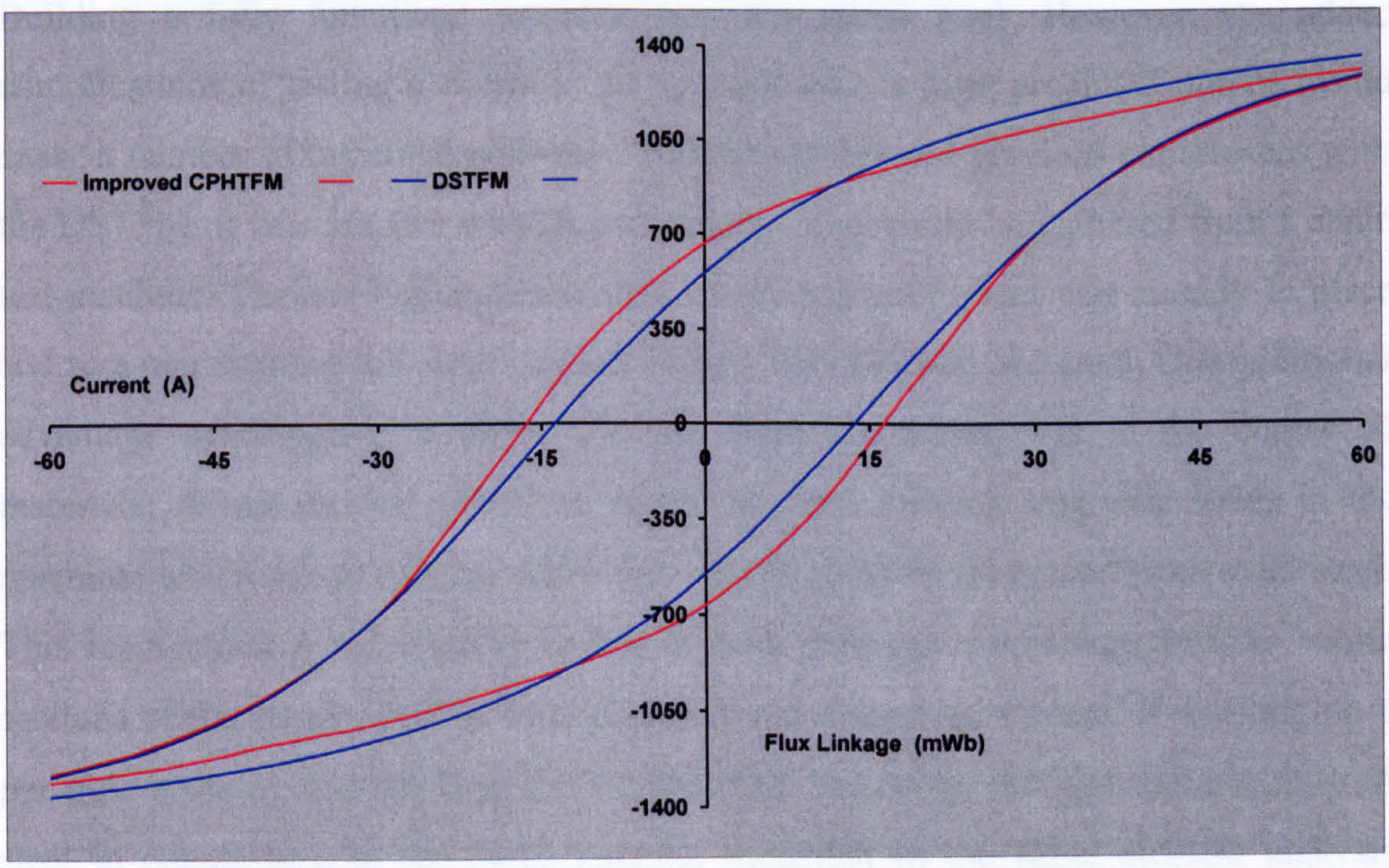

Figure 6.17 Positive and negative 'd' axis Ψ-I curves for the improved CPHTFM, compared with the DSTFM curves

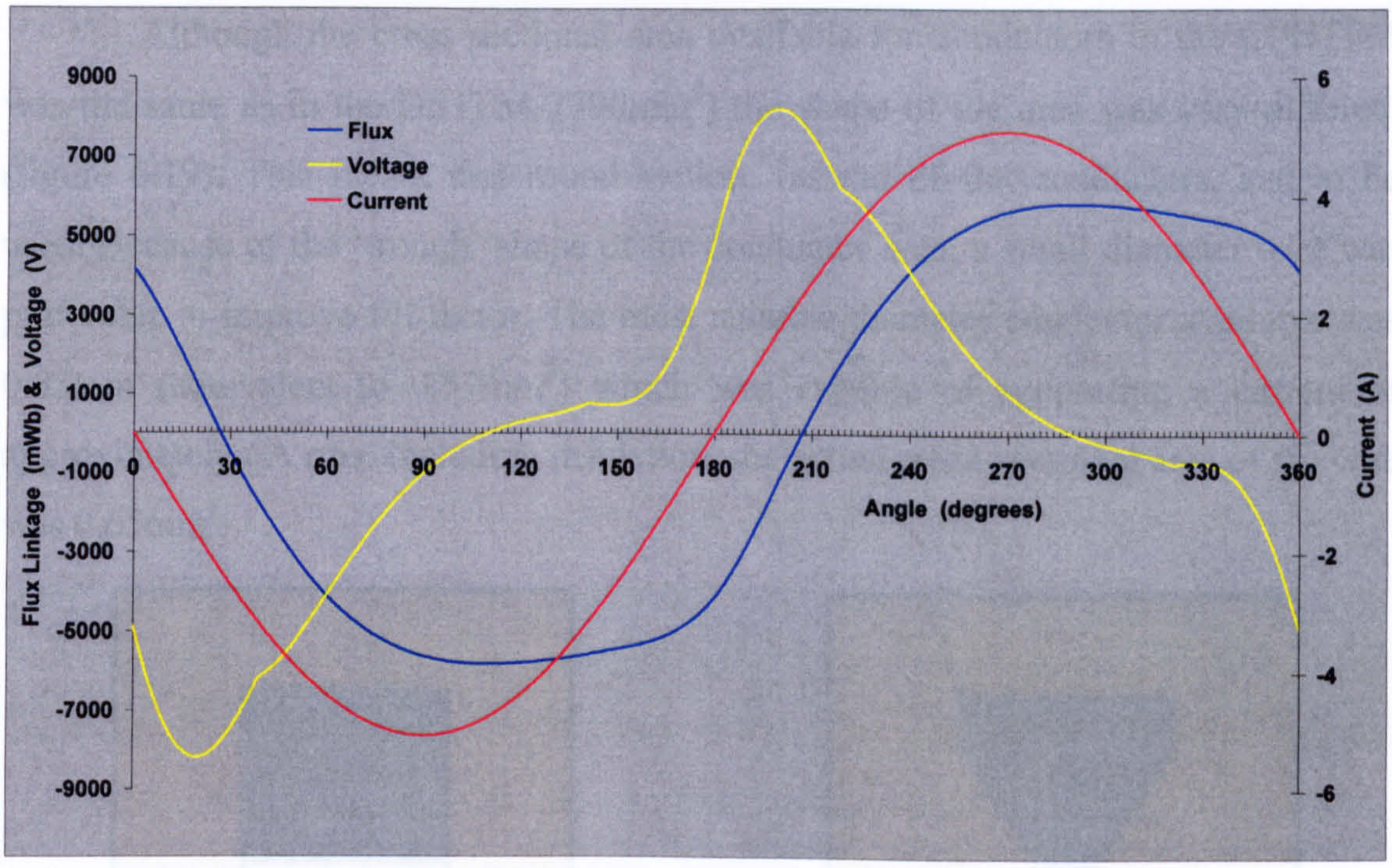

Figure 6.18 Derived flux and voltage waveforms for the improved CPHTFM

6.7 Construction and Testing of the Prototype

Promising results from theoretical analysis of the CPHTFM prompted the construction of a 100 pole single phase prototype machine to validate the topology. Building a fully functional machine was the initial goal. However, the added complications of testing a dynamic set up with such a high predicted output would cause a number of logistical problems. Because of this and previous experiences with the DSTFM, it was felt that enough performance data could be gathered from a static test machine. The test bed and analytical measuring equipment was already in place and so a non-rotating full sized version of the CPHTFM was designed. One additional advantage of designing a static machine from the outset was in the choice of materials. A non-rotating prototype meant no time varying magnetic fields in the machine, which meant that the entire iron circuit could be fabricated from solid steel. This represented a considerable saving in both cost and machining time, as whole sections of the stator could be manufactured and assembled instead of working on a per pole basis as was the case for the DSTFM. However, the high permeability of steel in comparison to the SMC material modelled in the finite element analysis would make comparative evaluation between theoretical and measured results harder.

6.7.1 Conductor Selection

Although the cross-sectional area available for conductors in the CPHTFM was the same as in the DSTFM, (390mm^2) the shape of the area was very different (figure 6.19). This meant that round-section, instead of flat conductors, had to be used. Because of the 'trough' shape of the conductor area, a small diameter wire was preferable to improve fill factor. The most suitable diameter conductor available was 0.85mm (equivalent to 0.57mm^2) which was capable of supporting a current of approximately 5A rms. Including insulation, the actual cross-sectional area of the wire was 0.65mm^2.

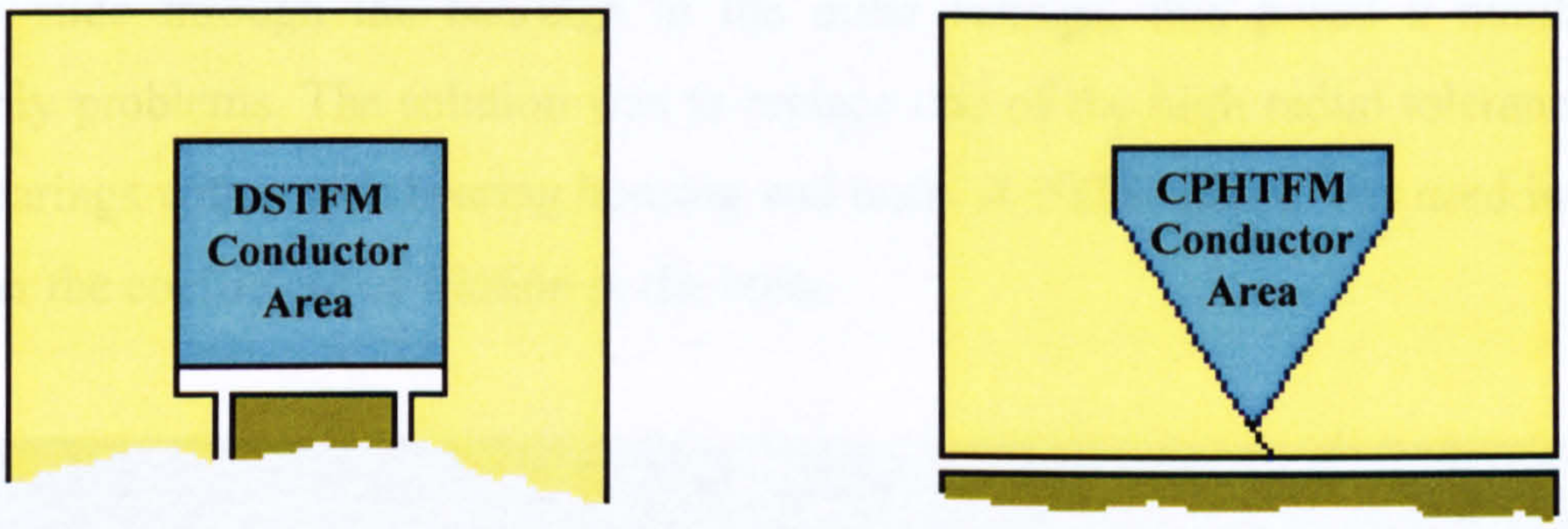

Figure 6.19 Comparison of the DSTFM and CPHTFM conductor area shapes

From the theoretical analysis, the specified electric loading for the CPHTFM was 2000Ampereturns. If an rms current of 5A was applied to the prototype, then it required 400 turns to attain this MMF, which equated to an overall conductor cross-sectional area of 260mm^2. Therefore, a conductor area fill factor of 0.66 was necessary in the prototype. By careful winding of the conductor into the stator, this value was actually exceeded.

6.7.2 Prototype Components

For ease of construction, the stator of the prototype consisted of only four major parts. These comprised of two coreback sections each spanning 180 mechanical degrees and two flanking rings (figure 6.20) each incorporating fifty stator teeth and their associated side-cheeks. A partially assembled stator is shown in figure 6.21.

The active rotor of the CPHTFM was produced in much the same way as the DSTFM, (Chapter 3, section 3.5.3) with individual iron and magnet sections being keyed and glued onto an indexed aluminium hub. Material data for the permanent magnets is presented in Appendix B.3. An annotated photograph of the completed

rotor is shown in figure 6.22. Engineering drawings of the component pieces of the stator and rotor are presented in Appendix C.3.4 and Appendix C.3.5 respectively. Figure 6.23, is a picture of the rotor and stator in detail during an assembly test run. The photograph shows the rotor in the aligned 'd' axis position. A cut away schematic of the complete machine is illustrated in figure 6.24.

In order to alleviate the problem of backlash experienced in the DSTFM prototype, the drive shaft on the CPHTFM dispensed with keyed interfaces in favour of flanged plates, welded to each end. These plates were then bolted to the aluminium hub at one end and the torque transducer at the other. As the drive shaft could not simply slide through the bearings in the outer casings, this posed a number of assembly problems. The solution was to replace one of the high radial tolerance ball race bearings with a split bearing housing and bush. A PTFE sleeve was used in order to lower the coefficient of friction in the bush.

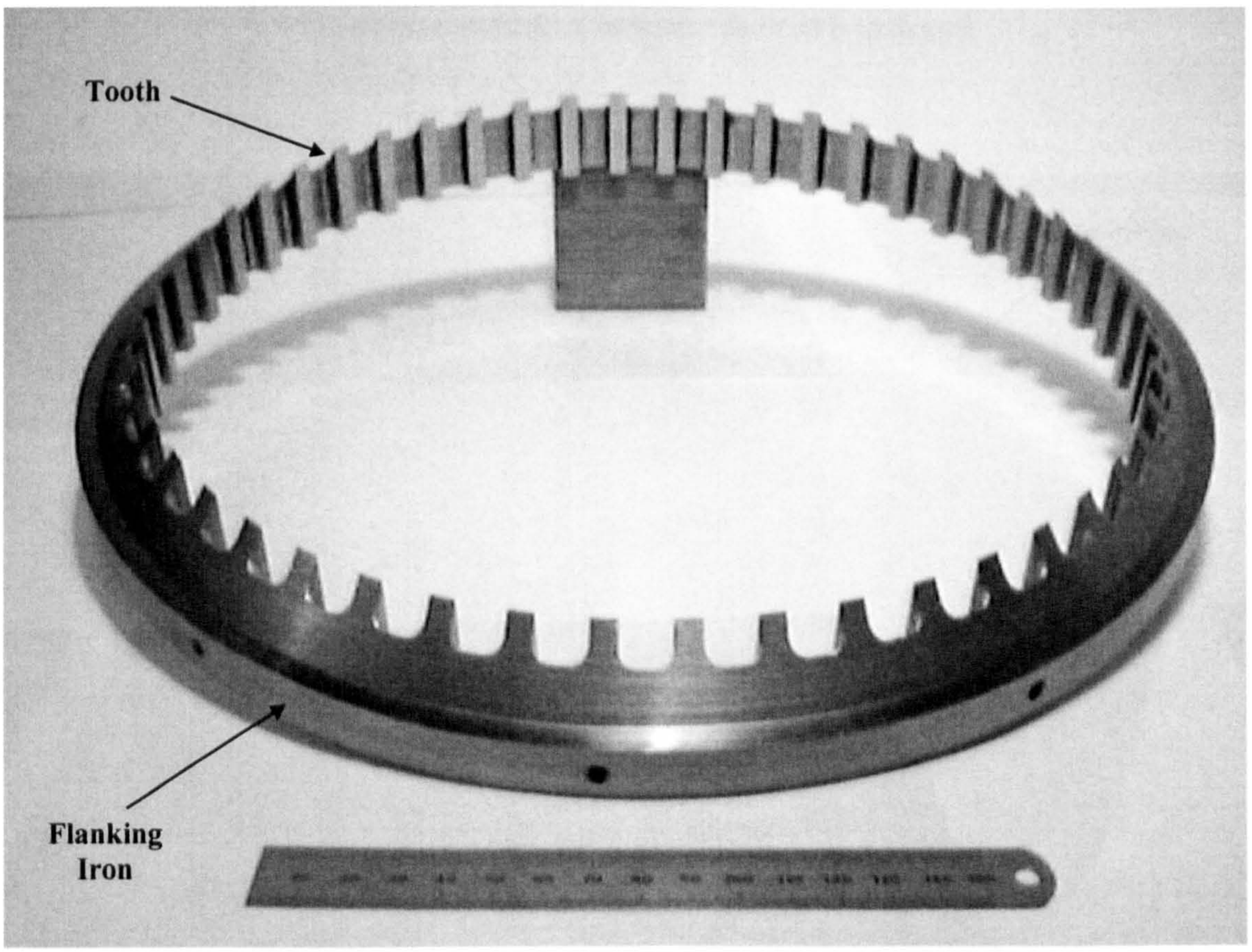

Figure 6.20 One of two stator rings used in the construction of the CPHTFM

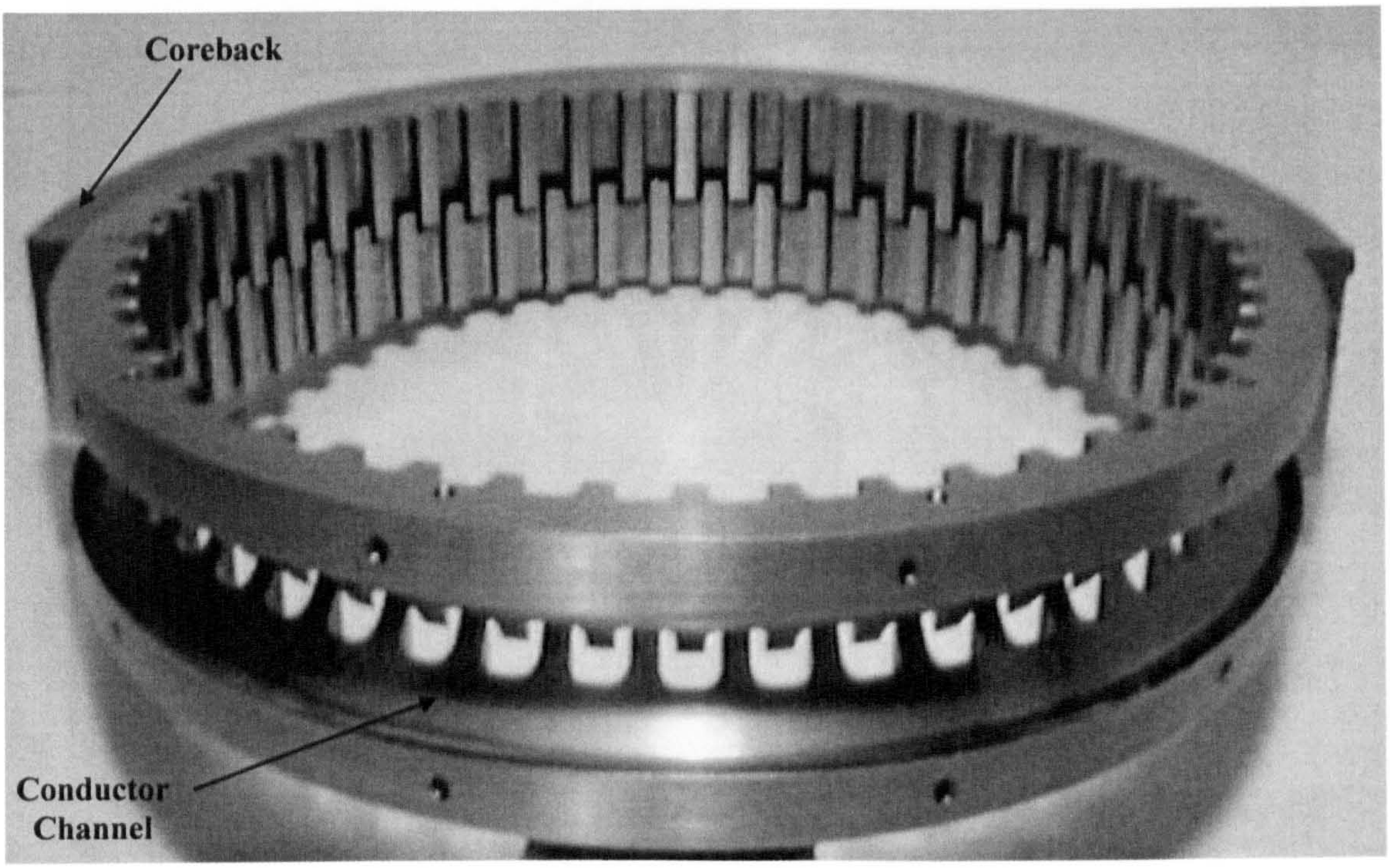

Figure 6.21 Both stator rings positioned together with one of the 180°(mech) corebacks. Conductor channel is indicated

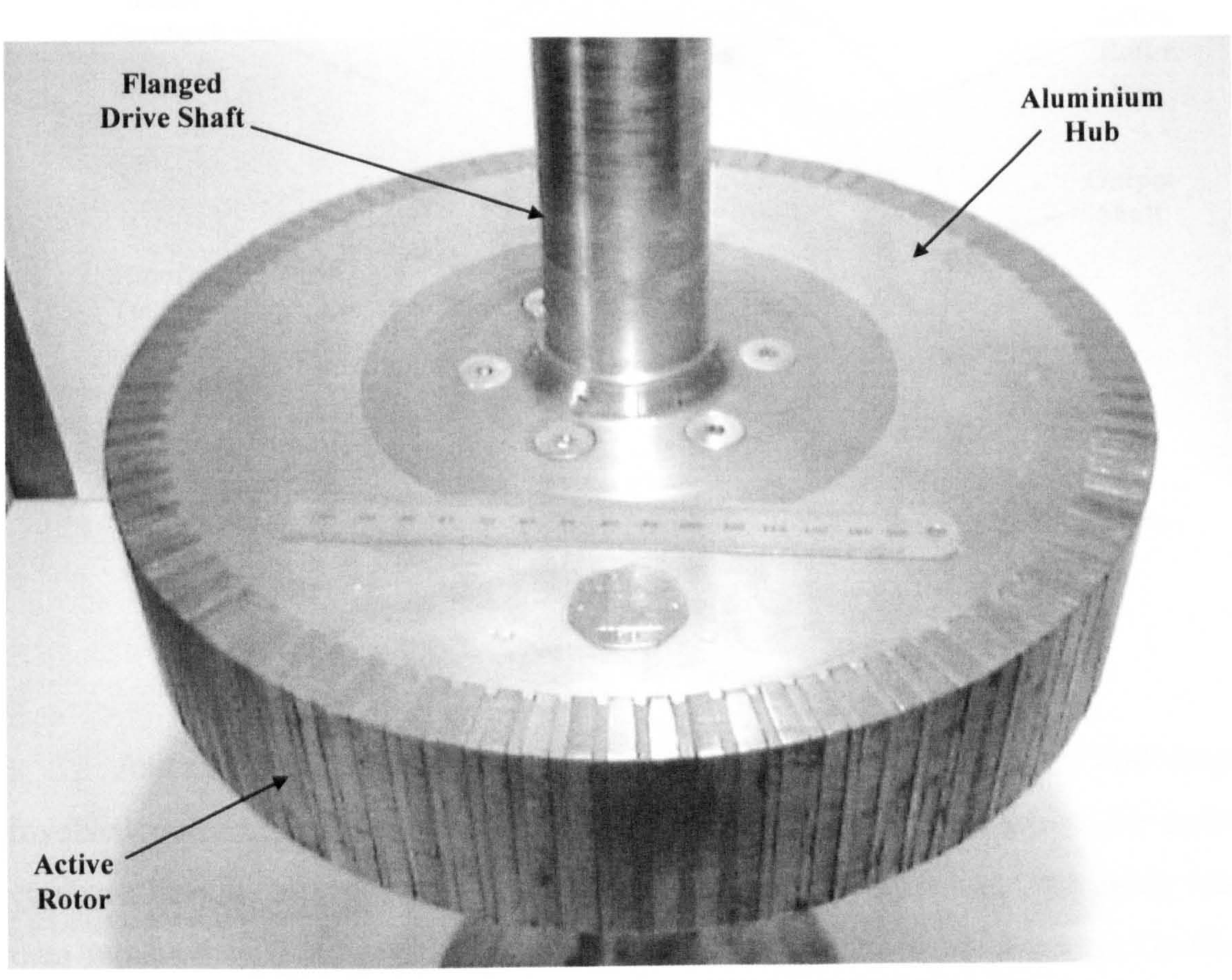

Figure 6.22 Completed rotor prior to assembly

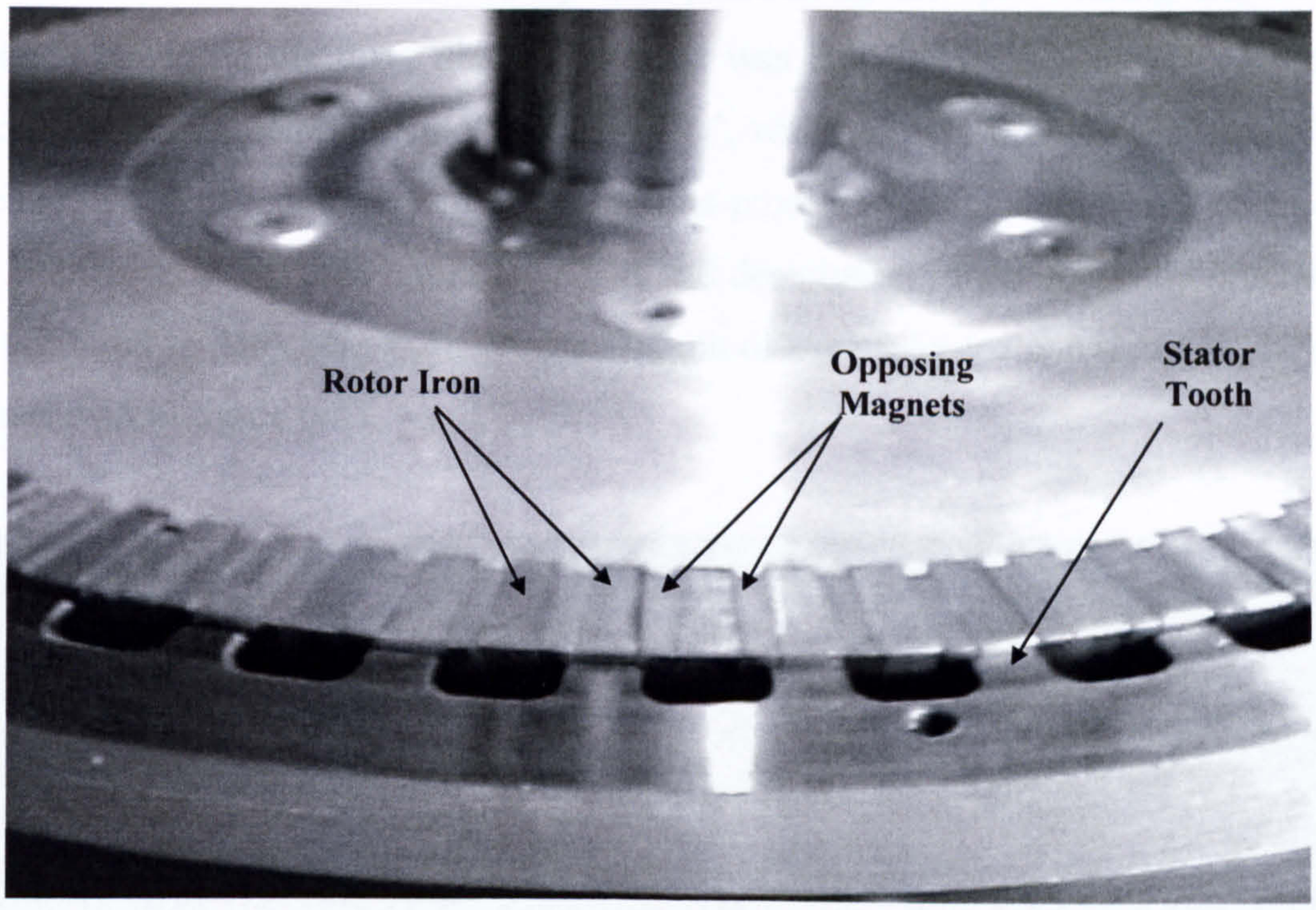

Figure 6.23 Detail photograph of the rotor and stator during the assembly procedure

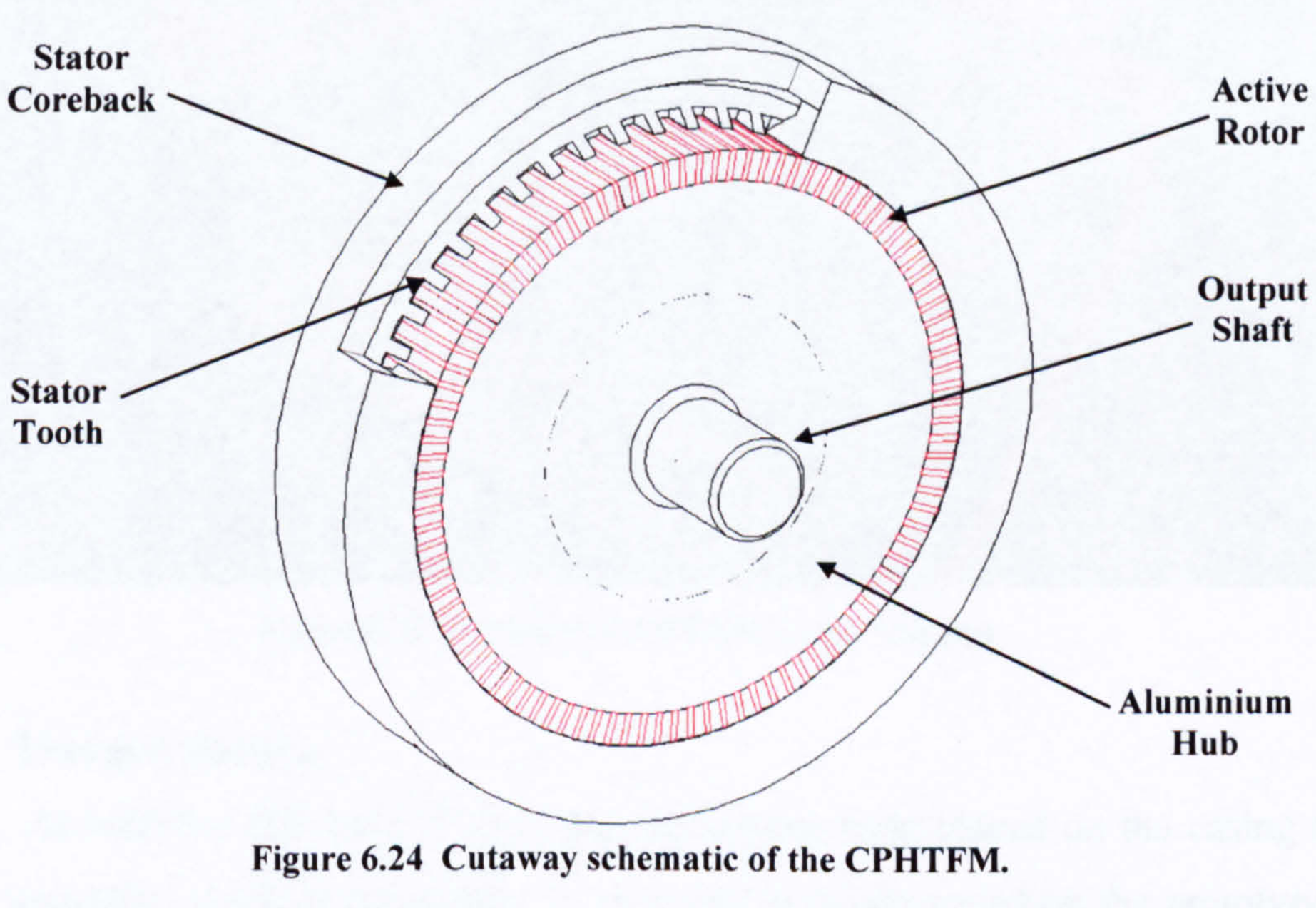

Figure 6.24 Cutaway schematic of the CPHTFM.

Assembly of the prototype was carried out in two stages. The first stage involved constructing the stator around a dummy rotor. This allowed the outer coreback ring segments to be removed, revealing the conductor area. The stator was then mounted in a lathe and the wire wound into the conductor channel. Careful positioning enabled 425 turns to be placed in the 390mm^2 area, giving a fill factor of

the real rotor. This was achieved by first positioning the split-bearing aluminium casing in place on the drive shaft. The rotor was then lowered into the completed conductor/stator assembly using 'jacking bolts', which slowly brought the two halves together. To limit radial movement during this procedure, both shafts were machined to a bearing fit along their entire length. A full description of the assembly procedure can be found in Appendix C.3.6. A photograph of the prototype connected to the test rig is shown in figure 6.25.

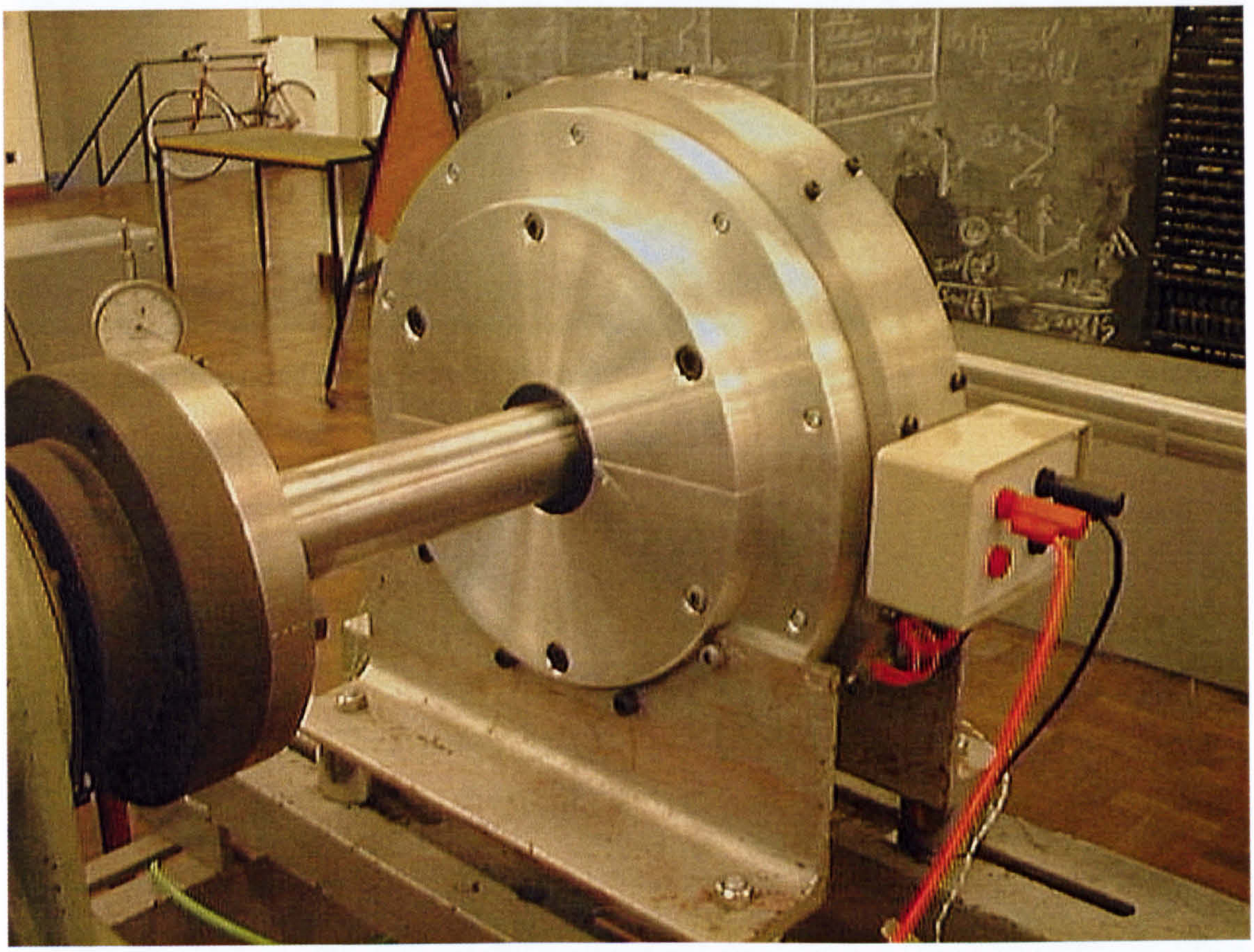

Figure 6.25 Prototype CPHTFM on the test bed

6.7.3 Thermal Testing

As with the DSTFM, 'T' type thermocouples were placed on the casing and during assembly, inside the machine. A 'heat run' was performed on the prototype at a nominal rms current of 3A; data from this test is presented in Appendix E.3.8. Thermal time constants of 3.5 minutes and 106 minutes were calculated for the winding core and outer casing respectively. Figures 6.26 and 6.27 show the measured and calculated curves from which these values were determined. The winding core

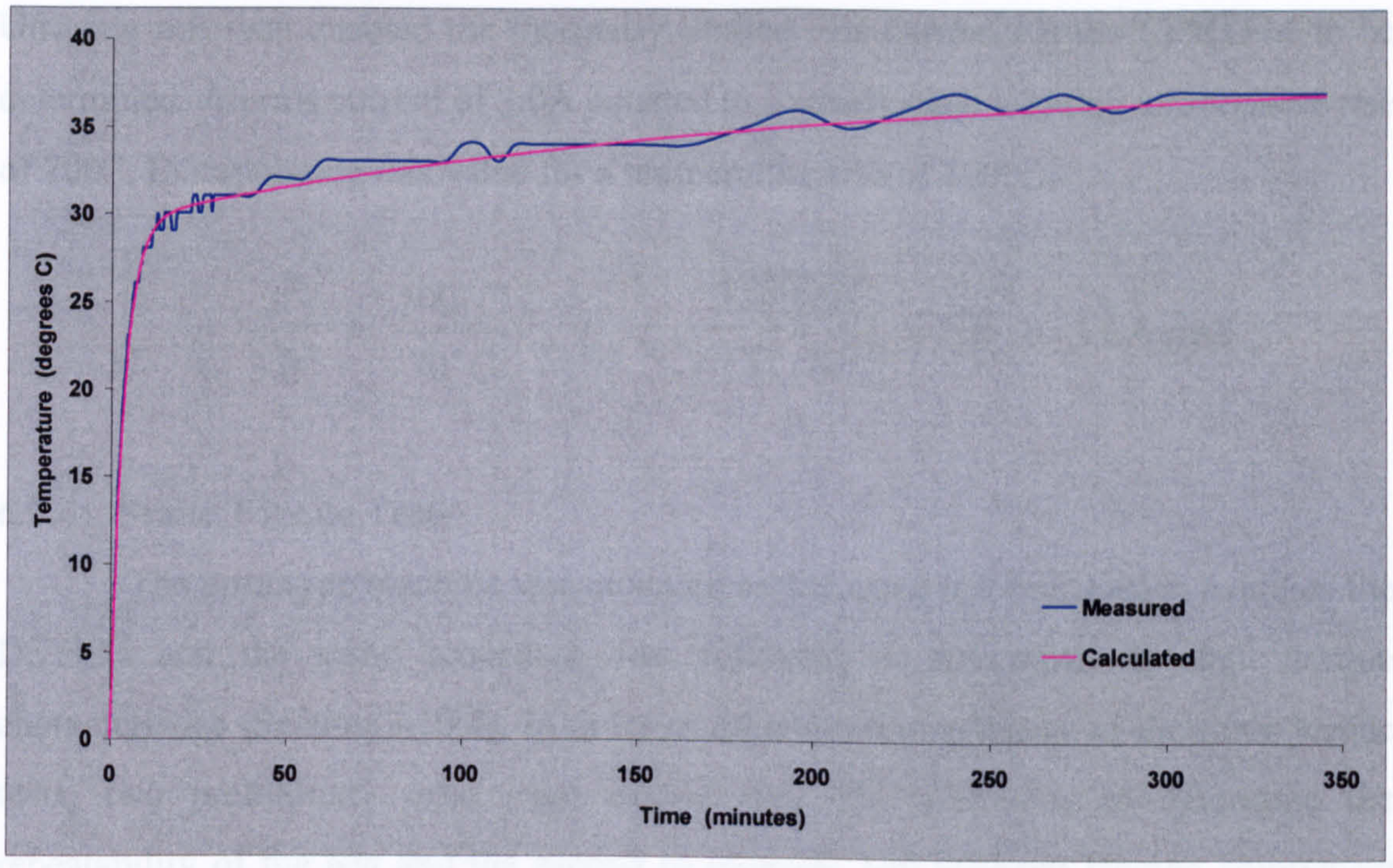

Figure 6.26 Measured and calculated exponential curves associated with the CPHTFM winding

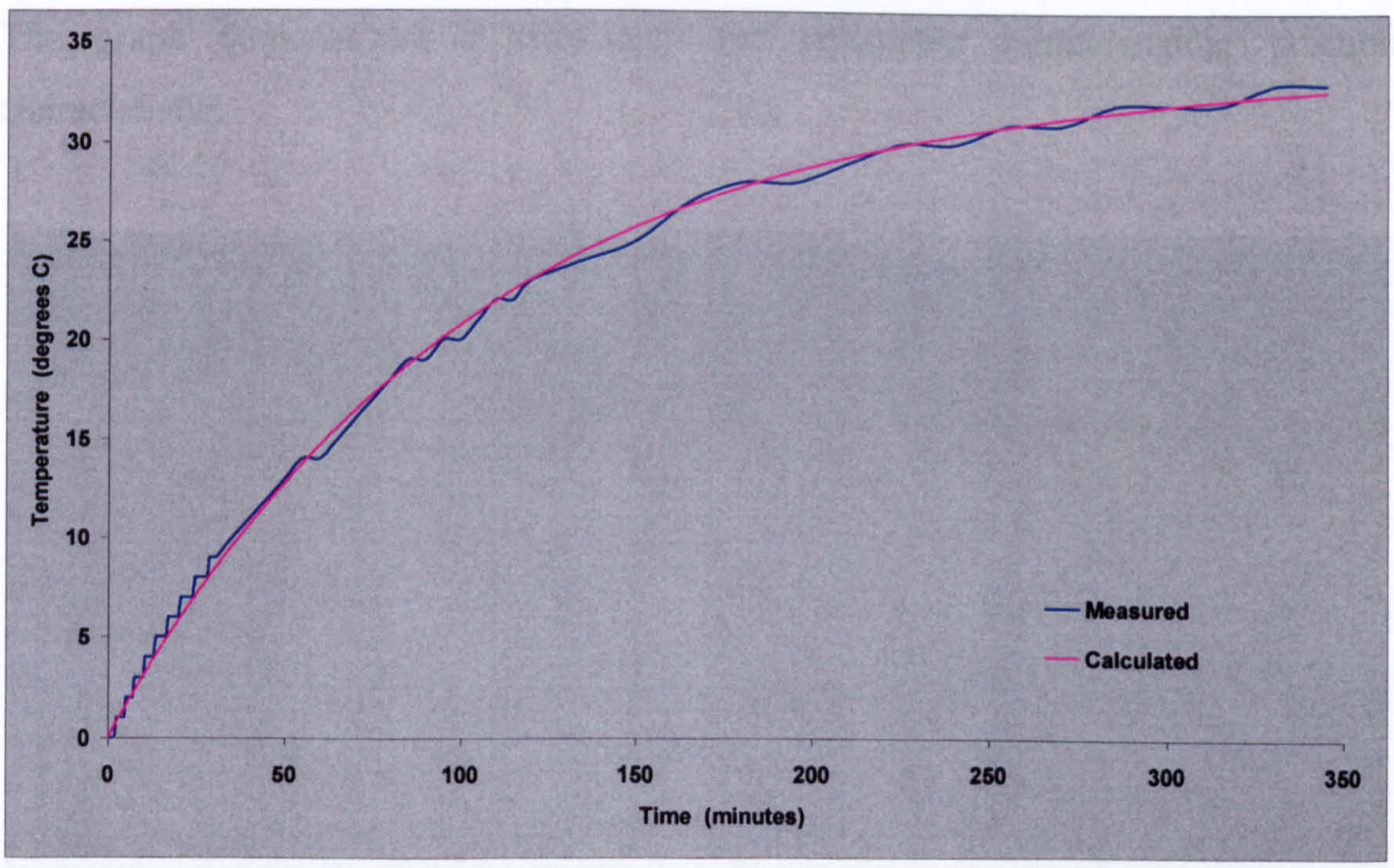

Figure 6.27 Measured and calculated exponential curves associated with the CPHTFM casing

actually exhibited two time constants, the most pronounced being 3.5 minutes. The second time constant was very much longer at 200 minutes. This second thermal time constant was due to a conduction path with a much larger thermal inertia. The most

likely source being the large aluminium hub to which the active rotor was attached. Utilising this data enabled the thermally limited rms current for the CPHTFM to be determined. An rms current of 3.0A equated to a steady state winding temperature rise of 70°C. Extrapolating this value for a temperature rise of 100°C:-

$$\frac{i^2}{3.0^2} = \frac{100^\circ C}{70^\circ C} \quad \therefore \quad i = \sqrt{\left(\frac{100}{70}\right)} \times 3.0 = 3.6\text{A rms}$$

6.7.4 Static Torque Tests

The prototype machine was mounted on the same test bed used to evaluate the DSTFM and the same procedure was followed to determine its static torque characteristics (Section 3.10.2). In order to ascertain the accuracy of the static torque tests, two preliminary tests were carried out. The first was to determine the repeatability of the test and the second to quantify any inherent friction component due to the PTFE sleeved bush. Figure 6.28 shows the magnitude of measured torque against angular position for two circumferentially consecutive poles of the CPHTFM. The graph demonstrates a consistent and repeatable torque/angular position characteristic.

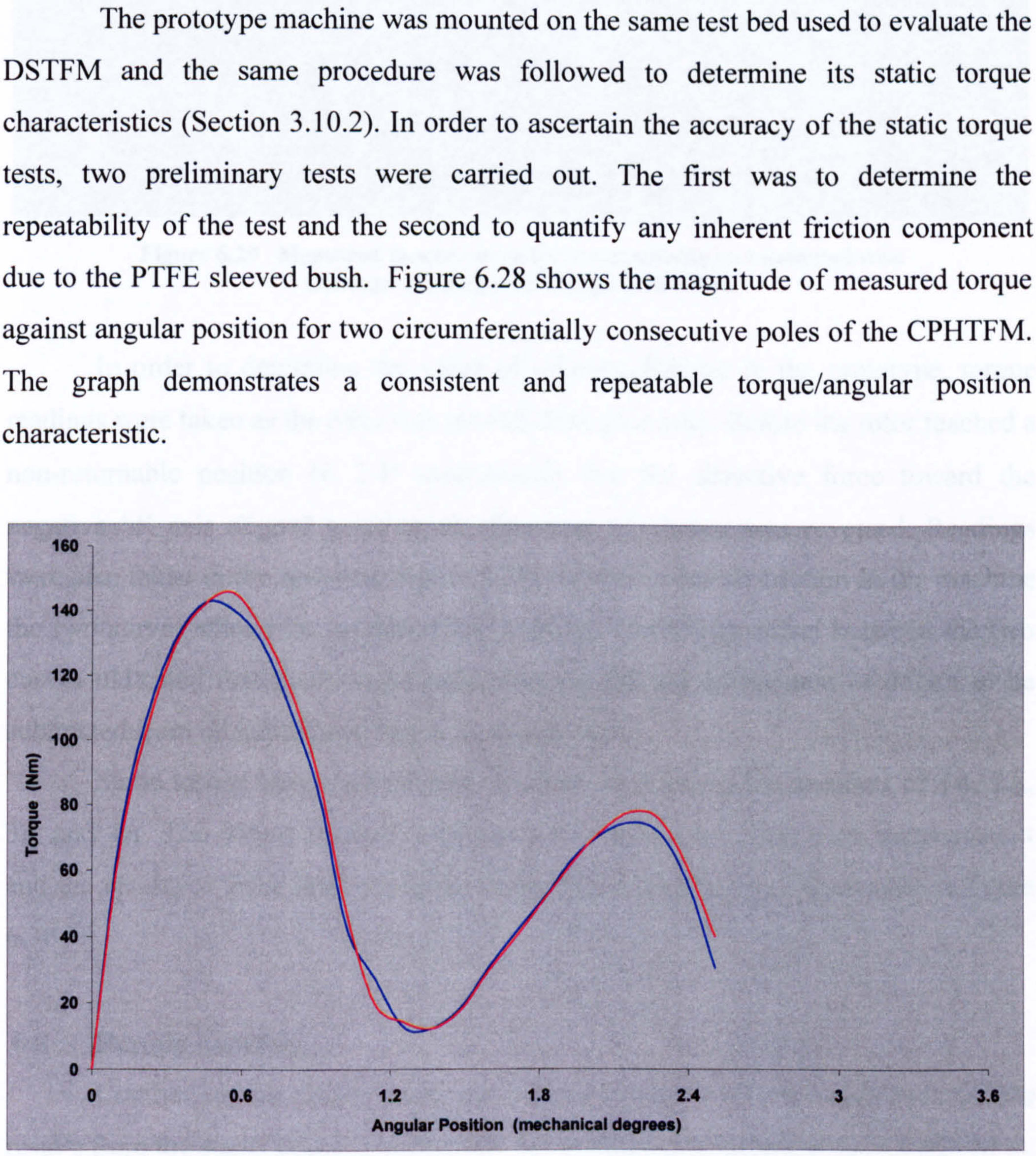

Figure 6.28 Measured torque curves for two consecutive poles of the CPHTFM

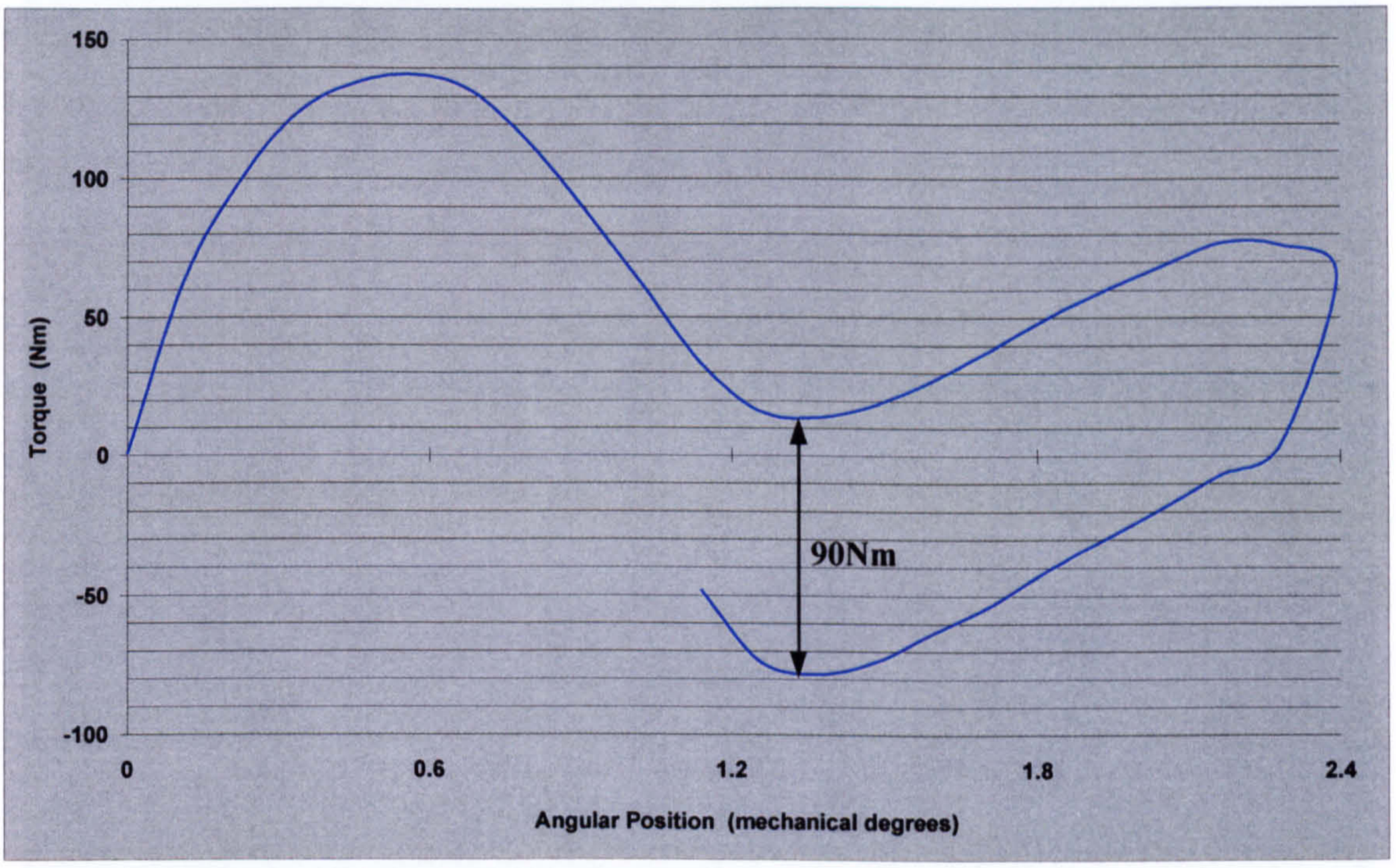

Figure 6.29 Measured torque curve from a clockwise and anticlockwise traverse of a single pole of the CPHTFM

In order to determine the value of inherent friction in the prototype, torque readings were taken as the rotor was moved through a pole. Before the rotor reached a non-returnable position (≡ 2.4° mechanical) due the attractive force toward the negative 'd' axis aligned position, its direction of rotation was reversed. Readings were also taken in the reversed (figure 6.29). If there were no friction in the machine the two curves should lie on top of one another. The 90Nm offset between the two curves indicated that there was a unidirectional friction component of 45Nm to be subtracted from all subsequent torque measurements.

Static torque tests were carried out at no load and at DC currents of 1A, 2A, 3A and 4A. The 45Nm friction component was subtracted from each measurement and the results of these tests are tabulated in Appendix E.3.9 and illustrated in figure 6.30.

6.8 Results Analysis

Combining the results from the thermal analysis of the machine with the results from the static torque tests enabled the working parameters of the CPHTFM to

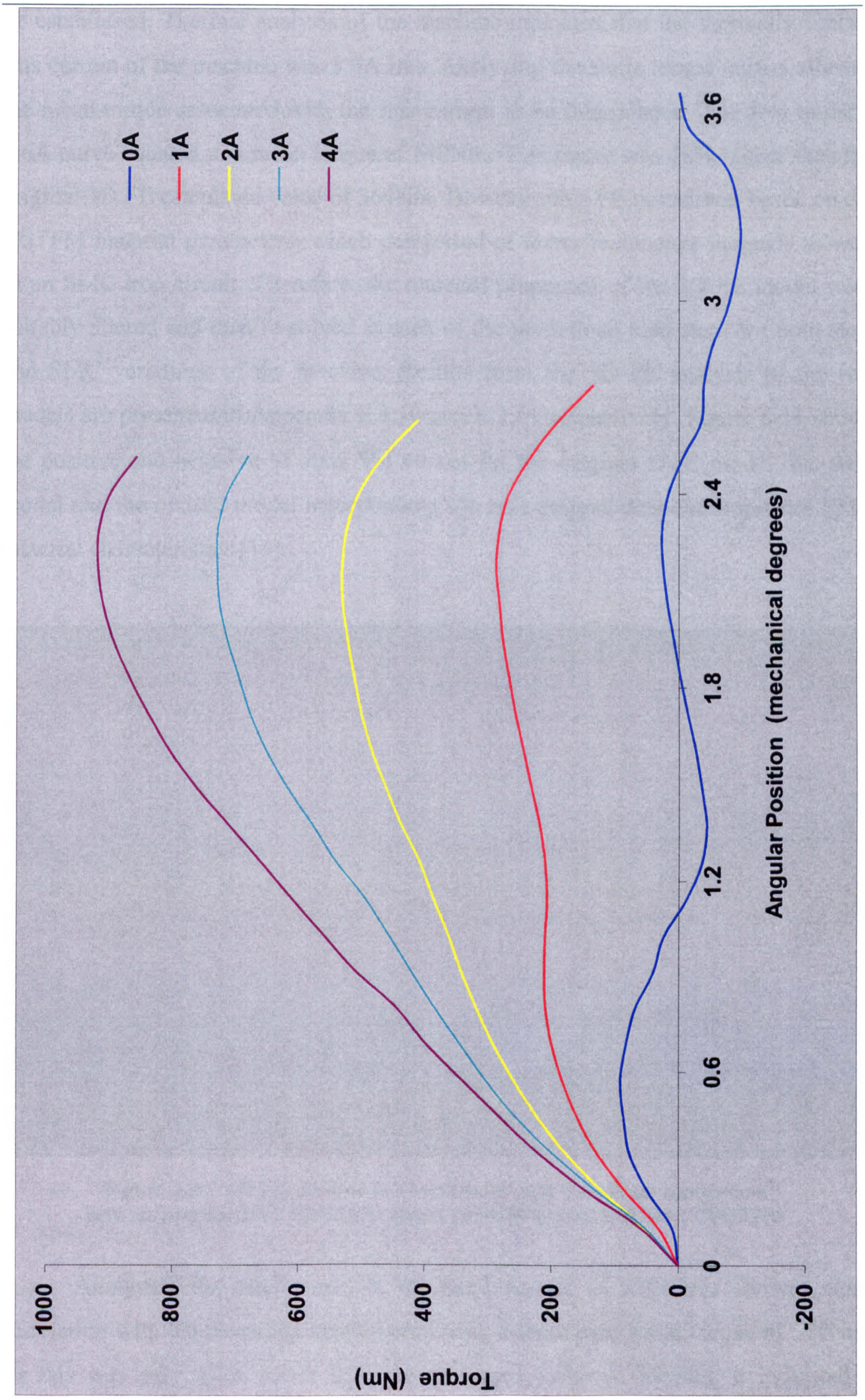

Figure 6.30 Measured static torque curves for the CPHTFM with the 45Nm friction component removed

be established. Thermal analysis of the machine indicated that the thermally limited rms current of the machine was 3.6A rms. Analysing the static torque curves allowed the mean torque associated with the rms current to be interpolated. The area under a 3.6A curve equated to a mean torque of 540Nm. This figure was 48% higher than the original 3D FE calculated value of 364Nm. However, this FE model was based on the DSTFM material parameters, which comprised of lower remanence magnets as well as an SMC iron circuit. Therefore, the material properties of the 3D FE model were suitably altered and then re-solved at each of the predefined load steps for both steel and SMC variations of the machine. Results from the 3D FE analysis of the two models are presented in Appendix E.3.10 and E.3.11 respectively. Figure 6.31 shows the positive and negative 'd' axis Ψ-I curves for the original SMC model, the steel model and the revised model incorporating the new magnet data and improved SMC material characteristics [14].

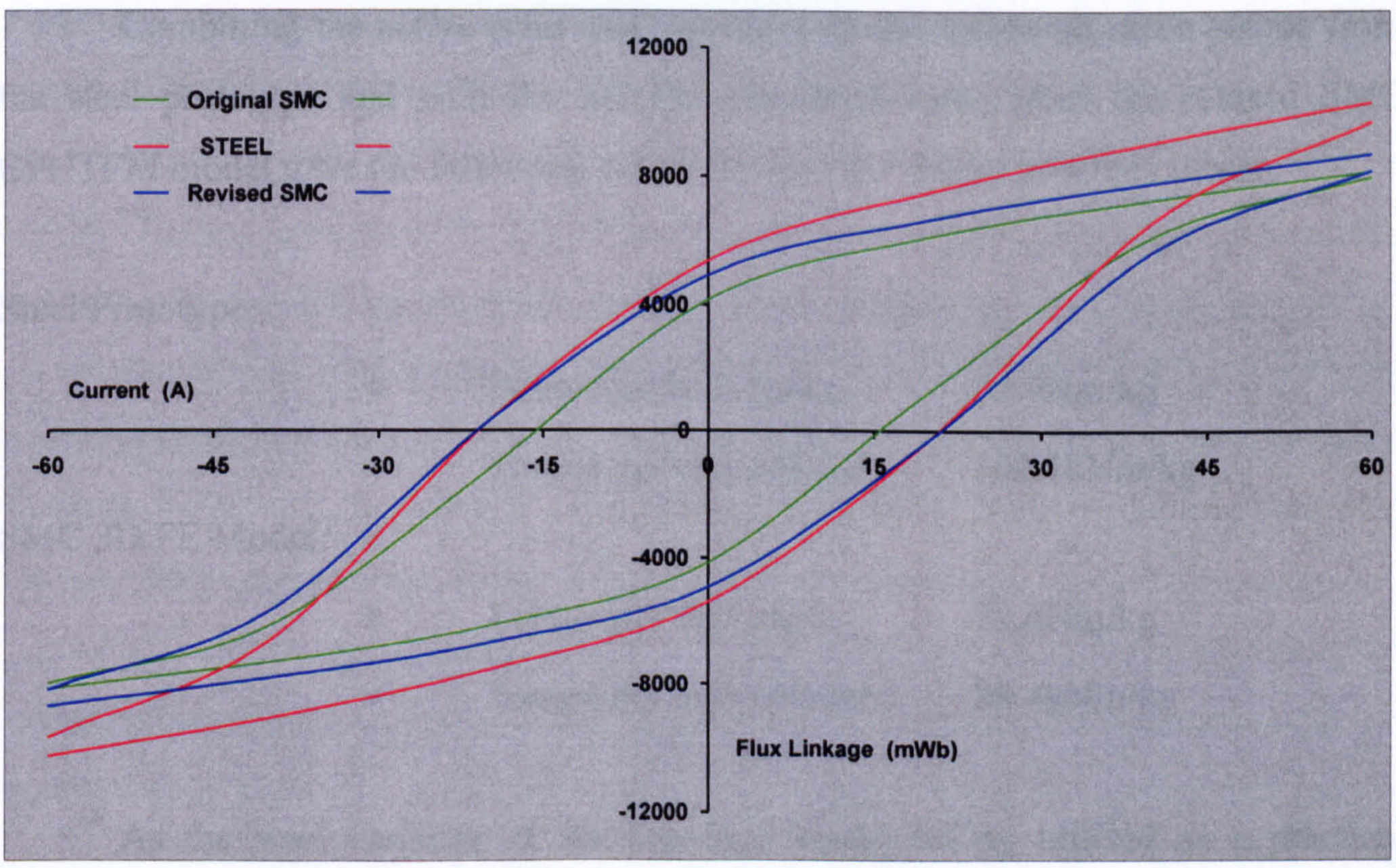

Figure 6.31 3D FE, positive and negative 'd' axis Ψ-I curves comparison between original SMC CPHTFM, steel CPHTFM and revised SMC CPHTFM

Analysing the steel model at the rated current of 3.6A rms showed close correlation with the measured results, producing a calculated mean torque of 518Nm. As this was only 4.1% lower than the measured value of 540Nm, it indicated a validation of the original SMC 3D FE model and the calculations based on that

model. The mean torque of the revised SMC CPHTFM model was calculated to be 467.4Nm.

The active components of the CPHTFM prototype were weighed in order to determine their mass (table 6.5). Active volume for the prototype was calculated at $5.289\times10^{-3}m^3$.

Table 6.5 Active masses of the CPHTFM prototype components

Rotor Iron	4.17kg
Stator Coreback	7.52kg
Stator Rings	5.19kg
Copper Conductor	1.91kg
Magnets	2.05kg
Total Active Mass	**20.84kg**

Combining the active mass and volume with the measured mean torque from the steel prototype and with the 3D FE calculated value from the revised SMC CPHTFM model gave the following values for specific output at rated current.

Steel Prototype:

- Torque per unit mass, 25.9Nm/kg
- Torque per unit volume, 102.1kNm/kg

SMC 3D FE Model:

- Torque per unit mass, 22.4Nm/kg
- Torque per unit volume, 88.4kNm/kg

As the steel variation of the topology could not be utilised as a practical rotating machine, the final 3D FE model, which incorporated the correct electric and magnetic loadings, was used to evaluate the CPHTFM.

Table 6.6 compares the five, 100 pole, TFM topologies that were investigated in Chapters 3, 5 and 6. The CPHTFM outperformed each of the alternative geometries in each classification. Its closest rival was the mechanically more complicated DSTFM, yet this still exhibited 30% less mean torque, a 15% reduction in power factor and a 29% lower torque per unit mass.

Table 6.6 Comparison of 3D FE generated results for five TFM topologies

TFM Model	Thermally Limited Mean Torque (Nm)	Power Factor	Torque per Unit Mass (Nm/kg)
CPHTFM	467.4	0.441	22.4
DSTFM	327.2	0.374	15.87
CPTFM	196.2	0.179	9.3
SSBTFM	140.1	0.305	9.27
SSTFM	131.8	0.294	9.28

6.9 Conclusions

A unique TFM topology based upon a claw pole geometry has been designed, constructed and tested, both practically and through extensive 3D FE analysis. For expediency, the magnetic circuit of the prototype test machine was fabricated from steel. Given this fact, the prototype was tested using a static test rig and DC current levels. Thermal analysis of the prototype machine, coupled with the results from static torque tests, enabled the rated rms output of the machine to be determined. A 4% correlation between the measured and calculated results ratified the 3D FE analysis and from this the predicted parameters of a dynamic version of the topology, utilising SMC materials in its iron circuit, were derived. Predicted power factor was improved by up to 59% over existing TFM variants under investigation.

The initial specification for the CPHTFM demanded a geometry with low armature leakage fields, a single radial airgap and low rotor pole to pole leakage. If these criteria were met, a machine with a high specific output, a relatively simple mechanical construction and an improved power factor would be the result. The CPHTFM design has fulfilled the first two of these requirements well, with some small reduction in the effect of the third. However, the overall result has been to produce a single-sided, radial airgap machine, with an improved power factor and a specific output 41% higher than its nearest TFM rival.

Chapter 7

Conclusions

7.1 General

The Transverse Flux Machine has the ability to fulfil an important role in the field of high torque, direct drive applications. A significantly high specific output also indicates the possibility of its use in areas where space is limited, or mass is a critical factor. However, the inherently low power factor exhibited by all TFMs is a major disadvantage with regard to the power rating requirements of its electronic drive components. This low power factor is the fundamental price of the high per pole MMF that enables these topologies to produce such large specific outputs. The specific output of these machines belies the fact that approximately half (51% in the CPHTFM) of the source magnet flux is lost in leakage flux fields around the rotor magnet and so never links with the stator winding. Therefore, further work into the limitation of this flux loss mechanism could produce radical improvements in both output and power factor.

Comparisons between the practical experimentation carried out and the non-linear 3D FE analysis, has validated the accuracy of the 3D FE models produced, and given credence to the detailed investigations into the flux distribution in the various TFM topologies that were examined. The use of Soft Magnetic Composite (SMC) materials throughout this research has freed the author from the dimensional design constraints imposed by a laminated steel magnetic circuit. However, the relatively low permeability of SMC when compared even to mild steel, does limit its output capabilities. This lower permeability can be compensated for by the isotropic nature of the material, which enables more iron to be incorporated into the magnetic circuit, delaying the onset of magnetic saturation.

7.2 Two Dimensional Finite Element Analysis

The 2D methodology developed to evaluate the performance of TFMs showed that it could produce results within 10% of those derived from the more rigorous process of 3D finite element analysis. Successful comparisons were made between 3D

FE solutions and the new 2D methodology-derived solutions for two separate DSTFM topologies. The gradients and energy envelopes of the Ψ-I curves determined from the 2D solutions were similar enough to those of the 3D FE that the 2D model could also be used to predict the level of armature reaction and hence the power factor in a topology. With similar saturation levels to those in the 3D model, the areas of saturation in the 2D model could be used to indicate where the 3D model should be adapted in order to minimise saturation losses.

It was felt that use of this methodology in the initial stages of new TFM analysis would be a worthwhile exercise, allowing the time set aside for the evaluation of a new topology to be used for additional optimisation before subjecting the model to more exacting 3D analysis.

7.3 The Double-Sided Transverse Flux Machine

After extensive 3D FE analysis, a double-sided transverse flux machine was designed and a non-rotating prototype constructed with the active iron parts of the machine fabricated from SMC material (ABM100.32). Combining results from thermal and static torque testing of the prototype showed that for a thermally limited 100°C rise the machine produced a mean torque of 327Nm. There was good correlation between the theoretical and practical analysis of the prototype, with an error of only 6% between the two sets of data in the region of the thermal limit.

Static torque analysis revealed a twice frequency saliency torque. This was attributed to two positions of rotor/stator alignment or stability over a single pole pitch. These positions corresponded to the positive (or negative) 'd' axis and to the positive (or negative) 'q' axis. Stability was maintained in this 'q' axis position by leakage flux around the axial face of a magnet linking with a stator tooth. The effect of this saliency torque when coupled with the machine's interaction torque was to offset the angle at which peak torque was produced.

Power factor for the machine, which was determined from the positive and negative 'd' axis Ψ-I curves generated from the 3D FE analysis, showed a disappointingly low value of 0.37 at the thermal limit. Despite this poor power factor, calculation of specific outputs for the DSTFM revealed a very high value of torque

per unit volume and a thus far unprecedented level of torque per unit of active mass. These two figures were respectively:

- Torque/unit volume = 52945Nm/m^3
- Torque/unit mass = 14.41Nm/kg

7.4 The Claw Pole Transverse Flux Machine

A prototype Claw Pole Transverse Flux Machine (CPTFM), exhibiting a torque per unit of active mass of 2.02Nm/kg was built and tested. In order to investigate the machine a range of 3D FE models were produced and evaluated. A close correlation was found between the theoretical 3D FE results and the measured values from the prototype machine. Consequently, the 3D FE model was employed to analyse the overall flux distribution in the CPTFM. This analysis revealed a number of distinct rotor and stator flux leakage paths. The most substantial of these were, respectively, the magnet leakage fields which accounted for 27% of the source magnet generated flux and the interpolar leakage path which permitted another 25% of the magnet flux to bypass the coreback.

The established accuracy of the three dimensional model, permitted further investigation into the CPTFM's fundamental parameters. The effect of pole number on machine performance showed that the rate of change of flux linkage and hence torque production of the CPTFM rose proportionally with pole number, but only at lower excitation levels. At higher MMFs, the armature reaction fields set up in the machine severely limited the value of $d\Psi/d\theta$. The impact of pole number on mean output of the CPTFM showed that the 24 poles of the prototype were close to ideal for this machine.

A series of 3D FE models were produced to investigate the importance of tooth width and shape. The circumferentially tapered teeth in the prototype CPTFM covered 120° electrical. This shape of tooth was directly compared with a rectangular profile tooth also with 120° pole arc coverage. Although there was a negligible difference in output between the two models, the airgap surface area of the rectangular profiled tooth was 11% smaller. It was shown that despite a larger surface area the output of the tapered tooth model was reduced because of increased airgap leakage flux. The effect of varying pole arc coverage showed little increase in net

output, as increased airgap surface area was generally offset by increased interpolar leakage.

An investigation was also carried out into the consequences of converting the existing, surface mounted permanent magnet rotor, into a flux concentrating permanent magnet rotor. This study showed that at light load, an improvement of the order of 5% in output could be made from using a flux concentrating configuration.

At 0.84, the power factor of the CPTFM was found to be much higher than that of its fellow TFMs. This elevated value was attributed to poor thermal performance in the prototype, which meant that the rated current for the CPTFM was low. As the machine was operating at a reduced level of electric loading, power factor produced by the 3D FE model was high.

7.5 Comparative Transverse Flux Machine Analysis

Four representative TFM topologies were selected and their 3D FE models constructed and analysed. Each model was established around benchmarked parameters to enable fair comparative evaluation between them. The models under scrutiny were:

- Single-Sided TFM (SSTFM)
- Single-Sided with Bridges TFM (SSBTFM)
- Claw Pole TFM (CPTFM)
- Double-Sided TFM (DSTFM)

Analysis of the four topologies revealed three major design requirements for an improved TFM geometry.

- Low armature leakage fields
- Low rotor pole to pole leakage
- Single radial airgap

Armature leakage fields tended to propagate most readily through interpolar leakage paths and so it was felt that a reduction in the effect of these paths would reduce the armature leakage and so improve both power factor and specific output. Utilising all of the magnets simultaneously, and in the case of surface mounted

configurations (SSTFM) reducing the pole arc of each magnet, would serve to limit rotor pole to pole flux leakage fields. A reduction in the viability of these flux leakage paths increased the flux travelling through the coreback and so increased specific output. From a construction/production standpoint a single radial airgap simplified the assembly process, as a single-sided machine with one radially active airgap would be much easier to produce than a machine with one or more axially active airgaps.

7.6 The Claw Pole Hybrid Transverse Flux Machine

A unique TFM topology based upon a claw pole geometry was designed and tested, both practically and through extensive 3D FE analysis. The innovation behind this new topology was that it allowed the claw teeth of the stator to be shortened, thus reducing their overlap and considerably reducing interpolar leakage flux. Additional flux was channelled axially along the rotor iron pole pieces to the stator teeth, compensating for their reduced area. For expediency, the magnetic circuit of the prototype test machine was fabricated from steel. Given this fact, the prototype was tested using a static test rig and DC current levels. Thermal analysis of the prototype machine, coupled with the results from static torque tests, enabled the rated rms output of the machine to be determined. A 4% correlation between the measured and calculated results ratified the 3D FE analysis and from this the predicted parameters of a dynamic version of the topology utilising SMC materials for its iron circuit were derived.

The initial specification for the CPHTFM demanded a geometry with low armature leakage fields, a single radial airgap and low rotor pole to pole leakage. If these criteria were met a machine with a high specific output, a relatively simple mechanical construction and an improved power factor would be the result. The single-sided, radial airgap, prototype design delivered a predicted power factor improvement of between 15% and 59% over the alternative TFMs under investigation and at 22.4Nm/kg, a specific output 41% higher than its nearest TFM rival.

7.7 Goals and Achievements

The aim of this thesis was to understand the characteristics of the Transverse Flux Machine and use that knowledge to design and build a TFM with the ability to outperform all existing TFM topologies.

To fulfil this task a large amount of detailed analysis has been carried out on a number of major TFM topologies: the Single-Sided TFM, the Single-Sided Bridged TFM, the Claw Pole TFM and the Double-Sided TFM. Studies involved some 2D FE work, but was mainly driven by non-linear 3D FE analysis of the topologies. Some of the areas covered in the course of the investigation were the effect of:

- Pole number
- Circumferential tooth overlap of rotor magnets
- Circumferential tooth width
- Axial tooth overlap
- Radial rotor magnet depth
- Stator coreback thickness
- Airgap length

In order to validate the extensive 3D FE analysis that was carried out, three prototype machines were built.

1. Double Sided TFM (DSTFM)
2. Claw Pole TFM (CPTFM)
3. Claw Pole Hybrid TFM (CPHTFM)

Both the DSTFM and CPHTFM were non-rotating 100 pole, single phase machines, whilst he CPTFM, was a 24 pole, single phase, rotating machine. Analysis of these machines took the form of static torque and thermal tests. The results from these practical measurements enabled validation of both 2D and 3D FE analysis. There was a close correlation between practical and theoretical work, which meant that further FE investigations into these machines could be carried out with confidence.

This three-year study of Transverse Flux Machines has established a detailed picture of how this family of machines operate and has enabled a totally original Transverse Flux Machine, displaying an extremely high specific output, to be designed and developed.

Appendix A

The Use Of Powder Metallurgy In Transverse Flux Machines

A.1 Introduction

One of the first examples of the use of Powder Metallurgy (PM) in an electrical engineering context was by Fritts in 1880 [30]. At the same time as Thomas Edison was suggesting the application of thin sheet steel laminations for the construction of machine cores, Fritts was producing soft magnetic cores from iron particles bonded and compacted together in a wax medium. Because this type of powdered core exhibited good high frequency characteristics it was used in radio engineering until it was superseded by soft magnetic ferrites. The production process, involves the compaction of granular metal powder to form either blocks of composite material in a predefined shape, or ingots which can be machined to shape.

In the field of electrical technology, the processes and materials of PM have been developed to such a stage over the last decade that machinable blocks of material can now be produced, which are effectively isotropically laminated.

For the electromagnetic design engineer, these Soft Magnetic Composite (SMC) materials offer a number of advantages over conventional steel laminations, although they do however have some shortcomings. Historically, one of the major advantages of PM production is the small amount of waste in both material and production time. This is because individual parts can be pressed to high precision tolerances without the need for any further machining which would entail both additional material and man-hours. This means that production is more economical, especially on long component runs. In the traditional production of iron cores for electrical machines, the level of waste encountered whilst punching out laminations can be as high as 60% or sometimes even 80% [18]. The assembly of the laminations themselves to produce a finished core is also a time consuming and complicated task. Therefore, streamlining of production techniques by the use of SMC materials can offer major profit increases in machine manufacture. However, the main technological

advantage of SMC materials, is their ability to support three dimensional magnetic fields and three dimensional thermal paths. Steel laminations will only facilitate magnetic flux flow along parallel two dimensional paths. These laminations also restrict the majority of thermal conduction to this parallel plane, with conduction normal to the plane generally an order of magnitude lower. This plane restriction in thermal conductivity is not usually a problem as heat is designed to be removed radially through the coreback. However, this is not the case with end or airgap windings. Due to the absence of iron around end windings, heat tends to flow back into the core, increasing its temperature. Encasing these regions in SMC material would lower the overall core temperature whilst aiding thermal dissipation to the casing. The isotropic magnetic properties of SMC materials are what make them so attractive when designing and constructing TFMs [16]. They allow an unprecedented freedom of movement of flux and so allow an entirely new range of topologies to be envisioned.

The disadvantages of SMC materials become apparent when their loss mechanisms are compared with those of laminated steels. The total loss in two iron cores; one built from high grade steel laminations, and one from SMC will be markedly different [49] with the SMC core displaying a total loss at lower frequencies (<500Hz) of up to 2 - 3 times more than that of the laminated core. This elevated level of loss is mainly caused by SMC materials having a much higher hysteresis loss than laminated steel. However, the situation is reversed as higher frequencies are reached (>1.2kHz) as frequency increases the eddy current loss in the laminated steel also increases whereas in the SMC this loss remains relatively constant.

A.2 Basic Production Technique

The principle behind SMC material is the electrical insulation and subsequent bonding of individual granules of iron. The insulation of the iron is achieved using a chemical reaction, which coats each 50-100μm diameter grain of iron with a layer of insulation approximately 15nm thick [31]. The depth of this coating is calculated to be thick enough to prevent eddy current propagation, yet thin enough that the attainable space factor of the finished material is not unduly affected. The basic production methods for SMC materials are well documented [16, 27, 31]. However, a brief description of the process at this stage would be appropriate. A composite mix of coated powdered iron and additives, namely a lubricant to reduce wear on the

compacting tools and a phenolic resin in order to increase the mechanical strength of the finished material, are delivered into a die where they are compacted at high pressure. This "Green", or uncured, material is then heat treated up to 500°C to complete the production process.

A.2.1 Effect of Pressure

The pressure exerted on the composite mix during the compacting process is between 600 and 800MPa [14]. The lower, 600Mpa, limit is predetermined by the need for adequate cohesion and strength in the finished material. However, the upper pressure limit is purely dependent upon the physical constraints of the die holding the charge. The higher the pressure exerted upon the composite mix the more dense the final product, and hence the better its space factor. A compaction pressure of 800MPa will typically produce a material with a density of 7.1g/cm^3 (common steels have a density of around 7.6g/cm^3). The density of compacted material has a marked effect on its permeability [27], with low density equating to a poor space factor and a permeability measured in hundreds, rather than in the thousands as attained by some high quality lamination steels.

A.2.2 Effect of Temperature

There are two main reasons; magnetic and physical, for heat-treating the material after it has been compacted. The physical benefits to material from being cured are that heat treating increases the final bond strength of the thermosetting resin added in the original composite mix [31]. From an electromagnetic perspective, the heat treatment of the solid powdered iron core provides partial stress relief within the material [31]. This stress relief allows the domains/grains greater freedom to orientate themselves when they are exposed to an alternating magnetic field, which in turn reduces hysteresis loss. As with compacting pressures, there are limitations on the temperature that the "Green" material can be cured at. The maximum temperature used in curing the material is 500°C, anything in excess of this value will be detrimental to the insulation coating the iron granules.

A great deal of research and development is being carried out in this field and consequently the performance and quality of SMC materials are improving all the time.

Appendix B

Materials Data

B.1 Double Sided Transverse Flux Machine

Permanent Magnets

The 100 Neodymium Iron Boron magnets used in the DSTFM had the following characteristics:

Residual Flux Density:	1.2 Tesla
Relative Permeability:	1.19
Max Coercive Force:	802 kA/m
Curie Temperature:	100°C (non-linear)
Dimensions:	(30 x 15 x 3) mm

Rotor and Stator Iron

The SMC material used in the iron circuit of the DSTFM was ABM100.32. Supplied by Swedish powder metallurgy company, Höganäs.
(Contact details: S-263 83, Höganäs, Sweden. Telephone: +46 42 33 80 00).

The material has very high compressive strength, a Tensile strength of 20N/mm², and very little resistance to shear stress. The first quadrant B-H characteristic and data for the material is reproduced in figure B1 and the specific B-H data in Table B1.

Table B1. B-H data for ABM100.32

H	0	1000	2000	3000	4000	6000	8000	10000	15000
B	0	0.53	0.88	1.03	1.11	1.21	1.27	1.32	1.41
H	20000	30000	40000	50000	60000	70000	80000	90000	100000
B	1.475	1.555	1.62	1.67	1.71	1.74	1.76	1.78	1.79

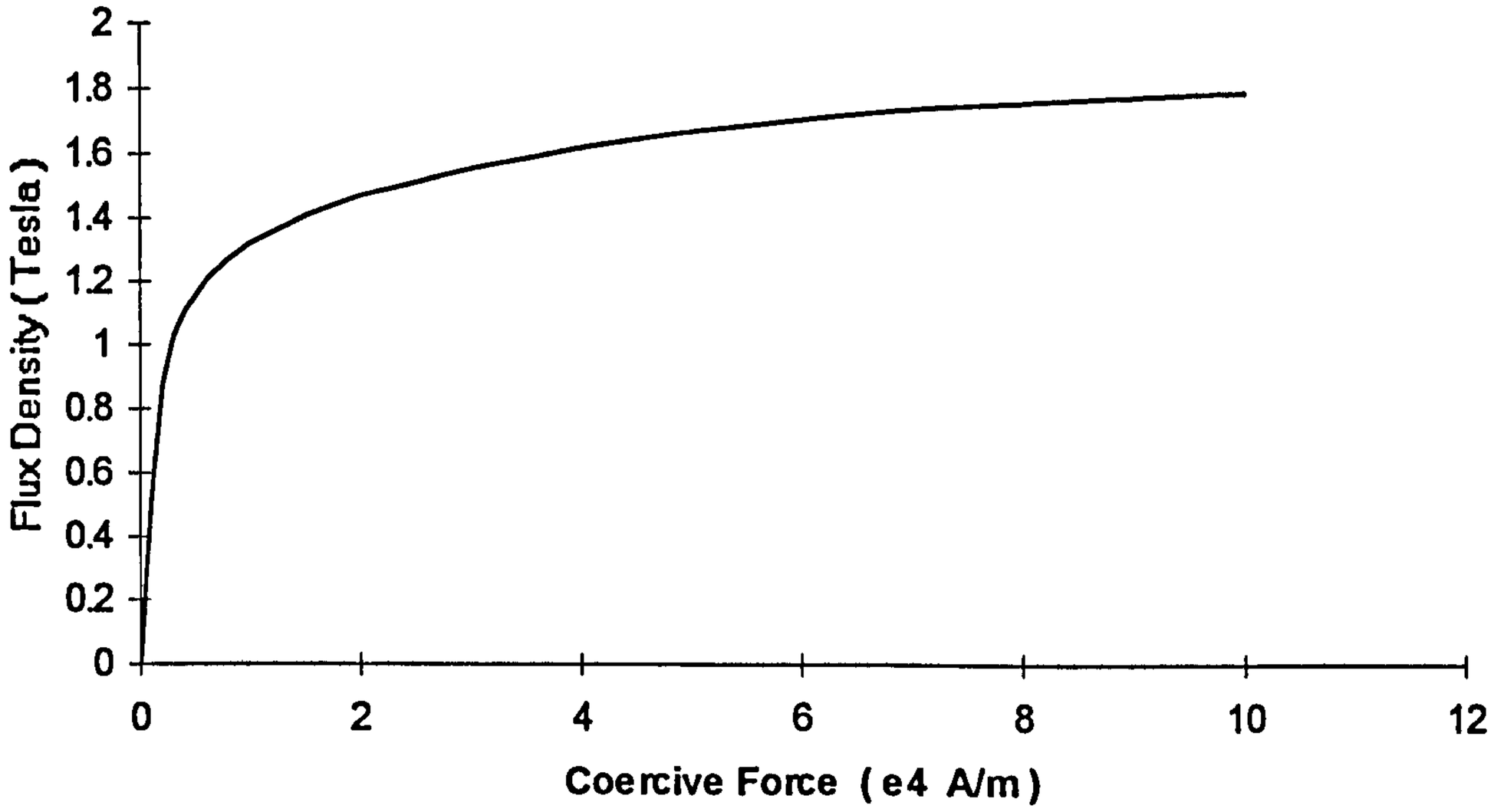

Figure B1. B-H characteristic for ABM100.32

Conductor Insulation

The flat copper conductor used in the DSTFM was electrically insulated with a Polyamide self adhesive tape, exhibiting the following characteristics.

- Backing: Polyamide
- Adhesive: Thermosetting Silicon
- Thickness: 0.06mm
- Tensile Strength: 5.3 kg/cm
- Elongation at Break: 70%
- Adhesion to Steel: 2.6 N/10mm
- Electric Strength: 120 kV/mm
- Insulation Resistance: 10^7 MΩ
- Specifications: UL recognised
- Temperature Range: -20°C to +310°C
- Cures: 24hrs at +230°C

[curing only required if tape to be used under extreme conditions]

B.2 Claw Pole Transverse Flux Machine

Permanent Magnets

The 24 Neodymium Iron Boron magnets used in the CPTFM had the following characteristics:

Residual Flux Density:	1.2 Tesla
Relative Permeability:	1.19
Max Coercive Force:	802 kA/m
Curie Temperature:	100°C (non-linear)
Dimensions:	(37.3 x 15.2 x 3.5) mm

Stator Iron

The SMC material used in the iron circuit of the CPTFM was ABM100.32. Supplied by Swedish powder metallurgy company, Höganäs.
(Contact details: S-263 83, Höganäs, Sweden. Telephone: +46 42 33 80 00).

The material has very high compressive strength, a Tensile strength of 20N/mm², and very little resistance to shear stress. The first quadrant B-H characteristic and data for the material is reproduced in figure B1 and the specific B-H data in Table B1.

B.3 Claw Pole Hybrid Transverse Flux Machine

Permanent Magnets

The 100 Vacodym 362HR Neodymium Iron Boron magnets used in the CPGTFM were supplied by Vacuumschmelze Hanau, Grüner Weg 37, D – 63450, Hanau, Germany. Each magnet has the following characteristics:

Residual Flux Density:	1.33 Tesla
Relative Permeability:	1.02
Max Coercive Force:	1277 kA/m
Curie Temperature:	120°C (non-linear)
Dimensions:	(60 x 15 x 3) mm

Appendix C

Technical Drawings and Schematics

C.1 Double Sided Transverse Flux Machine

Stator Side Plate

(Require 100 off)

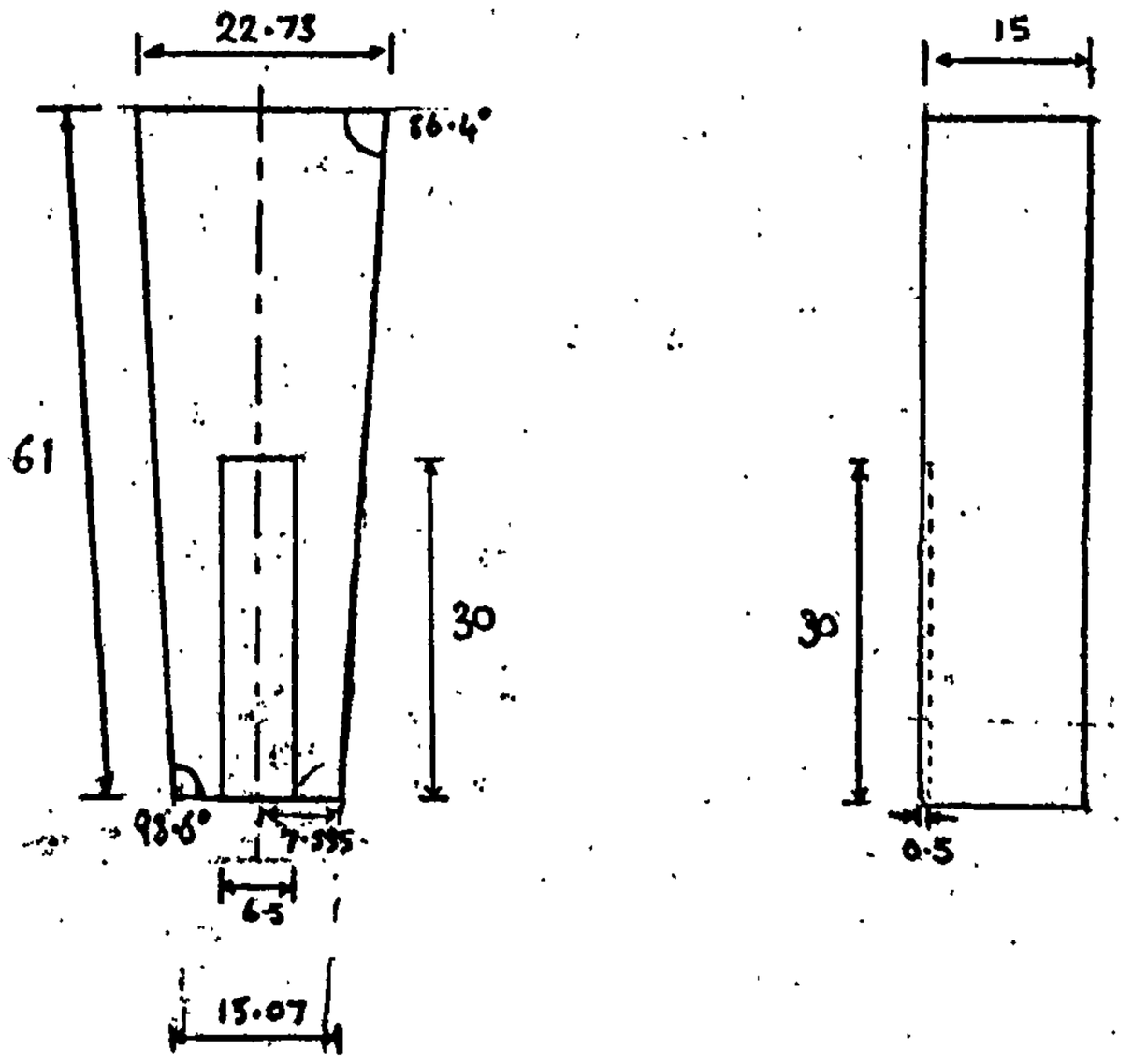

Stator Tooth

(Require 100 off)

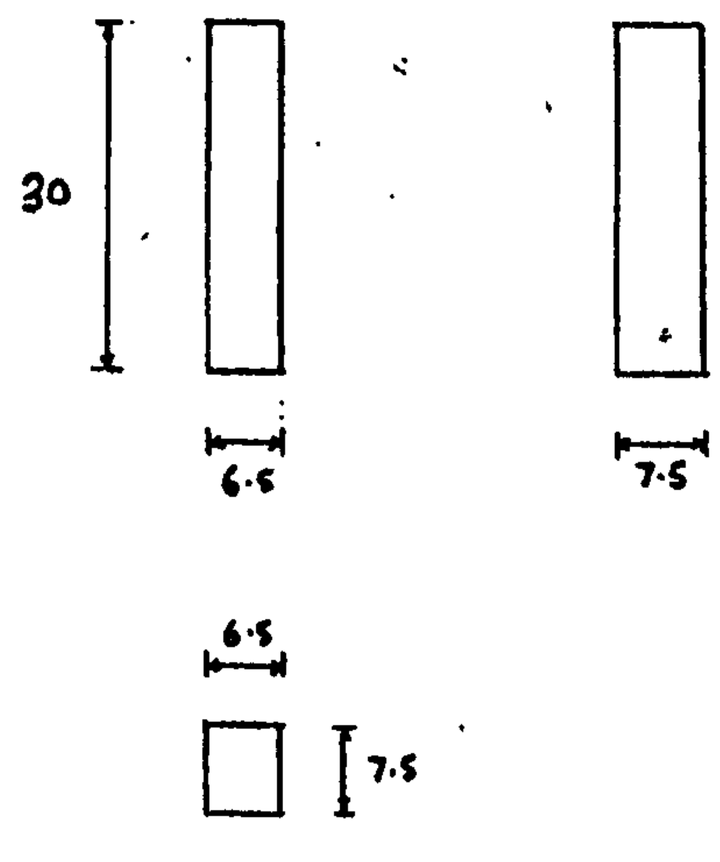

C.1 Double Sided Transverse Flux Machine (cont)

Stator Top Plate

(Require 50 off)

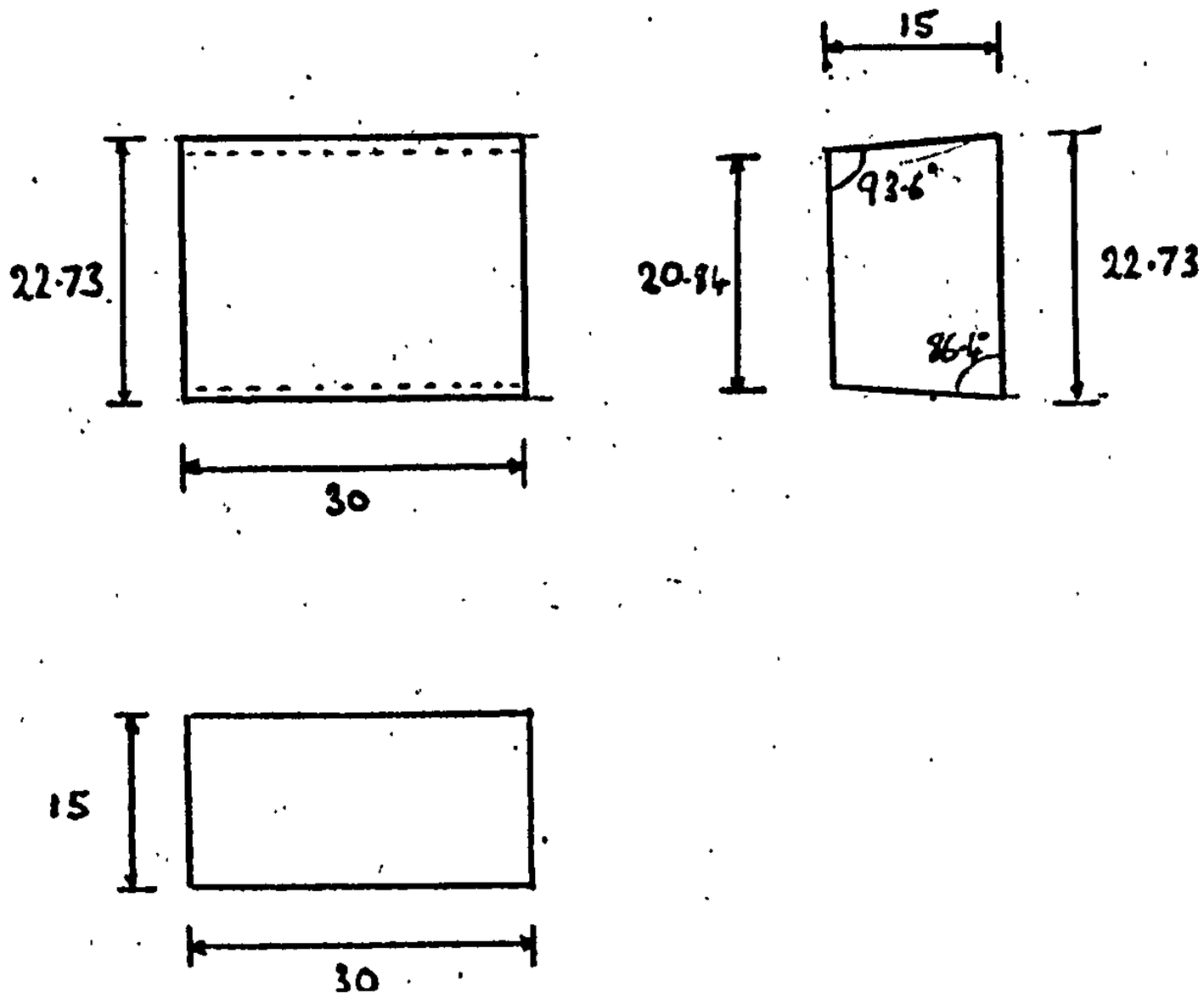

Rotor Segment

(Require 100 off)

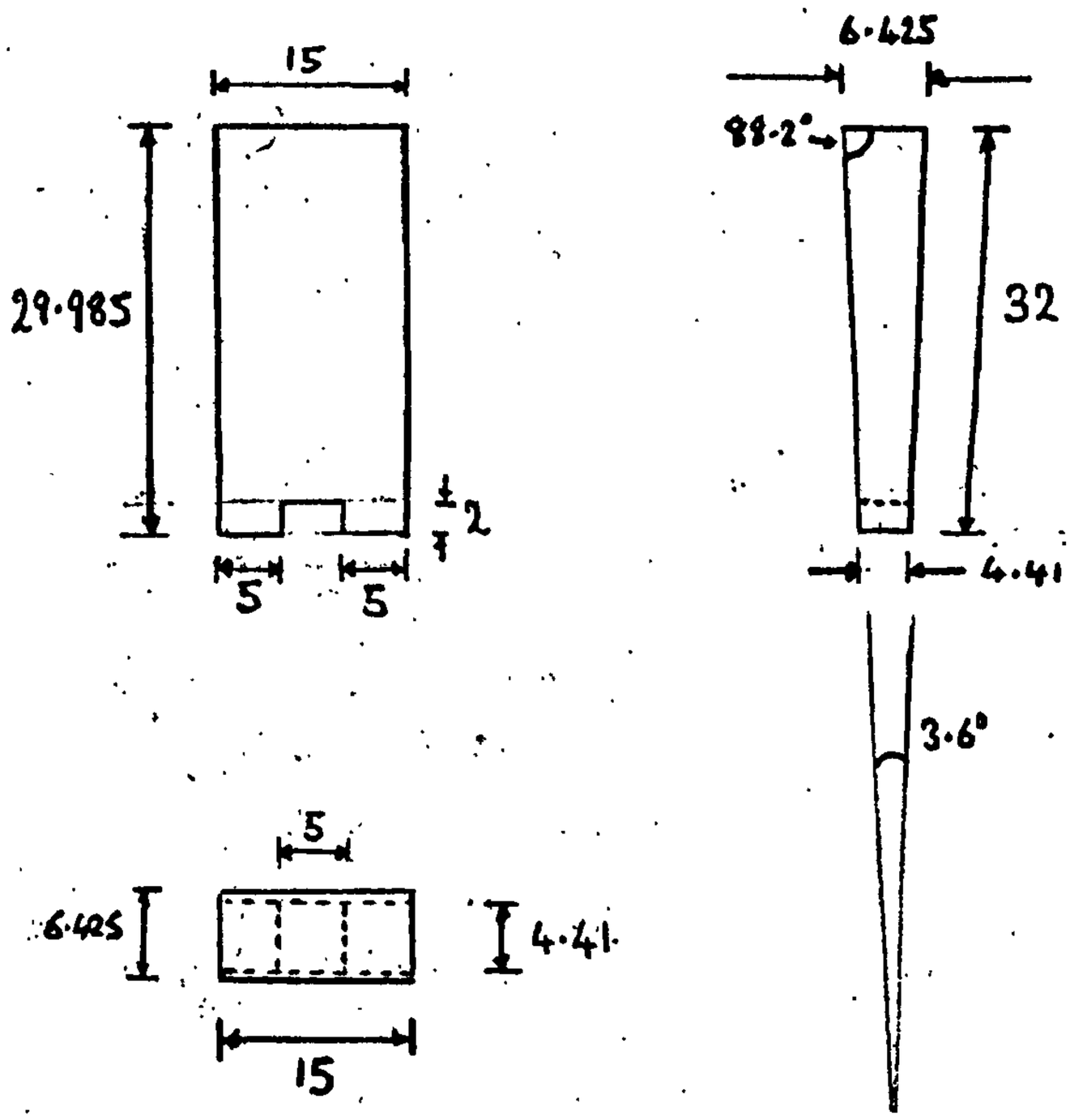

C.1 Double Sided Transverse Flux Machine (cont)

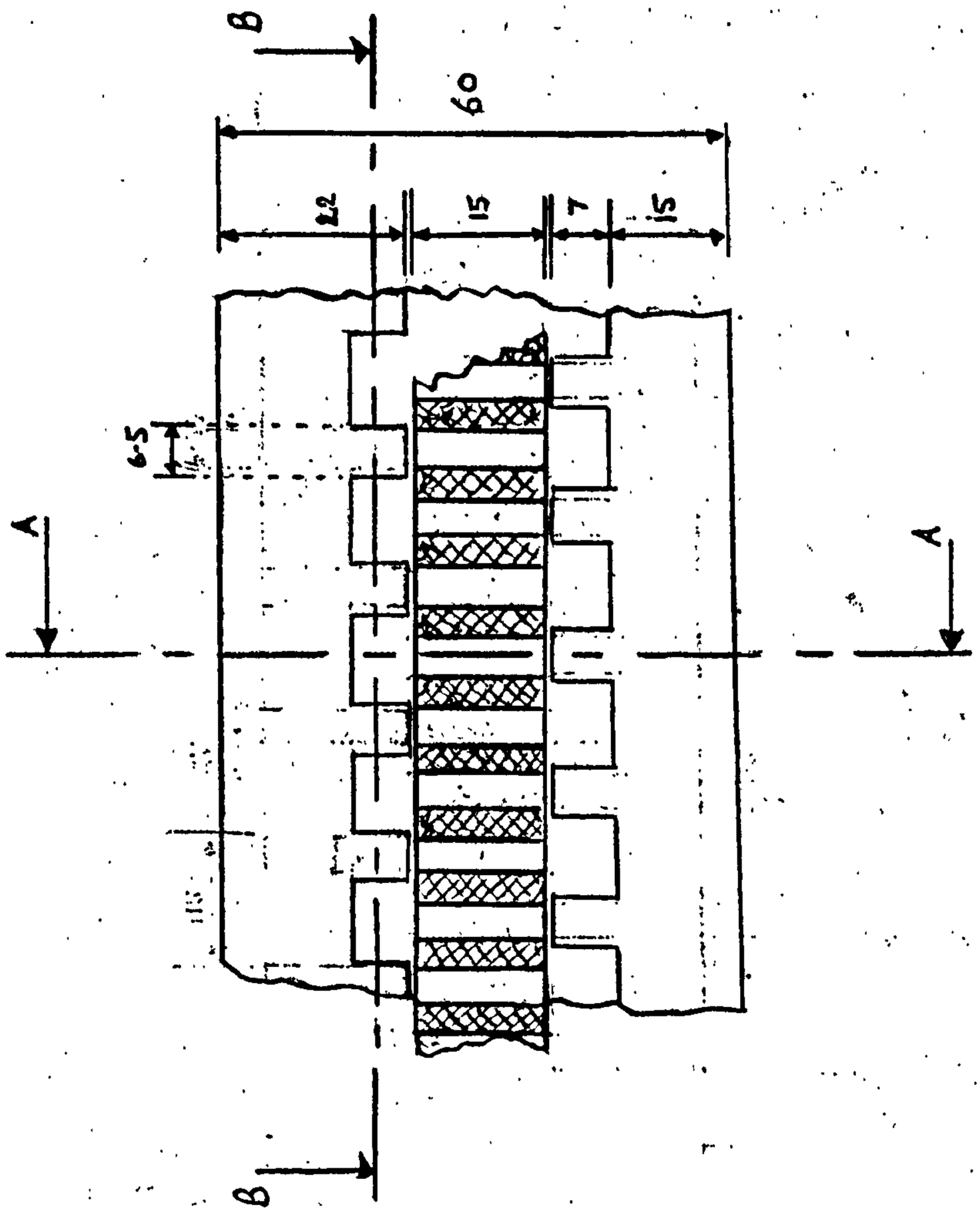

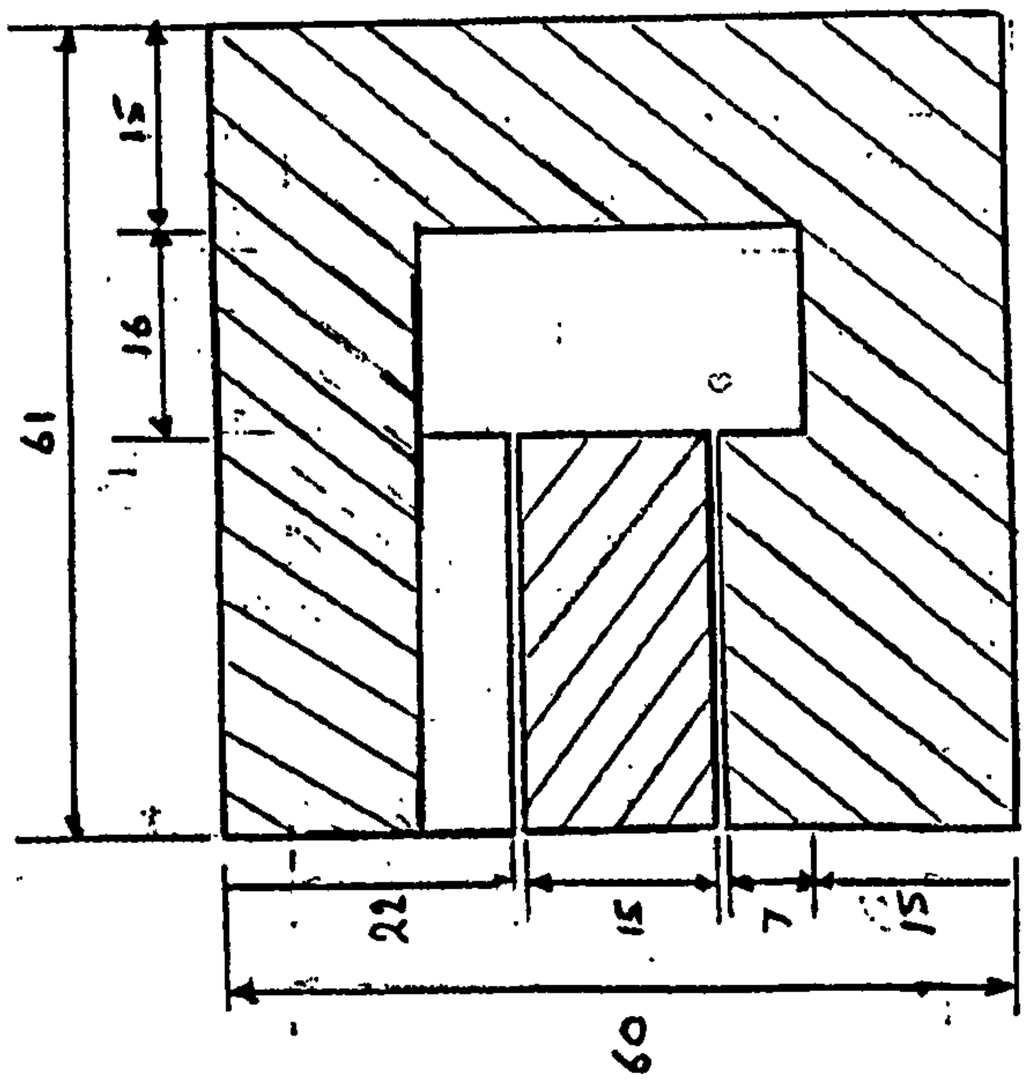

SECTION A-A

▨ INDICATES MAGNET

C.1 Double Sided Transverse Flux Machine (cont)

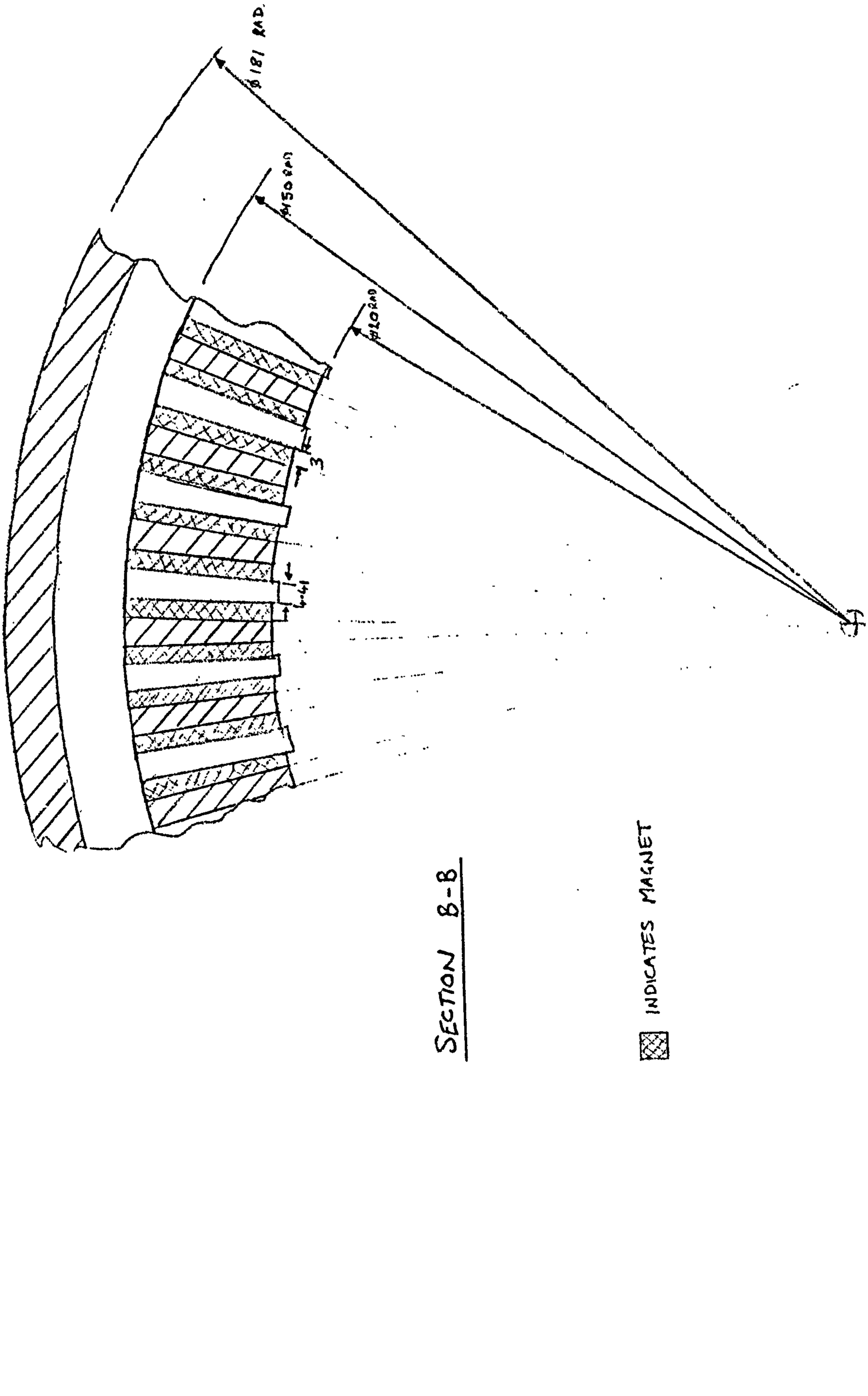

C.2 Claw Pole Transverse Flux Machine

A schematic showing the dimensions of one pole of the CPTFM. Dimensions not shown in the diagram are given below.

- Rotor outside diameter 116mm
- Stator inside diameter 117mm
- Stator outside diameter 200mm

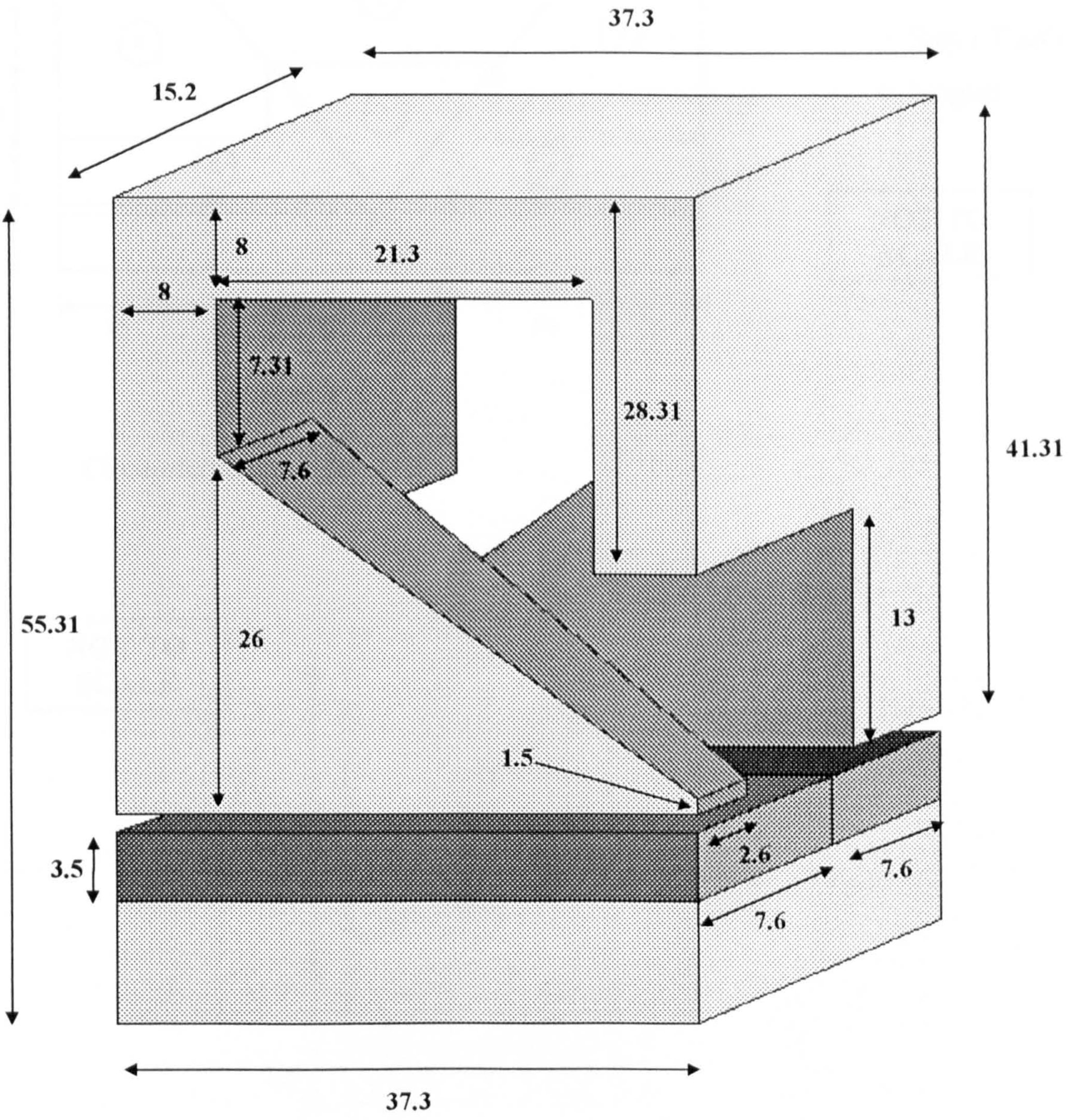

C.3 Claw Pole Hybrid Transverse Flux Machine

C.3.1 Schematic diagrams for the initial 3D FE model of the CPHTFM.

Axial/Radial Plane:

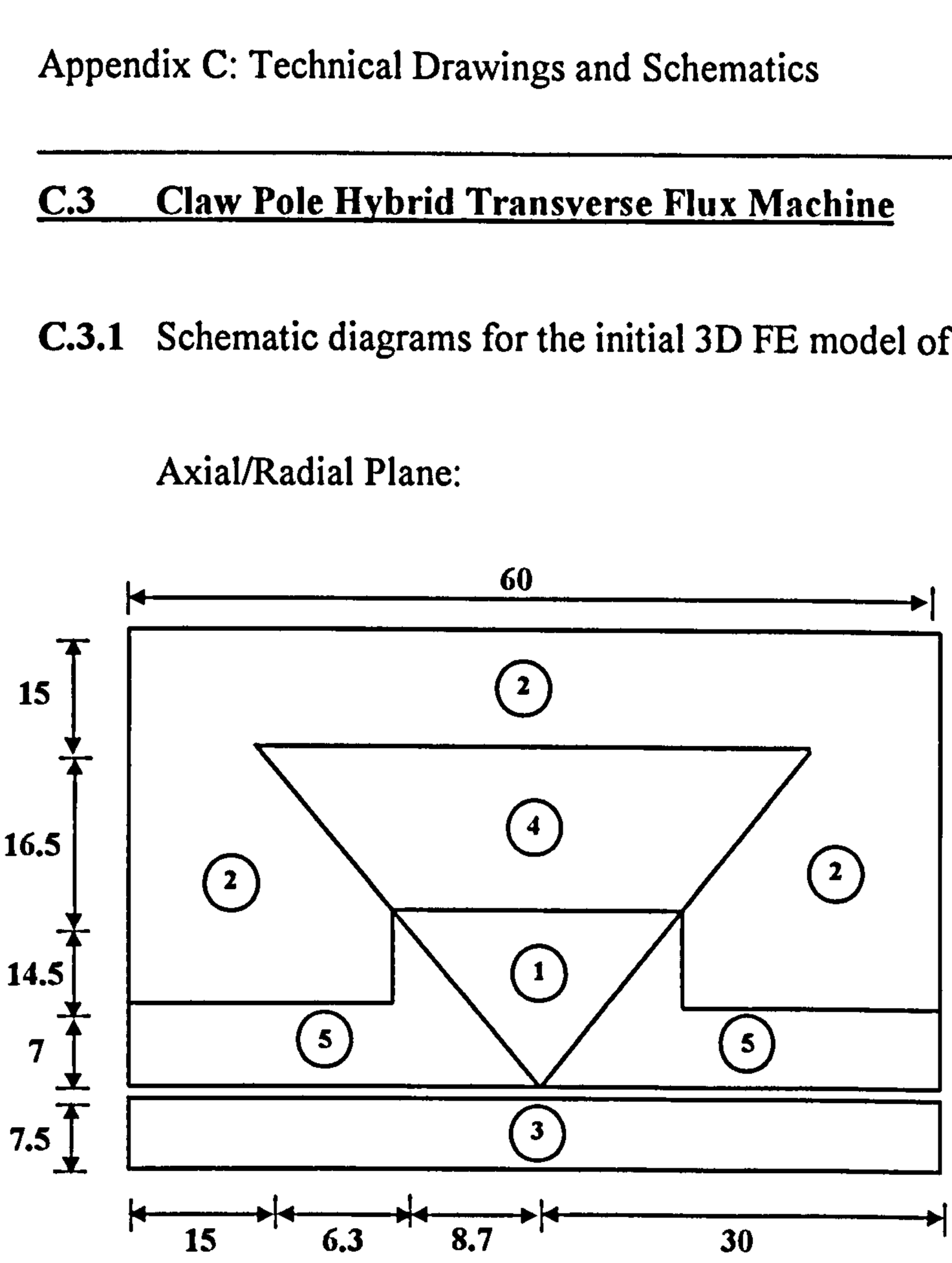

Materials:

1. Air
2. Stator Iron
3. Rotor Iron
4. Conductor
5. Stator Tooth
6. Magnet

NOT TO SCALE

Circumferential/Radial Plane:

NOT TO SCALE

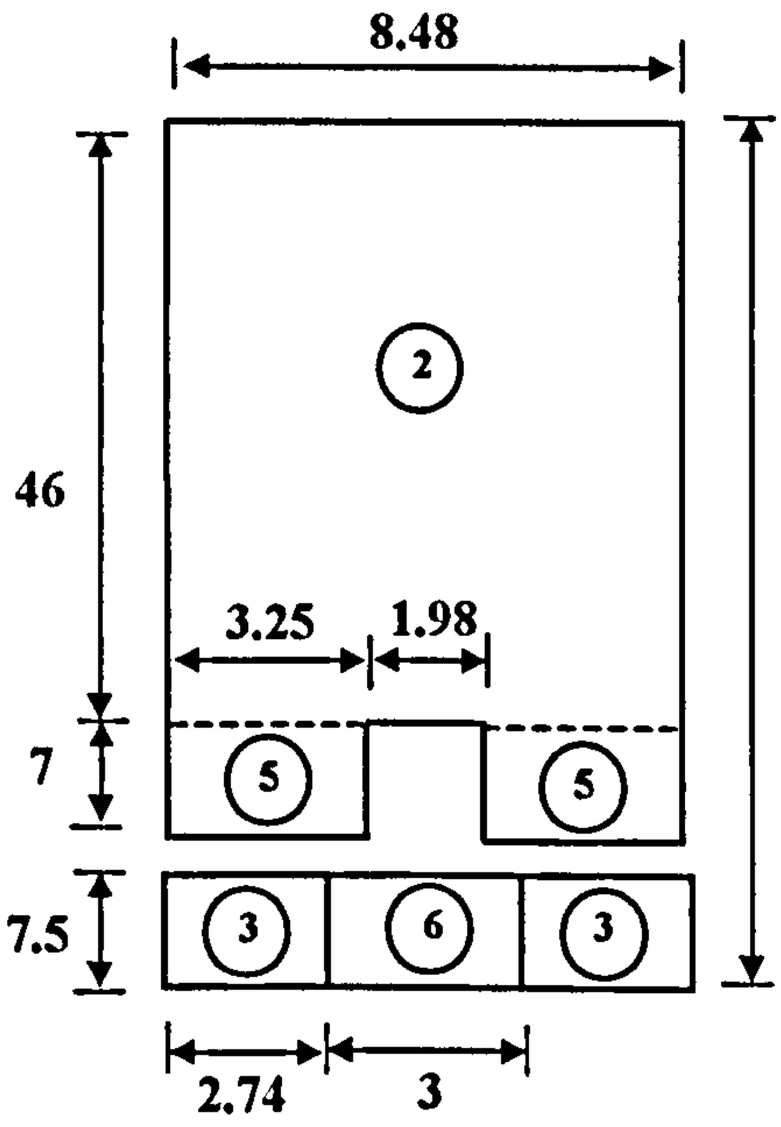

C.3.2 Schematic diagrams for the second 3D FE model of the CPHTFM.

Axial/Radial Plane:

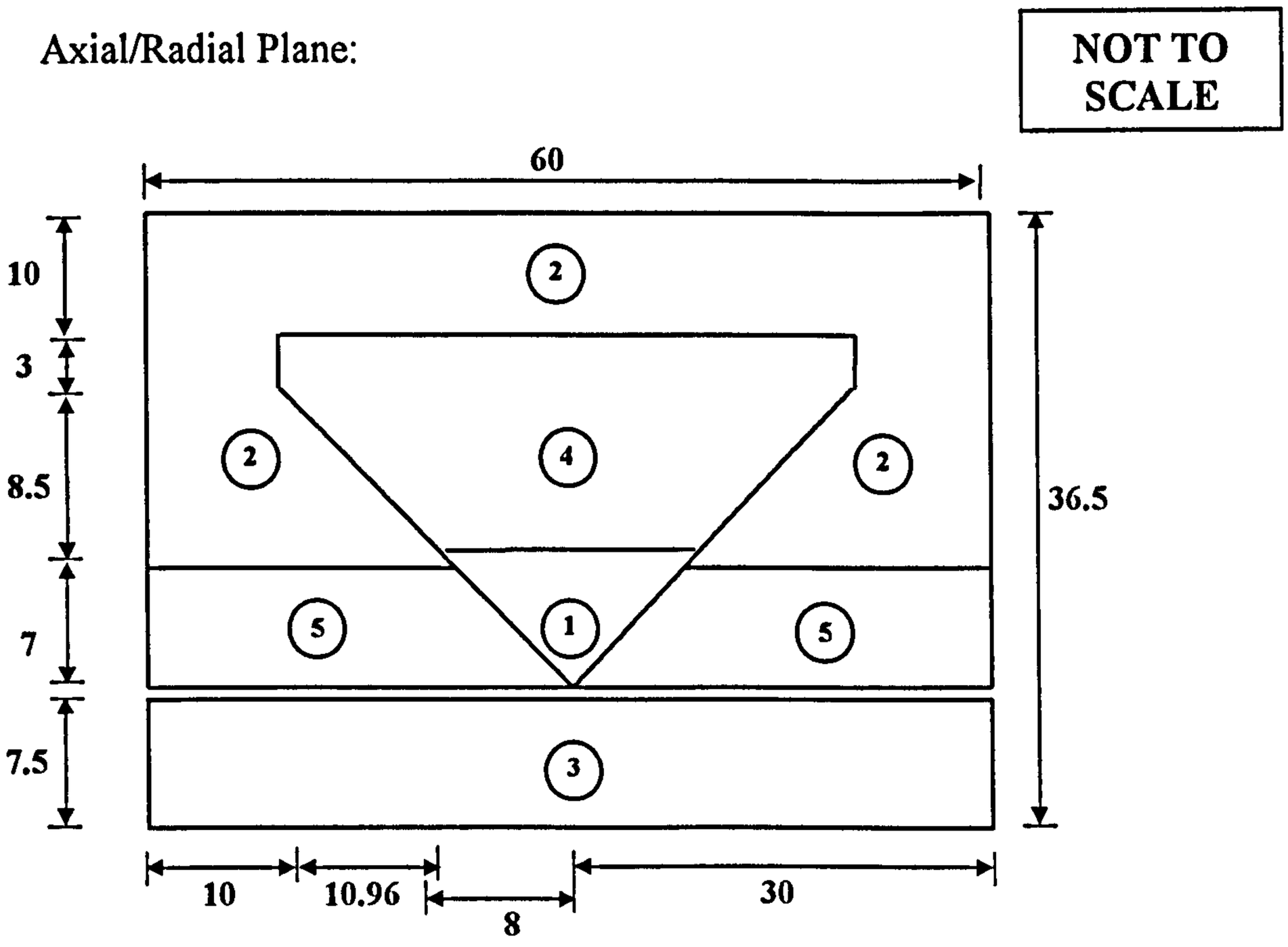

Materials:

1. Air
2. Stator Iron
3. Rotor Iron
4. Conductor
5. Stator Tooth
6. Magnet

Circumferential/Radial Plane:

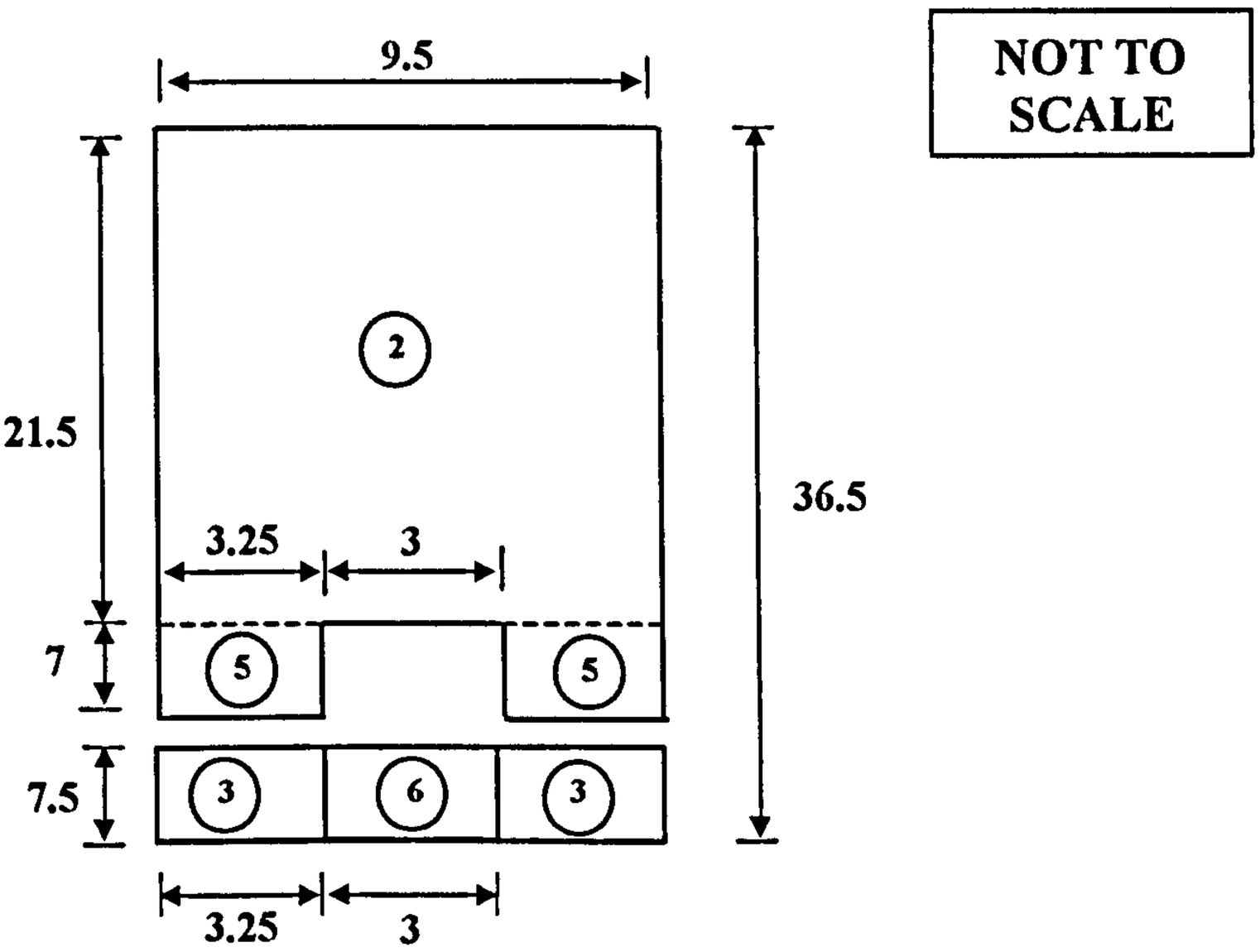

C.3.3 Schematic diagrams for the 3D FE model of the third version of the CPHTFM.

Axial/Radial Plane:

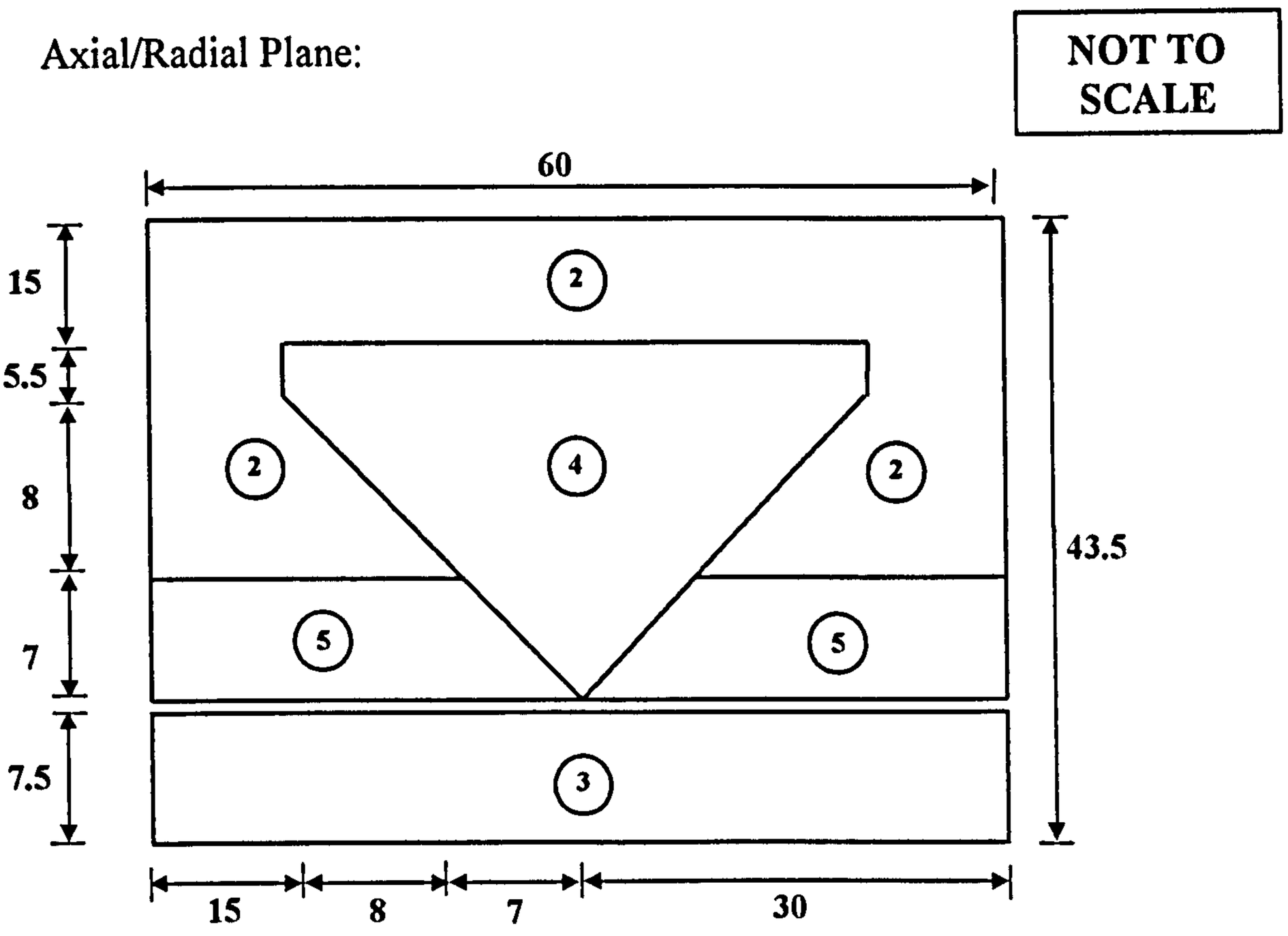

Materials:

1. Air
2. Stator Iron
3. Rotor Iron
4. Conductor
5. Stator Tooth
6. Magnet

Circumferential/Radial Plane:

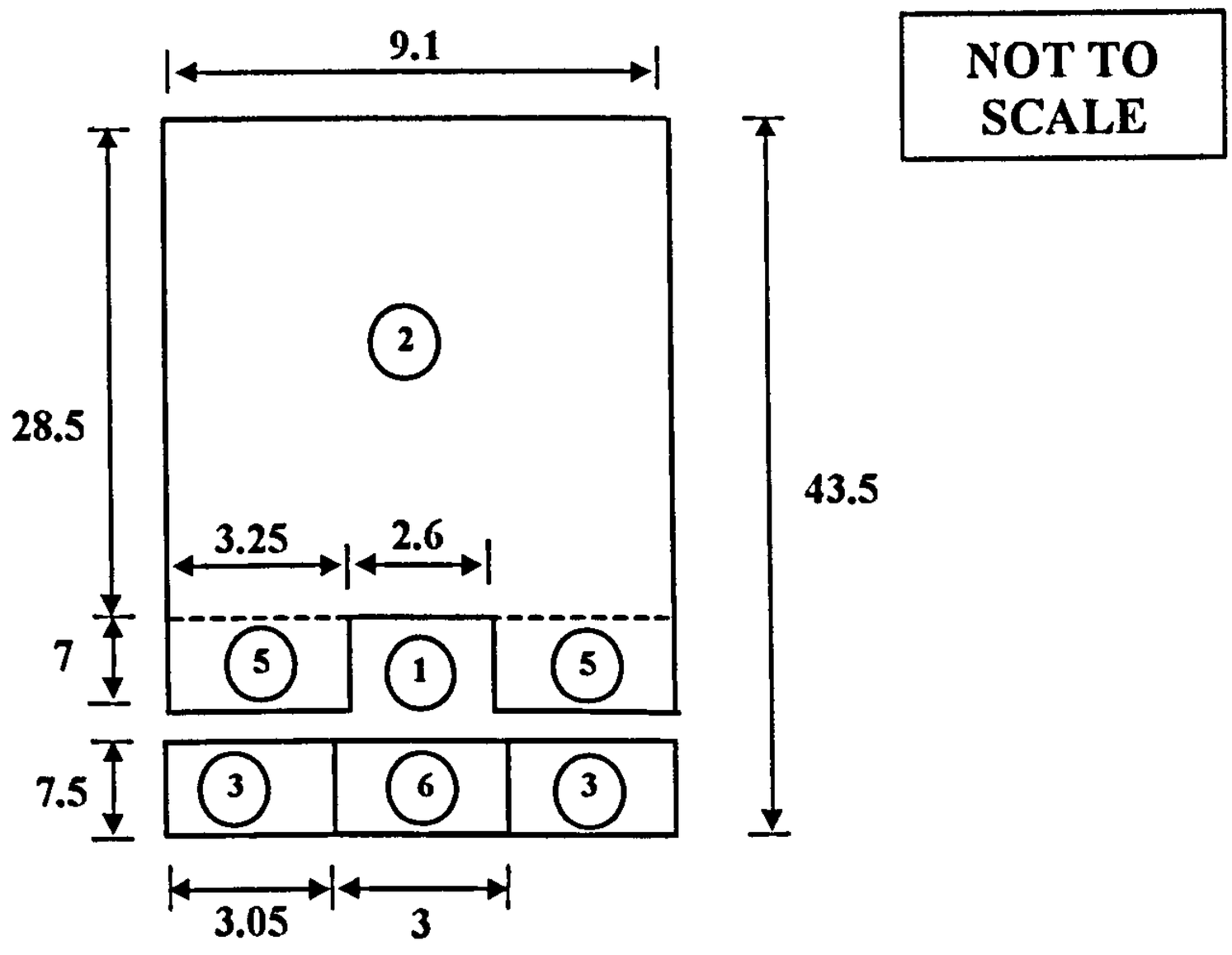

C.3.4 Engineering diagrams for the stator of the prototype CPHTFM.

Schematic of Assembled Stator

(radial / axial view)

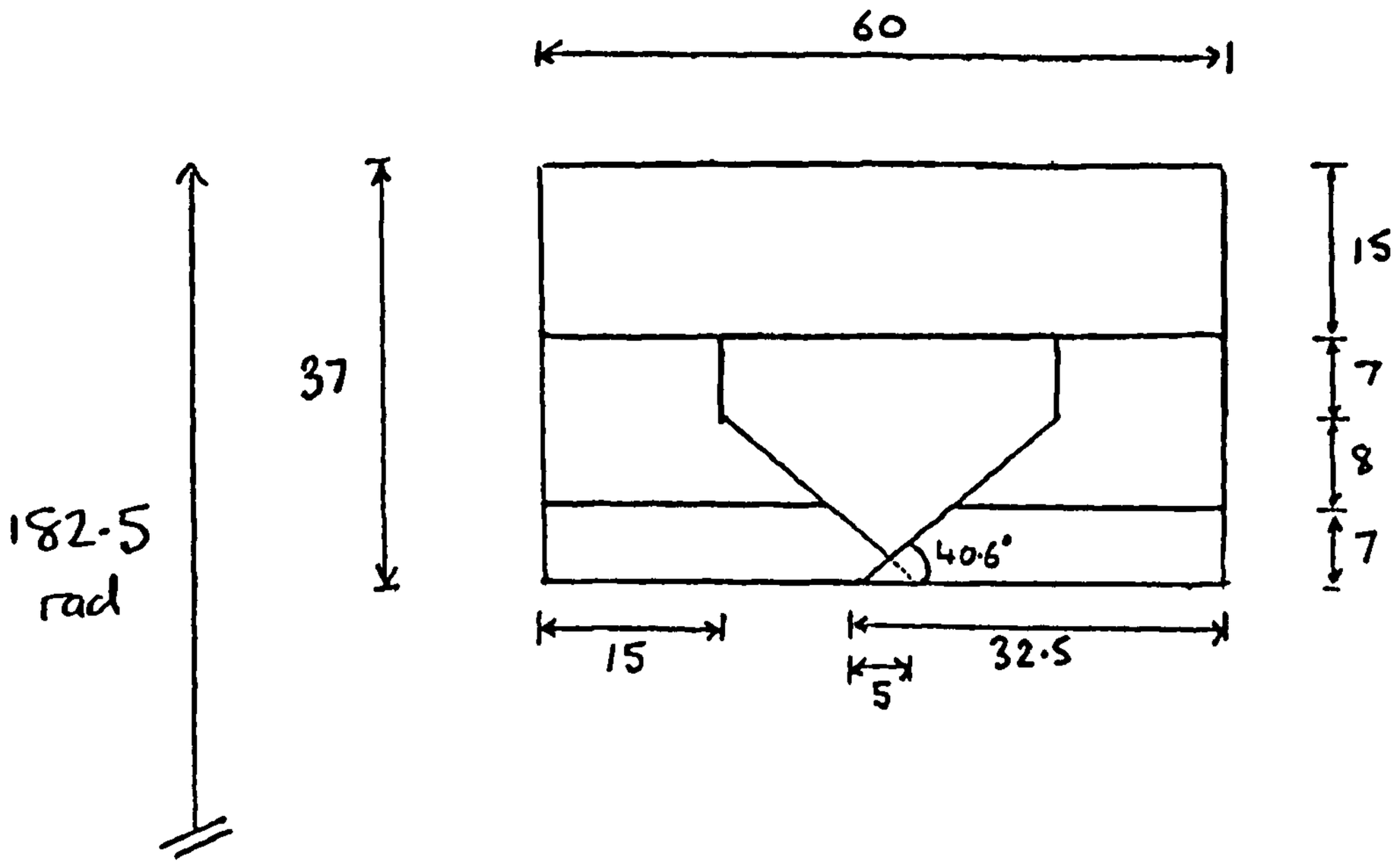

(circumferential / axial view)

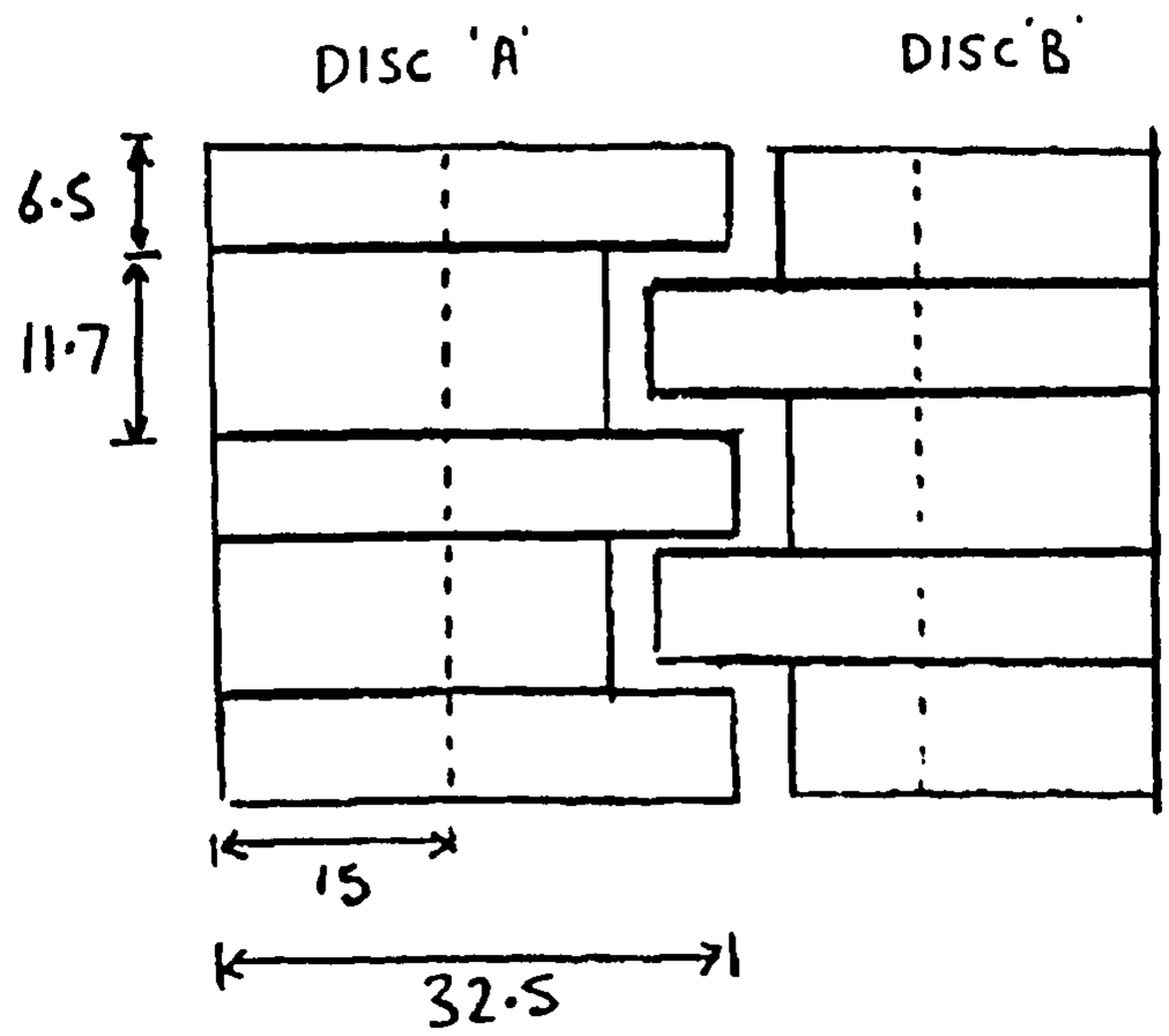

Portion of Stator Flanking Ring

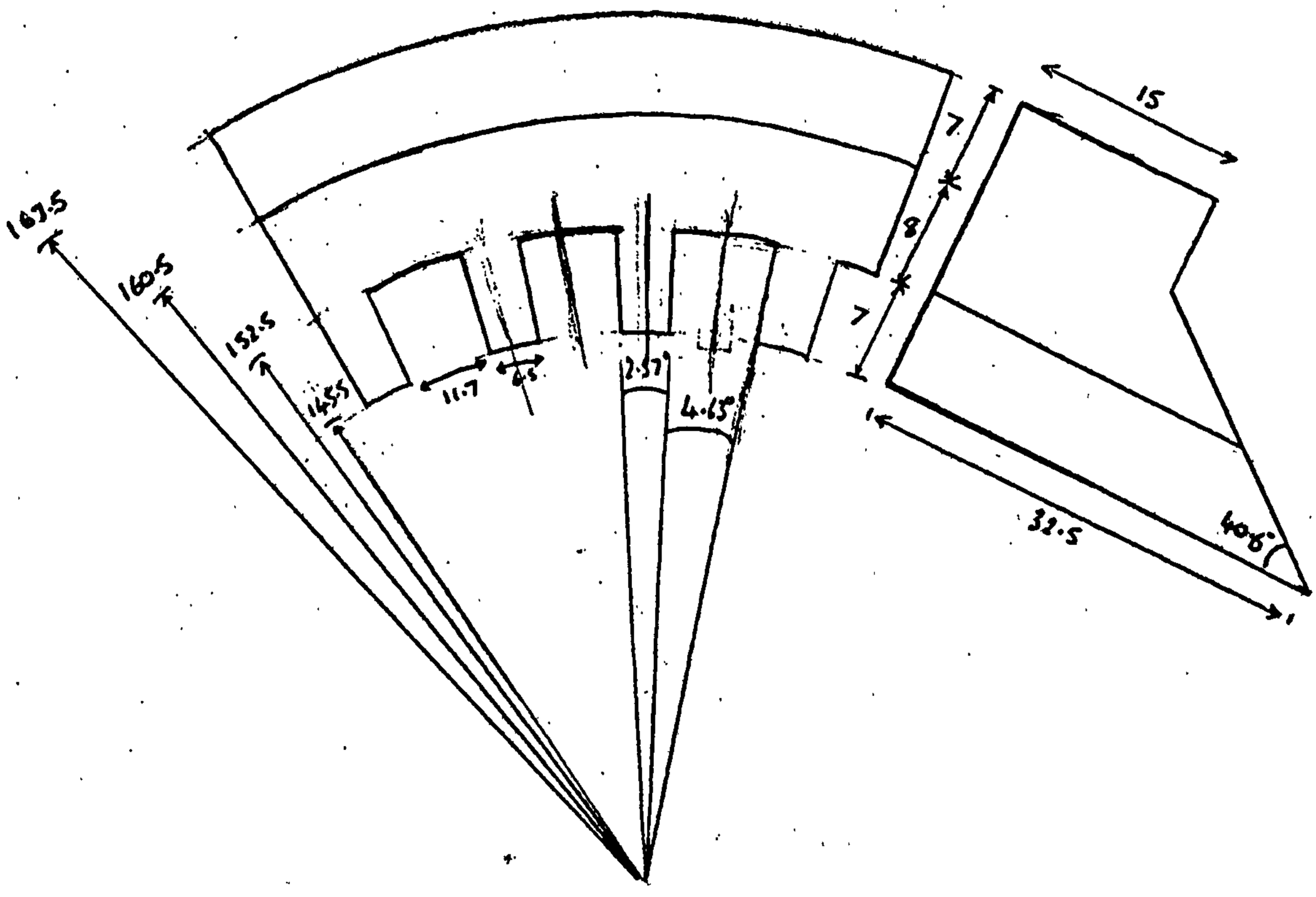

Engineering Drawing for Stator Flanking Ring

(Require 2 off)

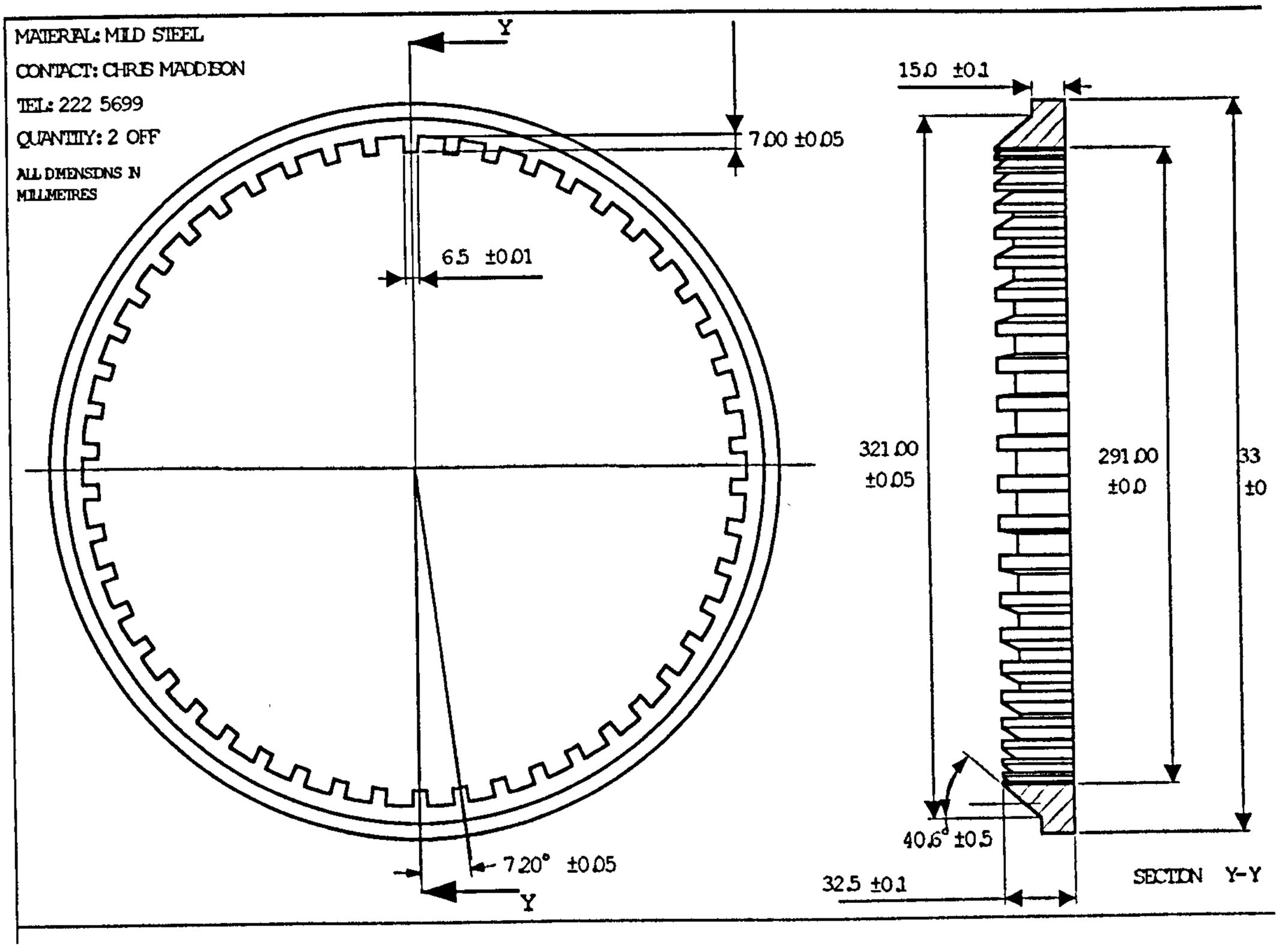

Portion of Stator Top Section

(each section spans 180°mech, Require 2 off)

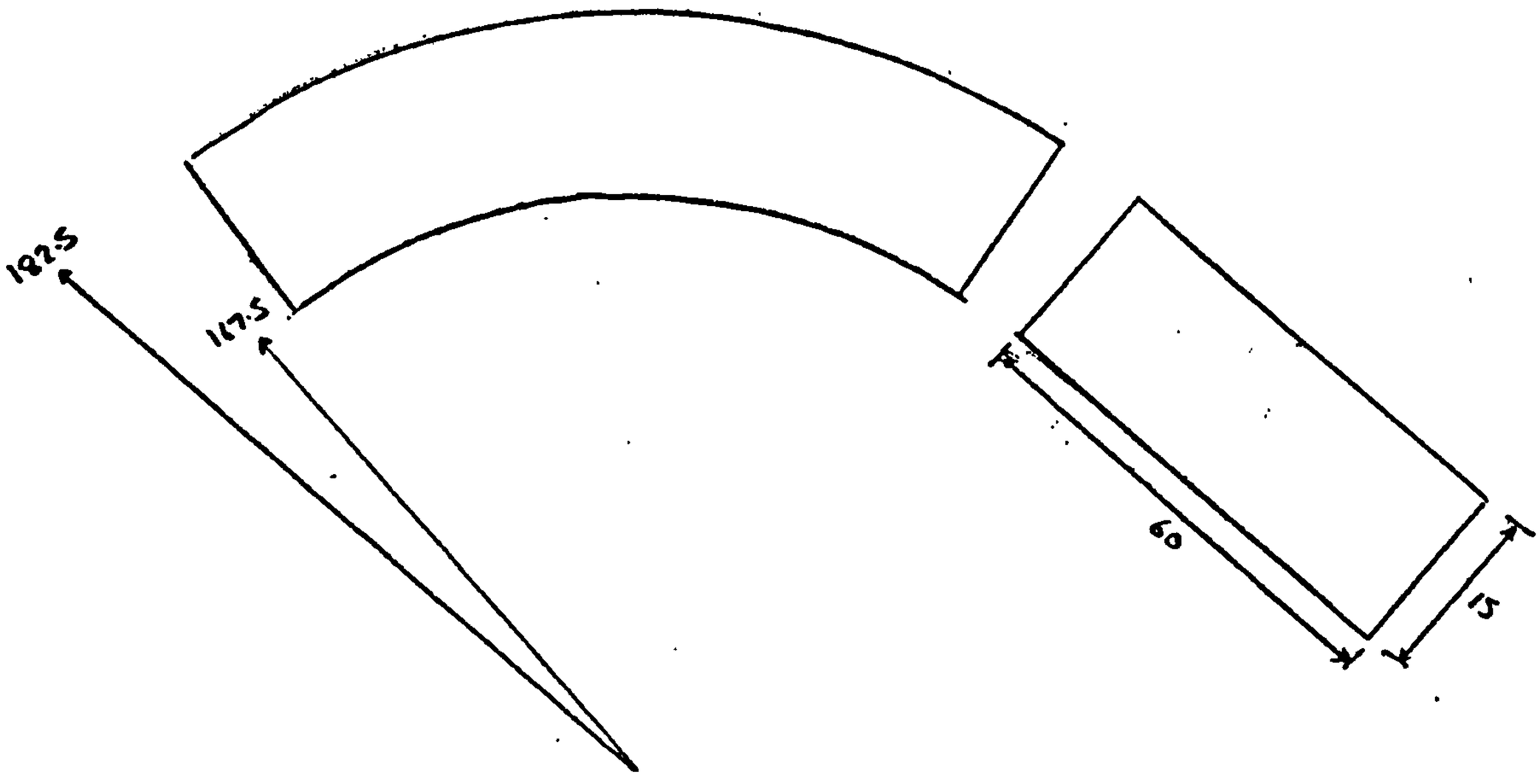

Assembled Stator Top Section

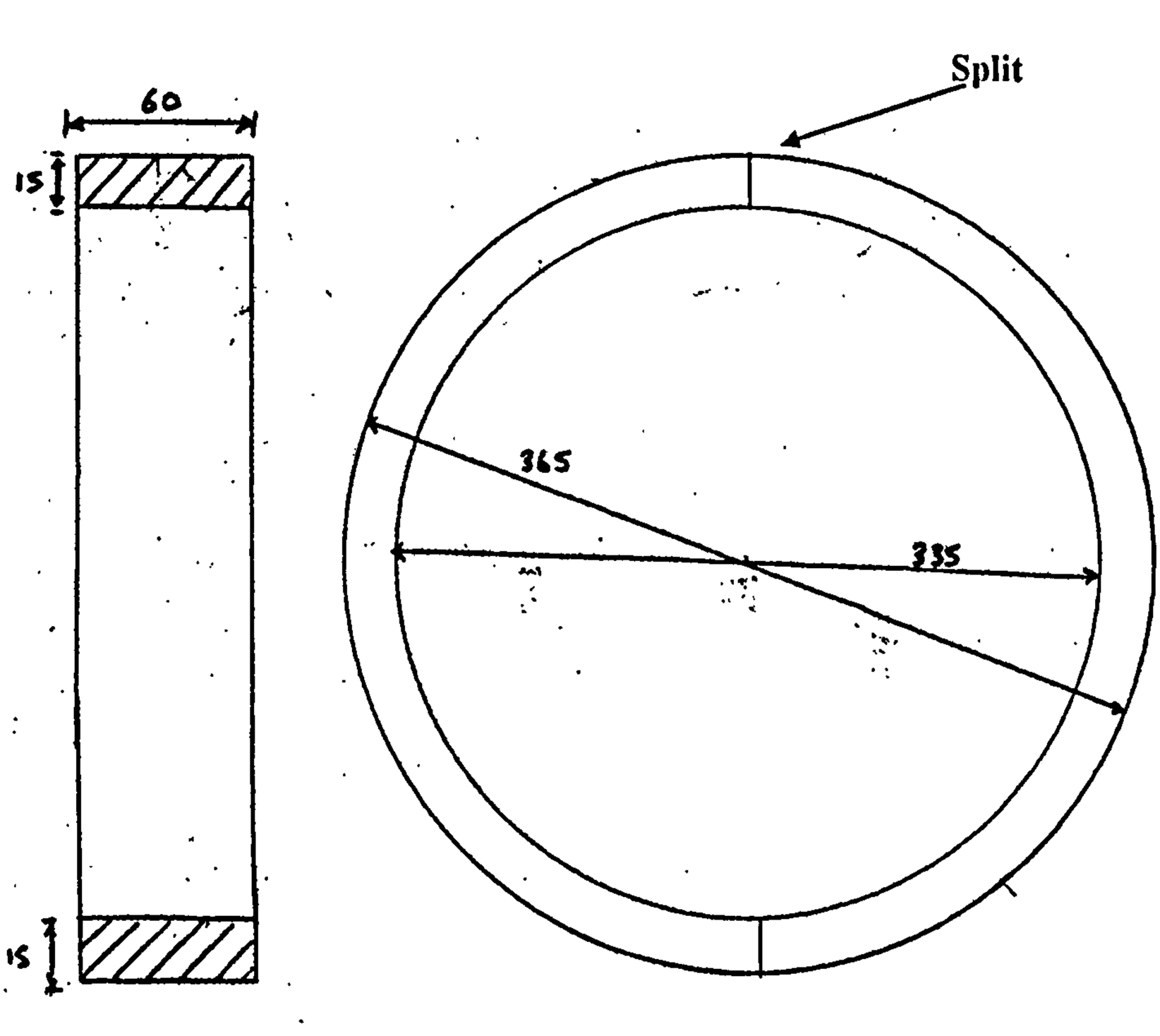

C.3.5 Engineering diagrams for the rotor of the prototype CPHTFM.

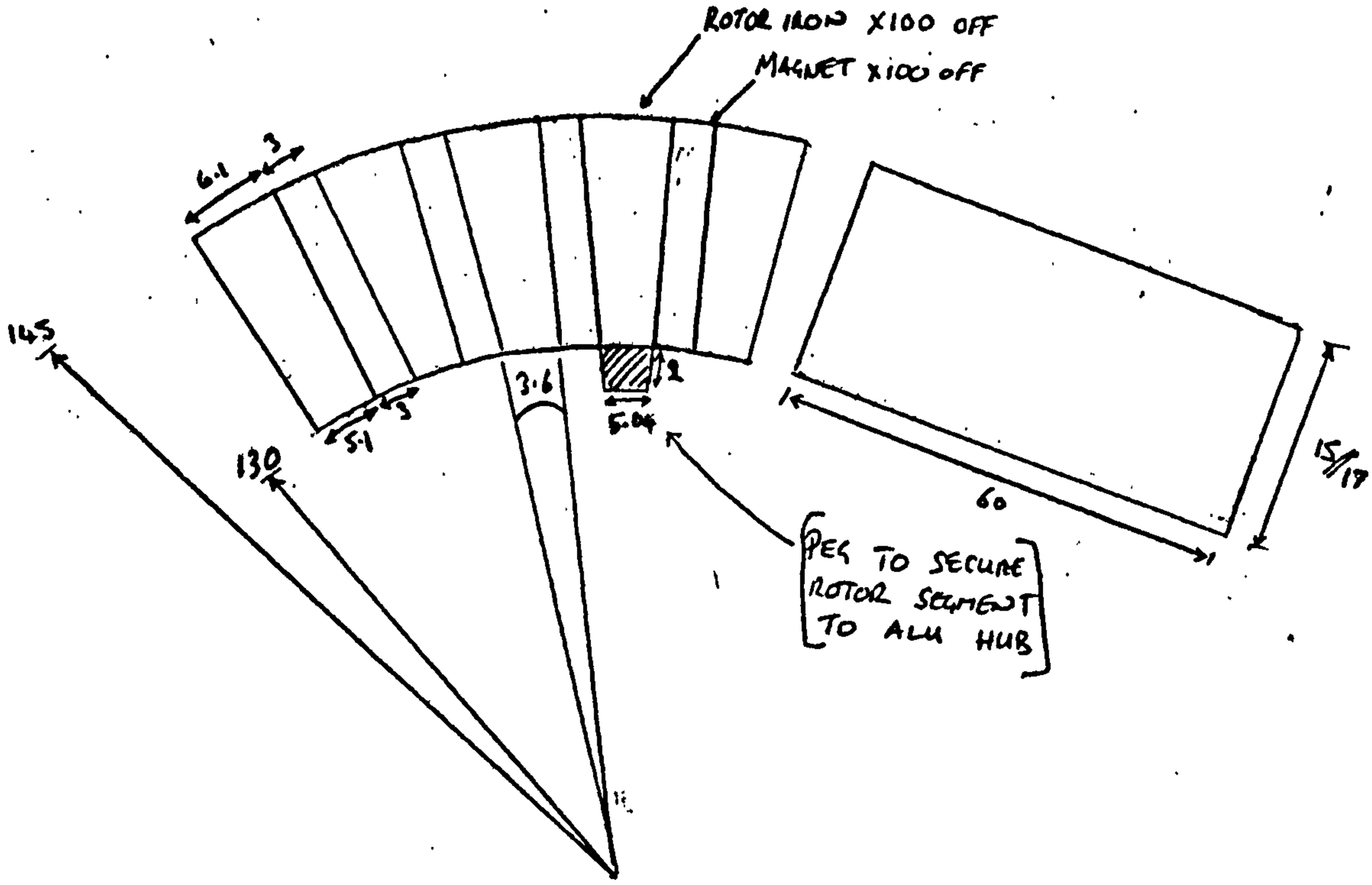

C.3.6 Assembly procedure for the prototype CPHTFM.

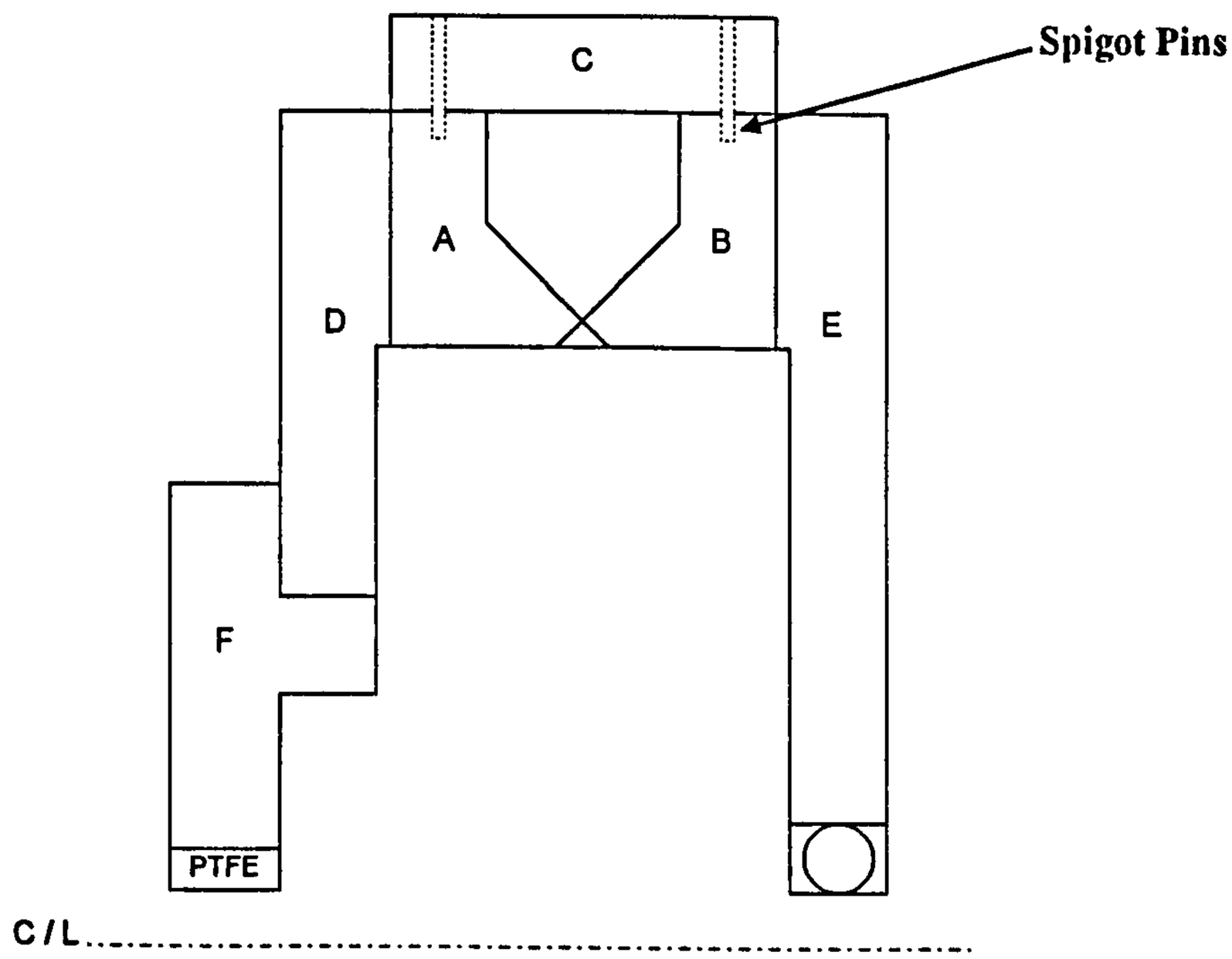

- Bolt Aluminium casing **D** to stator disc **A**.
- Bolt Aluminium casing **E** to stator disc **B**.
- Bolt bearing housing **F** to Aluminium casing **D**.
- Place a spigotted 'dolly' between assemblies **D / F** and **E** and clamp the two assemblies together.
- Without the conductor in place, torque down the Top Ring **C**, ensuring that the splits in **C** are at magnetically neutral positions, ie. between poles.
- Drill through the top ring **C** into the two stator discs **A** and **B**, in order to accept spigot pins later in assembly; these holes should also be in magnetically neutral parts of the coreback.
- Remove the top ring **C** and then wind in the conductor.
- With the winding in place, put the top ring **C** back in place and torque it down to the same level as before, allowing the winding to exit through the splits. Now put in the spigot pins.
- Unbolt casing **E** from stator disc **B**.
- Remove the 'dolly'.
- Unbolt bearing housing **F** from casing **D**.
- Slide complete rotor assembly into the machine until the torque transducer flange extends beyond casing **D**
- Clamp bearing housing **F** around the exposed rotor shaft; this part of the rotor shaft is 200mm long and should be sufficiently long to enable the shaft to be clamped without the active portion of the rotor entering the machine.
- Slide casing **E** onto the unflanged rotor shaft.
- Guide the rotor into the stator with four 'jacking bolts' and bolt casing **E** onto stator disc **B**.

Appendix D Miscellaneous Calculations

D.1 Mean areas in the DSTFM

Rotor Iron Mean Flux Path

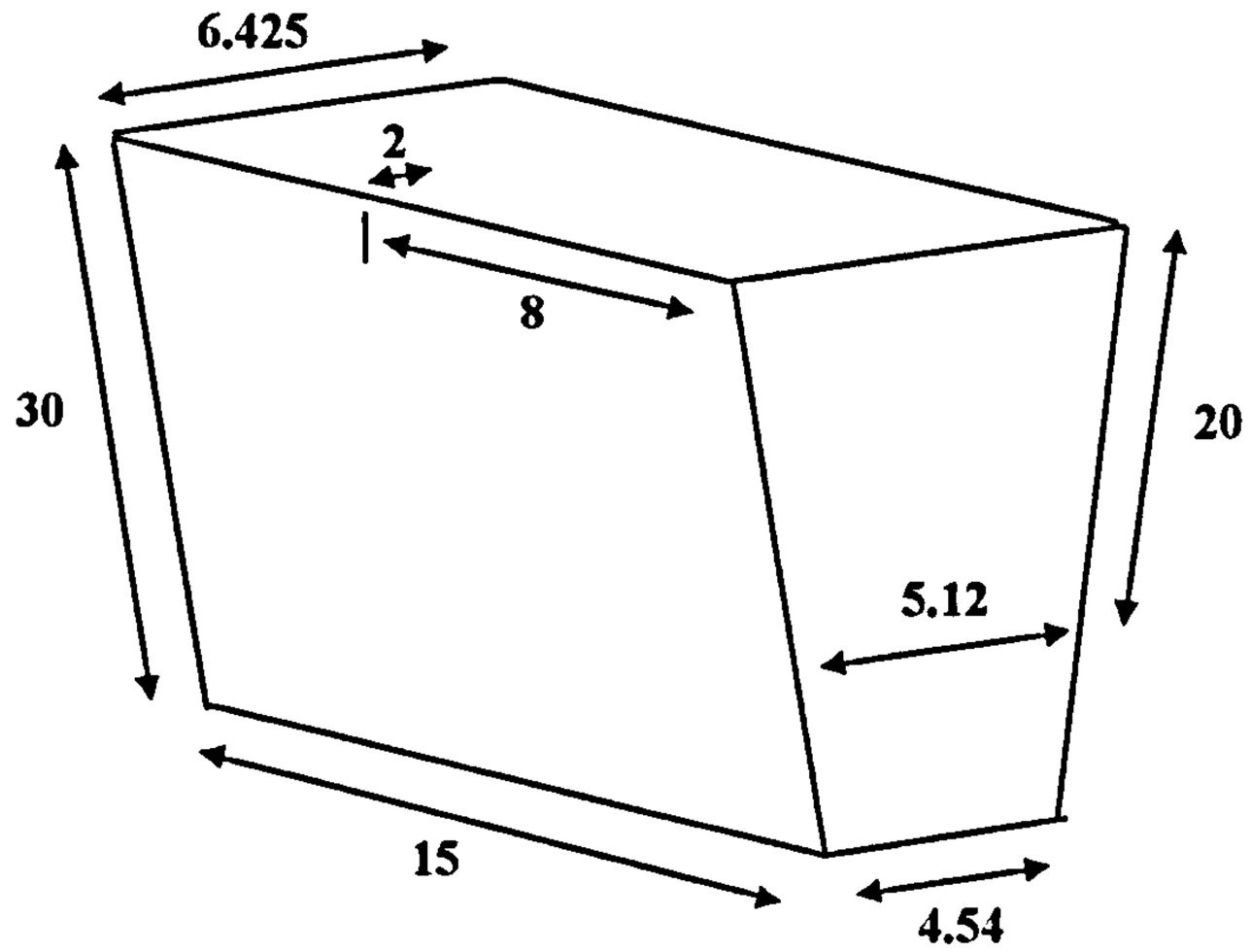

Figure D1.1 DSTFM rotor dimensions

Mean flux path length represents the path taken by the bulk of the flux from the magnet through the rotor and is approximately 10mm

Mean area represents the average area through which the magnet flux passes and this is taken to be:

$$\{\tfrac{1}{2}(6.425 + 5.12) \times 20\} \div 2 = \mathbf{57.7 \times 10^{-6}\ m^2}$$

10mm and 15mm Core Back Mean Flux Paths [15mm dimensions given in brackets]

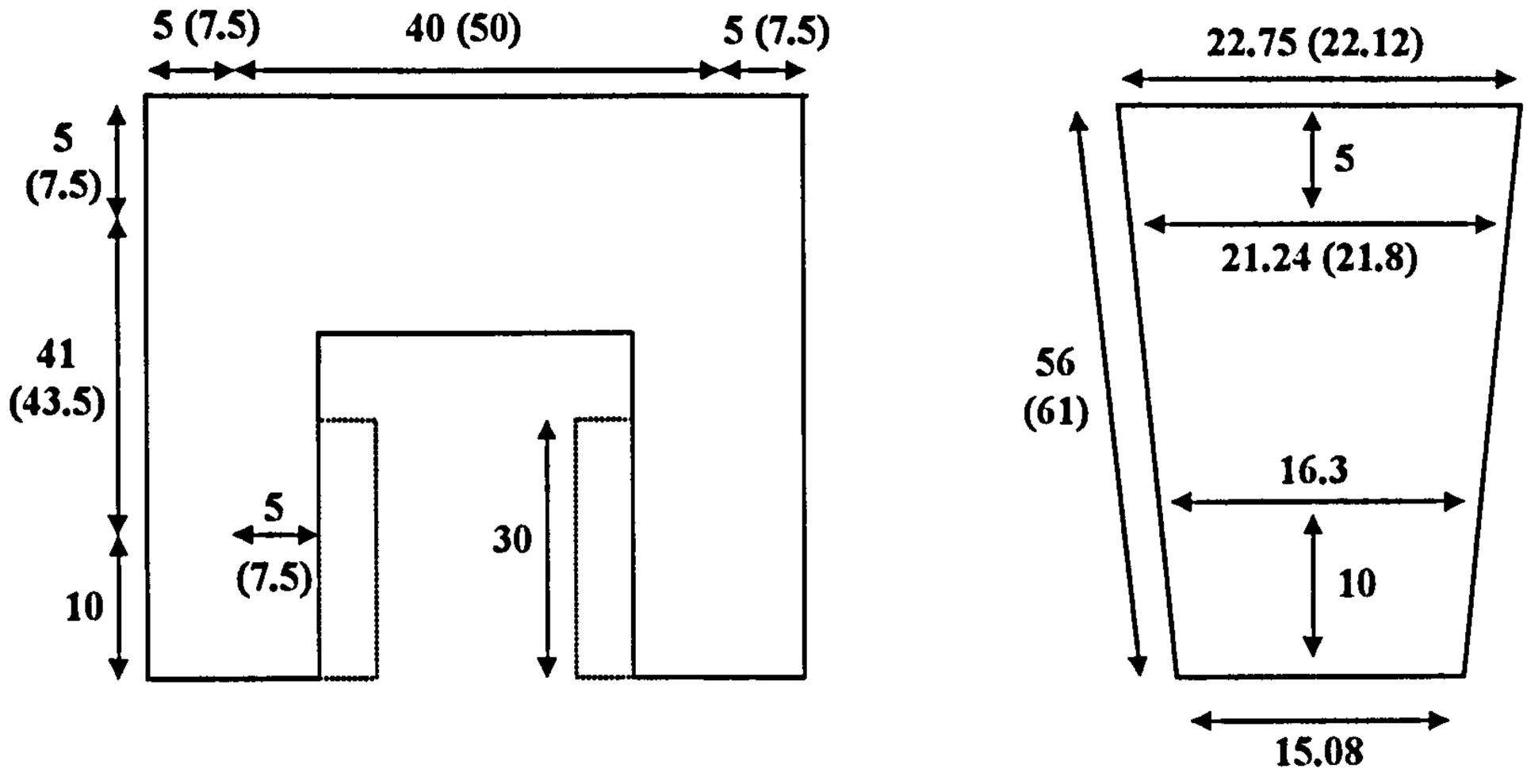

Figure D1.2 DSTFM stator dimensions

10mm mean length given by: $5 + 41 + 40 + 41 + 5 = \mathbf{131mm}$

15mm mean length given by: $7.5 + 43.5 + 50 + 43.5 + 7.5 = \mathbf{152mm}$

Mean area given by: $$\frac{\textbf{Average width} \times \textbf{Core Back Thickness}}{\textbf{2}}$$

So calculating the average widths from figure D1.2 gives the following values.

10mm average width: $$\frac{\left[2\left(\frac{(21.24+16.3)}{2}\right)+21.24\right]}{3} = \mathbf{19.59mm}$$

15mm average width: $$\frac{\left[2\left(\frac{(21.8+16.3)}{2}\right)+21.8\right]}{3} = \mathbf{20mm}$$

Therefore:

10mm average area: $(19.59 \times 10) / 2 = \mathbf{97.95\times10^{-6}\ m^2}$

15mm average area: $(20 \times 15) / 2 = \mathbf{150\times10^{-6}\ m^2}$

Tooth and Airgap Mean Flux Paths

Mean length of tooth: **7mm**

Mean length of airgap: **0.5mm**

The mean areas of the tooth and airgap can be considered equivalent to the rotor iron mean area. ie. $\mathbf{57.7\ x10^{-6}\ m^2}$

D.2 Calculation of DSTFM Aluminium Casing Thickness

The following are the results of calculations for section 3.5.1 of Chapter 3 and are derived from Roark [32].

Plate Deflection, $$y_b = \frac{-wa^3}{D}\left(\frac{C_1 L_6}{C_4} - L_3\right)$$

Where:

a = outer radius (201mm)

b = inner radius (35mm)

w = Unit line load

r_o = Radial location of load (120mm)

E = Young's modulus (70GN/m^2 for Al)

t = Plate thickness

υ = Poisson's ratio (0.33 for Al)

C_1 , C_4 , L_3 , L_6 = plate constants

$$D = \frac{E\ t^3}{12\left(1-\upsilon^2\right)} \qquad \text{(Plate Constant)}$$

$$W = 2\pi\ r_o\ w \qquad \text{(Total Load, 14683N)}$$

$$w = \frac{W}{2\pi\ r_o} = \frac{14682}{2\pi \times 120 \times 10^{-3}} = 19472.6 N/m$$

Plate Constants:

$$C_1 = \frac{1+\upsilon}{2}\frac{b}{a}Ln\left(\frac{a}{b}\right) + \frac{1-\upsilon}{4}\left(\frac{a}{b} - \frac{b}{a}\right)$$

$$C_4 = \frac{1}{2}\left[(1+\upsilon)\frac{b}{a} + (1-\upsilon)\frac{a}{b}\right]$$

$$L_3 = \frac{r_o}{4a}\left\{\left[\left(\frac{r_o}{a}\right)^2 + 1\right]Ln\left(\frac{a}{r_o}\right) + \left(\frac{r_o}{a}\right)^2 - 1\right\}$$

$$L_6 = \frac{r_o}{4a}\left[\left(\frac{r_o}{a}\right)^2 - 1 + 2Ln\left(\frac{a}{r_o}\right)\right]$$

With the load positioned at the inner radius of the stator and values of 'a' and 'b' 201mm and 35mm. These constants evaluate to:

$C_1 = 1.045$ $C_4 = 2.039$

$L_3 = 0.00837$ $L_6 = 0.05792$

Table D.2.1 Calculation of Aluminium Casing Axial Flex

Individual Plate Thickness (mm)	Total Thickness (mm)	Plate Constant	Plate Deflection (mm)
10	20	52370	0.06
12.5	25	102285	0.033
15	30	176748	0.019
17.5	35	280669	0.012
20	40	418958	0.008
22.5	45	596524	0.006
25	50	818277	0.004

D.3 Calculation Mechanical of Stresses

Calculation of Forces on Rotor Bearings in the DSTFM

The force exerted by the rotor magnets towards the stator was 14.68kN (from section 3.5.1, equation 3.21). If for example, the repulsive and attractive forces were unbalanced by a ratio of 3:1, then the force attracting the rotor to the stator will be:

$$\mathbf{14.68kN \times 0.75 = 11kN}$$ in one direction and

$$\mathbf{14.68kN \times 0.25 = 3.68kN}$$ in the opposite direction.

This gave an overall force in one direction of:

$$\mathbf{11000 - 3680 = 7.32kN}$$

The forces acting on the rotor bearings were determined with reference to figure D.3.1 by using the standard equations for calculating bending moments and static forces.

$$\mathbf{M1 = F1 \times X = F2 \times Y}$$

$$\mathbf{M1 = F1 \times X}$$

$$= \left(7.32 \times 10^{3}\right) \times \left(150 \times 10^{-3}\right) = \mathbf{1098Nm}$$

Therefore by transposition:

$$F2 = \frac{1098}{83\times10^{-3}} = 13.23kN$$

So the radial force exerted upon each thrust bearing is 13.23kN and the bending moment is 1098Nm.

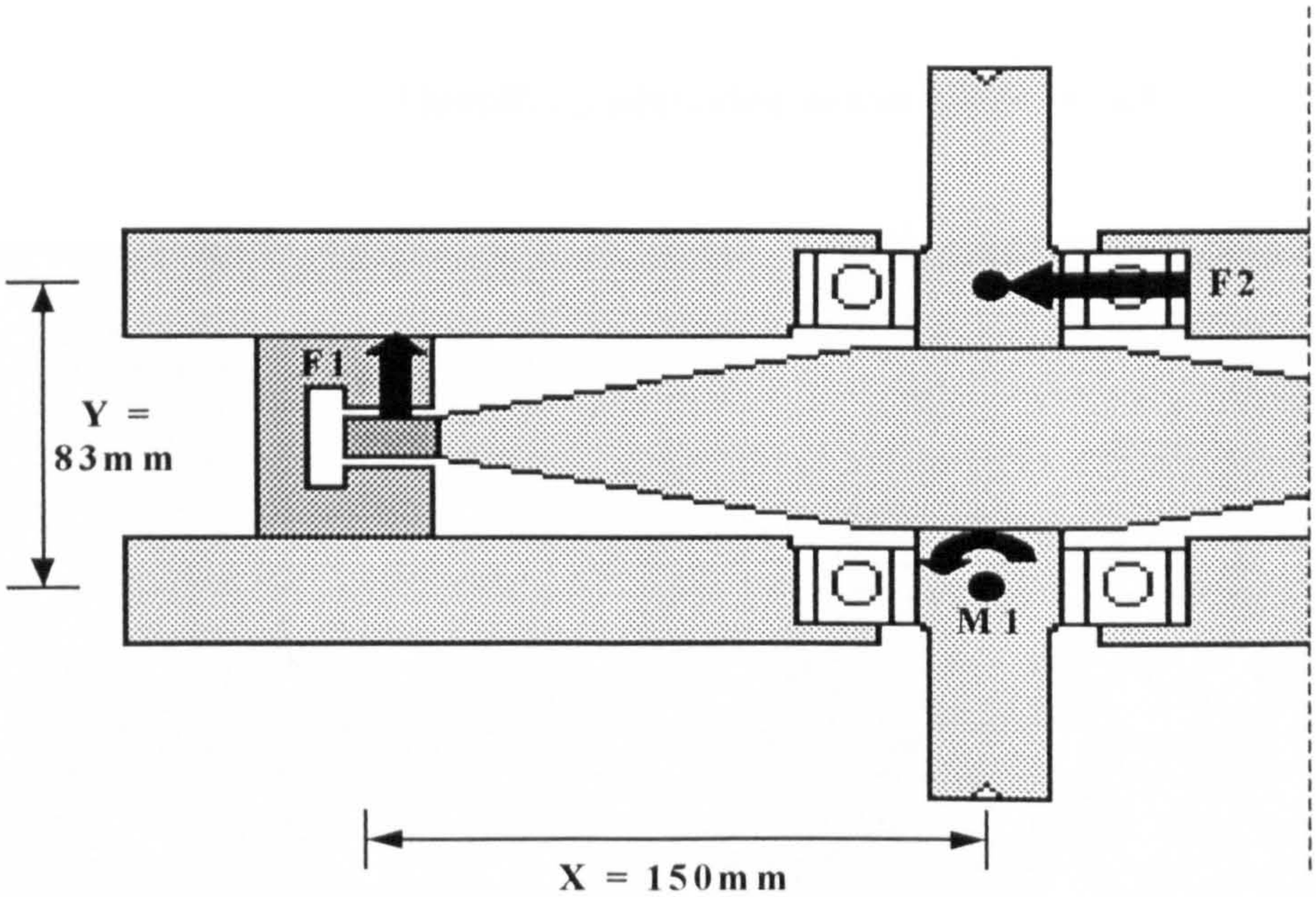

Figure D.3.1 Schematic diagram indicating bending moments and forces acting in the DSTFM

D.4 Example of Power Factor Derivation

In order to validate this methodology, a simple set of parallel Ψ-I curves incorporating a current locus were created (figure D.4.1). Because of the absence of saturation, this simple plot allowed the power factor to be calculated by derivation and by hand. Calculating the power factor by hand used an identical process to that used by Harris et al [11].

With reference to figure D.4.1, the value of E was positioned at a point of zero current and was therefore equivalent to the flux due solely to the magnet. Its magnitude was bounded by the 0° line which represents the positive 'd' axis aligned position. The magnitude of IX is bounded by the 90° line, which was equivalent to the 'q' axis unaligned position, and was situated at the rated current value. The determination of the power factor was as follows:

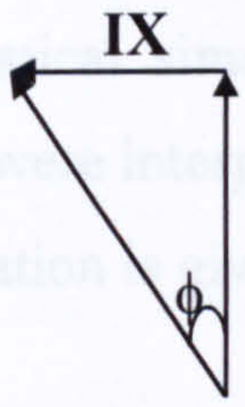

$$\text{Power Factor} = \cos\phi$$

$$\phi = \arctan\frac{IX}{E}$$

$$\phi = \arctan\frac{150}{300} = 26.5^{\circ}$$

Therefore, calculated power factor = **0.89**

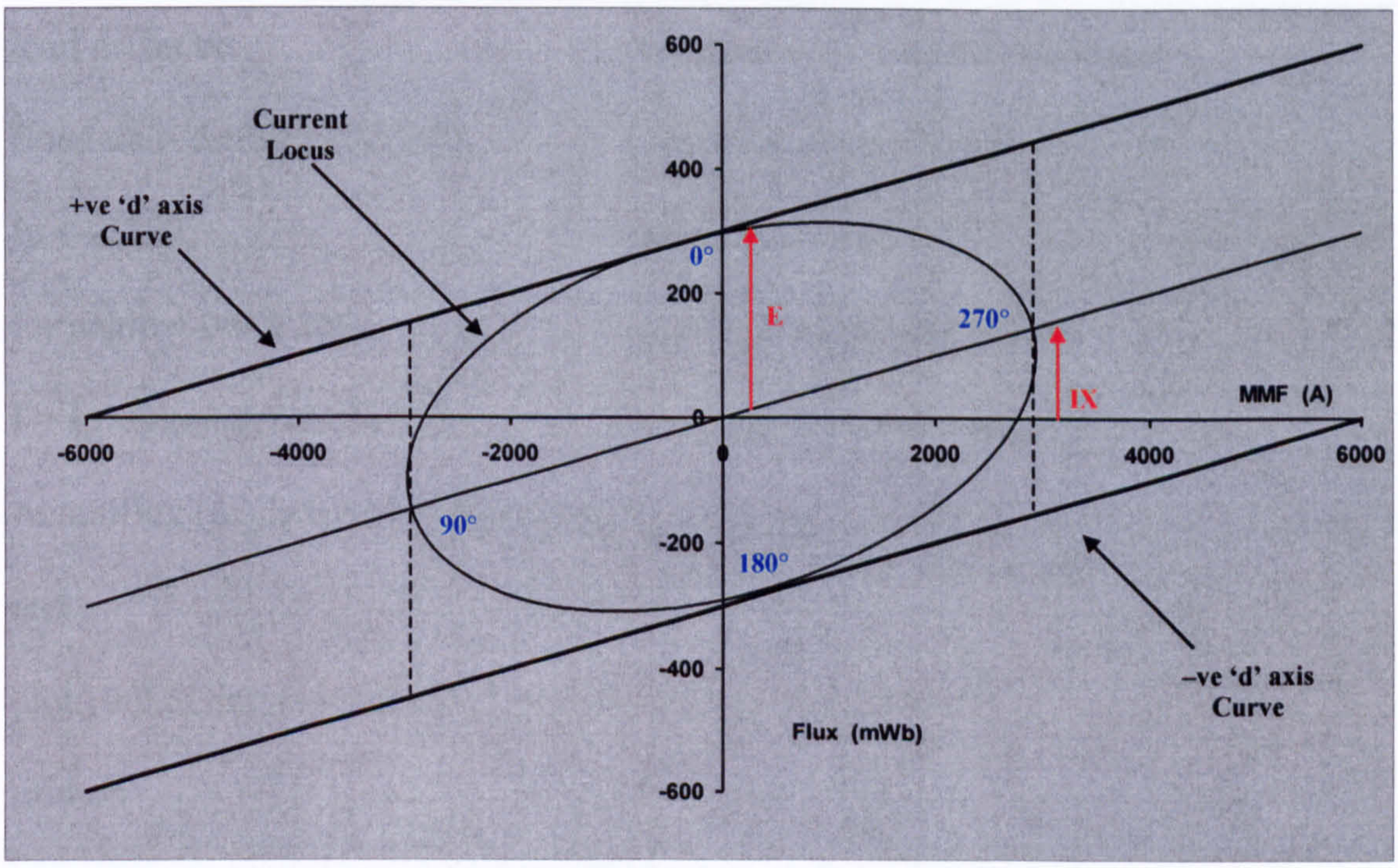

Figure D.4.1 Simple Ψ-I plot, including a current locus, to determine the validity of the power factor derivation methodology

In order to interpolate the value of flux accurately from the current locus, many more Ψ-I curves than the positive and negatively aligned curves needed to be generated. The flux between the two curves varied from a position of positive flux through zero to a position of equal and opposite negative flux. It was reasonable to assume that this 180° transition took the form of a cosine. Equation D.4 takes into account the different values of the two curves and allows a cosine variation to be plotted between them. The effect of this variation on the plot of figure D.4.1 can be seen in figure D.4.2.

$$\psi_\theta = \left(\frac{\psi_0 + \psi_{180}}{2}\right) + \left(\psi_0 - \left(\frac{\psi_0 + \psi_{180}}{2}\right) \times \cos\theta\right) \qquad \{D.4\}$$

The tabulated values of these curves were then imported into a proprietary mathematical simulation package such as 'Matlab' where the values of flux and current were interpolated for any given angle. The annotated code for performing this interpolation is given below:

'Matlab' Power Factor Interpolation Code

The following code was used in 'Matlab' to interpolate a flux linkage waveform from an enforced sinusoidal current for the DSTFM.

```
load dstfm.txt                          {loads cosine varying Ψ-I data table}

fluxdata = dstfm(2:722,2:8);            {data starts in row 2 column 2}

Ip = -2250;                             {set peak current}

for angle = 0:0.5:360                   {0.5° step loop from 0° to 360°}

I = Ip*sin(angle/360*2*pi);             {inst value of I for that angle}

Actualflux (angle/0.5+1)=interp1(-4080:1360:4080,fluxdata(angle/0.5+1,:),I,'cubic');
                                        {   see  *  below  for  details   }
end

plot((0:0.5:360),[Ip*sin((0:0.5:360)/360*2*pi)' Actualflux'])

grid on

zoom on
```

```
*       Actualflux (angle/0.5+1)=     { "Actualflux" for each step through the
                                              72 rows of the table data}

        interp1                       { interpolation instruction}

        (-4080:1360:4080,             {current data, -ve limit :increment size: +ve limit}

        fluxdata(angle/0.5+1,:),      {present fluxdata row ( colon indicates whole row)}

        I,                            {value of current to interpolate from}

        'cubic');                     { cubic interpolation selection}
```

In order to fit the locus of figure D.4.2, this interpolation took the form of a current sinusoid with I_{peak} set to the peak thermally limited value. In this case, with a thermally limited current of 1591A rms, the peak value was 2250A. The resultant flux data was then differentiated with respect to θ producing a voltage waveform derived from equation D.5.

$$V = \frac{\partial \psi}{\partial t} = \frac{\partial \psi}{\partial \theta} \times \frac{\partial \theta}{\partial t} = \frac{\partial \psi}{\partial \theta} \omega \qquad \{D.5\}$$

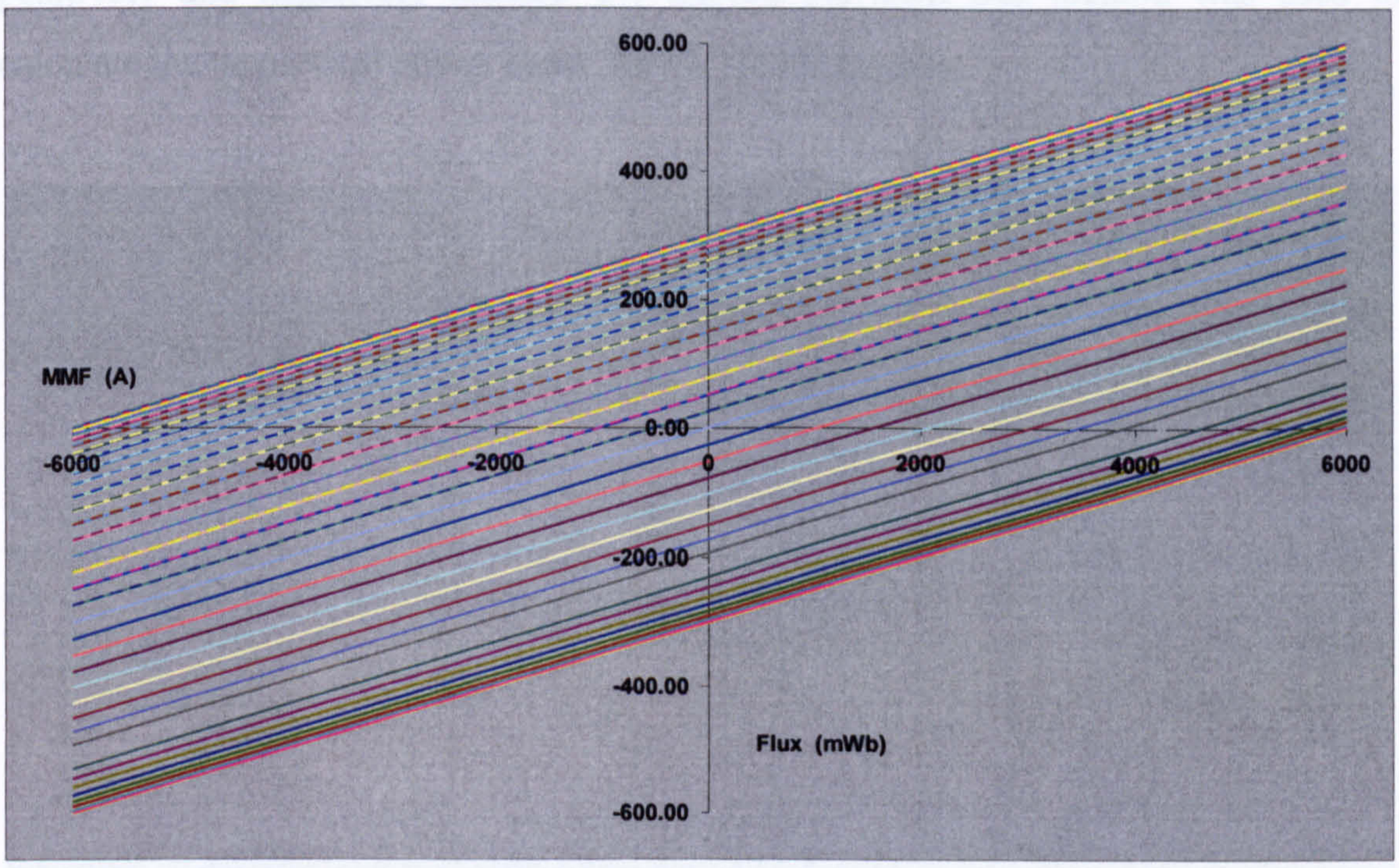

Figure D.4.2 Cosine interpolation of additional Ψ-I curves

Figure D.4.3 shows the three waveforms for flux, current and voltage on the same θ varying graph. This illustrates the phase difference between the current and voltage and hence the power factor of the model. For the test curves of figure D.4.1, the phase angle was 26.5° lagging which gave a power factor of 0.89. This exactly matched the hand calculated value. A further check of this number was to generate values of mean power, rms voltage and rms current from the data gathered. The mean power is equivalent to the average of the instantaneous product of voltage and current. Dividing this value by the product of the rms voltage and current provides a figure for power factor. The numbers generated from this process were:

- Mean Power = 7.844kW
- rms Voltage = 4.134V
- rms Current = 2121.32A

Therefore Power Factor $= \dfrac{\mathbf{7844}}{\mathbf{(4.134 \times 2121.32)}} = \mathbf{0.89}$

Again, this matched the hand calculated value exactly. The correlation of these three cross-checks pointed to a valid method for determining power factor from positively and negatively aligned Ψ-I curves. As such this method was used to calculate the theoretical power factor for all 3D FE models.

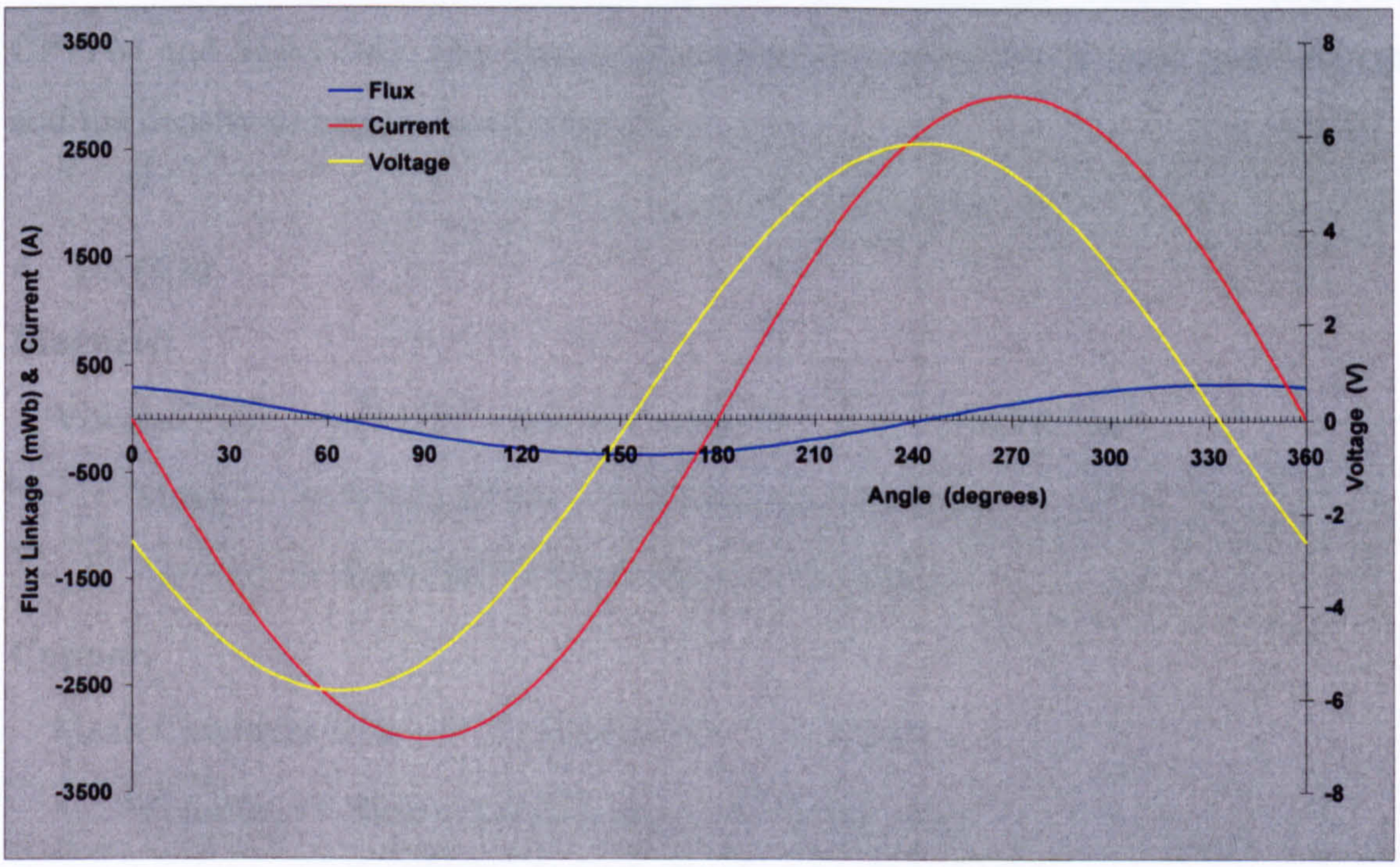

Figure D.4.3 Flux and voltage curves generated from a sinusoidal current waveform

D.5 Finite Element Solver

The solutions calculated for the models under scrutiny in this thesis have been produced by including the electric potential 'T' vector value to solve $\nabla.B = 0$

$$B = \mu H \qquad \{D6\}$$

$$H = -\nabla \phi \qquad \{D7\}$$

$$\nabla . B = 0 \qquad \{D8\}$$

$$\therefore \quad \nabla . (-\mu \nabla \phi) = 0 \qquad \{D9\}$$

$$\text{also,} \qquad \nabla \times H = J \qquad \{D10\}$$

$$\text{but,} \qquad \nabla \times (-\nabla \phi) = 0 \qquad \{D11\}$$

This implies that the current density (J) = 0 and so there are no sources in the problem. Introducing electric vector potential, T in the form, $H = T - \nabla \phi$, means that equation D7 can now be written as:

$$\nabla . B = \nabla . (\mu T - \mu \nabla \phi) = 0 \qquad \{D12\}$$

D.6 Calculation of Active Masses

The following are calculations of active mass based upon the rectilinear 3D Finite Element models derived in Chapter 3 (DSTFM) and Chapter 5 (SSTFM, CPTFM and SSBTFM). The density of iron/magnet components used was $7.6 g/cm^3$ and the density of copper was $8.93 g/cm^3$.

- **DSTFM**

Magnets:

$$\text{Volume/Pole} = \left(3\times10^{-3}\times15\times10^{-3}\times30\times10^{-3}\right) = 1.35\times10^{-6}\, m^3$$

$$\text{Mass} = \text{Volume/Pole} \times \text{Pole Number} \times \text{Density}$$

$$= 1.35\times10^{-6}\times100\times7600 = 1.026 kg$$

Copper:

$$\text{Mean Circumference} = 2\pi\times165.5\times10^{-3} = 1.04 m$$

$$\text{Volume} = \text{Mean circumference} \times N^{o} \text{ Turns} \times \text{csa}$$

$$= 1.04\times68\times3.15\times10^{-6} = 222.768\times10^{-6}\, m^3$$

$$\text{Mass} = 222.768\times10^{-6}\times8930 = 1.989 kg$$

Rotor Iron:

$$\text{Volume/Pole} = 2\times\left(2.74\times10^{-3}\times15\times10^{-3}\times30\times10^{-3}\right) = 2.466\times10^{-6}\, m^3$$

$$\text{Mass} = 2.466\times10^{-6}\times100\times7600 = 1.874 kg$$

Teeth:

$$\text{Volume/Pole} = 2\times\left(3.25\times10^{-3}\times7\times10^{-3}\times30\times10^{-3}\right) = 1.365\times10^{-6}\,m^3$$

$$\text{Mass} = 1.365\times10^{-6}\times100\times7600 = 1.037kg$$

Coreback:

$$\text{Volume/Pole} = \left(15\times10^{-3}\times8.48\times10^{-3}\times60\times10^{-3}\right)+2\times\left(15\times10^{-3}\times8.48\times10^{-3}\times46\times10^{-3}\right) = 19.33\times10^{-6}m^3$$

$$\text{Mass} = 19.33\times10^{-6}\times100\times7600 = 14.69kg$$

DSTFM Total Active Mass:

$$= 1.026 + 1.989 + 1.874 + 1.037 + 14.69 = 20.62\text{kg}$$

- **SSTFM**

Magnets:

$$\text{Volume/Pole} = 2\times\left(3\times10^{-3}\times8.48\times10^{-3}\times26.5\times10^{-3}\right) = 1.348\times10^{-6}\,m^3$$

$$\text{Mass} = \text{Volume/Pole} \times \text{Pole Number} \times \text{Density}$$

$$= 1.348\times10^{-6}\times100\times7600 = 1.025kg$$

Copper:

$$\text{Mean Circumference} = 2\pi\times150.45\times10^{-3} = 0.9453m$$

$$\text{Volume} = \text{Mean circumference} \times \text{N}^{\text{o}}\ \text{Turns} \times \text{csa}$$

$$= 0.9453\times68\times3.15\times10^{-6} = 202.48\times10^{-6}\,m^3$$

$$\text{Mass} = 202.48\times10^{-6}\times8930 = 1.808kg$$

Rotor Iron:

$$\text{Volume/Pole} = 9.1\times10^{-3}\times8.48\times10^{-3}\times60\times10^{-3} = 4.63\times10^{-6}\,m^3$$

$$\text{Mass} = 4.63\times10^{-6}\times100\times7600 = 3.519kg$$

Teeth:

$$\text{Volume/Pole} = 2\times\left[\left(9.1\times10^{-3}\times8.48\times10^{-3}\times60\times10^{-3}\right)+\left(\frac{9.5\times10^{-3}\times9.5\times10^{-3}}{2}\right)\times48\times10^{-3}\right] = 3.504\times10^{-6}\,m^3$$

$$\text{Mass} = 3.504\times10^{-6}\times100\times7600 = 2.663kg$$

Coreback:

$$\text{Volume/Pole} = \left(9.1\times10^{-3}\times8.48\times10^{-3}\times60\times10^{-3}\right)+2\times\left(9.1\times10^{-3}\times8.48\times10^{-3}\times10.9\times10^{-3}\right)$$
$$+2\times\left(\frac{7.9\times10^{-3}\times7.9\times10^{-3}\times8.48\times10^{-3}}{2}\right) = 6.8416\times10^{-6}\,m^3$$

$$\text{Mass} = 6.842\times10^{-6}\times100\times7600 = 5.199kg$$

SSTFM Total Active Mass:

$$= 1.025 + 1.808 + 3.519 + 2.663 + 5.199 = \mathbf{14.21kg}$$

- **CPTFM**

Magnets:

$$\text{Volume/Pole} = \left(3\times10^{-3}\times7.5\times10^{-3}\times60\times10^{-3}\right) = 1.35\times10^{-6}\,m^3$$

Mass = Volume/Pole × Pole Number × Density

$$= 1.35\times10^{-6}\times100\times7600 = 1.026kg$$

Copper:

$$\text{Mean Circumference} = 2\pi\times165\times10^{-3} = 1.0367m$$

Volume = Mean circumference × N° Turns × csa

$$= 1.0367\times68\times3.15\times10^{-6} = 222.07\times10^{-6}\,m^3$$

$$\text{Mass} = 222.07\times10^{-6}\times8930 = 1.983kg$$

Rotor Iron:

$$\text{Volume/Pole} = 2\times\left(2.74\times10^{-3}\times7.5\times10^{-3}\times60\times10^{-3}\right) = 2.466\times10^{-6}\,m^3$$

$$\text{Mass} = 2.466\times10^{-6}\times100\times7600 = 1.874kg$$

Teeth:

$$\text{Volume/Pole} =$$
$$2\times\left[\left(2.74\times10^{-3}\times10\times10^{-3}\times15\times10^{-3}\right)+\left(\frac{1.5\times10^{-3}+2.74\times10^{-3}}{2}\right)\times45\times10^{-3}\times30.05\times10^{-3}\right]$$

$$= 6.556\times10^{-6}\,m^3$$

$$\text{Mass} = 6.556\times10^{-6}\times100\times7600 = 4.982kg$$

Coreback:

Volume/Pole =

$$\left(15\times10^{-3}\times8.48\times10^{-3}\times60\times10^{-3}\right)+2\times\left(15\times10^{-3}\times8.48\times10^{-3}\times28\times10^{-3}\right)= 14.755\times10^{-6}\,m^3$$

$$\text{Mass} = 14.755\times10^{-6}\times100\times7600 = 11.214kg$$

CPTFM Total Active Mass:

$$= 1.026 + 1.983 + 1.874 + 4.982 + 11.214 = \mathbf{21.08kg}$$

- **SSBTFM**

Magnets:

$$\text{Volume/Pole} = 2\times\left(3\times10^{-3}\times15\times10^{-3}\times15\times10^{-3}\right) = 1.35\times10^{-6}\,m^3$$

Mass = Volume/Pole × Pole Number × Density

$$= 1.35\times10^{-6}\times100\times7600 = 1.026kg$$

Copper:

$$\text{Mean Circumference} = 2\pi\times157\times10^{-3} = 0.9865m$$

Volume = Mean circumference × N° Turns × csa

$$= 0.9865\times68\times3.15\times10^{-6} = 211.3\times10^{-6}\,m^3$$

$$\text{Mass} = 211.3\times10^{-6}\times8930 = 1.887kg$$

Rotor Iron:

$$\text{Volume/Pole} = 4\times\left(2.74\times10^{-3}\times15\times10^{-3}\times15\times10^{-3}\right) = 2.466\times10^{-6}\,m^3$$

$$\text{Mass} = 2.466\times10^{-6}\times100\times7600 = 1.874kg$$

Bridge:

Volume/Pole =

$$\left(2.74\times10^{-3}\times15\times10^{-3}\times30\times10^{-3}\right)+2\times\left(\frac{2.74\times10^{-3}\times15\times10^{-3}\times15\times10^{-3}}{2}\right) = 1.85\times10^{-3}\,m^3$$

$$\text{Mass} = 1.85\times10^{-6}\times100\times7600 = 1.406kg$$

Coreback:

Volume/Pole =

$$2\times\left(2.74\times10^{-3}\times15\times10^{-3}\times28\times10^{-3}\right)+2\times\left(5.74\times10^{-3}\times10.5\times10^{-3}\times15\times10^{-3}\right)$$
$$+\left(8.48\times10^{-3}\times15\times10^{-3}\times60\times10^{-3}\right)=\ 11.742\times10^{-6}\,m^3$$

Mass $= 11.742\times10^{-6}\times100\times7600 = 8.924kg$

SSBTFM Total Active Mass:

$= 1.026 + 1877 + 1.874 + 1.406 + 8.924 =$ **15.11kg**

D.7 Calculation of CPHTFM Active Masses

The following are calculations of active mass based upon the rectilinear 3D Finite Element models derived in Chapter 6 for the MKIII CPHTFM model and the final CPHTFM model. The density of iron/magnet components used was 7.6g/cm^3 and the density of copper was 8.93g/cm^3.

- **MKIII CPHTFM**

Magnets:

Volume/Pole $= \left(3\times10^{-3}\times7.5\times10^{-3}\times60\times10^{-3}\right) = 1.35\times10^{-6}\,m^3$

Mass = Volume/Pole × Pole Number × Density

$= 1.35\times10^{-6}\times100\times7600 = 1.026kg$

Copper:

Mean Circumference $= 2\pi\times160\times10^{-3} = 1.00m$

Volume = Mean circumference × N° Turns × csa

$= 1.00\times68\times3.15\times10^{-6} = 214.2\times10^{-6}\,m^3$

Mass $= 214.2\times10^{-6}\times8930 = 1.913kg$

Rotor Iron:

Volume/Pole $= 2\times\left(3.05\times10^{-3}\times7.5\times10^{-3}\times60\times10^{-3}\right) = 2.745\times10^{-6}\,m^3$

Mass $= 2.745\times10^{-6}\times100\times7600 = 2.086kg$

Teeth:

Volume/Pole =

$$2\times\left(\frac{.008\times.008}{2}+.008\times.015\right)\times9.31\times10^{-3}+\left(\frac{.007\times.007}{2}+.007\times.023\right)\times6.5\times10^{-3} = 3.972\times10^{-6}\,m^3$$

$$\text{Mass} = 3.972\times10^{-6}\times100\times7600 = 3.019kg$$

Coreback:

Volume/Pole =

$$\left(15\times10^{-3}\times9.1\times10^{-3}\times60\times10^{-3}\right)+2\times\left(15\times10^{-3}\times9.1\times10^{-3}\times5.5\times10^{-3}\right) = 9.692\times10^{-6}m^3$$

$$\text{Mass} = 9.692\times10^{-6}\times100\times7600 = 7.366kg$$

MKIII CPHTFM Total Active Mass:

$$= 1.026 + 1.913 + 2.086 + 3.019 + 7.366 = 15.41\text{kg}$$

D.8 DSTFM 2D Design Methodology Calculations

D.8.1 DSTFM 2D model iron widths, determined using the relative areas approach (Chapter 2, Section 2.4)

$$\text{Airgap Cross-sectional Area} = 0.00274\times0.03 = 82.2\times10^{-6}m^2$$

Tooth Calculations:

$$\text{Tooth Cross-sectional Area} = 0.00325\times0.03 = 97.5\times10^{-6}m^2$$

$$\therefore\ \text{2D Model Tooth Width} = 2.74\times10^{-3}\times\frac{97.5\times10^{-6}}{82.2\times10^{-6}} = 3.25mm$$

Side Cheek Calculations:

$$\text{Cheek Cross-sectional Area} = 0.00946\times0.015 = 141.9\times10^{-6}m^2$$

$$\therefore\ \text{2D Model Cheek Width} = 2.74\times10^{-3}\times\frac{141.9\times10^{-6}}{82.2\times10^{-6}} = 4.73mm$$

Flanking Piece Calculations:

$$\text{Cheek Cross-sectional Area} = 0.0109\times0.015 = 163.5\times10^{-6}m^2$$

$$\therefore\ \text{2D Model Flanking Width} = 2.74\times10^{-3}\times\frac{163.5\times10^{-6}}{82.2\times10^{-6}} = 5.45mm$$

D.8.2 Cross Slot Leakage

Rated MMF = 2000A

Conductor Area =

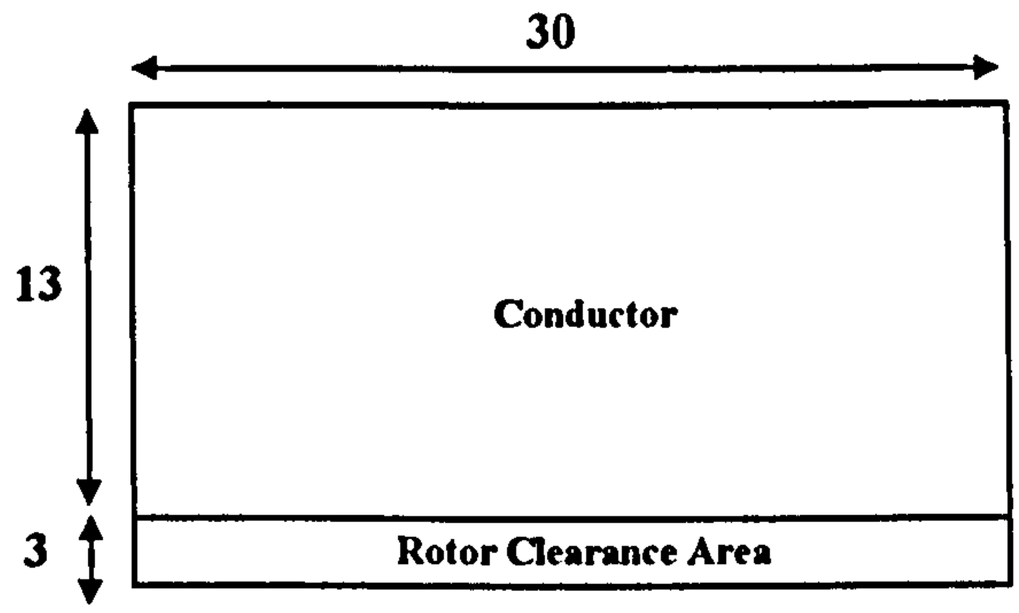

Cross slot flux density @ 2000A:

$$B = \mu H = \mu (I / length) = 4\pi \times 10^{-7} \times (2000/0.03) = 0.08T$$

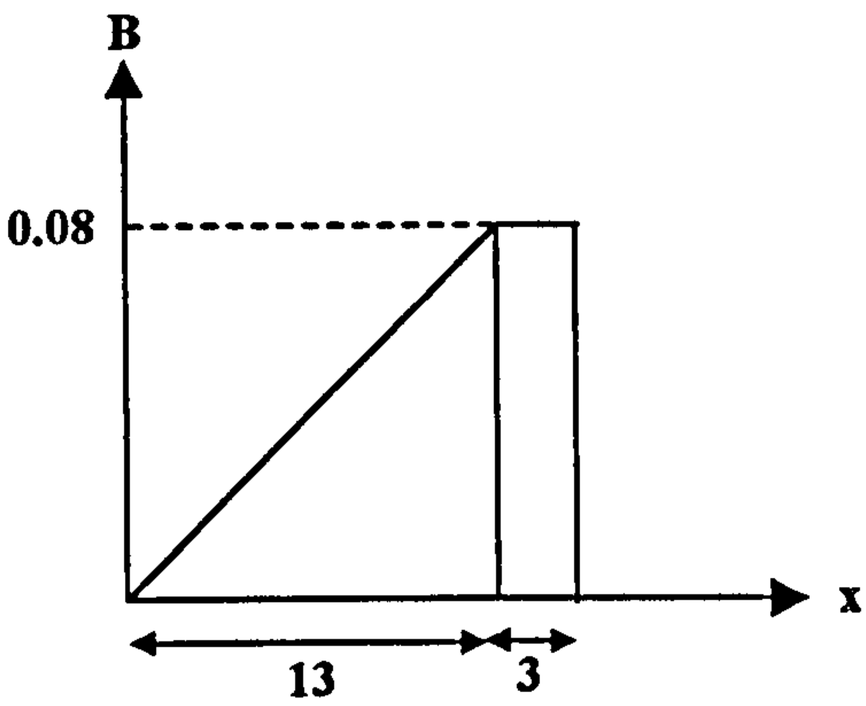

Therefore, flux per unit periphery =

$[(0.013/2)+0.003] \times 0.08 = 0.76mWb/m$

Peripheral length of conductor at a mean radius of 0.158m is 0.993m.

Therefore cross slot flux = $0.76 \times 10^{-3} \times 0.993 = 0.75mWb$

From the 2D FE model, this equates to 4.6% of the machine flux (16mWb) at rated MMF.

Appendix E

Test Results Data

E.1 Double-Sided Transverse Flux Machine

Table E.1.1 Flux and MMF results for the DSTFM 2D FEA model

Conductor MMF (A)	Average Vector Potential Of the Coil (Wb)	Total Flux (mWb) (Derived from Equation 2.5)
4080	6.3967×10^{-3}	19.19
2720	5.8865×10^{-3}	17.66
1360	5.0867×10^{-3}	15.26
0	3.2433×10^{-3}	9.73
-1360	-1.0133×10^{-3}	-3.04
-2720	-4.7695×10^{-3}	-14.31
-4080	-5.9334×10^{-3}	-17.8

Table E.1.2 Flux and MMF results for the DSTFM 3D FEA model

MMF (A)	Coreback Flux / Pole (Wb)	Total Flux Linkage in Machine (mWb)
60	0.18865×10^{-3}	1283.16
50	0.17281×10^{-3}	1175.04
40	0.14587×10^{-3}	992.12
30	0.10221×10^{-3}	694.96
20	0.42069×10^{-4}	286.28
10	-0.24123×10^{-4}	-163.88
0	-0.81553×10^{-4}	-554.88
-10	-0.12332×10^{-3}	-838.44
-20	-0.15053×10^{-3}	-1023.4
-30	-0.16885×10^{-3}	-1148.52
-40	-0.18208×10^{-3}	-1238.28
-50	-0.19185×10^{-3}	-1304.92
-60	-0.19920×10^{-3}	-1354.56

Thermal Test Results

With reference to these to tables E.1.3 and E.1.4:

"**Outer Temperature**" refers to the thermocouple temperature on the outer diameter of the winding, which is equivalent to the casing temperature.
"**Inner Temperature**" refers to the thermocouple temperature on the inner diameter of the winding.
"**Centre Temperature**" refers to the thermocouple temperature at the centre of the winding.
"**Difference**" refers to the temperature difference between the outer (casing) temperature and the centre (core) temperature.

Table E.1.3 15A Thermal Test on the DSTFM

Time (minutes)	0	1	2	3	4	5	6	7
Outer Temperature (°C)	16	18	19	19	20	20	21	21
Inner Temperature (°C)	16	22	25	27	29	30	31	32
Centre Temperature (°C)	16	24	27	31	32	34	35	36
Difference (°C)	0	6	8	12	12	14	14	15

Time (minutes)	8	9	10	11	12	13	14	15
Outer Temperature (°C)	21	21	21	22	22	22	22	22
Inner Temperature (°C)	32	33	33	33	33	33	33	34
Centre Temperature (°C)	36	37	37	38	38	38	38	39
Difference (°C)	15	16	16	16	16	16	16	17

Time (minutes)	20	25	30	35	40	45	50	55
Outer Temperature (°C)	23	23	24	25	25	26	27	27
Inner Temperature (°C)	34	35	36	36	37	38	38	38
Centre Temperature (°C)	39	40	40	41	42	43	43	43
Difference (°C)	16	17	16	16	17	17	16	16

Time (minutes)	60	75	90	105	120	135	150	165
Outer Temperature (°C)	28	29	31	32	33	34	35	36
Inner Temperature (°C)	39	40	42	43	44	46	46	47
Centre Temperature (°C)	44	46	47	48	49	51	52	53
Difference (°C)	16	17	16	16	16	17	17	17

Time (minutes)	180	195	210	225	240	255	270	285
Outer Temperature (°C)	37	37	38	38	39	40	40	40
Inner Temperature (°C)	48	48	49	50	50	51	51	52
Centre Temperature (°C)	53	54	55	55	56	56	57	57
Difference (°C)	16	17	17	17	17	16	17	17

Time (minutes)	300	315	330	345	360	375	390	405
Outer Temperature (°C)	40	40	41	41	41	41	41	41
Inner Temperature (°C)	52	52	52	52	52	52	52	52
Centre Temperature (°C)	57	57	58	58	58	58	58	58
Difference (°C)	17	17	17	17	17	17	17	17

Table E.1.4 20A Thermal Test on the DSTFM

Time (minutes)	0	1	2	3	4	5	6	7
Outer Temperature (°C)	19	22	23	24	25	25	26	27
Inner Temperature (°C)	19	28	34	38	42	44	46	47
Centre Temperature (°C)	19	29	38	43	48	51	53	55
Difference (°C)	0	7	15	19	23	26	27	28

Time (minutes)	8	9	10	11	12	13	14	15
Outer Temperature (°C)	27	28	28	28	28	29	29	29
Inner Temperature (°C)	48	48	49	49	50	50	51	51
Centre Temperature (°C)	56	57	58	58	59	59	60	60
Difference (°C)	29	29	30	30	31	30	31	31

Time (minutes)	20	25	30	35	40	45	50	60
Outer Temperature (°C)	31	32	33	34	35	36	37	39
Inner Temperature (°C)	52	53	54	56	57	58	59	61
Centre Temperature (°C)	62	63	64	65	66	67	68	70
Difference (°C)	31	31	31	31	31	31	31	31

Time (minutes)	65	83	90	105	120	135	150	165
Outer Temperature (°C)	40	43	44	46	48	49	51	52
Inner Temperature (°C)	61	64	66	68	69	71	72	73
Centre Temperature (°C)	71	74	75	78	79	81	83	84
Difference (°C)	31	31	31	32	31	32	32	32

Time (minutes)	180	195	210	225	240	255	270	285
Outer Temperature (°C)	53	54	55	56	57	57	58	58
Inner Temperature (°C)	75	75	76	77	78	78	79	79
Centre Temperature (°C)	85	86	87	88	88	89	90	90
Difference (°C)	32	32	32	32	31	32	32	32

Time (minutes)	300	315	330	360	375	390	420	435
Outer Temperature (°C)	59	59	59	60	60	60	60	60
Inner Temperature (°C)	80	80	80	81	81	81	81	81
Centre Temperature (°C)	91	91	91	92	92	92	92	92
Difference (°C)	32	32	32	32	32	32	32	32

Static Torque Tests

- Table E.1.5 contains the results from the No-Load test performed on the DSTFM in order to determine the level of 'stiction' in the prototype due to the inclusion of brass bushes as bearing surfaces instead of thrust bearings.
- Table E.1.6 shows the data collected from seven transitions of a single pole in the same direction of rotation. The armature current was increased incrementally for each transition by 5A. This data incorporates the 'stiction' effect and so 42.5Nm has been subtracted from each torque reading

Table E.1.5 Results from the investigation into the friction inherent in the DSTFM

Angle (degrees)	1st Pass (Nm)	2nd Pass (Nm)	3rd Pass (Nm)	4th Pass (Nm)	5th Pass (Nm)
2.394	100.48	22.70	102.00		
2.28	107.45	22.09	107.75	29.96	
2.166	106.23	14.83	106.23	20.28	
2.052	100.18	5.15	99.27	8.78	
1.938	89.29	-13.92	88.08	-8.17	
1.824	77.48	-26.03	75.67	-23.61	
1.71	64.77	-39.65	62.05	-38.44	
1.596	50.85	-54.48	46.31	-53.87	
1.482	36.92	-68.10	34.20	-66.59	
1.368	25.12	-75.36	22.40	-78.39	
1.254	19.07	-82.02	13.01	-83.54	
1.14	16.34	-80.81	11.20	-81.72	
1.026	20.58	-71.73	13.92	-75.97	
0.912	27.24	-60.23	21.19	-63.56	
0.798	36.02	-46.91	29.66	-50.54	29.36
0.684	43.89	-40.86	36.92	-43.89	36.62
0.57	49.03	-33.90	42.98	-35.41	42.07
0.456	52.36	-25.12	47.22	-27.24	46.31
0.342	53.57	-20.58	48.73	-22.09	48.43
0.228	52.97	-19.07	48.43	-19.37	49.64
0.114	48.43	-18.46	48.73	-19.07	48.73
0	0.00	-18.46	47.52	-19.67	47.52
-0.114		-20.88	45.10	-19.67	45.40
-0.228		-22.40	44.19	-21.79	43.89
-0.342		-24.82	42.98	-23.91	43.58
-0.456		-24.52	44.79	-24.21	45.70
-0.57		-23.31	49.33	-24.21	49.03
-0.684		-18.46	54.48	-19.07	56.30
-0.798		-13.92	65.68	-13.62	63.86
-0.912		-8.17	75.97	-8.17	76.88
-1.026		0.00	87.47	-0.91	88.68
-1.14		5.45	99.88	4.84	100.18
-1.254		7.57	106.23	8.17	106.54
-1.368		5.15	105.63	5.45	107.14
-1.482		-3.03	101.39	-3.03	101.39
-1.596		-16.65	91.10	-13.01	90.80
-1.71		-30.87	77.18	-28.15	77.18
-1.824		-45.40	62.65	-41.16	63.26
-1.938		-60.84	47.82	-58.41	47.52
-2.052		-74.76	34.50	-73.55	35.11
-2.166		-84.75	16.34	-82.63	17.86
-2.28		-92.62	3.93	-92.01	4.84
-2.394		-94.43	-8.17	-95.04	-4.24
-2.508		-91.71		-92.92	

Table E.1.6 Static Torque Test Results for the DSTFM

Angle (degrees)	Torque at 0A (Nm)	Torque at 5A (Nm)	Torque at 10A (Nm)	Torque at 15A (Nm)	Torque at 20A (Nm)	Torque at 25A (Nm)	Torque at 30A (Nm)
0	0.00	0.00	0.00	0.00	0.00	0.00	0.00
0.114	-5.27	5.32	22.57	32.26	40.73	48.60	56.17
0.228	-1.94	15.61	40.73	62.22	71.91	88.55	100.36
0.342	-2.25	25.60	57.38	87.34	103.38	125.48	136.07
0.456	-4.06	33.77	71.00	107.62	135.47	157.26	160.89
0.57	-8.30	38.61	88.86	123.66	160.89	185.41	187.52
0.684	-13.75	43.46	101.87	139.10	184.19	212.65	213.25
0.798	-21.92	44.67	113.07	156.05	203.87	238.37	243.52
0.912	-30.39	45.58	115.79	169.97	224.15	266.22	273.18
1.026	-37.96	48.30	120.64	186.01	244.73	294.36	307.08
1.14	-40.38	51.93	132.44	201.14	265.61	318.58	335.83
1.254	-37.66	57.08	143.34	214.76	284.38	341.88	361.56
1.368	-29.49	60.71	152.42	230.81	302.54	361.56	388.19
1.482	-18.89	67.97	167.25	247.45	322.51	385.77	413.92
1.596	-4.06	80.08	179.96	262.58	342.79	407.56	436.92
1.71	8.95	91.88	191.16	281.35	358.23	429.96	459.92
1.824	23.78	105.81	206.89	297.09	375.78	450.54	482.62
1.938	36.19	117.61	218.40	314.04	393.94	468.09	500.78
2.052	45.27	131.23	233.83	328.57	404.53	487.16	518.94
2.166	51.33	140.01	246.54	340.67	416.64	498.66	533.17
2.28	49.51	146.97	258.35	349.45	425.42	510.16	546.18
2.394	44.06	152.11	266.52	354.59	429.96	518.03	558.89
2.508	32.26	150.90	268.03	356.41	426.02	518.94	563.43
2.622	18.34	139.70	265.31	348.24	414.52	509.56	559.19
2.736	5.32	123.66	253.20	329.47	388.19	490.19	544.36
2.85	-4.97	99.75	231.71	297.09	349.15	457.80	515.31
2.964	-12.23	78.57	202.35	263.19	302.54	424.51	474.45
3.078	-16.77	53.75	165.73	222.94	256.53	379.72	
3.192	-17.68	38.01	137.89	169.36			
3.306	-17.08	21.06	105.81	143.94			
3.42	-15.87	6.83	77.96				
3.534	-13.75	-3.15	49.81				
3.648	-12.23	-12.84	25.90				
3.762	-12.54	-22.52	-0.13				

E.2 Clawpole Transverse Flux Machine

Table E.2.1 3D FE results from the 24 pole Clawpole machine

Current (A)	MMF (A)	Current Density (A/m^2)	Flux per Pole (Wb)	Total Flux (mWb)
60	2400	15.41×10^{6}	0.20252×10^{-3}	4.860
50	2000	12.85×10^{6}	0.19642×10^{-3}	4.714
40	1600	10.28×10^{6}	0.18929×10^{-3}	4.543
30	1200	7.707×10^{6}	0.18065×10^{-3}	4.336
25	1000	6.422×10^{6}	0.17292×10^{-3}	4.15
20	800	5.138×10^{6}	0.16949×10^{-3}	4.068
15	600	3.853×10^{6}	0.15625×10^{-3}	3.75
10	400	2.569×10^{6}	0.15327×10^{-3}	3.678
5	200	1.284×10^{6}	0.14155×10^{-3}	3.397
0	0	0	0.12559×10^{-3}	3.014
-5	-200	-1.284×10^{6}	0.10430×10^{-3}	2.503
-10	-400	-2.569×10^{6}	0.76664×10^{-4}	1.840
-15	-600	-3.853×10^{6}	0.43096×10^{-4}	1.034
-20	-800	-5.138×10^{6}	-0.45499×10^{-5}	0.1092
-25	-1000	-6.422×10^{6}	-0.35727×10^{-4}	-0.857
-30	-1200	-7.707×10^{6}	-0.73376×10^{-4}	-1.761
-40	-1600	-10.28×10^{6}	-0.13059×10^{-3}	-3.134
-50	-2000	-12.85×10^{6}	-0.16079×10^{-3}	-3.859
-60	-2400	-15.41×10^{6}	-0.17711×10^{-3}	-4.251

Table E.2.2 Results from the 7A Thermal Test on the CPTFM

The measured curve was curve matched using a calculated curve derived from the following exponential equation:

$$T_{rise} = 16 \times (1\text{-EXP}(-t/5.5)) + 6 \times (1\text{-EXP}(-t/80)) + 16.5 \times (1\text{-EXP}(-t/340))$$

Time (minutes)	0	2	4	6	8	10	12	14	16
Measured (°C)	0.00	4.37	8.55	11.23	13.13	14.41	15.42	16.18	16.57
Calculated (°C)	0.00	5.12	8.75	11.35	13.22	14.59	15.60	16.37	16.97

Time (minutes)	18	20	25	30	35	40	50	55	60
Measured (°C)	17.17	17.47	18.62	19.14	19.65	19.83	20.91	21.28	22.16
Calculated (°C)	17.45	17.85	18.61	19.20	19.71	20.18	21.04	21.45	21.83

Time (minutes)	75	90	105	120	150	180	215	240	270
Measured (°C)	23.10	23.65	25.09	26.05	26.81	27.98	29.74	30.24	30.82
Calculated (°C)	22.92	23.89	24.77	25.57	26.97	28.15	29.32	30.06	30.84

Time (minutes)	300	330	360	390	420	450	480
Measured (°C)	31.75	32.10	32.19	32.28	33.13	33.73	34.55
Calculated (°C)	31.53	32.15	32.71	33.21	33.67	34.09	34.46

Table E.2.3 Static Torque test results from the CPTFM using DC excitation current

Angle (°electrical)	Torque @ 0A (Nm)	Torque @ 5A (Nm)	Torque @ 10A (Nm)	Torque @ 15A (Nm)	Torque @ 20A (Nm)
0°	0	0	0	0	0
17°	1.30	4.05	4.10	5.69	7.00
34°	2.72	6.48	8.27	11.06	14.00
51°	3.25	8.19	11.32	15.13	19.00
69°	2.97	8.66	12.43	16.50	19.31
85°	0.64	5.69	9.18	11.92	15.92
102°	-1.70	2.52	5.60	9.03	11.99
119°	-4.03	-0.39	3.27	5.96	8.70

Table E.2.4 3D FE Flux linkage against MMF data regarding the effect of varying Pole Number for the aligned position (positive d-axis) only.

Current (A)	60	40	20	0	-20	-40	-60
12 Poles Flux Linkage (mWb)	186.8	175.2	155.6	120.96	59.6	-25.8	-107.2
18 Poles Flux Linkage (mWb)	190	178.8	159.6	116.84	34.04	-74	-146.8
24 Poles Flux Linkage (mWb)	190.8	180.4	158.8	107.6	-2	-117.2	-167.2
30 Poles Flux Linkage (mWb)	192	181.2	158.8	98.8	-40.4	-143.6	-177.6
36 Poles Flux Linkage (mWb)	190.8	180	156.8	88.24	-74.4	-156.8	-181.2

Table E.2.5 3D FE Flux linkage in mWb against MMF data regarding the effect of changing the tooth shape and pole arc coverage for the aligned position (positive d-axis) only.

Tooth Shape	Pole Arc Coverage	60A	40A	20A	0A	-20A	-40A	-60A
Rectangular	96°elec	189.2	178.4	158	108	-19.68	-134.8	-174
Rectangular	120°elec	183.6	170.4	148.4	105.6	10.64	-106	-161.6
Rectangular	144°elec	169.6	153.6	130.4	92.4	14.68	-89.2	-148.4

Table E.2.6 3D FE Flux linkage in mWb against MMF data relating to a flux concentrating rotor topology for the CPTFM for the aligned position (positive d-axis) only.

Current (A)	60	40	20	0	-20	-40	-60
Flux Linkage (mWb)	181.2	166.0	145.2	114.0	13.8	-132.5	-171.4

E.3 Claw Pole Hybrid Transverse Flux Machine

Table E.3.1 3D FE results from the initial CPHTFM model based solely upon the DSTFM. Values are for the aligned position (positive d-axis) only.

Current (A)	60	40	20	0	-20	-40	-60
Flux Linkage (mWb)	1219.2	957.4	410.7	-460.4	-862.9	-1126.1	-1297.4

Table E.3.2 3D FE results from the second CPHTFM model, incorporating a 10mm stator coreback and a 9.5mm pole pitch. Values are for the aligned position (positive d-axis) only.

Current (A)	60	40	20	0	-20	-40	-60
Flux Linkage (mWb)	932.96	843.2	710.6	467.16	-227.12	-695.64	-874.48

Table E.3.3 3D FE results for 90 and 80 pole CPHTFM models. Values are for the aligned position (positive d-axis) only.

Current (A)	60	40	20	0	-20	-40	-60
90 Pole Model Flux Linkage (mWb)	965.6	875.16	738.48	478.72	-242.76	-715.36	-891.48
80 Pole Model Flux Linkage (mWb)	975.8	888.08	752.08	482.8	-245.48	-724.88	-901

Table E.3.4 3D FE results from the third CPHTFM model, incorporating a 15mm stator coreback and a 9.1mm pole pitch. Values are for the aligned position (positive d-axis) only.

Current (A)	60	40	20	0	-20	-40	-60
Flux Linkage (mWb)	1073.1	941.12	769.76	497.76	-269.96	-778.6	-1013.2

Table E.3.5 3D FE results for the seven stator tooth axial overlap models. Overlaps investigated were 2.5mm, 5mm, 10mm, 15mm, 20mm, 40mm and 60mm. Values are for the aligned position (positive d-axis) only.

Current (A)	60	40	20	0	-20	-40	-60
2.5mm Flux Linkage (mWb)	1133.6	990.1	805.8	513.4	-311.4	-816.0	-1039.0
5mm Flux Linkage (mWb)	1177.1	1029.5	838.4	529.0	-340.7	-867.0	-1092.8
10mm Flux Linkage (mWb)	1222.6	1079.2	887.4	554.2	-397.8	-929.6	-1145.8
15mm Flux Linkage (mWb)	1280.4	1141.0	944.5	573.9	-467.2	-1003.0	-1215.8
20mm Flux Linkage (mWb)	1304.9	1165.5	969.0	591.6	-505.2	-1037.7	-1248.5
40mm Flux Linkage (mWb)	1230.8	1100.2	930.2	577.3	-575.3	-1013.9	-1200.2
60mm Flux Linkage (mWb)	1110.4	984.6	826.9	510.7	-605.9	-929.6	-1091.4

Table E.3.6 3D FE results for the four additional rotor radial depth models. Depths investigated were 10mm, 12.5mm, 15mm and 30mm. Values are for the aligned position (positive d-axis) only.

Current (A)	60	40	20	0	-20	-40	-60
10mm Flux Linkage (mWb)	1160.1	1027.5	858.8	569.8	-235.3	-864.3	-1096.8
12.5mm Flux Linkage (mWb)	1223.3	1089.4	916.0	612.0	-199.2	-914.6	-1173.7
15mm Flux Linkage (mWb)	1260.7	1123.4	941.1	635.1	-170.7	-937.0	-1222.0
30mm Flux Linkage (mWb)	1313.8	1159.4	960.2	669.8	-73.4	-948.6	-1281.8

Table E.3.7 3D FE results from the revised CPHTFM model, incorporating a 5mm axial stator tooth overlap, a 15mm radially deep active rotor, a 15mm stator coreback and a 9.1mm pole pitch. Values are for the aligned position (positive d-axis) only.

MMF (A)	60	50	40	30	20	10	0
Flux Linkage (mWb)	1302.88	1251.2	1166.88	1089.36	979.88	855.44	663.68
MMF (A)	-10	-20	-30	-40	-50	-60	
Flux Linkage (mWb)	322.32	-197.88	-691.56	-983.96	-1164.2	-1274.3	

Table E.3.8 3A Thermal Test on the CPHTFM

With reference to this table:

"**Centre Temperature**" refers to the thermocouple temperature at the centre of the winding.

"**Inner Temperature**" refers to the thermocouple temperature on the inner diameter of the winding.

"**Outer Temperature**" refers to the thermocouple temperature on the outer diameter of the winding.

"**Casing Temperature**" refers to the thermocouple temperature of the aluminium casing temperature.

Time (minutes)	0	0.5	1	1.5	2	2.5	3	3.5
Centre Temperature (°C)	25	29	33	36	39	42	44	46
Inner Temperature (°C)	25	27	29	29	30	30	31	32
Outer Temperature (°C)	25	27	28	29	30	31	32	32
Casing Temperature (°C)	25	25	25	25	25	26	26	26

Time (minutes)	4	4.5	5	5.5	6	6.5	7	7.5
Centre Temperature (°C)	47	49	50	51	52	53	53	54
Inner Temperature (°C)	32	33	33	34	34	35	35	35
Outer Temperature (°C)	32	32	33	34	34	35	35	35
Casing Temperature (°C)	26	26	27	27	27	27	27	28

Time (minutes)	8	8.5	9	9.5	10	10.5	11	11.5
Centre Temperature (°C)	55	55	56	56	56	57	57	58
Inner Temperature (°C)	36	36	36	36	36	36	36	36
Outer Temperature (°C)	36	36	36	36	36	36	36	37
Casing Temperature (°C)	28	28	28	28	28	29	29	29

Time (minutes)	12	12.5	13	13.5	14	14.5	15	15.5
Centre Temperature (°C)	58	58	59	59	59	59	60	60
Inner Temperature (°C)	36	36	36	36	36	37	37	37
Outer Temperature (°C)	37	37	37	38	38	38	38	38
Casing Temperature (°C)	29	29	29	30	30	30	30	30

Time (minutes)	16	16.5	17	17.5	18	18.5	19	19.5
Centre Temperature (°C)	60	60	60	60	60	61	61	61
Inner Temperature (°C)	37	37	37	38	38	38	38	38
Outer Temperature (°C)	38	39	39	39	39	39	40	40
Casing Temperature (°C)	30	30	31	31	31	31	31	31

Time (minutes)	20	20.5	21	21.5	22	22.5	23	23.5
Centre Temperature (°C)	61	62	62	62	62	62	63	63
Inner Temperature (°C)	38	39	39	39	39	39	39	39
Outer Temperature (°C)	40	40	40	40	40	40	41	41
Casing Temperature (°C)	31	32	32	32	32	32	32	32

Time (minutes)	24	24.5	25	25.5	26	26.5	27	27.5
Centre Temperature (°C)	63	63	63	63	64	64	64	64
Inner Temperature (°C)	40	40	40	40	40	40	40	40
Outer Temperature (°C)	41	41	41	41	41	42	42	42
Casing Temperature (°C)	32	33	33	33	33	33	33	33

Time (minutes)	28	28.5	29	29.5	30	30.5	35	40
Centre Temperature (°C)	64	64	65	65	65	65	66	67
Inner Temperature (°C)	41	41	41	41	42	42	43	44
Outer Temperature (°C)	42	42	43	43	43	44	44	45
Casing Temperature (°C)	33	34	34	34	34	34	35	36

Time (minutes)	24	24.5	25	25.5	26	26.5	27	27.5
Centre Temperature (°C)	63	63	63	63	64	64	64	64
Inner Temperature (°C)	40	40	40	40	40	40	40	40
Outer Temperature (°C)	41	41	41	41	41	42	42	42
Casing Temperature (°C)	32	33	33	33	33	33	33	33

Time (minutes)	45	50	55	60	65	70	75	80
Centre Temperature (°C)	69	70	71	72	73	74	75	76
Inner Temperature (°C)	45	46	47	48	49	50	51	52
Outer Temperature (°C)	46	47	48	49	50	51	52	53
Casing Temperature (°C)	37	38	39	39	40	41	42	43

Time (minutes)	85	90	95	100	105	110	115	120
Centre Temperature (°C)	77	77	78	79	80	80	81	82
Inner Temperature (°C)	53	54	54	55	56	57	57	58
Outer Temperature (°C)	54	55	56	56	57	58	58	59
Casing Temperature (°C)	44	44	45	45	46	47	47	48

Time (minutes)	135	150	165	180	195	210	225	240
Centre Temperature (°C)	83	84	86	88	89	89	91	92
Inner Temperature (°C)	59	61	63	64	65	66	67	67
Outer Temperature (°C)	60	62	63	64	65	66	67	68
Casing Temperature (°C)	49	50	52	53	53	54	55	55

Time (minutes)	255	270	285	300	315	330	345
Centre Temperature (°C)	92	93	93	94	94	95	95
Inner Temperature (°C)	68	69	69	70	70	71	71
Outer Temperature (°C)	68	69	69	70	70	71	71
Casing Temperature (°C)	56	56	57	57	57	58	58

Table E.3.9 Static Torque Tests for the CPHTFM

The 45Nm 'stiction' component, determined in Chapter 6, section 6.7.4, has been subtracted from the values in this table.

Angular Position (°mech)	Torque at 0A (Nm)	Torque at 1A (Nm)	Torque at 2A (Nm)	Torque at 3A (Nm)	Torque at 4A (Nm)
0	0	0	0	0	0
0.114	9.47	30.66	53.36	51.24	58.20
0.228	47.61	82.11	118.13	126.60	142.65
0.342	76.06	126.00	174.73	195.61	217.10
0.456	85.74	158.08	220.73	255.24	280.66
0.57	91.19	181.99	258.26	302.75	339.98
0.684	82.42	198.34	290.65	343.31	397.19
0.798	68.49	208.32	316.98	383.26	444.10
0.912	40.35	210.44	341.19	420.19	509.17
1.026	23.40	208.93	361.77	456.81	560.62
1.14	-11.71	205.90	385.38	494.34	610.87
1.254	-35.93	208.93	406.87	539.44	659.59
1.368	-44.10	217.10	435.62	576.36	709.53
1.482	-37.14	229.81	459.23	615.41	759.47
1.596	-27.75	241.92	481.63	649.00	801.85
1.71	-15.35	254.93	498.58	675.33	836.35
1.824	-3.24	265.53	510.08	693.80	867.52
1.938	6.75	275.21	520.67	711.96	892.95
2.052	16.74	280.66	528.54	724.36	909.59
2.166	24.00	285.50	529.15	727.69	917.46
2.28	26.12	280.66	521.88	726.79	915.95
2.394	16.74	265.83	502.21	711.05	897.79
2.508	-5.66	232.84	463.47	678.36	855.42
2.622	-35.32	189.56	408.99		
2.736	-39.35	133.87			
2.85	-51.45				
2.964	-74.76				
3.078	-88.68				
3.192	-97.46				
3.306	-92.01				
3.42	-72.64				
3.534	-16.65				
3.648	0.00				

Table E.3.10 3D FE results for the steel CPHTFM model, incorporating revised magnet data (see Appendix B.3). Values are for the aligned position (positive d-axis) only.

Current (A)	60	40	20	0	-20	-40	-60
Flux Linkage (mWb)	10272.3	9052.5	7522.5	5384.8	267.75	-6621.5	-9677.3

E.4 TFM Topology Comparisons

Table E.4.1 3D FE Flux linkage in mWb against MMF data relating to a 100 pole SSTFM topology for the aligned position (positive d-axis) only.

Current (A)	60	40	20	0	-20	-40	-60
Flux Linkage (mWb)	813.96	720.8	527	199.24	-197.9	-525.6	-722.8

Table E.4.2 3D FE Flux linkage in mWb against MMF data relating to a 100 pole, flux concentrating magnet, CPTFM topology for the aligned position (positive d-axis) only.

Current (A)	60	40	20	0	-20	-40	-60
Flux Linkage (mWb)	1268.7	1144.8	957.58	481.12	-743.3	-1126.6	-1276.2

Table E.4.3 3D FE Flux linkage in mWb against MMF data relating to a 100 pole, surface mounted magnet, CPTFM topology for the aligned position (positive d-axis) only.

Current (A)	60	40	20	0	-20	-40	-60
Flux Linkage (mWb)	1285.9	1157.4	952.68	425.0	-731.0	-1102.3	-1270.2

Table E.4.4 3D FE Flux linkage in mWb against MMF data relating to a 100 pole, surface mounted magnet, SSBTFM topology for the aligned position (positive d-axis) only.

Current (A)	60	40	20	0	-20	-40	-60
Flux Linkage (mWb)	695.10	607.19	492.13	259.18	-207.77	-548.52	-680.54

References

1) Bork M. "Electric machine", Patent No. WO 97/3951, Germany, 1997.

2) Bork M., Henneberger G. "New transverse flux concept for an electric vehicle drive system". Proceedings of the International Conference on Electrical Machines and Drives, pp: 308-313, 1996.

3) CIBA Polymers "Structural Adhesives". Company Literature, Publ No. A230b - GB, May 1995.

4) Fer A.F., Akay H.U. "Calculation of magnetic forces in a Lundell alternator using 3D finite elements". Proceedings of the IEEE, Vol: TA1, pp: 4.1-4.3. 1997.

5) Fitzgerald A.E., Kingsley C., Umans S.D. "Electric Machinery". Electrical Engineering Series, 5th Edition, McGraw-Hill, pp: 107-114, 1992.

6) Fothergill R.M. "The design and analysis of a novel permanent magnet machine". Final Year Undergraduate Project Thesis. Newcastle University, 1992.

7) Hadfield D. "Magnetic powder materials: Current status and development". Powder metallurgy: An overview. Book No. 492 (Jenkins I., Wood J.V.), Institute of Metals, pp: 346-351, 1991.

8) Hanselman, D. C. "Brushless Permanent Magnet Motor Design". Publisher McGraw-Hill, 1994.

9) Harris M., Pajooman G.H., Abu Sharkh S.M. "Comparison of alternative topologies for VRPM (transverse-flux) electrical machines". New topologies for permanent magnet machines (Organised by Professional Group P1 (Electrical machines)), IEE, London, 1997.

10) Harris M.R., Mecrow B.C. "Variable-reluctance permanent magnet motors for high specific output". IEE International Conference on Electrical Machines, (376), pp: 437-442, 1993.

11) Harris M.R., Pajooman G.H., Abu Sharkh S.M. "The problem of power factor in VRPM (transverse flux) machines". IEE Electrical Machines and Drives Conference, pp: 386-390, 1997.

12) Harris M.R., Pajooman G.H., Abu Sharkh S.M. "Performance and design optimisation of electric motors with heteropolar surface magnets and homopolar windings". IEE Proceedings of Electric Power Applications, Vol:143 (6), pp: 429-436, 1996.

13) Henneberger G. "Development of a new transverse flux motor". New topologies for permanent magnet machines (Organised by Professional Group P1 (Electrical machines)), IEE, London, 1997.

14) Höganäs AB S-26383, Höganäs, Sweden "Somaloy 500". Company Literature, SMC 97-1, AB Ruter Press, 1997.

15) Huang S., Luo J., Lipo T.A. "Evaluation of the transverse flux circumferential current machine by the use of sizing equations". Proceedings of the IEEE, Vol: WB2, pp: 15.1-15.3, 1997.

16) Jack A.G. "Experience with the use of soft magnetic composites in electrical machines". International Conference on Electrical Machines, Vol: 3/3, pp: 1441-1448, 1998.

17) Jack A.G., Mecrow B.C., Maddison C.P. "Claw pole armature permanent magnet machines exploiting soft iron powder metallurgy". IEEE Proceedings of International Conference on Electrical Machines and Drives, pp: MAI/5.1-5.3, 1997.

18) Krause R.F., Bularzik J.H., Kokal H.R. "A new soft magnetic material for AC and DC motor applications". Drives and Controls Conference, pp: 52-54, 1997.

19) Laithwaite E.R., Eastham J.F., Bolton H.R., Fellows T.G. "Linear motors with transverse flux". Proceedings of the IEE, Vol:118 (12), pp: 1761-1767, 1971.

20) Maddison C.P., Mecrow B.C., Jack A.G. "Claw pole geometries for high performance transverse flux machines". Proceedings of the International Conference on Electrical Machines and Drives, pp: 340-345, 1998.

21) McLean G.W. "Brushless d.c. drives using claw-type stator and disc rotor". Proceedings of the IEE, Vol:126 (7), pp: 683-689, 1979.

22) McLean G.W., Al-Abadi H.J. "Permanent magnet brushless drives using claw armatures". Proceedings of the International Conference on Electrical Machines and Drives, Vol:E4, pp: 5.1-5.10, 1978.

23) McLean G.W., Al-Abadi H., Taylor E.F. "A linear motor using claw stators and permanent magnet moving member". 7th International Conference on Electrical Variable Speed Drives, pp: 183-186, 1979.

24) Mecrow B.C., Jack A.G. "A new high torque density permanent magnet machine configuration". Proceedings of the International Conference on Electrical Machines and Drives, pp: 1046-1052, 1990.

25) Mecrow B.C., Jack A.G., Maddison C.P. "Permanent magnet machines for high torque, low speed applications". Proceedings of the International Conference on Electrical Machines and Drives, pp: 461-466, 1996.

26) Mitcham A.J. "Transverse-flux motors for electrical propulsion of ships". New topologies for permanent magnet machines (Organised by Professional Group P1 (Electrical machines)), IEE, London, 1997.

27) Oliver C.G. "Advances in powder metallurgy of soft magnetic materials". IEEE Transactions on magnetics, Vol:31 (6), pp: 3982-3984, 1995.

28) Parker D.S., Hodge C.G. "The electric warship". EMD97 Conference Publication No. 444, pp: 319-325, 1997.

29) Pajooman G. H. "Performance assessment and design optimisation of VRPM (transverse flux) machines by finite element computation". PhD Thesis, University of Southampton, June 1997.

30) Persson M. "SMC: More than material". Magnetic materials based on powder metallurgy. One-day seminar, The U.K. Magnetic Society, Oxfordshire, UK, 1998.

31) Persson M., Jansson P. "Soft magnetic composite materials - Use for electrical machines". IEE 7th International Conference on Electrical Machines and Drives, pp: 242-246, 1995.

32) Roark R.J. "Formulas for stress and strain". 5th Edition, McGraw-Hill, 1975.

33) Say M.G. "The performance and design of alternating current machines". 3rd Edition, Pitman, 1958

34) Spooner E., Chalmers B. J. "TORUS: A slotless, toroidal-stator, permanent-magnet generator". IEE Proceedings-B, Vol:139 (No. 6), pp: 497-506, 1992.

35) Spooner E., Chalmers B.J. "TORUS, A toroidal-stator, permanent-magnet machine for small scale power generation". International Conference on Electrical Machines, pp: 1053-1058, 1990.

36) Tasker J., Collyer T., Wearing A. "Cogging torques". EMD97 Conference Publication No. 444, pp: 205-209, 1997.

37) Thompson K.R. "Design of a novel permanent magnet machine". Final Year Undergraduate Project Thesis. Newcastle University, 1991.

38) Voith Turbo GmbH" ELVO-Drive. The electrical drive for buses: ecological, economic, ergonomic". Company Literature, Voith Turbo GmbH & Co KG, Commercial Vehicle Transmissions, P.O. Box 1930, D-89509, Heidenheim, Germany, 1998.

39) Walker J.H. "The theory of the inductor alternator". Journal of the Institute of Electrical Engineers - Power Engineering, Vol:89 (pt II), pp: 227-241, 1942.

40) Weglinski B. "Soft magnetic PM materials". Selected case studies in powder metallurgy. Book No. 491 (Jenkins I., Wood J.V.), Institute of Metals, pp:113-129, 1991.

41) Weh H. "Transversalfluxmaschine mit passivem Rotor", Patent No. DE 44 30 139 C2, Germany, 1998.

42) Weh H., May H. "Achievable force densities for permanent magnet excited machines in new configurations". Proceedings of the International Conference on Electrical Machines and Drives, pp: 1107-1111, 1986.

43) Weh H., Mosebach H., May H. "Design concepts and force generation in inverter-fed synchronous machines with permanent magnet excitation". IEEE Transactions on Magnetics, Vol:MAG-20 (5), pp: 1756-1761, 1984.

44) Weh H., Hoffmann H., Landrath J., Mosebach H., Poschadel J. "Directly driven permanent magnet excited synchronous generator for variable speed operation". European Community Wind Energy Conference, pp: 566-572, 1988.

45) Weh H., Hoffman H., Landrath J. "New permanent magnet excited synchronous machine with high efficiency at low speeds". Proceedings of the International Conference on Electrical Machines and Drives, pp: 35-40, 1988.

46) Weh H., Mosebach H., Niemann W., Tareilus A. "Field control in synchronous machines with permanent magnet excitation in flux concentration mode". Proceedings of the International Conference on Electrical Machines and Drives, pp: 143-148, 1990.

47) Weh H., May H., Shalaby M. "Highly effective magnetic circuits for permanent magnet excited synchronous machines". Proceedings of the International Conference on Electrical Machines and Drives, pp: 1040-1045, 1990.

48) Zenneck, "High frequency machines for undamped oscillations". Wireless Telegraphy, McGraw-Hill, UK, pp:213-219, 1915.

49) Zhu Z.Q., Ng K., Howe D. "Design and analysis of high speed brushless permanent magnet motors". IEE Electrical Machines and Drives Conference, pp: 381-385, 1997.